SYNTHESES AND STRUCTURES OF RHENIUM(VII) AND MANGANESE(VII) OXIDE FLUORIDES, MANGANESE(V, IV) FLUORIDES, AND THE FIRST OXIDE OF XENON(II)

SYNTHESES AND STRUCTURES OF RHENIUM(VII) AND MANGANESE(VII) OXIDE FLUORIDES, MANGANESE(V, IV) FLUORIDES, AND THE FIRST OXIDE OF XENON(II)

by

Maria V. Ivanova

A Thesis

Submitted to the School of Graduate Studies

in Partial Fulfillment of the Requirements

for the Degree

Doctor of Philosophy

McMaster University

DOCTOR OF PHYLOSOPHY — McMaster University

(Chemistry) — Hamilton, Ontario

TITLE: **SYNTHESES AND STRUCTURES OF RHENIUM(VII) AND MANGANESE(VII) OXIDE FLUORIDES, MANGANESE(V, IV) FLUORIDES, AND THE FIRST OXIDE OF XENON(II)**

AUTHOR: Maria V. Ivanova, B.Sc. (McMaster University)

SUPERVISOR: Professor Gary J. Schrobilgen

NUMBER OF PAGES: xxxvii, 406

ABSTRACT

This Thesis extends the chemistry of group VII transition metal oxide fluorides, namely ReO_3F and MnO_3F. The fundamental chemistry of ReO_3F has been significantly extended with the development of its high-yield and high-purity synthesis. This has been achieved by solvolysis of Re_2O_7 in anhydrous HF (aHF) followed by reaction of the water formed with dissolved F_2 at room temperature. The improved synthesis has allowed the Lewis acid and fluoride-ion donor-acceptor properties of ReO_3F to be further investigated. The Lewis acid-base complex, $(HF)_2ReO_3F{\cdot}HF$, was obtained by dissolution of ReO_3F in aHF at room temperature and was characterized by vibrational spectroscopy with aid of quantum-chemical calculations and single-crystal X-ray diffraction at −173 °C. The HF molecules are F-coordinated to rhenium, representing the only known example of an HF complex with rhenium. The study of the fluoride-ion acceptor properties of ReO_3F resulted in the syntheses and characterization of the $[\{ReO_3(\mu\text{-}F)\}_3(\mu_3\text{-}O)]^{2-}$, $[ReO_3F_3]^{2-}$, and $[ReO_3F_2]^-$ anions. The $[\{ReO_3(\mu\text{-}F)\}_3(\mu_3\text{-}O)]^{2-}$ anion was obtained as the $[N(CH_3)_4]^+$ salt by the reaction of stoichiometric amounts of ReO_3F and $[N(CH_3)_4]F$ in CH_3CN solvent. The anion was structurally characterized in CH_3CN solution by 1D and 2D ^{19}F NMR spectroscopy and in the solid state by Raman spectroscopy and a single-crystal X-ray structure determination of $[N(CH_3)_4]_2[\{ReO_3(\mu\text{-}F)\}_3(\mu_3\text{-}O)]{\cdot}CH_3CN$. The structure of the $[\{ReO_3(\mu\text{-}F)\}_3(\mu_3\text{-}O)]^{2-}$ anion consists of three ReO_3F units linked to each other through dicoordinate bridging fluorine atoms (F_μ) and a central tricoordinate bridging oxygen atom ($O_{\mu 3}$). Calculated vibrational frequencies and Raman intensities of the $[\{MO_3(\mu\text{-}F)\}_3(\mu_3\text{-}O)]^{2-}$ (C_{3v}) and $[\{MO_3(\mu\text{-}F)\}_3(\mu_3\text{-}F)]^-$ (C_{3v})

anions (M = Re, Tc) have been used to assign the Raman spectrum of $[N(CH_3)_4]_2[\{ReO_3(\mu\text{-}F)\}_3(\mu_3\text{-}O)]\cdot CH_3CN$. The *fac*-$[ReO_3F_3]^{2-}$ and $[ReO_3F_2]^-$ anions have been synthesized by the reactions of ReO_3F with CsF and KF in aHF, and by reaction of ReO_3F with NOF. Additionally, the $[ReO_3F_2]^-$ anion has been synthesized by the reaction of ReO_3F with $[NH_4]F$ in aHF. Both anions were characterized by Raman spectroscopy in the solid state and single-crystal X-ray diffraction. The calculated vibrational frequencies of the *fac*-$[ReO_3F_3]^{2-}$ (C_{3v}) and $[(\mu\text{-}F)_4(ReO_3F)_4]^{4-}$ (C_{4v}) anions were used to assign the Raman spectra of *fac*-$[ReO_3F_3]^{2-}$ and $[ReO_3F_2]^-$, respectively. The rhenium atoms in the open-chain, fluorine-bridged $[ReO_3F_2]^-$ anion and the monomeric *fac*-$[ReO_3F_3]^{2-}$ anion are six-coordinate with a facial arrangement of the oxygen ligands. The fluoride-ion donor properties were established by the reactions of ReO_3F with excess AsF_5 and SbF_5/SO_2ClF. Both reactions resulted in the formation of white friable solids, $\mu\text{-}O(ReO_2F)(AsF_5)\cdot 2AsF_5$ and $[ReO_3][Sb_3F_{16}]$. The $[ReO_3][Sb_3F_{16}]$ salt is stable at room temperature and decomposes to $[ReO_2F_2][SbF_5]$, when maintained at 45 ^oC under dynamic vacuum. The $\mu\text{-}O(ReO_2F)(AsF_5)\cdot 2AsF_5$, however, slowly decomposes at 0 ^oC to ReO_3F and AsF_5. Both products were characterized by Raman spectroscopy in the solid state with aid of quantum-chemical calculations. The vibrational analyses revealed that the geometry of $[ReO_3][Sb_3F_{16}]$ is consistent with a trigonal pyramidal arrangement of oxygen atoms around rhenium, whereas in $\mu\text{-}O(ReO_2F)(AsF_5)\cdot 2AsF_5$, ReO_3F interacts with one of the AsF_5 molecules through an O-bridge, which represents the first example of such type of bonding. The reactions of $\mu\text{-}O(ReO_2F)(AsF_5)\cdot 2AsF_5$ and $[ReO_3][Sb_3F_{16}]$

with CH_3CN resulted in the formation of the white salts, $[O_3Re(NCCH_3)_3][PnF_6]$ (Pn = As, Sb), which were characterized by Raman spectroscopy.

The reactivity of ReO_3F has been extended to the synthesis of a new Re(VII) oxide fluoride, $(\mu\text{-}F)_4\{[\mu\text{-}O(ReO_2F)_2](ReO_2F_2)_2\}$, which was synthesized by the reaction of 1:3 molar ratio of ReO_3F and ReO_2F_3. The compound, $(\mu\text{-}F)_4\{[\mu\text{-}O(ReO_2F)_2](ReO_2F_2)_2\}$, a rare example of an O-bridged rhenium oxide fluoride, has been characterized by single-crystal X-ray diffraction and solid-state Raman spectroscopy. The vibrational assignments of $(\mu\text{-}F)_4\{[\mu\text{-}O(ReO_2F)_2](ReO_2F_2)_2\}$ were confirmed by ^{18}O-enrichment and quantum-chemical calculations.

The improved synthesis of ReO_3F has also led to the synthesis and characterization of the novel $[XeOXeOXe]^{2+}$ cation as its $[\mu\text{-}F(ReO_2F_3)_2]^-$ salt by the low-temperature reaction of ReO_3F and XeF_2 in aHF. The $[XeOXeOXe]^{2+}$ cation provides an unprecedented example of a xenon(II) oxide and a noble-gas oxocation as well as a rare example of a noble-gas dication. The crystal structure of $[XeOXeOXe][\mu\text{-}F(ReO_2F_3)_2]_2$ consists of a planar, zigzag-shaped $[XeOXeOXe]^{2+}$ cation (C_{2h} symmetry) that is fluorine bridged through its terminal xenon atoms to two $[\mu\text{-}F(ReO_2F_3)_2]^-$ anions. The Raman spectra of the natural abundance and ^{18}O-enriched $[XeOXeOXe]^{2+}$ salts are consistent with a centrosymmetric (C_{2h}) cation geometry. Quantum-chemical calculations were used to aid in the vibrational assignments of $[Xe^{16/18}OXe^{16/18}OXe][\mu\text{-}F(Re^{16/18}O_2F_3)_2]_2$ and to assess the bonding in $[XeOXeOXe]^{2+}$ by NBO, QTAIM, ELF, and MEPS analyses. Ion pair interactions occur through $Re–F_\mu$---Xe bridges, which are predominantly electrostatic in nature and result from polarization of the F_μ-atom electron densities by the exposed

core charges of the terminal xenon atoms. Each xenon(II) atom is surrounded by a torus of xenon valence electron density comprised of the three valence electron lone pairs. The positive regions of the terminal xenon atoms and associated fluorine bridge bonds correspond to the positive σ-holes and donor interactions that are associated with "halogen bonding".

The reactions of MnO_3F with noble-gas fluorides, KrF_2 and XeF_6, have been studied as the possible synthetic routes to $MnOF_5$ and MnO_2F_3. The reaction of MnO_3F with KrF_2 yielded a red solid, which was isolated as a crystalline solid at room temperature and its crystal structure was assigned to manganese(V) fluoride, MnF_5. The crystal structure of polymeric MnF_5 consists of MnF_6-octahedra which are *trans*-coordinated through fluorine bridges. The geometrical parameters of MnF_5 could not be reliably determined due to unresolved twinning issues. The reaction of MnO_3F with KrF_2 in the presence of $K[HF_2]$ yielded a red-orange solid mixture of $K[MnF_6]$ (soluble in HF) and MnF_3 (insoluble in HF). The HF solution of the solid mixture was characterized by ^{19}F NMR spectroscopy and the resonance observed in the ^{19}F NMR spectrum was preliminary assigned to $[MnF_6]^-$ by comparison with the chemical shift observed in the ^{19}F NMR spectrum of MnO_3F. Additionally, MnO_3F was characterized by $^{19}F–^{55}Mn$ COSY NMR and ^{55}Mn NMR spectroscopies, the latter provided the first $^1J(^{19}F–^{55}Mn)$ coupling constant. The $K[MnF_6]$ salt was also characterized by single-crystal X-ray diffraction. The resulting octahedral geometry is imposed by symmetry, therefore, the anticipated Jahn-Teller distortion, which would result in D_{4h} symmetry for the $[MnF_6]^-$ anion, could not be observed. The reaction of MnO_3F with XeF_6 resulted in the

isolation of $[Xe_2F_{11}]_2[MnF_6]$ and $[XeF_5]_2[MnF_6]$. Both salts were characterized by low-temperature single-crystal X-ray diffraction. The $[Xe_2F_{11}]_2[MnF_6]$ salt was additionally characterized by low-temperature Raman spectroscopy with the aid of quantum-chemical calculations, whereas the assignment of the known Raman spectrum of $[XeF_5]_2[MnF_6]$ has been improved in the present work.

ACKNOWLEDGEMENTS

I sincerely thank Professor Gary J. Schrobilgen as my primary supervisor in learning the day-to day operations of the laboratory, for providing me with interesting and exciting avenues of research, as well as for his insight, guidance, enthusiasm, patience, and confidence in me.

I would like to thank the other members of my supervisory committee, Professors Kalaichelvi Saravanamuttu and David J. Emslie for their support, useful discussions, and interest in my research projects.

A heartfelt thanks to Dr. Hélène P. A. Mercier for her expertise and advice throughout the course of this work concerning vibrational analysis, refinement of the single-crystal X-ray diffraction data solutions, mentoring in quantum-chemical calculations. Also a special thanks for her help in development of my scientific writing skills.

I appreciate Prof. Tian Lu, Beijing Kein Research Center for Natural Sciences, Beijing, P. R. China for taking the time to provide me with his advice and guidance related to AIM and ELF calculations as implemented in Multiwfn 3.3.8.

I would like to thank Dr. Michael J. Hughes and Dr. Tobias Köhner for their initial training in experimental work and setting up quantum-chemical calculations, respectively.

Thanks also to other past and present members of the Schrobilgen research group, namely, Dr. Gregory L. Smith, John R. DeBackere, James T. Goettel, Jamie S. Haner, and Dr. Matic Lozinšek.

For their help in their respective fields, I appreciate help of Dr. Jim Britten (X-ray crystallographic facilities), Dr. Steve Kornic (NMR and spectroscopy facilities), and Michael Palme (Chemistry Glassblowing Shop).

I would like to acknowledge the Natural Science and Engineering Research Council of Canada (NSERC) and the Ontario Ministry of Education and Training – Ontario Graduate Scholarship (OGS), and the McMaster University Department of Chemistry and Chemical Biology for financial support in the form of bursaries and scholarships over the years.

A special thanks to my husband Nikolai Goupinets for his patience, understanding, incredible support, and full confidence in my abilities. Thanks a lot to my mother Liudmila Vorontsova for devoting her personal life to support my goal to become a scientist. Thanks also to my parents-in-law Veniamin and Galina Goupinets, to be there for me, when I needed their help. Finally, I would like to thank my children Sophia L. and Dimitry V. Goupinets for their appreciation of my hard work and for forgiving me the hours I could not spend with them.

PREFACE

The following Chapters have been published in whole by the American Chemical Society (ACS). The NMR chemical shift calculations for $[\{ReO_3(\mu\text{-}F)\}_3(\mu_3\text{-}O)]^{2-}$ and $[\{ReO_3(\mu\text{-}F)\}_3(\mu_3\text{-}F)]^{-}$ were done by Dr. Tobias Köchner.

Chapter 3: Ivanova, M. V.; Köchner, T.; Mercier, H. P. A.; Schrobilgen, G. J. *Inorg. Chem.* **2013**, *52*, 6806–6819.

Chapter 6: Ivanova, M. V.; Mercier, H. P. A.; Schrobilgen, G. J. *J. Am. Chem. Soc.* **2015**, *137*, 13398–13413.

LIST OF ABBREVIATIONS AND SYMBOLS

General

ax	axial
eq	equatorial
FT	Fourier transform
FEP	perfluoriethylene/perfluoropropylene copolymer
IR	infrared
Kel-F	chlorotrifluoroethylene
VSEPR	valence shell electron pair repulsion
N.A.	natural abundance (isotopic)
i.d.	inner diameter
o.d.	outer diameter
in.	inch

Raman Spectroscopy

$\Delta\nu$	frequency
cm^{-1}	wavenumber
ν	stretching mode
δ	in-plane bend
ρ_w	wagging mode
ρ_r	rocking mode

ρ_t	twisting mode
o.o.p.	out-of-plane
i.p.	in-plane

Nuclear Magnetic Resonance Spectroscopy

NMR	nuclear magnetic resonance
ppm	parts per milion
δ	chemical shift
I	nuclear spin quantum number
J	scalar coupling constant, in Hz
Hz	Hertz, or cycles per second
$\Delta\nu_{1/2}$	line width at half height

X-ray Crystallography

α, b, c, α, β, γ	unit cell parameters
V	unit cell volume
λ	wavelength
μ	absorption coefficient
ρ	density
Z	molecules per unit cell
mol. wt.	molecular weight
F	structure factor

R_1	conventional agreement index
wR_2	weighted agreement index

Computational

DFT	density functional theory
NBO	natural bond orbital
AIM	Atoms in Molecules
ELF	electron localization function
MEPS	molecular electrostatic potential surface

TABLE OF CONTENTS

page

LIST OF TABLES

LIST OF FIGURES

LIST OF SCHEMES

CHAPTER 1

INTRODUCTION

1.1. Technetium(VII) and Rhenium(VII) Oxide Fluorides

The highest oxidation state among the group VII elements, +7, is stabilized by several oxides and oxide fluorides in this group: M_2O_7 (M = Mn, Tc, Re), MOF_5, MO_2F_3, MO_3F (M = Tc, Re), and MnO_3F and their corresponding oxide fluoride cations and anions. The relative ease with which the +7 oxidation state is attained can be associated with the high oxophilicity of group VII transition metals. The stabilization of the highest oxidation states of group(VII) results from extensive pπ-dπ back bonding between filled p orbitals of the oxygen ligands and empty d orbitals of the metal atom. The +7 oxidation state is also stabilized in ReF_7, representing only the second known heptafluoride in the periodic table; the other being IF_7. In contrast to Re(VII) fluorides, ReF_7 and $[ReF_6]^+$, MnF_7 and TcF_7 are presently unkown.

1.1.1 Syntheses and Characterization of Technetium and Rhenium Oxide Pentafluorides

Technetium oxide pentafluoride was synthesized as a volatile orange solid (m.p. 57−58 ^oC) by Schrobilgen and co-workers[1,2] by the reaction of TcO_2F_3 with excess KrF_2 in aHF (eq 1.1). It was characterized in the solid state by Raman and single-crystal X-ray

$$TcO_2F_3 + KrF_2 \longrightarrow TcOF_5 + ½\,O_2 + Kr \qquad (1.1)$$

diffraction, in solution by ^{19}F and ^{99}Tc NMR and Raman spectroscopies, and in the gas-phase by infrared spectroscopy. The low-temperature ^{19}F NMR spectrum showed a well-

resolved doublet and a quintet corresponding to the equatorial (364.1 ppm) and axial (62.0 ppm) fluorine atoms, respectively. The ^{99}Tc NMR spectrum recorded at 35 ^{o}C in aHF and at 30 ^{o}C in SO_2ClF showed resonances at 394.5 and 433.8 ppm relative to $CFCl_3$, which are broadened by the partially quadrupole collapsed spin-spin coupling with the ^{99}Tc (100% abundance) nucleus. Technetium oxide pentafluoride has a pseudo-octahedral geometry; however, the crystal structure suffers from a twofold disorder with respect to a pseudo-mirror plane that contains one of the F_e−Tc−F_e axes (F_e, equatorial fluorine atom).[2] The location of two undistorted Tc−F_e bond lengths (1.81(1) Å) allowed the calculation of the Tc−F_a (F_a-axial fluorine atom) and Tc−O bond lengths (1.90(1) Å) and (1.67(1) Å).

The synthesis of $ReOF_5$ (m.p. 34.5 ^{o}C, b.p. 55 ^{o}C) was reported for the first time by Aynsley, Peacock, and Robinson,[3] who synthesized $ReOF_5$ in admixture with ReO_2F_3, by the fluorination of ReO_2 or K[ReO_4] at 100 ^{o}C (eq 1.2 and 1.3). Rhenium oxide

$$2ReO_2 + 4F_2 \xrightarrow{100\ ^{o}C} ReOF_5 + ReO_2F_3 + \tfrac{1}{2}O_2 \qquad (1.2)$$

$$2K[ReO_4] + 5F_2 \xrightarrow{100\ ^{o}C} ReOF_5 + ReO_2F_3 + 2KF + \tfrac{5}{2}O_2 \qquad (1.3)$$

pentafluoride (a minor cream-colored product) was separated from ReO_2F_3 (major product) by sublimation and analyzed for rhenium and fluorine. The fluorination of $ReOF_4$, ReO_2, and ReO_3 at high temperatures also resulted in the formation of $ReOF_5$ (eqs 1.4, 1.5, and 1.6, respectively).[4]

$$ReOF_4 + \tfrac{1}{2}F_2 \xrightarrow{300\ ^{o}C} ReOF_5 \qquad (1.4)$$

$$ReO_2 + 3F_2 \xrightarrow[25\ h]{250\ ^{o}C} ReOF_5 + \tfrac{1}{2}O_2 + \tfrac{1}{2}F_2 \qquad (1.5)$$

$$2ReO_3 + 4F_2 \xrightarrow[17\ h]{200\ ^oC} ReOF_5 + ReO_2F_3 + {}^3/_2\, O_2 \quad (1.6)$$

Recently, $ReOF_5$ was synthesized by fluorination of Re_2O_7 with ClF_3 (eq 1.7).[5] The reaction begins at −100 °C and proceeds with gas evolution and formation of ReO_2F_3 as

$$6Re_2O_7 + 20ClF_3 \xrightarrow[24\ h]{HF} 12ReOF_5 + 15O_2 + 10Cl_2 \quad (1.7)$$

the reaction intermediate which is converted to $ReOF_5$ at room temperature.

Rhenium oxide pentafluoride has also been characterized in low-temperature matrices by UV-vis spectroscopy,[6] infrared[6,7] and Raman spectroscopies,[7] solid state infrared spectroscopy,[8] and mass spectrometry.[4] The vibrational studies established that $ReOF_5$ has C_{4v} symmetry. Bartlett et al.[9] confirmed the C_{4v} geometry of $ReOF_5$ based on a ^{19}F NMR study and concluded that the axial Re−F bond is more polar, and thus longer than the equatorial Re−F bond lengths based on the relative chemical shifts of the axial (quintet, −362 ppm) and the equatorial (doublet, −160 ppm) fluorine ligands. The structural parameters of $ReOF_5$ were determined from a gas-phase electron diffraction study,[10] but the axial and equatorial Re−F bond lengths were refined as a single parameter and consequently could not be differentiated. A normal coordinate analysis[11] of the $ReOF_5$ vibrational frequencies indicated that the axial Re−F bond is shorter than the equatorial Re−F bonds, which contradicts the above ^{19}F NMR findings. A recent single-crystal X-ray structure determination of $ReOF_5$[12] unambiguously established that $ReOF_5$ (C_{4v}) has a monomeric structure with the axial Re−F bond being longer than the equatorial Re−F bonds.

1.1.2 Fluoride Ion Donor-Acceptor Properties of MOF_5 (M = Tc, Re)

The fluoride ion-donor properties of $ReOF_5$ and $TcOF_5$ were studied by reaction of MOF_5 (M = Re, Tc) with AsF_5 and SbF_5, and resulted in the formation of the $[ReOF_4][AsF_6]$,[13] $[\mu\text{-}F(TcOF_4)_2][Sb_2F_{11}]$,[2] $[\mu\text{-}F(ReOF_4)_2][Sb_2F_{11}]$,[13] and $[\mu\text{-}F(TcOF_4)_2][AsF_6]$[2] salts (eqs 1.8 -1.10). The $[ReOF_4][AsF_6]$ salt was characterized by

$$ReOF_5 + \text{xs } AsF_5 \longrightarrow [ReOF_4][AsF_6] \quad (1.8)$$

$$2MOF_5 + 2SbF_5 \longrightarrow [\mu\text{-}F(MOF_4)_2][Sb_2F_{11}] \text{ (M = Re, Tc)} \quad (1.9)$$

$$2TcOF_5 + AsF_5 \longrightarrow [\mu\text{-}F(TcOF_4)_2][AsF_6] \quad (1.10)$$

mass spectrometry and Raman spectroscopy.[13] The dinuclear $[\mu\text{-}F(MOF_4)_2]^+$ cations were characterized by Raman spectroscopy and single-crystal X-ray diffraction and were shown to consist of two fluorine-bridged MOF_4 units with the oxo ligands located trans to the bridging fluorine atom.[2,13] The $[\mu\text{-}F(TcOF_4)_2][Sb_2F_{11}]$ and $[\mu\text{-}F(TcOF_4)_2][AsF_6]$ salts were also characterized by ^{19}F and ^{99}Tc NMR spectroscopy.[2]

The synthesis of the $[TcOF_6]^-$ anion has been attempted by reaction of $Cs[TcO_2F_4]$ with KrF_2 in aHF, $TcOF_5$ with CsF in CH_3CN, and by fusion of $TcOF_5$ with dry CsF at 60 ^oC.[14] The reaction in aHF revealed that $TcOF_5$ is a weaker fluoro-acid than aHF and, as a result, only $Cs[HF_2]$ was formed. The reaction of $TcOF_5$ with CsF in CH_3CN and the fusion reaction resulted in reduction of $TcOF_5$ by the solvent or its decomposition, respectively. In contrast, $ReOF_5$ reacts with NOF,[15] NO_2F[15] (eq 1.11) and CsF[16] (eq 1.12)

$$ReOF_5 + NOF/NO_2F \longrightarrow [NO/NO_2][ReOF_6] \quad (1.11)$$

$$ReOF_5 + CsF \xrightarrow{60\ ^oC} Cs[ReOF_6] \quad (1.12)$$

to form $[ReOF_6]^-$. The $[ReOF_6]^-$ anion (C_{5v}) was characterized by Raman[15,16] and ^{19}F NMR spectroscopies[15,16] and by single-crystal X-ray diffraction.[16] The solid state geometry of the $[ReOF_6]^-$ anion is a pentagonal bipyramid (C_{5v}) with the oxygen atom in an apical position.

1.1.3. Syntheses and Characterization of Technetium and Rhenium Dioxotrifluoride

The high-yield synthesis of pure yellow TcO_2F_3 was achieved by Schrobilgen and Mercier,[17] who reacted Tc_2O_7 with XeF_6 in aHF at room temperature (eq 1.13-1.18).

$$Tc_2O_7 + 4HF \xrightarrow{HF} 2TcO_3F + [H_3O][HF_2] \quad (1.13)$$

$$[H_3O][HF_2] + XeF_6 \xrightarrow{HF} XeOF_4 + 4HF \quad (1.14)$$

$$TcO_3F + XeF_6 \xrightarrow{HF} TcO_2F_3 + XeOF_4 \quad (1.15)$$

$$[H_3O][HF_2] + XeOF_4 \xrightarrow{HF} XeO_2F_2 + 4HF \quad (1.16)$$

$$TcO_3F + XeOF_4 \xrightarrow{HF} TcO_2F_3 + XeO_2F_2 \quad (1.17)$$

$$XeO_2F_2 \longrightarrow XeF_2 + O_2 \quad (1.18)$$

The solvolysis of Tc_2O_7 in aHF initially produced TcO_3F along with water as a by-product (eq 1.13), which subsequently reacted with XeF_6 to form $XeOF_4$ (eq 1.14). Both XeF_6 and $XeOF_4$ further reacted with TcO_3F to yield TcO_2F_3 (eqs 1.15 and 1.17). Xenon dioxide difluoride, formed in eqs 1.16 and 1.17, decomposed to XeF_2 and O_2 which were removed under dynamic vacuum.

Technetium dioxide trifluoride was characterized by Raman spectroscopy,[17] ^{19}F and ^{99}Tc NMR spectroscopy,[18] and single-crystal X-ray diffraction.[17] The X-ray crystal

structure consists of open chains of *cis*-fluorine bridged TcO_2F_4 units, where Tc is in a pseudo-octahedral environment and the bridging fluorine atoms are trans to the oxygen atoms. However, in SO_2ClF solution, TcO_2F_3 forms cyclic fluorine bridged trimers (^{19}F NMR: F_t, 76.2 ppm; F_b, −148.6 ppm; ^{99}Tc NMR: 211.0 ppm).

High-purity ReO_2F_3 was synthesized in high yield by the room-temperature fluorination of Re_2O_7 with XeF_6 in aHF which is analogous to that used for the preparation of TcO_2F_3 (eq 1.13-1.18).[19] The synthesis of ReO_2F_3 by reaction of ReO_3Cl with XeF_2 (eq 1.19) avoids handling XeF_6, whose hydrolysis product, XeO_3, is explosive.

$$2ReO_3Cl + 3XeF_2 \xrightarrow{HF} ReO_2F_3 + 2Xe + O_2 + Cl_2 \qquad (1.19)$$

Rhenium dioxide trifluoride also forms as a product from the fluorination of ReO_2 (eq 1.2),[3] $K[ReO_4]$ (eq 1.3),[3] ReO_3 (eq 1.6),[4] and Re_2O_7 (eq 1.20).[6]

$$Re_2O_7 + 4F_2 \xrightarrow[16\ h]{200\ ^oC} 2ReO_2F_3 + {}^3/_2\, O_2 + F_2 \qquad (1.20)$$

Rhenium dioxide trifluoride was characterized in the gas-phase by UV-vis,[6] infrared,[6,20] and Raman[20] spectroscopies, mass spectrometry,[4] by ^{19}F NMR[18] spectroscopy in SO_2ClF solution, and in the solid state by Raman spectroscopy,[19,21] and single-crystal X-ray diffraction[9,21]. It has been shown by ^{19}F NMR spectroscopy that ReO_2F_3 has several modifications, which include open-chain oligomeric, cyclic trimeric and tetrameric compounds.[18] Additionally, small amounts of the pentanuclear oligomer were also observed.[18] Four structural modifications, two fluorine-bridged open chain-type[19,21] and two fluorine-bridged cyclic (trimers and tetramers),[21] have also been crystallographically characterized. In all of the above cases, the rhenium atoms occur in pseudo-octahedral

environments and the fluorine-bridge atoms are located *trans* to the doubly-bonded oxygen atoms.

1.1.4 Fluoride Ion Donor-Acceptor and Lewis Acid Properties of TcO_2F_3 and ReO_2F_3

The fluoride ion-donor properties of ReO_2F_3 and TcO_2F_3 have been studied by the room-temperature reactions of MO_2F_3 (M = Tc, Re) with PnF_5 (Pn = As, Sb) and XeO_2F_2 in aHF (eq 1.21) and resulted in the isolation and characterization of the $[MO_2F_2][PnF_6]$

$$MO_2F_3 + PnF_5 \xrightarrow{HF} [MO_2F_2][PnF_6] \quad (1.21)$$

salts and $TcO_2F_3 \cdot XeO_2F_2$.[22] Additionally, the $[TcO_2F_2][PnF_6] \cdot 2HF$ (Pn = As, Sb) salts have been obtained as products resulting from the solvolysis reactions of TcO_3F with PnF_5/aHF (eq 1.22).[23] The $[MO_2F_2][PnF_6]$[22,23] and $TcO_2F_3 \cdot XeO_2F_2$[22] salts were

$$TcO_3F + PnF_5 \xrightarrow{HF} [MO_2F_2][PnF_6] + [H_3O][PnF_6] \quad (1.22)$$

characterized by Raman spectroscopy and single-crystal X-ray diffraction. The structures of the $[MO_2F_2][SbF_6]$ salts consist of infinite chains of alternating MO_2F_2 and SbF_6 units, which are bridged through fluorine atoms. As observed in the crystal structures of MO_2F_3 (M = Tc, Re),[17,19,21,23] the metal centers are in pseudo-octahedral environments with the oxygen atoms bonded cis to one another and the fluorine bridge atoms bonded trans to the oxygen atoms. The structure of $TcO_2F_3 \cdot XeO_2F_2$ consists of infinite chains of TcO_2F_3 that run parallel to the *c*-axis and bridge to the XeO_2F_2 chains through long Tc−F···Xe contacts (2.848(8) Å). Additionally, the XeO_2F_2 chains interact through long Xe···F···Xe bridge contacts. This arrangement is in marked contrast with that observed in the crystal

structure of XeO_2F_2, where the XeO_2F_2 molecules interact through long Xe···O···Xe bridges.[24]

The aHF solutions of $[MO_2F_2][PnF_6]$ were studied by ^{19}F and ^{99}Tc NMR spectroscopy and SO_2ClF and CH_3CN solutions of $[ReO_2F_2][SbF_6]$ were studied by ^{19}F and ^{1}H, ^{13}C, and ^{19}F NMR spectroscopy, respectively. The peaks in the ^{19}F (109.2 ppm at −84 ^{o}C) and ^{99}Tc (140.3 ppm at −84 ^{o}C) spectra of $[TcO_2F_2][PnF_6]$[22] are more deshielded than those in the ^{19}F NMR spectra of $TcO_2F_3{\cdot}NCCH_3$ (25.3 and 37.3 ppm in CH_3CN at 30 ^{o}C) and $[TcO_2F_4]^-$ (sharp triplet at −14.1 ppm and partially collapsed triplet at −18.7 ppm assigned to the fluorine atoms located *trans* and *cis* to oxygen ligands, respectively; CH_3CN at 30 ^{o}C; 23 ^{o}C in HF)[25] and ^{99}Tc NMR spectrum of TcO_3F (43.7 ppm in aHF at 23 ^{o}C)[26] which is consistent with the formation of the $[TcO_2F_2]^+$ cation. Dissolution of $[ReO_2F_2][SbF_6]$ in SO_2ClF resulted in dissociation and self-association of the salt yielding the fluorine-bridged dinuclear $[\mu\text{-}F(ReO_2F_2)_2]^+$ cation, whereas in CH_3CN, the $[ReO_2F_2][SbF_6]$ salt formed the $[ReO_2F_2{\cdot}CH_3CN]^+$ adduct-cation.[22]

The study of the fluoride ion-acceptor properties of MO_2F_3 (M = Re, Tc) resulted in the isolation and characterization of the $[MO_2F_4]^-$ (M = Re, Tc), $[\mu\text{-}F(ReO_2F_4)_2]^-$, and $[(ReO_2F_2)(\mu\text{-}F)_2(ReO_2F_3)_2]^-$ anions. Salts of the $[ReO_2F_4]^-$ anion were synthesized by fusion of ReO_2F_3 with alkali metal fluorides (Na, K, Rb, Cs) at 120−150 ^{o}C[27] and by reactions of the alkali and alkaline metal perrhenates, $A[ReO_4]$ and $A[ReO_4]_2$ (A = Na, K, Rb, Cs, Ca, Sr, Ba), and $Ag[ReO_4]$ with BrF_3.[28] The formation of the above salts was confirmed by chemical[28] and elemental analyses[27,28] and infrared spectroscopy.[27] The $[MO_2F_4]^-$ anion were the products of the reactions of MO_2F_3 (M = Re, Tc) with alkali

metal fluorides (Re: Li, Na, Cs;[19] Tc: Li, Cs[25]) and $[(CH_3)_4N]F$[19,25] (eq 1.23) and the reaction of ReO_2F_3 with XeF_6 (eq 1.24) in aHF.[19] Both, $[ReO_2F_4]^-$ [19] and $[TcO_2F_4]^-$ [25]

$$ReO_2F_3 + A/[(CH_3)_4N]F \xrightarrow{HF} A/[(CH_3)_4N][ReO_2F_4] \quad (1.23)$$

$$XeF_6 + ReO_2F_3 \xrightarrow{HF} [XeF_5][ReO_2F_4] \quad (1.24)$$

were characterized by ^{19}F NMR and Raman spectroscopies and single-crystal X-ray diffraction.[19,25] The $[TcO_2F_4]^-$ anion was also characterized by ^{99}Tc and ^{17}O NMR spectroscopy.[25] The structures of the $[MO_2F_4]^-$ anions consist of *cis*-dioxo arrangements of M−O bonds. The equatorial M−F bonds are located trans to oxygen atoms and are longer than the axial M−F bonds due to the *trans*-influence of the oxygen atoms.[17]

The dinuclear and trinuclear anions, $[\mu\text{-}F(ReO_2F_4)_2]^-$ and $[(ReO_2F_2)(\mu\text{-}F)_2(ReO_2F_3)_2]^-$,[19] were synthesized by increasing the ReO_2F_3:F^- molar ratios to two and three (eq 1.25 and 1.26), respectively. Both anions were characterized by Raman

$$2ReO_2F_3 + KF/[(CH_3)_4N]F \xrightarrow{HF} K/[(CH_3)_4N][\mu\text{-}F(ReO_2F_4)_2] \quad (1.25)$$

$$3ReO_2F_3 + CsF \xrightarrow{HF} Cs[(ReO_2F_2)(\mu\text{-}F)_2(ReO_2F_3)_2] \quad (1.26)$$

spectroscopy and single-crystal X-ray diffraction. In addition, the $[\mu\text{-}F(ReO_2F_4)_2]^-$ anion was characterized in solution by ^{19}F NMR spectroscopy. The structures of the $[\mu\text{-}F(ReO_2F_4)_2]^-$ and $[(ReO_2F_2)(\mu\text{-}F)_2(ReO_2F_3)_2]^-$ anions are open chains, where the ReO_2F_3 units are connected through fluorine bridges located *trans* to doubly bonded oxygen ligands. As observed in the $[ReO_2F_4]^-$ anion,[19] the oxygen ligands are located cis to each other and the Re−F bonds are elongated due to the *trans*-influence of the oxygen atoms.[17]

The Lewis acid properties of ReO_2F_3 and TcO_2F_3 were demonstrated by the formation of the $ReO_2F_3{\cdot}NCCH_3$[19] and $TcO_2F_3{\cdot}NCCH_3$[25] adducts, which were

characterized by Raman and ^{19}F NMR spectroscopies. The $TcO_2F_3 \cdot NCCH_3$ adduct was also characterized by ^{99}Tc, ^{1}H, and ^{13}C NMR spectroscopy.[25]

1.1.5. Syntheses and Characterizations of TcO_3F and ReO_3F

Pertechnyl fluoride, TcO_3F (m.p. 18.3 ^{o}C; b.p. 100 ^{o}C), was first synthesized as a yellow compound in 1962 by Selig and Malm[29] by fluorination of technetium dioxide with fluorine gas in a nickel tube at 150 ^{o}C (eq 1.27). Selig and co- workers[30] also

$$TcO_2 + F_2 \xrightarrow{150\ ^{o}C} TcO_3F \qquad (1.27)$$

synthesized TcO_3F by solvolysis of $[NH_4][TcO_4]$ in aHF (eq. 1.28) and studied the

$$[NH_4][TcO_4] + aHF \longrightarrow TcO_3F + [NH_4]F + H_2O \qquad (1.28)$$

resulting pale yellow solution by Raman, infrared, and ^{19}F NMR spectroscopy. Mercier and Schrobilgen[17] obtained TcO_3F by solvolysis of Tc_2O_7 in aHF. The most recent synthesis of TcO_3F was reported by Seppelt and co-wokers,[23] who reacted $K[TcO_4]$ with aHF in the presence of BiF_5. Technetium trioxide fluoride was isolated from stable $K[BiF_6]$ and $[H_3O][BiF_6]$ salts at −78 ^{o}C (eq 1.29) and characterized by Raman

$$K[TcO_4] + 3HF + 2BiF_5 \longrightarrow TcO_3F + K[BiF_6] + [H_3O][BiF_6] \qquad (1.29)$$

spectroscopy and single-crystal X-ray diffraction. Technetium trioxide fluoride crystallizes as a dimer with bridging fluorine atoms trans to oxygen atoms. The Tc atom is in a pseudo-octahedral environment formed by five primary ligand bonds and an additional long contact (2.282(1) Å) with an oxygen atom of a neighboring dimer. When BiF_5 was used in stoichiometries ranging between 1:2 and 1:3, monomeric TcO_3F co-crystallized with the TcO_2F_3 chains, where TcO_3F molecules interact with the TcO_2F_3

chains through two long Tc---F contacts to complete the octahedral coordination sphere of the technetium atoms.

Although high-yield syntheses of $ReOF_5$ [5] and ReO_2F_3 [19] are well established and several other low-yield synthetic routes are found in the literature, a reliable high-yield, high-purity synthesis of ReO_3F was unknown. The first synthesis of ReO_3F was reported by Wiechert,[31] who prepared ReO_3F by reacting $K[ReO_4]$ with aHF according to eq 1.30.

$$K[ReO_4] + 2HF \xrightarrow{HF} KF \text{ (and/or } KHF_2) + ReO_3F + H_2O \quad (1.30)$$

However, isolation of the product was unsuccessful because ReO_3F hydrolyzed to form $H[ReO_4]$ and HF in the reverse reaction (eq 1.31) when HF was removed under vacuum.

$$ReO_3F + H_2O \xrightarrow{\text{HF removed}} H[ReO_4] + HF \quad (1.31)$$

Engelbrecht and Grosse[32] synthesized yellow ReO_3F (m.p. 147 ^oC; b.p. 164 ^oC) by reaction of ReO_3Cl with aHF (eq 1.32) and isolated it by vacuum sublimation. Perrhenyl

$$ReO_3Cl + aHF \xrightarrow{HF} ReO_3F + HCl \quad (1.32)$$

fluoride has also been obtained by refluxing finely divided $K[ReO_4]$ in IF_5 in the presence of trace amounts of aHF and at 100 ^oC (eq 1.33).[33] All by-products, IF_5 and IO_2F (eq 1.34), were removed under dynamic vacuum. Selig and El- Gad,[34] in their investigations

$$K[ReO_4] + IF_5 \xrightarrow{\text{HF, 100 }^oC} KF + ReO_3F + IOF_3 \quad (1.33)$$

$$2IOF_3 \xrightarrow{HF} IF_5 + IO_2F \quad (1.34)$$

of reaction 1.30, prepared solutions of $K[ReO_4]$ and Re_2O_7 in aHF (eqs 1.30, 1.35) and

$$Re_2O_7 + 2HF \xrightarrow{HF} 2ReO_3F + H_2O \quad (1.35)$$

studied these solutions directly by means of Raman and NMR spectroscopy. The assigned Raman frequencies of ReO_3F in HF solution suggested C_{3v} as the point symmetry for the

assumed ReO_3F monomer.[34] Rhenium trioxide fluoride is also a product of the reactions of Re_2O_7 with ReF_7 (3.6:1 molar ratio) (eq 1.36)[4] and Re_2O_7 with $ReOF_5$ (eq 1.37)[27] at

$$Re_2O_7 + ReF_7 \xrightarrow{150\ ^oC,\ 20\ h} ReO_3F + 2ReO_2F_3 \quad (1.36)$$

$$ReOF_5 + 2Re_2O_7 \xrightarrow{150 - 200\ ^oC} 5ReO_3F \quad (1.37)$$

high temperatures. Fluorination of a 1:1 mixture of Re_2O_7 and KBr with an excess of BrF_3

$$Re_2O_7 + KBr + 2BrF_3 \xrightarrow{BrF_3} 2ReO_3F + ½O_2 + Br_2 + KBrF_4 \quad (1.38)$$

(eq 1.38),[20] $K[ReO_4]$ with XeF_2 in CF_3CH_2Cl (eq 1.39),[35] and ReO_3 with F_2 (eq 1.40)[21] have also resulted in the formation of ReO_3F.

$$K[ReO_4] + XeF_2 \xrightarrow{CF_3CH_2Cl:ICl} ReO_3F + ½O_2 + KF + Xe \quad (1.39)$$

$$ReO_3 + F_2 \xrightarrow{<150\ ^oC} ReO_3F,\ ReO_2F_3,\ ReOF_5 \quad (1.40)$$

Seppelt[21] reviewed the known syntheses of ReO_3F and reinvestigated the known reactions (eqs 1.30, 1.32, 1.33, 1.36, and 1.40), concluding that all of these synthetic approaches do not yield ReO_3F in high purity.

Rhenium trioxide fluoride was characterized in the gas phase UV-vis,[6] infrared,[6,20] and Raman spectroscopy,[20] and mass spectrometry,[4,21] in solution by Raman[34] and ^{19}F NMR spectroscopy,[21,34] and in the solid state by Raman spectroscopy,[21] and single-crystal X-ray diffraction.[21] The crystal structure of ReO_3F consists of infinite polymer chains, where the ReO_3F units are bridged to each other through an oxygen and a fluorine atom maintaining the pseudo-octahedral environments around the Re atoms (Figure 1.1). The crystal structure was solved as a superposition of three sets of X-ray data with several light atoms being non-positively defined and therefore the refinement and structure may be problematic.

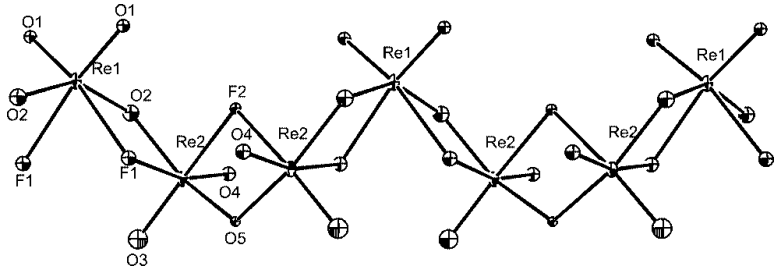

Figure 1.1. The X-ray crystal structure of ReO_3F. Reproduced with permission from Ref 21.

1.1.6. Fluoride Ion-Acceptor Properties of MO_3F (M = Tc, Re), Lewis Acid Properties of ReO_3F and Fluoride Ion-Donor Properties of TcO_3F

Although TcO_3F is the first oxide fluoride of technetium to have been synthesized, its chemistry is the least studied among the technetium(VII) oxide fluorides. While exploring the possibility of a simple synthesis for TcO_3F, Seppelt[23] investigated the fluoride-ion acceptor properties of TcO_3F by reacting $K/[NH_4][TcO_4]$ with aHF. Large yellow cubic-shaped crystals were grown by slow cooling of the solution to −30 ^oC. The crystal structure of the product corresponded to $K/[NH_4][\{TcO_3(\mu\text{-}F)\}_3(\mu_3\text{-}F)]\cdot 1.5TcO_3F$, which crystallized as a "cluster", where one $K/[NH_4]^+$ cation interacts with three fluorine atoms of three TcO_3F molecules and two fluorine atoms of two trimeric $[\{TcO_3(\mu\text{-}F)\}_3(\mu_3\text{-}F)]^-$ anions. The trimeric $[\{TcO_3(\mu\text{-}F)\}_3(\mu_3\text{-}F)]^-$ anion (Figure 1.2) consists of three TcO_3F-moieties linked to each other through dicoordinate bridging fluorine atoms and a central tricoordinate bridging fluorine atom, so that the coordination environment of each Tc is pseudo-octahedral. A striking feature of the "cluster" is the cis positions of

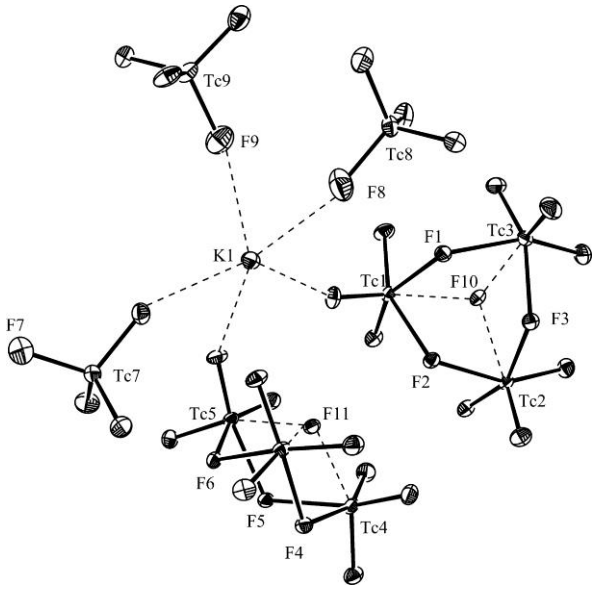

Figure 1.2. Asymmetric unit of $K[TcO_3(\mu\text{-}F)\}_3(\mu_3\text{-}F)]\cdot 1.5\ TcO_3F$. Reproduced with permission from ref. 23.

the two bulky $[\{TcO_3(\mu\text{-}F)\}_3(\mu_3\text{-}F)]^-$ anions which provide a significant amount of space to accommodate three TcO_3F molecules.

Preliminary evidence for the fluoride ion-acceptor properties of ReO_3F has been reported. Kuhlman and Sawodny[36] synthesized and isolated the $[ReO_3F_3]^{2-}$ anion as a colorless $K_2[ReO_3F_3]$ salt (eq 1.41) and characterized it at room temperature by Raman

$$K[ReO_4] + KF + IF_5 \xrightarrow{IF_5} K_2[ReO_3F_3] + IOF_3 \qquad (1.41)$$

and infrared spectroscopies. The $[ReO_3F_3]^{2-}$ anion has also been synthesized by the fusion of alkali metal fluorides with ReO_3F at elevated temperatures to give yellow $A_2[ReO_3F_3]$ salts (eq 1.42)[27] and by fluoride ion displacement of DMF from the $ReO_3F(DMF)_2$ adduct

$$ReO_3F + 2AF \xrightarrow{100\text{-}160\ ^oC} A_2[ReO_3F_3] \quad (A = K, Rb, Cs) \qquad (1.42)$$

(eq 1.43) by reaction with $[(CH_3)_4N]F$ in C_2H_5OH to form yellow-grey $[(CH_3)_4N]_2[ReO_3F_3]$ (1.44).[37] The products of both reactions were characterized by

$$Re_2O_7 + 2HF + 4DMF \longrightarrow 2ReO_3F(DMF)_2 + H_2O \quad (1.43)$$

$$ReO_3F(DMF)_2 + 2[(CH_3)_4N]F \longrightarrow [(CH_3)_4N]_2[ReO_3F_3] + 2DMF \quad (1.44)$$

infrared spectroscopy.

A meridional isomer (C_{2v}) was proposed for $[ReO_3F_3]^{2-}$,[27,36,37] based on the number of Re–O stretching bands observed in the infrared and Raman spectra. This assignment is, however, in marked contrast with the observed facial (C_{3v}) geometries of the $[ReO_3Cl_3]^{2-}$ [38] and *fac*-$[OsO_3F_3]^-$ [39] anions, which were unambiguously confirmed in the solid state by single-crystal X-ray diffraction. Additionally, the geometry of the *fac*-$[OsO_3F_3]^-$ anion has been established in solution by ^{19}F NMR spectroscopy.

Attempts to synthesize the $[ReO_3F_2]^-$ anion by reaction of ReO_3F with various alkali metal fluorides in 1:1 molar ratios and heating the mixtures to the melting point of ReO_3F were unsuccessful due to the thermal instabilities of the products at the synthesis temperature.[27] Although the synthesis of the $[ReO_3F_3]^{2-}$ anion was reported, a salt containing the $[ReO_3F_2]^-$ anion remained unknown.

The Lewis acid properties of ReO_3F have been studied and resulted in the isolation and characterization of several rhenium trioxide fluoride adducts: $ReO_3F{\cdot}2CH_3CN$,[19] $ReO_3F{\cdot}2(CH_2CH_3)_2O$,[21] $ReO_3F{\cdot}2(CH_3)_2O$,[21] and $ReO_3F{\cdot}2(CH_2)_4O$.[21] The adducts, $ReO_3F{\cdot}2CH_3CN$[19] and $ReO_3F{\cdot}2(CH_2CH_3)_2O$,[21] have been shown by single-crystal X-ray crystallography to possess facial arrangements of oxygen atoms and *trans*-oxo coordination of the Lewis bases to the rhenium atom.

Among the series of Tc(VII) oxide fluorides, TcO_3F has been shown to act as a fluoride ion-donor. Schrobilgen and co-workers[26] reacted TcO_3F with AsF_5 in aHF solution and studied this solution by ^{99}Tc and ^{17}O NMR spectroscopy. They concluded that the $[TcO_3]^+$ cation (D_{3h}) formed based on high-frequency shifts of the ^{99}Tc and ^{17}O resonances (^{99}Tc, 161 ppm; ^{17}O, 1214 ppm) relative to those of TcO_3F (^{99}Tc, 44 ppm; ^{17}O, 1048 ppm). A subsequent study of this reaction revealed that TcO_3F undergoes solvolysis in PnF_5/aHF (Pn = As, Sb) media to form $[TcO_2F_2][PnF_6]$ salts (eq 1.22).[23]

Strongly bonded $[ReO_3]^+$ and $[TcO_3]^+$ moieties are known and were characterized in $(\eta_5\text{-}C_5(CH_3)_5)ReO_3$,[40] $[(C_6H_{15}N_3)ReO_3]^+$ (Figure 1.3),[41] $[(C_6H_{12}S_3)ReO_3]^+$,[42] and $[TcO_3][SO_3F]$,[43] respectively. In all of the above salts, $[MO_3]^+$ (M = Tc, Re) is metal-bonded to the ligands and displays a trigonal pyramidal arrangement of oxygen atoms.

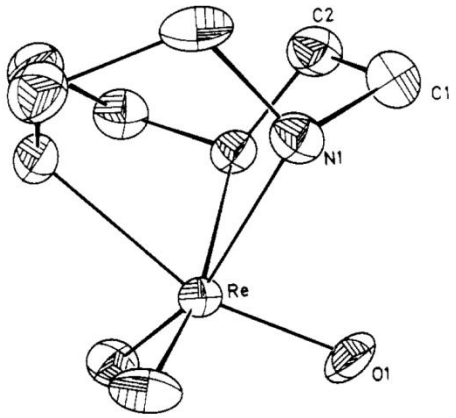

Figure 1.3. View of the $[(C_6H_{15}N_3)ReO_3]^+$ cation. Reproduced with permission from ref. 41a.

1.1.7 The -$OTeF_5$ Derivatives of ReO_2F_3, $ReOF_5$, and ReO_3F

The chemistries of ReO_2F_3, $ReOF_5$, and ReO_3F have been extended by use of the pentafluoroorthotellurate ligand, -$OTeF_5$, which resembles fluorine in its ability to stabilize the high oxidation states of the elements (the electronegativities of F and the -$OTeF_5$ group are estimated at 3.98 [44] and 3.88,[45] respectively, on the Pauling scale).

The -$OTeF_5$ derivative of ReO_2F_3 has been synthesized by reaction of ReF_7 with $B(OTeF_5)_3$ in $CFCl_3$ (eq 1.45).[46] The product was isolated as a yellow liquid (m.p. −63. 5

$$ReF_7 + {}^5/_3\, B(OTeF_5)_3 \xrightarrow{50\ ^oC,\ 3\ d} ReO_2(OTeF_5)_3 + {}^5/_3\, BF_3 + 2TeF_6 \qquad (1.45)$$

^oC and b.p. 30 ^oC). The elemental analysis, room-temperature Raman and ^{19}F NMR spectra; however, did not provide a definitive structural assignment.

Schrobilgen et al.[47] synthesized $ReO_2(OTeF_5)_3$ by the room-temperature reaction of ReO_2F_3 with $B(OTeF_5)_3$ in Freon-114 (eq 1.46) and provided its unambiguous structural

$$ReO_2F_3 + B(OTeF_5)_3 \xrightarrow{\text{Freon-114}} ReO_2(OTeF_5)_3 + BF_3 \qquad (1.46)$$

characterization in the solid state by Raman spectroscopy and in solution by ^{19}F and ^{125}Te NMR spectroscopy. The product was shown to possess a trigonal pyramidal geometry with oxygen atoms lying in the equatorial plane. Additionally, $ReO_2(OTeF_5)_3$ was shown to react with $[(CH_3)_4N][OTeF_5]$ in SO_2ClF yielding a light yellow solid, $[(CH_3)_4N][ReO_2(OTeF_5)_4]$ (eq 1.47),[47] which was characterized by ^{19}F and ^{125}Te NMR

$$ReO_2(OTeF_5)_3 + [(CH_3)_4N][OTeF_5] \xrightarrow{SO_2ClF} [(CH_3)_4N][ReO_2(OTeF_5)_4] \qquad (1.47)$$

and Raman spectroscopies and single-crystal X-ray diffraction. The structural analysis of the anion revealed pseudo-octahedral coordination around rhenium with two oxygen and

two -$OTeF_5$ ligands occupying equatorial positions and two -$OTeF_5$ ligands occupying axial positions.

Turowsky and Seppelt[48] synthesized the pentafluoroorthotellurate derivative of $ReOF_5$ by reaction of $ReO(OTeF_5)_4$ with $Xe(OTeF_5)_2$ (eq 1.48) in SO_2ClF. In contrast

$$ReO(OTeF_5)_4 + ½Xe(OTeF_5)_2 \xrightarrow{SO_2ClF} ReO(OTeF_5)_5 \quad (1.48)$$

with $ReO_2(OTeF_5)_3$, the oxygen atom in $ReO(OTeF_5)_5$ occupies the axial position as observed in its crystal structure.

Huppmann[49] claimed the synthesis of $ReO_3(OTeF_5)$ as a lime green solid by reaction of ReO_3F with $B(OTeF_5)_3$. The structural assignments were based on the percent composition of F, number of Re−O stretches and AB_4 pattern of the -$OTeF_5$ group observed in the ^{19}F NMR spectrum, and m/z = 476 (M^+) obtained from the mass spectrum.

1.2. Manganese(VII) Trioxide Fluoride and Its Reactivity

In contrast with Tc(VII) and Re(VII), for which several oxide fluorides are known, the only known oxide fluoride of Mn(VII) is MnO_3F. It is a dark-green liquid (m.p.−38 ^oC), which, in the pure state, explosively decomposes to MnF_2, MnO_2, and O_2 at temperatures above 0 ^oC. Manganese trioxide fluoride dissolves in aHF forming a deep-green solution, which slowly decolorizes with decomposition to MnF_2 and O_2 at temperatures above 0 ^oC.[31,32]

Manganese trioxide fluoride can be prepared by reaction of $K[MnO_4]$ with aHF (eq 1.49),[31,32] HSO_3F (eqs 1.50),[32] IF_5 (eq 1.51),[50] IF_7 (eq 1.52),[35] and XeF_2 (eq 1.53).[35]

$$K[MnO_4] + 4HF \longrightarrow MnO_3F + KF + [H_3O][HF_2] \quad (1.49)$$

$$K[MnO_4] + 2HSO_3F \longrightarrow MnO_3F + K[SO_3F] + H_2SO_4 \quad (1.50)$$

$$K[MnO_4] + IF_5 \longrightarrow MnO_3F + IOF_3 + KF \quad (1.51)$$

$$K[MnO_4] + IF_7 \xrightarrow{CH_2Cl_2} MnO_3F + IOF_3 + KF + F_2 \quad (1.52)$$

$$K[MnO_4] + XeF_2 \xrightarrow{CH_2Cl_2} MnO_3F + Xe + KF + \tfrac{1}{2}O_2 \quad (1.53)$$

The reactions of the lower oxidation state oxo-anions, $K_2[MnO_4]$ and $K_3[MnO_4]$ with IF_5 or HF also yield MnO_3F.[35] Permanganyl fluoride reacts with gaseous HCl to form MnO_3Cl. There is also evidence for the existence of $MnO_3F{\cdot}HF$;[51] however, it is unreactive towards PnF_5 (Pn = As, Sb) in aHF.[43] Permanganyl fluoride was characterized in the gas-phase by UV-vis,[6,52,53] microwave,[54,55] infrared,[6,52,56–58] photoelectron,[59] and resonance Raman[60] spectroscopy and in the solid state by infrared spectroscopy.[61] The above spectroscopic findings revealed a monomeric structure for MnO_3F (C_{3v}), which shows two strong O→Mn and F→Mn charge transfer transitions in the UV-vis spectrum at 15,500 and 33,300 cm^{-1}.[6] The monomeric structure of MnO_3F has been confirmed by single-crystal X-ray diffraction;[62] however, the Mn−F bond length could not be determined due to a O/F positional disorder.

1.3. Fluorides of Manganese, Technetium, and Rhenium

1.3.1. Fluorides of Rhenium and Technetium

The known high-oxidation-state technetium and rhenium fluorides, their syntheses

and methods of characterization are summarized in Table 1.1. Topics relating to the chemistries of rhenium and technetium fluorides having oxidation states below VII, which are beyond the scope of the present research work, are not discussed.

1.3.2. Manganese Fluorides

Manganese fluorides have been isolated and characterized in the +2, +3, and +4 oxidation states. The lowest oxidation state manganese(II) fluoride, MnF_2, precipitates as a pale pink solid upon addition of F^- to aqueous solutions containing Mn^{2+} ions.[121] Manganese difluoride has a rutile structure (Mn−F, 2.131(6) and 2.104(9) Å)[122] and a pale pink color which arises from electronic transitions between lower- and higher-lying d orbitals, which are otherwise forbidden in case of octahedral symmetry.[121] It is a fluoride-ion acceptor, which forms complexes with alkali metal fluorides, $A[MnF_3]$ and $A_2[MnF_4]$ (A = Na, K, Rb, Cs).[121,123] Grey MnF_3 is most conveniently prepared by reaction of MnF_2 with F_2 in aHF at room temperature.[124] It has a fluorine-bridged chain structure consisting of MnF_6 octahedra (Mn−F: 2.106(4), 1.923(5), 1.830(4) Å). The MnF_6 octahedra are tetragonally distorted by the Jahn-Teller effect and share all their corners with adjacent octahedra by means of fluorine bridges.[125-127] The structure of MnF_3 was also studied in matrix[128,129] and in the solid[124] state by infrared and Raman spectroscopies, and by high-temperature gas-phase electron diffraction.[130] The experimental geometrical and vibrational data were interpreted with the aid of quantum-chemical calculations.[131,132] Manganese trifluoride acts as a fluoride-ion acceptor in reactions with alkali metal

Table 1.1. Neutral Fluorides and Fluoro-Anions of Technetium and Rhenium

Fluoride	Color	Method of Preparation	Characterization	Ref.
Oxidation State VII				
ReF_7	yellow	Re + F_2 at 300 ^oC	IR, Raman, ^{19}F NMR, neutron and electron diffraction	63−70
$[ReF_6]^+$	white	ReF_7 + SbF_5	IR, Raman, MS, X-ray powder photography	13, 71−74
$[ReF_8]^-$	yellow	ReF_7 + CsF, NOF, NO_2F	X-ray, Raman, ^{19}F NMR	15, 75
Oxidation State VI				
ReF_6	yellow	Re + F_2 at 125 ^oC	X-ray, Raman, IR, UV-vis,	64, 76−84
$[ReF_7]^-$	orange	ReF_6 + AF (A = Na, K, Rb, Cs)	Raman, IR,	85−87
$[ReF_8]^{2-}$	violet	ReF_6 + 2AF (A = Na, K, Rb, Cs), 2NOF, $2NO_2F$	X-ray, Raman, IR	15, 75, 87−89
TcF_6	yellow	Tc + F_2 at 350−400 ^oC	X-ray, Raman, IR	79−83, 90−92
$[TcF_7]^-$	yellow	TcF_6 + NO_2F	IR, X-ray powder	92, 93
$[TcF_8]^{2-}$	off white	TcF_6 + 2NOF	IR, X-ray powder	93
Oxidation State V				
ReF_5	green	ReF_6 + $W(CO)_6$ in WF_6; ReF_6 + PF_3; ReF_6 + Si	MS, IR, X-ray powder	94−96
$[ReF_6]^-$	white	ReF_6 + 2AX (A = Na, K, Rb, Cs; X = Br, I) in SO_2 ReF_5 + CsF	X-ray powder, Raman	97−101
TcF_5	yellow	Tc + F_2 at 350−400 ^oC	Raman, X-ray powder, MS	92, 102−104
$[TcF_6]^-$	yellow	TcF_6 + ACl (A = Na, K, Rb, Cs), NO	IR, X-ray, Raman	92, 93, 99, 102, 105
Oxidation State IV				
ReF_4	blue	ReF_6 + $W(CO)_6$; thermal decomp. of ReF_5; ReF_5 + Si; hot fillament + ReF_6;	MS, IR, X-ray powder	94, 96
$[ReF_6]^{2-}$	white	$[NH_4]_2[ReI_6]$ + $A[HF_2]$ (A = Na, K, Rb, Cs) at 250 ^oC; $K[ReO_4]$ + KI + $K[HF_2]$ at 700 ^oC; ReF_6 + 2KI	Raman , IR, X-ray powder	101, 106−116
$[TcF_6]^{2-}$	lavender	$K_2[TcX_6]$ + $K[HF_2]$ 250 ^oC, (X = Cl, Br, I); $K_2[TcBr_6]$ + AgF	IR, X-ray powder	107−110, 117−120

fluorides, forming the violet $A_3[MnF_6]$, $A_2[MnF_5]$, and $A[MnF_4]$ (A = Na, K, Rb, Cs) salts.[121]

The highest oxidation state manganese fluorides that are known are in the +4 oxidation state and consist of neutral MnF_4 and the fluoro-anions, $[MnF_5]^-$, $[MnF_6]^{2-}$, and $[Mn_2F_9]^-$. High-purity MnF_4 is most conveniently prepared in high yield by fluorination of MnF_2 with F_2 in aHF under UV light (eq. 1.54)[124] or by oxidation of MnF_2 with KrF_2

$$MnF_2 + F_2 \xrightarrow{25\ ^oC,\ HF} MnF_4 \qquad (1.54)$$

(see section 1.3.4).[133] Manganese tetrafluoride was also a product of several synthetic procedures summarized by Rakov, Khaustov, and Ostropikov[134] in their study of the fluorination rate of powdered MnF_3 by gravimetric methods at 450−540 ^oC.

Manganese tetrafluoride has been characterized by magnetic measurements,[124,135-138] infrared[124,138] and Raman spectroscopies,[124] mass spectrometry,[138] and single-crystal X-ray diffraction.[139] Crystalline MnF_4 is dimorphic: tetragonal α-MnF_4 or rhombohedral β-MnF_4. The building blocks of α-MnF_4 are tetramers consisting of MnF_6 octahedra that are connected through *cis*-fluorine bridges. The tetramers are also interconnected to give a three-dimensional framework with terminal and bridging Mn−F bond lengths ranging between 1.677(1) − 1.704(1) Å and 1.845(2) − 1.948(1) Å, respectively. Although the unit cell parameters of β-MnF_4 have been reported, the structural parameters have not yet been defined.[139]

Manganese tetrafluoride is 10.5 ±2 kcal mol^{-1} less stable than MnF_3,[140] decomposing by F_2 elimination to MnF_3 according to eq 1.55. The equilibrium fluorine

$$MnF_4 \longrightarrow MnF_3 + \tfrac{1}{2}F_2 \qquad (1.55)$$

pressure above MnF_4 at room temperature was 10^{-9} bar, however, the decomposition temperature is ambiguous with the lowest decomposition temperatures reported at 52 [141] and 70 °C[142] with the highest decomposition temperature reported at 320 °C.[143]

1.3.3. Lewis Acid Properties of MnF_4

The fluoride ion-acceptor properties of MnF_4 have been studied and resulted in the syntheses and characterizations of the $[MnF_6]^{2-}$,[124,144−161] $[MnF_5]^-$,[123,162−164] and $[Mn_2F_9]^-$ [165] anions.

The alkali metal salts of $[MnF_6]^{2-}$ are most conveniently prepared in high yields by reaction of MnF_2/AF (A= Li, Na, K, Rb) with F_2 in aHF under UV light at room temperature.[124] Several other synthetic methods that yield $A_2[MnF_6]$ have been reviewed by Mazej[124] and Christe.[144] Alkaline earth and transition metal salts were synthesized by the high temperature reaction of $BaMnO_4$,[145] $SrMnO_3$,[145] and $CaCl_2/MnCl_2$ and $MgCl_2/MnCl_2$ [145] and $[Ni(NH_3)_6]Cl_2$/X,[146] $ZnCl_2$/X,[146] $HgCl_2$/X,[146] Ag[MnO_4]/X,[146] $CdCO_3$/X (X = $[NH_4][MnF_3]$)[146] mixtures with fluorine gas. The $[NO_2]_2[MnF_6]$ salt was synthesized by fluorination of MnF_2/NO_2F mixture with excess fluorine gas above 200 °C.[147] The $[MnF_6]^{2-}$ anion has also been synthesized by electrolytic oxidation of HF(40%)/$[NH_4]$F suspensions of MnF_3[148] or MnF_2[149] and by metathesis reactions of (i) $[NH_4][SbF_6]$ and $Cs_2[MnF_6]$ in aHF at room temperature[150] and (ii) $[O_2][SbF_6]$ and $Cs_2[MnF_6]$ in aHF at −78.[151]

The $[MnF_6]^{2-}$ anion was fully characterized by Raman,[124,150−154] infrared,[150,152−154] UV-vis,[152] and electronic[153−156] spectroscopies, X-ray powder photography,[157−160] and

single-crystal X-ray diffraction.[160,161] The single-crystal X-ray diffraction studies revealed that the $[MnF_6]^{2-}$ anion has two phases: cubic (Cs^+; K^+ and Rb^+, 100 to 70 ^oC) and hexagonal (K^+, Rb^+, 40 ^oC).

The $[MnF_5]^-$ anion was synthesized by fluorination of $A[MnF_3]$ (A = Na,[162] K,[123,162,163] Rb,[162] and Cs[123]) at 450 ^oC and fluorination of $K[MnO_4]$ with BrF_3[163] and characterized by X-ray powder diffraction,[163] magnetic measurements,[123] and electronic spectroscopy.[164]

The dinuclear hexafluoromanganate(IV) anion, $[Mn_2F_9]^-$, was synthesized as a ruby-red solid by treating MnO_2 or MnF_n (n = 2−4) with a F_2/O_2 gas mixture at 350−550 ^oC. The $[Mn_2F_9]^-$ anion was characterized by magnetic measurements, elemental analysis, Raman spectroscopy, and single-crystal X-ray diffraction.[165] The structure of the anion consists of double chains of MnF_6 octahedra which have a layered arrangement with the cations located between the layers.

Manganese tetrafluoride behaves as a Lewis acid in its reaction with pyridine, yielding $MnF_4 \cdot NC_5H_5 \cdot H_2O$.[162] The latter compound was characterized by elemental analysis, infrared spectroscopy, and magnetic measurements. The Lewis base properties of MnF_4 were investigated by reaction of MnF_4 with SbF_5, which resulted in the formation of $MnF_4 \cdot 4SbF_5$.[166] The $MnF_4 \cdot 4SbF_5$ adduct was only characterized by infrared spectroscopy.

1.3.4. Reactions of MnF_4 with the Noble-Gas Fluorides, KrF_2, XeF_2, and XeF_6

In contrast with the fluoride-ion acceptor properties of MnF_4, considerable scope

remains for the investigation of its fluoride-ion acceptor properties toward noble-gas fluorides.

Manganese difluoride has been shown to react with KrF_2 in aHF to form dark red oily $2KrF_2{\cdot}MnF_4$ and $KrF_2{\cdot}MnF_4$ which are stable below −45 and −25 °C, respectively.[133] The stoichiometric compositions of these adducts have been determined by examining their weight-loss versus time of pumping curves at −45 °C. The decompositions of both adducts yielded pure MnF_4, KrF_2, Kr, and F_2.

Manganese difluoride has also been shown to react with XeF_2 and XeF_6. The reaction of XeF_2 with MnF_2 resulted in the formation of $XeF_2{\cdot}MnF_4$ (eq 1.56), which was

$$MnF_2 + nXeF_2 \xrightarrow{130\ ^oC} XeF_2{\cdot}MnF_4 + (n\text{-}2)XeF_2 + Xe \qquad (1.56)$$

isolated by removal of excess XeF_2 at −196, −80 °C, and room temperature.[167,168] The 1:2 adduct, $XeF_2{\cdot}2MnF_4$, was obtained by pumping $XeF_2{\cdot}MnF_4$ under dynamic vacuum at 120 °C. The reaction stoichiometry was determined by comparing the weights of all reactants and products. The isolated compounds were characterized by X-ray powder diffraction, infrared spectroscopy, magnetic measurements, and elemental analyses.

The $4XeF_6{\cdot}MnF_4$ adduct[169,170] was synthesized by reaction of MnF_2 with XeF_6 at 60 °C and isolated under dynamic vacuum at 0 °C. The decomposition of $4XeF_6{\cdot}MnF_4$ occurred under dynamic vacuum in stages at room temperature, 60, and 140 °C and resulted in the formation of $nXeF_6{\cdot}MnF_4$ (n = 2, 1, 0.5), which have been characterized by X-ray powder diffraction, infrared spectroscopy, magnetic measurements, and elemental analyses.

The reaction between $[NH_4][MnF_3]$ and XeF_6 (eq 1.57) resulted in the formation of

$$[NH_4][MnF_3] + nXeF_6 \xrightarrow{0\text{ to }60\ ^oC} [NH_4][XeF_5][MnF_6] + XeF_x + Xe + XeF_6$$

$$n \geq 15,\ x = 2, 4 \qquad (1.57)$$

the yellow, room-temperature stable $[NH_4][XeF_5][MnF_6]$ salt.[171] The product was characterized by chemical analyses, magnetic susceptibility measurements, thermogravimetric studies, and infrared and room temperature Raman spectroscopy.

1.3.5. Existing Evidence for MnF_5 and Theoretical Studies

Indirect evidence was found for MnF_5 by mass spectrometry experiments while investigating the reactions of MnF_3 and MnF_4 with F_2 gas.[172,173] Although the $[MnF_4]^+$ cation, which contains manganese in the +5 oxidation state, was detected in the mass spectrum, the origin of this cation, MnF_4 or MnF_5, is unclear. Manganese pentafluoride was proposed to exist in the gas phase with the MnF_5 bond dissociation energy, D_0 (MnF_4−F), and the standard enthalpy of formation, $\Delta_f H^o$ (MnF_5, g), being 172 ±15 and −1062 ±15 kJ mol^{-1}, respectively.[173] It was also proposed that MnF_5 can be isolated in crystalline state at low temperature.

1.4. Purpose and Scope of Present Work

The present research expands the fundamental chemistry of group VII transition metal oxide fluorides. A significant body of the present research focuses on the fundamental chemistry of ReO_3F. The latter will be explored by the syntheses and characterization of its oxide and oxide fluoride derivatives. Additionally, the chemical reactivity of ReO_3F and MnO_3F will be investigated as possible routes to the syntheses of

the Xe(II) oxides, new Re(VII) and Mn(VII) oxide fluorides, and Mn(V) fluorides, respectively.

In contrast to the well-established chemistries of $ReOF_5$ and ReO_2F_3, the fundamental chemistry of the remaining known rhenium(VII) oxide fluoride, ReO_3F, is the least investigated due to the absence of a reliable high-yield, high-purity synthesis of this oxide fluoride. In view of the previous dubious claim that the $[ReO_3F_3]^{2-}$ anion possesses meridional symmetry,[27,36,37] the development of a reliable high-yield and high-purity synthesis of ReO_3F provides an opportunity to resynthesize salts of the $[ReO_3F_3]^{2-}$ anion and to unambiguously characterize its geometry by single-crystal X-ray diffraction in conjunction with Raman spectroscopy. The availability of pure ReO_3F in macroscopic amounts would allow expansion and deepening of our understanding of its Lewis acid behavior and fluoride-ion acceptor properties by synthesizing and characterizing previously unknown adducts and anions derived from ReO_3F.

The present research also investigates the reactivity of ReO_3F with Lewis acids such as BF_3, AsF_5, and SbF_5. The latter study is expected to yield the mononuclear $[ReO_3]^+$ and/or the dinuclear $[\mu\text{-}F(ReO_3)]^+$ cation stabilized by the weakly coordinating $[BF_4]^-$, $[PnF_6]^-$ (Pn = As, Sb), and $[Sb_2F_{11}]^-$ anions.

By analogy with the reaction of XeF_2 with $[H_3O][PnF_6]$ which yielded the first xenon(II) oxide fluoride, $[FXeOXeFXeF]^+$,[174] and considering the solvolytic behavior of ReO_3F under fluoro-basic conditions, the reaction of ReO_3F with XeF_2 will be investigated as a possible means to transfer oxygen to xenon(II). The reaction of ReO_3F

with ReO_2F_3 will also be investigated with the goal to prepare new "mixed" rhenium(VII) oxide fluorides.

Considering expected similarities between the chemistries of rhenium and technetium, as is observed for other pairs of row 5 and 6 transition elements, the development of rhenium oxide fluoride chemistry is expected to provide valuable insights into technetium chemistry, which is generally less developed due to the radioactivity of its long-lived isotope, ^{99}Tc (100% abundant, 0.29 MeV β^-, $t_{½}$ = $2.12x10^5$ yr). For example, detailed knowledge of the reactivity and properties of TcO_3F and its weakly radioactive analogue, ReO_3F (^{187}Re, 62.6%; ≤0.008 MeV β^-, $t_{½}$ = $7x10^{10}$ yr), is of particular interest to the nuclear industry for the removal of ^{99}Tc, a high-abundance fission product that must be removed from re-enriched UF_6 prior to refabrication into nuclear fuel elements composed of UO_2.[175] The latter process is heavily reliant upon the ability of TcO_3F to be absorbed on solid fluoride ion donor surfaces. Thus, fluoride ion donor-acceptor properties of TcO_3F and ReO_3F are of considerable interest in this field of applied research as well as to fundamental chemistry.

A final goal of the present research concerns the syntheses of the missing d^0 manganese oxide fluorides. This entails studies of the O/F methasesis reactions of MnO_3F with XeF_6 and KrF_2 as possible synthetic routes to new manganese oxide fluorides, such as $MnOF_5$ and MnO_2F_3, by analogy with the syntheses of $TcOF_5$ [1,2] and TcO_2F_3.[17] The latter reactions could result in the formation of high-valent Mn(V) and Mn(VI) fluorides by oxidative elimination of O_2. The reduction of Mn(VII) oxide fluorides is an alternative approach to previously known syntheses of high-valent manganese fluorides by oxidation

of MnF_2 with XeF_2, XeF_6, and KrF_2.[167−171] The highest oxidation state of manganese that has been attained as the result of the latter oxidation reactions is +4, which implies that a kinetic barrier hinders further oxidation of Mn(IV) to Mn(V) or (MnVI). Therefore, the reduction of Mn(VII) by reaction with noble-gas fluorides, such as XeF_6 and KrF_2, could be the only viable synthetic route to the syntheses of Mn(V) or Mn(VI) fluorides.

Structural characterizations of the compounds synthesized in this study will be achieved by use of Raman and ^{19}F spectroscopies, single-crystal X-ray diffraction, and quantum-chemical calculations in conjunction with Atoms in Molecules (AIM), electron localization function (ELF), and molecular electrostatic potential surface (MEPS) analyses.

CHAPTER 2

EXPERIMENTAL SECTION

2.1. Standard Techniques

2.1.1. Drybox and Vacuum Line Techniques

The compounds used and prepared during the course of this work were moisture- and temperature sensitive, and were handled under rigorously anhydrous conditions on glass and metal vacuum line systems or in the nitrogen atmosphere of a dry box (Vacuum Atmospheres Model DLX, oxygen and moisture <0.1 ppm) equipped with a glass cryowell. Low-temperature additions of potentially reactive solids were carried out in the dry box by use of a metal Dewar filled with 4.5 mm copper plated steel spheres (air rifle shot) that had been previously cooled to ca. –140 ^{o}C in the glass cryowell (–196 ^{o}C) of the dry box.

Transfers of volatile corrosive compounds and aggressively fluorinating solvents (e.g., HF and AsF_5) were carried out on metal vacuum lines constructed mainly from nickel and 316 stainless steel and fitted with 316 stainless steel valves (Autoclave Engineers Inc., Figure 2.1), which were themselves fitted with grease-free PTFE packings. Pressures were measured at ambient temperatures using MKS Model PDR-5B pressure transducers having inert wetted surfaces constructed of Inconel. The dynamic range of the pressure transducers was 0 – 1150 torr with an accuracy of ±0.5 torr over the entire pressure range. Two Edwards two-stage E2M8 direct-drive vacuum pumps functioned as a rough pump and as a high vacuum pump. The rough pump was primarily used to remove volatile fluoride compounds by pumping through a fluoride/fluorine trap

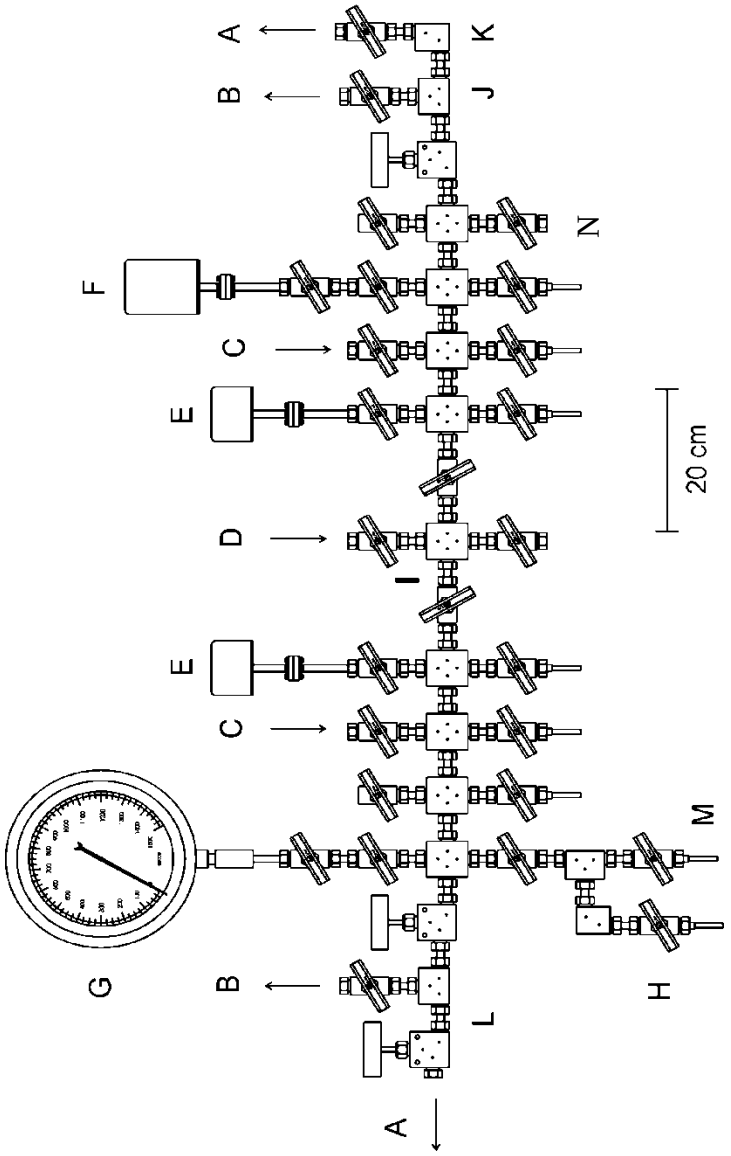

Figure 2.1. Schematic Diagram of the Metal Vacuum Line System: (A) outlet to liquid nitrogen and charcoal (Norit) traps followed by a two-stage direct-drive rotary vacuum pump (Edwards, E2M8) – hard vacuum, (B) outlet to soda lime and liquid nitrogen traps followed by a two-stage direct-drive rotary vacuum pump (Edwards, E2M8) – rough vacuum, (C) dry nitrogen inlet, (D) fluorine inlet, (E) MKS Model PDR-5B pressure transducer (0 –1000 torr), (F) MKS Model PDR-5B pressure transducer (0 – 10 torr), (G) Bourdon pressure gauge (0 – 1500 torr), (H) $^{3}/_{8}$-in. 316 stainless steel high pressure valve (Autoclave Engineers, 30BM6071), (I) 316 stainless steel cross, (J) 316 stainless steel T-piece, (K) 316 stainless steel L-piece, (L) nickel connectors, (M) ¼-in. o.d., $^{1}/_{8}$-in. i.d. nickel tube, (N) hot-wire reactor connection. Reproduced with permission from ref 14.

consisting of a stainless steel column packed with a soda lime absorbent (Fisher Scientific, 4-8 mesh), followed by a glass liquid nitrogen trap to remove any CO_2, water and other volatile products generated in the soda lime trap. The second vacuum pump provided a high vacuum source (ca. 10^{-4} torr) and was fitted with a glass liquid nitrogen trap and copper column, immediately before the pump, packed with activated charcoal (Norit).

Transfers of volatile compounds that did not attack glass were carried out on Pyrex glass vacuum lines (Figure 2.2) equipped with grease-free 6-mm J. Young glass stopcocks which were fitted with PTFE barrels. Vacuum (ca. 10^{-4} torr) was achieved using a single vacuum pump (Edwards two-stage E2M8 direct-drive) connected through a glass liquid nitrogen trap. Pressures inside the glass vacuum lines were monitored using a mercury manometer when backfilling reaction vessels.

2.1.2. Preparative Apparatus and Sample Vessels

All synthetic work was carried out in reactors constructed from lengths of ¼-in. o.d. FEP tubing which were heat-sealed at one end and heat-flared (45^o SAE) at the other. The tubing was connected to Kel-F valves, encased in aluminum housings, using brass flare fittings. All vessels were then connected to a glass vacuum line using ¼-in. stainless steel Swagelok Ultra-Torr unions fitted with Viton O-rings and were rigorously dried by pumping (a minimum of 6 h) under dynamic vacuum. Vessels were then connected to the metal vacuum line using a ¼-in. PTFE Swagelok union and passivated with ca. 1000 torr of F_2 for ca. 12 h. Once passivated, vessels were evacuated under dynamic vacuum to

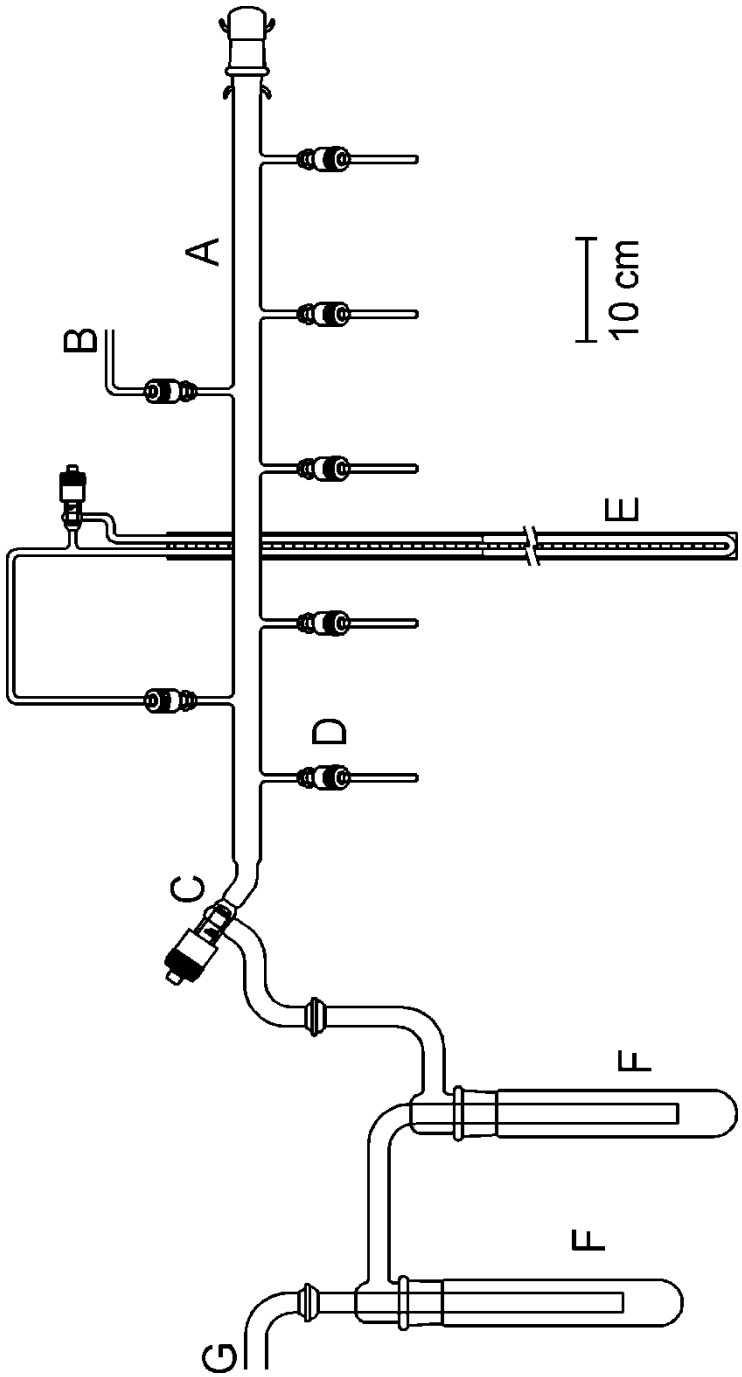

Figure 2.2. Glass vacuum line used for the manipulation of non-corrosive volatile materials. (A) Main vacuum manifold. (B) Dry N_2 inlet. (C) 15-mm greaseless J. Young valve with PTFE barrel. (D) 6-mm greaseless J. Young valve with PTFE barrel. (E) Mercury manometer. (F) Liquid N_2 cold traps. (G) Outlet to vacuum pump. Reproduced with permission from ref 14.

remove all volatile impurities and back-filled with dry N_2 (ca. 1000 torr) prior to use. Similarly, connections made to a metal vacuum line were dried under dynamic vacuum and passivated with F_2 gas overnight. Connections made to a glass vacuum line were dried under dynamic vacuum overnight. The glass vessels used to handle less corrosive materials were dried under dynamic vacuum for a minimum of 8 hr and were periodically heated (flamed out) with a Bunsen burner while under vacuum.

Nuclear magnetic resonance spectra were acquired using sample tubes prepared from 4-mm o.d. FEP tubing. One end of each tube was heat-sealed using the end of a heated thin-walled 5-mm o.d. glass NMR tube, while the other end was fused to ca. 5 cm of ¼-in. o.d. $^1/_8$-in i.d. thick-walled tubing. The open end was flared (45^o SAE) for connection to a Kel-F valve. Prior to acquisition of the NMR data, the sample tubes were heat-sealed under dynamic vacuum using a nichrome wire resistance furnace of appropriate diameter.

Low-temperature Raman spectra of solids (ca. −140 to −150 ^{o}C) were recorded on samples prepared in thin-walled ¼-in. o.d. FEP tubing.

All connections to vacuum lines were made using thick-walled ¼-in. o.d. $^3/_{16}$-in i.d. FEP tubing in conjunction with either a ¼-in. PTFE Swagelock unions outfitted with PTFE compression fittings (front and back ferrules) or ¼-in. stainless steel Swagelock Ultra-Torr connectors outfitted with stainless steel compression fittings and Viton rubber O-rings.

2.2. Synthesis and Purification of Starting Materials

2.2.1. Sources and Purification of Gases: N_2, Ar, F_2, Xe, and Kr

House nitrogen gas was generated by boiling off liquid nitrogen (Air Liquide) and was further dried through a freshly regenerated bed of type 4 Å molecular sieves. High-purity nitrogen gas (Praxair, 99.999%) and argon gas (VitalAire, 99.999%) were also employed for the back pressuring of reaction vessels and were used without further purification. Technical grade fluorine gas (Air Products, >98 %) and ultra-high purity Xe (Air Products, 99.995%) and Kr (Air Products, 99.995%) were used without further purification.

2.2.2. Purification of Solvents: Anhydrous HF, SO_2ClF, CH_3CN

HF. Commercial anhydrous hydrogen fluoride (Harshaw Chemical Co.) was purified by addition of ca. 5 atm of F_2 gas to a commercial HF sample contained in a nickel can and was allowed to stand for a minimum of ca. 48 h prior to use, converting residual water to HF and O_2. The reactor was subsequently cooled to −196 ^{o}C and all volatiles, such as O_2 and F_2, were removed under dynamic vacuum. After removal of O_2 and excess F_2 at −196 ^{o}C, anhydrous HF (aHF) was distilled into a dry Kel-F storage vessel equipped with a Kel-F valve and stored at room temperature for future use. Transfer of HF was accomplished by vacuum distillation from the Kel-F storage vessel, on a metal vacuum line, through a vacuum submanifold constructed from FEP, as shown in Figure 2.3.

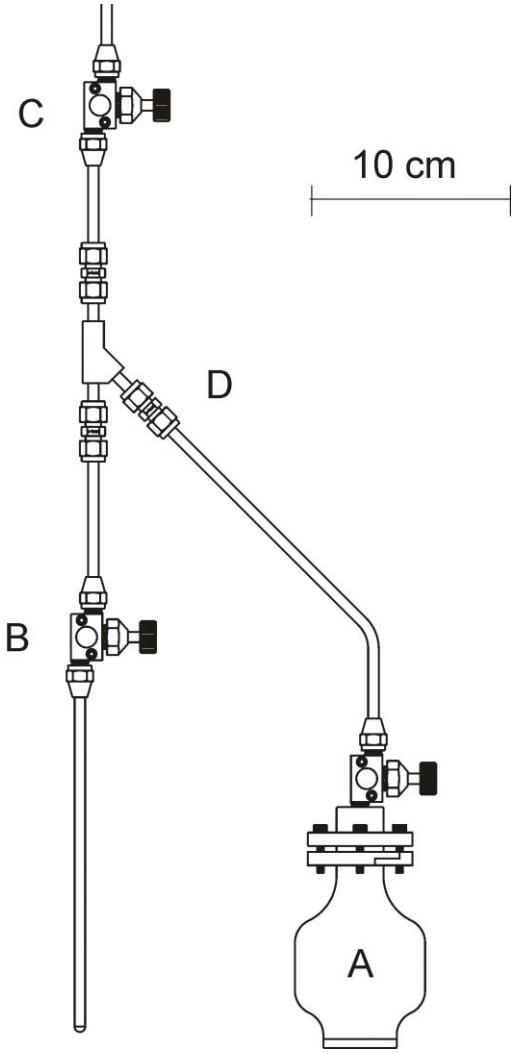

Figure 2.3. Hydrogen fluoride distillation apparatus. (A) Kel-F storage vessel containing HF. (B) FEP reaction vessel fitted with a Kel-F valve. (C) Kel-F valve connected to vacuum manifold. (D) ¼-in. Teflon union. Reproduced with permission from ref 14.

SO_2ClF. Sulfuryl chloride fluoride (Allied Chemical Co., Baker and Adams Division, >90%, ca. 100 g crude material) was purified by fractional distillation through two FEP U-tube traps cooled to –78 and –90 ^oC, respectively, effectively removing the inert impurity SO_2F_2. The remaining SO_2ClF was then condensed into an FEP U-tube containing ca. 80 g of SbF_5 at –78 ^oC and slowly warmed to room temperature with vigorous mixing to remove SO_2 by adduct formation with SbF_5 ($SO_2 \cdot (SbF_5)_n$), which is known to rapidly reduce xenon compounds. The purified SO_2ClF was then transferred to an FEP U-tube cooled to –78 ^oC and containing dried KF. Again, the mixture was slowly warmed to room temperature with vigorous mixing and allowed to stand with periodic mixing at room temperature for at least 2 h to remove any residual HF. The sample was again cooled to –78 ^oC and condensed into a 1¼-in. o.d. FEP reaction vessel containing XeF_2 (1.7 g) for 24 h to ensure all impurities, in particular SO_2, with reducing properties were oxidized ($SO_2 + XeF_2 \longrightarrow SO_2F_2 + Xe$). Finally, SO_2ClF was condensed by dynamic pumping at –78 ^oC into a glass vessel, outfitted with a 6-mm J. Young all glass stopcock, onto a bed of dry KF. The purity of the sample was assessed by ^1H, ^{17}O, and ^{19}F NMR spectroscopy of a neat sample recorded at –80 ^oC, in which only a small amount of SO_2F_2 (ca. 2 %) was found. Transfers were performed using a glass vacuum line by vacuum distillation of SO_2ClF through a submanifold comprised of a Y-shaped glass connection to the reaction vessel (Figure 2.4). The sample was stored at room temperature until used.

CH_3CN. Acetonitrile (Caledon, HPLC Grade) was purified according to the literature method,[176] stored over molecular sieves in a glass vessel outfitted with a grease-

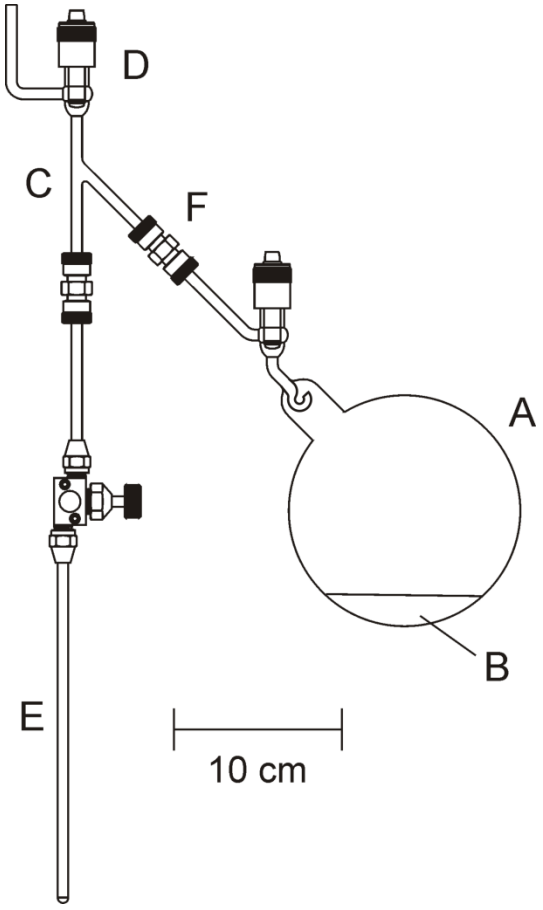

Figure 2.4. Apparatus used for the vacuum transfer of SO_2ClF solvent: (A) 250-mL glass vessel equipped with a grease-free 6-mm J. Young PTFE/glass stopcock outfitted with PTFE barrel, (B) bed of dry, powdered KF, (C) glass Y-connector, (D) 6-mm J. Young PTFE/glass valve, (E) FEP reaction vessel fitted with a Kel-F valve, and (F) stainless steel Swagelok Ultra-Torr Union. Reproduced with permission from ref 14.

free 6-mm J. Young glass/PTFE stopcock, and transferred under static vacuum using a glass vacuum line and a glass Y-piece into a smaller glass dispensing vessel outfitted with a grease-free 6-mm J. Young glass/PTFE stopcock. Acetonitrile was then dispensed, under static vacuum using a glass vacuum line and a glass Y-piece, into individual reaction vessels (Figure 2.5).

2.2.3. Purification of SbF_3, SbF_5, BF_3, CsF, and $K[MnO_4]$

SbF_3. Antimony trifluoride (Aldrich, 98%) was purified as previously described[177] by sublimation under dynamic vacuum and transferred into the dry box prior to use.

SbF_5. Antimony pentafluoride (Ozark-Mahoning Co.) was purified by the literature method[178] and stored in a glass vessel.

$K[MnO_4]$ and BF_3. Potassium permanganate (Shawinigan) and boron trifluoride (Matheson) were used without further purification.

CsF. Cesium fluoride (CsF, ICN-KCK Laboratories Inc., 99.9%) was dried by fusion in a platinum crucible, followed by immediate transfer of the melt to a dry box port which was immediately evacuated. Upon transferring to a nitrogen atmosphere dry box and solidification, the sample was ground to a fine powder in a dry mortar and pestel and stored in a PFA container inside the dry box until used.

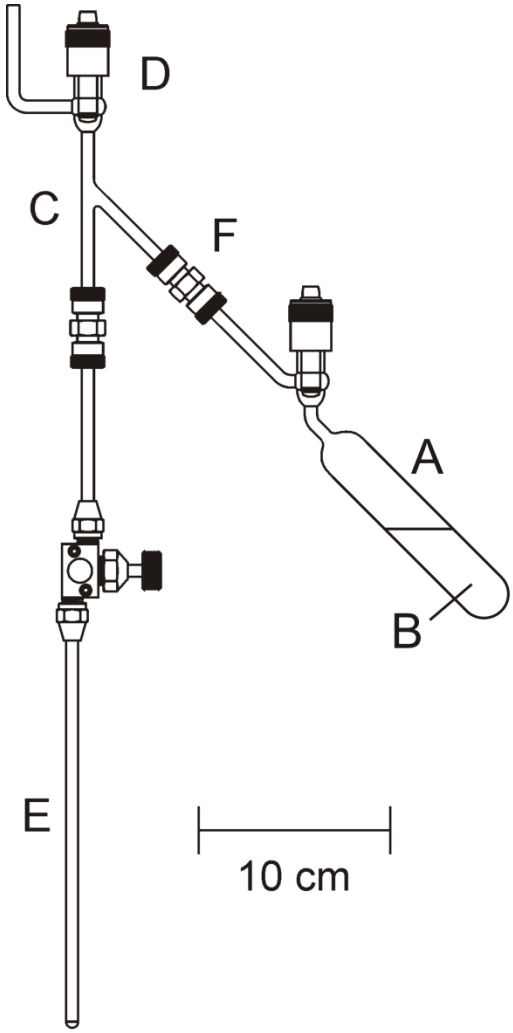

Figure 2.5. Apparatus used for the vacuum transfer of CH_3CN solvent: (A) 200-mL glass vessel equipped with a grease-free 6-mm J. Young PTFE/glass stopcock outfitted with PTFE barrel, (B) CH_3CN, (C) glass Y-connector, (D) 6-mm J. Young PTFE/glass valve, (E) FEP reaction vessel fitted with a Kel-F valve, and (F) stainless steel Swagelok Ultra-Torr Union. Reproduced with permission from ref 14.

2.2.4. Syntheses of Starting Materials: $[N(CH_3)_4]F$, AsF_5, ONF, $K[ReO_4]$, $[NH_4][ReO_4]$, $Re_2^{16/18}O_7$, XeF_2, KrF_2, XeF_6, ReO_2F_3, $Re^{16/18}O_3F$, and MnO_3F

$[N(CH_3)_4]F$. The naked fluoride ion source, $[N(CH_3)_4]F$, was prepared according to the literature method[179] and was stored in an FEP tube inside a dry box until used.

AsF_5. Arsenic pentafluoride was prepared as previously described,[180] by direct fluorination of purified AsF_3 with purified F_2 in a nickel can. The AsF_5 was used directly from the reaction can without further purification.

ONF. The synthesis of ONF was based on the published methods[181] using more rigorously purified starting materials. Nitrosyl fluoride, ONF, was prepared by twice reacting NO (0.0905 mol) and F_2 (0.0417 mol) in a nickel reactor (65 mL) to give a combined yield of 8.63 g (0.176 mol) of ONF. Trace amounts of O_2NF (ca. 0.2%) and ONF_3 (ca. 0.8%) found in the sample were estimated by recording the ^{19}F NMR spectrum of a sample of the neat liquid product at –80 ^{o}C. Transfers of ONF were carried out using a fluorine-passivated FEP submanifold (dedicated to this use) that was passivated once with ONF prior to transfer to an intermediate FEP vessel. This served to verify that passivation of the submanifold was complete. In the event of incomplete passivation, a distinct blue to light blue color appeared in the intermediate vessel that resulted from reaction of ONF with residual moisture and/or unpassivated metal surfaces to give intense blue N_2O_3. This procedure also allowed a controlled amount of ONF to be metered into the reaction vessel.

$K[ReO_4]$ and $[NH_4][ReO_4]$. The $K[ReO_4]$ and $[NH_4][ReO_4]$ salts were prepared and purified using procedures analogous to those used for preparation and purification of

pertechnetates.[26] These salts were subsequently dried under vacuum for 48 h. The salts were stored in glass vessels inside a dry box.

$Re_2^{16/18}O_7$. Synthesis of dirhenium heptoxide was carried out in a 15-mm o.d. quartz reaction tube equipped with a 6-mm J. Young glass valve equipped with a Teflon barrel (Figure 2.6). Rhenium powder (Cleveland Refractory Metals, 325 mesh; 2.178 g, 11.70 mmol) was added to the bottom of the reaction tube. Vessel was then connected to the metal vacuum line using a ¼-in. PTFE Swagelock union. Reduction of the metal powder surface was achieved by heating rhenium powder with a natural gas-oxygen torch in the presence of successive aliquots of H_2 (800–1000 torr) followed by removal of H_2O under vacuum while the quartz vessel was still hot. The reduction was repeated until water evolution ceased (no condensation was visible on the vessel walls when the reactor was cooled to room temperature). The metal powder was then reduced with two further aliquots of H_2 and flamed dried under dynamic vacuum. The metal powder was then quantitatively converted to Re_2O_7 by addition of successive aliquots of high-purity oxygen gas (Air Liquide, 99.995%), which had been further dried by passing it through a copper coil immersed in dry ice. The metal was heated to a dull red to yellow color with a natural gas-oxygen torch until combustion ceased. Dirhenium heptoxide condensed on the reaction walls as a bright yellow crystalline material in the cooler regions of the reactor. The procedure was repeated until all the powder metal had been converted to Re_2O_7. After complete combustion, the vessel was evacuated and Re_2O_7 was melted and purified by static vacuum distillation into a 8-mm outer diameter quartz side arm attached to the reaction vessel. The powdered solid was stored in a dry box until used. The synthesis of

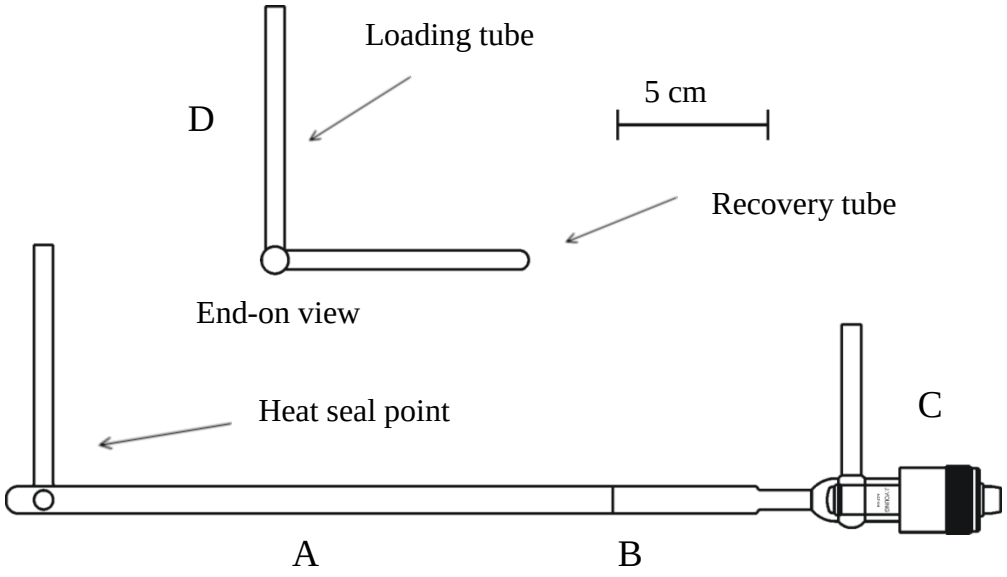

Figure 2.6. Reactor used for the preparation of Re_2O_7: (A) 9-mm o.d. quartz tube, (B) graded quartz to Pyrex seal, (C) 6-mm J. Young PTFE/glass valve, (D) front-end view showing the vertical loading tube and the horizontal recovery tube. Reproduced with permission from ref 14.

^{18}O-enriched Re_2O_7 was achieved by combustion of Re powder (Cleveland Refractory Metals, 325 mesh) in $^{18}O_2$ (Isotec, Inc.; 95-99% ^{18}O), and was similar to that used for the synthesis of natural abundance Re_2O_7 except that the scale of the reaction was reduced by approximately one-eighth.

XeF_2. Xenon difluoride was prepared according to the literature method[182] and stored in a Kel-F tube inside a dry box until needed.

KrF_2. Krypton difluoride was prepared by use of 316 stainless steel hot-wire reactor (Figure 2.7) equipped with a nickel filament, similar to that originally described[183] and subsequently modified.[184] The filament was fabricated from a $^1/_{16}$ -in nickel rod tightly wound about a second length of $^1/_{16}$-in rod that was, in turn, coiled and stretched into a helix. In a typical preparation, the hot-wire reactor was pressurized with 1000 torr (50 mmol) of krypton and then cooled to −196 ^oC in a 20-L Dewar. After reaching thermal equilibrium, the reactor was pressurized with 25 torr of F_2 and the DC power supply for the nickel filament was adjusted to ca. 6 V and 30 A (the filament was dull red in color under these conditions). The F_2 pressure increased to ca. 45 torr after the power supply was tuned on and was regulated between 35 and 45 torr by the periodic addition of F_2 during the synthesis. The decline in F_2 pressure was used to monitor the production of KrF_2, and additional amounts of Kr (1.0 to 2.0 mmol) were condensed into the reactor when the rate of KrF_2 production significantly slowed. Upon completion of the reaction (ca. 12 h), F_2 was removed under dynamic vacuum at −196 ^oC. The excess Kr and crude KrF_2 were recovered as a pink solid (the coloration arises from chromium oxide fluoride

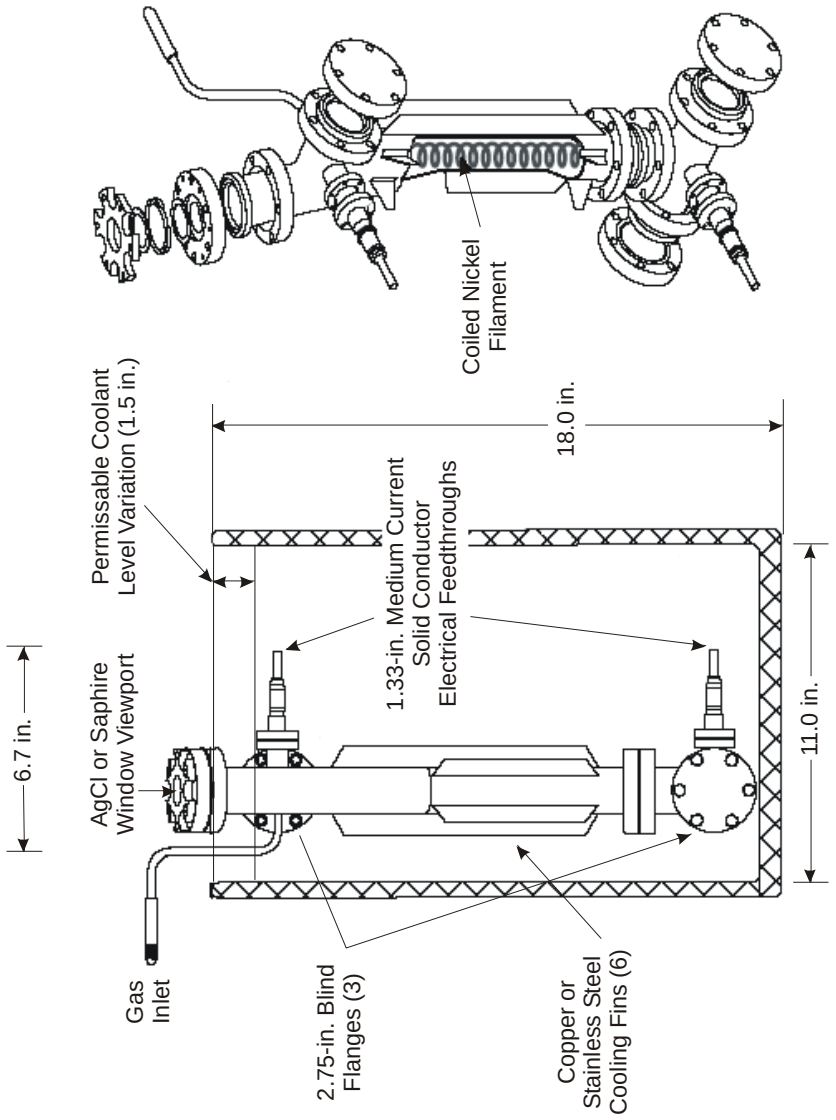

Figure 2.7. The stainless steel hot-wire reactor used for the preparation of KrF_2. (a) An external view and dimensions of a hot-wire reactor submerged in a liquid nitrogen coolant bath. (b) A perspective drawing of the hot-wire reactor showing the flange assembly and nickel filament (cut away region). Reproduced with permission from ref 185.

contamination; most likely CrO_2F_2 which is leached from the surfaces of the stainless steel reactor) by allowing the reactor to slowly warm to room temperature while dynamically pumping the volatile contents through a ½-in o.d. FEP U-trap (−196 °C). The Kr/KrF_2 mixture was then warmed to −78 °C under dynamic vacuum to remove the unreacted Kr. The crude KrF_2 was purified by briefly warming the sample to 0 °C and flash distilling off the more volatile chromium oxide fluorides. The remaining colorless KrF_2 was finally warmed to room temperature and rapidly sublimed into $^3/_8$-in o.d. FEP tube equipped with a Kel-F valve, where it was stored under 1000 torr of N_2 or Ar at −78 °C until used. This synthesis typically yields of ca. 3 to 4 g of pure KrF_2.

XeF_6. Xenon hexafluoride was synthesized by a method similar to that outlined by Chernick and Malm.[186] Xenon (620 torr) was condensed into a nickel vessel (825 mL) at −196 °C, followed by the condensation of excess F_2 gas (13000 torr) ($Xe:F_2$ = 1:22 molar ratio) reaching a total pressure of 56 atm at room temperature. The mixture was heated to 250 °C for 24 h and slowly cooled 47 °C over a period of 72 h before turning off the furnace and allowing the mixture to cool to room temperature. The nickel can, containing XeF_6 and excess F_2, was reconnected to the metal vacuum line through the FEP U-trap and cooled to −196 °C. The pressure of excess F_2 gas was slowly released through a U-trap precooled to −78 °C into a 5 L Monel storage vessel used to recover and recycle fluorine gas. Xenon hexafluoride was condensed in the FEP U-trap at −78 °C and the remaining unreacted F_2 was removed from the U-trap under vacuum at −78 °C. The product was vacuum distilled into a ½-in o.d. FEP storage vessel equipped with a Kel-F valve. The purity was assessed using Raman spectroscopy.

$Re^{16/18}O_2F_3$. Dirhenium heptoxide, Re_2O_7, (0.2670 g; 0.5511 mmol) was weighted inside a dry box into a ¼-in. o.d. FEP reactor. The reactor was connected to a metal vacuum line and ca. 0.35 mL of aHF was condensed onto the solid at –196 ^oC and the contents of the reactor were warmed to room temperature until all Re_2O_7 dissolved forming a pale yellow solution. The solution was frozen inside a dry box in a metal Dewar filled with 4.5 mm copper plated steel spheres (air rifle shot) that had been previously cooled to ca. –140 ^oC in the glass cryowell (–196 ^oC) of the dry box. Xenon difluoride, XeF_2, (0.2799 g; 0.1653 mmol) was weighed into the reactor. The reactor was very quickly removed from the dry box and connected to a metal vacuum line by means of a U-trap. The U-trap and all connections were passivated with ca. 1000 torr of F_2 for several hours. The contents of the reactor were then warmed to room temperature at which temperature all solids dissolved to form a pale yellow solution. As the color of the solution changed to yellow-orange, the reaction mixture rapidly evolved gas (O_2 and Xe), which was periodically released into a vacuum manifold. Over ca. 4 h, a white solid precipitated from the solution, which became very pale yellow to colorless, and gas evolution had ceased. The contents of the reactor were left under aHF and 1 atm of N_2 at room temperature overnight to ensure that the starting material completely reacted. The solvent was subsequently removed under dynamic vacuum at –78 ^oC, leaving behind a white friable solid. The solid was warmed to room temperature and only XeF_2 that remained was also removed under dynamic vacuum. The purity of the solid was checked by Raman spectroscopy. Synthesis of the ^{18}O enriched sample used 0.1627 g (0.3358 mmol) of $Re_2{}^{18}O_7$.

$Re^{16/18}O_3F$. Inside a dry box, Re_2O_7 (0.1399 g, 0.2887 mmol) was weighed into a ¼-in. o.d. FEP reactor equipped with a Kel-F valve. Anhydrous HF (ca. 1 mL) was condensed onto the solid at –196 °C. The solvolysis reaction was allowed to proceed at room temperature, giving a yellow solution. Three aliquots of F_2 (ca. 1050 torr each) were added to the reactor at 24 h intervals over 72 h at –78 °C followed by warming to room temperature. Anhydrous HF solvent was removed under dynamic vacuum at –78 °C. The resulting solid complex, $(HF)_2ReO_3F{\cdot}HF$, was further pumped in stages at –40, –20, 0 °C, and room temperature to remove weakly associated and coordinated HF. Further pumping at 50 °C ensured complete removal of HF and resulted in a pale yellow, friable solid. The Raman spectrum of the product was in excellent agreement with the previously published spectrum of ReO_3F.[21] Syntheses of the ^{18}O enriched samples used similar amounts of $Re_2{}^{18}O_7$.

MnO_3F. In a typical synthesis, $K[MnO_4]$ (~0.11 g, ~0.70 mmol) was weighed into a ¼-in. o.d. FEP reactor equipped with a Kel-F valve and was connected to a glass vacuum line and dried under dynamic vacuum over a period of 24 h. Anhydrous HF (ca. 0.5 mL) was condensed onto the solid at –196 °C. The reactor was subsequently pressurized with ca. 1050 torr of F_2 gas at −78 °C. After the reagents were warmed to −20 °C, solvolysis yielding a two-phase solution occurred. The dense metallic green bottom layer and the deep green transparent top layer consisted of Mn_2O_7 and MnO_3F/HF, respectively. The reaction temperature was maintained at −18 ±2 °C for ca. 6 h, after which it was cooled to –78 °C for ca. 18 h. Two additional aliquots of F_2 (ca. 1050 torr each) were added to the reactor at 24 h intervals over 36 h at –78 °C and the synthetic

steps following F_2 addition were repeated each time. When the reaction of $K[MnO_4]$ with aHF/F_2 was deemed to be complete, the MnO_3F/aHF mixture was isolated by distillation into a separate reactor maintained –196 °C. The aHF/MnO_3F solution was subsequently warmed to −20 °C and allowed to cool to –78 °C, at which temperature deep green needles of MnO_3F grew over a period of ca. 1h. The Raman spectrum was recorded on the crystalline material under frozen aHF.

2.3. Synthesis and Characterization of $(HF)_2ReO_3F{\cdot}HF$ and $[N(CH_3)_4]_2[\{ReO_3(\mu\text{-}F)\}_3(\mu_3\text{-}O)]$ and Attempted Synthesis of $[N(CH_3)_4][\{ReO_3(\mu\text{-}F)\}_3(\mu_3\text{-}F)]$ from ReO_3F and $[N(CH_3)_4]F$ in CH_3CN Solvent

2.3.1. Synthesis of $(HF)_2ReO_3F{\cdot}HF$

Inside a dry box, ReO_3F (0.0587 g, 0.2318 mmol) was weighed into a ¼-in. o.d. FEP reactor equipped with a side arm and a Kel-F valve. Anhydrous HF (ca. 1 mL) was condensed onto ReO_3F at –196 °C. Upon warming the reaction mixture to room temperature, the solid rapidly dissolved, yielding a yellow solution. Cooling of the solution to –78 °C resulted in the deposition of a crystalline white solid. Raman spectra were recorded on the crystalline solid under frozen aHF and on the solid that was subsequently isolated by removal of aHF under dynamic vacuum at –78 °C. Both spectra were identical and confirmed the formation of $(HF)_2ReO_3F{\cdot}HF$.

The $(HF)_2ReO_3F{\cdot}HF$ complex was also obtained in solution from three separate room-temperature aHF (ca. 1 mL) solvolysis reactions of $[NH_4][ReO_4]$ (0.0996 g, 0.3713 mmol), $K[ReO_4]$ (0.1343 g, 0.4641 mmol), and Re_2O_7 (0.1071 g, 0.2211 mmol). The

solutions were subsequently cooled to –78 ^{o}C, which resulted in the deposition of crystalline white solids. The Raman spectra of these solids, which were recorded under frozen aHF at –150 ^{o}C, and unit cell determinations of the single crystals confirmed the formation of $(HF)_2ReO_3F{\cdot}HF$.

2.3.2. Crystal Growth of $(HF)_2ReO_3F{\cdot}HF$ and $KF{\cdot}4HF$

$(HF)_2ReO_3F{\cdot}HF$. Crystals of $(HF)_2ReO_3F{\cdot}HF$ were grown from a pale yellow solution obtained by dissolving ReO_3F (0.0587 g, 0.2318 mmol) in aHF at room temperature. The solution was prepared in a ¼-in. o.d. FEP T-shaped reactor, which was pressurized with ca. 1 atm of dry nitrogen at −78 °C. The solution was slowly cooled to −36 °C inside a crystal growing apparatus (Figure 2.8),[185] whereupon colorless plates formed over a period of 4−5 h. Upon completion of crystal growth, the supernatant was decanted into the side arm, which had been precooled to –196 ^{o}C. The crystalline product was dried under dynamic vacuum at −44 °C before the side arm containing the frozen supernatant was heat-sealed off under dynamic vacuum. A crystal of $(HF)_2ReO_3F{\cdot}HF$ having the dimensions 0.37 x 0.33 x 0.06 mm^3 was selected for a low-temperature X-ray structure determination.

$KF{\cdot}4HF$. Crystals of $KF{\cdot}4HF$ were grown from a pale yellow solution obtained by dissolving 0.1343 g (0.4641 mmol) of $K[ReO_4]$ in ca. 2 mL of aHF at room temperature. The solution was prepared in a ¼-in. o.d. FEP T-shaped reactor which was pressurized with ca. 1 atm. of dry nitrogen at –78 ^{o}C. The solution was slowly cooled to –71 ^{o}C inside a low-temperature crystal growing apparatus (Figure 2.8),[185]

whereupon colorless plates formed over a period of 4−5 h. Upon completion of crystal growth, the supernatant was decanted into the side arm, which had been precooled to –196 ^{o}C. The crystalline product was dried under dynamic vacuum at −78 °C before the side arm containing the frozen supernatant was heat-sealed off under dynamic vacuum. A crystal of KF·4HF having the dimensions 0.04 x 0.17 x 0.16 mm^3 was selected for a low-temperature X-ray structure determination.

2.3.3. Synthesis of $[N(CH_3)_4]_2[\{ReO_3(\mu\text{-}F)\}_3(\mu_3\text{-}O)]$

Inside a dry box, ReO_3F (0.0484 g, 0.1912 mmol) and $[N(CH_3)_4]F$ (0.0182 g, 0.1958 mmol) were weighed into a ¼-in. o.d. FEP reactor at room temperature. The solids were removed from the dry box and cooled to and maintained at –78 ^{o}C until dry CH_3CN was condensed onto the solids at –196 ^{o}C. A white solid commenced to form upon warming the sample to –40 ^{o}C. The reactor was slowly warmed to –20 ^{o}C, at which temperature the solid became light beige in color. The solid had partial solubility at –10 ^{o}C, however, complete dissolution was only attained at room temperature. Acetonitrile was removed under dynamic vacuum at –40 ^{o}C and the product was completely dried by further pumping at room temperature. The low-temperature Raman spectrum of the dried product corresponded to a mixture of $[N(CH_3)_4]_2[\{ReO_3(\mu\text{-}F)\}_3(\mu_3\text{-}O)]\cdot CH_3CN$, $[N(CH_3)_4][ReO_4]$, and $[N(CH_3)_4][ReO_2F_4]$.[19]

2.3.4. Crystal Growth of $[N(CH_3)_4]_2[\{ReO_3(\mu\text{-}F)\}_3(\mu_3\text{-}O)]$ and $[N(CH_3)_4][ReO_4]$

$[N(CH_3)_4]_2[\{ReO_3(\mu\text{-}F)\}_3(\mu_3\text{-}O)]$. Crystals of $[N(CH_3)_4]_2[\{ReO_3(\mu\text{-}F)\}_3(\mu_3\text{-}O)]\cdot CH_3CN$ were grown from a bright yellow solution obtained by dissolution of 0.0694 g of a reaction mixture containing $[N(CH_3)_4]_2[\{ReO_3(\mu\text{-}F)\}_3(\mu_3\text{-}O)]$, $[N(CH_3)_4][ReO_4]$, and $[N(CH_3)_4][ReO_2F_4]$ (see Syntheses of ReO_3F, $(HF)_2ReO_3F$, and $[N(CH_3)_4]_2[\{ReO_3(\mu\text{-}F)\}_3(\mu_3\text{-}O)]$) in CH_3CN at room temperature. The solution was prepared in a ¼-in. o.d. FEP T-shaped reactor followed by pressurization with ca. 1 atm of dry nitrogen. Cooling the solution to −1 °C inside a crystal growing apparatus (Figure 2.8)[185] resulted in the formation of colorless plates over a period of 1.5−2 h. Upon completion of crystal growth, the supernatant was decanted into the side arm, which had been precooled to –196 °C. The crystalline product was dried under dynamic vacuum at −5 °C before the side arm containing the frozen supernatant was heat-sealed off under dynamic vacuum. A crystal of $[N(CH_3)_4]_2[\{ReO_3(\mu\text{-}F)\}_3(\mu_3\text{-}O)]\cdot CH_3CN$ having the dimensions 0.24 x 0.12 x 0.06 mm^3 was selected for a low-temperature X-ray structure determination.

$[N(CH_3)_4][ReO_4]$. Crystals of $[N(CH_3)_4][ReO_4]$ were obtained from the reaction of ReO_3F (0.0368 g, 0.1454 mmol) and $[N(CH_3)_4]F$ (0.0273 g, 0.2935 mmol) at −35 °C in CH_3CN in a ¼-in. o.d. FEP T-shaped reactor. The white solid partially dissolved in CH_3CN at room temperature forming a pale yellow solution. The solution was cooled to −3 °C inside a crystal growing apparatus,[185] whereupon colorless block-shaped crystals formed over a period of 3−4 h. The solution was further cooled to −5 °C for 1 h to ensure that crystallization is complete. Upon completion of crystal growth, the supernatant was decanted into the side arm, which had been precooled to –196 °C. The crystalline product

was dried under dynamic vacuum at −5 °C before the side arm containing the frozen supernatant was heat-sealed off under dynamic vacuum. A crystal of $[N(CH_3)_4][ReO_4]$ having the dimensions 0.15 x 0.30 x 0.31 mm^3 was selected for a low-temperature X-ray structure determination.

2.3.5. Attempted Synthesis of $[N(CH_3)_4][\{ReO_3(\mu\text{-}F)\}_3(\mu_3\text{-}F)]$ from ReO_3F and $[N(CH_3)_4]F$ in CH_3CN Solvent

Inside a dry box, ReO_3F (0.0853 g, 0.3369 mmol) and $[N(CH_3)_4]F$ (0.0110 g, 0.1179 mmol) were weighed into a ¼-in. o.d. FEP reactor equipped with a side arm and a Kel-F valve. The solid mixture was removed from the dry box and maintained at –78 ^oC until dry CH_3CN was condensed onto the mixture at –196 ^oC. A white solid formed upon warming to –35 ^oC. The reaction mixture was slowly warmed in stages to –20, –10 ^oC, and room temperature, at which temperature the product showed partial solubility. The low-temperature Raman spectrum of the precipitated product under CH_3CN corresponded to a mixture of $[N(CH_3)_4][ReO_4]$ and $(CH_3CN)_2ReO_3F$.

2.4. Syntheses and Characterization of $Cs[ReO_3F_2]$, $Cs_2[ReO_3F_3]$, $[NO][ReO_3F_2]$, $[NO]_2[ReO_3F_3]$, $M[ReO_3F_2]$ (M = K, $[NH_4]$), $K[H_3O][ReO_3F_3]$, and $(\mu\text{-}F)_4\{[\mu\text{-}^{16/18}O(Re^{16/18}O_2F)_2](Re^{16/18}O_2F_2)_2\}\cdot SO_2ClF$

Although the syntheses of the *fac*-$[ReO_3F_3]^{2-}$ (Cs^+, $[NO]^+$, and $K^+[H_3O]^+$) and $[ReO_3F_2]^-$ (Cs^+, $[NO]^+$, K^+, $[NH_4]^+$) anions were reproduced several times, the above salts always formed in admixtures with the corresponding salts of the $[ReO_2F_4]^-$ and/or [μ-

$F(ReO_2F_3)]^-$, and $[ReO_4]^-$ anions. The Raman frequencies and intensities of individual salts were assigned by comparison of the various Raman spectra recorded on the product mixtures resulting from the same reaction and/or the Raman spectra recorded on product mixtures resulting from different reactions. Additionally, the Raman bands were assigned by comparison with the previously published Raman frequencies and intensities for the $M[ReO_4]$ (M = $[NH_4]$, K, Cs),[187] $M[ReO_2F_4]$[19] (M = $[NH_4]$, K, Cs), and $K[\mu\text{-}F(ReO_2F_3)]$[19] salts.

Crystals of $\mu\text{-}F)_4\{[\mu\text{-}O(ReO_2F)_2](ReO_2F_2)_2\}\cdot SO_2ClF$ and $M[ReO_3F_2]$ (M = K, $[NH_4]$, [NO], Cs) and $K[H_3O][ReO_3F_3]$ were grown from their corresponding SO_2ClF and aHF solutions at room temperature by static distillation of aHF into the side arms of the reactors that were precooled to −78 °C (dry ice/acetone bath). The colorless crystals of $M[ReO_3F_2]$ (M = K, $[NH_4]$, [NO], Cs), $K[H_3O][ReO_3F_3]$, and $(\mu\text{-}F)_4\{[\mu\text{-}O(ReO_2F)_2](ReO_2F_2)_2\}\cdot SO_2ClF$ were isolated by heat-sealing the side arms at –196 °C and any residual solvent was removed under dynamic vacuum. The portion of the reactor containing the dry crystalline product was backfilled with dry N_2 and stored at –78 °C until the crystals could be mounted on the diffractometer.

2.4.1. Synthesis of $Cs[ReO_3F_2]$ and $Cs_2[ReO_3F_3]$

In a typical synthesis, ReO_3F (0.0638 g, 0.2519 mmol) and CsF (0.0385 g, 0.2534 mmol) corresponding to a 1:1 molar ratio and ReO_3F (0.0918 g, 0.3626 mmol) and CsF (0.0953 g, 0.6273 mmol) corresponding to a 1:2 molar ratio were weighed into two separate ¼-in. o.d. FEP T-shaped reactors inside a dry box. Anhydrous HF (ca. 0.3 and 0.4 mL,

respectively) was condensed onto the solids at –196 ^{o}C. The reactions proceeded at room temperature, yielding pale yellow solutions. When the solutions were cooled to –78 ^{o}C, a small amount of the colorless crystalline material formed in both reactors. The Raman spectra of these crystalline products under frozen aHF corresponded to only $Cs[ReO_2F_4]$. Subsequently, both reactors were rewarmed to –78 ^{o}C at which temperature aHF was removed under dynamic vacuum, leaving white solid products behind. The white products were subsequently dried under dynamic vacuum at room temperature. The low-temperature Raman spectra were assigned to the $Cs_2[ReO_3F_3]$, $Cs[ReO_3F_2]$, $Cs[ReO_2F_4]$ and $Cs[\mu\text{-}F(ReO_2F_3)]$ salts for both 1:1 and 1:2 molar ratios of ReO_3F and CsF. The product mixtures were subsequently re-dissolved in aHF at room temperature and crystals of $Cs[ReO_3F_2]$ were grown by static distillation of aHF into a pre-cooled side arm in admixture with $Cs_2[ReO_3F_3]$, $Cs[ReO_4]$, $Cs[ReO_2F_4]$, and $Cs[\mu\text{-}F(ReO_2F_3)]$ salts, which precipitated as white solids. The Raman spectra, where bands corresponding to $Cs_2[ReO_3F_3]$ and $Cs[ReO_3F_2]$, respectively, appear as the most intense bands were chosen for further vibrational analyses.

2.4.2. Crystal Growth of $Cs[ReO_3F_2]$

Crystals of $Cs[ReO_3F_2]$ were grown from a pale yellow solution prepared by reacting ReO_3F (0.0522 g, 0.2062 mmol) with CsF (0.0652 g, 0.4292 mmol) in aHF (ca. 0.4 mL). Colorless block-shaped crystal of $Cs[ReO_3F_2]$ grew over a period of 72 h. A crystal of $Cs[ReO_3F_2]$ having the dimensions 0.07 x 0.12 x 0.21 mm^3 was selected for a low-temperature X-ray structure determination.

2.4.3. Crystal Growth of $Cs[ReO_2F_4]$ and $Cs[\mu\text{-}F(ReO_2F_3)]$

Crystals of $Cs[ReO_2F_4]$ and $Cs[\mu\text{-}F(ReO_2F_3)_2]$ were grown from a pale yellow solution prepared by reacting ReO_3F (0.0602 g, 0.2376 mmol) with CsF (0.0698 g, 0.4597 mmol) in aHF in a ¼-in. o.d. FEP reaction vessel equipped with a side arm (T-shaped reactor)[X] and fitted with a Kel-F valve. The main arm of the reaction vessel containing the solution was placed inside the glass dewar of the crystal growing apparatus precooled to −33 °C and the temperature of the dewar and contents was slowly lowered to −40 °C to induce slow crystal growth. Colorless plates formed over a period of 5−6 h. Upon completion of crystal growth, the supernatant was decanted into the side arm, which had been precooled to –196 ^{o}C. The crystalline products were dried under dynamic vacuum at −45 °C before the side arm containing the frozen supernatant was heat-sealed off under dynamic vacuum. The portion of the reactor containing the dry crystalline products were backfilled with dry N_2 and stored at –78 ^{o}C until the crystals could be mounted. A crystal of $Cs[ReO_2F_4]$ having the dimensions 0.11 x 0.27 x 0.33 mm^3 and a crystal of $Cs[\mu\text{-}F(ReO_2F_3)_2]$ having the dimensions 0.12 x 0.31 x 0.31 mm^3 were selected for a low-temperature X-ray structure determination.

2.4.4. Synthesis of $[NO]_2[ReO_3F_3]$ and $[NO][ReO_3F_2]$

$[NO]_2[ReO_3F_3]$. Inside a dry box, ReO_3F (0.1071 g, 0.4230 mmol) was weighed into a ¼-in. o.d. FEP reactor equipped with a side arm and a Kel-F valve. The transfer of excess NOF was carried out by passing it through a fluorine-passivated FEP submanifold (dedicated to this use) that was passivated twice with NOF prior to its condensation into an intermediate

FEP vessel at −196 °C. This served to verify the passivation of the submanifold was complete. In the event of incomplete passivation, a distinct blue to light blue color appeared in the intermediate vessel that resulted from the reaction of NOF with residual moisture and/or unpassivated metal surfaces, to give intense blue N_2O_3.

The reactor was warmed to −20 °C and was held at this temperature until all, but trace amounts, of ReO_3F had reacted and a white solid formed (ca. 4 days). The Raman spectrum was assigned to $[NO]_2[ReO_3F_3]$ and to trace amounts of unreacted ReO_3F, $[NO][ReO_4]$ and $[NO][ReO_2F_4]$, which were assigned by comparison with the Raman spectra of known $[ReO_4]^-$ [187] and $[ReO_2F_4]^-$ [19] salts. The solid mixture was isolated as a white solid by removal of residual NOF under dynamic vacuum over a period of ca. 8 h at −78 °C. Upon distillation of aHF into the reactor, a portion of the white solid mixture dissolved at −78 °C. The Raman spectrum of the insoluble solid under frozen aHF was assigned to $[NO][ReO_3F_2]$. When aHF was removed under dynamic vacuum at −78 °C, a soluble product, which deposited on top of unsolvolyzed $[NO][ReO_3F_2]$, proved to be $[NO][ReO_2F_4]$ by Raman spectroscopy.

$[NO][ReO_3F_2]$. Inside a dry box, ReO_3F (0.0659 g, 0.2601 mmol) was weighed into a ¼-in. o.d. FEP reactor equipped with a side arm and a Kel-F valve. The transfer of excess NOF was carried out as described above. The reactor was warmed to −20 °C and was held at this temperature until all ReO_3F reacted (ca. 2 days) and white $[NO]_2[ReO_3F_3]$ formed in admixture with $[NO][ReO_2F_4]$ and $[NO][ReO_4]$. Pumping off residual NOF at −78, −20 °C, and room temperature for 19 h, provided a white solid mixture of $[NO][ReO_3F_2]$, $[NO][ReO_2F_4]$ and $[NO][ReO_4]$, which was confirmed by Raman spectroscopy. A Raman

spectrum, where the bands corresponded to by-products, $[NO][ReO_2F_4]$ and $[NO][ReO_4]$, were at concentration that were too low to be observed was used for the vibrational analysis.

2.4.5. Crystal Growth of $[NO][ReO_3F_2]$ and $[NO][ReO_2F_4]$

Crystals of $[NO][ReO_3F_2]$ were grown from a pale yellow solution obtained by dissolution of a reaction mixture prepared as described above (see Synthesis of $[NO][ReO_3F_2]$) in aHF (ca. 0.3 mL) at room temperature. Additionally, the crystals of one of the reaction by-products, $[NO][ReO_2F_4]$, also grew. Colorless blocks of $[NO][ReO_3F_2]$ and colorless plate-like crystals of $[NO][ReO_2F_4]$ grew over a period of 48 h. A crystal of $[NO][ReO_3F_2]$ having the dimensions 0.05 x 0.13 x 0.21 mm^3 was selected for a low-temperature X-ray structure determination and a crystal of $[NO][ReO_2F_4]$ having the dimensions 0.09 x 0.23 x 0.26 mm^3 was selected for the unit cell determination.

2.4.6. Syntheses of $M[ReO_3F_2]$ (M = K, $[NH_4]$) and $K[H_3O][ReO_3F_3]$

Inside a dry box, $[NH_4][ReO_4]$ (0.09959 g, 0.3713 mmol) and $K[ReO_4]$ (0.1343 g, 0.4641 mmol) were weighed into their respective ¼-in. o.d. FEP reactors equipped with a side arm and a Kel-F valve. Anhydrous HF (ca. 1.5 mL) was condensed onto each solid at –196 ^oC and the reactions were allowed to proceed at room temperature and resulted in yellow solutions. Upon cooling the solutions from −71 to –78 ^oC, $ReO_3F{\cdot}2HF$ crystallized in both reactors as was confirmed by Raman spectroscopy. White solid mixtures of $M[ReO_3F_2]$, $M[ReO_4]$, $M[\mu\text{-}F(ReO_2F_3)]$, $M[ReO_2F_4]$, (M = K, $[NH_4]$), and $K[H_3O][ReO_3F_3]$ were isolated in their corresponding reactors by removal of aHF under dynamic vacuum at –

78 ^{o}C and room temperature as confirmed by Raman spectroscopy. The product mixtures were subsequently re-dissolved in aHF at room temperature and the resultant yellow solutions were used for crystal growth. The Raman spectra were recorded on the crystalline material isolated in admixture with the precipitated white solid(s). A Raman spectrum, where the bands corresponded to a mixture of $K[ReO_3F_2]$ and $K[H_3O][ReO_3F_3]$ were of highest intensity was used for vibrational analysis.

2.4.7. Crystal Growth of $M[ReO_3F_2]$ (M = K, $[NH_4]$), $K[H_3O][ReO_3F_3]$, and $[NH_4][\mu\text{-}F(ReO_2F_3)_2]$

$[NH_4][ReO_3F_2]$ and $[NH_4][\mu\text{-}F(ReO_2F_3)_2]$. Crystals of $[NH_4][ReO_3F_2]$ were grown from a pale yellow solution obtained by dissolution of a mixture containing $[NH_4][ReO_3F_2]$, $[NH_4][ReO_2F_4]$ and/or $[NH_4][\mu\text{-}F(ReO_2F_3)_2]$, and $[NH_4][ReO_4]$ in aHF (see Syntheses of $M[ReO_3F_2]$ (M = K, $[NH_4]$) and $K[H_3O][ReO_3F_3]$). In the process, the crystals of one of the reaction by-products, $[NH_4][\mu\text{-}F(ReO_2F_3)_2]$, also grew. Colorless plates of $[NH_4][ReO_3F_2]$ and $[NH_4][\mu\text{-}F(ReO_2F_3)_2]$ grew over a period of 72 h. A crystal of $[NH_4][ReO_3F_2]$ and $[NH_4][\mu\text{-}F(ReO_2F_3)_2]$ having the dimensions 0.16 x 0.19 x 0.37 mm^3 and 0.12 x 0.31 x 0.28 mm^3 were selected for a low-temperature X-ray structure determination and a unit cell determination, respectively.

$K[ReO_3F_2]$ and $K[H_3O][ReO_3F_3]$. Crystals of $K[ReO_3F_2]$ and $K[H_3O][ReO_3F_3]$ were grown from a pale yellow solution obtained by dissolution of a reaction mixture containing $K[ReO_3F_2]$, $K[ReO_2F_4]$ and/or $K[\mu\text{-}F(ReO_2F_3)_2]$, $K[ReO_4]$, and $K[H_3O][ReO_3F_3]$ (see Syntheses of $M[ReO_3F_2]$ (M = K, $[NH_4]$) and $K[H_3O][ReO_3F_3]$).

Colorless crystalline blocks of $M[ReO_3F_2]$ (M = K, $[NH_4]$) and $K[H_3O][ReO_3F_3]$ grew over a period of 72 h. Crystals of $K[ReO_3F_2]$ and $K[H_3O][ReO_3F_3]$ having the dimensions 0.10 x 0.11 x 0.11 mm^3 and 0.18 x 0.25 x 0.32 mm^3, respectively, were selected for a low-temperature X-ray structure determination.

2.4.8. Synthesis of $(\mu\text{-}F)_4\{[\mu\text{-}^{16/18}O(Re^{16/18}O_2F)_2](Re^{16/18}O_2F_2)_2\}$ and Crystal Growth of $(\mu\text{-}F)_4\{[\mu\text{-}O(ReO_2F)_2](ReO_2F_2)_2\}\cdot SO_2ClF$

Inside a dry box, ReO_3F (0.0401 g 0.1580 mmol) and ReO_2F_3 (0.1304 g (0.4739 mmol) were weighed into a ¼-in. o.d. FEP T-shaped reactor equipped with a side arm and a Kel-F valve. The solid mixture was removed from the dry box and maintained at –78 ^oC until SO_2ClF was condensed onto the solids at –78 ^oC. The solid mixture slowly dissolved upon warming the reactor to room temperature forming a colorless solution. The product was isolated as colorless needle-shaped crystals by static distillation of the solvent into the reactor side arm, which had been pre-cooled to −78 °C under ca. 1 atm of dry N_2 followed by removal of the solvent under dynamic vacuum. The reactor was consequently backfilled with ca. 1 atm of dry N_2 and a Raman spectrum was recorded on the crystalline compound. The dry crystalline product was stored at –78 ^oC until the crystals could be mounted. A crystal of $(\mu\text{-}F)_4\{[\mu\text{-}O(ReO_2F)_2](ReO_2F_2)_2\}\cdot SO_2ClF$ having the dimensions 0.024 x 0.036 x 0.121 mm^3 was selected for a low-temperature X-ray structure determination. The ^{18}O-enriched sample, $(\mu\text{-}F)_4\{[\mu\text{-}^{18}O(Re^{18}O_2F)_2](Re^{18}O_2F_2)_2\}$, was synthesized from enriched $Re^{18}O_3F$ (0.0485 g, 0.1936 mmol) and $Re^{18}O_2F_3$ (0.1598 g, 0.5807 mmol).

Crystals of $(\mu\text{-}F)_4\{[\mu\text{-}O(ReO_2F)_2](ReO_2F_2)_2\}\cdot SO_2ClF$ were grown from a SO_2ClF solution of the product formed in the reaction of ReO_3F 0.0401 g (0.1580 mmol) with ReO_2F_3 0.1304 g (0.4739 mmol). Colorless, needle-shaped crystals of $(\mu\text{-}F)_4\{[\mu\text{-}O(ReO_2F)_2](ReO_2F_2)_2\}\cdot SO_2ClF$ having the dimensions 0.024 x 0.036 x 0.121 mm^3 were selected for a low-temperature X-ray structure determination.

2.5. Syntheses of $\mu\text{-}O(ReO_2F)(AsF_5)\cdot 2AsF_5$, $[ReO_3][Sb_3F_{16}]$, and $[O_3Re(NCCH_3)_3][PnF_6]$ (Pn = As, Sb)

2.5.1. Synthesis of $\mu\text{-}O(ReO_2F)(AsF_5)\cdot 2AsF_5$

In the dry box, 0.0916 g (0.3616 mmol) of ReO_3F was weighed into a ¼-in. o.d. FEP T-shaped reactor equipped with a Kel-F valve. An excess of AsF_5 (860 torr, 0.9598 mmol) was condensed onto ReO_3F at –196 ^oC. An insoluble, dense white solid started to form upon warming to −50 ^oC, but the reaction was completed after reacting ReO_3F with AsF_5 at −20 ^oC until no ReO_3F remained. Excess AsF_5 was removed under dynamic vacuum at –78 ^oC. The white solid was found to be unstable toward dissociation into the starting materials at 0 ^oC, however, the reaction is reversible at –78 ^oC. Complete removal of AsF_5 under dynamic vacuum at room temperature led to the formation of ReO_3F, which was confirmed by low-temperature Raman spectroscopy. The white solid was identified as $\mu\text{-}O(ReO_2F)(AsF_5)\cdot 2AsF_5$. This compound is insoluble in aHF up to –25 ^oC, at which temperature solvolysis takes place, yielding ReO_2F_3 and $[H_3O][AsF_6]$. The $\mu\text{-}O(ReO_2F)(AsF_5)\cdot 2AsF_5$ salt is also insoluble in SO_2ClF and CH_2Cl_2.

2.5.2. Synthesis of $[ReO_3][Sb_3F_{16}]$

In the dry box, 0.2454 g (0.9692 mmol) of ReO_3F was weighed into a ¼-in. o.d. FEP reactor equipped with a Kel-F valve. Antimony pentafluoride, SbF_5, (0.8386 g, 3.399 mmol) was condensed onto ReO_3F at –196 ^oC. Subsequently ca. 0.8 mL of SO_2ClF (see Figure 2.4) was condensed onto a mixture of SbF_5 and ReO_3F at –78 ^oC. The reactor was allowed to warm to room temperature, at which temperature the solid became white over period of 1 h. The solvent and excess SbF_5 were removed under dynamic vacuum at room temperature leaving a dry friable solid behind. The Raman spectrum of the solid (0.7596 g, 0.8408 mmol) was attributed to $[ReO_3][Sb_3F_{16}]$. The $[ReO_3][Sb_3F_{16}]$ salt is insoluble in SO_2ClF and CH_2Cl_2. The solid slowly decomposes to $[ReO_2F_2][SbF_5]$ at temperature above 40 ^oC.

2.5.3 Syntheses and Crystal Growth of $[O_3Re(NCCH_3)_3][PnF_6]$ (Pn = As, Sb)

The μ-$O(ReO_2F)(AsF_5)\cdot 2AsF_5$ and $[ReO_3][Sb_3F_{16}]$ salts were prepared in their corresponding ¼-in. o.d. FEP T-shaped reactors from 0.0572 g (0.2259 mmol) and 0.0907 g (0.3582 mmol) of ReO_3F as described in sections 2.6.1 and 2.6.2, respectively. Acetonitrile (ca. 0.5 mL) was distilled onto both solids at –196 ^oC. The contents of both reactors were subsequently warmed to room temperature, at which temperature both solids dissolved forming viscous yellow solutions. The Raman spectra recorded on the products precipitated at –78 ^oC were assigned to $[O_3Re(NCCH_3)_3][PnF_6]$ (Pn = As, Sb). Both compounds were isolated as white solids by removal of CH_3CN under dynamic

vacuum at room temperature. The Raman spectra of the dry products were identical to those recorded under frozen CH_3CN.

Crystals of both salts were grown from their respective yellow solutions from −10 to −15 °C in low-temperature baths over a 4 to 5 h period under ca. 1 atm of dry nitrogen. The crystals of both compounds were isolated by decanting the solvent at –15 ^{o}C under dry nitrogen into the side arms of the FEP vessels, which were immersed in liquid nitrogen, followed by drying of the crystalline products under dynamic vacuum at –15 ^{o}C before the side arms were heat-sealed under dynamic vacuum at –196 ^{o}C. The portion of the reactor containing the dry crystalline products were backfilled with dry N_2 and stored at –78 ^{o}C until the crystals could be mounted. The examination of the crystalline products under microscope revealed that the crystals were covered in residual frozen solvent that could not be pumped off at –15 ^{o}C. This resulted in failed attempts to mount isolated single crystals. An attempt to remove the solvent at temperatures above –15 ^{o}C resulted in formation of white solid.

An attempt to dissolve the mixture of $[O_3Re(NCCH_3)_3][SbF_6]$ and $[ReO_2F_2][SbF_6]$ salts in CH_2Cl_2 resulted in formation of a colorless suspension under a yellow solution. The reaction content was left at –78 ^{o}C for ca. 3 weeks, however, no crystals grew over this period of time.

2.5.4. Attempted Synthesis of $[ReO_3][AsF_6]$ by the Reaction of ReO_3F with AsF_5 in aHF

Inside a dry box, 0.1031 g (0.4072 mmol) of ReO_3F was weighed into a ¼-in. o.d. FEP T-shaped reactor equipped with a Kel-F valve. Anhydrous HF (ca. 0.3 mL) was condensed onto the solid at –196 ^oC. Rhenium trioxide fluoride readily dissolved at room temperature giving rise to a yellow solution. The solution was cooled to –196 ^oC and one equivalent of AsF_5 (400 torr, 0.414 mmol) was condensed into the reactor. An insoluble, dense white solid began to form at –78 ^oC. The low-temperature Raman spectrum of the solid revealed that the only product of the reaction at –78 ^oC was ReO_2F_3.[19] Upon warming the reaction mixture to room temperature, excess AsF_5 reacted with ReO_2F_3 forming the $[ReO_2F_2][AsF_6]$[22] salt.

2.5.5. Attempted Synthesis of $[ReO_3][SbF_6]$ by the 1:1 Molar Ratio Reaction of ReO_3F with SbF_5 in aHF

Rhenium trioxide fluoride (0.0547 g, 0.2162 mmol) was transferred inside a N_2 filled dry box onto a frozen HF solution of SbF_5 (0.045 g, 0.2069 mmol) contained in a ¼-in. o.d. FEP T-shaped reactor fitted with a Kel-F valve. The SbF_5 solution had been prepared by distilling ca. 0.5 mL of HF onto SbF_3 (0.0367 g, 0.2069 mmol) followed by the addition of 1000 torr of F_2 every ½ h for 1½ h. The reactor was quickly removed from the dry box and allowed to warm up to –78 ^oC, at which temperature a white solid formed. The solid was subsequently warmed to room temperature, at which temperature

the reaction was complete. The low-temperature Raman spectrum of the solid corresponded to ReO_2F_3.[19]

2.5.6. Attempted Synthesis of $[ReO_3][Sb_2F_{11}]$ by the 1:2 Molar Ratio Reaction of ReO_3F with SbF_5 in aHF

Rhenium trioxide fluoride (0.14013 g, 0.7840 mmol) was transferred inside a N_2 filled dry box onto a frozen HF solution of SbF_5 (0.09926 g, 0.3920 mmol) contained in a ¼-in. o.d. FEP T-shaped reactor fitted with a Kel-F valve. The SbF_5 solution had been prepared by distilling ca. 0.5 mL of aHF onto SbF_3 (0.09926 g, 0.3920 mmol) followed by the addition of 1000 torr of F_2 every ½ h for 3 h. The reactor was quickly removed from the dry box and allowed to warm to –78 ^oC. The reaction commenced at –78 ^oC with the formation of an insoluble white product, which was isolated at –78 ^oC under dynamic vacuum. The Raman spectrum recorded on the product corresponded to $[H_3O][SbF_6]$ and a rhenium oxide fluoride, which was tentatively assigned to $[ReO_2F_2 \cdot HF][SbF_6]$. The product mixture was subsequently warmed to –60 ^oC and kept at this temperature for ca. 30 min. The Raman spectrum recorded on the solid corresponded to $[ReO_2F_2][SbF_6]$.[22] Finally, the contents of the reactor were warmed to room temperature and droplets of liquid (presumably aHF) appeared on the reactor's wall. The Raman spectrum of the room temperature solid also corresponded to $[ReO_2F_2][SbF_6]$.[22]

2.5.7. Attempted Synthesis of [μ-F(ReO_3)][SbF_6] by the 2:1 Molar Ratio Reaction of ReO_3F with SbF_5 in aHF

Rhenium trioxide fluoride (0.0999 g, 0.3946 mmol) was transferred inside a N_2 filled dry box onto a frozen aHF solution of SbF_5 (0.043 g, 0.1973 mmol) contained in a ¼-in. o.d. FEP T-shaped reactor fitted with a Kel-F valve. The SbF_5 solution had been prepared by distilling ca. 0.5 mL of HF onto SbF_3 (0.03527 g, 0.1973 mmol), followed by the addition of 1000 torr of F_2 every ½ h for 1½ h. The resulting SbF_5 was in slight excess (8 mol%) relative to ReO_3F. The reactor was quickly removed from the dry box and allowed to warm successively to –78, –50, and –40 ^oC, until the reaction was complete. The white solid mixture that had formed dissolved at room temperature forming a pale yellow solution. The Raman spectrum of the products that precipitated from the pale yellow solution at –78 ^oC was assigned to $[H_3O][ReO_2F_4]\cdot[H_3O][SbF_6]$, $[H_3O][ReO_2F_4]$, and an unidentified rhenium oxide fluoride.

Crystals of $[H_3O][ReO_2F_4]\cdot[H_3O][SbF_6]$ were grown from the pale yellow solution (see section 2.6.4.) in a ¼-in. o.d. FEP T-shaped reactor that was placed at a 45^o angle with respect to the horizontal plane in a Dewar containing a dry ice/acetone bath. The previous solution, which was saturated at ca. –15 ^oC, was slowly cooled from –15 to –25 ^oC over the course of 6 h. When crystal growth was deemed complete, the reactor was quickly transferred into a crystal growing apparatus[185] that was previously cooled to −25 ^oC. Colorless crystals were isolated by decanting the solvent at –35 ^oC under dry nitrogen into the side arm of the FEP vessel, which was immersed in liquid nitrogen. This was followed by drying of the crystalline product under dynamic vacuum at –35 ^oC

before the side arm was heat-sealed under dynamic vacuum at –196 ^{o}C. The portion of the reactor containing the dry crystalline product was backfilled with dry N_2 and stored at –78 ^{o}C until the crystals were mounted. A crystal of $[H_3O][ReO_2F_4]\cdot[H_3O][SbF_6]$ having the dimensions 0.168 x 0.189 x 0.340 mm^3 was selected for a low-temperature X-ray structure determination. Attempted crystallization of an unidentified rhenium oxide fluoride at temperatures between –78 ^{o}C to 0 ^{o}C was unsuccessful.

2.5.8. Attempted Synthesis of $[ReO_3][BF_4]$ by the Reaction of ReO_3F with BF_3 in aHF

Inside a N_2 filled dry box, 0.0711 g (0.2808 mmol) of ReO_3F was weighed into a ¼-in. o.d. FEP T-shaped reactor equipped with a Kel-F valve. Anhydrous HF (ca. 0.3 mL) was condensed onto the solid at –196 ^{o}C. Rhenium trioxide fluoride, ReO_3F, readily dissolved at room temperature giving rise to a yellow solution. The solution was cooled to –196 ^{o}C and a sixfold excess of BF_3 was condensed onto the ReO_3F at –196 ^{o}C. An insoluble, dense, white solid formed upon warming to −78 ^{o}C. Excess BF_3 was then removed under dynamic vacuum at –78 ^{o}C. The low-temperature Raman spectrum of the solid corresponded to ReO_2F_3.[19] When all BF_3 was removed under dynamic vacuum at room temperature, some unreacted ReO_3F still remained in the reactor.

2.5.9. Attempted Syntheses of $[ReO_3][BF_4]$ by the Reaction of ReO_3F with BF_3

Inside a N_2 filled dry box, 0.0465 (0.1836 mmol) of ReO_3F was weighed into a ¼-in. o.d. FEP T-shaped reactor equipped with a Kel-F valve. Boron trifluoride, BF_3, (1052

torr) was condensed directly onto ReO_3F at –196 ^oC in the absence of a solvent. The contents of the reactor were warmed to −78 ^oC and maintained at this temperature for ca. 24 h. When the temperature of the reaction mixture was gradually increased to 80 ^oC, ReO_3F remained inert towards BF_3. The Raman spectrum of the solid corresponded to unreacted ReO_3F.

2.6. Synthesis and Characterization of $[Xe^{16/18}OXe^{16/18}OXe][\mu\text{-}F(Re^{16/18}O_2F_3)_2]_2$

2.6.1. Synthesis and Crystal Growth of $[Xe^{16/18}OXe^{16/18}OXe][\mu\text{-}F(Re^{16/18}O_2F_3)_2]_2$

The salt, $[XeOXeOXe][\mu\text{-}F(ReO_2F_3)_2]_2$, was synthesized by reaction of XeF_2 with ReO_3F (Chapter 6, eqs 6.1−6.5). A range of reactant ratios was explored to determine if other xenon(II) oxide cations could be formed; however, only $[XeOXeOXe][\mu\text{-}F(ReO_2F_3)_2]_2$ was isolated. The following molar ratios of reactants were investigated: XeF_2: ReO_3F = 2.11:1.00, [0.1208 g, 0.7136 mmol: 0.0857 g, 0.3385 mmol]; 1.19:1.00, [0.0570 g, 0.3366 mmol: 0.0694 g, 0.2827 mmol]; 1.18:1.00, [0.0893 g, 0.5275 mmol: 0.1132 g, 0.4471 mmol], 1.14:1.00 [0.0638 g, 0.3769 mmol: 0.0839 g, 0.3315 mmol], 1.02:1.00 [0.0546 g, 0.3222 mmol: 0.0805 g, 0.3179 mmol], and 0.56:1.00 [0.0361 g, 0.2131 mmol: 0.0964 g, 0.3806 mmol]; XeF_2: $Re^{18}O_3F$ = 1.00:0.66, [0.1706 g, 1.007 mmol: 0.1701 g, 0.6717 mmol].

The general synthetic procedure follows: Anhydrous HF (ca. 0.3 mL) was condensed into a ¼-in. o.d. FEP reactor at −196 °C. Inside a dry box, aHF was frozen in a metal Dewar filled with 4.5 mm copper plated steel spheres (air rifle shot) that had been cooled to ca. −140 °C in the glass cryowell of the dry box with liquid N_2. Rhenium

trioxide fluoride, ReO_3F, was weighed into the reactor, and its frozen contents were briefly warmed to room temperature whereupon ReO_3F dissolved to form a pale yellow solution. The solution was immediately refrozen at −140 °C, and XeF_2 was weighed into the reactor. The reactor and its frozen contents were rapidly removed from the dry box and warmed to −30 °C at which temperature the reactants dissolved over a period of ca. 5−10 min forming a pale-yellow solution. As the reaction proceeded to completion (2−4 h), the color of the solution changed to bright yellow-orange. Upon completion of the reaction, a red-orange, microcrystalline powder irreversibly precipitated, and the supernatant decolorized when the yellow-orange solution was cooled to −78 °C. Low-temperature Raman spectra were obtained for the dry red-orange solids that formed when XeF_2 and ReO_3F (2.11:1.00, 1.18:1.00) had fully reacted. The solids were isolated by removal of HF under dynamic vacuum at −78 °C and were assigned to $[XeOXeOXe][\mu\text{-}F(ReO_2F_3)_2]_2$.

Low-temperature Raman spectra were also recorded for the red-orange solids that formed when XeF_2 and ReO_3F (1.19:1.00, 1.14:1.00) were only partially reacted at −30 °C. The red-orange precipitates were obtained when the reaction mixtures were cooled to −78 °C (see above) and frozen under their yellow-orange supernatants at −140 °C. The frozen supernatants contained unreacted XeF_2 and $ReO_3F(FH)_2$, which were not observed when the laser was focused on the red-orange precipitates. The Raman spectra of the dry products and those recorded under the frozen HF solutions were identical and were assigned to $[XeOXeOXe][\mu\text{-}F(ReO_2F_3)_2]_2$. The solution samples were subsequently slowly warmed to room temperature for ca. 5 min, whereupon they decomposed. Their

solute mixtures were isolated by removal of HF and residual XeF_2 under dynamic vacuum at room temperature. The Raman spectra of the resulting mixtures corresponded to ReO_2F_3 and unreacted ReO_3F.

The decomposition of solid $[XeOXeOXe][\mu\text{-}F(ReO_2F_3)_2]_2$ was also investigated. The product was obtained from the reaction of a 1:1.33 molar ratio of XeF_2:ReO_3F [0.0689 g, 0.4068 mmol: 0.1373 g, 0.5423 mmol] in aHF and was isolated by removal of HF under dynamic vacuum at −78 °C. Warming the solid to room temperature for 1 h resulted in a solid, white mixture. The Raman spectrum of the mixture corresponded to ReO_2F_3 and XeF_2. The ^{18}O-enriched salt, $[Xe^{18}OXe^{18}OXe][\mu\text{-}F(Re^{18}O_2F_3)_2]_2$, was synthesized from enriched $Re^{18}O_3F$ using the aforementioned procedure ($Re^{18}O_3F$, 0.1627 g, 0.3358 mmol; XeF_2, 0.1706 g, 1.007 mmol).

Crystals of $[XeOXeOXe][\mu\text{-}F(ReO_2F_3)_2]_2$ were grown in ¼-in. i.d. FEP reaction vessels equipped with side arms to give T-shaped reaction vessels that were fitted with Kel-F valves. Crystals grew as red-orange plates upon cooling bright yellow-orange HF solutions of XeF_2:ReO_3F (0.56:1.00 and 1.02:1.00) from −30 to −35 °C in a low-temperature bath over a 5 h period under ca. 1 atm of dry nitrogen. Upon completion of crystal growth, the supernatants were decanted into the side arms of the reactors, which had been cooled to −196 °C. The crystalline products were dried under dynamic vacuum at −50 °C before the side arms containing the frozen supernatants were heat-sealed off under dynamic vacuum. The crystalline products were stored at −78 °C under 1 atm of dry nitrogen until suitable crystals could be mounted on the X-ray diffractometer. Red-orange colored plates having the dimensions 0.045 × 0.058 × 0.097 mm^3 (XeF_2:ReO_3F =

0.56:1.00) and 0.052 × 0.176 × 0.320 mm^3 (XeF_2:ReO_3F = 1.02:1.00) were selected for structure determinations.

2.7. Reactions of MnO_3F with Noble-Gas Fluorides, KrF_2 and XeF_6

2.7.1. Reaction of MnO_3F with KrF_2 in aHF

Manganese trioxide fluoride was prepared as described in Section 2.2.4, using 0.1078 g (0.6821 mmol) of K[MnO_4]. The deep green HF solution of MnO_3F and Mn_2O_7 was distilled into a separate ¼-in. o.d. FEP T-shaped reactor equipped with a Kel-F valve at –196 ^oC. The reactor was subsequently warmed to –78 ^oC and was stored at this temperature under 1 atm of dry nitrogen until KrF_2 could be added. The reactor was evacuated at –196 ^oC and excess KrF_2 was condensed into the reactor at –196 ^oC in small aliquots. After each addition of KrF_2, the reactor and contents were warmed to room temperature, resulting in rapid evolution of condensable (Kr) and non-condensable (O_2) gases, which were periodically released into a vacuum manifold after temporarily quenching the reaction at –196 ^oC. The solution turned pale pink over a period of ca. 3 h and a small amount of pink-red oil also formed. The reaction was quenched by cooling the reactor to –196 ^oC. The Raman spectrum, recorded on the oil under the frozen solution, was assigned to KrF_2 (464 and 131 cm^{-1}) and an unknown manganese fluoride (weak bands assignable to Mn−F stretches occurred at 732, 727 sh, 596 sh, 584 sh, 578 cm^{-1}, see Figure E1, Appendix E). The reactor was subsequently connected to the metal vacuum line and the reaction was allowed to proceed until the solution and the oil colors turned red-violet and gas evolution ceased. The Raman spectrum was recorded on the

isolated product after removal of HF under dynamic vacuum at room temperature (see Figure E2, Appendix E) and was similar to that of $[O_2][Mn_2F_9]$.[139]

A fresh aliquot of aHF (ca. 0.3 mL) was distilled onto the solid at –196 ^{o}C and the contents of the reactor were allowed to warm to room temperature. While the solution remained red-violet in color, a small amount of grey solid immediately precipitated. The grey solid was separated by decanting the supernatant and the solid into the side arm and then decanting the supernatant back into the main tube of the reactor. Crystallization was attempted by allowing the supernatant to stand at –78 ^{o}C; however, no crystalline material formed. The grey solid was then transferred back into the red-violet solution. This unexpectedly resulted in the dissolution of the grey solid and the color of the solution changed from red-violet to very pale green. The resulting solution was allowed to stand at –78 ^{o}C for ca. 24 h, but no crystals grew at this temperature. Needle-shaped red crystals (ca. <1 %); however, grew under ca. 1 atm of N_2 over a period of 24 h by static distillation of the solvent into the precooled (–78 ^{o}C) side arm of the reactor. A very small amount of friable pale pink/grey solid was also observed. Two red crystals having the dimensions 0.08 x 0.13 x 0.28 mm^3 and 0.06 x 0.11 x 0.16 mm^3 were selected for structure determinations. Both crystal structures suffered from twinning issues, therefore, only preliminary solutions revealing the presence of MnF_5 could be obtained. Subsequent attempts to reproduce the above synthesis of MnF_5 failed. Instead, and based on their characteristic colors, the reaction of MnO_3F with KrF_2 in aHF only resulted in the formation of MnF_3 and MnF_4.

2.7.2. Reaction of MnO_3F with KrF_2 and $K[HF_2]$ in aHF

A mixture of MnO_3F, Mn_2O_7, and $K[HF_2]$ was prepared as described in Section 2.2.4., using 0.1026 g (0.6492 mmol) of $K[MnO_4]$. Excess KrF_2 was condensed into the reactor in small portions at –196 ^oC. After each addition of KrF_2, the contents of the reactor were warmed to room temperature, resulting in the rapid evolution of condensable (Kr) and non-condensable (O_2) gases, which were periodically released into the vacuum line manifold after temporary cooling of the solution to –196 ^oC and followed by pumping at –196 ^oC. Over ca. 4 h, the solution became orange and a dark red oil separated and settled to the bottom of the reaction vessel. An attempt to record a Raman spectrum on the red oil under the frozen solution failed due to the very weak scattering ability of the product. The reactor was connected to a vacuum line and the orange product was isolated by removal of HF under dynamic vacuum at −78 ^oC and subsequent drying at room temperature. The broad Raman spectrum of the dry material was assigned to a new manganese fluoride or a mixture of manganese fluorides (see Figure E3, Appendix E).

The product was transferred into a ¼-in. i.d. FEP T-shaped reaction vessel fitted with a Kel-F valve. Anhydrous HF (ca. 0.2 mL) was condensed onto the solid resulting in the deposition of a small amount of grey solid under a clear orange solution. Crystals of $K[MnF_6]$ grew as colorless to pale pink cubes upon cooling of the orange HF solution from −25 to −35 °C in a crystal-growing apparatus over a 4 h period under ca. 1 atm of dry nitrogen. Upon completion of crystal growth, the supernatant was decanted into the side arm of the reactor, which had been cooled to −196 °C. The crystalline product was

dried under dynamic vacuum at −40 °C before the side arm containing the frozen supernatant was heat-sealed off under dynamic vacuum. The crystalline product was stored at −78 °C under 1 atm of dry nitrogen until suitable crystals could be mounted on the X-ray diffractometer. A crystal having the dimension 0.11 × 0.11 × 0.12 mm^3 was selected for structure determination.

In a subsequent attempt, 0.0353 g (0.2234 mmol) of $K[MnO_4]$ was dissolved in aHF (ca. 0.3 mL) yielding MnO_3F, Mn_2O_7, and $K[HF_2]$. The reactor was subsequently pressurized with 1080 torr of F_2 gas at −78 ^oC. The reactor and contents were maintained under F_2 at −78 ^oC for ca. 24 h. Krypton difluoride (0.0754 g, 0.6191 mmol) was condensed into the reactor in small aliquots at –196 ^oC. The reaction was carried out as described above. The Raman spectrum (see Figure E4, Appendix E) of the orange product (0.0392 g) that was isolated at room temperature showed several broad bands that were in common with those described above (see Figure E3, Appendix E) and three sharp bands corresponding to $K_2[MnF_6]$ (601, 516, 309 cm^{-1}). An attempt to crystallize the product mixture from HF while maintaining the solution at −78 ^oC over a 48 h period and by very slow removal of HF at −78 ^oC under dynamic vacuum failed.

All other attempts to synthesize $K[MnF_6]$ in HF resulted in the formation of yellow $K_2[MnF_6]\cdot 2HF$ (identified by determination of the crystallographic unit cell and by Raman spectroscopy) and a grey, insoluble material that is presumed to be MnF_3.

2.7.3. Reaction of MnO_3F with XeF_6 in aHF: Syntheses of $[Xe_2F_{11}]_2[MnF_6]$ and $[XeF_5]_2[MnF_6]$ and Crystal Growths

On a metal vacuum line, 0.3275 g (1.335 mmol) of XeF_6 was sublimed into a ¼-in. o.d. FEP weighing vessel. The weighing vessel was connected through a ¼-in. o.d. x ⅛-in. i.d. FEP h-shaped connector to a reaction vessel containing a MnO_3F/HF solution prepared from 0.0642 g (0.4062 mmol) of K[MnO_4] (see 2.2. Synthesis of MnO_3F) and maintained at −78 °C. Xenon hexafluoride was sublimed from the weighing vessel into the reaction vessel pre-cooled to −196 °C. The reaction mixture was slowly warmed from −78 to 15 ^{o}C over a period of 5 days; however, MnO_3F and XeF_6 did not react at the above temperatures as indicated by Raman spectroscopy. The reactor was subsequently warmed to room temperature, at which temperature a slow reaction took place accompanied by very slow gas evolution. The reaction was quenched after ca. 1 h by cooling the reaction mixture to −78 °C. The Raman spectrum recorded on the solids precipitated under frozen aHF corresponded to MnO_3F, XeF_6·1.5HF, $XeOF_4$[188] and/or $XeOF_4$·XeF_6[188,189] and $[Xe_2F_{11}]_2[MnF_6]$ (Figure E5, Appendix E). The reaction mixture was subsequently warmed to room temperature and was kept at this temperature until the solution turned from dark green to orange, indicating that the reaction had gone to completion. The yellow product was isolated by removal of aHF under dynamic vacuum at −78 °C. The color of the product changed from yellow to orange upon warming the sample above −50 °C; the color change was reversible when cooled to low temperature. The Raman spectrum corresponded to a mixture of XeF_6·1.5HF, $XeOF_4$[188] and/or $XeOF_4$·XeF_6[188,189] (white solids) and $[Xe_2F_{11}]_2[MnF_6]$ (orange solid).

Crystals of $[Xe_2F_{11}]_2[MnF_6]$ were grown from a bright orange solution obtained by dissolution of XeF_6 and $[Xe_2F_{11}]_2[MnF_6]$ that had been synthesized in Section 2.7.4. in ca 0.4 mL of aHF at −10 °C under 1 atm of N_2. Cooling the solution to −15 °C inside a crystal growing apparatus (Figure 2.8)[185] resulted in the formation of bright orange needles over a period of 3−4 h. The solution was subsequently cooled to –60 °C which resulted in a second growth of colorless needle-shaped crystals. The supernatant was decanted into the precooled (–196 °C) side arm of the reaction vessel upon completion of crystal growth. The crystalline products were dried under dynamic vacuum at −65 °C before the side arm containing the frozen supernatant was heat-sealed off under dynamic vacuum. The low-temperature Raman spectrum was recorded on the crystalline material confirming the formation of $[Xe_2F_{11}]_2[MnF_6]$, $XeF_6 \cdot 1.5HF$, and $XeOF_4$[188] and/or $XeOF_4 \cdot XeF_6$[188,189] (Figure 7.1). A crystal of $[Xe_2F_{11}]_2[MnF_6]$ (orange needle) having the dimensions 0.069 x 0.117 x 0.502 mm^3 and a crystal of $XeF_6 \cdot 1.5HF$ (colorless needle) was selected for a low-temperature X-ray structure and unit cell determinations, respectively.

For the synthesis of $[XeF_5]_2[MnF_6]$, 0.2528 g (1.0307 mmol), XeF_6 was allowed to react with a MnO_3F/aHF solution prepared from 0.0543 g (0.3436 mmol) of $K[MnO_4]$ (see Section 2.2) yielding $[Xe_2F_{11}]_2[MnF_6]$ as described above. The reactor containing $[Xe_2F_{11}]_2[MnF_6]$ was connected to a vacuum line and XeF_6 was removed under dynamic vacuum at room temperature over a period of ca. 8 h. The Raman spectrum of the final product corresponded to the previously known $[XeF_5]_2[MnF_6]$ (yellow at −78 °C and orange at > −50 °C).[171]

A bright orange solution of $[XeF_5]_2[MnF_6]$ was prepared by dissolving the solid in ca 0.3 mL of aHF at room temperature under 1 atm of N_2. The orange needle-shaped crystals were grown by removal of aHF by static distillation into a precooled (–78 ^oC) side arm of the FEP reaction vessel. The side arm containing the supernatant was then cooled to –196 ^oC and subsequently heat-sealed off under dynamic vacuum. The crystalline material was characterized by low-temperature Raman spectroscopy (Figure E6, Appendix E). A crystal of $[XeF_5]_2[MnF_6]$ having the dimensions 0.058 x 0.143 x 0.169 mm^3 was selected for a low-temperature X-ray structure determination.

2.7.4. Synthesis and Crystal Growth of $K_2[MnF_6]\cdot 2HF$

The salt, $K_2[MnF_6]\cdot 2HF$, was always obtained as a by-product of the solvolysis reaction of $K[MnO_4]$ in aHF and crystallized by allowing the solution to stand at −78 ^oC for ca 48 h. Upon completion of crystal growth, the supernatant was decanted into the side arm of the reaction vessel, which had been precooled to –196 ^oC. The crystalline product was dried under dynamic vacuum at −65 °C before the side arm containing the frozen supernatant was heat-sealed off under dynamic vacuum at –196 ^oC. The low-temperature Raman spectrum was recorded on the crystalline solid (Figure E7, Appendix E) A crystal of $K_2[MnF_6]\cdot 2HF$ having the dimensions 0.169 x 0.171 x 0.177 mm^3 was selected for a low-temperature X-ray structure determination.

2.8. X-ray Crystallography

2.8.1. Crystal Growth

Unless otherwise noted, crystals for structure determination by single-crystal X-ray diffraction were grown in the low-temperature crystal growing apparatus depicted in Figure 2.8. The following procedure summarizes the general approach used to grow crystals from solutions using the thermal gradient method. The solvent (ca. 0.5 mL) was condensed onto the compound (ca. 0.3 mmol) at –196 ^{o}C that had been synthesized in situ in one arm of a ¼-in o.d. FEP T-shaped reactor fitted with a Kel-F valve. The reactor was warmed to just initiate dissolution, and while maintained at that temperature, the reactor was attached to a vacuum line and pressurized to ca. 1 atm with dry nitrogen. The arm containing the solution was inclined at ca. 5^{o} from the horizontal inside the glass dewar of a crystal growing apparatus[185] which had been previously adjusted to the same temperature. The temperature was then lowered by slowly increasing the flow of cold gaseous nitrogen over a period of time, usually several hours, whereupon crystals began to grow on the walls of the FEP vessel. The reactor was then held for a further period of time to allow for more complete crystallization. Crystals were isolated by decanting the solvent under dry nitrogen into the side arm of the FEP vessel which was immersed in liquid nitrogen, followed by evacuation and vacuum drying of the crystalline product under dynamic vacuum before the side arm containing the supernatant was heat-sealed off the vessel containing the dried

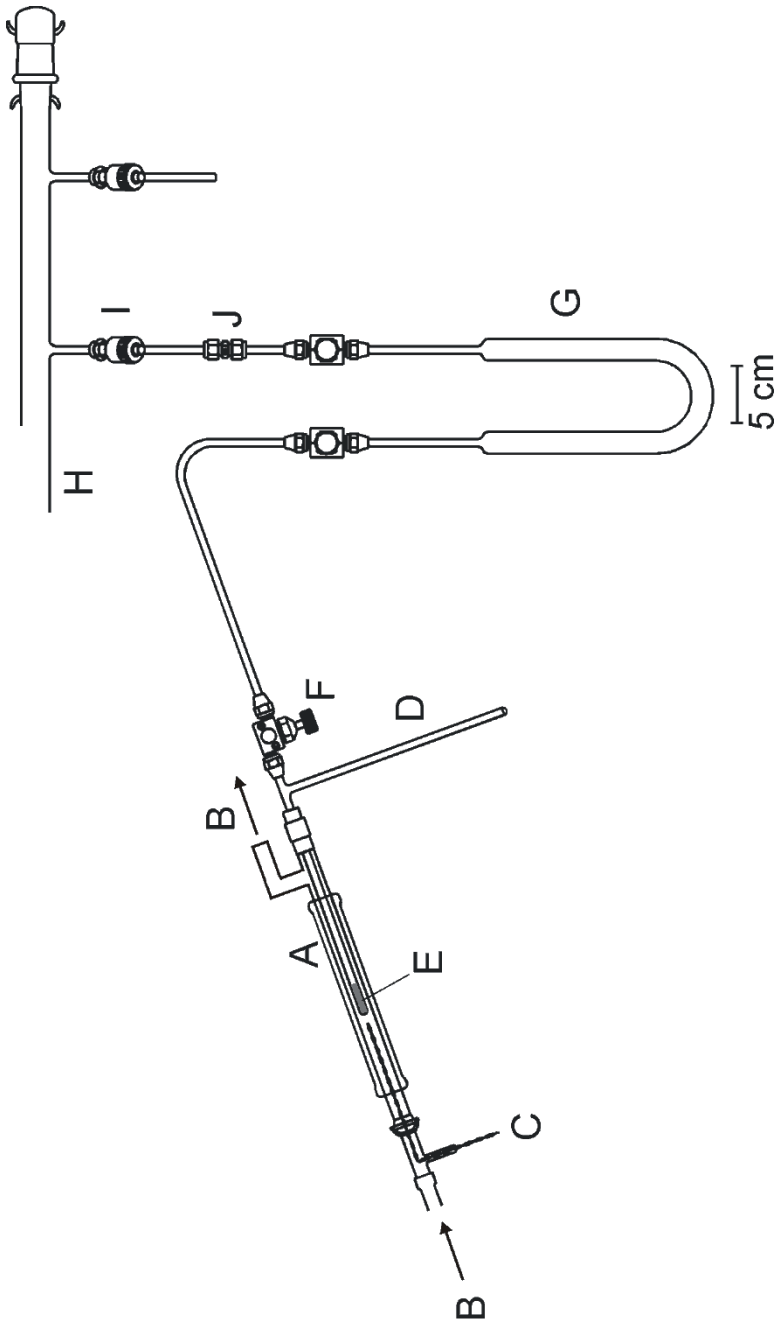

Figure 2.8. Low-temperature crystal growing apparatus. (A) Glass-jacketed dewar. (B) Nitrogen cold flow. (C) Thermocouple lead. (D) T-shaped FEP reaction vessel with side arm. (E) Sample region. (F) Kel-F valve. (G) FEP U-trap. (H) Vacuum manifold. (I) Greaseless J-Young valve with PTFE barrel. (J) ¼″ PTFE Swagelok or ¼-in. stainless steel Swagelok Ultra-Torr connector. Reproduced with permission from ref 185.

crystalline product. The crystals were selected at –104 ±2 ^{o}C for low- temperature X-ray structure determination and were mounted in a cold stream (–173 ^{o}C) on a goniometer head as described in the next section.

2.8.2. Low-Temperature Crystal Mounting

Because the majority of compounds investigated in this work were thermally unstable and/or moisture sensitive, their crystals were mounted at low temperature using the apparatus depicted in Figures 2.9 and 2.10. The reaction vessels containing the samples were first cut open below the Kel-F valve under a flow of dry argon gas, using an inverted glass funnel, while maintaining the sample at –78 ^{o}C. The sample was then quickly dumped into the aluminum trough of the crystal mounting apparatus under a stream of dry argon, precooled (–104 ±2 ^{o}C) by the regulated passage of dry nitrogen gas flow through a 5-L dewar filled with liquid N_2 (Figure 2.9). The temperature inside the trough was measured using a copper-constantan thermocouple positioned in the sample region of the trough. Crystals were then selected using a stereo-zoom microscope and mounted on a glass fibre (0.05 to 0.1-mm o.d.) using perfluorinated polyether oil (Ausimont Inc., Fomblin Z15 or Z25) which served as an adhesive upon freezing at low temperature. The glass fibre had been previously mounted with epoxy cement to a copper pin fitted to a magnetic base and affixed to the end of a magnetic wand (Hampton Research). The magnetic wand could be fastened to an adjustable support stage such that samples could be inspected in the dry nitrogen cold stream under the stereo-zoom microscope once affixed to the glass fibre. The mounted crystal and magnetic pin were

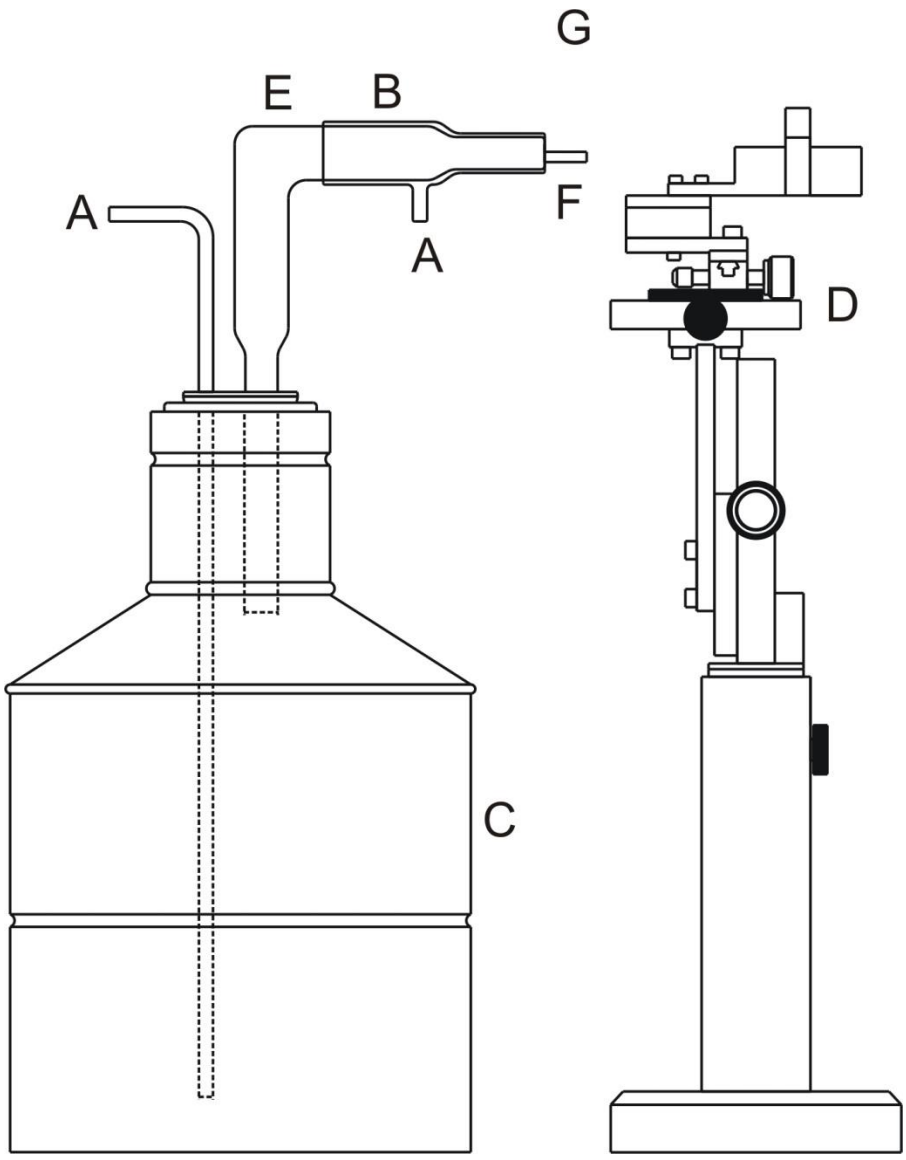

Figure 2.9. Low-temperature crystal mounting apparatus. (A) Nitrogen inlet. (B) Glass sleeve for ambient nitrogen flow. (C) Liquid N_2 dewar. (D) Adjustable support stage. (E) Silvered dewar (glass). (F) Aluminum trough. (G) Stereo-zoom microscope. Reproduced with permission from ref 185.

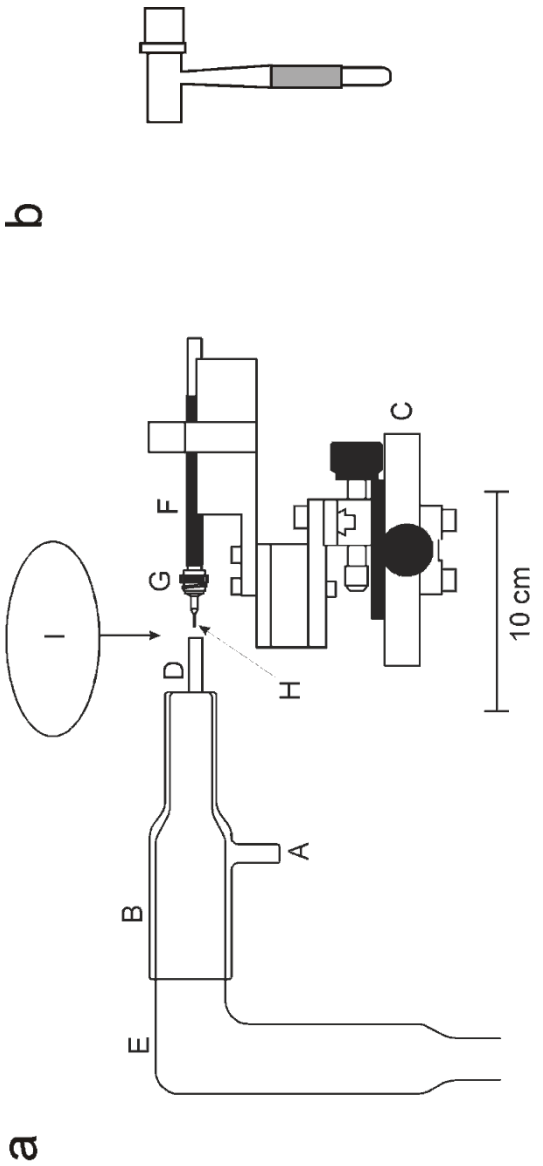

Figure 2.10. (a) Enlarged view of the crystal mounting apparatus; (A) ambient nitrogen gas flow inlet, (B) glass sleeve for ambient nitrogen gas flow, (C) adjustable support stage, (D) aluminum trough, (E) silvered glass jacketed dewar, (F) magnetic-tipped wand affixed to (G) the magnetic-based copper pin-fibre assembly, (H) glass fibre. (I) stereo-zoom microscope, (b) cryotongs employed in the transfer of the copper pin-fibre assembly with adhered crystal from the support stage to the goniometer head. Reproduced with permission from ref 185.

quickly (ca. 5 to 10 s) transferred from the crystal mounting apparatus to the magnetic mount of the goniometer by means of a cryotongs (Hampton Research) which had been precooled in liquid N_2 prior to use. The crystals were maintained at low temperature on the goniometer head by a cold N_2 gas flow provided by a Molecular Structure Corporation cryostat system.

2.8.3. Data Collection

2.8.3.1. Bruker SMART APEX II Diffractometer

The crystallographic data acquired during the course of this Thesis were collected using Bruker SMART APEX II diffractometer, which was equipped with Oxford Cryosystems low-temperature cryostream accessory that provided a stream of cold, gaseous N_2 for low-temperature data collection. The instrument was controlled by a Cryostream Controller 700 (Oxford Cryosystems).

The Bruker SMART APEX II diffractometer was equipped with an APEX II 4K CCD area detector and a triple-axis goniometer, controlled by the APEX2 Graphical Use Interface (GUI) software,[190] and a sealed tube X-ray source (Mo target) emitting Kα radiation monochromated (λ = 0.71073 Å) by a graphite crystal. A Bruker Triumph curved crystal monochromator with a Mo Kα (λ = 0.71073 Å) radiation source was also used. Diffraction data were collected at –173 ^{o}C and consisted of a full ϕ-rotation at a fixed $\chi = 54.74^{o}$ with 0.36^{o}, followed by a series of short ω scans at various φ settings to fill the gaps for $([N(CH_3)_4]_2[\{ReO_3(\mu\text{-}F)\}_3(\mu_3\text{-}O)]\cdot CH_3CN$, $[N(CH_3)_4][ReO_4]$, $(HF)_2ReO_3F\cdot HF$, $KF\cdot 4HF$, $K[MnF_6]$, MnF_5, $(M[ReO_3F_2])_\infty$, (M = [NO], Cs, K, $[NH_4]$),

$K[H_3O][ReO_3F_3]$, $Cs[ReO_2F_4]$, and $Cs[\mu\text{-}F(ReO_2F_3)]$ (Table 2.1) and of ω-scans collected at 0.5° intervals at fixed $\chi = 54.74^{o}$ for ($[XeOXeOXe][\mu\text{-}F(ReO_2F_3)_2]_2$, $(\mu\text{-}F)_4\{[\mu\text{-}O(ReO_2F)_2](ReO_2F_2)_2\}\cdot SO_2ClF$), $[Xe_2F_{11}]_2[MnF_6]$, $[XeF_5]_2[MnF_6]$, and $[K\cdot 2HF]_2[MnF_6]$ (Table 2.1). The crystal-to-detector distance ranged from 4.951 to 4.955 cm, and the data collection was carried out in a 512 ×512 pixel mode using 2 × 2 pixel binning. Processing of the raw data was completed using the APEX2 GUI software,[190] which applied Lorentz and polarization corrections to three-dimensionally integrated diffraction spots. The program SADABS[191] was used for the scaling of diffraction data, the application of a decay correction, and an empirical absorption correction based on the intensity ratios of redundant reflections.

2.8.3.2. Solution and Refinement of Structures

The XPREP[192] program was used to confirm the unit cell dimensions and the crystal lattices. The final refinements were obtained by introducing anisotropic parameters for all the atoms except hydrogen, an extinction parameter, and the recommended weight factor. The maximum electron densities in the final difference Fourier maps were located around the heavy atoms. All calculations were performed using the SHELXTL-plus,[192] software package for the structure determination, refinement, and molecular graphics. Structure solutions were obtained by direct methods which located the Re, Mn, Xe, Sb, K, and Cs atoms. Successive difference Fourier syntheses revealed the positions of the carbon, nitrogen, oxygen, and fluorine atoms.

Table 2.1. Summary of Selected X-Ray Data Collection Parameters

Compound	Total Number of Frames	
	ω	ϕ
$([N(CH_3)_4]_2[\{ReO_3(\mu\text{-}F)\}_3(\mu_3\text{-}O)]\cdot CH_3CN$	900	771
$[N(CH_3)_4][ReO_4]$	900	158
$(HF)_2ReO_3F\cdot HF$	1250	3046
$KF\cdot 4HF$	1000	1010
$K[MnF_6]$	900	727
MnF_5	900	1466
$K[H_3O][ReO_3F_3]$	418	
$([NO][ReO_3F_2])_\infty$	900	2193
$([NH_4][ReO_3F_2])_\infty$	720	2193
$(Cs[ReO_3F_2])_\infty$	1124	3197
$(K[ReO_3F_2])_\infty$	900	727
$Cs[ReO_2F_4]$	2351	2514
$Cs[\mu\text{-}F(ReO_2F_3)]$	900	1466
$([XeOXeOXe][\mu\text{-}F(ReO_2F_3)_2]_2$	4040	
$(\mu\text{-}F)_4\{[\mu\text{-}O(ReO_2F)_2](ReO_2F_2)_2\}\cdot SO_2ClF)$	4188	
$[Xe_2F_{11}]_2[MnF_6]$	2020	720
$[XeF_2]_2[MnF_6]$	3636	720
$[K\cdot 2HF]_2[MnF_6]$	2424	

The space group choice was confirmed using Platon from the WinGX software package.[193]

The hydrogen atoms could not be located in the case of $(HF)_2ReO_3F\cdot HF$ and $KF\cdot 4HF$, but their positions were calculated in the case of $[N(CH_3)_4]_2[\{ReO_3(\mu\text{-}F)\}_3(\mu_3\text{-}O)]\cdot CH_3CN$, $[NH_4][ReO_3F_2]$, and $[N(CH_3)_4][ReO_4]$. In the case of the $(HF)_2ReO_3F\cdot HF$ structure, the axial oxygen and fluorine atoms are positionally disordered, although not related by symmetry. A similar disorder was observed for the HF molecules. Attempts to resolve the O/F positions into two components were unsuccessful. The possibility of twinning was also explored. The initial solution and refinement of the $(\mu\text{-}F)_4\{[\mu\text{-}O(ReO_2F)_2](ReO_2F_2)_2\}\cdot SO_2ClF$ structure in the tetragonal *P*4/n space group resulted in a

relatively high wR_2 value (*ca*. 20%) and F_{obs} being higher than F_{calcd}. Moreover, the SO_2ClF molecule was found to be positionally disordered (50/50) between two orientations. Because there is one symmetry axis in the *P*4/n space group, the structure was resolved in the monoclinic *P*2/n space group, "mimicking" the higher symmetry tetragonal *P*4/n space group as a result of pseudomerohedral twinning (BASF ~ 41%). With the introduction of the twin matrix (0010-10-100) characteristic of a pseudomerohedral twin, the refinement gave rise to a drastic drop in R_1 to 0.0273, indicating the correct law had been applied.

2.9. Raman Spectroscopy

Low-temperature Raman spectra were recorded on a Bruker RFS 100 FT Raman spectrometer employing a quartz beam splitter and a liquid-nitrogen cooled Ge diode detector. The 1064-nm line of a Nd-YAG laser was used for excitation with a laser spot of <0.1 mm at the sample and configured such that only the 180^o-backscattered radiation was detected. The scanner velocity was 5 kHz and the wavelength range was 5894 to 10394 cm^{-1} relative to the laser line at 9394 cm^{-1}, resulting in a spectral range of 3501 to –999 cm^{-1}. Fourier transformations were processed using a Blackman Harris 4-term apodization and a zero-filling factor of 2. Typical acquisitions used 1.0 cm^{-1} resolution and a laser power of 300 mW for all samples, except $[ReO_3][Sb_3F_{16}]$, $([XeOXeOXe][\mu\text{-}F(ReO_2F_3)_2]_2$, and $(\mu\text{-}F)_4\{[\mu\text{-}O(ReO_2F)_2](ReO_2F_2)_2\}\cdot SO_2ClF)$, for which a power of 500 mW was used. The acquisitions involved 600 scans for strongly scattering samples and 1200–1600 scans for weakly scattering samples. Low-temperature spectra were acquired

using a Bruker I0121 low-temperature accessory which provided temperatures ranging from −130 to –150 ^{o}C for routine samples, with an estimated error of ±1 ^{o}C.

2.10. Nuclear Magnetic Resonance Spectroscopy

2.10.1. NMR Instrumentation and Spectral Acquisitions

The ^{19}F NMR spectrum of an equimolar mixture of $[N(CH_3)_4]F$ and ReO_3F in CH_3CN **(1)** was acquired on a Bruker Avance II 600 MHz NMR spectrometer, equipped with a TBI-Z probehead and BCU05 temperature unit. The spectrum was externally at 25 ^{o}C referenced to $CFCl_3$. The ^{19}F NMR spectra of MnO_3F **(2)** and a new manganese fluoride **(3)** and ^{55}Mn **(4)** and ^{19}F–^{55}Mn COSY **(5)** spectra of MnO_3F were acquired on a Bruker Avance II 500 MHz NMR spectrometer equipped with a Brucker 5-mm combination ^{1}H/^{19}F probe, or a Bruker 5-mm broad band inverse probe. The ^{55}Mn NMR spectrum was externally referenced at 25 ^{o}C to $K[MnO_4]$. The ^{19}F NMR spectra were externally referenced at 25 ^{o}C to $CFCl_3$. The chemical shift convention used is that a positive (negative) sign indicates a chemical shift to high (low) frequency of the reference compound. A summary of spectroscopic parameters used for the spectra acquired for this Thesis is provided in Table 2.2. Spectra in the present study often used Gaussian multiplication to enhance spectral resolution.

2.10.2. NMR Sample Preparation

Samples of product mixtures resulting from the reactions of ReO_3F with $[N(CH_3)_4][ReO_4]$ in CH_3CN (containing the reaction products, $[N(CH_3)_4]_2[\{ReO_3(\mu$-

Table 2.2. Summary of Parameters Used for NMR Data Acquisition

Parameters[a]	(1)	(2)	(4)	(5)		(3)
	^{19}F	^{19}F	^{55}Mn	^{19}F	^{55}Mn	^{19}F
SF (MHz)	564.686	470.51	123.98	470.51	123.98	470.56
TD	128	8192	65536	8192	256	65536
SW (kHz)	85	9	0.8	9	2	25
RD (s)	0.77	0.81	0.33	0.44	0.07	1.31
Hz/pt	0.64	1.14	3.05	1.14	7.26	0.76
PW (μs)	4.53	8.07	15	8.07		8.07
NS	128	128	1024	16		1024
LB (Hz)	1.0	5.0	100	5.0		15.0

[a] The abbreviations denote spectral frequency (SF), time domain (TD), sweep width (SW), pulse width (PW), relaxation delay (RD), line broadening (LB), and number of scans (NS).

F)}$_3$(μ_3-O)]·CH_3CN, $[N(CH_3)_4][ReO_4]$, and $[N(CH_3)_4][ReO_2F_4]$) were prepared in ¼-in. o.d. FEP reactors as described above. NMR samples were prepared by transfer of the reaction mixture solutions under anhydrous conditions into 4-mm o.d. FEP NMR sample tubes which were then outfitted with Kel-F valves as previously described.[194] The NMR sample tubes were connected to a glass vacuum line through their valve assemblies, cooled to –196 °C, heat-sealed under dynamic vacuum, and stored at –196 °C until NMR spectra could be obtained. Samples were rapidly dissolved at room temperature just prior to data acquisition at 27 ^{o}C. When recording the spectra, the 4-mm o.d. FEP tubes were inserted into 5-mm o.d. thin-wall precision glass NMR tubes (Wilmad).

2.11. Quantum-Chemical Calculations

All calculations were performed using the Gaussian 03[195] or Gaussian 09[196] software packages. Geometries were fully optimized using density functional theory

(B3LYP and PBE1PBE) and aug-cc-pVTZ (O, F, Mn), aug-cc-pVDZ (O, F), aug-cc-pVTZ(-PP) (Re, Tc, As, Sb), aug-cc-pVDZ(-PP) (Re, Xe), and def2-SVP (Mn, F) basis sets. The combined use described is indicated by aug-cc-pVT(D)Z(-PP). Basis sets were obtained online from the EMSL Basis Set Exchange (https://bse.pnl.gov/bse/portal).[197−199] Fundamental vibrational frequencies were calculated along with Raman intensities. Natural bond orbital analyses were performed with the NBO program (version 6.0).[200] The molecular electrostatic potential surfaces (MEPS) were calculated using the cubegen utility as implemented in G09 and formatted Gaussian 09 checkpoint files as input. The G09 checkpoint files were created upon optimization of the geometries at the B3LYP (PBE1PBE)/aug-cc-pVDZ(-PP) levels. Atoms in molecules (AIM) and electron localization function (ELF) analyses were performed as implemented in the Multiwfn package[201] using formatted Gaussian 09 wave function files as input. The G09 wave function files were created by performing single-point calculations at the B3LYP (PBE1PBE)/aug-cc-pVDZ(-PP) levels of theory on optimized geometries. The GaussView[202] program was used to visualize the vibrational displacements that form the basis for the vibrational mode descriptions. The MEPS and NBO diagrams were drawn with Jmol[203] and Chimera,[204] respectively.

Calculations of NMR chemical shifts were carried out using the Amsterdam Density Functional (ADF) 2010.2 program package[205-208] and the implemented NMR module.[208-212] Single point energies were obtained for the B3LYP/aug-cc-pVTZ geometries at the PBE0 level of theory utilizing Slater type all electron TZ2P basis sets.

Relativistic effects were included with the spin-orbit coupled zeroth-order regular approximation (ZORA) methodology.

The calculated chemical shifts (δ_{calcd}) reported in this work (see NMR Spectroscopy) were obtained according to eq 2.1 where δ_{ref} is the experimental chemical

$$\delta_{calcd} = \delta_{ref} + \sigma_{ref} - \sigma_{rcalcd} \quad (2.1)$$

shift (−141.2 ppm) of the reference,[19] μ-F in $[(ReO_2F_3)_2(\mu\text{-}F)]^-$; σ_{ref} is the calculated NMR shielding of the reference nucleus (296.71 ppm); σ_{calcd} is the calculated NMR shielding of the nucleus under study, i.e., $\sigma_{\mu\text{-}F}$ = 334.76 ppm in $[\{ReO_3(\mu\text{-}F)\}_3(\mu_3\text{-}O)]^{2-}$ and $\sigma_{\mu\text{-}F}$ = 351.40 ppm and $\sigma_{\mu_3\text{-}F}$ = 359.35 ppm in $[\{ReO_3(\mu\text{-}F)\}_3(\mu_3\text{-}F)]^-$; giving calculated chemical shifts of $\delta_{\mu\text{-}F}$ = −179.3 ppm for $[\{ReO_3(\mu\text{-}F)\}_3(\mu_3\text{-}O)]^{2-}$ and $\delta_{\mu\text{-}F}$ = −179.3 ppm and $\sigma_{\mu_3\text{-}F}$ = −203.9 ppm for $[\{ReO_3(\mu\text{-}F)\}_3(\mu_3\text{-}F)]^-$.

CHAPTER 3

THE SYNTHESIS AND LEWIS ACID PROPERTIES OF ReO_3F AND THE X-RAY CRYSTAL STRUCTURES OF $(HF)_2ReO_3F{\cdot}HF$ AND $[N(CH_3)_4]_2[\{ReO_3(\mu\text{-}F)\}_3(\mu_3\text{-}O)]{\cdot}CH_3CN$

3.1. Introduction

Rhenium trioxide fluoride has been known for more than 60 years,[31] but its chemistry has been little studied. The fluoride-ion acceptor properties of ReO_3F have been investigated for several alkali metal fluorides (K,[27,36] Rb,[27] Cs[27]) and $[N(CH_3)_4]F$.[37] The resulting complexes were characterized by infrared[27,36,37] and Raman[36] spectroscopy and formulated as salts of the [*mer*-$ReO_3F_3]^{2-}$ anion,[27,36,37] although the isoelectronic $[OsO_3F_3]^-$ anion has since been shown to exclusively exist as the *fac*-isomer.[39] No further structural characterization of $[ReO_3F_3]^{2-}$ has been reported. More recently, the donor-acceptor complexes, $(CH_3CN)_2ReO_3F_7$ and L_2ReO_3F (L = $(C_2H_5)_2O$, $(CH_3)_2O$, THF),[21] were characterized by single-crystal X-ray diffraction, establishing the Lewis acid character of ReO_3F. Unlike the previously reported meridional geometries proposed for the $[ReO_3F_3]^{2-}$ anion, $(CH_3CN)_2ReO_3F$ and L_2ReO_3F have *cis*-trioxo arrangements. No studies of the fluoride-ion donor properties of ReO_3F have been forthcoming.

Several low-yield syntheses of ReO_3F have been reported in the literature,[4,31–33] but none provide a reliable high-yield, high-purity synthesis of this compound, which has likely contributed to the slow development of its chemistry. For a summary of prior ReO_3F syntheses, see ref 21. Among the synthetic routes available for ReO_3F, two are

particularly relevant to the present study. The solvolyses of $K[ReO_4]$ and Re_2O_7 in aHF (eqs 3.1 and 3.2) have been documented by means of Raman and ^{19}F NMR spectroscopy;

$$K[ReO_4] + (2 + x)HF \xrightarrow{aHF} K[F(HF)x] + ReO_3F + H_2O \quad (3.1)$$

$$Re_2O_7 + 2HF \xrightarrow{aHF} 2ReO_3F + H_2O \quad (3.2)$$

however, ReO_3F was not isolated from these solutions.[34] The Raman assignments reported in the latter study were based on an assumed C_{3v} point symmetry for ReO_3F in aHF solution.

More recently, another synthesis of ReO_3F was reported which entailed the reaction of ReO_3 with F_2 at temperatures between 90 and 150 °C.[21] The oxidative fluorination of ReO_3 resulted in the formation of ReO_3F, which was isolated from the reaction by-products, $ReOF_5$ and ReO_2F_3, upon condensation of ReO_3F as a glassy sublimate in the cooler regions of the quartz reactor. The X-ray crystal structure, Raman spectrum, and mass spectrum of ReO_3F were reported. The crystal structure was determined on a 3-fold twinned crystal and is reported to consist of a fluorine- and oxygen-bridged chain polymer having hexacoordinated rhenium atoms.

The present chapter describes a simplified and reliable synthesis of ReO_3F and extends the Lewis acid and fluoride-ion acceptor properties of ReO_3F by the structural characterization of $(HF)_2ReO_3F{\cdot}HF$ and the cage anion, $[\{ReO_3(\mu\text{-}F)\}_3(\mu_3\text{-}O)]^{2-}$, which represent the only example of rhenium coordinated to HF and the only example of rhenium oxide fluoride species containing a tricoordinated oxygen atom.

3.2. Results and Discussion

3.2.1. Syntheses of ReO_3F, $(HF)_2ReO_3F{\cdot}HF$, and $[N(CH_3)_4]_2[\{ReO_3(\mu\text{-}F)\}_3(\mu_3\text{-}O)]$

Reaction progress and product purities were routinely monitored by recording the Raman spectra of the solids at −150 °C.

ReO_3F. The synthesis of ReO_3F was achieved by solvolysis of Re_2O_7 in aHF followed by room-temperature fluorination of this solution with F_2 gas to oxidatively fluorinate H_2O to O_2 and HF (eqs 3.2 and 3.3). Hydrogen fluoride solvent and associated

$$H_2O + F_2 \xrightarrow{aHF} 2HF + \tfrac{1}{2}O_2 \qquad (3.3)$$

HF in the complex, $(HF)_2ReO_3F{\cdot}HF$ (vide infra), were removed under dynamic vacuum in stages at temperatures ranging from −78 °C to room temperature. The product was further pumped on at 50 °C to ensure complete removal of coordinated HF. Rhenium trioxide fluoride was obtained as a pale yellow, friable powder that gave a broad Raman spectrum (Figure A1, Appendix A) identical to the previously reported spectrum.[21]

$(HF)_2ReO_3F{\cdot}HF$. The complex, $(HF)_2ReO_3F{\cdot}HF$, was synthesized by dissolution of ReO_3F in aHF (eq 3.4) and was isolated as pale yellow to colorless plates upon

$$ReO_3F + 3HF \longrightarrow (HF)_2ReO_3F{\cdot}HF \qquad (3.4)$$

removal of aHF under vacuum at −78 °C. The product was characterized by single-crystal X-ray diffraction and Raman spectroscopy. The Raman spectrum of the crystalline material (Table 3.1) was in good agreement with the reported solution spectra resulting from the solvolyses of Re_2O_7 or $K[ReO_4]$ in aHF solvent, which had previously been assigned to monomeric ReO_3F.[34] The $(HF)_2ReO_3F{\cdot}HF$ complex was also synthesized by the solvolyses of $M[ReO_4]$ ($M = [NH_4]^+, K^+$) and Re_2O_7 in aHF (eqs 3.1 and 3.2) and was

confirmed from the Raman spectra of the products, which crystallized from aHF at −78 °C, and by unit cell determinations of the single crystals.

$[N(CH_3)_4]_2[\{ReO_3(\mu\text{-}F)\}_3(\mu_3\text{-}O)]$. The salt, $[N(CH_3)_4]_2[\{ReO_3(\mu\text{-}F)\}_3(\mu_3\text{-}O)]$, was obtained, along with minor amounts of $[N(CH_3)_4][ReO_4]$ and $[N(CH_3)_4][ReO_2F_4]$, by the reaction of stoichiometric quantities of ReO_3F and $[N(CH_3)_4]F$ in CH_3CN. The product mixture was partially soluble in CH_3CN at −10 °C. Upon slow warming of the mixture to room temperature, all products dissolved forming a bright yellow solution. The salt, $[N(CH_3)_4]_2[\{ReO_3(\mu\text{-}F)\}_3(\mu_3\text{-}O)]$, was obtained in admixture with $[N(CH_3)_4][ReO_4]$ and $[N(CH_3)_4][ReO_2F_4]$ upon removal of CH_3CN at −40 to −35 °C. Subsequent drying of the mixture at room temperature yielded a friable light beige powder. The reaction of ca. 50 mg of ReO_3F and $[N(CH_3)_4]F$ in 0.2−0.3 mL of CH_3CN led to the formation of $[N(CH_3)_4]_2[\{ReO_3(\mu\text{-}F)\}_3(\mu_3\text{-}O)]$ as the major product, whereas larger amounts (80−100 mg) of ReO_3F and $[N(CH_3)_4]F$ in 0.3−0.4 mL of CH_3CN favored the formation of $[N(CH_3)_4][ReO_4]$ and $[N(CH_3)_4][ReO_2F_4]$. All products were characterized by single-crystal X-ray diffraction and Raman spectroscopy. Fluorine-19 NMR spectroscopy was also employed to obtain the spectra of $[N(CH_3)_4]_2[\{ReO_3(\mu\text{-}F)\}_3(\mu_3\text{-}O)]$ and $[N(CH_3)_4][ReO_2F_4]$ (see NMR Spectroscopy).

A plausible reaction pathway leading to $[\{ReO_3(\mu\text{-}F)\}_3(\mu_3\text{-}O)]^{2-}$ is given in Scheme 3.1. The proposed reaction sequence is initiated by dissolution of ReO_3F in CH_3CN at −40 °C to give $(CH_3CN)_2ReO_3F$. The latter coordination complex was previously formed

Table 3.1. Experimental Raman Frequencies and Intensities for ReO_3F and $(HF)_2ReO_3F{\cdot}HF$ and Calculated Vibrational Frequencies, Intensities, and Assignments for Monomeric ReO_3F

ReO_3F	$(HF)_2ReO_3F{\cdot}HF$ exptl[a,b,c,d]					monomeric ReO_3F calcd[a,e]	monomeric ReO_3F assgnts (C_{3v})[c,f]
	g	*h*	*i*	*j*	*k*		
996(100)	1017(100)	1017(100)	1017(100)	1017(100)	1009	1059(43)[16]	$\nu_s(ReO_3)$
969 sh	981(40)	981(51)	981(44)	981(49)	980	1011(10)[169]	ν_{as}(ReO3 – ReO1)
908(26) br							
813(26) br							
664(6)	669(13)	669(24)	669(16)	669(16)	666	706(3)[100]	ν(ReF)
386(21) br	400(13)	400(19)	400(15)	399(15)	403	357(4)[2]	δ(O3ReO1) – δ(O2ReO3)
354(17) br	341 sh	341(8)	341(3)	341(4)			
313(11) br	326(21)	326(28)	326(25)	326(22)	321	318(1)[12]	$\delta(ReO_3)_{umb}$
	323 sh	323 sh	323 sh	323 sh			
						243(2)[6]	δ(FReO2) + ρ_w(O3ReO1)
234(2) br	215(<1)	215(5)	215(2)	215(3)			
190(3)	190(4)	190(7)	190(3)	190(5)			lattice modes
177(5)	177(4)	177(7)	177(5)	177(5)			

[a] Frequencies are given in cm^{-1}. [b] Values in parentheses denote relative Raman intensities. [c] The abbreviations denote shoulder (sh), broad (br), stretch (ν), bend (δ), symmetric (s), asymmetric (as), wag (ρ_w), and umbrella (umb). [d] Raman spectra were recorded in FEP sample tubes at –150 °C using 1064-nm excitation. [e] Values in parentheses denote calculated Raman intensities ($Å^4\ u^{-1}$). Values in square brackets denote calculated infrared intensities (km mol^{-1}). The B3LYP/aug-cc-pVTZ(-PP) level was used. [f] The atom numbering corresponds to that used in Figure A1 where O1, O2, and O3 correspond to the three equivalent oxygen atoms of the O_3Re-group. [g] From $[NH_4][ReO_4]$ dissolved in HF. [h] From $K[ReO_4]$ dissolved in HF. [i] From Re_2O_7 dissolved in HF. [j] From ReO_3F dissolved in HF. [k] From an HF solution of Re_2O_7; ref 34.

by the hydrolysis of ReO_2F_3 in CH_3CN solution and characterized by single-crystal X-ray diffraction.[19] In the present work, it was shown by Raman spectroscopy and single-crystal X-ray diffraction that ReO_3F dissolves in CH_3CN to give $(CH_3CN)_2ReO_3F$ (eq 3.5).

$$ReO_3F + 2CH_3CN \xrightarrow{CH_3CN} (CH_3CN)_2ReO_3F \quad (3.5)$$

A second reaction, also initiated at −40 °C, leads to disproportionation of ReO_3F in the presence of F^- ion and the formation of equimolar amounts of $[N(CH_3)_4][ReO_4]$ and $[N(CH_3)_4][ReO_2F_4]$ (eq 3.6) as confirmed by the Raman spectrum of the product

$$2ReO_3F + 2[N(CH_3)_4]F \xrightarrow[-40\ °C]{CH_3CN} [N(CH_3)_4][ReO_4] + [N(CH_3)_4][ReO_2F_4] \quad (3.6)$$

mixture under CH_3CN at −150 °C. A third reaction (Scheme 3.1), presumably involves F^- ion attack at rhenium in $(CH_3CN)_2ReO_3F$, resulting in the formation of $[(CH_3CN)ReO_3F_2]^-$ as an intermediate. The $[(CH_3CN)ReO_3F_2]^-$ anion subsequently reacts with a second equivalent of $(CH_3CN)_2ReO_3F$ to form the anionic intermediate, $[\{(CH_3CN)ReO_3F\}_2(\mu\text{-}F)]^-$. The $[ReO_4]^-$ anion functions as a nucleophile, attacking $[\{(CH_3CN)ReO_3F\}_2(\mu\text{-}F)]^-$ at rhenium to form the open chain trirhenium intermediate, $[(ReO_3)(\mu\text{-}O)(ReO_3F)(\mu\text{-}F)\{(CH_3CN)ReO_3F\}]^{2-}$, which undergoes cyclolization to $[\{ReO_3(\mu\text{-}F)\}_3(\mu_3\text{-}O)]^{2-}$. A likely alternative reaction pathway that initially involves nucleophilic attack by F^- and $[ReO_4]^-$ ion on two independent $(CH_3CN)_2ReO_3F$ molecules and pursuant condensation and cyclolization reactions that lead to the $[\{ReO_3(\mu\text{-}F)\}_3(\mu_3\text{-}O)]^{2-}$ anion is outlined in Scheme A1 (see Appendix A).

In view of the existence of the $[\{TcO_3(\mu\text{-}F)\}_3(\mu_3\text{-}F)]^-$ anion,[23] attempts were made to synthesize the rhenium analogue, $[\{ReO_3(\mu\text{-}F)\}_3(\mu_3\text{-}F)]^-$. Initially, ReO_3F was allowed to react with $[N(CH_3)_4]F$ in CH_3CN in a 3:1 molar ratio between −40 and −35 °C. The

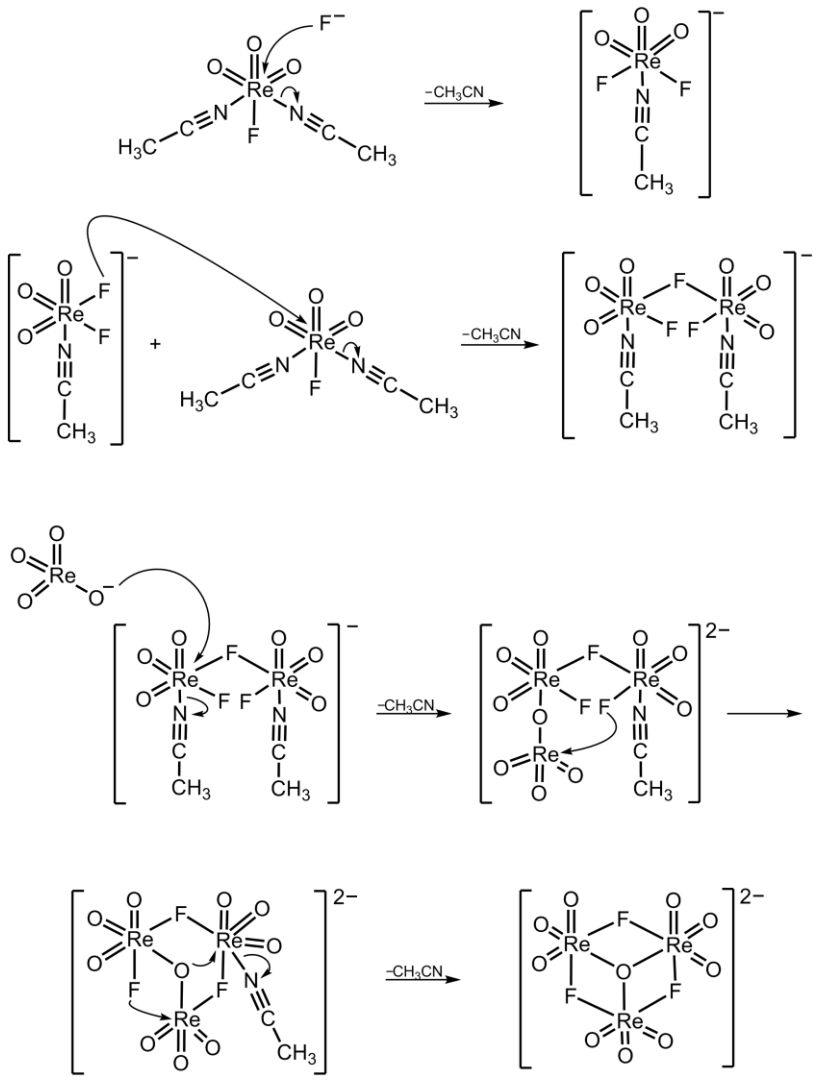

Scheme 3.1. Proposed reaction pathway leading to the formation of the $[\{ReO_3(\mu\text{-}F)\}_3(\mu_3\text{-}O)]^{2-}$ anion. The $[ReO_4]^-$ is formed in eq (3.6).

only products observed by Raman spectroscopy and single-crystal X-ray diffraction were the known $[N(CH_3)_4][ReO_4]$ salt[213] and $(CH_3CN)_2ReO_3F$.[19] A second attempt involved a reaction analogous to that used to synthesize the $[\{TcO_3(\mu\text{-}F)\}_3(\mu_3\text{-}F)]^-$ anion in aHF[23] (see Scheme A2, for a plausible reaction pathway). Thus, $K[ReO_4]$ or $[NH_4][ReO_4]$ were allowed to react with aHF at room temperature. Upon removal of aHF under dynamic vacuum, mixtures of $K/[NH_4][ReO_4]$, $K/[NH_4][ReO_3F_2]$, $K/[NH_4][ReO_2F_4]$, and $K[H_3O][ReO_3F_3]$ were recovered as the only reaction products. The product identities were confirmed by the Raman spectra of the mixtures and by the single-crystal X-ray structures of these salts. The structures of the $K/[NH_4][ReO_3F_2]$ and $K[H_3O][ReO_3F_3]$ salts are discussed in Chapter 4.

A major difference between the two reaction pathways (Schemes 3.1 and A2) lies in the nature of the reaction media. In the basic solvent, CH_3CN, the $[ReO_4]^-$ anion serves as a source of the tricoordinate oxygen bridge in its reaction with the intermediate anion, $[\{(CH_3CN)ReO_3F\}_2(\mu\text{-}F)]^-$, whereas in acidic (aHF) solution, the $[MO_4]^-$ (M = Tc, Re) anion immediately undergoes HF solvolysis to form MO_3F and $[H_3O]^+$.[30,34]

3.2.2. NMR Spectroscopy

The ^{19}F NMR spectrum (Figure 3.1) of a solution resulting from the reaction of $[N(CH_3)_4]F$ and ReO_3F (1:1 stoichiometry) was recorded in CH_3CN at 27 °C and consisted of a broad signal ($\delta(^{19}F) = -182.8$ ppm, $\nu_{½} = 213$ Hz) and two sharp ($\nu_{½} = 5.0$ Hz), equal-intensity triplets ($\delta(^{19}F) = -53.0$ ppm ($F_{c,t}$); $\delta(^{19}F) = -66.1$ ppm ($F_{c,c}$) and

$^{2}J(^{19}F_{c,t}-19F_{c,c})$ = 87 Hz, where the c and t subscripts denote cis and trans to oxygen, respectively) that are unambiguously assigned to [*cis*-$ReO_2F_4]^-$, in agreement with the published ^{19}F NMR spectrum.[19] The broad singlet at −182.8 ppm is tentatively assigned to a fluorine bridge environment by comparison with the bridging fluorine resonance of $[\mu\text{-}F(ReO_2F_3)_2]^-$ (−141.2 ppm).[19] The ^{19}F NOE and ^{19}F–^{19}F COSY spectra did not show any NOE or correlation between the two triplets of [*cis*-$ReO_2F_4]^-$ and the broad singlet, thus confirming their independence and the presence of a single fluorine environment in the unknown species. The NMR findings are in accordance with the X-ray crystal structure of $[\{ReO_3(\mu\text{-}F)\}_3(\mu_3\text{-}O)]^{2-}$ (Structure I), which contains three equivalent bridging fluorine atoms (see X-ray Crystallography) and which was also observed, along with $[ReO_4]^-$, in the room temperature Raman spectrum of the reaction mixture dissolved in CH_3CN.

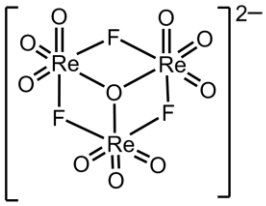

I

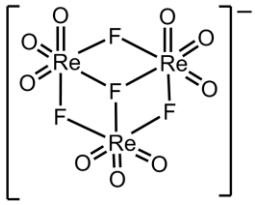

II

To further investigate the nature of the species associated with the ^{19}F resonance at −182.8 ppm, the ^{19}F NMR chemical shift of $[\{ReO_3(\mu\text{-}F)\}_3(\mu_3\text{-}O)]^{2-}$ was calculated at the PBE0/SO/ZORA/TZ2P level. The chemical shift obtained was referenced to the chemical shift of the bridging fluorine of the structurally related $[\mu\text{-}F(ReO_2F_3)_2]^-$ anion of its $[N(CH_3)_4]^+$ salt in CH_3CN solvent at −40 °C (−141.2 ppm with respect to $CFCl_3$; also see Experimental and Computational Results).[19] The calculated ^{19}F chemical shift of the

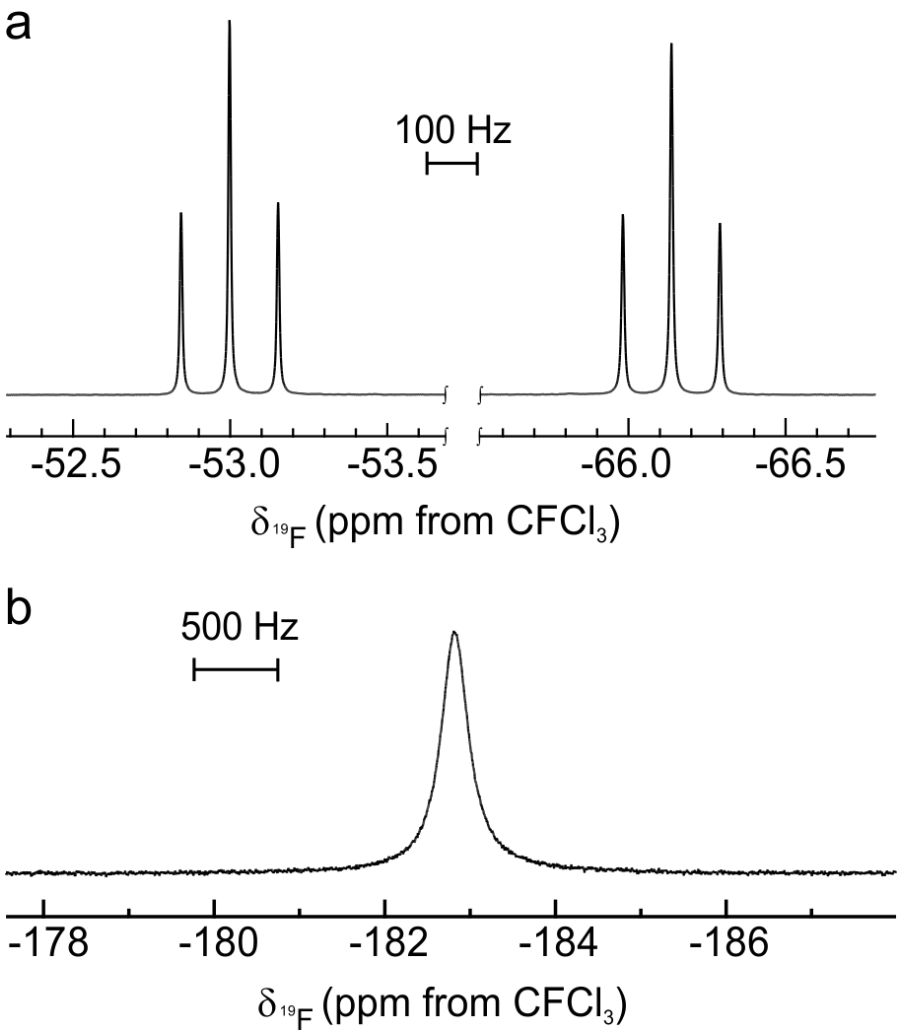

Figure 3.1. The ^{19}F NMR spectra (470.599 MHz) of the (a) $[ReO_2F_4]^-$ and (b) $[\{ReO_3(\mu F)\}_3(\mu_3\text{-}O)]^{2-}$ anions in $[N(CH_3)_4][ReO_2F_4]$ and $[N(CH_3)_4]_2[\{ReO_3(\mu\text{-}F)\}_3(\mu_3\text{-}O)]$, respectively, recorded at 27 ^oC in CH_3CN.

three equivalent bridging F_{μ} atoms of $[\{ReO_3(\mu\text{-}F)\}_3(\mu_3\text{-}O)]^{2-}$ is −179.3 ppm, in very good agreement with the experimental value, −182.8 ppm.

For comparison, the isotropic ^{19}F chemical shifts of the three bridging F_{μ} atoms (−203.9 ppm) and the central three coordinate bridging F_{μ_3} atom (−195.9 ppm) in the related $[\{ReO_3(\mu\text{-}F)\}_3(\mu_3\text{-}F)]^{-}$ anion (Structure II) were also calculated. Taking into account the estimated error in the calculated chemical shift (±20 ppm),[214,215] the observed broad resonance at −182.8 ppm, in principle, could also be assigned to the $[\{ReO_3(\mu\text{-}F)\}_3(\mu_3\text{-}F)]^{-}$ anion, with the broadening of the resonance arising from intramolecular fluorine chemical exchange between the F_{μ} and F_{μ_3} environments of $[\{ReO_3(\mu\text{-}F)\}_3(\mu_3\text{-}F)]^{-}$. Unfortunately, variable temperature experiments, which may have led to splitting or further coalescence of the resonance, could not be performed because crystalline material deposited at 0 °C and slow decomposition took place above ca. 40 °C.

On the basis of ^{19}F NMR chemical shifts alone, it is not possible to unambiguously determine the solution structure of the anion, nor is it possible to differentiate between $[\{ReO_3(\mu\text{-}F)\}_3(\mu_3\text{-}O)]^{2-}$ and $[\{ReO_3(\mu\text{-}F)\}_3(\mu_3\text{-}F)]^{-}$; however, from Raman spectroscopic findings, the X-ray crystal structure, and synthetic considerations (see 2.3.3. Synthesis of $[N(CH_3)_4]_2[\{ReO_3(\mu\text{-}F)\}_3(\mu_3\text{-}O)]$), it is reasonable to conclude that the $[\{ReO_3(\mu\text{-}F)\}_3(\mu_3\text{-}O)]^{2-}$ anion retains its solid state structure in solution.

3.2.3. X-ray Crystallography

Details of the data collection and other crystallographic information for $(HF)_2ReO_3F{\cdot}HF$, $[N(CH_3)_4]_2[\{ReO_3(\mu\text{-}F)\}_3(\mu_3\text{-}O)]{\cdot}CH_3CN$, $[N(CH_3)_4][ReO_4]$, and

KF·4HF are given in Table 3.2, and important bond lengths and bond angles for $(HF)_2ReO_3F{\cdot}HF$ and $[\{ReO_3(\mu\text{-}F)\}_3(\mu_3\text{-}O)]^{2-}$ are provided in Tables 3.3 and 3.4. The crystal structure of KF·4HF is given in Figure A2.

The crystal structure of $[N(CH_3)_4]_2[\{ReO_3(\mu\text{-}F)\}_3(\mu_3\text{-}O)]{\cdot}CH_3CN$ consists of well-separated $[N(CH_3)_4]^+$ cations, $[\{ReO_3(\mu\text{-}F)\}_3(\mu_3\text{-}O)]^{2-}$ anions, and CH_3CN molecules (Figure A3), and the crystal structure of $[N(CH_3)_4][ReO_4]$ consists of well-separated $[N(CH_3)_4]^+$ cations and $[ReO_4]^-$ anions (Figure A4). In both structures, the tetrahedral $[N(CH_3)_4]^+$ cations lie on C_3-axes. The N−C bond lengths are equal within experimental error and are comparable to those given in the literature.[39,47,216] The geometrical parameters of the CH_3CN molecule are also in good agreement with the literature values.[19,217]

3.2.3.1. $[N(CH_3)_4][ReO_4]$

The $[ReO_4]^-$ anion has T_d symmetry with a Re−O bond length (1.726(3) Å) that is in good agreement with the Re−O bond lengths of other $[ReO_4]^-$ salts (K^+, 1.719(5) Å, at 20 °C;[218] $[NH_4]^+$, 1.737(5) Å, at −138 °C and 1.720(5) Å, at 22 °C[219]).

3.2.3.2. $(HF)_2ReO_3F{\cdot}HF$

The crystal structure of $(HF)_2ReO_3F{\cdot}HF$ reveals that the coordination sphere of rhenium is a distorted octahedron consisting of three oxygen atoms that are cis to one another, a fluorine atom, and two HF molecules that are cis to one another and trans to oxygen ligands (Figure 3.2). The HF molecules are coordinated to the rhenium atom

Table 3.2. Summary of Crystal Data and Refinement Results for $[N(CH_3)_4]_2[\{ReO_3(\mu\text{-}F)\}_3(\mu_3\text{-}O)]\cdot CH_3CN$ **(1)**, $[N(CH_3)_4]\,[ReO_4]$ **(2)**, $(HF)_2ReO_3F\cdot HF$ **(3)**, and $KF\cdot 4HF$ **(4)**

chem formula	**(1)**	**(2)**	**(3)**	**(4)**
space group	$P2_1/c$	$Pbcm$	$P2_1/c$	$I4_1/a$
a (Å)	9.1792(5)	5.7222(3)	4.9381(3)	6.287(5)
b (Å)	20.3457(12)	11.8535(5)	4.9392(3)	6.287(5)
c (Å)	14.3432(6)	12.4754(6)	20.716(1)	12.937(5)
β (deg)	124.3(3)	90	91.906(2)	90
V (Å)^3	2212.8(2)	845.57(7)	505.02(8)	511.4(1)
molecules/unit cell	4	4	4	4
mol wt (g mol^{-1})	964.95	1297.38	1252.90	536.40
calcd density (g cm^{-3})	2.896	2.548	4.120	1.742
T (^{o}C)	–173	–173	–173	–173
μ (mm^{-1})	16.44	14.33	24.08	1.02
R_1[a]	0.0371	0.0338	0.0371	0.0299
wR_2[b]	0.0782	0.0841	0.0931	0.0838

[a] R_1 is defined as $\Sigma \| F_o | - | F_c \| \Sigma | F_o |$ for $I > 2\sigma(I)$. [b] wR_2 is defined as $[\Sigma[w(F_o^2 - F_c^2)^2]/\Sigma w(F_o^2)^2]^{1/2}$ for $I > 2\sigma(I)$.

Table 3.3. Experimental Bond Lengths (Å) and Bond Angles (deg) for $(HF)_2ReO_3F{\cdot}HF$ and Calculated Bond Lengths (Å) and Bond Angles (deg) for Monomeric ReO_3F

exptl[a]		calcd[b]	
$(HF)_2ReO_3F{\cdot}HF$		ReO_3F (C_{3v})	
Bond Lengths (Å)			
Re(1)−O(1)	1.669(5)	Re−O1	1.693
Re(1)−O(2)	1.662(5)	Re−O2	1.693
Re(1)−O/F(3)	1.838(5)	Re−O3	1.693
Re(1)−O/F(4)	1.837(4)	Re−F	1.844
Re(1)---F(1)	2.045(4)		
Re(1)---F(2)	2.014(4)		
Bond Angles (deg)			
O(1)−Re(1)−O(2)	102.9(3)	O1−Re−O2	109.0
O(1)−Re(1)−O(3)	95.9(3)	O1−Re−O3	109.0
O(2)−Re(1)−O(3)	96.7(3)	O2−Re−O3	109.0
O(3)−Re(1)−F(4)	159.1(3)	O3−Re−F	109.9
O(1)−Re(1)−F(4)	97.1(3)	O1−Re−F	109.9
O(2)−Re(1)−F(4)	96.5(3)	O2−Re−F	109.9
F(1)---Re(1)---F(2)	75.2(2)		
F(4)−Re(1)---F(2)	81.7(2)		
O(3)−Re(1)---F(2)	81.8(2)		
O(2)−Re(1)---F(1)	166.9(2)		
O(2)−Re(1)---F(2)	91.7(2)		
O(1)−Re(1)---F(1)	90.0(2)		
O(1)−Re(1)---F(2)	165.3(2)		
O(3)−Re(1)---F(1)	82.1(2)		
F(1)---Re(1)−F(4)	81.3(2)		

[a] The labeling scheme corresponds to that used in Figure 3.2. [b]B3LYP/aug-cc-pVTZ(-PP). The labeling scheme corresponds to that used in Figure A1.

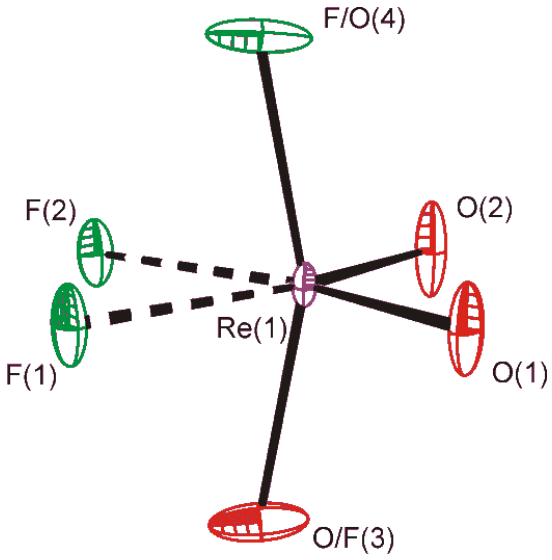

Figure 3.2. Structural unit in the X-ray crystal structure of $(HF)_2ReO_3F \cdot HF$ with thermal ellipsoids drawn at the 30% probability level. The F/O(4) and O/F(3) positions are twofold disordered.

Table 3.4. Experimental Structural Parameters for the $[\{ReO_3(\mu\text{-}F)\}_3(\mu_3\text{-}O)]^{2-}$ Anion in $[N(CH_3)_4]_2[\{ReO_3(\mu\text{-}F)\}_3(\mu_3\text{-}O)]\cdot CH_3CN$ and Calculated Structural Parameters for the $[\{ReO_3(\mu\text{-}F)\}_3(\mu_3\text{-}O)]^{2-}$ and $[\{ReO_3(\mu\text{-}F)\}_3(\mu_3\text{-}F)]^{-}$ Anions

exptl[a]		calcd[b]			
$[\{ReO_3(\mu\text{-}F)\}_3(\mu_3\text{-}O)]^{2-}$		$[\{ReO_3(\mu\text{-}F)\}_3(\mu_3\text{-}O)]^{2-}$		$[\{ReO_3(\mu\text{-}F)\}_3(\mu_3\text{-}F)]^{-}$	
Bond Lengths (Å)					
Re(1)−O(1)	1.711(4)	Re_1-O_A	1.707	Re_1-O_A	1.701
Re(1)−O(2)	1.706(4)	Re_1-O_B	1.715	Re_1-O_B	1.702
Re(1)−O(3)	1.713(4)	Re_1-O_C	1.707	Re_1-O_C	1.701
Re(2)−O(4)	1.705(4)	Re_2-O_A	1.707	Re_2-O_A	1.701
Re(2)−O(5)	1.716(4)	Re_2-O_B	1.715	Re_2-O_B	1.702
Re(2)−O(6)	1.705(4)	Re_2-O_C	1.707	Re_2-O_C	1.701
Re(3)−O(7)	1.703(4)	Re_3-O_A	1.707	Re_3-O_A	1.701
Re(3)−O(8)	1.666(5)	Re_3-O_B	1.715	Re_3-O_B	1.702
Re(3)−O(9)	1.700(4)	Re_3-O_C	1.707	Re_3-O_C	1.701
Re(1)−O(10)	2.079(4)	Re_1-O_D	2.106	Re_1-F_4	2.322
Re(2)−O(10)	2.072(4)	Re_2-O_D	2.106	Re_2-F_4	2.322
Re(3)−O(10)	2.078(4)	Re_3-O_D	2.106	Re_3-F_4	2.322
Re(1)−F(1)	2.139(3)	Re_1-F_1	2.165	Re_1-F_1	2.127
Re(1)−F(2)	2.166(3)	Re_1-F_2	2.165	Re_1-F_2	2.127
Re(2)−F(2)	2.163(3)	Re_2-F_2	2.165	Re_2-F_2	2.127
Re(2)−F(3)	2.148(3)	Re_2-F_3	2.165	Re_2-F_3	2.127
Re(3)−F(3)	2.144(3)	Re_3-F_3	2.165	Re_3-F_3	2.127
Re(3)−F(1)	2.140(3)	Re_3-F_1	2.165	Re_3-F_1	2.127
Bond Angles (deg)					
O(1)−Re(1)−O2	102.6(2)	$O_A-Re_1-O_B$	104.3	$O_A-Re_1-O_B$	105.1
O(2)−Re(1)−O(3)	105.4(2)	$O_B-Re_1-O_C$	104.3	$O_B-Re_1-O_C$	105.1
O(3)−Re(1)−O(1)	104.0(2)	$O_C-Re_1-O_A$	102.2	$O_C-Re_1-O_A$	103.1
O(1)−Re(1)−O(10)	95.4(2)	$O_A-Re_1-O_D$	95.8	$O_A-Re_1-F_4$	89.9
O(2)−Re(1)−O(10)	148.2(2)	$O_B-Re_1-O_D$	147.5	$O_B-Re_1-F_4$	155.1
O(3)−Re(1)−O(10)	94.4(2)	$O_C-Re_1-O_D$	95.8	$O_C-Re_1-F_4$	89.9
O(4)−Re(2)−O(5)	104.2(2)	$O_A-Re_2-O_B$	104.3	$O_A-Re_2-O_B$	105.1
O(5)−Re(2)−O(6)	105.1(2)	$O_B-Re_2-O_C$	104.3	$O_B-Re_2-O_C$	105.1
O(6)−Re(2)−O(4)	102.7(2)	$O_C-Re_2-O_A$	102.2	$O_C-Re_2-O_A$	103.1
O(4)−Re(2)−O(10)	94.4(2)	$O_A-Re_2-O_D$	95.8	$O_A-Re_2-F_4$	89.9
O(5)−Re(2)−O(10)	148.4(2)	$O_B-Re_2-O_D$	147.5	$O_B-Re_2-F_4$	155.4
O(6)−Re(2)−O(10)	95.2(2)	$O_C-Re_2-O_D$	95.8	$O_C-Re_2-F_4$	90.0
O(7)−Re(3)−O(8)	104.6(2)	$O_A-Re_3-O_B$	104.3	$O_A-Re_3-O_B$	105.1
O(8)−Re(3)−O(9)	105.2(2)	$O_B-Re_3-O_C$	104.3	$O_B-Re_3-O_C$	105.1
O(9)−Re(3)−O(7)	103.2(2)	$O_C-Re_3-O_A$	102.2	$O_C-Re_3-O_A$	103.1
O(7)−Re(3)−O(10)	94.9(2)	$O_A-Re_3-O_D$	95.8	$O_A-Re_3-F_4$	89.9
O(8)−Re(3)−O(10)	147.5(2)	$O_B-Re_3-O_D$	147.5	$O_B-Re_3-F_4$	155.4
O(9)−Re(3)−O(10)	95.1(2)	$O_C-Re_3-O_D$	95.8	$O_C-Re_3-F_4$	89.9
O(1)−Re(1)−F(2)	87.3(2)	$O_A-Re_1-F_2$	88.3	$O_A-Re_1-F_2$	88.0

Table 3.4. (continued…)

O(2)−Re(1)−F(2)	86.0(2)	O_B−Re_1−F_2	85.9	O_B−Re_1−F_2	93.7
O(3)−Re(1)−F(2)	162.3(2)	O_C−Re_1−F_2	162.8	O_C−Re_1−F_2	154.6
O(10)−Re(1)−F(2)	69.9(1)	O_D−Re_1−F_2	69.3	F_4−Re_1−F_2	67.0
O(1)−Re(1)−F(1)	162.2(2)	O_A−Re_1−F_1	162.8	O_A−Re_1−F_1	154.6
O(2)−Re(1)−F(1)	84.6(2)	O_B−Re_1−F_1	85.9	O_B−Re_1−F_1	93.7
O(3)−Re(1)−F(1)	89.7(2)	O_C−Re_1−F_1	88.3	O_C−Re_1−F_1	88.0
O(10)−Re(1)−F(1)	69.9(1)	O_D−Re_1−F_1	69.3	F_4−Re_1−F_1	67.0
O(4)−Re(2)−F(2)	88.9(2)	O_A−Re_2−F_2	88.3	O_A−Re_2−F_2	88.0
O(5)−Re(2)−F(2)	84.8(2)	O_B−Re_2−F_2	85.9	O_B−Re_2−F_2	93.7
O(6)−Re(2)−F(2)	162.1(2)	O_C−Re_2−F_2	162.8	O_C−Re_2−F_2	154.6
O(10)−Re(2)−F(2)	70.0(1)	O_D−Re_2−F_2	69.3	F_4−Re_2−F_2	67.0
O(4)−Re(2)−F(3)	161.9(2)	O_A−Re_2−F_3	162.8	O_A−Re_2−F_3	154.6
O(5)−Re(2)−F(3)	86.2(2)	O_B−Re_2−F_3	85.9	O_B−Re_2−F_3	93.7
O(6)−Re(2)−F(3)	88.6(2)	O_C−Re_2−F_3	88.3	O_C−Re_2−F_3	88.0
O(10)−Re(2)−F(3)	70.2(1)	O_D−Re_2−F_3	69.8	O_4−Re_2−F_3	67.0
O(7)−Re(3)−F(3)	162.3(2)	O_A−Re_3−F_3	162.8	O_A−Re_3−F_3	154.6
O(8)−Re(3)−F(3)	85.2(2)	O_B−Re_3−F_3	85.9	O_B−Re_3−F_3	93.7
O(9)−Re(3)−F(3)	87.9(2)	O_C−Re_3−F_3	88.3	O_C−Re_3−F_3	88.0
O(10)−Re(3)−F(3)	70.2(1)	O_D−Re_3−F_3	69.3	F_4−Re_3−F_3	67.0
O(7)−Re(3)−F(1)	88.2(2)	O_A−Re_3−F_1	88.3	O_A−Re_3−F_1	88.0
O(8)−Re(3)−F(1)	84.3(2)	O_B−Re_3−F_1	85.9	O_B−Re_3−F_1	93.7
O(9)−Re(3)−F(1)	162.5(2)	O_C−Re_3−F_1	162.8	O_C−Re_3−F_1	154.6
O(10)−Re(3)−F(1)	70.4(1)	O_D−Re_3−F_1	69.3	F_4−Re_3−F_1	67.0
F(1)−Re(1)−F(2)	77.7(1)	F_1−Re_1−F_2	78.5	F_1−Re_1−F_2	73.6
F(2)−Re(2)−F(3)	77.1(1)	F_2−Re_2−F_3	78.5	F_2−Re_2−F_3	73.6
F(3)−Re(3)−F(1)	78.1(1)	F_3−Re_3−F_1	78.5	F_3−Re_3−F_1	73.6
Re(1)−O(10)−Re(2)	110.6(2)	Re_1−O_D−Re_2	110.2	Re_1−F_4−Re_2	103.9
Re(2)−O(10)−Re(3)	109.6(2)	Re_2−O_D−Re_3	110.2	Re_2−F_4−Re_3	103.8
Re(3)−O(10)−Re(1)	109.1(2)	Re_3−O_D−Re_1	110.2	Re_3−F_4−Re_1	103.8
Re(1)−F(2)−Re(2)	104.1(1)	Re_1−F_2−Re_2	105.9	Re_1−F_2−Re_2	118.5
Re(2)−F(3)−Re(3)	104.4(1)	Re_2−F_3−Re_3	105.9	Re_2−F_3−Re_3	118.4
Re(3)−F(1)−Re(1)	104.4(1)	Re_3−F_1−Re_1	105.9	Re_3−F_1−Re_1	118.5

[a] For the atom labeling scheme, see Figure 3.3. [b] For the atom labeling scheme, see Figure 3.4. B3LYP/aug-cc-pVTZ(-PP) basis sets.

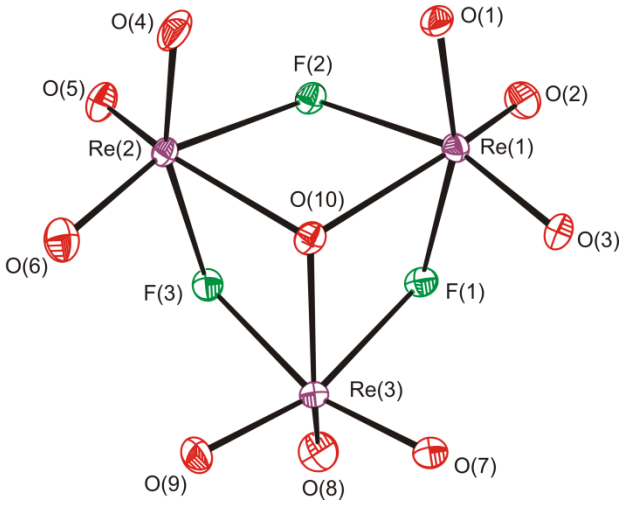

Figure 3.3. The $[\{ReO_3(\mu\text{-}F)\}_3(\mu_3\text{-}O)]^{2-}$ anion in the crystal structure of $[N(CH_3)_4]_2[\{ReO_3(\mu\text{-}F)\}_3(\mu_3\text{-}O)]\cdot CH_3CN$; thermal ellipsoids are shown at the 50% probability level.

a

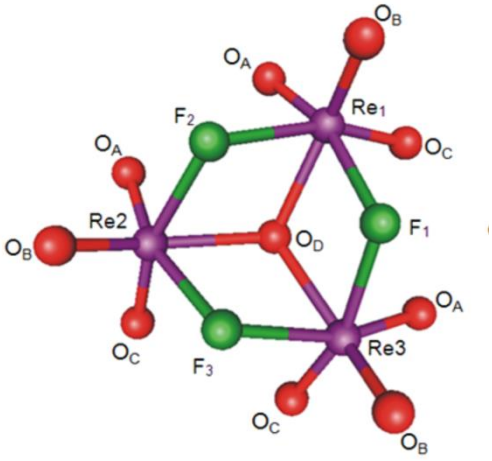

b

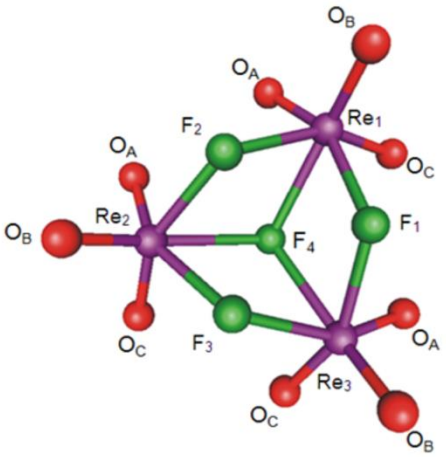

Figure 3.4. Calculated structures of the (a) $[\{ReO_3(\mu\text{-}F)\}_3(\mu_3\text{-}O)]^{2-}$ and (b) $[\{ReO_3(\mu\text{-}F)\}_3(\mu_3\text{-}F)]^{-}$ anions (B3LYP/aug-cc-pVTZ(-PP)).

through their F atoms, representing the only known example of HF coordinated to rhenium. Several examples in which HF is coordinated to alkaline earth and lanthanide metal cations[220] and to Os(VIII)[221] are also known. The facial arrangement of oxygen atoms is the result of equal competition of the filled p orbitals of the oxygen atoms for the three empty approximately $d_{t_{2g}}$ orbitals of rhenium.[17] The rhenium atom is found to lie in the [F(1), F(2), O(1), O(2)] plane and is equidistant from the disordered F/O(3, 4) atoms. The Re−O(1, 2) bond lengths trans to the two HF molecules (1.669(5) and 1.662(5) Å) are very similar to the Re−O bond lengths in polymeric ReO_2F_3 (1.667(8) and 1.675(8) Å)[19] and (1.669(9)−1.676(9) Å),[21] but are somewhat shorter than those of $(CH_3CN)_2ReO_3F$ (1.705(4) and 1.788(5) Å)[19] and $(OEt_2)_2ReO_3F$ (1.703(3), 1.708(3), and 1.778(2) Å).[21] The third Re−O bond length could not be accurately determined due to a 2-fold positional disorder between O/F(3) and F/O(4). These bond lengths (1.838(5) and 1.837(4) Å) are the average of the Re−O (1.788(5) Å) and Re−F (1.880(5) Å)[19] bond lengths of $(CH_3CN)_2ReO_3F$.[19] The Re---F(1, 2) distances (2.045(4) and 2.014(4) Å) are comparable to the Re---F bridging distances in oligomeric ReO_2F_3 (2.085(6)−2.118(7) Å)[19] (2.075(7)−2.109(6) Å)[21] and ReO_3F (2.141(7)−2.142(7) Å).[21] The O/F(3)−Re−F/O(4) bond angle (159.1(3)^o) is bent away from the Re−O(1, 2) double bond domain toward the less repulsive Re---F(1, 2) bonds. The O(1)−Re−O(2) angle (102.9(3)^o) is considerably more open than the F(1)---Re---F(2) angle (75.2(2)^o) as a result of greater repulsions between the Re−O(1) and Re−O(2) double bond domains, with weaker repulsions occurring between the longer and more polar Re---F(1, 2) bond domains. In turn, the small F(1)---Re---F(2) angle is a consequence of repulsive

interactions between the Re---F(1, 2) bond domains and the Re−O(1, 2) double bond domains.

3.2.3.3. $[N(CH_3)_4]_2[\{ReO_3(\mu\text{-}F)\}_3(\mu_3\text{-}O)]\cdot CH_3CN$

The $[\{ReO_3(\mu\text{-}F)\}_3(\mu_3\text{-}O)]^{2-}$ anion is positioned on a C_3-axis and consists of three ReO_3F units linked to each other through dicoordinate bridging fluorine atoms (F_μ) and a central tricoordinate bridging oxygen atom (O_{μ_3}). The bridge-head O_{μ_3} atom is located on the C_3-axis, and the coordination environments of the rhenium atoms are pseudo-octahedral (Figure 3.3).

A closely related structure with a triply coordinated oxygen bridge atom has been reported for the $[\{WF_3(\mu\text{-}O)\}_3(\mu_3\text{-}O)]^{5-}$ anion in $[NH_4]_5[\{WF_3(\mu\text{-}O)\}_3(\mu_3\text{-}O)]\cdot[NH_4]F\cdot H_2O$.[222] The Re atoms of $[\{ReO_3(\mu\text{-}F)\}_3(\mu_3\text{-}O)]^{2-}$ form a triangle with Re···Re distances of 3.4128(3) Å (Re(1)···Re(2)), 3.3910(4) Å (Re(2)···Re(3)), and 3.3870(3) Å (Re(3)···Re(1)). The Re···Re distances are significantly longer than the W···W distances (2.514(2) Å) of the W_3-triangle in $[\{WF_3(\mu\text{-}O)\}_3(\mu_3\text{-}O)]^{5-}$,[222] which is indicative of significant W−W bonding. Rhenium in $[\{ReO_3(\mu\text{-}F)\}_3(\mu_3\text{-}O)]^{2-}$ is in the +7 oxidation state (Re, $5d^0$), where the terminal coordination sites are occupied by doubly bonded oxygen ligands and the μ-bridge positions are occupied by bridging fluorine ligands. In contrast, tungsten in $[\{WF_3(\mu\text{-}O)\}_3(\mu_3\text{-}O)]^{5-}$ is in the +4 oxidation state (W, $5d^2$) where the terminal coordination sites are occupied by fluorine ligands and the μ-bridge positions are occupied by oxygen ligands. The influence of O_{μ_3} on both structures is minor. The structural parameters are dominated by the metal oxidation state. Thus, the

availability of the d^2 valence electrons of $[\{WF_3(\mu\text{-}O)\}_3(\mu_3\text{-}O)]^{5-}$ allows metal−metal bond formation among the tungsten metal centers, resulting in W···W distances that are substantially shorter than the Re···Re distances in $[\{ReO_3(\mu\text{-}F)\}_3(\mu_3\text{-}O)]^{2-}$. Presently, neither tungsten oxide fluorides in higher oxidation states nor rhenium oxide fluorides in lower oxidation states having similar structural motifs, which could substantiate the observed trend, are known. However, several examples of similar trends occur among rhenium and tungsten chlorides and chloroanions. Rhenium(III) trichloride exists as a Re_3Cl_9 cluster with Re···Re distances of 2.489(6) Å,[223] whereas Re(V)Cl_5 contains Re_2Cl_{10} units with a substantially longer Re···Re distance of 3.739(2) Å.[224] In comparison, the W···W distances are 2.409(5) Å in $K_3[W_2(III)Cl_9]$,[225] and 2.8703(6)−2.9054(6) Å in the octahedral W_6-cluster of $K_2[W_6(III)Cl_{18}]$.[226] The central bridging O_{μ_3} and bridging F_μ atoms of $[\{ReO_3(\mu\text{-}F)\}_3(\mu_3\text{-}O)]^{2-}$ coordinate trans to the terminal oxygen atoms (O_t) of the facial ReO_3 group so that the filled oxygen p orbitals of the O_t atoms compete equally for the three empty $d_{2_{tg}}$ orbitals of rhenium.[17] The Re(1), Re(2), and Re(3) atoms lie in the [F(1), F(2), O(1), O(3)], [F(2), F(3), O(4), O(6)], and [F(3), F(1), O(7), O(9)] planes, respectively. The Re−O_t bonds are comparable in length to those in oligomeric ReO_3F (1.667(7)−1.715(8) Å),[21] ReO_2F_3 (1.667(8)−1.675(8) Å)[19] and (1.669(9)−1.676(9) Å),[21] $[ReO_4]^-$ (1.726(3) Å, this work), $[ReO_2F_4]^-$ (1.678(9) Å),[19] and $[(ReO_2F_2)(\mu\text{-}F)_2(ReO_2F_3)_2]^-$ (1.669(8)−1.715(8) Å).[19] The bridging Re−F_μ bond lengths are comparable to the Re−F_μ bond lengths in ReO_3F (2.141(7) and 2.142(7) Å),[21] ReO_2F_3 (2.085(6)−2.118(7) Å,[19] 2.075(7)−2.109(6) Å[21]), $[\mu\text{-}F(ReO_2F_3)_2]^-$ (2.155(4)−2.150(4) Å),[19] and $[(ReO_2F_2)(\mu\text{-}F)_2(ReO_2F_3)_2]^-$ (2.039(6)−2.151(6) Å).[19]

A tricoordinate bridge-head oxygen atom, O_{μ_3}, has not been previously observed in a rhenium oxide fluoride structure. The rhenium atoms of $[\{ReO_3(\mu\text{-}F)\}_3(\mu_3\text{-}O)]^{2-}$ are equidistant (within ±3σ) from O_{μ_3} (2.072(4)−2.079(4) Å). These Re−O_{μ_3} bonds are comparable in length to the Re−O_μ bonds of Re_2O_7 (2.05(2)−2.16(3) Å),[227] and to the Re−O_{μ_3} bonds of $[NEt_4]_2[\{Re(CO)_3(\mu\text{-}H)\}_3(\mu_3\text{-}O)]$ (2.12 Å),[228] and $\{(t\text{-}Bu)_2SiO_2\}_2(\mu\text{-}O)_4(\mu_3\text{-}O)_2\{ReO(NAr)\}_2\{Re(NAr)\}_2$ (Ar = 2,6-iPr_2−C_6H_3; 2.170(5) Å).[229] The Re−O_{μ_3} bridge bonds of $[\{ReO_3(\mu\text{-}F)\}_3(\mu_3\text{-}O)]^{2-}$ are longer than the terminal Re−O_t bonds and slightly shorter than the Re−F_μ bonds of this anion. These bond length trends differ from those of the related $[\{TcO_3(\mu\text{-}F)\}_3(\mu_3\text{-}F)]^-$ anion where the Tc−F_{μ_3} bonds (2.223(3)−2.266(3) Å) are longer than the Tc−F_μ bonds (2.098(3)−2.132(3) Å).[23] The experimental bond length trends for $[\{ReO_3(\mu\text{-}F)\}_3(\mu_3\text{-}O)]_2^-$ and $[\{TcO_3(\mu\text{-}F)\}_3(\mu_3\text{-}F)]^-$ are reproduced by quantum-chemical calculations (see Computational Results).

The O_t−Re−O_t angles of $[\{ReO_3(\mu\text{-}F)\}_3(\mu_3\text{-}O)]^{2-}$ are greater than the O_t−Re−F_μ and F_μ−Re−F_μ angles due to the greater spatial requirements of the terminal oxygen double bond domains which result in greater repulsive interactions with other bond pair domains as observed in $[ReO_2F_4]^-$,[19] $[\mu\text{-}F(ReO_2F_3)_2]^-$,[19] $[(ReO_2F_2)(\mu\text{-}F)_2(ReO_2F_3)_2]^-$,[19] ReO_2F_3,[19,21] and ReO_3F.[21] Compression of the F_μ−Re−F_μ angles of $[\{ReO_3(\mu\text{-}F)\}_3(\mu_3\text{-}O)]^{2-}$ relative to the F_μ−Re−F_μ (70.4(1)−77.7(1)°) angles of $[\mu\text{-}F(ReO_2F_3)_2]^-$, $[(ReO_2F_2)(\mu\text{-}F)_2(ReO_2F_3)_2]^-$, and ReO_2F_3 is also attributable to the greater spatial requirements of the Re−O_t double bond domains and to constraints imposed by the anion cage. The latter factor also influences the O_{μ_3}−Re−F_μ angles, which are the smallest of the anion cage angles (69.3°). The largest cage angles occur for the Re−O_{μ_3}−Re angles

(109.1(2)−110.6(2)°), which are more open than the angles subtended at O_{μ_3} in {(t-Bu)$_2$SiO$_2$}$_2$(μ-O)$_4$(μ$_3$-O)$_2${ReO(NAr)}$_2${Re(NAr)}$_2$ (104.8(2)°).[229]

3.2.4. Raman Spectroscopy

The low-temperature Raman spectra of $(HF)_2ReO_3F\cdot HF$ and $[N(CH_3)_4]_2[\{ReO_3(\mu\text{-}F)\}_3(\mu_3\text{-}O)]\cdot CH_3CN$ are shown in Figures 3.5 and 3.6. The observed and calculated frequencies and mode descriptions for $(HF)_2ReO_3F\cdot HF$, $[ReO_4]^-$, and $[\{ReO_3(\mu\text{-}F)\}_3(\mu_3\text{-}O)]^{2-}$ are provided in Tables 3.1, A1, and 3.5, respectively. Spectral assignments for the $[N(CH_3)_4]^+$ cation[230−232] and CH_3CN[217] were made by comparison with previously published assignments. Spectral assignments for $[\{ReO_3(\mu\text{-}F)\}_3(\mu_3\text{-}O)]^{2-}$ were made by comparison with the calculated frequencies and Raman intensities of the energy-minimized gas-phase geometries of $[ReO_4]^-$ (T_d) and $[\{ReO_3(\mu\text{-}F)\}_3(\mu_3\text{-}O)]^{2-}$ (C_{3v}), where gas-phase $[ReO_4]^-$ was used as a benchmark. The vibrational assignments for $[ReO_4]^-$ are provided in Table A1 and in the ensuing discussion provided in the Appendix A, and agree with the previously published assignments.[233,234]

3.2.4.1. $(HF)_2ReO_3F\cdot HF$

The Raman spectrum of solid $(HF)_2ReO_3F\cdot HF$ is similar to those reported for solutions of Re_2O_7 and $K[ReO_4]$ in aHF.[34] The present study, however, establishes that the previously reported solution spectra correspond to a $ReO_3F\cdot$aHF complex and not to ReO_3F (C_{3v}), as proposed by the authors.[34] In the present study, the spectrum is simpler

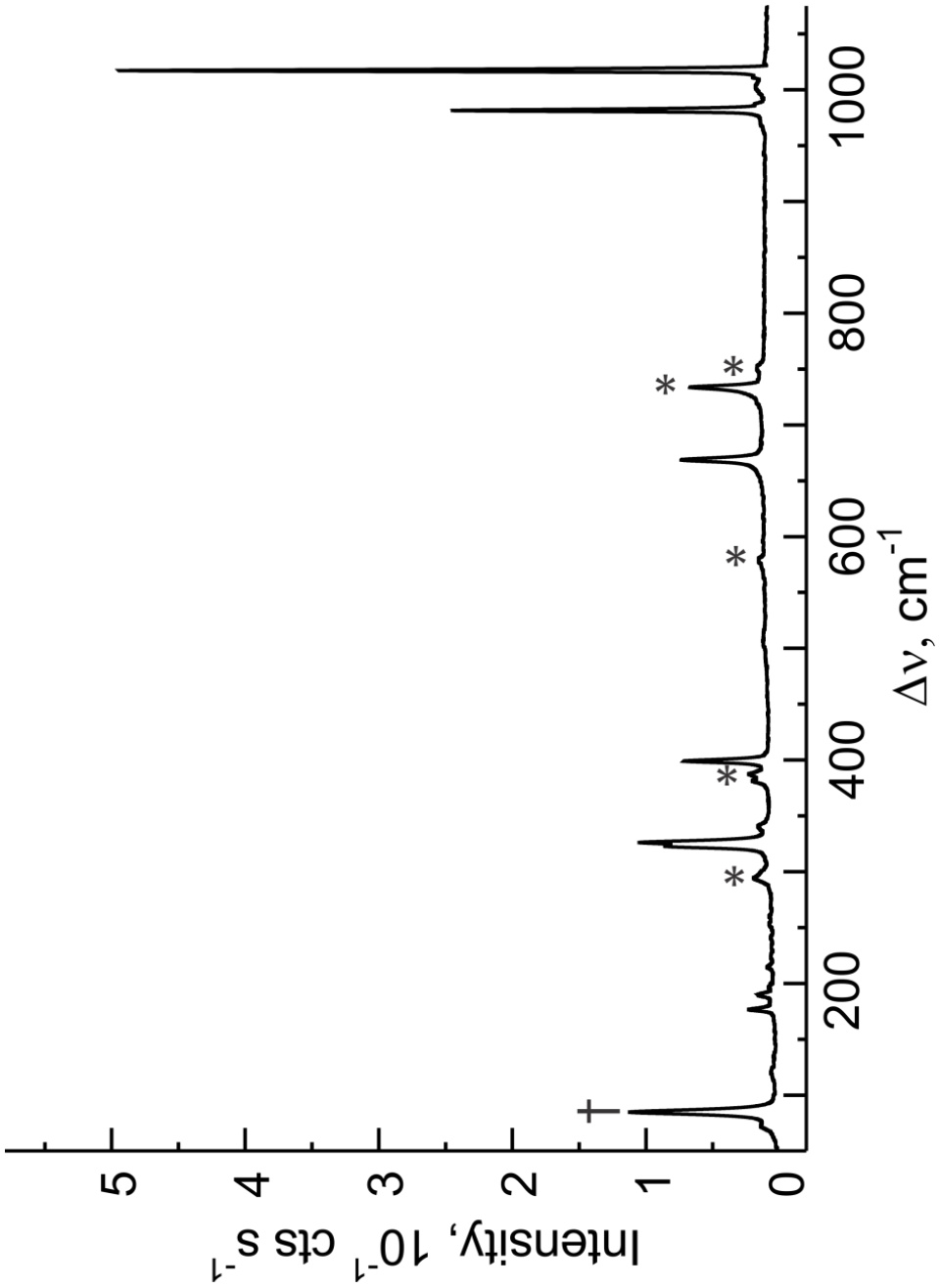

Figure 3.5. Raman spectrum of $(HF)_2ReO_3F{\cdot}HF$ obtained from the solvolysis of ReO_3F in aHF and isolated by removal of aHF under dynamic vacuum at –78 °C. The spectrum is recorded at –160 °C using 1064-nm excitation. Symbols denote an FEP sample tube line (*) and an instrumental artifact (†).

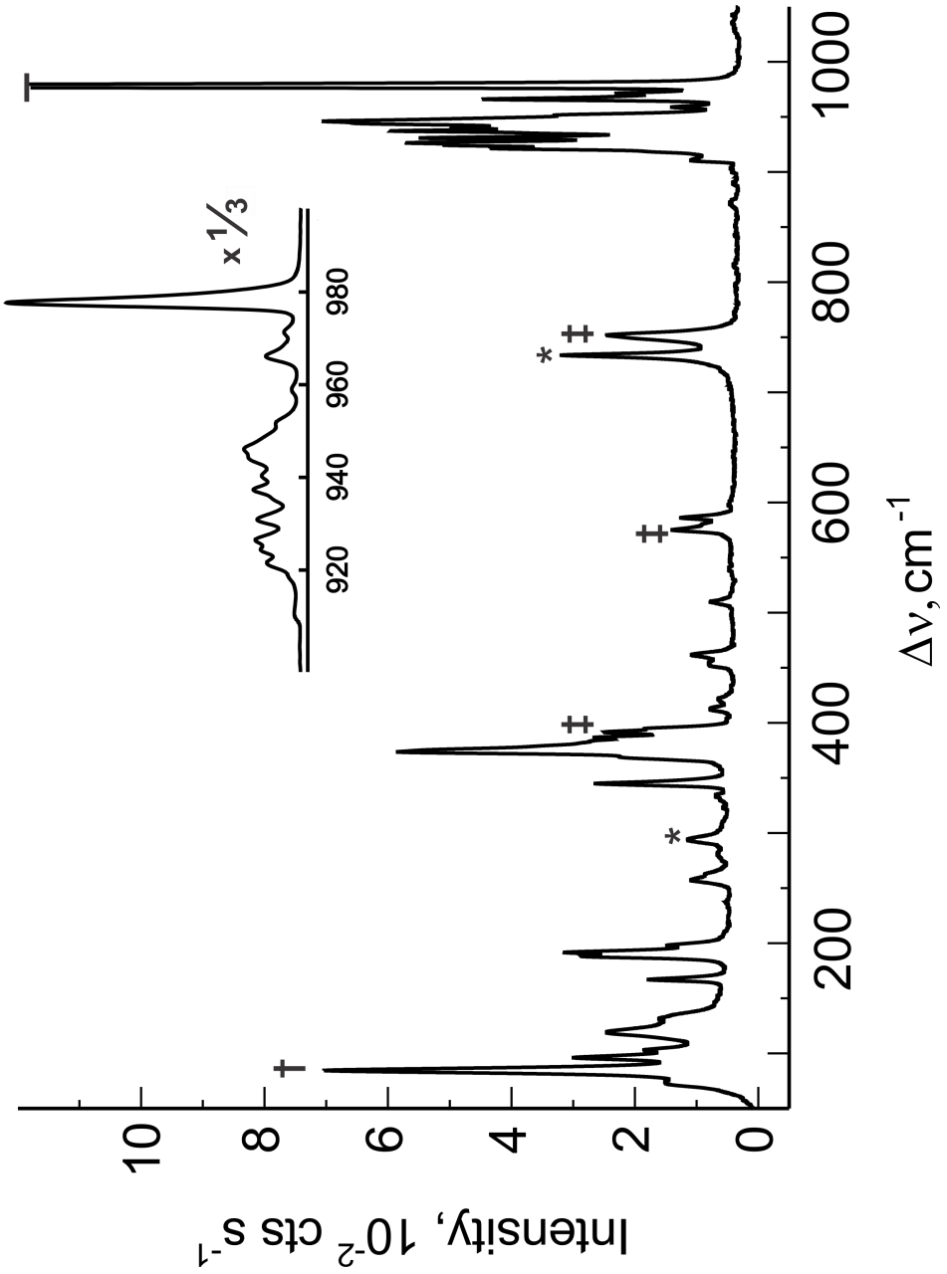

Figure 3.6. Raman spectrum of $[N(CH_3)_4]_2[\{ReO_3(\mu\text{-}F)\}_3(\mu_3\text{-}O)]\cdot CH_3CN$ recorded at –160 °C under frozen CH_3CN using 1064-nm excitation. Symbols denote an FEP sample tube line (*), instrumental artifact (†), and overlap of a $[N(CH_3)_4]_2[\{ReO_3(\mu\text{-}F)\}_3(\mu_3\text{-}O)]\cdot CH_3CN$ line with an FEP sample tube line (‡).

Table 3.5. Experimental Raman Frequencies and Intensities for the $[\{ReO_3(\mu\text{-}F)\}_3(\mu_3\text{-}O)]^{2-}$ Anion in $[N(CH_3)_4]_2[\{ReO_3(\mu\text{-}F)\}_3(\mu_3\text{-}O)]\cdot CH_3CN$ and Calculated Vibrational Frequencies and Infrared and Raman Intensities for the $[\{ReO_3(\mu\text{-}F)\}_3(\mu_3\text{-}O)]^{2-}$ and $[\{ReO_3(\mu\text{-}F)\}_3(\mu_3\text{-}F)]^{-}$ Anions

$[\{ReO_3(\mu\text{-}F)\}_3(\mu_3\text{-}O)]^{2-}$				$[\{ReO_3(\mu\text{-}F)\}_3(\mu_3\text{-}F)]^{-}$	
exptl[a,b]	calcd[c]		assgnts (C_{3v})[b,d]	calcd[c]	
978(100) 971(6)	1018(171)[44]	$\nu_1(A_1)$	$\nu(Re_1O_AO_BO_C) + \nu(Re_2O_AO_BO_C) + \nu(Re_3O_AO_BO_C)$	$\nu_1(A_1)$	1048(155)[11]
966(13)[e] 959(4) 951(9)[f] 946(20)	1005(3)[133]	$\nu_{10}(E)$	$\nu(Re_1O_AO_BO_C) - \nu(Re_2O_AO_BO_C) + \nu(Re_3O_AO_BO_C)$	$\nu_{10}(E)$	1041(1)[72]
944 sh 941(14) 937(17) 931(16)	967(35)[270]	$\nu_{11}(E)$	$\nu(Re_1O_A) - \nu(Re_1O_C) - \nu(Re_2O_A) + \nu(Re_2O_C)$	$\nu_{11}(E)$	999(28)[225]
926(16)[e] 924(15)	959(14)[558]	$\nu_2(A_1)$	$\nu(Re_1O_B) + \nu(Re_2O_B) + \nu(Re_3O_B)$	$\nu_2(A_1)$	997(6)[459]
921(12)[g] 918 sh[g] 911(3) br	942(36)[92]	$\nu_{12}(E)$	$\nu(Re_1O_B) - \nu(Re_2O_B) + \nu(Re_2O_A) + \nu(Re_2O_C) + \nu(Re_3O_B) - \nu(Re_3O_C)$	$\nu_{12}(E)$	985(20)[73]
586(3) 580 sh 575(3)	558(6)[215]	$\nu_{13}(E)$	$[\nu(Re_2O_D) - \nu(Re_3O_D)] + [\nu(Re_1F_1) + \nu(Re_3F_1) - \nu(Re_1F_2) - \nu(Re_2F_2)]$		
			$[\nu(Re_2F_4) - \nu(Re_3F_4)] + [\nu(Re_1F_1) + \nu(Re_3F_1) - \nu(Re_1F_2) - \nu(Re_2F_2)]$	$\nu_{13}(E)$	464(<1)[239]
510(2)	516(1)[1]	$\nu_3(A_1)$	$[\nu(Re_1O_D) + \nu(Re_2O_D) + \nu(Re_3O_D)] + [\nu(Re_1F_1) + \nu(Re_3F_1) + \nu(Re_2F_3) + \nu(Re_3F_3) + \nu(Re_1F_2) + \nu(Re_2F_2)]$		
			$[\nu(Re_1F_4) + \nu(Re_2F_4) + \nu(Re_3F_4)] + [\nu(Re_1F_1) + \nu(Re_3F_1) + \nu(Re_2F_3) + \nu(Re_3F_3) + \nu(Re_1F_2) + \nu(Re_2F_2)]$	$\nu_3(A_1)$	438(1)[7]
	407(1)[59]	$\nu_{14}(E)$	$[\nu(Re_1F_1) + \nu(Re_2F_3)] - [\nu(Re_3F_1) + \nu(Re_3F_3)]$		
395 sh[g] 392(7)[g]	401(2)[27]	$\nu_4(A_1)$	$\delta(O_ARe_1O_C) + \delta(O_ARe_2O_C) + \delta(O_ARe_3O_C)$	$\nu_4(A_1)$	403(5)[8]
			$\delta(O_ARe_1O_C) + \rho_w(Re_1O_B) + \delta(O_ARe_1O_C) + \rho_w(Re_1O_B)$ $\delta(O_ARe_3O_B) + \rho_w(Re_3O_C)$	$\nu_{14}(E)$	396(5)[1]

Table 3.5. (continued ...)

387(4)[g] 374(17)	388(1)[50]	ν_{15}(E)	$\delta(O_ARe_2O_C) - \delta(O_ARe_3O_C)$	ν_{15}(E)	391(<0.1)[14]
	384(5)[1]	$\nu_5(A_1)$	$\delta(O_AO_CRe_1O_B) + \delta(O_AO_CRe_2O_B) + \delta(O_AO_CRe_3O_B)$	$\nu_5(A_1)$	380(2)[1]
368 sh	380(1)[1]	ν_{16}(E)	$\delta(O_CRe_2O_B) + \delta(O_CRe_3O_B) - \delta(O_AO_CRe_1O_B)$	ν_{16}(E)	375(<0.01)[11]
	379(3)[82]	ν_{17}(E)	$\delta(O_CRe_1O_B) + \delta(O_CRe_3O_B) - \delta(O_AO_CRe_2O_B)$	ν_{17}(E)	365(2)[8]
	367(<1)[33]	$\nu_6(A_1)$	$\rho_w(O_ARe_1O_C) + \rho_w(O_ARe_2O_C) + \rho_w(O_ARe_3O_C)$	$\nu_6(A_1)$	351(<1)[25]
345(7)	332(3)[11]	ν_{18}(E)	$[\delta(O_ARe_1O_B) - \delta(O_BRe_1O_C) - \delta(O_ARe_3O_B) + \delta(O_BRe_2O_C) - \delta(O_BRe_2O_C)] + [\nu(Re_1F_3) + \nu(Re_3F_3) - \nu(Re_2F_2) - \nu(Re_3F_2)]$	ν_{18}(E)	275(2)[67]
262 sh	251(1)[12]	ν_{19}(E)	$\rho_r(O_ARe_1O_C) + \rho_r(O_ARe_2O_C) + \rho_r(Re_3O_B) + [\nu(Re_1F_2) + \nu(Re_2F_2)] - [\nu(Re_2F_3) + \nu(Re_3F_3)]$		
257(3)	248(2)[<1]	$\nu_7(A_1)$	$[\nu(Re_1F_2) + \nu(Re_2F_2)] + [\nu(Re_2F_3) + \nu(Re_3F_3)] + [\nu(Re_3F_1) + \nu(Re_1F_1)]$	ν_{19}(E)	252(<1)[3]
			$[\nu(Re_1F_2) + \nu(Re_2F_2)] + [\nu(Re_2F_3) + \nu(Re_3F_3)] + [\nu(Re_3F_1) + \nu(Re_1F_1)] - [\nu(Re_1F_4) + \nu(Re_2F_4) + \nu(Re_3F_4)]$	$\nu_7(A_1)$	286(<1)[12]
197(4) 191(9)	190(2)[<1]	$\nu_8(A_1)$	$\rho_w(Re_1O_B) + \rho_w(Re_2O_B) + \rho_r(Re_3O_B)$	$\nu_8(A_1)$	175(2)[1]
188(8)	182(2)[<0.1]	ν_{20}(E)	$\rho_r(O_ARe_1O_B) + \rho_r(O_AO_BRe_2O_C) + \rho_r(O_AO_BRe_3O_C)$	ν_{20}(E)	173(1)[<1]
	153(2)[<0.1]	$\nu_9(A_1)$	$\rho_r(O_AO_BRe_1O_C) + \rho_r(O_AO_BRe_2O_C) + \rho_r(O_AO_BRe_3O_C)$	$\nu_9(A_1)$	119(1)[<0.001]
	118(<1)[<0.1]	ν_{21}(E)	$\rho_r(O_AO_BRe_1O_C) - \rho_r(O_AO_BRe_3O_C)$	ν_{21}(E)	97(1)[<0.1]
	95(<1)[<1]	ν_{22}(E)	deformation modes	ν_{22}(E)	96(<1)[<1]
	80(<1)[<0.1]	ν_{23}(E)		ν_{23}(E)	44(<1)[<1]

[a] Frequencies are given in cm^{-1}. Values in parentheses denote relative Raman intensities. The Raman spectrum was recorded in an FEP sample tube at −150 °C using 1064-nm excitation. The $[N(CH_3)_4]^+$ cation modes were observed at ν_8(E), 377(1); $\nu_{19}(T_2)$, 463(5), 460(5), 455(5); $\nu_3(A_1)$, 750(3), 757(12); $\nu_{18}(T_2)$, 949(8), 943(1); ν_7(E), 1174(1), 1182(2); $\nu_{17}(T_2)$, 1285(1), 1288(2); $\nu_{16}(T_2)$, 1407(5), 1401(3); $\nu_2(A_1)$, ν_6(E), 1461(9), 1467(8), 2830(2), 2979(9), 2983(9), 2993(8), 3010(7), 3014(7), 3039(17), 3047(10); many combination bands were also observed. The CH_3CN modes were observed at 2938(33), 2737(2), 2294(24), 1457(6), 1454(4), 921(12), 394(5), 392(7). [b] The abbreviations denote a shoulder (sh), broad (br), stretch (ν), bend (δ), rocking (ρ_r), and wag (ρ_w). [c] Values in parentheses denote calculated Raman intensities ($Å^4\ u^{-1}$). Values in square brackets denote calculated infrared intensities (km mol^{-1}). The B3LYP/aug-cc-pVTZ(-PP) level was used. [d] For the atom labeling scheme, see Figure 3.4. [e] Band overlapping with the $[ReO_4]^-$ anion mode. [f] Band overlapping with the $[N(CH_3)_4]^+$ cation mode. [g] Band overlapping with CH_3CN.

than that of ReO_3F,[21] lacking modes in the Re−O−Re and Re−F−Re bridging stretching regions.

The $(HF)_2ReO_3F$ complex has 21 fundamental vibrational modes under C_{2v} symmetry belonging to the irreducible representations $8A_1 + 4B_1 + 3A_2 + 6B_2$, where all modes are Raman active and the A_1, B_1, and B_2 modes are infrared active. The four anions occupy C_1 sites in the crystallographic unit cell of $(HF)_2ReO_3F{\cdot}HF$. A factor-group analysis was carried out (Table A2) based on the crystal structure (see X-ray crystal structure of $(HF)_2ReO_3F{\cdot}HF$). Correlation of the gas-phase symmetry of the complex (C_{2v}) to the crystal site symmetry (C_1) results in no additional splittings for the A_1, B_1, A_2, and B_2 modes. Correlation of the site symmetry to the crystal (unit cell) symmetry (C_{2h}) shows that the A_1, B_1, A_2, and B_2 modes are split into Raman-active A_g and B_g components and into infrared-active A_u and B_u components. Only 10 of the 21 Raman-active vibrational modes predicted for $(HF)_2ReO_3F$ in the gas phase were observed. Modes associated with the coordinated HF molecules are expected to be weak and were not observed in the Raman spectrum. Vibrational coupling within the unit cell of $(HF)_2ReO_3F{\cdot}HF$ is apparently weak, and, consequently, the splittings are too small to be resolved on many of the bands. The bands at 981 and 1017 cm^{-1} are assigned to the asymmetric and symmetric Re−O stretching modes, respectively, and appear at higher frequencies than in ReO_3F (969−996 cm^{-1}). The intense band at 669 cm^{-1} is in good agreement with the 664 cm^{-1} band observed in ReO_3F and is assigned to an Re−F stretching mode. The bands between 215 and 399 cm^{-1} are assigned to O−Re−O and

F−Re−O deformation modes which are similar to those observed in ReO_3F (234−386 cm^{-1}).

3.2.4.2. $[N(CH_3)_4]_2[\{ReO_3(\mu\text{-}F)\}_3(\mu_3\text{-}O)]\cdot CH_3CN$

The anion, $[\{ReO_3(\mu\text{-}F)\}_3(\mu_3\text{-}O)]^{2-}$, possesses 42 fundamental vibrational modes belonging to the irreducible representations $9A_1 + 5A_2 + 14E$ under C_{3v} symmetry, where the A_1 and E modes are Raman and infrared active and the A_2 modes are inactive. The four anions occupy C_1 sites in the crystallographic unit cell of $[N(CH_3)_4]_2[\{ReO_3(\mu\text{-}F)\}_3(\mu_3\text{-}O)]\cdot CH_3CN$. As a result of site symmetry lowering, all E modes are expected to be split into two A components. In order to assign the additional bands that could not be accounted for by symmetry lowering alone, the possibility of vibrational coupling within the unit cell was investigated by undertaking a factor-group analysis (Table A3) based on the crystal structure of $[N(CH_3)_4]_2[\{ReO_3(\mu\text{-}F)\}_3(\mu_3\text{-}O)]\cdot CH_3CN$. Although correlation of the gas-phase anion symmetry (C_{3v}) to its crystal site symmetry (C_1) cannot result in splittings for the A_1 and A_2 modes, correlation of the site symmetry to the unit cell symmetry (C_{2h}) showed that the A_1 and A_2 modes are each split into Raman-active A_g and B_g components and into infrared-active A_u and B_u components under C_{2h} crystal symmetry. Each E mode is split into two A_g and two B_g components that are Raman-active and two A_u and two B_u components that are infrared-active. The factor-group splittings predicted for the Raman spectrum were observed on the highest intensity bands, namely, $\nu_1(A_1)$ (971/978), $\nu_{10}(E)$ (946/951/959/966), $\nu_{11}(E)$ (931/937/941/944), $\nu_2(A_1)$

(924/926), ν_4(A1) (392/395), ν_8(A1) (191/197), ν_{12}(E) (911/918/921), and ν_{13}(E) (575/580/586).

The bands between 911 and 978 cm^{-1} are assigned to the out-of-phase and in-phase terminal Re−O stretching modes. The two factor-group split bands at highest frequency (971, 978 cm^{-1}) correspond to the totally symmetric $\nu_{in\text{-}phase}$ (Re−O) stretching mode. The calculated frequencies reproduce the trend $\nu_{in\text{-}phase}$(Re−O) > $\nu_{out\text{-}of\text{-}phase}$(Re−O), although, as observed for $[ReO_4]^-$ (Table A1), the calculated frequencies appear 30−40 cm^{-1} higher than the experimental values (exptl, 911−978 cm^{-1}; calcd, 942−1018 cm^{-1}). The $\nu_{in\text{-}phase}$(Re−O) and $\nu_{out\text{-}of\text{-}phase}$(Re−O) frequencies are comparable to those observed for $[N(CH_3)_4][ReO_2F_4]$ (972 and 939 cm^{-1}, respectively).[7] The terminal $\nu_{in\text{-}phase}$(Re−O) stretching mode (971/978 cm^{-1}) is shifted to lower frequency when compared with the corresponding modes in ReO_3F (996 cm^{-1}), and ReO_2F_3 (1025 cm^{-1}),[7] in accordance with the enhanced negative charge on oxygen that arises from the net −2 charge of the anion, resulting in somewhat weaker Re−O double bonds.

The factor-group split bands at 575/580/586 cm^{-1} correspond to a mode resulting from asymmetric coupling of $\nu(Re{-}O_{\mu_3})$ and $\nu(Re{-}F_{\mu})$, in agreement with the calculated frequency (558 cm^{-1}). The symmetrically coupled $\nu(Re{-}O_{\mu_3})$ and $\nu(Re{-}F_{\mu})$ mode is assigned to a weak band at 510 cm^{-1} which quantum-chemical calculations predict to occur as a weak band at 516 cm^{-1} (see Computational Results). The coupled $\nu(Re{-}O_{\mu_3})$ and $\nu(Re{-}F_{\mu})$ stretching modes are comparable to the coupled $\nu(Re{-}F_t)$ and $\nu(Re{-}F_{\mu})$ stretching modes in $[\mu\text{-}F(ReO_2F_3)_2]^-$ (554 cm^{-1})[19] and $[(ReO_2F_2)(\mu\text{-}F)_2(ReO_2F_3)_2]^-$ (568

cm^{-1}).[19] Raman bands occurring between 188 and 395 cm^{-1} are assigned to deformation modes, in accordance with the calculated frequencies (182−401 cm^{-1}).

3.2.5. Computational Results

3.2.5.1. Calculated Structures of $[\{MO_3(\mu\text{-}F)\}_3(\mu_3\text{-}O)]^{2-}$ and $[\{MO_3(\mu\text{-}F)\}_3(\mu_3\text{-}F)]^-$ (M = Re, Tc)

The geometries of the $[\{MO_3(\mu\text{-}F)\}_3(\mu_3\text{-}O)]^{2-}$ and $[\{MO_3(\mu\text{-}F)\}_3(\mu_3\text{-}F)]^-$ anions (M = Re, Tc) (Figures 3.4 and A5) were optimized under C_{3v} symmetry at the B3LYP/aug-cc-pVTZ(-PP) level of theory and resulted in stationary points with all frequencies real (Tables 3.5 and A5). The starting geometries for $[\{MO_3(\mu\text{-}F)\}_3(\mu_3\text{-}O)]^{2-}$ and $[\{MO_3(\mu\text{-}F)\}_3(\mu_3\text{-}F)]^-$ were the crystallographic geometries of the $[\{ReO_3(\mu\text{-}F)\}_3(\mu_3\text{-}O)]^{2-}$ and $[\{TcO_3(\mu\text{-}F)\}_3(\mu_3\text{-}F)]^-$ anions in their respective $[N(CH_3)_4]^+$ (see X-ray Crystallography) and K^+ [23] salts.

$[\{ReO_3(\mu\text{-}F)\}_3(\mu_3\text{-}O)]^{2-}$. Overall, there is very good agreement between the calculated and experimental Re−O bond lengths and angles (Table 3.4). Among the experimental trends in geometrical parameters that are reproduced by the calculations are the following: (a) bond lengths; $Re{-}F_\mu > Re{-}O_\mu > Re{-}O_t$ and (b) bond angles; $O_t{-}Re{-}O_t > O_t{-}Re{-}F_\mu > F_\mu{-}Re{-}F_\mu > F_\mu{-}Re{-}O_{\mu_3}$.

$[\{ReO_3(\mu\text{-}F)\}_3(\mu_3\text{-}F)]^-$: Calculated Geometry of $[\{ReO_3(\mu\text{-}F)\}_3(\mu_3\text{-}F)]^-$ and Comparison with that of $[\{ReO_3(\mu\text{-}F)\}_3(\mu_3\text{-}O)]^{2-}$. The calculated $Re{-}O_t$ bond lengths in the $[\{ReO_3(\mu\text{-}F)\}_3(\mu_3\text{-}F)]^-$ anion are equal to or slightly shorter than those calculated for the $[\{ReO_3(\mu\text{-}F)\}_3(\mu_3\text{-}O)]^{2-}$ anion (Table 3.4). The $Re{-}O_t$ bonds are equal, whether or

not they are trans to Re−F_{μ_3} or Re−F_{μ} bonds, whereas the Re−F_{μ} bond lengths in $[\{ReO_3(\mu\text{-}F)\}_3(\mu_3\text{-}F)]^-$ are significantly shorter than in $[\{ReO_3(\mu\text{-}F)\}_3(\mu_3\text{-}O)]^{2-}$ due to the lower negative charge of the [{ReO3(μ-F)}3(μ3-F)]− anion relative to that of $[\{ReO_3(\mu\text{-}F)\}_3(\mu_3\text{-}O)]^{2-}$. The Re−$F_{\mu_3}$ bond lengths of $[\{ReO_3(\mu\text{-}F)\}_3(\mu_3\text{-}F)]^-$ are significantly longer than the Re−O_{μ_3} bond lengths of $[\{ReO_3(\mu\text{-}F)\}_3(\mu_3\text{-}O)]^{2-}$ because of the greater polarity of the Re−F_{μ_3} bond relative to that of Re−O_{μ_3}. The calculated bond length trend for $[\{ReO_3(\mu\text{-}F)\}_3(\mu_3\text{-}F)]^-$, i.e., Re−$F_{\mu_3}$ > Re−F_{μ} > Re−O_t , where all Re−O_t bonds are equal, is the same as that observed in the X-ray crystal structure of $[\{TcO_3(\mu\text{-}F)\}_3(\mu_3\text{-}F)]^-$.[23]

All O_t−Re−O_t angles are essentially equal for both rhenium anions. The O_t−Re−F_{μ} angles (where each O_t is trans to F_{μ}) in $[\{ReO_3(\mu\text{-}F)\}_3(\mu_3\text{-}F)]^-$ are smaller than the corresponding O_t−Re−O_{μ} angles in $[\{ReO_3(\mu\text{-}F)\}_3(\mu_3\text{-}O)]^{2-}$. The O_t−Re−F_{μ_3} angles $[\{ReO_3(\mu\text{-}F)\}_3(\mu_3\text{-}F)]^-$ are larger than the related O_t−Re−$O_{\mu 3}$ angle (where O_t is trans to $O_{\mu 3}$) in $[\{ReO_3(\mu\text{-}F)\}_3(\mu_3\text{-}O)]^{2-}$. The Re−$F_{\mu}$−Re bond angles in $[\{ReO_3(\mu\text{-}F)\}_3(\mu_3\text{-}F)]^-$ are significantly larger than the Re−F_{μ}−Re bond angles in $[\{ReO_3(\mu\text{-}F)\}_3(\mu_3\text{-}O)]^{2-}$, whereas the Re−$F_{\mu_3}$−Re angles are smaller than the Re−O_{μ_3}−Re angle.

$[\{ReO_3(\mu\text{-}F)\}_3(\mu_3\text{-}F)]^-$: Calculated Vibrational Spectrum of $[\{ReO_3(\mu\text{-}F)\}_3(\mu_3\text{-}F)]^-$ and Comparison with That of $[\{ReO_3(\mu\text{-}F)\}_3(\mu_3\text{-}O)]^{2-}$. The $[\{ReO_3(\mu\text{-}F)\}_3(\mu_3\text{-}F)]^-$ anion possesses 42 fundamental vibrational modes belonging to the irreducible representations $9A_1 + 5A_2 + 14E$ under C_{3v} symmetry, where the A_1 and E modes are Raman and infrared active and the A_2 modes are inactive. The calculated ν(Re−O_t) stretches of $[\{ReO_3(\mu\text{-}F)\}_3(\mu_3\text{-}F)]^-$ (985−1048 cm^{-1}) are expected to appear at higher frequencies (30−43 cm^{-1}) than the calculated ν(Re−O_t) stretches of the $[\{ReO_3(\mu\text{-}F)\}_3(\mu_3$-

$O)]^{2-}$ anion (Table 3.5). This is attributed to less electron density donation into the rhenium $d_{t_{2g}}$ orbitals by F_{μ_3} than by O_{μ_3}. In addition, the higher negative charge of $[\{ReO_3(\mu\text{-}F)\}_3(\mu_3\text{-}O)]^{2-}$ also contributes to enhancement of the Re−O_t bond polarities in $[\{ReO_3(\mu\text{-}F)\}_3(\mu_3\text{-}O)]^{2-}$ and lowering of the O_3Re-group stretching frequencies. Although it is possible to distinguish the two anions based on their ν(Re−O_t) stretching frequencies, the major spectral differences arise from stretching modes involving the triply bridged central atom. In both cases, the ν(Re−F_μ) stretches are predicted to be in-phase and out-of-phase coupled to ν(Re−X_{μ_3}) (X = O; 516 and 558 cm^{-1}, respectively and X = F; 438 and 464 cm^{-1}, respectively). The modes in $[\{ReO_3(\mu\ F)\}_3(\mu_3\text{-}F)]^-$ are not only predicted to occur ca. 100 cm^{-1} lower than in $[\{ReO_3(\mu\text{-}F)\}_3(\mu_3\text{-}O)]^{2-}$, their band intensities are also predicted to be extremely weak. In the experimental spectrum, four bands are observed at 510, 575, 580, and 586 cm^{-1}, and no bands are observed between 400 and 500 cm^{-1}, confirming that the experimental spectrum is that of $[\{ReO_3(\mu\text{-}F)\}_3(\mu_3\text{-}O)]^{2-}$, in accord with the X-ray crystal structure. The deformation mode frequencies are similar in both anions.

$[\{TcO_3(\mu\text{-}F)\}_3(\mu_3\text{-}O)]^{2-}$ and $[\{TcO_3(\mu\text{-}F)\}_3(\mu_3\text{-}F)]^-$. There is overall good agreement between the calculated and the experimental[23] Tc−O and Tc−F bond lengths of the $[\{TcO_3(\mu\text{-}F)\}_3(\mu_3\text{-}F)]^-$ anion (Table A4). All bond length and bond angle trends of $[\{TcO_3(\mu\text{-}F)\}_3(\mu_3\text{-}O)]^{2-}$ and $[\{TcO_3(\mu\text{-}F)\}_3(\mu_3\text{-}F)]^-$ follow those calculated for their rhenium analogues. The bond angles of both isomers are essentially identical.

3.2.5.2. Natural Bond Orbital (NBO) Analyses

The bonding in the $[\{MO_3(\mu\text{-}F)\}_3(\mu_3\text{-}O)]^{2-}$ and $[\{MO_3(\mu\text{-}F)\}_3(\mu_3\text{-}F)]^{-}$ anions (M = Re, Tc) was examined by NBO analyses using the B3LYP/aug-cc-pVTZ(-PP) substitute. The respective NPA charges, valencies, and bond orders (Table 3.6) are in accordance with anticipated trends: (a) the positive charges are located on the metal atoms (Re, 2.13/2.16; Tc, 1.82/1.82), (b) the three terminal oxygen atoms are doubly bonded (O_t valence, ca. 1.0) to the metal atom (valencies: Re, 3.93/3.78; Tc, 3.73/3.63), (c) the dicoordinate bridging fluorine atoms (F_μ valence: Re, 0.55/ 0.61; Tc, 0.58/0.61) are equivalently bonded to two metal centers ($M-F_\mu$ bond order, ca. 0.3).

Significant differences are found for O_{μ_3} and F_{μ_3} bridge-head atoms. For the $[\{MO_3(\mu\text{-}F)\}_3(\mu_3\text{-}O)]^{2-}$ anions, the highest negative charge occurs on O_{μ_3} (Re, −0.99; Tc, −0.95). The O_{μ_3} valencies (Re, 1.34; Tc, 0.99) and the $M-O_{\mu_3}$ bond orders (Re, 0.42; Tc, 0.31) of $[\{MO_3(\mu\text{-}F)\}_3(\mu_3\text{-}O)]^{2-}$ show that O_{μ_3} is equivalently bonded to the three M atoms. The highest negative charges in the $[\{MO_3(\mu\text{-}F)\}_3(\mu_3\text{-}F)]^{-}$ anions are also located on the bridge-head atom, here F_{μ_3} (Re, −0.65; Tc, −0.64), and are significantly lower than the O_{μ_3} charges in the $[\{MO_3(\mu\text{-}F)\}_3(\mu_3\text{-}O)]^{2-}$ anions. The F_{μ_3} valencies are only slightly higher (Re and Tc, 0.62) than those of the F_μ atoms (valencies: Re and Tc, 0.61; $M-F_\mu$ bond orders: Re, 0.30; Tc, 0.28) and are equally shared among the three metal centers ($M-F_{\mu_3}$ bond orders: Re, 0.20; Tc, 0.19).

Table 3.6. NBO Natural Charges, Natural Bond Orders, and Valencies for the $[\{MO_3(\mu\text{-}F)\}_3(\mu_3\text{-}O)]^{2-}$ and $[\{MO_3(\mu\text{-}F)\}_3(\mu_3\text{-}F)]^{-}$ (M= Re, Tc) Anions[a]

	$[\{ReO_3(\mu\text{-}F)\}_3(\mu_3\text{-}O)]^{2-}$ [b]		$[\{ReO_3(\mu\text{-}F)\}_3(\mu_3\text{-}F)]^{-}$ [b]		$[\{TcO_3(\mu\text{-}F)\}_3(\mu_3\text{-}O)]^{2-}$ [c]		$[\{TcO_3(\mu\text{-}F)\}_3(\mu_3\text{-}F)]^{-}$ [c]	
Atom	Charges	Valencies	Charges	Valencies	Charges	Valencies	Charges	Valencies
$M_{1,2,3}$	2.13	3.93	2.16	3.78	1.82	3.73	1.82	3.63
$F_{1,2,3}$	−0.62	0.55	−0.60	0.61	−0.61	0.58	−0.59	0.61
O_A	−0.60	1.02	−0.57	1.02	−0.49	1.03	−0.44	1.02
O_B	−0.64	1.00	−0.54	1.04	−0.57	1.00	−0.46	1.02
O_C	−0.60	1.02	−0.57	1.02	−0.49	1.03	−0.44	1.02
O_D/F_4	−0.99	1.34	−0.65	0.62	−0.95	0.99	−0.64	0.62
	Bond order							
$M_1-O_{A,C}$	0.98		0.98		0.96		0.96	
M_1-O_B	0.96		0.99		0.93		0.95	
$M_2-O_{A,C}$	0.98		0.98		0.96		0.96	
M_2-O_B	0.96		0.99		0.93		0.95	
$M_3-O_{A,C}$	0.98		0.98		0.96		0.96	
M_3-O_B	0.96		0.99		0.93		0.95	
M_1-O_D/F_4	0.42		0.20		0.31		0.19	
M_2-O_D/F_4	0.42		0.20		0.31		0.19	
M_3-O_D/F_4	0.42		0.20		0.31		0.19	
$M_1-F_{1,2}$	0.28		0.30		0.28		0.28	
$M_2-F_{2,3}$	0.28		0.30		0.28		0.28	
$M_3-F_{1,3}$	0.28		0.30		0.28		0.28	

[a] B3LYP/aug-cc-pVTZ(-PP), (C_{3v}). [b] For the atom labeling scheme, see Figure 3.4. [c] For the atom labeling scheme, see Figure A5.

3.3. Conclusion

The solvolysis of Re_2O_7 in aHF in the presence of F_2 gas has provided a facile, high-yield, and high-purity synthesis of ReO_3F which has enabled further investigation of its Lewis acid and fluoride ion acceptor properties. The complex resulting from coordination of HF to the metal center, $(HF)_2ReO_3F{\cdot}HF$, was characterized by Raman spectroscopy and single-crystal X-ray diffraction. The study of the fluoride ion acceptor properties of ReO_3F in CH_3CN has led to the isolation of the novel $[\{ReO_3(\mu\text{-}F)\}_3(\mu_3\text{-}O)]^{2-}$ anion as its $[N(CH_3)_4]^+$ salt, and its characterization in the solid state by Raman spectroscopy and single-crystal X-ray diffraction. The $[\{ReO_3(\mu\text{-}F)\}_3(\mu_3\text{-}O)]^{2-}$ anion was also observed in CH_3CN solvent by ^{19} F NMR spectroscopy. The $[\{ReO_3(\mu\text{-}F)\}_3(\mu_3\text{-}O)]^{2-}$ anion provides the only example of a rhenium oxide fluoride species containing a triply coordinated oxygen atom. Quantum-chemical calculations have been used to model the $[\{ReO_3(\mu\text{-}F)\}_3(\mu_3\text{-}O)]^{2-}$ anion and have provided an energy minimized geometry that is in very good agreement with the experimental structure. The Raman spectrum of the salt has been fully assigned based on the calculated vibrational modes. The proposed reaction pathways are consistent with the formation of the $[\{ReO_3(\mu\text{-}F)\}_3(\mu_3\text{-}O)]^{2-}$ anion in the basic solvent medium, CH_3CN. Attempts to synthesize the $[N(CH_3)_4]^+$ salt of $[\{ReO_3(\mu\text{-}F)\}_3(\mu_3\text{-}F)]^-$ by analogy with the known technetium analogue failed in CH_3CN and aHF solvents. Quantum-chemical calculations for the known $[\{ReO_3(\mu\text{-}F)\}_3(\mu_3\text{-}O)]^{2-}$ and $[\{TcO_3(\mu\text{-}F)\}_3(\mu_3\text{-}F)]^-$ anions are in very good agreement with their experimental geometries. Quantum-chemical calculations also show that the related, but unknown,

$[\{ReO_3(\mu\text{-}F)\}_3(\mu_3\text{-}F)]^-$ and $[\{TcO_3(\mu\text{-}F)\}_3(\mu_3\text{-}O)]^{2-}$ anions are expected to be stable in the gas phase.

CHAPTER 4

SYNTHESES AND STRUCTURAL CHARACTERIZATION OF THE $[ReO_3F_2]^-$ AND *fac*–$[ReO_3F_3]^{2-}$ ANIONS AND $(\mu\text{-}F)_4\{[\mu\text{-}O(ReO_2F)_2](ReO_2F_2)_2\}$

4.1. Introduction

The recent synthesis of high-yield, high-purity ReO_3F[235] opened an avenue to examine its fluoride-ion acceptor properties in detail. In a prior study, the reaction of ReO_3F with $[N(CH_3)_4]F$ was shown to form the trirhenium dianion, $[\{ReO_3(\mu\text{-}F)\}_3(\mu_3\text{-}O)]^{2-}$,[235] which was characterized by Raman and ^{19}F NMR spectroscopy. A single-crystal X-ray diffraction study confirmed the facial arrangement of the oxygen ligand atoms on rhenium.

There have also been several prior studies of the fluoride-ion acceptor behavior of ReO_3F. Salts of the $[ReO_3F_3]^{2-}$ anion were claimed to be synthesized by fusion of alkali metal fluorides with ReO_3F at 150−160 °C (eq 4.1).[27] The starting material, which was

$$ReO_3F + 2MF \xrightarrow{150-160\ ^oC} M_2[ReO_3F_3] \qquad (M = K, Rb, Cs) \qquad (4.1)$$

identified as ReO_3F by chemical analysis, infrared spectroscopy, and a melting point determination, was synthesized by reaction of $ReOF_5$ with Re_2O_7 at 150−200 °C for 2−3 h (eq 4.2). The experimental data supporting the above finding was not provided by the

$$ReOF_5 + 2Re_2O_7 \xrightarrow{150-200\ ^oC} 5ReO_3F \qquad (4.2)$$

authors, moreover, in the present work it has been shown by Raman spectroscopy that ReO_3F decomposes to Re_2O_7 at temperatures > 112 °C. In a recent overview of the known syntheses of ReO_3F, Seppelt[21] has commented on the melting and boiling points of ReO_3F

he had obtained by differential scanning calorimetry and concluded that the previously determined melting (147 ^{o}C) and boiling (164 ^{o}C) points of ReO_3F must be revised; therefore, the assignment of the product resulting from eq 2, based on melting point alone, is suspect. The products resulting from the reactions of ReO_3F with alkali metal fluorides KF, RbF, and CsF,[27] were pale yellow in color and were characterized by chemical analyses (Re, K, Rb, Cs, and F) and infrared spectra of the products which were only generally assigned and which showed two absorption band regions consisting of three peaks, at 425−550 (Re−F stretching region) and 880−1000 cm^{-1} (Re−O stretching region).

In another study, the $[ReO_3F_3]^{2-}$ anion has also been claimed to form by reaction of KF with ReO_3F. The latter was formed in situ by reaction of $K[ReO_4]$ with IF_5 at room temperature (eq 4.3).[36] The resulting $K_2[ReO_3F_3]$ salt was isolated from KIO_3 and IO_2F,

$$5K[ReO_4] + 6KF + 2IF_5 \xrightarrow{IF_5} 5K_2[ReO_3F_3] + KIO_3 + IO_2F \qquad (4.3)$$

which were identified by infrared spectroscopy, by reduction and dissolution of KIO_3 and IO_2F with KF in anhydrous CH_3CN, in which $K_2[ReO_3F_3]$ proved to be insoluble. It is noteworthy that there was no definitive characterization of ReO_3F provided in the latter work. The product, $K_2[ReO_3F_3]$, was reported to decompose at 220–230 ^{o}C. The salt was characterized by gravimetric analyses (Re, K, and F) and by Raman and infrared spectroscopies.

The reaction of $ReO_3F{\cdot}2DMF$ with $[(CH_3)_4N]F$ in ethanol was also reported to result in the formation of the yellow-grey $[(CH_3)_4N]_2[ReO_3F_3]$ salt (eq 4.4), which was

$$ReO_3F{\cdot}2DMF + 2[(CH_3)_4N]F \longrightarrow [(CH_3)_4N]_2[ReO_3F_3] + 2DMF \qquad (4.4)$$

isolated by washing the solid in ethanol and drying the product at 150 °C under vacuum.[37] The DMF adduct was synthesized by reaction of DMF with ReO_3F. The latter was formed by reaction of Re_2O_7 with HF (eq 4.5). The adduct was isolated by removal of H_2O under

$$Re_2O_7 + 2HF + 4DMF \longrightarrow 2ReO_3F{\cdot}2DMF + H_2O \quad (4.5)$$

vacuum and characterized by infrared spectroscopy and elemental analyses (Re, C, H, and N). Although it was claimed that the synthesis of $[(CH_3)_4N]_2[ReO_3F_3]$ was carried out under anhydrous conditions; however, the first synthesis of truly anhydrous $[(CH_3)_4N]F$ was only accomplished 13 years later;[179] therefore, the reaction described in eq 4 could have instead resulted in the formation of $[(CH_3)_4N][ReO_4]$ by hydrolysis of $[(CH_3)_4N]_2[ReO_3F_3]$ (eq 4.6).[36]

$$[(CH_3)_4N]_2[ReO_3F_3] + H_2O \longrightarrow [(CH_3)_4N][ReO_4] + HF + [(CH_3)_4N][HF_2] \quad (4.6)$$

Failed attempts to synthesize the $[ReO_3F_3]^{2-}$ anion by reactions of $Na[ReO_4]$ with CsF, RbF, $[(C_6H_5)_3As]F$, and $[R_4N]F$ have also been reported.[236]

All of the aforementioned studies proposed that ligand arrangement was meridional for the $[ReO_3F_3]^{2-}$ anion based on the number of Re–O stretching bands observed in the corresponding infrared and Raman spectra. However, these early findings contrast with the facial geometry subsequently reported for isoelectronic $[OsO_3F_3]^-$,[39] $[ReO_3Cl_3]^{2-}$,[237–239] and $[\{ReO_3(\mu\text{-}F)\}_3(\mu_3\text{-}O)]^{2-}$.[235]

Attempts to synthesize the $[ReO_3F_2]^-$ anion by reaction of ReO_3F with alkali metal fluorides in 1:1 molar ratios and heating the mixtures to 150−160 °C were unsuccessful due to the thermal instability of the $[ReO_3F_2]^-$ anion at the synthetic temperature.[27]

Although several unconfirmed syntheses of $[ReO_3F_3]^{2-}$ salts have been reported, salts containing an isolated $[ReO_3F_2]^-$ anion are unknown.

In the present study, access to high-purity ReO_3F[235] has enabled the reinvestigation of the $[ReO_3F_3]^{2-}$ anion and the unlikely possibility that its geometry is meridional. For this reason, the $K^+[H_3O]^+$, Cs^+, and $[NO]^+$ salts of the $[ReO_3F_3]^{2-}$ anion were synthesized. The study also provides the first synthesis of the presently unknown $[ReO_3F_2]^-$ anion as its Cs^+, K^+, $[NH_4]^+$, and $[NO]^+$ salts.

Until now, it was thought that the list of structurally characterized neutral rhenium(VII) oxide fluorides, ReO_3F, ReO_2F_3, and $ReOF_5$, was complete.[19] The present study; however, reports the synthesis of a new neutral rhenium(VII) oxide fluoride, $(\mu\text{-}F)_4\{[\mu\text{-}O(ReO_2F)_2](ReO_2F_2)_2\}$, a rare example of an O-bridged rhenium oxide fluoride.

In no case has $[ReO_3F_3]^{2-}$ been definitely characterized. In the present work, both the $[ReO_3F_3]^{2-}$ and $[ReO_3F_2]^-$ anions and $(\mu\text{-}F)_4\{[\mu\text{-}O(ReO_2F)_2](ReO_2F_2)_2\}$ were unambiguously characterized for the first time by single-crystal X-ray diffraction and Raman spectroscopy.

4.2. Results and Discussion

4.2.1. Syntheses of $M[ReO_3F_2]$ (M = Cs, [NO], K, and $[NH_4]$), $Cs_2[ReO_3F_3]$, $[NO]_2[ReO_3F_3]$, and $K[H_3O][ReO_3F_3]$

The reactions of ReO_3F with CsF and NOF and $K/[NH_4][ReO_4]$ with aHF always resulted in the formation of mixtures of several salts. The individual components of each reaction mixture have been identified by Raman spectroscopy and single-crystal X-ray

diffraction and are discussed in their respective sections. The Raman spectra indicated that the sample compositions were not homogeneous. Spectra were recorded in sample regions in which the concentration of the species of interest was optimal.

4.2.1.1 $Cs[ReO_3F_2]$ and $Cs_2[ReO_3F_3]$

The $Cs[ReO_3F_2]$ and $Cs_2[ReO_3F_3]$ salts were formed in admixture with $Cs[ReO_2F_4]$, $Cs[\mu\text{-}F(ReO_2F_3)]$, and $Cs[ReO_4]$[187] (eq 4.7), and resulted from the reaction of ReO_3F with

$$ReO_3F + 1(2)CsF \xrightarrow{HF} Cs[ReO_3F_2], Cs_2[ReO_3F_3], Cs[ReO_2F_4], Cs[ReO_4], Cs[\mu\text{-}F(ReO_2F_3)] \quad (4.7)$$

CsF at room temperature. Both $Cs[ReO_3F_2]$ and $Cs_2[ReO_3F_3]$ were isolated as the major products when ReO_3F and CsF were reacted in 1:1 and 1:2 molar ratios, respectively. Other salts, $Cs[ReO_2F_4]$, $Cs[ReO_4]$, and $Cs[\mu\text{-}F(ReO_2F_3)]$, also formed in eq 4.7, are apparently the products of competing HF solvolysis reactions of ReO_3F in the presence of F^-.[235] The product mixtures were soluble in aHF at room temperature forming yellow to pale yellow solutions. All attempts to crystallize $Cs[ReO_3F_2]$ and $Cs_2[ReO_3F_3]$ by cooling the solutions at temperatures ranging from −10 °C to −78 °C only resulted in the crystallization of $Cs[ReO_2F_4]$ and $Cs[\mu\text{-}F(ReO_2F_3)]$ (see Appendix B), whose anion structures were already known.[19] The $Cs[ReO_3F_2]$ salt was, however, isolated in crystalline form at room temperature in admixture with $Cs_2[ReO_3F_3]$ and other reaction products, which deposited as white solids, upon removal of aHF by static distillation into the side arm of the reaction vessel which had been pre-cooled to −78 °C.

4.2.1.2. $[NO]_2[ReO_3F_3]$ and $[NO][ReO_3F_2]$

$[NO]_2[ReO_3F_3]$. The salt, $[NO]_2[ReO_3F_3]$, was synthesized along with $[NO][ReO_2F_4]$ and $[NO][ReO_4]$ by the reaction of ReO_3F with excess NOF at −20 °C over a period of four days. It was isolated as a white solid upon removal of unreacted NOF under dynamic vacuum at −78 °C (eq 4.8) and was characterized by Raman

$$ReO_3F + \text{xs NOF} \xrightarrow{-20\ ^oC} [NO]_2[ReO_3F_3], [NO][ReO_2F_4], [NO][ReO_4] \quad (4.8)$$

spectroscopy. Additional Raman bands that could not be assigned to $[NO]_2[ReO_3F_3]$, were assigned to $[NO][ReO_2F_4]$ and $[NO][ReO_4]$ by analogy with the known Raman spectra of $[ReO_2F_4]^-$ [19] and $[ReO_4]^-$.[187] Attempts to dissolve $[NO]_2[ReO_3F_3]$ in aHF at −78 °C resulted in the formation of $[NO][ReO_3F_2]$, which was insoluble at that temperature, and the soluble salt, $[NO][ReO_2F_4]$, as the only reaction products.

$[NO][ReO_3F_2]$. The salt, $[NO][ReO_3F_2]$, formed in admixture with $[NO][ReO_2F_4]$ and $[NO][ReO_4]$ (eq 4.8) upon removal of one equivalent of NOF under dynamic vacuum at room temperature (eq 4.9) from $[NO]_2[ReO_3F_3]$ which was formed in eq 4.8. The solid

$$[NO]_2[ReO_3F_3] \longrightarrow [NO][ReO_3F_2] + NOF \quad (4.9)$$

mixture containing $[NO][ReO_4]$, $[NO][ReO_3F_2]$, and $[NO][ReO_2F_4]$ readily dissolved in aHF at room temperature forming a pale yellow solution. Crystals of $[NO][ReO_3F_2]$ and $[NO][ReO_2F_4]$ were grown by static distillation of aHF into the pre-cooled side arm of the FEP reaction vessel, whereas $[NO][ReO_4]$ precipitated as a white solid. The resulting product mixture was characterized by Raman spectroscopy and suitable crystals of $[NO][ReO_3F_2]$ and $[NO][ReO_2F_4]$ were obtained for a single-crystal X-ray structure determination and a unit-cell determination, respectively.

4.2.1.3. $M[ReO_3F_2]$ (M = K, $[NH_4]$) and $K[H_3O][ReO_3F_3]$

The $M[ReO_4]$ (M = K and $[NH_4]$) salts were solvolyzed in aHF in an attempt to synthesize the $[\{ReO_3(\mu\text{-}F)\}_3(\mu_3\text{-}F)]^-$ anion. The solvolyses of $M[TcO_4]$ (M = K and $[NH_4]$) in aHF have been previously shown to yield the analogous technetium anion, $[\{TcO_3(\mu\text{-}F)\}_3(\mu_3\text{-}F)]^-$, which has been characterized by single-crystal X-ray diffraction.[23] The reactions of $M[ReO_4]$ with aHF (eq 4.10 and 4.11), however, resulted in the

$$[NH_4][ReO_4] + xsHF \longrightarrow [NH_4][ReO_3F_2],\ [NH_4][ReO_2F_4] \text{ and/or } [NH_4][\mu\text{-}F(ReO_2F_3)],\ [NH_4][ReO_4] \quad (4.10)$$

$$K[ReO_4] + xsHF \longrightarrow K[ReO_3F_2],\ K[ReO_2F_4] \text{ and/or } K[\mu\text{-}F(ReO_2F_3)],\ K[ReO_4],\ K[H_3O][ReO_3F_3] \quad (4.11)$$

formation of $M[ReO_3F_2]$ (M = K, $[NH_4]$), and $K[H_3O][ReO_3F_3]$ in admixture with $[M][ReO_2F_4]$ and/or $[M][\mu\text{-}F(ReO_2F_3)]$, and $M[ReO_4]$, which were isolated by removal of aHF under dynamic vacuum at −78 °C followed by drying the solid mixtures at room temperature. The individual components of the solid mixtures were identified by Raman spectroscopy. Although it seemed plausible, the $[ReO_3F_3]^{2-}$ anion was not identified as a product of the HF solvolysis of $[NH_4][ReO_4]$ (eq 4.10) by either Raman spectroscopy or X-ray diffraction.

The salt mixtures readily dissolve in aHF at room temperature forming yellow solutions. Crystals of $M[ReO_3F_2]$ and $K[H_3O][ReO_3F_3]$ along with the crystals of a by-product, $[NH_4][\mu\text{-}F(ReO_2F_3)]$, whose anion structure is known, were grown by static distillation of aHF into the pre-cooled side arms of their corresponding reactors, whereas $M[ReO_4]$ and $M[ReO_2F_4]$ precipitated as white solids. The isolated product mixtures were

characterized by Raman spectroscopy and suitable crystals of $M[ReO_3F_2]$, $K[H_3O][ReO_3F_3]$, and $[NH_4][\mu\text{-}F(ReO_2F_3)]$ were obtained for single-crystal X-ray structure determinations.

4.2.1.4. Synthesis of $(\mu\text{-}F)_4\{[\mu\text{-}O(ReO_2F)_2](ReO_2F_2)_2\}\cdot SO_2ClF$

The new neutral rhenium oxide fluoride, $(\mu\text{-}F)_4\{[\mu\text{-}O(ReO_2F)_2](ReO_2F_2)_2\}\cdot SO_2ClF$, was synthesized by reaction of ReO_2F_3 with ReO_3F in a 3:1 stoichiometric ratio in SO_2ClF at room temperature (eq 4.12). The colorless SO_2ClF solvate crystallized at room

$$3ReO_2F_3 + ReO_3F \longrightarrow (\mu\text{-}F)_4\{[\mu\text{-}O(ReO_2F)_2](ReO_2F_2)_2\}\cdot SO_2ClF \qquad (4.12)$$

temperature upon slow static distillation of SO_2ClF (under 1.1 atm of N_2 gas) into the cooled (–78 ^{o}C) side arm of the FEP reaction vessel. The isolated crystalline material, $(\mu\text{-}F)_4\{[\mu\text{-}O(ReO_2F)_2](ReO_2F_2)_2\}\cdot SO_2ClF$, was characterized by Raman spectroscopy and was used to obtain its single-crystal X-ray structure (see Experimental Section).

4.2.2. X-ray Crystallography

Details of the data collection and other crystallographic information for $[NH_4][ReO_3F_2]$, $K[H_3O][ReO_3F_3]$, $(\mu\text{-}F)_4\{[\mu\text{-}O(ReO_2F)_2](ReO_2F_2)_2\}\cdot SO_2ClF$, $Cs[ReO_2F_4]$, and $Cs[\mu\text{-}F(ReO_2F_3)]$ are provided in Table 4.1. Important bond lengths and bond angles are provided in Tables 4.2−4.4, B1, and B2. The crystal structures of the

Table 4.1. Summary of Crystal Data and Refinement Results for $[NH_4][ReO_3F_2]$ **(1)**, $Cs[ReO_2F_4]\cdot 3HF$ **(2)**, $Cs[\mu\text{-}F(ReO_2F_3)_2]\cdot 2HF$ **(3)**, $K[H_3O][ReO_3F_3]$ **(4)**, and $(\mu\text{-}F)_4\{[\mu\text{-}O(ReO_2F)_2](ReO_2F_2)_2\}\cdot SO_2ClF$ **(5)**

formula	**(1)**	**(2)**	**(3)**	**(4)**	**(5)**
space group	*P*bcn	$P2_1/n$	*C*2/c	$P\bar{a}3$	*P*2/n
a (Å)	13.5016(4)	51189(1)	14.026(3)	9.986(2)	20.1534(4)
b (Å)	5.50180(10)	20.5650(5)	14.677(4)	9.986(2)	7.1226(1)
c (Å)	12.1493(3)	7.5969(2)	5.2053(11)	9.986(2)	20.1732(4)
α (deg)	90	90	90	90	
β (deg)	90	91.7064(9)	83.380(13)	90	90.031(1)
γ (deg)	90	90	90	90	
V (Å)^3	902.49(4)	799.37(3)	1064.0(4)	995.8(4)	2895.75(9)
molecules/unit cell	8	4	4	8	2
mol wt (g mol^{-1})	2321.94	1948.54	2961.24	2562.10	4433.71
calcd density (g cm^{-3})	4.272	4.048	4.634	4.273	5.085
T (^{o}C)	−173	–173	–173	−173	–173
μ (mm^{-1})	26.88	19.77	26.23	24.82	33.58
R_1[a]	0.0274	0.0315	0.0827	0.0328	0.0273
wR_2[b]	0.0581	0.0711	0.2142	0.0670	0.0658

[a] R_1 is defined as $\Sigma \| F_o | - | F_c \| \Sigma | F_o |$ for $I > 2\sigma(I)$. [b] wR_2 is defined as $[\Sigma[w(F_o^2 - F_c^2)^2]/\Sigma w(F_o^2)^2]^{1/2}$ for $I > 2\sigma(I)$.

Table 4.2 Experimental Geometrical Parameters for the $[ReO_3F_2]^-$ Anion in $[NH_4][ReO_3F_2]$ and Calculated Bond Lengths and Bond Angles for $[(\mu\text{-}F)_4(ReO_3F)_4]^{4-}$

	exptl[a]	calcd[b]	
		$[(\mu\text{-}F)_4(ReO_3F)_4]^{4-}$ (C_{4v})	
		B3LYP	PBE1PBE
Bond Lengths (Å)			
Re_1-O_1	1.705(2)	1.722	1.709
Re_1-O_2	1.703(2)	1.722	1.709
Re_1-O_3	1.726(2)	1.712	1.700
Re_1-F_1	1.939(2)	1.949	1.933
Re_1-F_2	2.182(2)	2.177	2.156
Re_1-F_{2A}	2.163(2)	2.177	2.156
Bond Angles (deg)			
$O_1-Re_1-O_2$	103.3(1)	100.7	100.8
$O_1-Re_1-O_3$	101.9(1)	101.7	101.8
$O_2-Re_1-O_3$	103.2(1)	101.7	101.8
$O_1-Re_1-F_1$	95.2(1)	93.2	93.3
$O_2-Re_1-F_1$	95.1(1)	93.2	93.3
$O_3-Re_1-F_1$	151.2(1)	156.3	156.1
$O_1-Re_1-F_2$	87.9(1)	89.0	89.1
$O_2-Re_1-F_2$	165.2(1)	166.6	166.4
$O_3-Re_1-F_2$	83.6(1)	85.0	85.0
$O_1-Re_1-F_{2A}$	164.8(1)	166.6	166.4
$O_2-Re_1-F_{2A}$	88.9(1)	89.0	89.1
$O_3-Re_1-F_{2A}$	84.2(1)	85.0	85.0
$F_1-Re_1-F_2$	74.1(1)	76.9	76.7
$F_2-Re_1-F_{2A}$	74.0(1)	80.0	79.7
$F_{2A}-Re_1-F_1$	78.84(3)	76.9	76.7
$Re_1-F_2-Re_{1B}$	137.2(1)	165.3	164.8

[a] For the atom labeling scheme see Figure 4.1a. [b] The aug-cc-pVTZ(-PP) basis set was used. For the atom labeling scheme see Figure 4.1b.

a

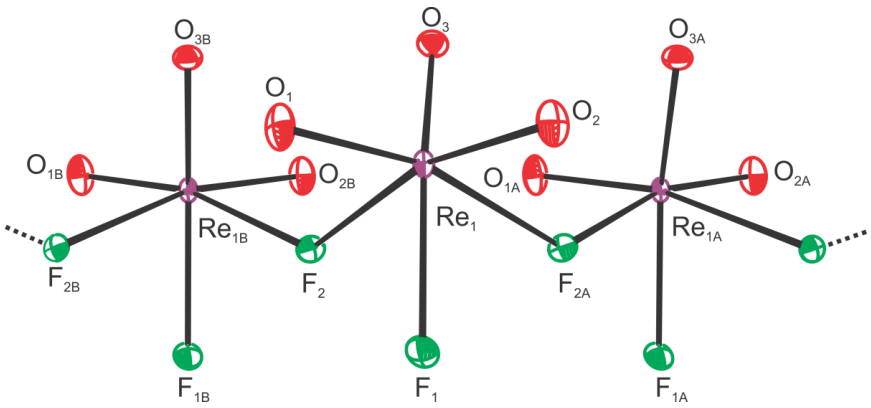

b

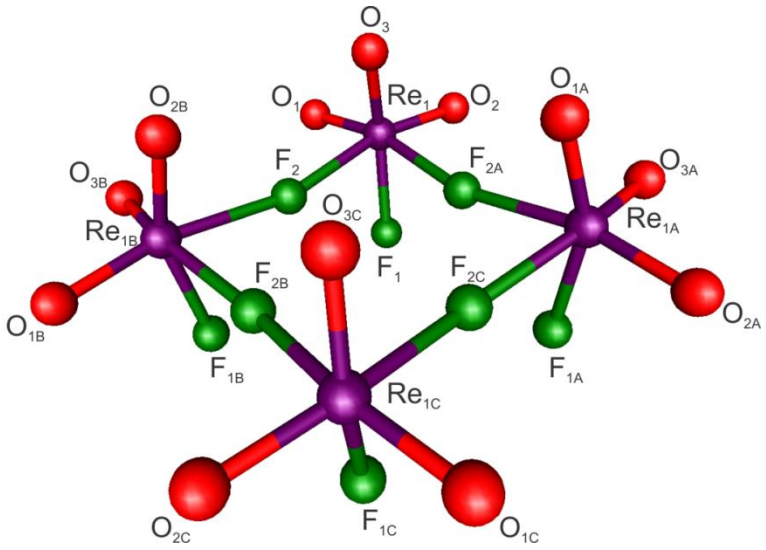

Figure 4.1. (a) A part of the oligomeric $[ReO_3F_2]^-$ anion in the crystal structure of $[NH_4][ReO_3F_2]$. Thermal ellipsoids are shown at the 50% probability level. (b) Calculated structure of the hypothetical $[(\mu\text{-}F)_4(ReO_3F)_4]^{4-}$ anion (B3LYP/aug-cc-pVTZ(-PP)).

Table 4.3. Experimental and Calculated (C_{3v}) Bond Lengths (Å) and Bond Angles (deg) for the *fac*-$[ReO_3F_3]^{2-}$ Anion

	exptl[a]	calcd[b]	
		B3LYP	PBE1PBE
Bond lengths (Å)			
$Re_1–O_1$	1.743(4)	1.735	1.722
$Re_1–F_1$	1.964(4)	2.035	2.017
$K---O_1$	2.840(4)		
$K---F_2$	2.893(4)		
Bond Angles (°)			
$O_1–Re_1–O_{1A}$	98.9(2)	100.9	101.0
$O_1–Re_1–F_1$	166.6(2)	89.0	89.0
$O_1–Re_1–F_{1A}$	88.3(2)	164.2	164.0
$O_1–Re_1–F_{1B}$	91.0(2)	89.0	89.0
$F_1–Re_1–F_{1A}$	80.3(2)	78.8	78.6

[a] For the atom labeling scheme see Figure 4.2a. [b] For the atom labeling scheme see Figure 4.2b. The aug-cc-pVTZ(-PP) basis set was used.

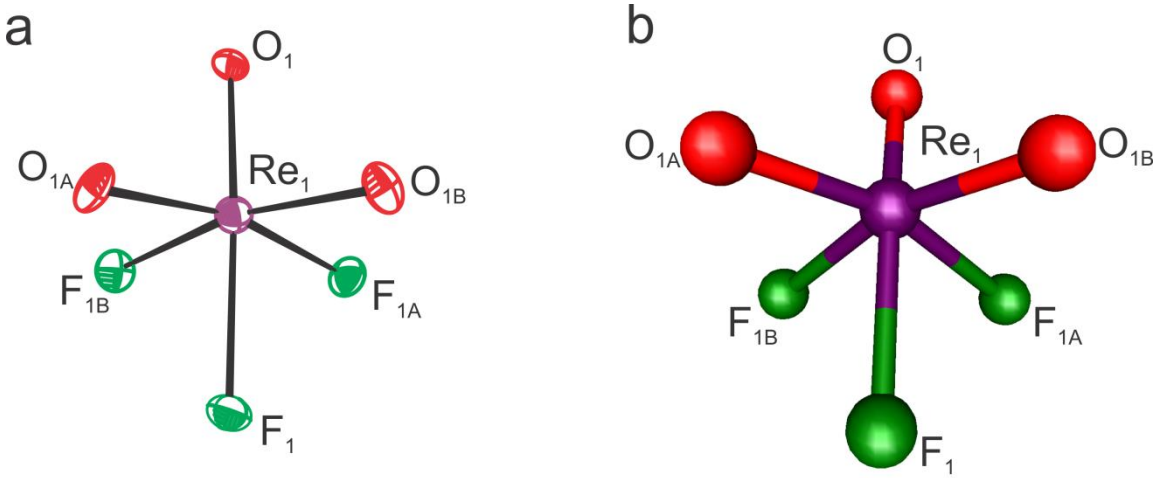

Figure 4.2. (a) The *fac*–$[ReO_3F_3]^{2-}$ anion in the crystal structure of $K[H_3O][ReO_3F_3]$. Thermal ellipsoids are shown at the 50% probability level. (b) Calculated structure of the *fac*–$[ReO_3F_3]^{2-}$ anion (B3LYP/aug-cc-pVTZ(-PP)).

Table 4.4. Experimental Geometrical Parameters for $(\mu\text{-}F)_4\{[\mu\text{-}O(ReO_2F)_2](ReO_2F_2)_2\}$ in $(\mu\text{-}F)_4\{[\mu\text{-}O(ReO_2F)_2](ReO_2F_2)_2\}\cdot SO_2ClF$ and Calculated Geometrical Parameters for $(\mu\text{-}F)_4\{[\mu\text{-}O(ReO_2F)_2](ReO_2F_2)_2\}$ (C_{2v})

exptl[a]				calcd[b]	
				B3LYP	PBE1PBE
Bond Lengths (Å)					
Re_1-O_1	1.667(11)	Re_3-O_5	1.648(13)	1.671	1.659
Re_1-O_2	1.640(13)	Re_3-O_6	1.676(13)	1.671	1.659
Re_2-O_3	1.654(12)	Re_4-O_7	1.671(12)	1.674	1.662
Re_2-O_4	1.653(12)	Re_4-O_8	1.642(12)	1.674	1.662
Re_2-O_9	1.868(10)	Re_4-O_9	1.871(11)	1.876	1.862
Re_1-F_1	1.832(10)	Re_3-F_4	1.819(9)	1.840	1.826
Re_1-F_2	1.870(11)	Re_3-F_5	1.849(11)	1.850	1.836
Re_2-F_3	1.856(8)	Re_4-F_6	1.863(9)	1.844	1.831
Re_1-F_7	2.080(9)	Re_3-F_8	2.095(8)	2.115	2.097
Re_1-F_{10}	2.062(9)	Re_3-F_9	2.079(9)	2.115	2.097
Re_2-F_7	2.099(9)	Re_4-F_9	2.087(9)	2.131	2.112
Re_2-F_8	2.107(8)	Re_4-F_{10}	2.071(10)	2.131	2.112

[a] For the atom labeling scheme, see Figure 4.3a. [b] For the atom labeling scheme, see Figure 4.3b. The aug-cc-pVTZ(-PP) basis set was used.

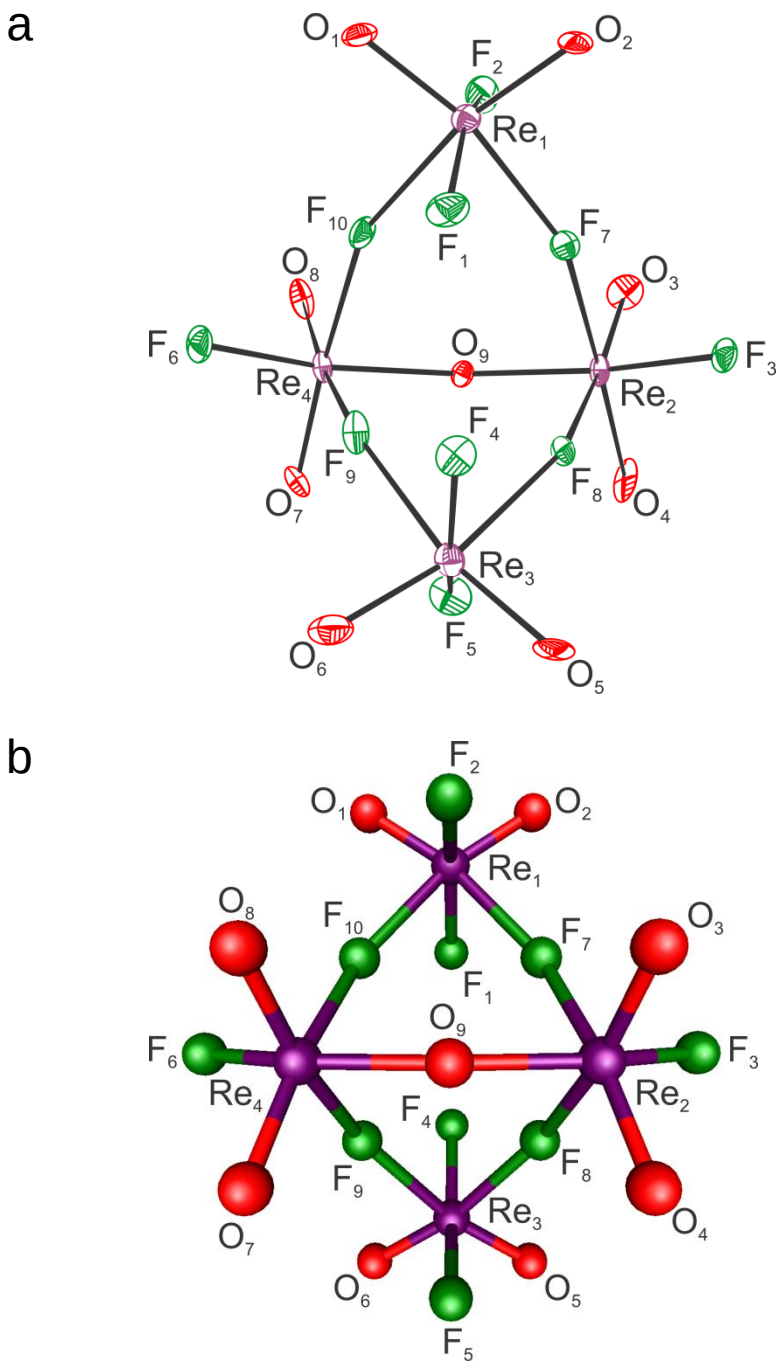

Figure 4.3. (a) The $(\mu\text{-}F)_4\{[\mu\text{-}O(ReO_2F)_2](ReO_2F_2)_2\}$ molecule in the crystal structure of $(\mu\text{-}F)_4\{[\mu\text{-}O(ReO_2F)_2](ReO_2F_2)_2\}\cdot SO_2ClF$. Thermal ellipsoids are shown at the 50% probability level. (b) Calculated structure of $(\mu\text{-}F)_4\{[\mu\text{-}O(ReO_2F)_2](ReO_2F_2)_2\}$ (B3LYP/aug-cc-pVTZ(-PP)).

$Cs[ReO_2F_4]$ and $Cs[\mu\text{-}F(ReO_2F_3)]$ salts (Figure B2) are discussed in the Appendix B.

4.2.2.1. $[NH_4][ReO_3F_2]$

Crystal Packing and Secondary Contacts. The crystal structure of $[NH_4][ReO_3F_2]$ consists of infinite chains of the $[ReO_3F_2]^-$ anions running along the *b*-axis with the $[NH_4]^+$ cations stacked between the chains along the same axis (Figures B3). The chains interact with the cations through weak contacts ($(H_4)N\cdots F$, 2.882(3) Å; $(H_4)N\cdots O$, 2.813(3) Å), where the contacts are comparable to the sums of the Waddington ($[NH_4]^+$, 1.43 Å[240]) and van der Waals radii (O, 1.52 Å); F, 1.47 Å)[241] ($(H_4)N\cdots F$, 2.90 Å; $(H_4)N\cdots O$, 2.95 Å). There are also other weak contacts between the ReO_3F_2-units within the same chain, the shortest being O···O (2.844(3) Å), O···F (2.627(3) Å), and F···F (2.478(2) Å). The O···O contacts are close to the sum of the van der Waals radii (3.04 Å),[241] whereas the F···O and F···F contacts are significantly shorter than the sums of their van der Waals radii (2.99 and 2.94 Å, respectively).[241]

$[ReO_3F_2]^-$. The $[ReO_3F_2]^-$ anion has an open chain structure, where the ReO_3F_2-units are bridged through fluorine atoms (Figure 4.1). Each ReO_3F_2-unit consists of a rhenium atom bonded to three oxygen atoms that are cis to one another and trans to terminal (1x) or bridging fluorine (2x) atoms, providing a pseudo-octahedral environment around the Re atom. The facial arrangement of the oxygen atoms in the $[ReO_3F_2]^-$ anion provides a greater degree of π-bonding with the empty set of $d_{t_{2g}}$ orbitals on rhenium than a meridional arrangement would provide.[17]

The Re–O bond length trans to the terminal fluorine atom (Re–O_t, 1.726(2) Å) is comparable to those of $[\mu\text{-}F(ReO_2F_3)_2]^-$ (1.753(9) Å)[19] and $[(ReO_2F_2)(\mu\text{-}F)_2(ReO_2F_3)_2]^-$ (1.715(8) and 1.695(9) Å),[19] but longer than the Re–O_t bond lengths of $[ReO_2F_4]^-$ (1.678(9) Å)[19] and $[ReOF_6]^-$ (Cs^+, 1.671(7) Å).[16] The Re–O bond lengths trans to the bridging fluorine atoms (Re–O_{tb}, 1.703(2) and 1.705(2) Å) are shorter than the Re–O_t bond length and comparable to those of $[(ReO_2F_2)(\mu\text{-}F)_2(ReO_2F_3)_2]^-$ (1.678(7), 1.694(8), 1.669(8), and 1.683(7) Å),[19] $[\{ReO_3(\mu\text{-}F)\}_3(\mu_3\text{-}O)]^{2-}$ (1.700(4)–1.713(4) Å),[235] ReO_2F_3 (1.675(8),[19] 1.675(8)–1.682(6) Å[21]), and ReO_3F (1.715(8), 1.685(9) Å).[21]

The terminal Re−F bond length (1.939(2) Å) is comparable to the terminal Re−F_{ax} bond length of $[ReOF_6]^-$ (Cs^+,1.923(6) Å)[16] and intermediate with respect to those of $[\mu\text{-}F(ReO_2F_3)_2]^-$ (1.893(8) Å)[19] and $[ReO_2F_4]^-$ (2.002(7) Å).[19] The bridging Re−F_μ bond lengths are comparable to those of $(\mu\text{-}F)_4\{[\mu\text{-}O(ReO_2F)_2](ReO_2F_2)_2\}$ (2.062(9)–2.139(8) Å), ReO_3F (2.141(7), 2.142(7) Å),[21] and $[\{ReO_3(\mu\text{-}F)\}_3(\mu_3\text{-}O)]^{2-}$ (2.139(3)–2.166(3) Å).[235]

As predicted by the VSEPR model, the O–Re–O angles are greater than 90° due to the greater steric requirements of oxygen double bond domains and their associated double bond−double bond repulsion.

4.2.2.2. $K[H_3O][ReO_3F_3]$

The potassium cation in the crystal structure of $K[H_3O][ReO_3F_3]$ forms twelve contacts with four anions: six contacts with oxygen atoms (6x 2.840(5) Å) and six contacts with fluorine atoms (6x 2.893(4) Å) (Figure B4). There are also several weak

F···O(H_3) contacts between the anions and the $[H_3O]^+$ cations. The shortest F···O(H_3) (2.682(4) Å) contacts is near the sum of the van der Waals radii (2.99 Å).[241]

The crystal structure of the *fac*-$[ReO_3F_3]^{2-}$ anion consists of a rhenium atom bonded to three oxygen atoms that are cis to one another and trans to three fluorine atoms, providing a pseudo-octahedral environment around the Re atom (Figure 4.2a). The facial arrangement of the oxygen atoms allows a greater degree of π-bonding with the empty set of $d_{t_{2g}}$ orbitals on rhenium and is in agreement with the facial geometries observed in *fac*-$[ReO_3Cl_3]^{2-}$,[237–239] $[\{ReO_3(\mu\text{-}F)\}_3(\mu_3\text{-}O)]^{2-}$,[235] $[ReO_3F_2]^-$, and isoelectronic *fac*-$[OsO_3F_3]^-$.[39] The observed *fac*-coordination contradicts the previous spectroscopic interpretations which reported a meridional arrangement of oxygen atoms for *mer*-$[ReO_3F_3]^{2-}$ (see above).[27,36,37]

The Re–O bonds (3x 1.743(4) Å) are comparable, within ±3σ, to the Re–O bonds of $Cs_2[ReO_3Cl_3]$ (1.698(21) and 1.704(17) Å)[238] and $[NH_4][ReO_3F_2]$. The Re–O bonds are, however, longer than those of $[NH_4]_3[ReO_3Cl_3]Cl$ (1.720(2) Å),[239] which may be explained by the stronger cation-anion interactions that occur in $K[H_3O][ReO_3F_3]$ (O···K, 2.840(4) Å) when compared to the cation-anion interactions in $[NH_4]_3[ReO_3Cl_3]Cl$ (O···N(H_4), (3.065(2) Å)).

The Re−F bonds (3x 1.964(4) Å) in $K[H_3O][ReO_3F_3]$ are significantly longer than the terminal Re−F bonds in $(\mu\text{-}F)_4\{[\mu\text{-}O(ReO_2F)_2](ReO_2F_2)_2\}$ (1.816(9)–1.870(11) Å), $[\mu\text{-}F(ReO_2F_3)_2]^-$ (1.893(8) Å),[19] and are comparable, within ±3σ, to those of $[ReO_3F_2]^-$ (1.943(2) Å).

The O–Re–O angles (3x 98.9(2)^o) are greater than 90^o and are bent away from the oxygen double bond moiety toward the terminal fluorine atoms, as observed in other rhenium oxide fluoride anions (see above). The angles are comparable, within ±3σ, to the O–Re–O bond angles of $Cs_2[ReO_3Cl_3]$ (103.7(9)^o)[238] and $[NH_4]_3[ReO_3Cl_3]Cl$ (103.5(1)^o).[239] The F_t–Re–F_t (3x 80.3(2)^o) angles are comparable to the Cl–Re–Cl angles in $[NH_4]_3[ReO_3Cl_3]Cl$ (79.8(1)^o)[239] and the F_t–Re–F_t angles in $[ReO_2F_4]^-$ (82.8(3)^o),[19] $[\mu\text{-}F(ReO_2F_3)_2]^-$ (82.3(4)^o),[19] and $[(ReO_2F_2)(\mu\text{-}F)_2(ReO_2F_3)_2]^-$ (82.0(4)^o, 82.4(3)^o, 82.7(3)^o, and 83.0(4)^o).[19]

4.2.2.3. $(\mu\text{-}F)_4\{[\mu\text{-}O(ReO_2F)_2](ReO_2F_2)_2\}\cdot SO_2ClF$

The crystal structure of $(\mu\text{-}F)_4\{[\mu\text{-}O(ReO_2F)_2](ReO_2F_2)_2\}\cdot SO_2ClF$ consists of well-separated $(\mu\text{-}F)_4\{[\mu\text{-}O(ReO_2F)_2](ReO_2F_2)_2\}$ cages and SO_2ClF molecules whose shortest intermolecular contact distances (Table B1) are near the sums of the O, F, and Cl van der Waals radii (O···O, 3.04; O···Cl, 3.27; F···Cl, 3.22; F···F, 2.94, and F···O, 2.99 Å).[241] The $(\mu\text{-}F)_4\{[\mu\text{-}O(ReO_2F)_2](ReO_2F_2)_2\}$ and SO_2ClF molecules are packed along the *b*-axis, where the SO_2ClF molecules occupy voids between the cages. The SO_2ClF molecules are positionally disordered (50/50; Figure B1) and their bond lengths and bond angles are in good agreement with previously published values,[242] requiring no further discussion.

Each $(\mu\text{-}F)_4\{[\mu\text{-}O(ReO_2F)_2](ReO_2F_2)_2\}$ cage consists of two oxygen-bridged ReO_2F-units that are also fluorine bridged to two ReO_2F_2-units to give a distorted tetrahedron whose vertices are occupied by four six-coordinate rhenium atoms (Figure 4.3a). The terminal Re–O bonds (1.640(13)–1.700(11) Å) are cis to one another and trans

to bridging Re−F_μ bonds (2.062(9)–2.139(8) Å) (Tables 4.4 and B1). The terminal Re–O, Re–F (1.816(9)–1.870(11) Å), and bridging Re−F_μ bond lengths are similar to those previously reported for ReO_2F_3 (phases I−IV)[21] and K[μ-F(ReO_2F_3)$_2$]·2ReO_2F_3.[19] The trend observed among the O−Re−O > O−Re−F > F−Re−F_μ bond angles (Tables 4.4 and B1) is in accordance with the trend observed in the structurally related tetramer, (ReO_2F_3)$_4$ (phase IV).[21]

The Re–O_μ bond lengths (1.853(10)–1.883(10) Å) are intermediate with respect to the terminal Re–O and Re–F_μ bond lengths (see above), and are comparable to the Re−O_μ bond lengths of ReO_3F (1.865(7)–1.907(7) Å),[21] the only other neutral rhenium oxide fluoride that contains an oxygen bridge. As expected, the Re−O_μ bonds of (μ-F)$_4${[μ-O(ReO_2F)$_2$](ReO_2F_2)$_2$}·SO_2ClF are shorter than the Re−O_{μ_3} bonds of [{ReO_3(μ-F)}$_3$(μ$_3$-O)]$^{2-}$ (2.072(4)−2.079(4) Å).[235] The Re–O_μ–Re angles of (μ-F)$_4${[μ-O(ReO_2F)$_2$](ReO_2F_2)$_2$} (162.7(6) and 160.6(6)^o) are more open than those of ReO_3F (117.7(3) and 115.9(6)^o)[21] and [{ReO_3(μ-F)}$_3$(μ$_3$-O)]$^{2-}$ (109.1(2)–110.6(2)^o)[235] due to less constraint than in the latter species.

4.2.3. Raman Spectroscopy

The low-temperature Raman spectra shown in Figures 4.4, B5, B6, B7, 4.5, and B8 were recorded on product mixtures (see Experimental Section), where the compounds of interest, M[ReO_3F_2] (M = [NO], [NH_4], and Cs), K[H_3O][ReO_3F_3] and K[ReO_3F_2], [NO]$_2$[ReO_3F_3], Cs_2[ReO_3F_3], are the major species in their respective spectra. The low-temperature Raman spectra of (μ-F)$_4${[μ-$^{16/18}$O($Re^{16/18}O_2F$)$_2$]($Re^{16/18}O_2F_2$)$_2$}·SO_2ClF are

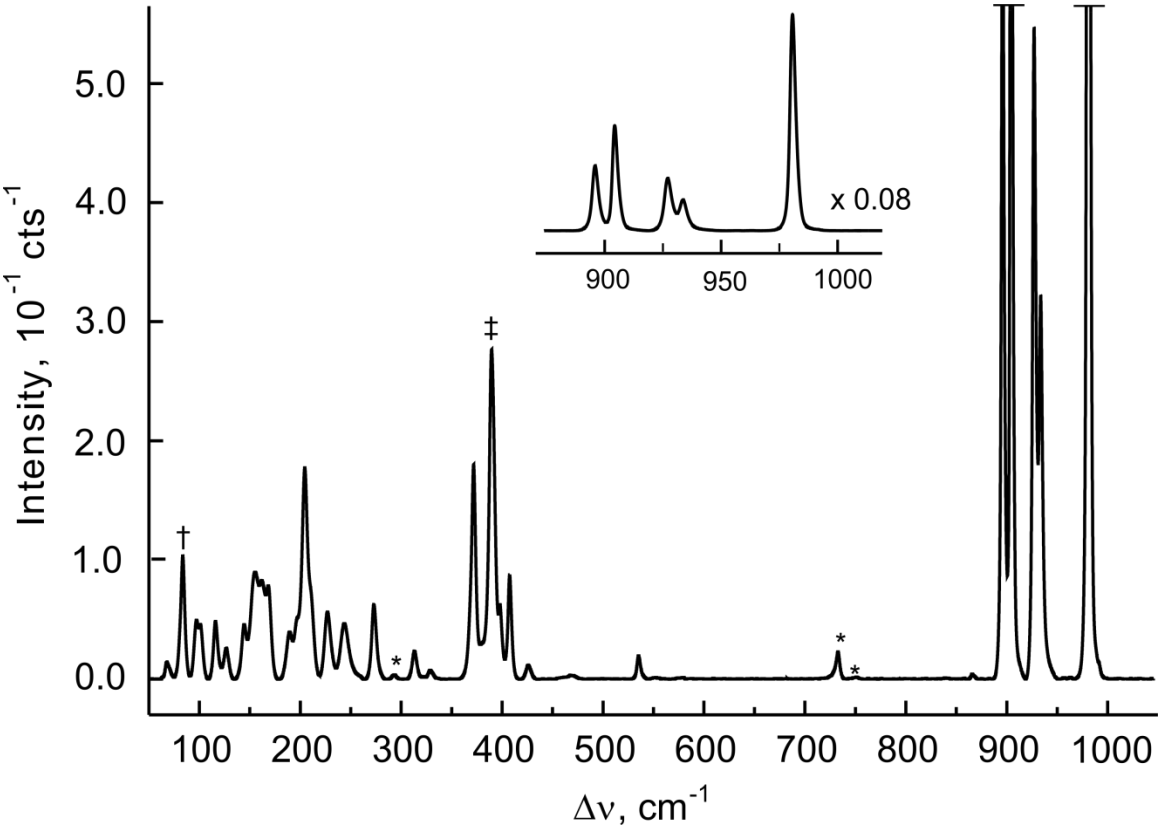

Figure 4.4 Raman spectrum of crystalline $[NO][ReO_3F_2]$ recorded at –150 ^{o}C using 1064-nm excitation. Symbols denote an FEP sample tube line (*), instrumental artifact (†), overlap of a $[NO][ReO_3F_2]$ line with an FEP sample tube line (‡). The $[NO]^+$ bands appear at 2251(11), 2268(95), and 2285(5) cm^{-1}.

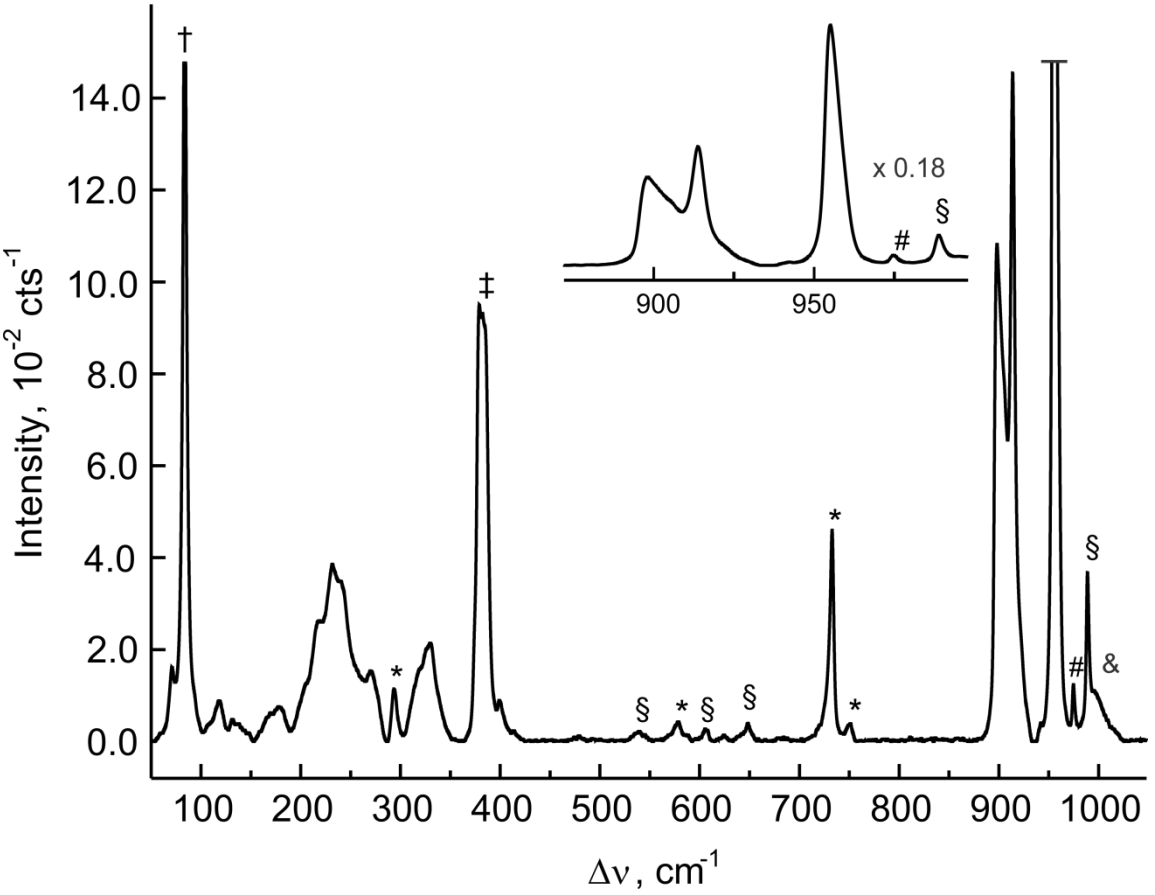

Figure 4.5. Raman spectrum of a solid mixture of crystalline $[NO]_2[ReO_3F_3]$ recorded at –150 ^oC using 1064-nm excitation. Symbols denote an FEP sample tube line (*), instrumental artifact (†), overlap of a $[NO]_2[ReO_3F_3]$ line with an FEP sample tube line (‡), a $[NO][ReO_4]$ line (#), a $[NO][ReO_2F_4]$ line (§), and a $(ReO_3F)_\infty$ line (&). The $[NO]^+$ bands appear at 2282(35) and 2304(75) cm^{-1}.

shown in Figure 4.6. The observed and calculated frequencies and mode descriptions for $M[ReO_3F_2]$ (M = Cs, [NO], K, $[NH_4]$), $M_2[ReO_3F_3]$ (M = Cs, [NO], $K[H_3O]$), and $(\mu\text{-}F)_4\{[\mu\text{-}^{16/18}O(Re^{16/18}O_2F)_2](Re^{16/18}O_2F_2)_2\}\cdot SO_2ClF$ are provided in Tables 4.5−4.7 and B3. Spectral assignments were made by comparison with the calculated frequencies and Raman intensities for $[(\mu\text{-}F)_4(ReO_3F)_4]^{4-}$ (C_{4h}) (Table 4.5), *fac*-$[ReO_3F_3]^{2-}$ (C_{3v}) (Table 4.6), *mer*-$[ReO_3F_3]^{2-}$ (C_s) (Table B3), $[ReO_3F_2]^-$ (C_s) (Table B4), and $(\mu\text{-}F)_4\{[\mu\text{-}^{16/18}O(Re^{16/18}O_2F)_2](Re^{16/18}O_2F_2)_2\}$ (C_{2v}) (Table 4.7 and B2), which were optimized at the B3LYP/aug-cc-pVTZ(-PP) and PBE1PBE/aug-cc-pVTZ(-PP) levels of theory. Spectral assignments for SO_2ClF,[243] $[NH_4]^+$ [234] and $[NO]^+$ [100,244,245] were made by comparison with previously published assignments and require no further discussion. The vibrational assignments for $(\mu\text{-}F)_4\{[\mu\text{-}O(ReO_2F)_2](ReO_2F_2)_2\}\cdot SO_2ClF$ were also confirmed by an ^{18}O-enrichment study.

4.2.3.1. $[ReO_3F_2]^-$

The monomeric $[ReO_3F_2]^-$ anion (C_s) possesses 12 fundamental vibrational modes that span the irreducible representations 8A' + 4A", where all vibrations are Raman and infrared active (Table B4, Appendix B). In view of the chain-like structure, and although the Raman spectrum of $[ReO_3F_2]^-$ could be assigned based on the calculated frequencies and intensities of monomeric $[ReO_3F_2]^-$ (C_s), another model, the cyclic $[(\mu\text{-}F)_4(ReO_3F)_4]^{4-}$ (C_{4v}) anion, was also considered to account for possible coupling between bridging ReO_3F_2-units of the open-chain structure (Figure 4.1).

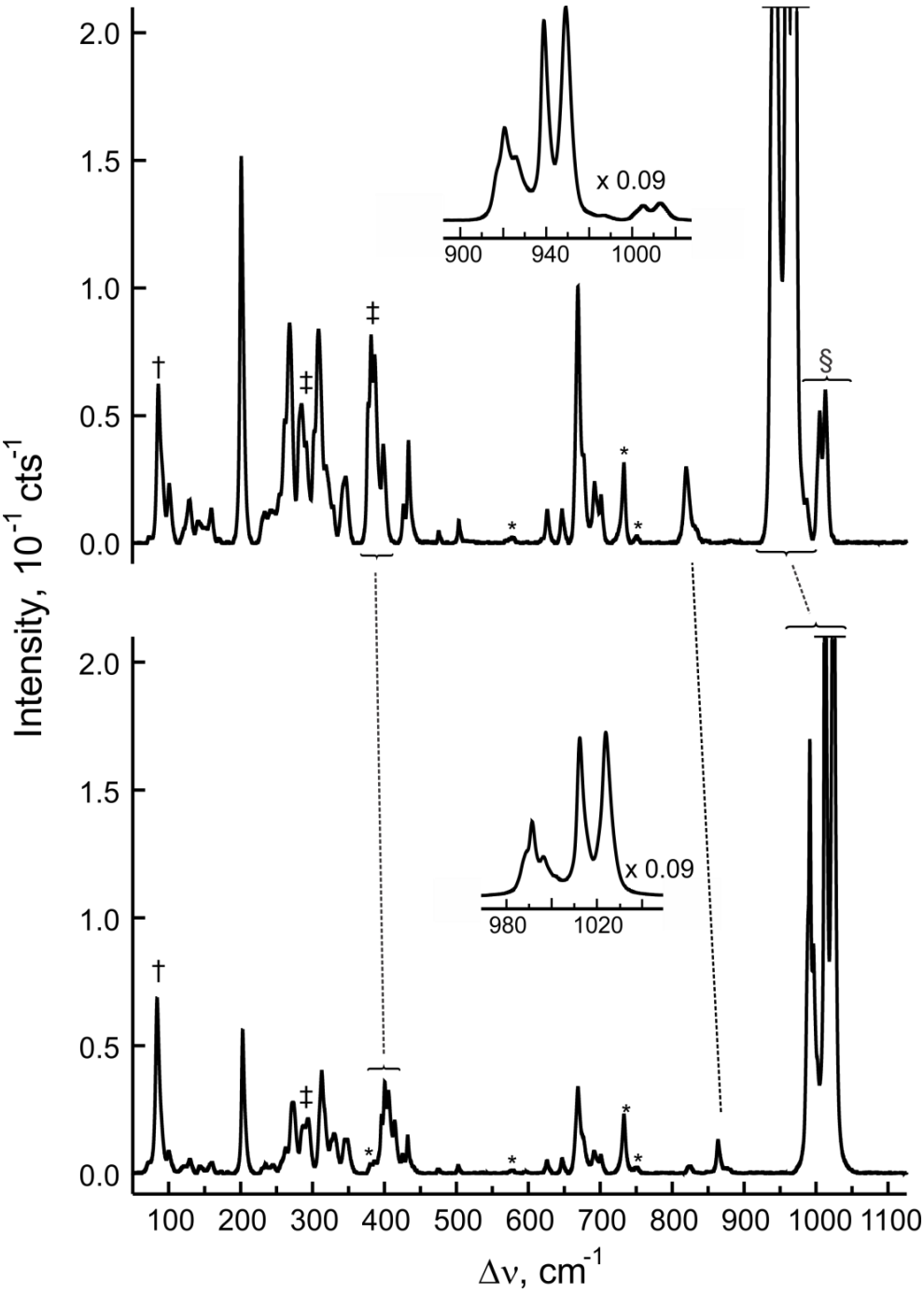

Figure 4.6. Raman spectra of $(\mu\text{-}F)_4\{[\mu\text{-}O(ReO_2F)_2](ReO_2F_2)_2\}\cdot SO_2ClF$ recorded at −140 °C using 1064-nm excitation for natural abundance (lower trace) and ~97% ^{18}O-enriched (upper trace). Symbols denote an FEP sample tube line (*), instrumental artifact (†), overlap of a $(\mu\text{-}F)_4\{[\mu\text{-}O(ReO_2F)_2](ReO_2F_2)_2\}\cdot SO_2ClF$ line with an FEP sample tube line (‡), and small quantities of ^{16}O and $^{16/18}O$ isotopomers (§).

Table 4.5. Experimental Raman Frequencies and Intensities for $M[ReO_3F_2]$ (M = $[NH_4]$, K, Cs, [NO]) and Calculated Raman and Infrared Frequencies, Intensities, and Assignments for the Hypothetical $[(\mu\text{-}F)_4(ReO_3F)_4]^{4-}$ Anion

exptl[a,b]				calcd[a,c]		assgnts (C_{4v})[d]
Cs^+	$[NO]^+$ [e]	$[NH_4]^+$ [f]	K^+	$[(\mu\text{-}F)_4(ReO_3F)_4]^{4-}$		
				B3LYP	PBE1PBE	
980(100)	981(88)	986(100)	980(100)	996(249)[202]	1027(238)[197]	$[\nu(Re_1O_1) + \nu(Re_1O_2) + \nu(Re_1O_3)]_{i.p}$
				988(<1)[54]	1020(<1)[60]	$\nu(Re_1O_1) + \nu(Re_1O_2) + \nu(Re_1O_3)$
				984(1)[0]	1015(1)[0]	$[\nu(Re_1O_1) + \nu(Re_1O_2) + \nu(Re_1O_3)]_{o.o.p.}$
933(12)	933(13)	948(4)	936(24)	945(117)[382]	972(101)[413]	$[\nu(Re_1O_1) + \nu(Re_1O_2) - \nu(Re_1O_3)]_{i.p.}$
922(55)	927(21)	938(14)	931(22) sh			
				928(<1)[478]	954(<1)[503]	$[\nu(Re_1O_1) + \nu(Re_1O_2) - \nu(Re_1O_3)]$
914(4)	904(42)	925(39)	925(14)[g]	918(145)[0]	945(130)[0]	$[\nu(Re_1O_1) - \nu(Re_1O_2)]_{o.o.p.}$
910 sh	896(27)		897(12)[g]	918(<1)[0]	944(<1)[0]	$[\nu(Re_1O_1) + \nu(Re_1O_2) - \nu(Re_1O_3)]_{o.o.p.}$
				911(1)[513]	937(1)[533]	$[\nu(Re_1O_1) - \nu(Re_1O_2)]$
				896(0)[0]	922(0)[0]	$[\nu(Re_1O_1) - \nu(Re_1O_2)]_{i.p.}$
				552(7)[382]	568(6)[395]	$[\nu(Re_1F_1)]_{i.p.}$
531(1)	535(1)	525(<1)		542(<1)[75]	557(<1)[80]	$[\nu(Re_1F_1)]$
				539(<1)[0]	555(<1)[0]	$[\nu(Re_1F_1)]_{o.o.p.}$
				416(<1)[0]	431(<1)[0]	$[\nu(Re_1F_2) + \nu(Re_1F_{2A})]_{o.o.p.}$
				403(<1)[92]	416(<1)[192]	$[\nu(Re_1F_2) + \nu(Re_1F_{2A})]_{o.o.p.}$ + $\delta(O_1O_2Re_1O_3)$
				400(1)[31]	407(1)[29]	$[\delta(O_1O_2Re_1O_3)]_{i.p.}$
394(5) sh	407(3)	402(4)	401 sh	396(2)[27]	403(2)[21]	$\delta(O_1O_2Re_1O_3)$
391(8)	398(2)	391(6)	386(23)	394(1)[0]	401(<1)[0]	$[\delta(O_1O_2Re_1O_3)]_{o.o.p.}$
386(13)	390(11)	386(11)	380 sh	394(<1)[8]	401(<1)[7]	$[\delta(O_1Re_1O_2)]_{i.p.}$
380 sh				391(1)[0]	398(1)[0]	$[\delta(O_1Re_1O_3) - \delta(O_2Re_1O_3)]_{o.o.p.}$
				389(4)[32]	396(4)[32]	$[\delta(O_1Re_1O_3) - \delta(O_2Re_1O_3)] + [\delta(O_{1A}Re_{1A}O_{2A}) - \delta(O_{1B}Re_{1B}O_{2B})]$
				379(20)[0]	388(19)[0]	$[\delta(O_1Re_1O_2)]_{o.o.p.}$
				382(0)[0]	390(0)[0]	$[\delta(O_1Re_1O_3) - \delta(O_2Re_1O_3)]_{i.p.}$
371(11)	372(7)	364(7)		377(3)[235]	387(4)[170]	$[\delta(O_1Re_1O_3) - \delta(O_2Re_1O_3)] + [\nu(Re_1F_2) - \nu(Re_1F_{2A})]_{o.o.p.} + [\delta(O_{1B}Re_{1B}O_{3B}) - \delta(O_{2A}Re_{1A}O_{3A})]$
				346(0)[0]	358(0)[0]	$[\delta(O_1Re_1F_1) - \delta(O_2Re_1F_1) + \nu(Re_1F_2) - \nu(Re_1F_5)]_{i.p.}$
	313(1)	303(1)		322(1)[10]	332(<1)[10]	$[\delta(O_3Re_1F_2F_{2A}) - \delta(F_1Re_1F_2F_{2A})]_{i.p.}$
				300(2)[0]	306(1)[0]	$[\delta(F_1Re_1F_2) - \delta(F_1Re_1F_{2A})]_{o.o.p.}$

Table 4.5. (continued…)

				297(1)[27]	306(1)[23]	$\delta(F_2F_{2A}Re_1F_1) + \rho_t(F_{2A}Re_{1A}F_{2C}) + \rho_t(F_{2B}Re_{1B}F_2)$
	273(2)			292(3)[11]	298(3)[12]	$[\delta(F_2Re_1F_{2A}) + \delta(O_3Re_1F_1)_{small}]_{i.p.}$
260(4)			267(2) br	264(1)[98]	268(1)[99]	$[\delta(O_1Re_1F_1) - \delta(O_2Re_1F_1)] + \delta(O_{3A}Re_{1A}F_{1A}) - \delta(O_{3B}Re_{1B}F_{1B})$
245(<1)	244(2)			253(<1)[0]	259(<1)[0]	$[\rho_t(F_{2A}Re_1F_2) - \rho_t(O_2Re_1O_1)]_{o.o.p.}$
	227(2)			239(<1)[171]	245(<1)[164]	$\delta(O_3Re_1F_1) + \delta(F_2Re_1F_{2A}) + \rho_r(F_{2C}Re_{1A}F_{2A}) - \rho_r(F_2Re_{1B}F_{2B})$
	211 sh 204(7)	203(1)	201(1)	202(2)[9]	207(2)[9]	$[\delta(O_3Re_1F_1) + \delta(F_2Re_1F_{2A})]_{i.p.}$
	197 sh 189(2)			196(1)[0]	201(1)[0]	$\delta(O_3Re_1F_1)_{o.o.p.}$
				190(<1)[0]	192(<1)[0]	$[\rho_r(F_2Re_1F_{2A}) + \rho_w(O_3Re_1F_1)_{small}]_{o.o.p.}$
				182(<1)[0]	189(<1)[0]	$[\rho_r(O_3Re_1F_1)]_{o.o.p.}$
164(<1)	168(3) 162(3)			179(<1)[103]	184(<1)[96]	$[\rho_r(F_2Re_1F_{2A}) + \rho_w(O_3Re_1F_1)_{small}]_{i.p.} + [\delta(F_{2C}Re_{1A}F_{2A}) - \delta(O_{3A}Re_{1A}F_{1A})] + [\delta(O_{3B}Re_{1B}F_{1B}) - \delta(F_{2B}Re_{1B}F_2)]$
				151(0)[0]	157(0)[0]	$[\rho_w(O_3Re_1F_1) + \rho_r(F_{2A}Re_1F_2)]_{i.p.}$
134(1)	155(4) 144(2)	136(1)		142(<1)[4]	146(<1)[5]	$\rho_r(O_1Re_1O_2O_3) + \rho_r(O_{3A}Re_{1A}F_{1A}) + \rho_r(O_{3B}Re_{1B}F_{1B})$
	127(1)		122(2) br	121(<1)[24]	125(<1)[21]	$[\rho_r(O_1Re_1O_2F_1)$
	116(2)	112(1)		112(0)[0]	115(0)[0]	$[\rho_r(O_1Re_1O_2O_3)]_{i.p.}$
	101(2)			92(1)[0]	95(1)[0]	lattice modes
	96(2)	96(1)		87(1)[<1]	90(1)[<1]	
				69(<1)[1]	71(<1)[1]	
				53(1)[0]	52(1)[0]	
				50(0)[0]	69(0)[0]	
				41(<1)[0]	42(<1)[0]	
				41(<1)[0]	40(<1)[0]	
				40(1)[1]	39(1)[1]	
				37(<1)[<1]	36(<1)[<1]	
				6(<1)[0]	9(<1)[0]	

Table 4.5. (continued…)

[a] Frequencies are given in cm^{-1}. [b] Values in parentheses denote relative Raman intensities. Raman spectra were recorded in the FEP sample tubes at −150 °C using 1064-nm excitation. The abbreviations denote shoulder (sh) and broad (br). [c] Values in parentheses denote calculated Raman intensities ($Å^4\ u^{-1}$). Values in square brackets denote calculated infrared intensities (km mol^{-1}). The aug-cc-pVTZ(-PP) basis set was used. [d] The atom numbering corresponds to that used in Figure 4.1b. The abbreviations denote stretch (ν), bend (δ), wagg (ρ_w), rock (ρ_r), twist (ρ_t), in-phase (i.p.) and out-of-phase (o.o.p.) with respect to the $[Re_{1A}O_3F]$ and $[Re_{1B}O_3F]$ units. [e] The $[NO]^+$ cation modes were observed at 2251(11), 2268(95), 2285(5) cm^{-1}. Peaks observed at 327(<1), 426(<1), 866 (<1), 2210(<1), 2229(<1), and 2293(<1) cm^{-1} were unassigned. [f] The $[NH_4]^+$ cation modes were observed at 214 sh, 265(1), 1439(<1), 3137(1), 3191(1) cm^{-1}. [g] Overlap with an $[ReO_4]^-$ mode.

Table 4.6. Experimental Raman Frequencies and Intensities for $M_2[fac\text{-}ReO_3F_3]$ (M = Cs, [NO]) and $K[H_3O][fac\text{-}ReO_3F_3]$ and Calculated Raman and Infrared Frequencies, Intensities, and Assignments for $[fac\text{-}ReO_3F_3]^{2-}$

exptl[a,b]			calcd[a,c]		assgnts (C_{3v})[d]
Cs^+	$[NO]^+$ [e]	$K^+[H_3O]^+$	B3LYP	PBE1PBE	
957(5) 949(100)	955(100) br	951 sh 945 sh	949(76)[107]	980(72)[110]	$[\nu(Re_1O_1) + \nu(Re_1O_{1A}) + \nu(Re_1O_{1B})]$
905(51) 886(45)	921 sh 914(50) 905 sh 898(37) br	921 sh 887 sh 869(6) 855 sh br	882(33)[383]	907(29)[402]	$[\nu(Re_1O_1) + \nu(Re_1O_{1A}) - \nu(Re_1O_{1B})]$
			479(<1)[245]	495(<1)[252]	$[\nu(Re_1F_1) + \nu(Re_1F_{1A}) + \nu(Re_1F_{1B})]$
391(5)[f]	398(3)		404(1)[53]	417(1)[63]	$[\nu(Re_1F_1) + \nu(Re_1F_{1A}) - \nu(Re_1F_{1B})$
384(44)[g]	382(33)		388(2)[14]	394(2)[13]	$\delta(O_1O_{1A}Re_1O_{1B})$
381 sh	379(33) br		379(5)[26]	387(5)[20]	$\delta(O_1Re_1O_{1B}) - \delta(O_{1A}Re_1O_{1B})$
310(3)	329(7) br				
307 sh	317 sh		290(1)[51]	295(1)[50]	$\delta(O_{1A}Re_1F_1F_{1A}) - \delta(O_1O_{1B}Re_1F_1F_{1A})$
296(3)[g]	270(5)		288(1)[7]	295(1)[7]	$\delta(F_1F_{1A}Re_1F_{1B})$
290(4)					
233(3)	240(12)				
224(2)	232(13)		197(1)[10]	201(1)[11]	$\delta(F_{1A}Re_1F_{1B}) - \delta(F_1Re_1O_{1B})$
214(1)	217(9)				
212(1)	204 sh				
			172(0)[0]	174(0)[0]	$\rho_r(O_1O_{1A}Re_1O_{1B}) + \rho_r(F_1F_{1A}Re_1F_{1B})$
120(2)	180(3) br				
102(3)	132(4)				lattice modes
	116(11)				

[a] Frequencies are given in cm^{-1}. [b] Values in parentheses denote relative Raman intensities. Raman spectra were recorded in the FEP sample tubes at −150 °C using 1064-nm excitation. The abbreviations denote shoulder (sh) and broad (br). [c] Values in parentheses denote calculated Raman intensities ($Å^4\ \mu^{-1}$). Values in square brackets denote calculated infrared intensities (km mol^{-1}). The aug-cc-pVTZ(-PP) basis set was used. The atom numbering scheme corresponds to that used in Figure 4.2b. The abbreviations denote stretch (ν), bend (δ), and rock (ρ_r). [e] The $[NO]^+$ cation modes were observed at 2283(34) and 2304(74) cm^{-1}. [f] Band overlapping with the $[ReO_3F_2]^-$ anion mode. [g] Band overlapping with the $[ReO_3F_2]^-$ anion mode and an FEP mode.

Table 4.7. Selected Experimental Raman Frequencies and Intensities for (μ-F)$_4${[μ-^{18}O(Re$^{16/18}$O$_2$F)$_2$](Re$^{16/18}$O$_2$F$_2$)$_2$} in (μ-F)$_4${[μ-$^{16/18}$O(Re$^{16/18}$O$_2$F)$_2$](Re$^{16/18}$O$_2$F$_2$)$_2$}·SO$_2$ClF and Calculated Raman and Infrared Frequencies, Intensities, and Assignments for (μ-F)$_4${[μ-$^{16/18}$O(Re$^{16/18}$O$_2$F)$_2$](Re$^{16/18}$O$_2$F$_2$)$_2$}

exptl[a,b]			calcd[a,c]			assgnts (C_s)[d]
			B3LYP	PBE1PBE		
^{16}O	^{18}O	Δν	^{16}O	^{18}O	Δν	
			1077.9(159)[9]	1020.2(143)[8]	−57.7	[ν(Re$_1$O$_1$) + ν(Re$_1$O$_2$)] + [ν(Re$_3$O$_5$) + ν(Re$_3$O$_6$)]
1024.0(100)	969.1(100)	−54.9	1075.1(14)[115]	1017.4(13)[101]	−57.7	[ν(Re$_1$O$_1$) + ν(Re$_1$O$_2$)] – [ν(Re$_3$O$_5$) + ν(Re$_3$O$_6$)]
			1072.1(11)[<1]	1014.1(10)[<1]	−58.0	[ν(Re$_2$O$_3$) + ν(Re$_2$O$_4$)] – [ν(Re$_4$O$_7$) + ν(Re$_4$O$_8$)] + [ν(Re$_2$O$_9$) − ν(Re$_4$O$_9$)]$_{small}$
1012.6(97)	958.8(94)	−53.8	1066.0(58)[145]	1008.7(50)[132]	−57.3	[ν(Re$_2$O$_3$) + ν(Re$_2$O$_4$)] + [ν(Re$_4$O$_7$) + ν(Re$_4$O$_8$)]
996.3(24)	945.8(30)	−50.5	1042.2(7)[328]	988.6(6)[301]	−53.6	[ν(Re$_1$O$_1$) − ν(Re$_1$O$_2$)] + [ν(Re$_3$O$_6$) – ν(Re$_3$O$_5$)]
			1041.5(44)[0]	988.1(39)[0]	−53.4	[ν(Re$_1$O$_1$) − ν(Re$_1$O$_2$)] + [ν(Re$_3$O$_5$) − ν(Re$_3$O$_6$)]
991.3(46)	940.5(44)	−50.8	1032.0(23)[330]	978.9(20)[307]	−53.1	[ν(Re$_2$O$_3$) − ν(Re$_2$O$_4$)] + [ν(Re$_4$O$_8$) − ν(Re$_4$O$_7$)]
988.7 sh	937.0 sh	−51.7	1028.5(4)[0]	975.3(3)[0]	−53.2	[ν(Re$_2$O$_3$) − ν(Re$_2$O$_4$)] + [ν(Re$_4$O$_7$) − ν(Re$_4$O$_8$)]
863.7(4)	819(4)[e]	−44.7	887.2(5)[813]	841.1(4)[709]	−46.1	[ν(Re$_2$O$_9$) − ν(Re$_4$O$_9$)]
700.8(2)	700.8(2)	0.0	704.0(7)[198]	704.0(7)[198]	−0.0	[ν(Re$_1$F$_1$) − ν(Re$_1$F$_2$)] + [ν(Re$_3$F$_4$) − ν(Re$_3$F$_5$)]
691.3(2)	691.7(3)	0.0	695.3(8)[133]	695.2(8)[134]	−0.1	[ν(Re$_2$F$_3$) + ν(Re$_4$F$_6$)] – [ν(Re$_1$F$_1$) + ν(Re$_1$F$_2$)] + [ν(Re$_3$F$_4$) + ν(Re$_3$F$_5$)]
			690.0(1)[166]	690.0(1)[165]	0.0	[ν(Re$_1$F$_1$) − ν(Re$_3$F$_4$)]
675.9 sh	675.9 sh	0.0	676.1(<1)[4]	676.0(<1)[4]	−0.1	[ν(Re$_1$F$_2$) − ν(Re$_3$F$_5$)]
668.5(9)	668.4(13)	−0.1	675.3(13)[54]	675.2(13)[54]	−0.1	[ν(Re$_1$F$_2$) + ν(Re$_3$F$_5$)] + [ν(Re$_2$F$_3$) + ν(Re$_4$F$_6$)]
			672.7(1)[303]	671.9(1)[327]	−0.8	[ν(Re$_2$F$_3$) − ν(Re$_4$F$_6$)]
			505.1(1)[191]	504.2(1)[197]	−0.9	[ν(Re$_1$F$_{10}$) + ν(Re$_1$F$_7$)] – [ν(Re$_2$F$_7$) + ν(Re$_2$F$_8$)] + [ν(Re$_3$F$_8$) + ν(Re$_3$F$_9$)] – [ν(Re$_4$F$_9$) + ν(Re$_4$F$_{10}$)]
			467.2(<1)[341]	466.2(<1)[355]	−1.0	[ν(Re$_1$F$_{10}$) + ν(Re$_1$F$_7$)] + [ν(Re$_2$F$_8$) − ν(Re$_2$F$_7$)] − [ν(Re$_3$F$_8$) + ν(Re$_3$F$_9$)] + [ν(Re$_4$F$_9$) − ν(Re$_4$F$_{10}$)]
			439.3(<1)[28]	437.2(<1)[25]	−2.1	[ν(Re$_1$F$_{10}$) − ν(Re$_1$F$_7$)] + [ν(Re$_2$F$_7$) + ν(Re$_2$F$_8$)] + [ν(Re$_3$F$_9$) − ν(Re$_3$F$_8$)] − [ν(Re$_4$F$_9$) + ν(Re$_4$F$_{10}$)]
414.2(5)	397.5(5)	−16.7	421.1(2)[22]	402.2(2)[12]	−18.9	[ν(Re$_2$O$_9$) + ν(Re$_4$O$_9$)] + [δ(O$_3$Re$_2$O$_4$) + δ(O$_7$Re$_4$O$_8$)]

Table 4.7. (continued…)

			415.3(1)[0]	412.9(1)[0]	−2.4	$[\nu(Re_1F_{10}) - \nu(Re_1F_7)] + [\nu(Re_2F_7) - \nu(Re_2F_8)] + [\nu(Re_3F_8) - \nu(Re_3F_9)] + [\nu(Re_4F_9) - \nu(Re_4F_{10})]$
405.4(9)	385.2(9)	−20.2	413.6(2)[<1]	393.4(2)[1]	−20.2	$\delta(O_1Re_1O_2) + \delta(O_3Re_2O_4) + \delta(O_5Re_3O_6) + \delta(O_7Re_4O_8)$
400.2(10)	380.1(10)	−20.1	411.0(1)[17]	391.5(1)[14]	−19.5	$\delta(O_1Re_1O_2) - \delta(O_5Re_3O_6)$
395.7(6)	376.6(7)	−19.1	407.6(1)[2]	386.7(1)[2]	−20.9	$\delta(O_3Re_2O_4) - \delta(O_7Re_4O_8)$
			407.1(6)[2]	386.4(5)[3]	−20.7	$[\delta(O_1Re_1O_2) + \delta(O_5Re_3O_6)] - [\delta(O_3Re_2O_4) + \delta(O_7Re_4O_8)] + [\nu(Re_2O_9) + \nu(Re_4O_9)]$
			402.3(<1)[7]	384.2(<1)[<1]	−18.1	$[\delta(O_3Re_2O_9) - \delta(O_4Re_2O_9)] + [\delta(O_8Re_4O_9) - \delta(O_7Re_2O_9)]$

[a] Frequencies are given in cm^{-1}. $\Delta\nu^{16/18} = \nu(^{18}O) - \nu(^{16}O)$. [b] Values in parentheses denote relative Raman intensities. Raman spectra were recorded in the FEP sample tubes at –140 °C using 1064-nm excitation. The abbreviation denotes shoulder (sh). The SO_2ClF modes were observed at 424(3), 431(4), 474(<1), 502(1), 626(1), 824(1), 1218(4), 1444(1) cm^{-1}. [c] Values in parentheses denote calculated Raman intensities ($Å^4\ u^{-1}$). Values in square brackets denote calculated infrared intensities (km mol^{-1}). The B3LYP/aug-cc-pVTZ(-PP) method was used. [d] The atom numbering scheme corresponds to that used in Figure 4.3b. The abbreviations denote stretch (ν) and bend (δ). [e] Overlap with SO_2ClF.

In contrast with the Raman spectra of $A[ReO_2F_4]$ (A = Li, K, Cs) and $[(CH_3)_4N][ReO_2F_4]$,[19] where the Re−O stretching frequencies correlate with the polarizing strength of the cation, no such correlation was observed for the $[ReO_3F_2]^-$ salts. The most intense Raman bands at 980, 980 and 981 cm^{-1} for the K^+, Cs^+, and $[NO]^+$ salts, respectively, and at 986 cm^{-1} for the $[NH_4]^+$ salt are assigned to the symmetric, in-phase, $\nu(ReO_3)$ stretching mode, which is predicted to appear at 996 cm^{-1} as the most intense band. The experimental frequency is comparable to that observed for $K[ReO_2F_4]$ (987 cm^{-1}).[19] The corresponding in-phase and out-of-phase asymmetric $\nu(ReO_3)$ stretching modes are predicted at 945 and 918 cm^{-1} which are in good agreement with the experiment (Cs^+, 922/933 and 910/914 cm^{-1}; $[NO]^+$, 927/933 and 896/904 cm^{-1}; $[NH_4]^+$, 925 cm^{-1}; K^+, 931/936 and 897/925 cm^{-1}). The terminal $\nu(ReF_t)$ stretches are predicted to be significantly weaker than the $\nu(ReO_3)$ stretches and appear at 525 ($[NH_4]^+$), 531 (Cs^+), and 535 ($[NO]^+$) cm^{-1} as very weak bands (calcd, 552 cm^{-1}). Overall, the terminal $\nu(ReF)$ stretches are expected to occur at lower frequencies than the $\nu(ReF_t)$ stretches in $A[ReO_2F_4]$ (A = Li, K, Cs),[19] $[(CH_3)_4N][ReO_2F_4]$,[19] $K[\mu\text{-}F(ReO_2F_3)_2]$,[19] $K[\mu\text{-}F(ReO_2F_3)_2]\cdot 2ReO_2F_3$,[19] and $Cs[(ReO_2F_2)(\mu\text{-}F)_2(ReO_2F_3)_2]$.[19] Both the $\nu(ReO_3)$ and the $\nu(ReF_t)$ stretches are predicted to couple with the respective $\nu(ReO_3)$ and the $\nu(ReF_t)$ stretching modes of their adjacent ReO_3F_2-moieties and are well reproduced by their calculated values. The bridging $\nu(ReF_\mu)$ stretches (calcd, 403 and 416 cm^{-1}), which are predicted to be very weak, were not observed. As predicted, all deformation modes appear below 400 cm^{-1}.

4.2.3.2. *fac*-$[ReO_3F_3]^{2-}$

The *fac*-$[ReO_3F_3]^{2-}$ anion (C_{3v}) possesses 15 fundamental vibrational modes that span the irreducible representations $4A_1 + A_2 + 5E$, where the A_1 and E vibrations are Raman and infrared active and the A_2 vibration is inactive.

The large number of bands observed in the Raman spectra of the Cs^+, $K^+[H_3O]^+$, and $[NO]^+$ salts suggests site symmetry lowering or factor-group splitting. In the absence of crystal structures for $Cs_2[ReO_3F_3]$ and $[NO]_2[ReO_3F_3]$ salts, a factor-group analysis could only be carried out for $K[H_3O][ReO_3F_3]$ (Table B5, Appendix B). Correlation of the gas-phase anion symmetry (C_{3v}) to its crystal site symmetry (C_3) revealed that the observed band splittings do not result from site symmetry lowering alone but are attributable to vibrational coupling within the unit cell (factor-group splitting). Correlation of the site symmetry to the unit cell symmetry (T_h) of $K[H_3O][ReO_3F_3]$ revealed that the fundamental modes, ν_1–ν_5, are each split into two A_g, A_u, T_g, and T_u components. The ν_6–ν_{10} fundamentals are each split into two E_g, E_u, T_g, and T_u components. The A_g, E_g, and T_g components are Raman active, the A_u and E_u components are inactive, and only the T_u components are infrared active. Thus, 40 Raman-active and 20 infrared-active bands are predicted. The splittings of the $\nu_1(A_1)$ (945/951) and $\nu_6(E)$ (855/869/887/921) modes in the Raman spectrum of $K[H_3O][ReO_3F_3]$ are attributed to coupling within the unit cell (factor-group splitting).

The corresponding Re–O stretches are comparable among the Cs^+, $[NO]^+$, and $K^+[H_3O]^+$ salts and the corresponding Re–F stretches are comparable in the Cs^+ and $[NO]^+$ salts. The highest frequency and most intense bands at 949/957 (Cs^+) and 955

($[NO]^+$) cm^{-1} are assigned to the symmetric $\nu_s(ReO_3)$ mode, in agreement with the calculated value at 949 [980] cm^{-1}. By comparison, the shoulders at 945/951 cm^{-1} in the $K^+[H_3O]^+$ salt are also assigned to the symmetric $\nu_s(ReO_3)$ mode. The $\nu_s(ReO_3)$ stretches of the *fac*-$[ReO_3F_3]^{2-}$ anion are shifted to much lower frequencies than in neutral ReO_3F (996 cm^{-1}),[21,235] consistent with increased Re−O bond polarities resulting from the charge of the anion. The corresponding asymmetric mode, $\nu_{as}(ReO_3)$, is observed as a split band in all salts (886/905 (Cs^+), 898/905/914/921 ($[NO]^+$), and 855/869/887/921 ($K^+[H_3O]^+$) cm^{-1}). The average value agrees well with the calculated frequency (882 [907] cm^{-1}). Both symmetric and asymmetric Re−O stretches appear at higher frequency than those in $Cs_2[ReO_3Cl_3]$ (925(vs) and 895(s) cm^{-1}),[236] consistent with a decrease in the polarity of the Re−O bonds resulting from the higher electronegativity and lower basicities of the fluoride ligands when compared with those of the chloride ligands.

Both the symmetric, $\nu_s(ReF_3)$, and asymmetric, $\nu_{as}(ReF_3)$, stretching modes are expected to be very weak with the symmetric mode occurring at higher frequency (calcd, 479 [495] cm^{-1}) than the asymmetric mode (calcd, 404 [417] cm^{-1}). Only the $\nu_{as}(ReF_3)$ mode was observed at 391 cm^{-1} in the Cs^+ salt and at 398 cm^{-1} in the $[NO]^+$ salt. As expected, the Re−F stretching modes appear at significantly lower frequencies than those of the $[ReO_2F_4]^-$ anion (500−600 cm^{-1} region).[19]

The symmetric bend, $\delta_s(ReO_3)$, is predicted to occur at higher frequency (calcd, 388 [394] cm^{-1}) than the asymmetric bend, $\delta_{as}(ReO_3)$, (calcd, 379 [386] cm^{-1}), in good agreement with the frequencies observed for the Cs^+ ($\delta_s(ReO_3)$, 384 cm^{-1}; $\delta_{as}(ReO_3)$, 381 cm^{-1}) and $[NO]^+$ ($\delta_s(ReO_3)$, 382 cm^{-1}; $\delta_{as}(ReO_3)$, 379 cm^{-1}) salts. The asymmetric

$\delta_{as}(ReF_3)$ bend is coupled to the asymmetric $\delta_{as}(F{-}Re{-}O)$ bend (calcd, 290 [295] cm^{-1}) and is expected to occur at a frequency similar to that of the symmetric $\delta_s(ReF_3)$ bend (288 [295] cm^{-1}). Both modes are assigned to factor-group split at 212/214/224/233 cm^{-1} in the Cs^+ salt and at 204/217/232/240 cm^{-1} in the $[NO]^+$ salt.

4.2.3.3 $(\mu\text{-}F)_4\{[\mu\text{-}^{16/18}O(Re^{16/18}O_2F)_2](Re^{16/18}O_2F_2)_2\}\cdot SO_2ClF$

The $(\mu\text{-}F)_4\{[\mu\text{-}O(ReO_2F)_2]\ (ReO_2F_2)_2\}$ molecule possesses C_{2v} symmetry which results in 63 fundamental vibrational modes belonging to the $19A_1 + 13A_2 + 15B_1 + 16B_2$ irreducible representations, where all modes are infrared and Raman active, except for the A_2 modes which are only Raman active.

The calculated frequencies associated with the terminal and bridging Re−O stretching modes are overestimated (Table 4.7); however, the observed frequency trends and isotopic shifts are well reproduced by quantum-chemical calculations. These are the highest frequency and most intense bands in the Raman spectrum exhibiting the largest isotopic shifts (Tables 4.7 and B3). Their frequencies are comparable to their $ReO_3F(FH_2)$[235] and ReO_2F_3[19,21] counterparts. The broad band at 864 cm^{-1} (calcd, 887 [911] cm^{-1}) is particularly noteworthy because no bands are observed in this region for rhenium oxide fluorides other than ReO_3F (813 cm^{-1}) which exhibits $Re–O_\mu$ bridge bonding.[21] This band shows a large $\Delta\nu^{16/18}$ isotopic shift (exptl, −44.7 cm^{-1}; calcd −46.1 [−47.2] cm^{-1}), and is assigned to the asymmetric $[\nu(Re_2O_\mu){-}\nu(Re_4O_\mu)]$ stretching mode of the $Re–O_\mu–Re$ bridge. This frequency is also consistent with the asymmetric $Re–O_\mu–Re$ stretching frequencies of Re_2O_7 (782 to 895 cm^{-1}, this work; 798 to 880 cm^{-1} [246]) and

ReO_3F (813 cm^{-1}).[21,235] As expected, the asymmetric Re–O_μ–Re stretching mode of (μ-F)$_4${[μ-O$(ReO_2F)_2$]$(ReO_2F_2)_2$} appears at higher frequency than the asymmetric doubly degenerate Re–O_{μ_3}–Re stretching mode of the $[\{ReO_3(\mu\text{-}F)\}_3(\mu_3\text{-}O)]^{2-}$ anion (575/580/586 cm^{-1}),[235] which is substantially lower due to the formal negative charge of the anion and the corresponding lower bond valencies of the Re–O_{μ_3} bonds and coupling with the asymmetric ν(Re−F_μ−Re) stretching modes of this anion. The symmetric [ν(Re_2O_μ) + ν(Re_4O_μ)] stretch of (μ-F)$_4${[μ-O$(ReO_2F)_2$]$(ReO_2F_2)_2$} (exptl, 414, −16.7 cm^{-1}; calcd, 421 [429], −18.9 [−18.9] cm^{-1}) is weakly coupled to the [δ($O_3Re_2O_4$) + δ($O_7Re_4O_8$)] deformation mode and is comparable to the symmetric O−Re−O stretching frequency of Re_2O_7 (solid, 401/412/421 cm^{-1} (Table B10); gas phase, 456 cm^{-1} [246]). As expected, the terminal ν(Re−F) stretches are more intense and appear at higher frequency than the bridging ν(Re−F_μ) stretches (Table 4.7, B3), which were not observed.

4.2.4. Computational Results

Quantum-chemical calculations for $[(\mu\text{-}F)_4(ReO_3F)_4]^{4-}$ (C_{4h}) (Table 4.5), *fac*-$[ReO_3F_3]^{2-}$ (C_{3v}) (Table 4.6), (μ-F)$_4${[μ-O$(ReO_2F)_2$]$(ReO_2F_2)_2$} (C_{2v}) (Table 4.7, B3), *mer*-$[ReO_3F_3]^{2-}$ (C_s) (Table B3), and $[ReO_3F_2]^-$ (C_s) (Table B4) were carried out using the B3LYP and PBE1PBE (values are given in brackets) methods and the aug-cc-pVTZ(-PP) basis sets and resulted in the corresponding stationary points with all frequencies real.

4.2.4.1. Geometry Optimizations for $[ReO_3F_2]^-$, $[(\mu\text{-}F)_4(ReO_3F)_4]^{4-}$, *fac*-$[ReO_3F_3]^{2-}$ (C_{3v}), *mer*-$[ReO_3F_3]^{2-}$ (C_s), and (μ-F)$_4${[μ-O$(ReO_2F)_2$]$(ReO_2F_2)_2$}

$[ReO_3F_2]^-$ and $[(\mu\text{-}F)_4(ReO_3F)_4]^{4-}$. Initially, the optimization of the unknown $[(\mu\text{-}F)_2(ReO_3F)(ReO_3F_2)_2]^{4-}$ (C_1) anion was attempted in order to reproduce and assign the experimental vibrational spectra of $[ReO_3F_2]^-$, also taking into account possible coupling between bridging ReO_3F_2-units of the open-chain structure. This approach has been previously used to assign the Raman spectra of $(OsO_3F_2)_\infty$[247] and $(MoSF_4)_\infty$.[248] The starting geometry used for $[(\mu\text{-}F)_2(ReO_3F)(ReO_3F_2)_2]^{4-}$ was part of the crystallographic geometry of the $[ReO_3F_2]^-$ anion in the $[NH_4]^+$ salt (see X-ray Crystallography) which reproduced the geometry of the central ReO_3F_2-moiety. However, all attempts resulted in dissociation of the hypothetical trimeric-chain anion into one central ReO_3F_3- and two terminal ReO_3F_2-groups. Therefore, the hypothetical tetrameric anion, $[(\mu\text{-}F)_4(ReO_3F)_4]^{4-}$ (C_{4h}), was calculated instead. The monomeric $[ReO_3F_2]^-$ (C_s) anion was also calculated in order to assess the effect of oligomerization (Table B6).

The calculated Re−O bond lengths, which are trans to the terminal fluorine atom (1.712 [1.700] Å) are slightly shorter than those trans to the bridging fluorine atoms (1.722 [1.709] Å). The opposite trend was observed among the experimental Re−O bond lengths (1.726(2) vs. 1.704(2) and 1.705(2) Å), which is most likely due to interionic contacts in the crystal structures. The calculated terminal and bridging Re−F bond lengths (1.949 [1.933] Å and 2.177 [2.156] Å, respectively), however, well reproduce the experimental values. Trends among all bond angles are also reproduced by the calculations, except the Re−F−Re angles (165.3° [164.8°]), which are more open in the calculated $[(\mu\text{-}F)_4(ReO_3F)_4]^{4-}$ (C_{4h}) anion model than in the crystal structure of $[NH_4][ReO_3F_2]$ (137.2(1)°).

***fac*-$[ReO_3F_3]^{2-}$ (C_{3v}) and *mer*-$[ReO_3F_3]^{2-}$ (C_s).** The Re–O bond lengths of the *fac*-$[ReO_3F_3]^{2-}$ anion (1.735 [1.722] Å) are in excellent agreement with the experimental values, whereas the calculated Re–F bond lengths (2.035 [2.017] Å) are longer than the experimental Re–F bond lengths (1.964(4) Å). The O−Re–O, F−Re−O, and F−Re−F bond angles are in very good agreement with experiment (Table 4.3).

The optimization of *mer*-$[ReO_3F_3]^{2-}$ to C_{2v} geometry gave one imaginary frequency. Attempts to follow this imaginary frequency resulted in lowering of the anion symmetry from C_{2v} to C_s, to give a local minimum for the *mer*-$[ReO_3F_3]^{2-}$ anion, which is more stable by 5.7 [6.1] kJ mol^{-1} than the *mer*-$[ReO_3F_3]^{2-}$ (C_{2v}) anion. The *mer*-$[ReO_3F_3]^{2-}$ (C_s) anion is, however, predicted to be less stable by 85.6 [88.4] kJ mol^{-1} than the *fac*-$[ReO_3F_3]^{2-}$ (C_{3v}) anion. Overall the Re–O and the Re–F bond lengths of the *mer*-$[ReO_3F_3]^{2-}$ anion (Table B7) are longer than those of the *fac*-$[ReO_3F_3]^{2-}$ anion. The Re–O bonds, which are trans to each other, are longer than the Re–O bond that is trans to a fluorine atom, whereas the opposite trend is observed for the Re–F bond lengths. This behavior is consistent with the trans influence of the oxygen atoms,[17] which are much stronger pπ→dπ donors than the fluorine atoms.

$(\mu\text{-}F)_4\{[\mu\text{-}O(ReO_2F)_2](ReO_2F_2)_2\}$. The optimized geometry of $(\mu\text{-}F)_4\{[\mu\text{-}O(ReO_2F)_2]\ (ReO_2F_2)_2\}$ agrees very well with the experimental geometry and is consistent with the cage being well isolated in the crystal structure (see X-ray Crystallography). The calculated terminal Re−O bonds have similar lengths (1.671 [1.659] and 1.674 [1.662] Å) and are longer than the bridging Re−O_μ bond (1.876 [1.862] Å), agreeing well with the experimental trend. The terminal Re−F bonds that are trans to

one another are slightly different (1.840 and 1.850 Å) which also reproduces the experimental trend. The calculated bridging Re−F bonds are significantly longer than the calculated bridging Re−O_μ bond, supporting the experimental findings.

All calculated trends among bond angles well reproduce the experimental trends, i.e., O−Re−O > O_μ−Re−O > O−Re−F > O−Re−F_μ > F−Re−F_μ > F_μ−Re−F_μ.

4.2.4.2. Calculated Vibrational Spectrum of *mer*-$[ReO_3F_3]^{2-}$ and Comparison with That of *fac*-$[ReO_3F_3]^{2-}$

The *mer*-$[ReO_3F_3]^{2-}$ anion possesses 15 fundamental vibrational modes belonging to the irreducible representations 10A' + 5A" under C_s symmetry where the A' and A" modes are Raman and infrared active.

The most intense Re−O stretching band, $\nu_s(ReO_3)$, (928 [958] cm^{-1}) and both $\nu_{as}(ReO_3)$ stretches (872 [900] and 835 [860] cm^{-1}) of *mer*-$[ReO_3F_3]^{2-}$ (Table B3) are predicted to occur at lower frequencies than those of *fac*-$[ReO_3F_3]^{2-}$ (Table 4.6). The $\nu(ReF_3)$ stretches of the *mer*-$[ReO_3F_3]^{2-}$ anion are more intense and appear at higher frequency (462 [475] and 506 [522] cm^{-1}) than the symmetric $\nu_s(ReF)$ (404 [417] cm^{-1}) and asymmetric $\nu_{as}(ReF)$ (479 [595] cm^{-1}) stretches of the *fac*-$[ReO_3F_3]^{2-}$ anion. Contrary to the *fac*-$[ReO_3F_3]^{2-}$ anion, the δ(OReO) and δ(FReF) bends couple in the *mer*-$[ReO_3F_3]^{2-}$ anion. It is also noteworthy that contrary to what is observed experimentally, bands of reasonable intensity should also be observed around 462, 506, and 835 cm^{-1} in the case of the *mer*-isomer (Table B3). All of the above points relating to the vibrational analysis concur with the conclusion that only the *fac*-$[ReO_3F_3]^{2-}$ anion is stable.

4.2.4.3. NBO Charges, Wiberg Valencies, and Bond Indices. The NBO charges and Wiberg valencies and bond indices for $[(\mu\text{-}F)_4(ReO_3F)_4]^{4-}$ (C_{4h}) (Table B8), [*fac*-$ReO_3F_3]^{2-}$ (C_{3v}) (Table B9), and $(\mu\text{-}F)_4\{[\mu\text{-}O(ReO_2F)_2](ReO_2F_2)_2\}$ (C_{2v}) (Table B10) were determined for the B3LYP/aug-cc-pVTZ(-PP) and PBE1PBE/aug-cc-pVTZ(-PP) optimized gas-phase geometries. The trends in calculated charges, valencies, and bond orders for the above species are consistent at both levels of theory.

As expected, the positive charge is located on rhenium and the negative charges are located on the electronegative ligands (Tables B8−B10). The negative charges are evenly shared among all oxygen and fluorine atoms in $[(\mu\text{-}F)_4(ReO_3F)_4]^{4-}$ and *fac*-$[ReO_3F_3]^{2-}$, whereas the highest negative charge (−0.78) in $(\mu\text{-}F)_4\{[\mu\text{-}O(ReO_2F)_2](ReO_2F_2)_2\}$, is located on the doubly bridging oxygen atom (O_μ).

Although the Wiberg valencies (v.) and the bond indices (b.i.) of the terminal oxygen atoms decrease from the neutral $(\mu\text{-}F)_4\{[\mu\text{-}O(ReO_2F)_2](ReO_2F_2)_2\}$ molecule (v., 2.36 and 2.37; b.i., ca. 1.80) to the $[(\mu\text{-}F)_4(ReO_3F)_4]^{4-}$ (v., 2.08 and 2.15; b.i., 1.52 and 1.56) and $[ReO_3F_3]^{2-}$ (v., 2.04; b.i., 1.47) anions, overall the calculations are consistent with the double-bond characters of the terminal Re−O bonds. A similar trend is observed for the terminally bonded fluorine atoms, where the valencies and the bond indices of the neutral $(\mu\text{-}F)_4\{[\mu\text{-}O(ReO_2F)_2](ReO_2F_2)_2\}$ molecule (v., 1.02, 1.01 and 0.98; b.i., 0.71, 0.70, 0.69) are higher than in the $[(\mu\text{-}F)_4(ReO_3F)_4]^{4-}$ (v., 0.75; b.i., 0.50) and *fac*-$[ReO_3F_3]^{2-}$ (v., 0.60; b.i., 0.40) anions.

The Wiberg valence of the bridging O_μ (2.11) in $(\mu\text{-}F)_4\{[\mu\text{-}O(ReO_2F)_2](ReO_2F_2)_2\}$ is similar, whereas the Re−O_μ bond index (0.74) is significantly smaller than those of the

terminal oxygen atoms, in accordance with the Re−O_μ bonds being longer and weaker than the terminal Re−O bonds.

The bridging fluorine atoms of (μ-F)$_4${[μ-O(ReO_2F)$_2$](ReO_2F_2)$_2$} (v., 0.76; b.i., 0.25 and 0.24) and of [(μ-F)$_4$(ReO_3F)$_4$]$^{4-}$ (v., 0.72; b.i., 0.24) are equivalently bonded to the rhenium atoms.

4.3. Conclusion

The development of a high-yield, high-purity synthesis of ReO_3F has significantly extended the number of structurally documented Re(VII) oxide fluorides. The study of the fluoride-ion acceptor properties of ReO_3F has led to the isolation of several salts of the *fac*-[ReO_3F_3]$^{2-}$ (Cs^+, $[NO]^+$, and $K^+[H_3O]^+$) and [ReO_3F_2]$^-$ (Cs^+, $[NO]^+$, K^+, $[NH_4]^+$) anions and their characterization in the solid state by Raman spectroscopy, where the vibrational assignments were aided by quantum-chemical calculations. The salts, $K[H_3O][ReO_3F_3]$ and $[NH_4][ReO_3F_2]$, were structurally characterized by single-crystal X-ray diffraction. The arrangement of oxygen ligand atoms was shown to be facial in the [ReO_3F_3]$^{2-}$ anion. This contrasts with the meridional geometry previously reported for its K^+, Rb^+, Cs^+,[27,36] and $[N(CH_3)_4]^+$ [37] salts, which was erroneously arrived at based on the assignments of their infrared and Raman spectra. The [ReO_3F_2]$^-$ anion represents an example of an open-chain structure, in which the ReO_3F-units are fluorine bridged to each other.

The reaction of ReO_3F with ReO_2F_3 in SO_2ClF yielded a new neutral rhenium(VII) oxide fluoride, (μ-F)$_4${[μ-O(ReO_2F)$_2$](ReO_2F_2)$_2$}, which also provides a rare example of

an O-bridged rhenium oxide fluoride. This oxide fluoride was characterized by single-crystal X-ray diffraction and solid-state Raman spectroscopy. The vibrational assignments of the Raman spectrum of $(\mu\text{-}F)_4\{[\mu\text{-}O(ReO_2F)_2](ReO_2F_2)_2\}$ were supported by ^{18}O-enrichment studies.

CHAPTER 5

FLUORIDE ION-DONOR PROPERTIES OF ReO_3F

5.1. Introduction

The discovery of a high-yield, high-purity synthesis of ReO_3F[235] (Chapter 3) has facilitated the investigation of its Lewis acid and fluoride ion-acceptor properties. In the process, the $[\{ReO_3(\mu\text{-}F)\}_3(\mu_3\text{-}O)]^{2-}$,[235] $[ReO_3F_2]^-$ (Chapter 4), and *fac*-$[ReO_3F_3]^{2-}$ (Chapter 4) anions and the $(HF)_2ReO_3F$ adduct[235] (Chapter 4) were synthesized and structurally characterized by single-crystal X-ray diffraction.

Although no rhenium(VII) cations derived from ReO_3F were known, cations of other high-valent rhenium(VII) oxide fluorides, $ReOF_5$ and ReO_2F_3, had been previously synthesized and characterized, namely, $[ReOF_4]^+$,[13] $[\mu\text{-}F(ReOF_4)_2]^+$,[13] $[ReO_2F_2]^+$,[22] and $[\mu\text{-}F(ReO_2F_2)_2]^+$.[22] The coordination spheres of the rhenium atoms in these cations are distorted octahedra. The oxygen ligands in the $[ReO_2F_2]^+$ [22] and $[\mu\text{-}F(ReO_2F_2)_2]^+$ [22] cations are located cis to one another allowing a greater degree of π-bonding with the empty set of $d_{t_{2g}}$ orbitals on rhenium. The bridging fluorine atoms in the dinuclear cations, $[\mu\text{-}F(ReOF_4)_2]^+$ [13] and $[\mu\text{-}F(ReO_2F_2)_2]^+$,[22] are always located trans to the oxygen ligands.

The strongly bonded $[MO_3]^+$ (M = Tc, Re) moieties are known and have been intensively studied in several rhenium(VII) complexes, e.g., CH_3ReO_3,[249] $(\eta_5\text{-}C_5(CH_3)_5)ReO_3$,[40,249b] $[(C_6H_{15}N_3)ReO_3]X$ (X = Cl, $[ReO_4]$,[41] $[ReO_3][ClO_4]$,[250]

$[(C_6H_{12}S_3)ReO_3][BF_4]$,[42] and in the only known technetium(VII) salt, $[TcO_3][SO_3F]$.[43] In all of the aforementioned salts, the ReO_3- and TcO_3-moieties adopt pyramidal geometries.

The technetium analog of ReO_3F, TcO_3F, has been shown to react with AsF_5 in aHF forming the $[TcO_3]^+$ cation, which was characterized in solution by ^{99}Tc and ^{17}O NMR spectroscopy.[26] In a subsequent study, it was shown that TcO_3F solvolyses in PnF_5/aHF (Pn = As, Sb) media formed the $[TcO_2F_2][PnF_6]$ salts.[23]

This Chapter investigates the fluoride ion-donor properties of ReO_3F in its reactions with the Lewis acids, SbF_5 and AsF_5. The study resulted in the synthesis, isolation, and characterization of μ-$O(ReO_2F)(AsF_5)\cdot 2AsF_5$ and the salts, $[ReO_3][Sb_3F_{16}]$ and $[O_3Re(NCCH_3)_3][PnF_6]$ (Pn = As, Sb). The products were characterized by Raman spectroscopy, where vibrational assignments were made with the aid of quantum-chemical calculations.

5.2. Results and Discussion

Reaction progress was routinely monitored by low-temperature Raman spectroscopy.

5.2.1. Attempted Syntheses of $[ReO_3][PnF_6]$ (Pn = As, Sb), $[\mu$-$F(ReO_3)_2][SbF_6]$, $[ReO_3][Sb_2F_{11}]$, and $[ReO_3][BF_4]$ in aHF

All attempts to synthesize either the $[ReO_3]^+$ or $[\mu$-$F(ReO_3)_2]^+$ cations by reaction of ReO_3F with BF_3, excess AsF_5, or SbF_5 (ReO_3F:SbF_5, 1:1, 1:2, and 2:1 molar ratios) in aHF at –78 ^{o}C resulted in the solvolysis of ReO_3F. Solvolysis reactions were also

previously reported for TcO_3F, which was shown to undergo O/F metathesis in the superacidic media, aHF/PnF_5 (Pn = As, Sb), to give $[TcO_2F_2][PnF_6]$ and $[H_3O][PnF_6]$.[23]

Anhydrous HF solutions of ReO_3F and BF_3/PnF_5 were allowed to react at –78 °C which resulted in the formation of ReO_2F_3 and $[H_3O][BF_4]/[H_3O][PnF_6]$ (eq 5.1). Upon

$$ReO_3F + BF_3/PnF_5 \xrightarrow[-78\ ^oC]{aHF} ReO_2F_3 + [H_3O][BF_4]/[H_3O][PnF_6] \quad (5.1)$$

warming HF solutions of the reaction mixtures to room temperature, ReO_2F_3 reacted with excess AsF_5 and SbF_5 (ReO_3F:SbF_5, 1:2) (eq 5.2) forming the known $[ReO_2F_2][PnF_6]$

$$ReO_3F + \text{xs } AsF_5/2SbF_5 \xrightarrow{aHF} [ReO_2F_2][PnF_6] + [H_3O][PnF_6]$$

$$(Pn = As, Sb) \quad (5.2)$$

salts (Pn = As, Sb).[22]

The reaction of ReO_3F with SbF_5 in a 2:1 molar ratio at −40 °C yielded a white solid, which dissolved in aHF at room temperature forming a bright orange solution (eq 5.3). The solution was cooled to –78 °C whereupon several white products precipitated.

$$2ReO_3F + SbF_5 \xrightarrow[-40\ ^oC]{aHF} [H_3O][ReO_2F_4]\cdot[H_3O][SbF_6] + \text{unidentified product(s)} \quad (5.3)$$

The precipitate was assigned to a mixture of rhenium oxide fluorides based on the Raman spectrum of the dry precipitate; however, not all of the products could be identified by Raman spectroscopy. Crystallization of the products was attempted at various temperatures which resulted in the crystallization of $[H_3O][SbF_6]$ at –78 °C and $[H_3O][ReO_2F_4]\cdot[H_3O][SbF_6]$ at –50 , –30, and –10 °C. All attempts to crystallize the remaining unidentified product(s) from HF were unsuccessful.

Rhenium trioxide fluoride failed to react with BF_3 gas at temperatures from –78 up to 80 °C.

5.2.2. Syntheses of μ-O(ReO_2F)(AsF_5)·2AsF_5 and [ReO_3][Sb_3F_{16}]

In order to circumvent solvolysis of ReO_3F in aHF, ReO_3F was reacted with neat AsF_5 at –20 °C which resulted in the formation of μ-O(ReO_2F)(AsF_5)·2AsF_5 over the course of several days (eq 5.4). The product was isolated by removing AsF_5 under

$$ReO_3F + 3AsF_5 \xrightarrow[-20\ ^oC]{AsF_5} \mu\text{-}O(ReO_2F)(AsF_5)\cdot 2AsF_5 \quad (5.4)$$

dynamic vacuum at –50 °C. The salt, μ-O(ReO_2F)(AsF_5)·2AsF_5, is unstable with respect to dissociation at 0 °C, at which temperature different oligomeric $(ReO_3F)_x$ units start to assemble. When the ReO_3F and AsF_5 mixture was cooled from 0 °C to –78 °C and maintained at –78 °C for several days, μ-O(ReO_2F)(AsF_5)·2AsF_5 reformed, as confirmed by Raman spectroscopy. Complete dissociation into the starting materials, ReO_3F and AsF_5, occurred when AsF_5 was removed under dynamic vacuum at room temperature. The original product was insoluble up to –25 °C in aHF and up to –20 °C in SO_2ClF and CH_2Cl_2. An attempt to dissolve μ-O(ReO_2F)(AsF_5)·2AsF_5 in aHF at temperatures higher than –25 °C resulted in the formation of ReO_2F_3[3,4,6,19] and [H_3O][AsF_6] (eq 5.5).

$$\mu\text{-}O(ReO_2F)(AsF_5)\cdot 2AsF_5 + 3HF \xrightarrow[>\ -25\ ^oC]{aHF} ReO_2F_3 + [H_3O][AsF_6] + 2AsF_5 \quad (5.5)$$

Rhenium trioxide fluoride very slowly reacted with SbF_5 at ca. 40 °C which resulted in a mixture of [ReO_3][Sb_3F_{16}] and [ReO_2F_2][SbF_6].[22] The salt, [ReO_3][Sb_3F_{16}], was insoluble in SbF_5, whereas [ReO_2F_2][SbF_6] dissolved in excess SbF_5 as it formed. However, the pure product, [ReO_3][Sb_3F_{16}], can be synthesized by reaction of ReO_3F with SbF_5 in SO_2ClF at room temperature (eq 5.6) and was isolated by removal of the

$$ReO_3F + SbF_5 \xrightarrow[RT]{SO_2ClF} [ReO_3][Sb_3F_{16}] \quad (5.6)$$

solvent under dynamic vacuum. The $[ReO_3][Sb_3F_{16}]$ salt is insoluble in both SO_2ClF and CH_2Cl_2, which prevented its structural characterization by single-crystal X-ray diffraction. Attempts to crystallize $[ReO_3][Sb_3F_{16}]$ by sublimation (45 ^oC) resulted in the formation of colorless crystals of $[ReO_2F_2][SbF_6]$.[22]

5.2.3. Syntheses of $[O_3Re(NCCH_3)_3][PnF_6]$ (Pn = As, Sb)

The μ-$O(ReO_2F)(AsF_5)\cdot 2AsF_5$ and $[ReO_3][Sb_3F_{16}]$ salts were shown to react with CH_3CN forming pale yellow-brown and light brown colored viscous solutions, respectively. Removal of the solvent under dynamic vacuum at room temperature resulted in the isolation of the colorless $[O_3Re(NCCH_3)_3][PnF_6]$ (Pn = As, Sb) salts along with $PnF_5\cdot CH_3CN$[251−253] (eq 5.7 and 5.8). Although the compounds crystallize at –15 ^oC,

$$[ReO_3][Sb_3F_{16}] \xrightarrow[RT]{CH_3CN} [O_3Re(NCCH_3)_3]SbF_6] + 2SbF_5\cdot CH_3CN \quad (5.7)$$

$$\mu\text{-}O(ReO_2F)(AsF_5)\cdot 2AsF_5 \xrightarrow[RT]{CH_3CN} [O_3Re(NCCH_3)_3][AsF_6] + 2AsF_5\cdot CH_3CN \quad (5.8)$$

all attempts to isolate crystals from their viscous solutions at temperatures ≥ −15 ^oC were unsuccessful. Raman spectra were recorded on the crystalline products, $[O_3Re(NCCH_3)_3][PnF_6]$, under a small amount of frozen CH_3CN. The product could not be dried by pumping at −15 ^oC. An attempt to isolate crystals of $[O_3Re(NCCH_3)_3][AsF_6]$ was made by slowly removing CH_3CN at temperatures > −15 ^oC. This resulted in the formation of a white solid, $[O_3Re(NCCH_3)_3][AsF_6]$, which was further dried by pumping at room temperature.

The synthesis of $[O_3Re(NCCH_3)_3][SbF_6]$ was attempted by condensing a small amount of CH_3CN into a reactor containing $[ReO_3][Sb_3F_{16}]$ under CH_2Cl_2. This resulted in the formation of a white suspension in a yellow solution. Attempts to grow crystals from the yellow solution at −78 ^oC over a period of several weeks failed.

5.2.4. Computational Results

In view of the fact that $[ReO_3][Sb_3F_{16}]$, μ-$O(ReO_2F)(AsF_5)\cdot 2AsF_5$, and $[O_3Re(NCCH_3)_3][PnF_6]$ (Pn = As, Sb) failed to crystallize, the structures of the aforementioned compounds were initially inferred by Raman spectroscopy and further supported by quantum-chemical calculations.

5.2.4.1. Calculated Structures of $[ReO_3][Sb_3F_{16}]$ (1), μ-$O(ReO_2F)(AsF_5)\cdot 2AsF_5$ (2) and $[O_3Re(NCCH_3)_3]^+$ (3)

The geometries of **(1)** (C_s), **(2)** (C_s), **(3)** (C_{3v}) (Figures 5.1a, 5.1b and 5.1c), $[ReO_3]^+$ (C_{3v}) (Figure C1), $[Sb_3F_{16}]^-$ (C_s) (Figure C2), hypothetical $\{[ReO_3][AsF_6]_3\}^{2-}$ (C_{3v}) (Figure C3a), and CH_3CN (C_{3v}) (Figure C4) were optimized at the B3LYP/aug-cc-pVTZ(-PP) and only these values are referred to in the discussion, and the PBE1PBE/aug-cc-PVTZ(-PP) levels of theory and resulted in stationary points with all frequencies real (Tables 5.1, 5.2, 5.3, C1, C2, C3, C4, C5 and C6, Appendix C). The optimization of $\{[ReO_3][SbF_6]_3\}^{2-}$ (C_{3v}) (Figure C3b) gave three imaginary frequencies at both levels of theory. The optimization of the "$[ReO_3][As_3F_{16}]$" and $[As_3F_{16}]^-$ models at the B3LYP/aug

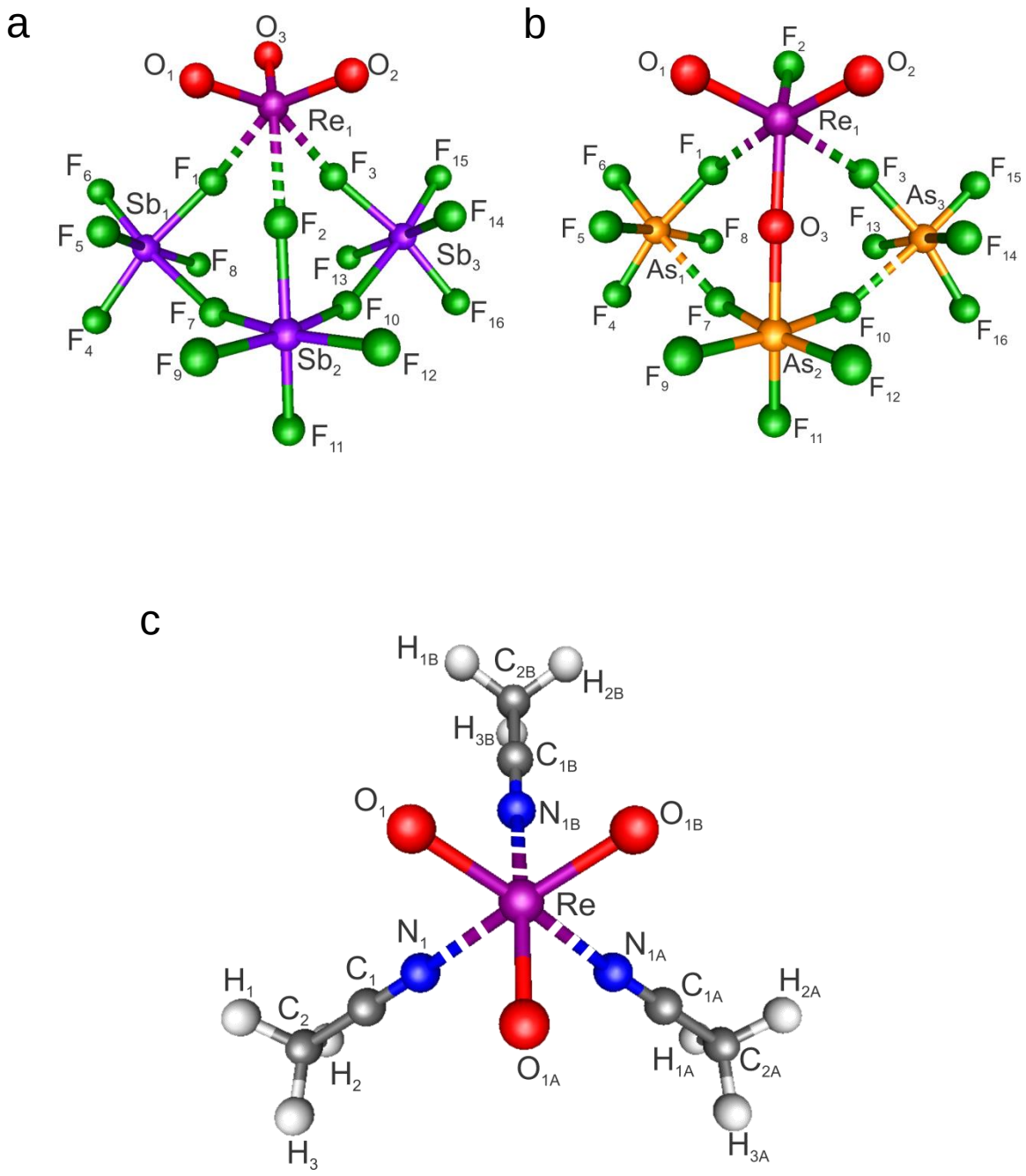

Figure 5.1. The energy-minimized structures of (a) $[ReO_3][Sb_3F_{16}]$, (b) the μ-$O(ReO_2F)(AsF_5)\cdot 2AsF_5$ adduct and (c) the $[O_3Re(NCCH_3)_3]^+$ adduct-cation (B3LYP/aug-cc-pVTZ(-PP)).

Table 5.1. Selected Experimental Raman Frequencies and Intensities and Calculated Vibrational Frequencies, Intensities, and Assignments for the $[ReO_3]^+$ Cation in the $[ReO_3][Sb_3F_{16}]$ Ion-Pair (C_s)

exptl[a,b]	calcd[a,c]		assgnts[d]
1038(100) 1018(14) 1010(40)	1066(55)[19]	A'	$\nu(Re_1O_1) + \nu(Re_1O_2) + \nu(Re_1O_3)$
972(11)	1014(18)[156]	A''	$\nu(Re_1O_1) - \nu(Re_1O_2)$
	1011(21)[139]	A'	$\nu(Re_1O_1) + \nu(Re_1O_2) - \nu(Re_1O_3)$
406(8)	388(3)[2]	A'	$\delta(O_1Re_1O_2)$
	383(3)[5]	A''	$\delta(O_1Re_1O_3) - \delta(O_2Re_1O_3)$
	375(2)[18]	A'	$\delta(Re_1O_1O_2O_3)$

[a] Frequencies are given in cm^{-1}. [b] Values in parentheses denote relative Raman intensities. The Raman spectrum was recorded in an FEP sample tube at –140 °C using 1064-nm excitation. A full list of frequencies and assignments is provided in Table C4. [c] Values in parentheses denote calculated Raman intensities ($Å^4\ u^{-1}$). Values in square brackets denote calculated infrared intensities (km mol^{-1}). The B3LYP/aug-cc-pVTZ(-PP) method was used. [d] The abbreviations denote stretch (ν) and bend (δ). The atom numbering corresponds to that used in Figure 5.1a.

Table 5.2. Selected Experimental Raman Frequencies and Intensities and Calculated Vibrational Frequencies, Intensities, and Assignments for μ-$O(ReO_2F)(AsF_5)$ $2AsF_5$ (C_s)

exptl[a,b]	calcd[a,c]		assgnts[d]
1038(5) 1030(100)	1082(51)[37]	A'	$\nu(Re_1O_1) + \nu(Re_1O_2)$
1015(29) 1006(15) 1002(3)	1045(21)[140]	A"	$\nu(Re_1O_1) - \nu(Re_1O_2)$
886(2) 878(3)	938(4)[609]	A'	$\nu[(Re_1O_3) - \nu(As_2O_3)$
	703(2)[141]	A'	$\nu(Re_1F_2)$
535(1)	549(1)[93]	A'	$[\nu(Re_1F_1) + \nu(Re_1F_3)] - [\nu(As_1F_1) + \nu(As_3F_3)] + \nu(As_2F_7) + \nu(As_2F_{10})] - [\nu(As_1F_7) + \nu(As_3F_{10})]$
523(1)	523(4)[155]	A"	$[\nu(Re_1F_1) + \nu(As_3F_3)] - [\nu(Re_1F_3) + \nu(As_1F_1)]$
510(3)	520(20)[36]	A'	$[\nu(Re_1F_1) + \nu(Re_1F_3)] - [\nu(As_1F_1) + \nu(As_3F_3)] - [\nu(As_2F_7) + \nu(As_2F_{10})] + [\nu(As_1F_7) + \nu(As_3F_{10})]$
	472(3)[9]	A"	$[\nu(As_2F_7) - \nu(As_2F_{10})] - [\nu(As_1F_7) - \nu(As_3F_{10})]$
423(2)	420(1)[11]	A'	$[\nu(Re_1O_3) + \nu(As_2O_3)]$
	417(<1)[6]	A"	$[\delta(F_1Re_1O_3) + \delta(F_7Re_1O_3)] - [\delta(F_3Re_1O_3) + \delta(F_{10}Re_1O_3)]$
407(13)	407(2)[3]	A'	$\delta(O_1Re_1O_2)$
	403(1)[111]	A'	$[\nu(As_1F_7) + \nu(As_2F_7)] + [\nu(As_3F_{10}) + \nu(As_2F_{10})] + \delta(O_1Re_1O_2)_{small}$
333(2)	338(2)[46]	A'	$\delta(Re_1O_1O_2F_3) + \delta(FAsF)$
312(4)	322(1)[36]	A"	$\delta(O_1Re_1O_3) - \delta(O_2Re_1O_3) + \delta(FAsF) + \rho_t(FAs_2F)$
	307(1)[51]	A'	$\delta(Re_1O_2F_2) - \delta(O_3Re_1F_2) + \delta(O_3As_2F)$
290(18)	294(1)[120]	A"	$\delta(O_1Re_1O_2F_2) - \delta(O_2Re_1F_2) + \delta(FAsF)$
	286(1)[31]	A"	

[a] Frequencies are given in cm^{-1}. [b] Values in parentheses denote relative Raman intensities. The Raman spectrum was recorded in an FEP sample tube at –140 °C using 1064-nm excitation. A full list of frequencies and assignments is provided in Table C5. [c] Values in parentheses denote calculated Raman intensities ($Å^4$ u^{-1}). Values in square brackets denote calculated infrared intensities (km mol^{-1}). The B3LYP/aug-cc-pVTZ(-PP) method was used. [d] The abbreviations denote stretch (ν), bend (δ), and twist (ρ_t). The atom numbering corresponds to that used in Figure 5.1b.

Table 5.3. Experimental Raman Frequencies and Intensities for the $[O_3Re(NCCH_3)_3]^+$ Cation in $[O_3Re(NCCH_3)_3][PnF_6]$ (Pn = As, Sb) and Calculated Vibrational Frequencies, Intensities, and Assignments for the $[O_3Re(NCCH_3)_3]^+$ Cation

$[O_3Re(NCCH_3)_3][PnF_6]$		$[O_3Re(NCCH_3)_3]^+$ (C_{3v})		
exptl[a,b]		calcd[a,c]		assgnts[d]
$[SbF_6]^-$ [e]	$[AsF_6]^-$ [f]	B3LYP	PBE1PBE	
3007 sh 2997(20)[g]	3011(17)	3125(164)[7] 3125(12)[2] 3123(100)[7] 3123(0)[0]	3154(158)[12] 3154(11)[2] 3151(97)[11] 3151(0)[0]	$\nu_{as}(CH_3)$ $\nu_{as}(CH_2)$
2953 sh 2939(78) 2934(100)	2954 sh 2941(100)	3049(699)[3] 3049(32)[14]	3066(695)[5] 3066(33)[19]	$\nu_s(CH_3)$
2330(38) 2303(16)	2329(76) 2300(36)	2405(394)[87] 2400(171)[214]	2433(389)[94] 2428(170)[230]	$\nu(CN)$
1412(2)	1413(5)	1458(2)[35] 1458(10)[2] 1457(7)[23] 1457(0)[0]	1447(2)[38] 1447(9)[3] 1446(7)[25] 1446(0)[0]	$\delta_{as}(CH_3)$
1370(11) 1366(9) 1361(8)	1360(21)	1408(22)[3] 1407(14)[5]	1395(19)[4] 1394(13)[7]	$\delta_s(CH_3)$
1037(1)	1035(2)	1059(1)[9] 1058(1)[2] 1055(1)[7] 1054(0)[0]	1047(1)[10] 1047(1)[3] 1043(1)[8] 1042(0)[0]	$\rho_r(CH_3)$
975(27)	974(55)	1039(68)[26]	1069(66)[30]	$\nu(ReO_1) + \nu(ReO_{1A}) + \nu(ReO_{1B})$
946(43)	946(71)	993(19)[202]	1019(18)[218]	$\nu(ReO_1) - \nu(ReO_{1A})$
935(20)	936(33) 931 sh	950(18)[12]	975(20)[12]	$\nu_s(CC)$
922 sh	922(4)	946(2)[11]	971(2)[11]	$\nu_{as}(CC)$
424(4)	424(8)	434(2)[6] 433(2)[1]	439(2)[6] 438(2)[1]	$\delta_s(NCC)_{ip}$ $\delta_s(NCC)_{oop}$
399(2)	408(2) br	424(<1)[4] 421(0)[0]	429(<1)[3] 426(0)[0]	$\delta_{as}(NCC)_{ip}$ $\delta_{as}(NCC)_{oop}$
390(8) 386(3)[g,h] 380 sh[h]	385(8) 381(9)	386(2)[33]	393(2)[34]	$\delta_s(ReO_1O_{1A}O_{1B})$
371(14) 365(14)	367(44)[i]	377(5)[6]	383(5)[6]	$\delta_{as}(ReO_1O_{1A}O_{1B})$
		251(<1)[8]	256(<1)[7]	$\delta(OReN)$
		250(<1)[12]	258(<1)[11]	$\nu_s(Re\text{---}N)$
213(2)	209(4)	213(1)[9]	220(1)[11]	$\nu_{as}(Re\text{---}N)$
		199(<1)[1]	205(<1)[1]	$\delta_s(ReNC)_{ip}$
		178(0)[0]	181(0)[0]	$\rho_r(ReO_1O_{1A}O_{1B}) - \rho_r(CH_3CN)$

Table 5.3. (continued ...)

		158(1)[13]	166(1)[13]	δ(OReN)
		71(<1)[<1]	72(<1)[<1]	δ(OReN)
		69(0)[0]	70(0)[0]	$\rho_r(ReO_1O_{1A}O_{1B})$ + $\rho_r(CH_3CN)$
		43(3)[15]	43(3)[15]	CH_3CN deformation modes
		38(4)[4]	38(4)[4]	
		22(<1)[<1]	16(<1)[<1]	
		21(0)[0]	14(0)[0]	
129 sh				lattice modes
114(5)[g]	117(16) br			
106(9)				
99 sh				

[a] Frequencies are given in cm^{-1}. [b] Values in parentheses denote relative Raman intensities. The Raman spectra were recorded in FEP sample tubes at –140 °C using 1064-nm excitation. The abbreviation denotes shoulder (sh). [c] Values in parentheses denote calculated Raman intensities ($Å^4$ u^{-1}). Values in square brackets denote calculated infrared intensities (km mol^{-1}). The aug-cc-pVTZ(-PP) basis set was used. [d] The atom numbering corresponds to that used in Figure 5.1c. The abbreviations denote stretch (ν), symmetric (s), asymmetric (as), bend (δ), rock (ρ_r), in-plane (ip), and out-of-plane (oop). [e] The spectrum was recorded on a crystalline material under a small amount of frozen CH_3CN. Modes associated with frozen CH_3CN are given in Table C6. A broad band at 668(1) cm^{-1} was assigned to $SbF_5{\cdot}NCCH_3$. Modes associated to the $[SbF_6]^-$ anion were observed at $\nu_1(A_{1g})$, 645(23); $\nu_2(E_g)$, 574(2); $\nu_5(T_{2g})$, 278(4) cm^{-1}. A combination band was observed at 2732(2) cm^{-1}. [f] The spectrum was recorded on a dry solid. Modes associated to the $[AsF_6]^-$ anion were observed at $\nu_1(A_{1g})$, 681(18) cm^{-1} and $\nu_2(E_g)$, 577(3) cm^{-1}. The band at 628(1) cm^{-1} was assigned to $AsF_5{\cdot}NCCH_3$. Combination bands were observed at 2711(1), 2274 sh, 1753(4), and 1444(2) cm^{-1}. The bands at 544(1) and 534(1) cm^{-1} were not assigned. [g] Band overlapping with free CH_3CN. [h] Band overlaps with an FEP line. [i] Band overlaps with the $\nu_5(T_{2g})$ mode of $[AsF_6]^-$.

-cc-pVTZ(-PP) level of theory failed because the gas-phase species dissociated.

$[ReO_3][Sb_3F_{16}]$ (1). Initially, the hypothetical $\{[ReO_3][SbF_6]_3\}^{2-}$ ion-pair (Figure C3a) was calculated, as it is expected that the $[ReO_3]^+$ cation will interact with the fluorine atoms associated with more than one $[SbF_6]^-$ anion in order to attain a pseudo-octahedral environment of the Re atom. Overall, the calculated frequencies and intensities of the $\{[ReO_3][SbF_6]_3\}^{2-}$ ion-pair are in reasonable accord with the experimental values. Because some experimental frequencies and intensities were comparable with those of $Cs[Sb_3F_{16}]$,[254] the $[ReO_3][Sb_3F_{16}]$ ion-pair was also calculated (Tables 5.1 and C4). The resulting frequencies and intensities are in very good agreement with experiment (see Raman Spectroscopy).

The calculated Re−O bond lengths (1.686 Å) are longer (Table 5.4, C7) and therefore more polar than the calculated Re−O bond lengths of the free $[ReO_3]^+$ cation (1.677 Å) (Figure C1), which is consistent with ion-pair formation. The calculated Re−O bond lengths are comparable to the experimental ones $\{C_6H_2(CH_3)_3\}ReO_3$ (1.681(5) and 1.683(5) Å)[255] and $(\eta_5\text{-}C_5H_5)ReO_3$ (1.693(4) Å).[249c] The calculated O−Re−O bond angles (104.8 and 105.3°) are consistent with a trigonal pyramidal arrangement of oxygen atoms and are comparable to those of the calculated gas-phase $[ReO_3]^+$ cation (106.1°). The calculated O−Re−O bond angles are also similar to the experimental O−Re−O bond angles of $(\eta_5\text{-}C_5H_5)ReO_3$ (103.5(3) and 104.6(2)°),[249c] $(\eta_5\text{-}C_5(CH_3)_5)ReO_3$ (103.7(6)°),[256] and $(\eta_5\text{-}C_5(CH_3)H_4)ReO_3$ (105.7(1) and 104.5(1)°.[257]

Table 5.4. Selected Calculated [a] Bond Lengths and Bond Angles of $[ReO_3][Sb_3F_{16}]$ **(1)**, μ-$O(ReO_2F)(AsF_5)\cdot 2AsF_5$ **(2)**, and $[O_3Re(NCCH_3)_3]^+$ **(3)**

	(1) (C_s)[b]	**(2)** (C_s)[b]		**(3)** (C_{3v})[c]	
Bond Length (Å)					
Re_1-O_1	1.686	Re_1-O_1	1.670	$Re-O_1$	1.695
Re_1-O_2	1.686	Re_1-F_2	1.835	$Re---N_1$	2.299
Re_1---F_1	2.197	Re_1---F_1	2.381	N_1-C_1	1.144
Re_1---F_2	2.401	Re_1-O_3	1.791	C_1-C_2	1.447
Sb_1-F_1	2.006	As_1-F_1	1.805	C_2-H_1	1.090
Sb_1-F_4	1.872	As_1-F_4	1.698		
Sb_1-F_5	1.873	As_1-F_5	1.704		
Sb_1-F_6	1.868	As_1-F_6	1.687		
Sb_1-F_8	1.870	As_1-F_8	1.698		
Sb_1-F_7	2.147	As_1---F_7	2.165		
Sb_2-F_2	1.939	As_2-O_3	1.848		
Sb_2-F_{11}	1.866	As_2-F_{11}	1.699		
Sb_2-F_9	1.865	As_2-F_9	1.702		
Sb_2-F_{12}	1.865	As_2-F_{12}	1.702		
Sb_2-F_7	2.017	As_2-F_7	1.830		
Bond Angles (deg)					
$O_1-Re_1-O_2$	104.8	$O_1-Re_1-O_2$	103.5	O_1-Re-O_2	105.5
$O_1-Re_1-O_3$	105.3	$O_1-Re_1-F_2$	100.7	$O_1-Re---N_1$	86.6
$O_1-Re_1---F_1$	88.8	$O_1-Re_1---F_1$	88.8	$O_1-Re---N_{1A}$	86.6
$O_1-Re_1---F_2$	85.8	$O_1-Re_1-O_3$	103.1	$O_1-Re---N_{1B}$	159.4
$O_1-Re_1---F_3$	153.1	$O_1-Re_1---F_3$	166.7	$Re---N_1-C_1$	164.4
$O_3-Re_1---F_1$	93.0	$F_2-Re_1---F_1$	71.8	$C_1-N_1-C_2$	179.3
$O_3-Re_1---F_2$	161.2	$F_2-Re_1-O_3$	141.0	N_1-C_2-H	109.3
$F_1---Re_1---F_2$	71.9	$F_1---Re_1-O_3$	78.3	$H_1-C_2-H_2$	109.2
$F_1---Re_1---F_3$	70.4	$F_1---Re_1---F_3$	78.5		
$Re_1---F_1-Sb_1$	152.5	$Re_1---F_1-As_1$	142.1		
$Re_1---F_2-Sb_2$	156.2	$Re_1-O_3-As_2$	164.5		
$Sb_1-F_7-Sb_2$	146.5	$As_1-F_7-As_2$	144.6		

[a] B3LYP/aug-cc-aVTZ(-PP). For the atom labeling scheme, see Figures 5.1. The bond lengths and bond angles around Pn_3 (Pn = As, Sb) are equal to those around Pn_1 by symmetry. [b] See table C7 for the PBE1PBE/aug-cc-pVTZ(-PP) values. [c] See table C9 for the PBE1PBE/aug-cc-pVTZ(-PP) values.

The calculated lengths of the Re−$F_{\mu t}$ bridging bonds between the Re and the "terminal" $Sb_{1,3}$ atoms (2.197 Å) are comparable to those of the experimental Re−$F_{\mu t}$ bridging bonds in $[ReO_2F_2][SbF_6]$ (2.210(5) and 2.200(5) Å) salt,[22] and are shorter than the calculated Re−$F_{\mu c}$ bridging bond between Re and the central Sb_2 atom (2.401 Å). The calculated O−Re−$F_{\mu c}$ (161.2° and 85.8°) and O−Re−$F_{\mu t}$ (153.1°, 93.0°, and 88.8°) bond angles are also comparable to those observed in the crystal structure of $[ReO_2F_2][SbF_6]$ (164.5(2), 168.2(2), 92.3(2), and 88.5(2)°).[22]

Overall, the calculated terminal Sb−F (1.868−1.873 Å) bond lengths and bridging Sb−F_{μ} bond lengths between two Sb atoms (2.017 and 2.147 Å) and the F−Sb−F, F−Sb−F_{μ}, F_{μ}−Sb−F_{μ}, and Sb−F_{μ}−Sb bond angles of the $[ReO_3][Sb_3F_{16}]$ ion-pair (Tables 5.4 and C7) are comparable to the corresponding bond lengths and bond angles calculated for the $[Sb_3F_{16}]^-$ anion (Table C8). The only notable difference occurs for the Sb−$F_{\mu t}$ and Sb−$F_{\mu c}$ (2.006 and 1.939 Å) bond lengths which elongate upon ion-pair formation (calcd $[Sb_3F_{16}]^-$, 1.891 and 1.879 Å). The calculated bond lengths and bond angles of the $[Sb_3F_{16}]^-$ anion in $[ReO_3][Sb_3F_{16}]$ are comparable to the experimental bond lengths and bond angles of $Cs[Sb_3F_{16}]$.[254]

μ-O(ReO$_2$F)(AsF$_5$)·2AsF$_5$ (2). Initially, the hypothetical $\{[ReO_3][AsF_6]_3\}^{2-}$ ion-pair (Figure C4a) was calculated by analogy with $\{[ReO_3][SbF_6]_3\}^{2-}$. Although it was optimized with all frequencies real (Figure C4a), several experimental Raman bands could not be accounted for. Attempts to optimize the $[ReO_3][As_3F_{16}]$ ion pair resulted in the dissociation of the $[As_3F_{16}]^-$ anion into a central AsF_5 molecule (C_{4v}) that interacts with an ReO_3F molecule through a long Re---F_2(As) contact (2.777 Å) and two terminal

AsF_5 molecules (D_{3h}) that interact through very long Re---$F_{1,3}$(As) contacts (3.290 Å) (Figure C5). Moreover, attempts to optimize (B3LYP/aug-cc-pVTZ(-PP)) the unknown $[As_3F_{16}]^-$ anion also resulted in a dissociated model (Figure C6) where a central $[AsF_6]^-$ anion (As−F_t, 1.713 and 1.716 Å; As−F_b, 1.854 Å) interacts through long As---F_b contacts (2.105 Å) with two adjacent AsF_5 molecules (C_{4v}). The Raman spectrum of the product isolated from the reaction of ReO_3F with AsF_5 showed two bands at 886 and 878 cm^{-1} that do not correspond to terminal Re−O stretches. Instead, these bands are reminiscent of a band at 864 cm^{-1} in $(\mu\text{-}F)_4\{[\mu\text{-}O(ReO_2F)_2](ReO_2F_2)_2\}$ (Chapter 4) which is associated with a Re−O_μ−Re stretch. A model was therefore calculated in which one of the oxygen atoms of the ReO_3F-moiety is oxygen-bridged to the central AsF_5 molecule and the fluorine atom is terminal. The remaining two terminal AsF_5 molecules interact with the ReO_3F-moiety through two F_μ---Re contacts to complete the pseudo-octahedral environment around the Re atom. This model accounts for all of the observed frequencies (see Raman Spectroscopy).

The calculated As_2−O_μ bond length (1.848 Å) is comparable to the As_2−F_μ bond lengths (1.830 Å), whereas the Re−O_μ bond (1.791 Å) is longer than the Re−O_t bond (1.670 Å). As expected, the Re---F_μ contacts (2.381 Å) are significantly longer than the terminal Re−F_t bond (1.835 Å) (Tables 5.4 and C7). The $As_{1,3}$−F_μ bonds of two terminal AsF_5 molecules elongate upon coordination to the Re atom ($As_{1,3}$−F_μ, 1.805 Å; $As_{1,3}$−F_t, 1.687, 1.698, and 1.704 Å), however, they are significantly shorter than the As−F_μ bridging bonds between As_1---F_7 and As_3---F_{10} (2.165 Å).

The calculated terminal Re−O_t bond lengths (1.670 Å) (Table 5.4) are comparable to the experimental Re−O_t bond lengths of ReO_3F (1.667(7) and 1.685(7) Å),[21] and ReO_2F_3 (1.667(8), 1.675(8) Å;[19] 1.669(9)−1.676(9) Å[21]). They are slightly shorter than the Re−O_t bond lengths of $[ReO_3][Sb_3F_{16}]$ (1.686 Å) (Table 5.4), which is consistent with reduction of the Re charge in $[ReO_3][Sb_3F_{16}]$ (2.14, see Table C9, Appendix C) upon ion-pair formation when compared to that of neutral μ-$O(ReO_2F)(AsF_5)\cdot 2AsF_5$ (2.27, see Table C9, Appendix C). The calculated bridging Re−O_μ (1.791 Å) bond length is significantly longer than the Re−O_t bond lengths, consistent with the loss of double-bond character, and is significantly shorter than the calculated bridging Re−O_μ bond lengths of $(\mu\text{-}F)_4\{[\mu\text{-}O(ReO_2F)_2](ReO_2F_2)_2\}$ (1.876 Å) (Chapter 4). The calculated terminal Re−F_t bond length (1.835 Å) is also comparable to the experimental Re−F_t bond length of $(\mu\text{-}F)_4\{[\mu\text{-}O(ReO_2F)_2](ReO_2F_2)_2\}$ (1.816(9)–1.870(11) Å) (Chapter 4) and ReO_2F_3 (1.831(6), 1.854(6) Å;[19] (1.828(8)−1.867(8) Å[21]).

The calculated bridging As_2−O_μ (1.848 Å) bond length is comparable to the experimental bridging As_2−O_μ bond lengths in $[AsCl_4][As(OTeF_5)_6]$ (av. 1.801(6) Å),[258] $[AsBr_4][As(OTeF_5)_6]$ (av. 1.805(9) Å),[258] $[N(CH_3)_4][As(OTeF_5)_6]$ (1.791(9) Å),[259] and is considerably longer than the terminal As−O bond in $AsOCl_3$ (1.633(3) Å).[260] The terminal AsF_5 molecules interact with the central AsF_5 molecule through long As−F_μ bridges (2.165 Å). Overall, the terminal As−F bond lengths are comparable to those of $CF_3SNSO\cdot AsF_5$[261] and $CH_3SCN\cdot AsF_5$.[262] Considering the above bond length and contact distance trends, the compound appears to be best formulated as μ-$O(ReO_2F)(AsF_5)\cdot 2AsF_5$.

$[O_3Re(NCCH_3)_3]^+$ (3). The energy-minimized gas-phase structure of the $[O_3Re(NCCH_3)_3]^+$ adduct-cation has a facial arrangement of oxygen atoms, with the CH_3CN molecules coordinated trans to the oxygen ligands, giving rise to a distorted octahedral environment around the rhenium atom (Figure 5.4c). The calculated Re−O bond lengths (1.695 Å) (Tables 5.4 and C9) are comparable to the calculated Re−O bond lengths (1.686 Å) of $[ReO_3][Sb_3F_{16}]$ and are longer than those in the free $[ReO_3]^+$ cation (1.677 Å, Figure C1), consistent with the adduct-cation formation. The calculated O−Re−O bond angles (105.4°) in $[O_3Re(NCCH_3)_3]^+$ are comparable to those in $[ReO_3][Sb_3F_{16}]$ (104.8 and 105.3°) and $[ReO_3]^+$ (106.1°) and in agreement with the trigonal pyramidal arrangement of oxygen atoms. The calculated Re−O bond lengths are shorter than those in $[(C_6H_{15}N_3)ReO_3]^+$ (1.724(3), 1.730(3), and 1.719(3) Å)[41b] and $[\{C_6H_8(CH_3)_5N_3\}ReO_3]^+$ (1.725(2), 1.721(2), and 1.703(2) Å),[41c] which is in agreement with the shift of the ν(ReO) stretches to higher frequency in the Raman spectrum of $[O_3Re(NCCH_3)_3]^+$ when compared with the Raman spectra of other adduct-cations (see Section 5.2.5.3).

The calculated Re---N bond lengths (2.299 Å) are comparable to those of the $ReO_3F(NCCH_3)_2{\cdot}CH_3CN$ adduct (2.294(4) Å),[19] and slightly longer than those of $[(C_6H_{15}N_3)ReO_3]^+$ (2.241(3), 2.254(1), and 2.231(3) Å)[41b] and $[\{C_6H_8(CH_3)_5N_3\}ReO_3]^+$ (2.273(2), 2.289(3), and 2.267(2) Å).[41c] The C−N bonds (1.144 Å) in **(3)** are comparable, whereas the C−C (1.447 Å) bonds are slightly shorter than those of the calculated free CH_3CN molecule (C−N, 1.149 Å; C−C, 1.455 Å; Table C3), which is in agreement with C−C bond strengthening upon coordination of CH_3CN. Although the C−N and C−C bond

lengths of CH_3CN do not change significantly upon the adduct-cation formation, significantly high-frequency shifts are observed for the ν(CN) and ν(CC) stretching modes in the Raman spectrum of **(3)** (see Raman Spectroscopy). Analogous behaviour has been observed for $OsO_3F_2{\cdot}NCCH_3$[217] and $TcO_2F_3(NCCH_3)$.[25]

5.2.5. Raman Spectroscopy

The low-temperature Raman spectra of $[ReO_3][Sb_3F_{16}]$ **(1)**, μ-$O(ReO_2F)(AsF_5){\cdot}2AsF_5$ **(2)**, $[O_3Re(NCCH_3)_3][PnF_6]$ (Pn = As. Sb) **(3)** are shown in Figures 5.2, 5.3, 5.4, and C7, respectively. The observed and calculated frequencies and mode descriptions are provided in Tables 5.1, 5.2, 5.3, C4, C5, and C6. Spectral assignments were made by comparison with the calculated frequencies and Raman intensities of **(1)** (C_s) (Tables 5.1 and C4), **(2)** (C_s) (Tables 5.2 and C5), **(3)** (C_{3v}) (Tables 5.3 and C6), $[ReO_3]^+$ (C_{3v}) (Table C1), $[Sb_3F_{16}]^-$ (C_s) (Table C2), and CH_3CN (Table C3), which were optimized at the B3LYP/aug-cc-pVTZ(-PP) and PBE1PBE/aug-cc-pVTZ(-PP) levels of theory. Overall there is better agreement with the B3LYP/aug-cc-pVTZ(-PP) values, therefore only the B3LYP/aug-cc-pVTZ(-PP) values were used in the following discussion. In the absence of crystal structures, it was not possible to carry out factor-group analyses which may account for a number of splittings observed in the Raman spectra of **(1)**, **(2)**, and **(3)**.

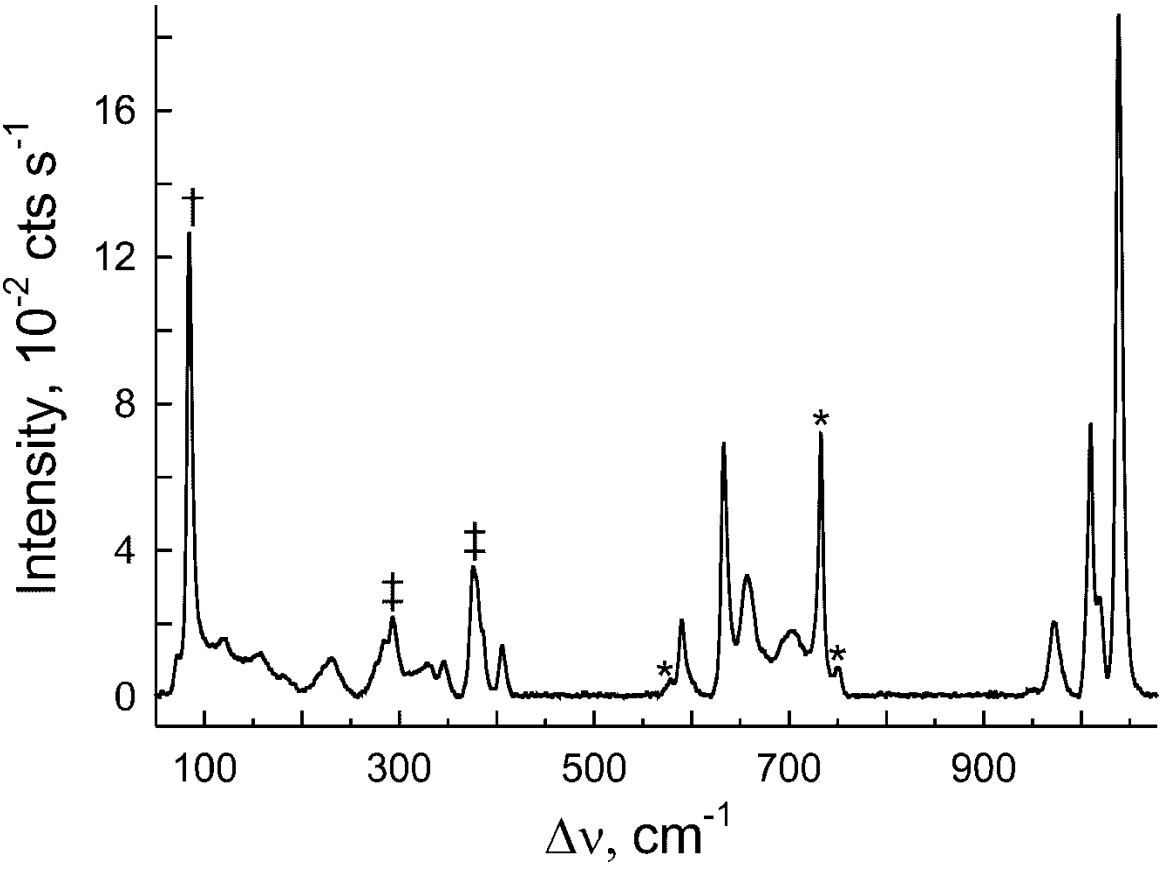

Figure 5.2. Raman spectrum of $[ReO_3][Sb_3F_{16}]$ recorded at –140 ^{o}C using 1064-nm excitation. Symbols denote an FEP sample tube line (*), a $[ReO_3][Sb_3F_{16}]$ line overlaps with an FEP sample tube line (‡), and an instrumental artifact (†).

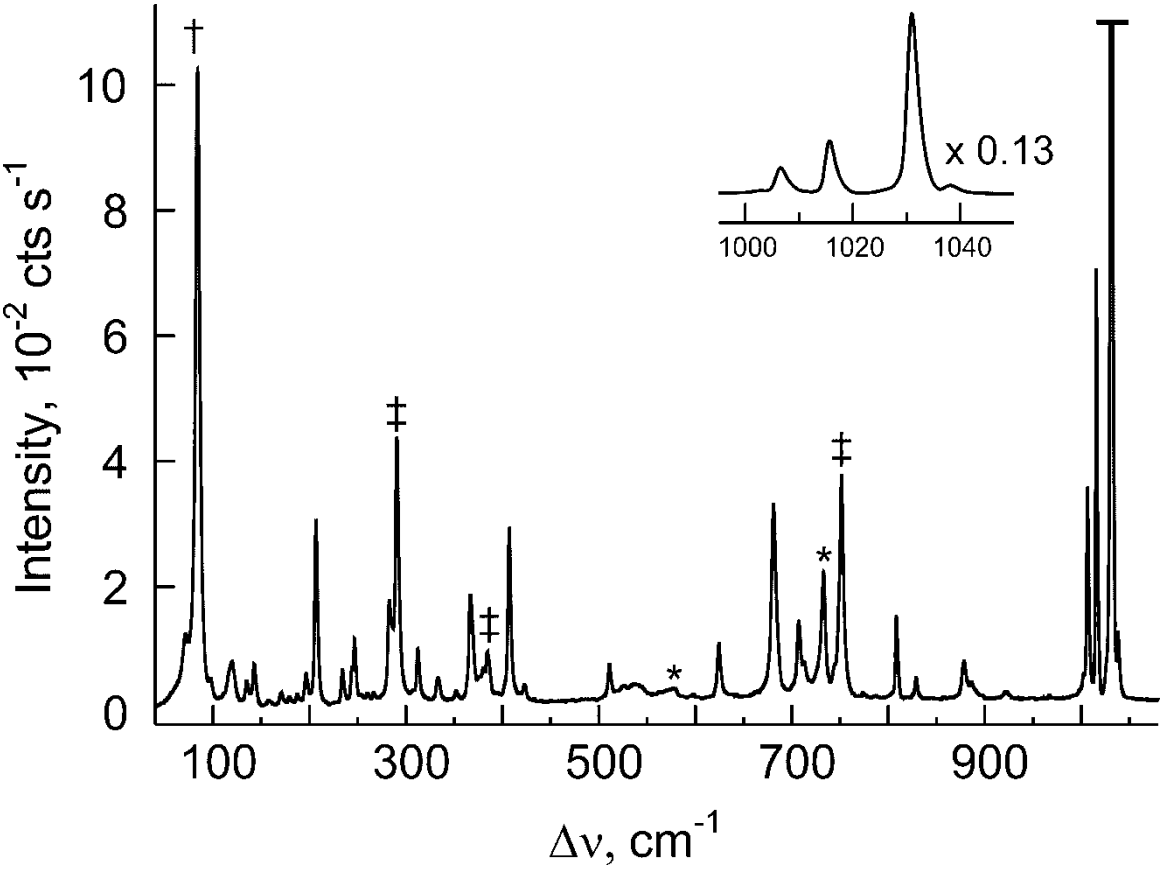

Figure 5.3. Raman spectrum of μ-O(ReO_2F)(AsF_5)·2AsF_5 recorded at –140 ^oC using 1064-nm excitation. Symbols denote an FEP sample tube line (*), a μ-O(ReO_2F)(AsF_5)·2AsF_5 line overlaps with an FEP sample tube line (‡), and an instrumental artifact (†).

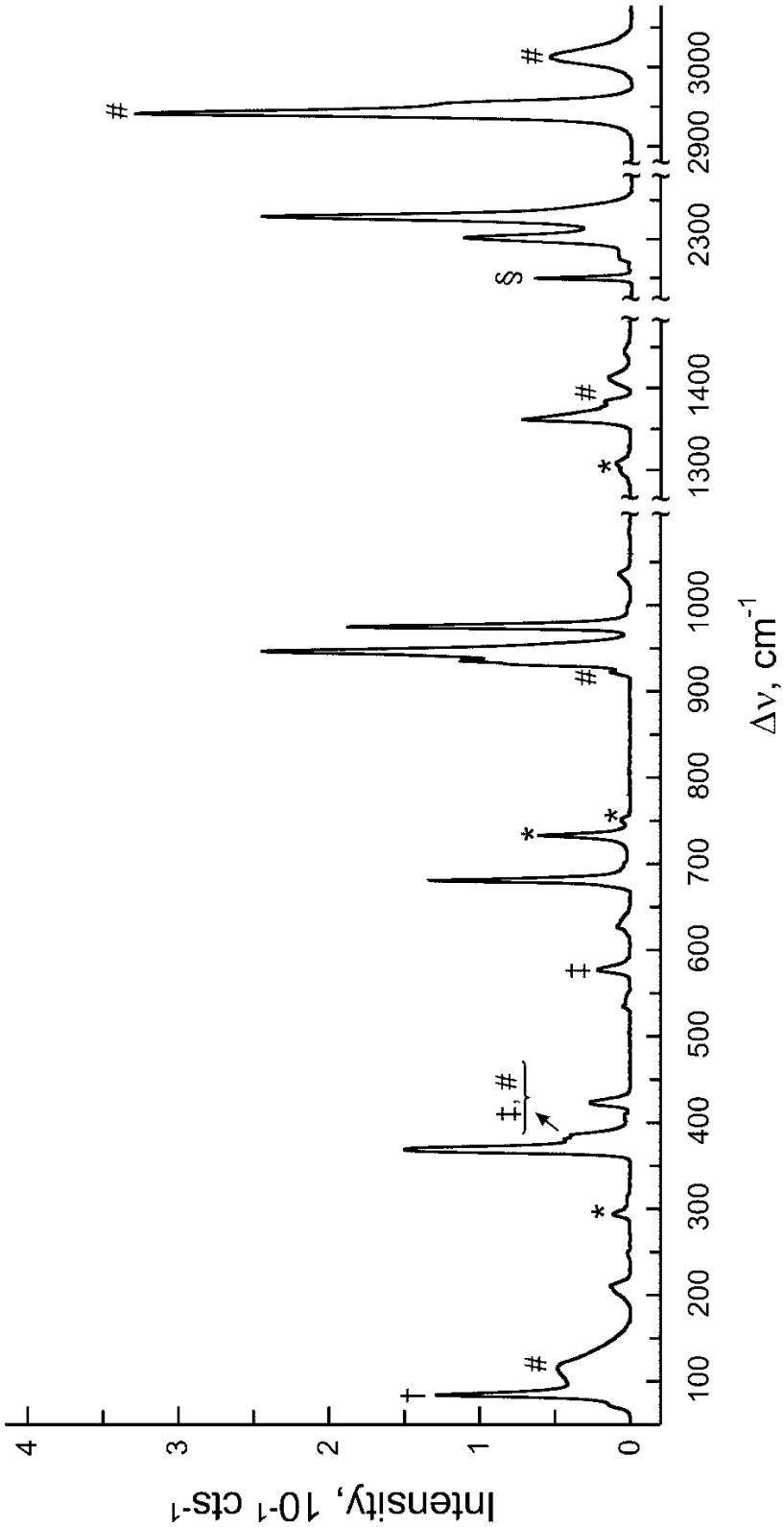

Figure 5.4. Raman spectrum of $[O_3Re(NCCH_3)_3][AsF_6]$ recorded at −140 °C using 1064-nm excitation. Symbols denote an FEP sample tube line (*), a $[O_3Re(NCCH_3)_3][AsF_6]$ line that overlaps with an FEP sample tube line (‡) or with a CH_3CN line (#), free CH_3CN (2248 cm^{-1}) (§), and an instrumental artifact (†).

5.2.5.1. $[ReO_3][Sb_3F_{16}]$ (1)

The $[ReO_3][Sb_3F_{16}]$ ion-pair (Figure 5.1a) possesses C_s symmetry which results in 63 fundamental vibrational modes belonging to the 34A' + 29A" irreducible representation, where all modes are infrared and Raman active.

The experimental frequencies associated with the terminal Re−O stretching modes are overestimated by the calculations; however, the observed frequency trends are well reproduced. The highest frequencies and most intense bands are assigned to the symmetric $\nu(ReO_3)$ stretching mode (exptl, 1010/1018/1038 cm^{-1}; calcd, 1066 cm^{-1}). The band at 972 cm^{-1} is assigned to the corresponding asymmetric modes which could not be distinguished experimentally (calcd, 1011 and 1014 cm^{-1}). The calculated Re−O stretching frequencies are shifted to lower frequency than those of the free $[ReO_3]^+$ cation (1084 and 1016 cm^{-1}), consistent with ion-pair formation. Both stretching modes appear at higher frequencies than the corresponding modes in the Raman spectrum of ReO_3F (996 and 969 cm^{-1}),[21,235] reflecting the greater covalent character of the Re−O bonds in the $[ReO_3][Sb_3F_{16}]$ ion-pair than in ReO_3F. The symmetric and asymmetric Re−O stretching modes also appear at lower frequencies than those of $[ReO_3][ClO_4]$ (1001 and 982 cm^{-1}),[250] CH_3ReO_3 (995 and 950/957 cm^{-1}),[249d] $(\eta_5\text{-}C_5H_5)ReO_3$ (914 and 875/885cm^{-1}),[263] and $(\eta_5\text{-}C_5(CH_3)_5)ReO_3$ (905 and 873/887 cm^{-1})[263] which result from the weaker donor ability (lower basicity) of the $[Sb_3F_{16}]^-$ anion relative to $[ClO_4]^-$, $[CH_3]^-$, $[(\eta_5\text{-}C_5H_5)]^-$, and $[(\eta_5\text{-}C_5(CH_3)_5)]^-$.

The band appearing at 406 cm^{-1} is associated with $\delta(ReO_2)$ and $\delta(ReO_3)$ deformation modes and is well reproduced by the calculations (375, 383, and 388 cm^{-1}).

The bending mode frequencies are comparable to those observed in $(\eta_5\text{-}C_5(CH_3)_5)ReO_3$ (395 cm^{-1})[263] and $(\eta_5\text{-}C_5H_5)ReO_3$ (386 cm^{-1}).[263]

Overall, the modes associated with the $[Sb_3F_{16}]^-$ anion are comparable to those of the calculated free $[Sb_3F_{16}]^-$ anion and those observed for $Cs[Sb_3F_{16}]$.[254]

5.2.5.2. μ-O(ReO$_2$F)(AsF$_5$)·2AsF$_5$ (2)

The μ-O(ReO_2F)(AsF_5)·2AsF_5 molecule (Figure 5.1b) possesses C_s symmetry which results in 63 fundamental vibrational modes which span the 34A' + 29A" irreducible representation with all modes being infrared and Raman active.

The experimental frequencies associated with the terminal symmetric (exptl, 1030/1038 cm^{-1}) and asymmetric (1002/1006/1015 cm^{-1}) Re−O stretching modes are overestimated by the calculations (ν_s(Re−O), 1082 cm^{-1}; ν_{as}(Re−O), 1045 cm^{-1}) as was observed for the $[ReO_3][Sb_3F_{16}]$ ion-pair. Both modes are shifted to higher frequency when compared to those observed for ReO_3F (996 and 969 cm^{-1}),[21,235] $ReO_3F(FH_2)$ (1017 and 981 cm^{-1}),[235] and (μ-F)$_4${[μ-O(ReO_2F)$_2$](ReO_2F_2)$_2$}(1012/1024 and 996 cm^{-1}) (Chapter 4), and are consistent with the lower polarity of the Re−O bonds in μ-O(ReO_2F)(AsF_5)·2AsF_5. The weak bands at 878 and 886 cm^{-1} (calcd, 938 cm^{-1}) were assigned to the asymmetric bridging stretching mode, $\nu(ReO_\mu) - \nu(AsO_\mu)$, which appears at higher frequency than $\nu(ReO_\mu) - \nu(Re'O_\mu)$ in ReO_3F (813 cm^{-1}),[21,235] (μ-F)$_4${[μ-O(ReO_2F)$_2$](ReO_2F_2)$_2$} (864 cm^{-1}) (Chapter 4), and Re_2O_7 (783 to 895 cm^{-1} (see Figure C11, Appendix C); 798 to 880 cm^{-1} [246]). The symmetric $\nu(AsO_\mu) + \nu(ReO_\mu)$ stretching band is expected to be very weak and was observed as a weak band at 423 cm^{-1} (calcd,

420 cm^{-1}). The δ(OReO) deformation mode involving the terminal oxygen atoms (calcd, 407 cm^{-1}) appears at 407 cm^{-1}, whereas the δ($OReO_{\mu}$) deformation mode is coupled to the δ(FAsF) and ρ_t(FAsF) deformation modes and appears at 312 cm^{-1} (calcd, 322 cm^{-1}). The δ(OReO) deformation modes are comparable to those observed in ReO_3F (313, 354, 386 cm^{-1}),[21,235] $(\mu\text{-}F)_4\{[\mu\text{-}O(ReO_2F)_2](ReO_2F_2)_2\}$ (396, 400, and 405 cm^{-1}) (Chapter 4), and $ReO_3F(FH_2)$ (326, 341, and 400 cm^{-1}).[235] The bridging ν(ReF_{μ}) − ν(AsF_{μ}) stretching modes (510, 523, and 535 cm^{-1}) are well reproduced by the calculations (520, 523, and 549 cm^{-1}) and appear at slightly higher frequency than the bridging ν(ReF_{μ}) − ν($Re'F_{\mu}$) stretching modes in $K[\mu\text{-}F(ReO_2F_4)_2]\cdot 2ReO_2F_3$ (554 cm^{-1})[19] and $Cs[(ReO_2F_2)(\mu\text{-}F)_2(ReO_2F_3)_2]$ (568 cm^{-1}).[19] The terminal ν(ReF) stretching mode (calcd, 703 cm^{-1}) is predicted to be weak and was not observed.

The terminal ν(AsF_{eq}) (exptl, 829 cm^{-1}; calcd, 777 and 783 cm^{-1}) and ν(AsF_{ax}) (exptl, 808; calcd, 761 and 762 cm^{-1}) stretching modes of the "terminal" AsF_5 groups are comparable to those of ν(AsF_{eq}) (exptl, 812 cm^{-1}; calcd, 776 cm^{-1}) and ν(AsF_{ax}) (exptl, 739 cm^{-1}; calcd, 754 cm^{-1}) in AsF_5. The ν(AsF_{eq}) and ν(AsF_{ax}) stretching modes appear at higher frequencies than the ν(AsF) stretching modes of the $[AsF_6]^-$ (exptl, 679 and 565 cm^{-1}; calcd, 640 and 546 cm^{-1}) and $[As_2F_{11}]^-$ (exptl, 736 and 683 cm^{-1}; calcd, 733, 721 and 696, 681 cm^{-1}) anions.

5.2.5.3. $[O_3Re(NCCH_3)_3]^+$ (3)

In the following discussion, values associated with the $[AsF_6]^-$ salt are given in parentheses. The frequencies of the $[PnF_6]^-$ anion are consistent with O_h symmetry (Table

C6), indicating that the $[O_3Re(NCCH_3)_3]^+$ adduct-cations are well isolated from the $[PnF_6]^-$ anions (Figure 5.1c). The $[O_3Re(NCCH_3)_3]^+$ adduct-cation possesses 60 fundamental vibrational modes belonging to the irreducible representation $13A_1 + 7A_2 + 20E$ under C_{3v} symmetry where the A_1 and E modes are Raman and infrared active and the A_2 modes are inactive.

The bands at 975 (974) and 946 (946) cm^{-1} (calcd, 1039 and 993 cm^{-1}) are assigned to the symmetric and asymmetric terminal Re−O stretching modes, respectively. Both $\nu(ReO_3)$ stretching modes appear at higher frequencies than those observed in the Raman spectrum of the $[(C_6H_{12}S_3)ReO_3]^+$ adduct-cation (920/934, and 909 cm^{-1})[42] indicative of stronger covalent character of the Re−O bond in **(3)** than in $[(C_6H_{12}S_3)ReO_3]^+$. The Re−O stretching modes also appear at higher frequencies than the corresponding stretches observed in the infrared spectra of $[(C_6H_{12}S_3)ReO_3]^+$ (933, 902 cm^{-1}),[42] $[(C_6H_{15}N_3)ReO_3]^+$ (945, 920 cm^{-1}),[41a] and $[\{HC(3,5\text{-}(CH_3)_2C_3N_2H)_3\}ReO_3]^+$ (929, 920 cm^{-1}).[41c]

The symmetric and asymmetric δ(OReO) deformation modes (exptl, 380/386/390 (381/385), 365/371 (367) cm^{-1}; calcd, 386 and 377 cm^{-1}) appear at lower frequency than the $\delta(ReO_2)$ and $\delta(ReO_3)$ deformation modes in $[ReO_3][Sb_3F_{16}]$ (exptl, 406 cm^{-1}; calcd, 375, 383, 388 cm^{-1}).

The ν(CN) stretching mode of the coordinated CH_3CN molecules (exptl, 2303/2330 (2300/2329) cm^{-1}; calcd, 2400/2405 cm^{-1}) is shifted by 69 (66) cm^{-1} (calcd, 40 cm^{-1}) to higher frequency relative to that observed in free CH_3CN (exptl, 2248 cm^{-1}; calcd, 2363 cm^{-1}). The shift to higher frequency results from the donation of electron

density by the nitrogen atoms to the rhenium atom, resulting in increased σ-bond character and strengthening of the C−N bonds rather than to π back donation from rhenium into the nitrogen π* orbitals, which would cause a low-frequency shift for the ν(CN) stretch. The symmetric ν(CC) stretching mode (exptl, 935 (931/936) cm^{-1}; calcd, 950 cm^{-1}) is also slightly shifted to higher frequency (Δν(CC) = 15 (14) cm^{-1}; calcd, 22 cm^{-1}) upon coordination of CH_3CN which results from C−C bond strengthening. Comparable high-frequency shifts of the ν(CN) and ν(CC) stretching modes have previously been observed in $MO_2F_3{\cdot}NCCH_3$ [M = Tc (Δν(CN) = 13 cm^{-1}, Δν(CC) = 20 cm^{-1};[25] M = Re (Δν(CN) = 75 cm^{-1}, Δν(CC) = 23 cm^{-1})][19] and $OsO_3F_2{\cdot}NCCH_3$ (Δν(CN) = 84 cm^{-1}, Δν(CC) = 34 cm^{-1}).[217] The δ(NCC) deformation modes occur at 424 cm^{-1} (408, 423) cm^{-1} and are well reproduced by the calculations (421/424/433/434 cm^{-1}). The Re---N stretching modes are predicted to occur as weak bands (calcd, 213 and 250 cm^{-1}) and were observed as weak bands 213 cm^{-1} (209) cm^{-1} and are comparable to those observed in $ReO_2F_3{\cdot}NCCH_3$ (212 and 221 cm^{-1}).[19]

5.2.6. NBO Charges, Wiberg Valencies, and Bond Indices

The NBO analyses for $[ReO_3][Sb_3F_{16}]$ (C_s), μ-O(ReO_2F)(AsF_5)·2AsF_5 (C_s), $[O_3Re(NCCH_3)_3]^+$ (C_{3v}), $[ReO_3]^+$ (C_{3v}), $[Sb_3F_{16}]^-$ (C_{3v}), and CH_3CN (C_{3v}) were carried out for the B3LYP/aug-cc-pVTZ(-PP) and PBE1PBE/aug-cc-pVTZ(-PP) optimized gas-phase geometries. The trends in calculated charges, valencies, and bond indices for the above molecules are consistent at both levels of theory (Tables C10−C15, Appendix C); therefore, only the B3LYP results are referred to in the ensuing discussion.

5.2.6.1. $[ReO_3][Sb_3F_{16}]$ (Figure 5.1a)

Positive charges are located on the rhenium (2.14) and antimony (3.07 and 3.09) atoms, whereas negative charges are located on the electronegative atoms (O, −0.49 and −0.50; F, −0.60, −0.61, and −0.65) with the highest negative charge residing on the bridging fluorine atoms. The Re, Sb and F atom charges are comparable to those of the free $[ReO_3]^+$ cation (Re, 2.12) and free $[Sb_3F_{16}]^-$ anion (Sb, 3.06 and 3.08; F, −0.62, and −0.66), respectively. The charges on the O atoms of $[ReO_3][Sb_3F_{16}]$ are, however, more negative than those of free $[ReO_3]^+$ (−0.37), consistent with donation of electron density from the $[Sb_3F_{16}]^-$ anion to the $[ReO_3]^+$ cation. The Re and O valencies of the $[ReO_3][Sb_3F_{16}]$ ion pair (Re, 5.51; O, 2.27) are slightly greater than that of the free $[ReO_3]^+$ cation (Re, 5.47; O, 2.34). The Sb valencies of the ion pair (2.80) are smaller whereas the F valencies are similar to those of the free $[Sb_3F_{16}]^-$ anion (Sb, 3.06 and 3.08).

The Wiberg bond indices of the Re−O (1.68 and 1.69) and Sb−F_μ (0.32 and 0.41) bonds decrease upon ion-pair formation ($[ReO_3]^+$, 1.82; $[Sb_3F_{16}]^-$, 0.52 and 0.55), in agreement with increases in the corresponding calculated Re−O and Sb−F_μ bond lengths of $[ReO_3][Sb_3F_{16}]$ (Re−O, 1.686 Å; Sb−F_μ, 2.017 and 2.147 Å), when compared with those of $[ReO_3]^+$ (1.677 Å) and $[Sb_3F_{16}]^-$ (1.891 and 1.879 Å).

5.2.6.2. μ-$O(ReO_2F)(AsF_5)\cdot 2AsF_5$ (Figure 5.1b)

The positive charges reside on rhenium (2.27) and arsenic (2.70 and 2.68). As in the $[ReO_3][Sb_3F_{16}]$ ion-pair, the negative charges are dispersed over both terminal oxygen

atoms (−0.41) and terminal fluorine atoms bonded to As (−0.52, −0.53, and −0.54). The charges on the bridging fluorine atoms are slightly more negative (−0.59 and −0.60) than those on the terminal fluorine atoms, whereas the highest negative charge is on the bridging oxygen atom (−0.86). The overall negative charge distributions are comparable to those of $(\mu\text{-F})_4\{[\mu\text{-O}(ReO_2F)_2](ReO_2F_2)_2\}$ (Chapter 4). The charge on the terminal fluorine atom (−0.43) is also comparable to those observed in $(\mu\text{-F})_4\{[\mu\text{-O}(ReO_2F)_2](ReO_2F_2)_2\}$ (Chapter 4). The Re valence (5.50) is comparable to that observed in $(\mu\text{-F})_4\{[\mu\text{-O}(ReO_2F)_2](ReO_2F_2)_2\}$ (5.54). The valencies of the As atoms of the terminal AsF_5 are slightly smaller than that of the central AsF_5 molecule. The terminal F valencies (0.78, 079, and 0.80) are only slightly greater than those of the fluorine atoms bridging Re and terminal AsF_5 molecules (0.73) and those bridging the terminal AsF_5 and the central AsF_5 (0.74) molecules. The terminal O valencies are significantly greater than that of the bridging O_μ atom (1.96). The higher valence of the bridging O_μ atoms is in accordance with its higher coordination number.

The Wiberg bond indices of the terminal Re−O and As−F bonds (O, 1.79; F, ca. 0.64) are in agreement with their double- and single-bond character, respectively. The $As_2{-}F_\mu(As)$ Wiberg bond indices (0.42) are higher than the $As_{1,3}{-}F_\mu(As)$ Wiberg bond indices (0.16), which is in accordance with the calculated $As_2{-}F_\mu(As)$ (1.830 Å) and $As_{1,3}{-}F_\mu(As)$ ($As_{1,3}{-}F_\mu$, 2.165 Å) bond lengths. Noticeable difference is observed between the Re---F_μ (0.11) and Re−O_3 (0.97) bridge bond indices, in agreement with the proposed structure description of $\mu\text{-O}(ReO_2F)(AsF_5)\cdot 2AsF_5$.

5.2.6.3. $[O_3Re(NCCH_3)_3]^+$ (Figure 5.1c)

Upon adduct formation, the charges on the Re atom (1.93) decrease and the charges on the O atoms (−0.50) become more negative, when compared to those of the free $[ReO_3]^+$ cation (Re, 2.12; O, −0.37) and are consistent with the electron density donation by the CH_3CN ligands. The Re valencies (5.64) in $[O_3Re(NCCH_3)_3]^+$ slightly increase, whereas the O valencies (2.28) slightly decrease upon the adduct-cation formation ($[ReO_3]^+$: Re, 5.47; O, 2.34). The Re−O Wiberg bond index (1.62) is comparable to that in the $[ReO_3][Sb_3F_{16}]$ ion-pair (1.68 and 1.69) and smaller than in the free $[ReO_3]^+$ cation (1.82). The Re---N Wiberg bond index (0.25) indicates that the Re---N bond has some covalent character.

The charges on the N atoms in $[O_3Re(NCCH_3)_3]^+$ (−0.44) are more negative, whereas the charge on the C directly bonded to N becomes more positive (0.51) than those in free CH_3CN (N, −0.33; C_1, 0.28), consistent with the overall electron density flow from the C−N triple bond to the N atom. The polarization of CH_3CN is also indicated by the decreased Wiberg bond index of the C−N bond (2.74), increase of N valencies (3.26), and decrease of C_1 valence (3.91), when compared to that of free CH_3CN (bond index, 2.90; valence: N, 3.02; C_1, 4.00). The charge, valencies, and bond indices of the CH_3-group do not change upon adduct formation.

5.3. Conclusion

The study of the fluoride ion-donor properties of ReO_3F has led to the isolation of the first rhenium trioxide cation, $[ReO_3]^+$, as its $[Sb_3F_{16}]^-$ salt, and a novel μ-

$O(ReO_2F)(AsF_5)\cdot 2AsF_5$ molecule, which provides the first example of AsF_5 molecule coordinated to a transition metal through an O atom. The aforementioned compounds have been synthesized by the reaction of ReO_3F with SbF_5 in SO_2ClF and AsF_5, respectively. Both solids were insoluble in SO_2ClF and CH_2Cl_2 and solvolyzed in aHF to form $[ReO_2F_2][PnF_6]$ (Pn = As, Sb),[22] preventing crystal growth. The $[ReO_3][Sb_3F_{16}]$ salt is stable at room temperature, whereas μ-$O(ReO_2F)(AsF_5)\cdot 2AsF_5$ slowly dissociates into ReO_3F and AsF_5, at temperatures above 0 ^oC. An attempt to grow crystals of $[ReO_3][Sb_3F_{16}]$ by sublimation at 45 ^oC resulted in the formation of $[ReO_2F_2][SbF_6]$.[22] The dissolution of the $[ReO_3][Sb_3F_{16}]$ ion-pair and μ-$O(ReO_2F)(AsF_5)\cdot 2AsF_5$ in CH_3CN yielded the $[O_3Re(NCCH_3)_3][PnF_6]$ salts, which both contain the novel $[O_3Re(NCCH_3)_3]^+$ adduct-cation. All of the above compounds were unambiguously characterized by Raman spectroscopy with the aid of quantum-chemical calculations. The structural characterization of these compounds revealed that the ReO_3-moiety is retained in the $[ReO_3][Sb_3F_{16}]$ ion-pair and in the $[O_3Re(NCCH_3)_3]^+$ adduct-cation, whereas in μ-$O(ReO_2F)(AsF_5)\cdot 2AsF_5$, the ReO_2F-moiety is bridged to AsF_5 through an O atom. In the $[O_3Re(NCCH_3)_3]^+$ adduct-cation, the CH_3CN ligands are bonded trans to the oxygen atoms.

CHAPTER 6

$[XeOXeOXe]^{2+}$, THE MISSING OXIDE OF XENON(II); SYNTHESIS, RAMAN SPECTRUM, AND X-RAY CRYSTAL STRUCTURE OF $[XeOXeOXe][\mu\text{-}F(ReO_2F_3)_2]_2$

6.1. Introduction

Noble-gas compounds have generated considerable interest since the discovery of noble-gas reactivity by Neil Bartlett in 1962.[264] Over the ensuing decades, the syntheses of the binary xenon fluorides, KrF_2, and oxide fluorides of xenon have provided a diverse derivative chemistry.[265] Although thermodynamically unstable with respect to their elements, xenon oxides have also been isolated and characterized in macroscopic quantities for every known oxidation state of xenon except the +½ and +2 oxidation states, i.e., $Xe^{IV}O_2$,[266] $Xe^{VI}O_3$,[267-272] $Xe^{VIII}O_4$,[273-279] $(\eta^2\text{-}O_2)Xe^{VIII}O_3$,[279] and $[Xe^{VIII}O_6]^{4-}$.[270,280-297] No isolable oxides of krypton are known.[298] Both XeO_3 and XeO_4 are shock-sensitive, decomposing explosively with the release of 402[269] and 642[275] kJ mol^{-1}, respectively, whereas water-insoluble XeO_2 quiescently decomposes under water at 0 ^oC[265] over several minutes. In contrast, $[Xe^{VIII}O_6]^{4-}$ salts are kinetically and thermodynamically stable at ambient temperatures and pressures,[270] and have been characterized by X-ray crystallography,[280-285,288] Raman,[289,290,296] infrared,[286,289,296] photoelectron,[291,296] Auger,[291] Mössbauer,[30] ^{129}Xe NMR,[292,297] and UV[295] spectroscopy. Xenon tetroxide is generated by the reaction of concentrated H_2SO_4 with $Na_4[XeO_6]$ and has been isolated as a pale yellow, volatile solid and its molecular structure has been

obtained from an electron diffraction study of XeO_4 in the gas phase.[276] Xenon tetroxide has also been characterized by infrared,[273,279] Raman,[277,278] ^{129,131}Xe NMR spectroscopy,[278] and mass spectrometry.[274] Photolysis of XeO_4 in noble-gas matrices at 365 nm yielded the Xe(VIII) peroxo-compound, (η^2-O_2)XeO_3 and XeO_3.[279] The former was characterized by infrared spectroscopy. Xenon trioxide, XeO_3, has been synthesized as a colorless crystalline solid and characterized by single-crystal X-ray diffraction,[268] Raman,[271] and infrared[272] spectroscopy. Recently, XeO_2 has been synthesized as a bright yellow solid at 0 ^{o}C.[266] The characterization of XeO_2 by Raman spectroscopy revealed that XeO_2 is polymeric, possessing an extended structure in which Xe is bonded to four oxygen atoms having a local square-planar XeO_4 geometry around the central Xe atom.

The xenon(II) oxide, XeO, has been postulated as an intermediate in some oxidation reactions of XeO_3.[270] Its gas-phase UV and vacuum UV emission spectra have been attributed to emissions from $Xe^{+}O^{-}$ ion pair states.[299,300] Monomeric XeO has not been synthesized in macroscopic amounts, but has been obtained in an argon matrix[301] where UV spectroscopic evidence suggested that the ground state of XeO is essentially a van der Waals molecule with a bond length considerably longer than the excited state value. Xenon monoxide was subsequently shown by gas-phase quantum-chemical calculations to have an unbound $^3\Pi$ ground state. The only bound state is the excited $1^1\Sigma^+$ state.[299,300]
In a prior study, the first xenon(II) oxide fluoride species, $[FXeOXeFXeF]^+$, was synthesized as its $[PnF_6]^-$ (Pn = As, Sb) salts by reaction of XeF_2 with $[H_3O][PnF_6]$ in HF.[302] The $[FXeOXeFXeF][PnF_6]$ salts were characterized by single-crystal X-ray diffraction, Raman spectroscopy, and quantum-chemical calculations. Although the

oxygen and fluorine atoms bonded to the central Xe atom of $[FXeOXeFXeF]^+$ are positionally disordered in both $[PnF_6]^-$ salts the presence of a bridging oxygen atom was corroborated by $^{16/18}O$ isotopic shifts obtained from the Raman spectrum and by isotopic shift values obtained from quantum-chemical calculations. It was proposed that XeF_2 is hydrolyzed by $[H_3O]^+$ to form FXeOH, an intermediate in the formation of the $[FXeOXeFXeF]^+$ cation.

In the quest for a xenon(II) oxide, the reaction of ReO_3F with XeF_2 was investigated as a possible means to transfer oxygen to xenon(II). A reliable synthesis of high-purity ReO_3F in anhydrous HF (aHF) has been recently developed,[235] which has allowed its chemistry to be more widely explored. The HF solvate, $ReO_3F(FH)_2$, has also been isolated and characterized by single-crystal X-ray diffraction and Raman spectroscopy.

The present study reports the synthesis and characterization of the first xenon(II) oxide, $[XeOXeOXe]^{2+}$ as its $[\mu\text{-}F(ReO_2F_3)_2]^-$ salt. The salt has been structurally characterized by low-temperature single-crystal X-ray diffraction and Raman spectroscopy. Vibrational assignments have been made with the aid of quantum-chemical calculations, which were supported by ^{18}O-enrichment studies. The nature of the bonding in $[XeOXeOXe][\mu\text{-}F(ReO_2F_3)_2]_2$ has been examined using Natural Bond Orbital (NBO), Quantum Theory of Atoms in Molecules (QTAIM), Electron Localization Function (ELF), and Molecular Electrostatic Potential Surface (MEPS) analyses.

6.2. Results and Discussion

6.2.1 Synthesis of $[XeOXeOXe][\mu\text{-}F(ReO_2F_3)_2]_2$

Reaction progress and product purities were monitored by recording the Raman spectra of the solids under aHF in FEP reaction vessels at –140 °C.

The salt, $[XeOXeOXe][\mu\text{-}F(ReO_2F_3)_2]_2$, was obtained by the reaction of ReO_3F[235] with XeF_2 in aHF at −30 °C according to a three-step reaction sequence (eqs 6.1–6.3), with the overall synthesis summarized in eq 6.4. A range of XeF_2:$ReO_3F(FH)_2$ molar

$$ReO_3F + 2HF \longrightarrow ReO_3F(FH)_2 \quad (6.1)$$

$$3XeF_2 + 4ReO_3F(FH)_2 \longrightarrow [XeOXeOXe][\mu\text{-}F(ReO_2F_3)_2]_2 + 2[H_3O][HF_2] \quad (6.2)$$

$$2XeF_2 + 2[H_3O][HF_2] \longrightarrow 2Xe + O_2 + 8HF \quad (6.3)$$

$$5XeF_2 + 4ReO_3F(FH)_2 \longrightarrow [XeOXeOXe][\mu\text{-}F(ReO_2F_3)_2]_2 + 2Xe + O_2 + 8HF \quad (6.4)$$

ratios was surveyed to determine whether or not other xenon(II) oxide or oxide fluoride cations could be formed.

The molar ratios of the reactants, XeF_2:ReO_3F, were 2.11:1.00, 1.19:1.00, 1.18:1.00, 1.14:1.00, 1.02:1.00, and 0.56:1.00. Upon warming the reaction mixtures to −30 °C, ReO_3F and XeF_2 dissolved in aHF over a period of ca. 5–10 min, forming pale yellow solutions. As the reactions progressed over a period of 2–4 h at −30 °C, the solution colors changed from pale yellow to yellow-orange. Rapid cooling of the solutions (XeF_2:ReO_3F = 2.11:1.00, 1.19:1.00, 1.18:1.00, 1.14:1.00) to −78 °C resulted in irreversible precipitation of red-orange colored microcrystalline powders that was accompanied by solution color changes from yellow-orange to colorless upon complete

precipitation. The low-temperature Raman spectra of the red-orange crystalline products under frozen aHF (XeF_2:ReO_3F = 1.19:1.00, 1.14:1.00) and products isolated under dynamic vacuum at −78 °C (XeF_2:ReO_3F = 2.11:1.00, 1.18:1.00) were identical and were assigned to [XeOXeOXe][μ-F(ReO_2F_3)$_2$]$_2$. Crystals of [XeOXeOXe][μ-F(ReO_2F_3)$_2$]$_2$ that were of a quality suitable for an X-ray structure determination were grown by slowly cooling the yellow-orange solutions (XeF_2:ReO_3F = 0.56:1.00 and 1.02:1.00) from −30 to −35 °C over a 5 h period. The ^{18}O-enriched salt, [Xe^{18}OXe^{18}OXe][μ-F(Re$^{18}O_2F_3$)$_2$]$_2$, was also synthesized from enriched Re$^{18}O_3F$ using a modification of a published synthetic procedure[235] (also see Experimental Section).

A plausible reaction pathway leading to [XeOXeOXe][μ-F(ReO_2F_3)$_2$]$_2$ is provided in Scheme 6.1. The reaction sequence is presumably initiated by XeF_2 coordination to $ReO_3F(FH)_2$, followed by intramolecular rearrangements that lead to [OXeFReO_2F_2(FH)]. Subsequent HF solvolysis yields ReO_2F_3(FH) and HOXeF. The HOXeF molecule has also been invoked as a key reaction intermediate in the synthesis of the [FXeOXeFXeF]$^+$ cation.[302] The reaction of HOXeF with a second equivalent of $ReO_3F(FH)_2$ provides [HOXeFReO_3F(FH)], which, in turn, undergoes condensation with HOXeF to yield [FXeOXeFReO_3F(FH)]. The latter product undergoes intramolecular rearrangement and subsequent HF solvolysis to form ReO_2F_3(FH) and FXeOXeOH. Fluorine coordination of FXeOXeOH to Lewis acidic μ-F(ReO_2F_3)(ReO_2F_2) results in a positive charge on the XeOXeOH unit of μ-F(XeOXeOH)[μ-F(ReO_2F_3)(ReO_2F_2)] which promotes a further FXeOH condensation/H_2O elimination reaction to give μ-F(FXeOXeOXe)[μ-F(ReO_2F_3)(ReO_2F_2)].

Scheme 6.1. Proposed Reaction Pathway Leading to the Formation of [XeOXeOXe][μ-F(ReO_2F_3)$_2$]$_2$.

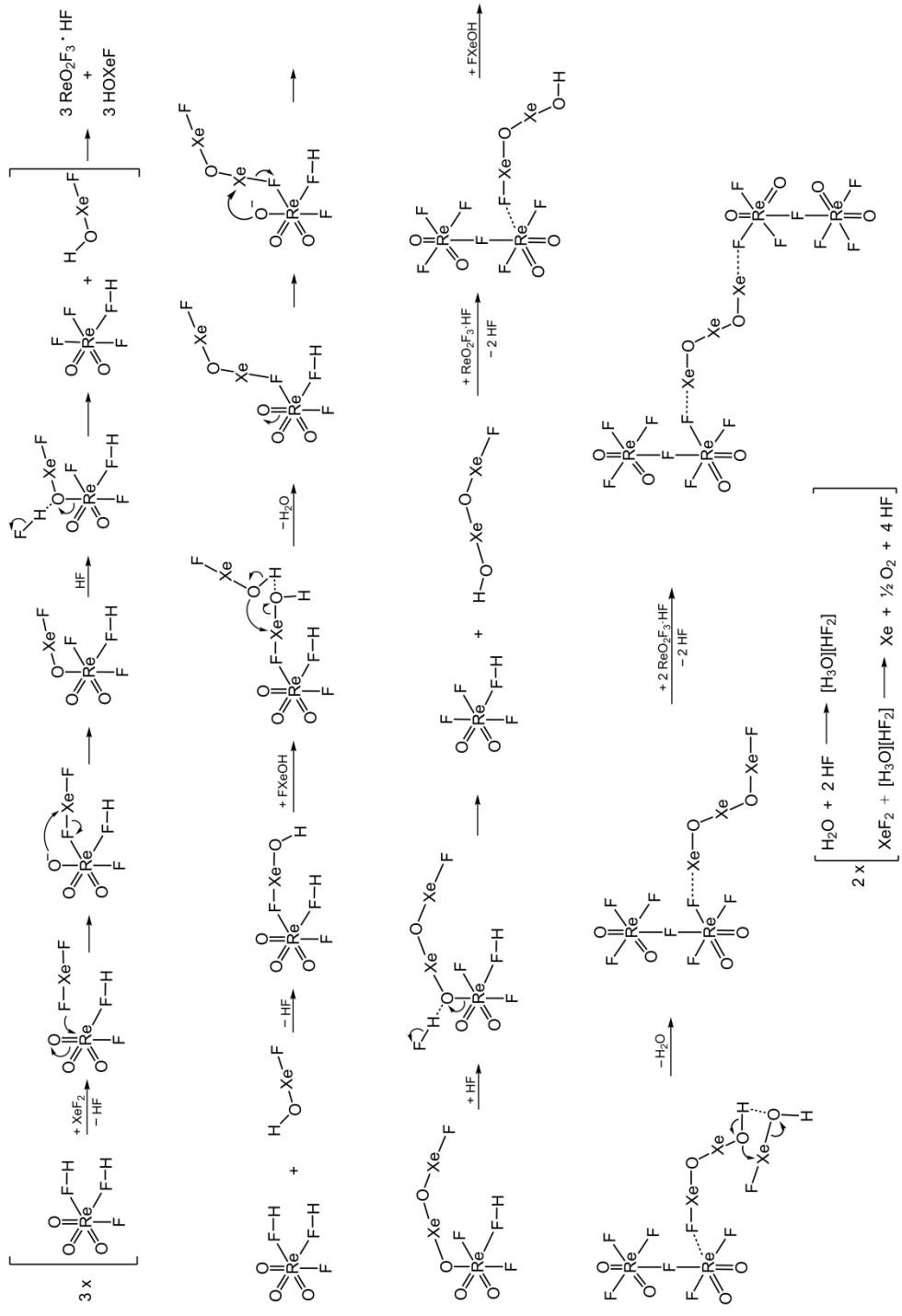

In view of the stabilities of the $[\mu\text{-}F(ReO_2F_3)_2]^-$ salts,[19] the latter complex may be reformulated as $[FXeOXeOXe][\mu\text{-}F(ReO_2F_3)_2]$, where it is understood that there is a Xe---F–Re fluorine bridge interaction between the cation and the anion. In the final step, $[FXeOXeOXe]^+$ undergoes fluoride ion abstraction by two equivalents of $ReO_2F_3(FH)$, which undergo HF elimination to give $[XeOXeOXe][\mu\text{-}F(ReO_2F_3)_2]_2$. Water generated in Scheme 6.1 is protonated in HF,[303,304] forming $[H_3O][HF_2]$ which reacts with XeF_2 according to eq 6.3 to form Xe, O_2, and HF. Although the $[FXeOXeFXeF]^+$ cation may be formed as an intermediate, its $[AsF_6]^-$ and $[SbF_6]^-$ salts have been shown to rapidly decompose, with gas evolution, above –30 °C.[302]

The $[XeOXeOXe][\mu\text{-}F(ReO_2F_3)_2]_2$ salt decomposes as a solid or in HF solvent to ReO_2F_3, XeF_2 (both confirmed by Raman spectroscopy), O_2, and Xe at temperatures above −20 °C (eq 6.5). Xenon formation was confirmed by condensation from the

$$[XeOXeOXe][\mu\text{-}F(ReO_2F_3)_2]_2 \longrightarrow 4ReO_2F_3 + XeF_2 + O_2 + 2Xe \qquad (6.5)$$

evolved gas mixture at –196 °C. In a separate study, ReO_2F_3 and XeF_2 were shown to be unreactive in aHF at room temperature and when equimolar amounts were fused at 80 °C. In instances (XeF_2: ReO_3F = 1.19:1.00, 1.14:1.00), where $[XeOXeOXe][\mu\text{-}F(ReO_2F_3)_2]_2$ had been isolated before the reaction sequence (eqs 6.2-6.4) had gone to completion (ca. 1h at –35 °C), the solution samples were allowed to decompose (–20 °C to room temperature) and were pumped on at room temperature to remove HF, XeF_2, Xe, and O_2. The Raman spectra of the resulting solids consisted of mixtures of ReO_2F_3 and unreacted ReO_3F.

6.2.2 X-ray Crystallography

Details of the data collection and other crystallographic information for $[XeOXeOXe][\mu\text{-}F(ReO_2F_3)_2]_2$ are given in Table 6.1 and important bond lengths and bond angles are provided in Table 6.2. The salt, $[XeOXeOXe][\mu\text{-}F(ReO_2F_3)_2]_2$, crystallizes in the triclinic space group $P\bar{1}$ (Z = 1) (Figure 6.1a). The unit cell consists of a well-isolated $[XeOXeOXe][\mu\text{-}F(ReO_2F_3)_2]_2$ ion pair, where the $[XeOXeOXe]^{2+}$ cation interacts through fluorine bridges with two symmetry-equivalent $[\mu\text{-}F(ReO_2F_3)_2]^-$ anions. The $[XeOXeOXe][\mu\text{-}F(ReO_2F_3)_2]_2$ ion pairs occupy parallel *b*,*c*-planes and stack along the *a*-axis (Figure D1). The shortest intermolecular ligand atom distances occur for $O_{(1)}\cdots O_{(4C)}$ (2.962(8) Å) and $F_{(7)}\cdots O_{(2K)}$ (2.882(8) Å), which are close to the corresponding sums of the van der Waals radii (O···O, 3.04 and O···F, 2.99 Å).[241] The central $Xe_{(1)}$ atom has six Xe···O (3.324(6)–3.663(6) Å) and four Xe···F (3.119(5)–3.429(5) Å) long contacts and the terminal $Xe_{(2,2A)}$ atoms have two Xe···O (3.311(6), 3.239(6) Å) and five Xe···F (3.114(5)–3.419(5) Å) long contacts so that the total coordination numbers of $Xe_{(1)}$ and $Xe_{(2)}$ are 12 and 9, respectively (Figure D2). These contacts are somewhat shorter than the sums of the Xe···O (3.68 Å) and Xe···F (3.63 Å) van der Waals radii.[241] In the absence of these contacts, both xenon atoms are under bonded, having bond valences[305] of 1.56 ($Xe_{(1)}$) and 1.57 ($Xe_{(2,2A)}$) (Table D1). The introduction of the aforementioned long contacts results in total bond valences of 1.84 ($Xe_{(1)}$) and 1.81 ($Xe_{(2,2A)}$). The next closest Xe---O and Xe---F distances have bond valences less than 0.01, and are too long to be considered as contacts.

Table 6.1. Summary of Crystal Data and Refinement Results for [XeOXeOXe] [μ-F(ReO_2F_3)$_2$]$_2$

Compound	[XeOXeOXe][μ-F(ReO_2F_3)$_2$]$_2$
space group	$P\bar{1}$
a (Å)	7.7142(2)
b (Å)	8.0991(2)
c (Å)	10.0494(2)
α (deg)	88.2797(13)
β (deg)	69.1278(12)
γ (deg)	62.0249(12)
V (Å)^3	510.91(2)
molecules/unit cell	1
mol wt (g mol^{-1})	1564.7
calcd density (g cm^{-3})	5.086
T (^{o}C)	–173
μ (mm^{-1})	28.67
R_1[a]	0.0283
wR_2[b]	0.0597

[a] R_1 is defined as $\Sigma \| F_o \| - \| F_c \| \Sigma \| F_o \|$ for $I > 2\sigma(I)$. [b] wR_2 is defined as $[\Sigma[w(F_o^2 - F_c^2)^2]/\Sigma w(F_o^2)^2]^{1/2}$ for $I > 2\sigma(I)$.

Table 6.2. Experimental and Calculated Geometrical Parameters for [XeOXeOXe][μ-F(ReO_2F_3)$_2$]$_2$ (C_i), $[XeOXeOXe]^{2+}$ (C_{2h}), and FXeOXeOXeF (C_i)

	[XeOXeOXe][μ-F(ReO_2F_3)$_2$]$_2$ [a]			[XeOXeOXe]$^{2+}$ [b]		[μ-F(ReO_2F_3)$_2$]$^-$ [b]		FXeOXeOXeF [b]	
	exptl	calcd							
		c	*d*	*c*	*d*	*c*	*d*	*c*	*d*
Bond Lengths (Å)									
$Xe_{(1)}$–$O_{(1)}$	2.135(6)	2.174	2.139	2.207	2.169			2.155	2.119
$Xe_{(2)}$–$O_{(1)}$	1.987(6)	2.034	2.007	2.021	1.994			2.098	2.068
$Xe_{(2)}$---$F_{(1)}$	2.392(4)	2.310	2.279					2.086	2.057
$Re_{(1)}$–$F_{(1)}$	2.007(4)	2.112	2.097			1.920	1.908		
$Re_{(1)}$–$O_{(3)}$	1.676(6)	1.680	1.668			1.689	1.677		
$Re_{(1)}$–$O_{(2)}$	1.673(6)	1.678	1.666			1.696	1.683		
$Re_{(1)}$–$F_{(3)}$	1.859(4)	1.863	1.852			1.880	1.866		
$Re_{(1)}$–$F_{(4)}$	1.852(5)	1.860	1.844			1.880	1.865		
$Re_{(1)}$–$F_{(2)}$	2.048(4)	2.073	2.059			2.136	2.119		
$Re_{(2)}$–$O_{(4)}$	1.750(6)	1.687	1.675			1.696	1.683		
$Re_{(2)}$–$O_{(5)}$	1.661(6)	1.678	1.666			1.689	1.677		
$Re_{(2)}$–$F_{(2)}$	2.174(5)	2.243	2.218			2.136	2.119		
$Re_{(2)}$–$F_{(7)}$	1.815(5)	1.888	1.877			1.880	1.865		
$Re_{(2)}$–$F_{(5)}$	1.863(5)	1.859	1.845			1.880	1.866		
$Re_{(2)}$–$F_{(6)}$	1.883(5)	1.941	1.926			1.920	1.908		
Bond Angles (deg)									
$O_{(1)}$–$Xe_{(1)}$–$O_{(1A)}$	180.0	180.0	180.0	180.0	180.0			180.0	180.0
$Xe_{(1)}$–$O_{(1)}$–$Xe_{(2)}$	115.6(3)	118.7	118.0	123.6	122.5			118.1	117.0
$O_{(1)}$–$Xe_{(2)}$---$F_{(1)}$	176.7(2)	175.3	175.2					177.1	177.4
$Xe_{(2)}$---$F_{(1)}$–$Re_{(1)}$	134.8(2)	130.7	129.1						
$O_{(3)}$–$Re_{(1)}$–$O_{(2)}$	101.6(3)	102.8	102.9			101.9	102.0		
$O_{(3)}$–$Re_{(1)}$–$F_{(1)}$	90.7(3)	88.9	89.0			96.2	96.5		
$O_{(3)}$–$Re_{(1)}$–$F_{(2)}$	168.1(3)	165.5	165.3			173.5	173.5		
$O_{(3)}$–$Re_{(1)}$–$F_{(3)}$	96.3(3)	97.1	97.2			96.8	97.0		
$O_{(3)}$–$Re_{(1)}$–$F_{(4)}$	97.6(3)	97.4	97.6			96.5	96.6		
$O_{(2)}$–$Re_{(1)}$–$F_{(1)}$	167.7(2)	168.3	168.1			161.8	161.5		
$O_{(2)}$–$Re_{(1)}$–$F_{(2)}$	90.2(2)	91.6	91.8			84.5	84.5		
$O_{(2)}$–$Re_{(1)}$–$F_{(3)}$	96.4(2)	97.8	97.8			94.1	94.1		
$O_{(2)}$–$Re_{(1)}$–$F_{(4)}$	96.4(3)	97.8	98.1			94.4	94.6		
$F_{(1)}$–$Re_{(1)}$–$F_{(2)}$	77.5(2)	76.7	76.3			77.3	77.0		

Table 6.2. (continued….)

$F_{(1)}$–$Re_{(1)}$–$F_{(3)}$	82.4(2)	80.4	80.1	83.4	83.2
$F_{(1)}$–$Re_{(1)}$–$F_{(4)}$	81.5(2)	80.5	80.5	83.7	83.5
$F_{(2)}$–$Re_{(1)}$–$F_{(3)}$	80.5(2)	80.5	80.2	82.7	82.6
$F_{(2)}$–$Re_{(1)}$–$F_{(4)}$	82.7(2)	80.6	80.5	82.7	82.5
$F_{(3)}$–$Re_{(1)}$–$F_{(4)}$	158.9(2)	155.8	155.2	162.3	162.0
$Re_{(1)}$–$F_{(2)}$–$Re_{(2)}$	158.3(3)	151.8	148.6	150.6	146.7
$O_{(5)}$–$Re_{(2)}$–$O_{(4)}$	100.2(3)	103.2	103.2	101.9	102.0
$O_{(5)}$–$Re_{(2)}$–$F_{(5)}$	98.7(3)	99.0	99.0	96.8	97.0
$O_{(5)}$–$Re_{(2)}$–$F_{(6)}$	98.4(3)	98.6	98.9	96.2	96.5
$O_{(5)}$–$Re_{(2)}$–$F_{(7)}$	99.2(3)	98.1	98.0	96.5	96.6
$O_{(5)}$–$Re_{(2)}$–$F_{(2)}$	177.6(3)	174.0	174.0	173.5	173.5
$O_{(4)}$–$Re_{(2)}$–$F_{(2)}$	82.0(2)	82.7	82.7	84.5	84.5
$O_{(4)}$–$Re_{(2)}$–$F_{(5)}$	91.6(3)	95.9	96.1	94.1	94.1
$O_{(4)}$–$Re_{(2)}$–$F_{(6)}$	161.2(3)	158.1	157.6	161.8	161.5
$O_{(4)}$–$Re_{(2)}$–$F_{(7)}$	94.3(3)	93.9	93.7	94.4	94.6
$F_{(5)}$–$Re_{(2)}$–$F_{(2)}$	80.3(2)	81.0	80.9	82.7	82.6
$F_{(5)}$–$Re_{(2)}$–$F_{(6)}$	83.2(3)	83.2	83.2	83.4	83.2
$F_{(5)}$–$Re_{(2)}$–$F_{(7)}$	159.8(3)	157.8	157.9	162.3	162.0
$F_{(2)}$–$Re_{(2)}$–$F_{(6)}$	79.3(2)	75.5	75.1	77.3	77.0
$F_{(2)}$–$Re_{(2)}$–$F_{(7)}$	81.4(2)	80.6	80.7	82.7	82.5
$F_{(6)}$–$Re_{(2)}$–$F_{(7)}$	85.1(3)	80.3	80.2	83.7	83.5

Intermolecular Contacts(Å)

$Xe_{(1)}$---$O_{(1E)}$	3.324(6)
$Xe_{(1)}$---$O_{(1F)}$	3.324(6)
$Xe_{(1)}$---$O_{(4J)}$	3.330(6)
$Xe_{(1)}$---$O_{(4C)}$	3.330(6)
$Xe_{(1)}$---$O_{(2E)}$	3.663(6)
$Xe_{(1)}$---$O_{(2I)}$	3.663(6)
$Xe_{(1)}$---$F_{(3D)}$	3.429(5)
$Xe_{(1)}$---$F_{(3B)}$	3.429(5)

Table 6.2. (continued….)

$Xe_{(1)}$---$F_{(7D)}$	3.119(5)
$Xe_{(1)}$---$F_{(7B)}$	3.119(5)
$Xe_{(2)}$---$O_{(3J)}$	3.239(6)
$Xe_{(2)}$---$O_{(1F)}$	3.311(6)
$Xe_{(2)}$---$F_{(1B)}$	3.248(5)
$Xe_{(2)}$---$F_{(4C)}$	3.419(5)
$Xe_{(2)}$---$F_{(5C)}$	3.114(5)
$Xe_{(2)}$---$F_{(6B)}$	3.168(5)
$Xe_{(2)}$---$F_{(3B)}$	3.266(5)

[a] See Figure 6.1 for the atom labeling scheme. [b] See Figure D3 for the atom labeling scheme. [c] The B3LYP/aug-cc-pVDZ(-PP) level of theory was used. [d] The PBE1PBE/aug-cc-pVDZ(-PP) level of theory was used.

a

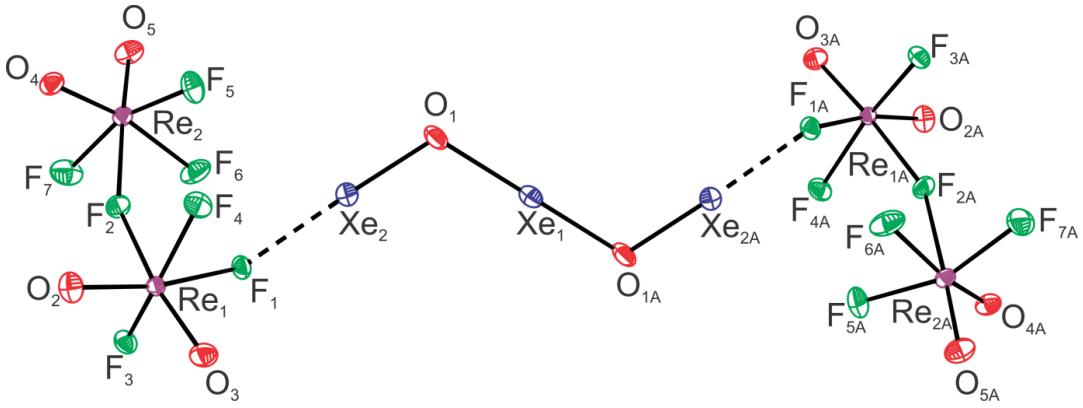

b

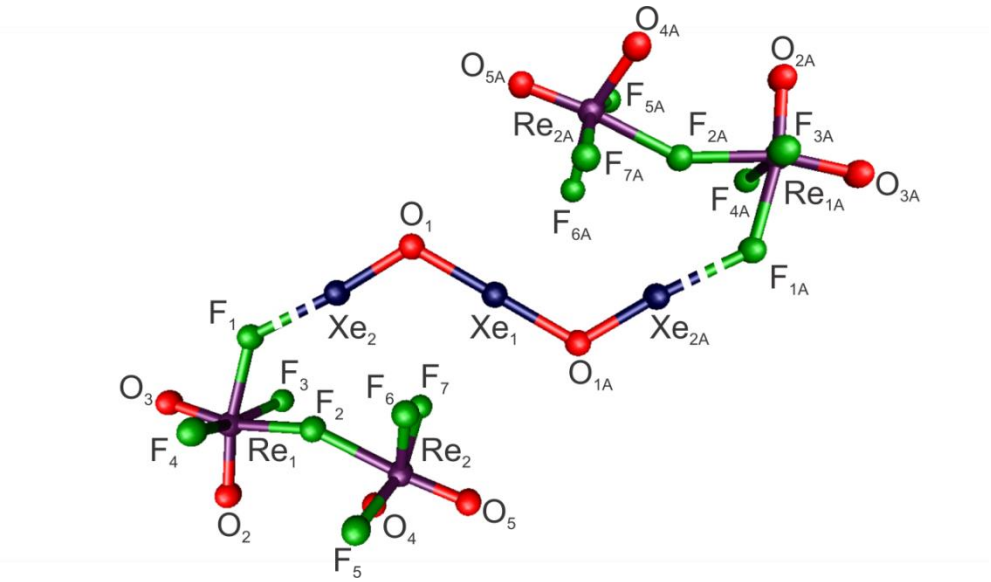

Figure 6.1. (a) The crystal structure of [XeOXeOXe][μ-F(ReO_2F_3)$_2$]$_2$. Thermal ellipsoids are shown at the 50% probability level. (b) Calculated gas-phase structure of [XeOXeOXe][μ-F(ReO_2F_3)$_2$]$_2$ (B3LYP/aug-cc-pVDZ(-PP)). The experimental and calculated geometric parameters are provided in Table 6.2.

The central xenon atom of $[XeOXeOXe]^{2+}$ is located on an inversion center, whereas all other atoms of the cation and anion are on general positions, giving C_i symmetry for the ion pair. The $[XeOXeOXe]^{2+}$ cation is planar by symmetry and, when considered in isolation, has C_{2h} symmetry. The central $Xe_{(1)}–O_{(1,1A)}$ bonds (2.135(6) Å) are significantly longer and more polar than the terminal $Xe_{(2,2A)}–O_{(1,1A)}$ bonds (1.987(6) Å), in accordance with the dominant resonance contributions, **(1)** and **(2)**.

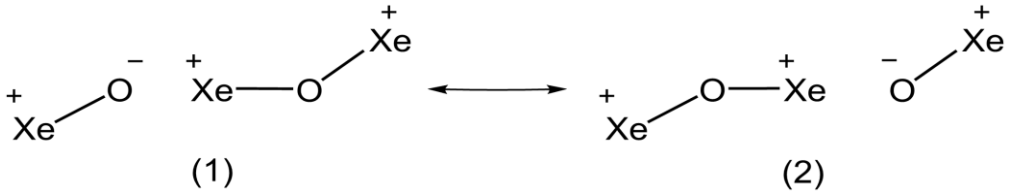

The central $Xe_{(1)}–O_{(1,1A)}$ bond lengths are equal, within ±3σ, to the Xe−O bond lengths of $Xe(OTeF_5)_2$ (2.119(11) Å),[306] $FXeOSO_2F$ (2.155(8) Å),[307] $Xe(OSO_2F)_2$ (2.1101(13), 2.1225(13) Å),[308] and $FXeONO_2$ (2.126(4) Å).[309] The terminal $Xe_{(2,2A)}–O_{(1,1A)}$ bond lengths are equal, within ±3σ, to the Xe−O bond lengths of $[XeOTeF_5][Sb(OTeF_5)_6]\cdot SO_2ClF$ (1.969(4) Å).[242] The $Xe_{(2,2A)}–O_{(1,1A)}$ bonds are slightly shorter than the Xe−O bonds of $Xe(OTeF_5)_2$,[306] $Xe(OTeF_5)_4$ (2.039(5), 2.026(5) Å),[310] and $O_2Xe(OTeF_5)_2$ (2.024(5), 2.020(4) Å),[310] but are significantly shorter than the Xe−O bonds of $FXeOSO_2F$[307] and $FXeONO_2$.[309]

The $Xe_{(2,2A)}$---$F_{(1,1A)}$ bridge bonds between the $[XeOXeOXe]^{2+}$ cation and the $[\mu\text{-}F(ReO_2F_3)_2]^-$ anions (2.392(4) Å) are considerably longer and more polar than the terminal Xe−F bonds of XeF_2 (1.999(4) Å).[311] Overall, the $Xe_{(2,2A)}$---$F_{(1,1A)}$ cation-anion

bridge bonds are slightly longer than the Xe---F bridge bonds in a number of $[XeF]^+$ salts, e.g., $[XeF][AsF_6]$ (2.208(3),[311] 2.212(5) Å[312]), $[XeF][SbF_6]$ (2.278(2) Å),[311] $[XeF][BiF_6]$ (2.204(7) Å),[311] $[XeF][Sb_2F_{11}]$ (2.343(4) Å),[311] and $[XeF][Bi_2F_{11}]$ (2.253(5) Å),[311] consistent with the dominant electrostatic nature of the $Xe_{(2,2A)}$---$F_{(1,1A)}$ interaction in $[XeOXeOXe][\mu\text{-}F(ReO_2F_3)_2]_2$ (also see Computational Results).

The $O_{(1)}$–$Xe_{(1)}$–$O_{(1A)}$ bond angle is linear by symmetry, whereas the $O_{(1,1A)}$–$Xe_{(2,2A)}$---$F_{(1,1A)}$ bridge bond angles slightly deviate from linearity (176.7(2)°). Both bond angles are consistent with linear AX_2E_3 VSEPR arrangements[313] in which three valence electron lone pairs of xenon occupy equatorial positions and two bonding electron pairs occupy axial positions. Similar near-linear fluorine bridge angles occur for F–Xe^{II}---F and O–Xe^{II}---F in $[FXeOXeFXeF][PnF_6]$ (As, 177.4(5)°, 178.3(5)°, 178.2(5)°; Sb, 178.6(3)°, 177.9(1)°),[302] $[XeF][AsF_6]$ (179.1(2)°,[311] 178.9(7)°[312]), $[XeF][SbF_6]$ (177.94(9)°),[311] $[XeF][BiF_6]$ (178.4(3)°),[311] $[XeF][Sb_2F_{11}]$ (179.3(2)°),[311] $[XeF][Bi_2F_{11}]$ (178.9(3)°),[311] and $FXeOSO_2F$ (177.4(3)°).[307]

The bent $Xe_{(1)}$–$O_{(1,1A)}$–$Xe_{(2,2A)}$ (115.6(3)°) and $Xe_{(2,2A)}$---$F_{(1,1A)}$–$Re_{(1,1A)}$ (134.8(2)°) bond angles are in accordance with AX_2E_2 VSEPR arrangements at the oxygen and fluorine atoms.[313] The $Xe_{(1)}$–$O_{(1,1A)}$–$Xe_{(2,2A)}$ bond angles are slightly smaller than the Xe–O–Ch (Ch = S, Se, or Te) angles in $Xe(OTeF_5)_2$ (121.2(6)°, 122.3(5)°),[306] $Xe(OSO_2F)_2$ (119.74(7), 119.18(7)°),[308] $FXeOSO_2F$ (123.7(5)°),[307] $Xe(OSeF_5)_2$ (123.9(13)°),[306] and are also less than the $Xe_{(1)}$–$O_{(1)}/F_{(1)}$–$Xe_{(2)}$ bond angle in $[FXeOXeFXeF][PnF_6]$ (As, 123.5(6)°, 123.6(6)°; Sb, 2 x 124.6(3)°).[302] The $Xe_{(2,2A)}$---$F_{(1,1A)}$–$Re_{(1,1A)}$ angles and related fluorine bridge angles are expected to be more open than the $Xe_{(1)}$–$O_{(1,1A)}$–$Xe_{(2,2A)}$ angle

owing to reduced lone-pair—bond-pair repulsions between the bridge bonds and the electron lone pairs of the bridging fluorine atoms. The fluorine-bridge angles that occur between the $[XeF]^+$ cation and its anion in $[XeF]^+$ salts are more open, e.g., $[XeF][AsF_6]$ ($133.6(2)^o$,[311] $134.8(2)^o$ [312]), $[XeF][SbF_6]$ ($136.9(1)^o$),[311] $[XeF][BiF_6]$ ($156.1(4)^o$),[311] $[XeF][Sb_2F_{11}]$ ($148.1(2)^o$),[311] and $[XeF][Bi_2F_{11}]$ ($151.3(3)^o$.[311]

The $[XeOXeOXe]^{2+}$ cation bridges to two $[\mu\text{-}F(ReO_2F_3)_2]^-$ anions through fluorine atoms that are trans to oxygen atoms of the anions. The preference for *trans*- versus *cis*-coordination is attributed to the trans influence of the doubly bonded oxygen atoms.[17] The bridging fluorine atom is a weaker $p_\pi \rightarrow d_\pi$ donor than the doubly bonded oxygen atom, therefore, more effective competition of the oxygen atom for the same two $d_{t_{2g}}$ orbitals of rhenium enhances the negative charge and basicity of the fluorine atom trans to it. In contrast, the terminal fluorine atoms cis to the oxygen atom and trans to each other are less basic and, therefore, less favorable for fluorine-bridge formation. Such *trans*-oxo fluorine bridges are found in other transition metal oxide fluorides: ReO_2F_3,[19,21] TcO_2F_3,[17] OsO_3F_2,[314] $[\mu\text{-}F(TcOF_4)_2][Sb_2F_{11}]$,[2] $[\mu\text{-}F(ReOF_4)_2][Sb_2F_{11}]$,[13] $[\mu\text{-}F(OsO_2F_3)_2][Sb_2F_{11}]$,[177] and $[XeF_5][\mu\text{-}F(OsO_3F_2)_2]$.[315]

The $[\mu\text{-}F(ReO_2F_3)_2]^-$ anions of $K[\mu\text{-}F(ReO_2F_3)_2]$[19] and $K[\mu\text{-}F(ReO_2F_3)_2]\cdot 2ReO_2F_3$[19] have been structurally characterized by X-ray crystallography. Both salts display cation-anion interactions that are essentially Coulombic in nature. In contrast, the $[\mu\text{-}F(ReO_2F_3)_2]^-$ anions of $[XeOXeOXe][\mu\text{-}F(ReO_2F_3)_2]_2$ interact with the $[XeOXeOXe]^{2+}$ cation by means of fluorine bridges that lower the anion symmetries from C_{2v} to C_1. Despite a conformational change and symmetry lowering, the structural parameters and

trends among the $[\mu\text{-}F(ReO_2F_3)_2]^-$ anion bond lengths and bond angles of the $[XeOXeOXe]^{2+}$ salt are comparable to those reported for $K[\mu\text{-}F(ReO_2F_3)_2]$ and $K[\mu\text{-}F(ReO_2F_3)_2]\cdot 2ReO_2F_3$, and are not further discussed.

In contrast with $K[\mu\text{-}F(ReO_2F_3)_2]$ and $K[\mu\text{-}F(ReO_2F_3)_2]\cdot 2ReO_2F_3$, where the Re−F−Re bridge bonds are equal by symmetry, the $Re_{(1,1A)}-F_{(2,2A)}-Re_{(2,2A)}$ bridge bonds of $[XeOXeOXe][\mu\text{-}F(ReO_2F_3)_2]_2$ are asymmetric. The fluorine bridge asymmetry is, to a large extent, indicative of the strength of the Xe---F bridging interactions between $[XeOXeOXe]^{2+}$ and $[\mu\text{-}F(ReO_2F_3)_2]^-$, showing shorter $Re_{(1,1A)}-F_{(2,2A)}$ bridge bonds that are proximate to the cation-anion bridges ($Re_{(1,1A)}-F_{(2,2A)}$, 2.048(4); $Re_{(2,2A)}-F_{(2,2A)}$, 2.174(5) Å). Similar asymmetries are found for the anions of $[XeF][Pn_2F_{11}]$ (Pn = Sb, Bi),[311] where the Pn−F−Pn bridge asymmetry is more pronounced in $[XeF][Bi_2F_{11}]$ (2.092(6), 2.195(6) Å) than in $[XeF][Sb_2F_{11}]$ (2.010(3), 2.066(3) Å), and is attributed to the greater ionic character of $[XeF][Sb_2F_{11}]$ and its weaker Xe---F bridge bond (Xe---F_{Sb}, 2.343(4) Å; Xe---F_{Bi}, 2.253(5) Å).[311]

6.2.3. Raman Spectroscopy

The low-temperature Raman spectra of $[Xe^{16/18}OXe^{16/18}OXe][\mu\text{-}F(Re^{16/18}O_2F_3)_2]_2$ are shown in Figure 6.2. The observed and calculated frequencies and mode descriptions are provided in Tables 6.3, D2, and D3. Spectral assignments were made by comparison with the calculated frequencies and Raman intensities of $[Xe^{16/18}OXe^{16/18}OXe][\mu\text{-}F(Re^{16/18}O_2F_3)_2]_2$ (C_i) (Tables 6.3, D2, and D3), $[Xe^{16/18}OXe^{16/18}OXe]^{2+}$ (C_{2h}) (6.4, D4, and D5), and $[\mu\text{-}F(Re^{16/18}O_2F_3)_2]^-$ (C_1) (Table D6), which were optimized at the

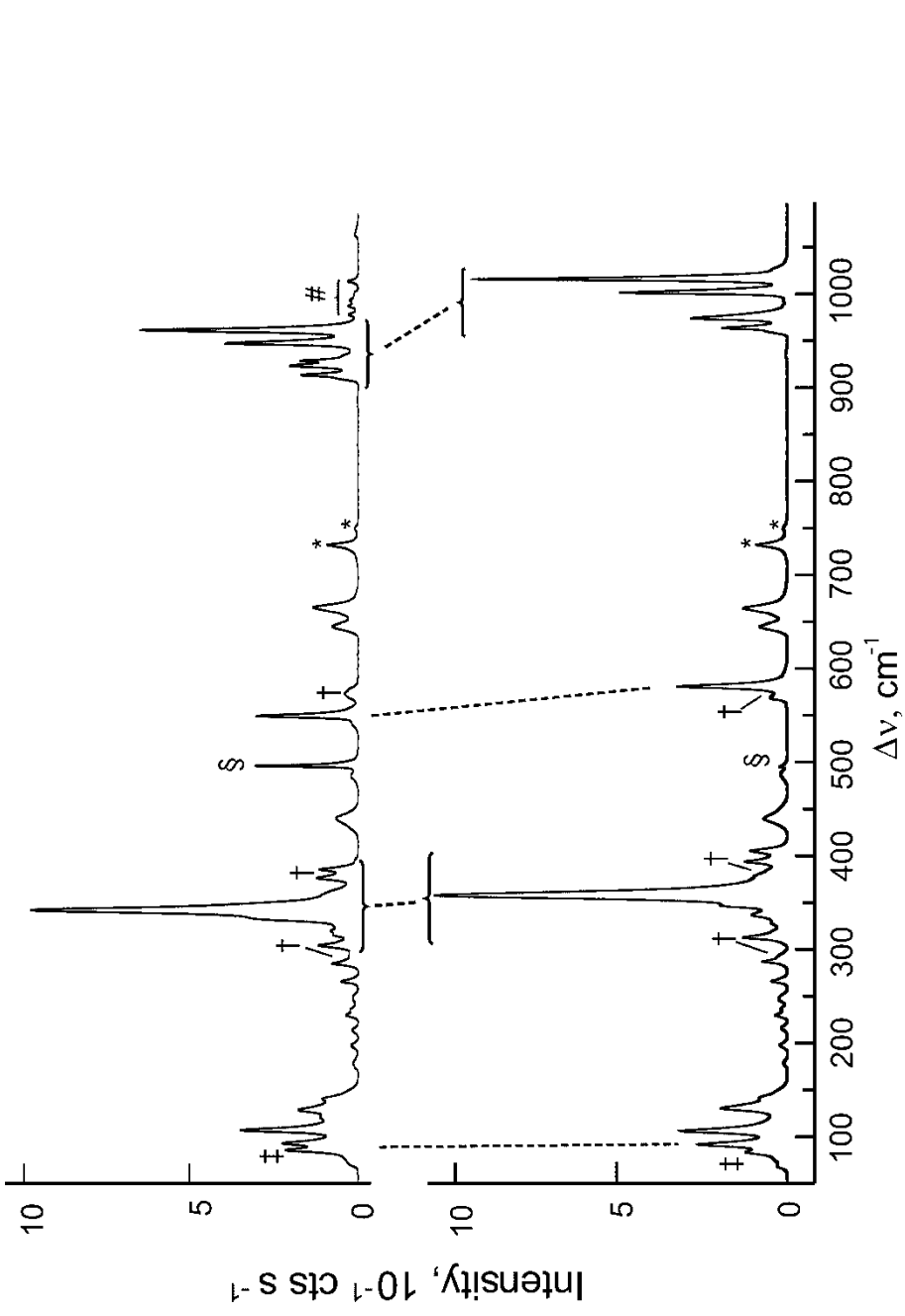

Figure 6.2. Raman spectra of $[XeOXeOXe][\mu\text{-}F(ReO_2F_3)_2]_2$ recorded at −140 °C using 1064-nm excitation for natural abundance (lower trace) and ~97% ^{18}O-enriched (upper trace). Symbols denote FEP sample tube lines (*), instrumental artifact (‡), overlap of $[XeOXeOXe][\mu\text{-}F(ReO_2F_3)_2]_2$ lines with FEP sample tube lines (†), unreacted XeF_2 (§), and small quantities of ^{16}O and mixed $^{16/18}O$ isotopomers of the $[\mu\text{-}F(ReO_2F_3)_2]^-$ anion (#).

PBE1PBE/aug-cc-pVDZ (values given in square brackets) and B3LYP/aug-cc-pVDZ(-PP) levels of theory. The vibrational modes of $[\mu\text{-}F(ReO_2F_3)_2]^-$, which had been previously assigned with the aid of LDFT and NLDFT calculations,[19] have been improved in the present work and are provided in Table D6, but are not further discussed.

The centrosymmetric, zigzag-shaped $[XeOXeOXe]^{2+}$ gas-phase cation possesses C_{2h} symmetry. Its nine fundamental vibrational modes span the irreducible representations $\Gamma = 3A_g + 2A_u + 4B_u$, where the A_u and B_u modes are infrared active and only the A_g modes are Raman active. The $\nu_1(A_g)$ band, corresponding to the symmetric out-of-phase $[\nu(Xe_1O_1) + \nu(Xe_1O_{1A})] - [\nu(Xe_2O_1) + \nu(Xe_{2A}O_{1A})]$ stretching mode, occurs at 581.6 cm^{-1} and exhibits a ^{18}O isotope shift of –32.3 cm^{-1}. The most intense band in the Raman spectrum occurs at 358.7 cm^{-1} with a ^{18}O isotope shift of –17.8 cm^{-1} and is assigned to $\nu_2(A_g)$. This band corresponds to $[\nu(Xe_1O_1) + \nu(Xe_1O_{1A})] + [\nu(Xe_2O_1) + \nu(Xe_{2A}O_{1A})]$, and is the in-phase counterpart of $\nu_1(A_g)$. The $\nu_3(A_g)$ band, corresponding to the symmetric in-phase $[\delta(Xe_2O_1Xe_1) + \delta(Xe_{2A}O_{1A}Xe_1)]_{i.p.}$ bending mode, occurs at 92.8 cm^{-1} with a ^{18}O isotope shift of –2.5 cm^{-1}.

The calculated gas-phase $^{16/18}O$ isotopic shifts of the free $[XeOXeOXe]^{2+}$ cation are in good agreement with their experimental values ($\nu_1(A_g)$, –29.7 [–32.2] cm^{-1}; $\nu_2(A_g)$, –18.1 [–19.5] cm^{-1}; $\nu_3(A_g)$, –0.4 [–0.3] cm^{-1}). There is also good agreement between the experimental and calculated frequencies of the free $[XeOXeOXe]^{2+}$ cation for $\nu_1(A_g)$ (565.3 [611.3] cm^{-1}) and $\nu_2(A_g)$ (326.1 [353.6] cm^{-1}); however, the calculated frequency of $\nu_3(A_g)$ is underestimated (71.3 [74.9] cm^{-1}) by both methods. Optimization of the $[XeOXeOXe][\mu\text{-}F(ReO_2F_3)_2]_2$ ion pair resulted in similar $^{16/18}O$ isotopic shifts ($\nu_1(A_g)$, –

Table 6.3. Selected Experimental and Calculated Vibrational Frequencies, $^{16/18}$O Isotopic Shifts ($\Delta\nu^{16/18}$), and Assignments[a] for $[XeOXeOXe]^{2+}$ in $[XeOXeOXe][\mu\text{-}F(ReO_2F_3)_2]_2$

exptl[b]			calcd (C_i)[c]			
^{16}O	^{18}O	$\Delta\nu^{16/18}$	^{16}O	^{18}O	$\Delta\nu^{16/18}$	assgnts[d]
581.6(31)	549.3(30)	−32.3	580.1(110)[0]	550.3(94)[0]	−29.8	$[\nu(Xe_1O_1) + (Xe_1O_{1A})] - [\nu(Xe_2O_1) + (Xe_{2A}O_{1A})]$
			565.0(0)[322]	535.6(0)[304]	−29.4	$[\nu(Xe_1O_1) - (Xe_1O_{1A})] - [\nu(Xe_2O_1) - (Xe_{2A}O_{1A})]$
			465.5(0)[201][e]	440.1(0)[165][e]	−25.4	$[\nu(Xe_1O_1) - (Xe_1O_{1A})] + [\nu(Xe_2O_1) - (Xe_{2A}O_{1A})]$
358.7(100)	340.9(100)	−17.8	376.2(139)[0]	357.3(125)[0]	−18.9	$[\nu(Xe_1O_1) + (Xe_1O_{1A})] + [\nu(Xe_2O_1) + (Xe_{2A}O_{1A})]$
			173.4(0)[8][f]	172.7(0)[7][f]	−0.7	$[\delta(Xe_2O_1Xe_1) - \delta(Xe_{2A}O_{1A}Xe_1)]_{i.p.}$
			169.7(0)[4]	162.4(0)[4]	−7.3	$[\delta(Xe_2O_1Xe_1) - \delta(Xe_{2A}O_{1A}Xe_1)]_{o.o.p.}$
92.8(25)	90.3(23)	−2.5	89.9(24)[0]	89.6(24)[0]	−0.3	$[\delta(Xe_2O_1Xe_1) + \delta(Xe_{2A}O_{1A}Xe_1)]_{i.p.}$
			87.0(0)[9][g]	86.6(0)[9][g]	−0.4	$[\rho_r(Xe_2O_1Xe_1) - \rho_r(Xe_{2A}O_{1A}Xe_1)]$

A full list of frequencies and assignments is provided in Table D2. Vibrational frequencies and isotopic shifts are given in cm^{-1}; $\Delta\nu^{16/18} = \nu(^{18}O) - \nu(^{16}O)$. [b] The Raman spectrum was recorded in an FEP sample tube at −140 °C using 1064-nm excitation. Values in parentheses denote relative experimental Raman intensities. [c] B3LYP/aug-cc-pVDZ(-PP); the PBE1PBE values are given in Table D3. Values in parentheses denote calculated Raman intensities (Å amu^{-1}). Values in square brackets denote calculated infrared intensities (km mol^{-1}). [d] Bond elongations and angle openings are denoted by plus (+) signs, and bond contractions and angle compressions are denoted by minus (–) signs. Abbreviations denote stretch (ν), bend (δ), rock (ρ_r), twist (ρ_t), in-plane (i.p.), and out-of-plane (o.o.p.). The atom labeling scheme is given in Figure 6.1. [e] There is also a small contribution from $[\nu(Xe_2F_1) - \nu(Re_1F_1)] + [\nu(Re_1F_2) - \nu(Re_2F_2)] + [\nu(Xe_{2A}F_{1A}) - \nu(Re_{1A}F_{1A})] - [\nu(Re_{1A}F_{2A}) - \nu(Re_{2A}F_{2A})]$ for this mode in the ion pair. [f] There is also a contribution from $[\rho_t(F_7Re_2F_6) - \rho_t(F_{7A}Re_{2A}F_{6A})]$ for this mode in the ion pair. [g] There is also a small contribution from $[\rho_r(Re_2O_4O_5F_5F_6F_7) - \rho_r(Re_{2A}O_{4A}O_{5A}F_{5A}F_{6A}F_{7A})]$ for this mode in the ion pair (Table D2).

Table 6.4. Selected Experimental and Calculated Vibrational Frequencies, $^{16/18}$O Isotopic Shifts ($\Delta\nu^{16/18}$), and Assignments[a] for Gas-Phase $[XeOXeOXe]^{2+}$

exptl[b]			calcd (C_{2h})[c]			
^{16}O	^{18}O	$\Delta\nu^{16/18}$	^{16}O	^{18}O	$\Delta\nu^{16/18}$	assgnts[d]
581.6(31)	549.3(30)	−32.3	565.3(20)[0]	535.6(17)[0]	−29.7	$[\nu(Xe_1O_1) + (Xe_1O_{1A})] - [\nu(Xe_2O_1) + (Xe_{2A}O_{1A})]$
			548.0(0)[18]	519.5(0)[16]	−28.5	$[\nu(Xe_1O_1) - (Xe_1O_{1A})] - [\nu(Xe_2O_1) - (Xe_{2A}O_{1A})]$
			407.1(0)[90]	387.4(0)[83]	−19.7	$[\nu(Xe_1O_1) - (Xe_1O_{1A})] + [\nu(Xe_2O_1) - (Xe_{2A}O_{1A})]$
358.7(100)	340.9(100)	−17.8	326.1(30)[0]	308.0(27)[0]	−18.1	$[\nu(Xe_1O_1) + (Xe_1O_{1A})] + [\nu(Xe_2O_1) + (Xe_{2A}O_{1A})]$
			160.3(0)[4]	159.9(0)[4]	−0.4	$[\delta(Xe_2O_1Xe_1) - \delta(Xe_{2A}O_{1A}Xe_1)]_{i.p.}$
			115.0(0)[6]	110.4(0)[6]	−4.6	$[\delta(Xe_2O_1Xe_1) - \delta(Xe_{2A}O_{1A}Xe_1)]_{o.o.p.}$
92.8(25)	90.3(23)	−2.5	71.3(35)[0]	70.9(35)[0]	−0.4	$[\delta(Xe_2O_1Xe_1) + \delta(Xe_{2A}O_{1A}Xe_1)]_{i.p.}$
			34.5(0)[<1]	34.3(0)[<1]	−0.2	$[\rho_r(Xe_2O_1Xe_1) - \rho_r(Xe_{2A}O_{1A}Xe_1)]$
			11.3(0)[3]	11.2(0)[3]	−0.1	$[\rho_t(Xe_2O_1Xe_1) - \rho_t(Xe_{2A}O_{1A}Xe_1)]$

A full list of frequencies and assignments is provided in Table D4. Vibrational frequencies and isotopic shifts are given in cm^{-1}; $\Delta\nu^{16/18} = \nu(^{18}O) - \nu(^{16}O)$. [b] The Raman spectrum was recorded in an FEP sample tube at −140 °C using 1064-nm excitation. Values in parentheses denote relative experimental Raman intensities. [c] B3LYP/aug-cc-pVDZ(-PP); the PBE1PBE values are given in Table D5. Values in parentheses denote calculated Raman intensities (Å amu^{-1}). Values in square brackets denote calculated infrared intensities (km mol^{-1}). [d] Bond elongations and angle openings are denoted by plus (+) signs, and bond contractions and angle compressions are denoted by minus (–) signs. Abbreviations denote stretch (ν), bend (δ), rock (ρ_r), twist (ρ_t), in-plane (i.p.), and out-of-plane (o.o.p.). The atom labeling scheme is given in Figure 6.1.

29.8 [–32.5] cm^{-1}; $\nu_2(A_g)$, –18.9 [–17.3] cm^{-1}; $\nu_3(A_g)$, –0.3 [–0.3] cm^{-1}) and in slightly higher vibrational frequencies ($\nu_1(A_g)$, 580.1 [621.8] cm^{-1}; $\nu_2(A_g)$, 376.2 [397.4] cm^{-1}; $\nu_3(A_g)$, 89.9 [94.4] cm^{-1}) that are in better agreement with the experimental values. Non of the symmetric modes of the cation are coupled to anion modes in the ion pair. The frequency and isotopic shift of $[\nu(Xe_1O_1) + \nu(Xe_{1A}O_{1A})] - [\nu(Xe_2O_1) + \nu(Xe_2O_{1A})]$ are comparable to those of the antisymmetric $[\nu(Xe_1O_1) - \nu(Xe_2O_1)]$ stretching mode of $[FXeOXeFXeF]^+$ (595.8 cm^{-1}; $\Delta\nu^{16/18}$, –27.0 and –31.4 cm^{-1}).[302] The corresponding symmetric mode of $[FXeOXeFXeF]^+$ was coupled to Xe–F stretches and consequently occurred at higher frequency than that of $[XeOXeOXe][\mu\text{-}F(ReO_2F_3)_2]_2$ (418.7 and 429.8 cm^{-1}; $\Delta\nu^{16/18}$, –24.8 and –27.8 cm^{-1}, respectively). The anion bands have been fully assigned (Table D2 and D3) and are in good agreement with those of $K[\mu\text{-}F(ReO_2F_3)_2]$,[19] $K[\mu\text{-}F(ReO_2F_3)_2]\cdot 2ReO_2F_3$,[19] and $ReO_3F(FH)_2$.[235]

6.2.4. Computational Results

Quantum-chemical calculations for $[Xe^{16/18}OXe^{16/18}OXe][\mu\text{-}F(Re^{16/18}O_2F_3)_2]_2$ (C_i) and $[Xe^{16/18}OXe^{16/18}OXe]^{2+}$ (C_{2h}) were carried out using the PBE1PBE (values in square brackets) and B3LYP methods and the aug-cc-pVDZ(-PP) basis set. Although the optimizations of $[Xe^{16/18}OXe^{16/18}OXe]^{2+}$ (C_{2h}) resulted in stationary points with all frequencies real (Tables 6.4, D4. and D5.; Figure D3a.), the optimizations of $[Xe^{16/18}OXe^{16/18}OXe][\mu\text{-}F(Re^{16/18}O_2F_3)_2]_2$ (C_i) (Tables 6.3, D2, and D3; Figure 6.1) each gave one imaginary frequency. Attempts to follow the imaginary frequencies resulted in conformers that were severely twisted about their $Xe_{(2,2A)}$---$F_{(1,1A)}$ bridge bonds; thus, all

subsequent NBO, QTAIM, ELF, and MEPS calculations were carried out using the calculated C_i geometry. The hypothetical $FXe^{16/18}OXe^{16/18}OXeF$ (C_{2h}) molecule was also calculated in order to better assess the nature of the Xe---F bridge bonds in the ion pair (Tables D7 and D8.; Figure D3b.). The $[\mu\text{-}F(ReO_2F_3)_2]^-$ anion was also calculated to aid with the anion mode assignments of the ion pair (Table D6.; Figure D3c.).

6.2.4.1. Geometry Optimizations

The calculated symmetry of the ion pair is C_i and the local symmetry of the $[XeOXeOXe]^{2+}$ cation is C_{2h}. The local gas-phase symmetry of $[XeOXeOXe]^{2+}$ is the same as in the crystal structure. Although the calculated gas-phase ion pair and the solid-state ion pair have the same point group symmetry, their conformations differ. In the calculated ion-pair, the Xe and Re atoms of both anions are coplanar, whereas the Re---F---Re axis in the solid-state structure is approximately perpendicular to the $Xe_{(2)}$---$Xe_{(1)}$---$Xe_{(2A)}$ axis (Figure 6.1). The calculated bond valences of $Xe_{(1)}$ and $Xe_{(2,2A)}$ (Table D1.) suggest that the reorientation of the anions most likely stems from the need for each Xe atom to complete its valency requirement through additional long intramolecular Xe---F contacts. In the crystal structure, similar intermolecular Xe---F contacts occur between neighboring ion pairs (see X-ray Crystallography); however, in the calculated gas-phase ion pair, the xenon atoms can only achieve their valence complements through intramolecular contacts (Table D1.), resulting in a conformation that substantially differs with respect to the crystallographic conformation.

Despite the conformational difference between the calculated and experimental ion pairs, all experimental bond length and bond angle trends were well reproduced by the quantum-chemical calculations (Tables 6.2). The central $Xe_{(1)}{-}O_{(1,1A)}$ bond lengths (calcd, 2.174 [2.139] Å; exptl, 2.135(6) Å) are longer than the terminal $Xe_{(2,2A)}{-}O_{(1,1A)}$ bond lengths (calcd, 2.034 [2.007] Å; exptl, 1.987(6) Å). The $O_{(1)}{-}Xe_{(1)}{-}O_{(1A)}$ angle is linear by symmetry, whereas the $Xe_{(1)}{-}O_{(1,1A)}{-}Xe_{(2,2A)}$ bond angles (calcd, 118.7 [118.0]^{o}; exptl, 115.6(3)^{o}) are significantly bent. The calculated $Xe_{(2)}{---}F_{(1,1A)}$ bridge bond lengths (2.310 [2.279] Å) are slightly overestimated compared to the experimental values (2.392(4) Å). The calculated $F_{(1,1A)}{---}Xe_{(2,2A)}{-}O_{(1,1A)}$ bond angles are also in very good agreement with experiment (calcd, 175.3 [175.2]^{o}; exptl, 176.7(2)^{o}). A comparison of the geometrical trends of the calculated ion pair with those of the free $[XeOXeOXe]^{2+}$ cation ($Xe_{(1)}{-}O_{(1,1A)}$, 2.207 [2.169] Å; $Xe_{(2,2A)}{-}O_{(1,1A)}$, 2.021 [1.994] Å; $Xe_{(1)}{-}O_{(1,1A)}{-}Xe_{(2,2A)}$, 123.6 [122.5]^{o}) shows that the central $Xe_{(1)}{-}O_{(1,1A)}$ bond lengths and $Xe_{(1)}{-}O_{(1,1A)}{-}Xe_{(2,2A)}$ bond angles slightly decrease upon ion pair formation, but the terminal $Xe_{(2,2A)}{-}O_{(1,1A)}$ bond lengths remain essentially unchanged.

In order to assess the degree of ion pairing, the energy-minimized geometry of the hypothetical FXeOXeOXeF molecule was calculated. Although the O−Xe−O (180.0^{o}), Xe−O−Xe (118.1 [117.0]^{o}), and O−Xe−F (177.1 [177.4]^{o}) bond angles are comparable to those of the ion pair, fluoride ion coordination affects the Xe−O bond lengths. The central $Xe_{(1)}{-}O_{(1,1A)}$ bond lengths are shorter (2.155 [2.119] Å) whereas the terminal $Xe_{(2,2A)}{-}O_{(1,1A)}$ bond lengths are longer (2.098 [2.068] Å) than those of $[XeOXeOXe]^{2+}$; however, the relative bond length order, $Xe_{(1)}{-}O_{(1,1A)} > Xe_{(2,2A)}{-}O_{(1,1A)}$ remains

unchanged. The $Xe_{(2,2A)}$−$F_{(1,1A)}$ bond lengths (2.086 [2.057] Å) of FXeOXeOXeF are considerably shorter and more covalent than the $Xe_{(2,2A)}$---$F_{(1,1A)}$ bridge bonds (2.310 [2.279] Å) of the gas-phase ion pair, [XeOXeOXe][μ-F(ReO_2F_3)$_2$]$_2$.

The geometrical parameters and trends within the [μ-F(ReO_2F_3)$_2$]$^-$ anions (Re−O < Re−F < Re−F_μ; O−Re−O > O−Re−F > O−Re−F_μ > F−Re−F_μ) of the calculated ion pair are similar to those of the experimental structure (Tables 6.2).

6.2.4.2. Natural Bond Orbital (NBO) Analyses

The NBO analyses for the [XeOXeOXe][μ-F(ReO_2F_3)$_2$]$_2$ ion pair (C_i), $[XeOXeOXe]^{2+}$ (C_{2h}), and FXeOXeOXeF (C_i) were carried out for the B3LYP/aug-cc-pVDZ(-PP) and PBE1PBE/aug-cc-pVDZ(-PP) optimized gas-phase geometries and are compared with those of the $[FXeOXeFXeF]^+$ cation.[302] The trends in calculated charges, valences, and bond orders for the above molecules are consistent at both levels of theory (Tables D9).

Overall, the $Xe_{(1)}$, $Xe_{(2,2A)}$, $O_{(1,1A)}$, and $F_{(1,1A)}$ charges of [XeOXeOXe][μ-F(ReO_2F_3)$_2$]$_2$, $[XeOXeOXe]^{2+}$, and FXeOXeOXeF are nearly half of the formal charges expected for purely ionic interactions (Xe, +2; O, −2; F, −1) and are consistent with semi-ionic bonding. The $Xe_{(1)}$ and $Xe_{(2,2A)}$ charges of the free cation (+1.085 and +1.095, respectively) are in accordance with resonance structures (**1**) and (**2**) and do not change significantly when $[XeOXeOXe]^{2+}$ forms fluorine bridges with the [μ-F(ReO_2F_3)$_2$]$^-$ anions of the ion pair (+1.061 and +1.095), but decrease significantly upon formation of the hypothetical FXeOXeOXeF molecule (+0.966 and +1.044). The O charges become

more negative upon ion-pair formation ($[XeOXeOXe]^{2+}$, −0.638; $[XeOXeOXe][\mu\text{-}F(ReO_2F_3)_2]_2$, −0.792), and are most negative in the neutral FXeOXeOXeF molecule (−0.911). The $F_{(1,1A)}$ charges of the ion pair (−0.621) are similar to those of FXeOXeOXeF (−0.616). The positive charge transferred from the XeOXeOXe-moiety of the ion pair (+0.333) to its anions is considerably less than that transferred from the XeOXeOXe-moiety of FXeOXeOXeF (+0.768) to its F-ligands.

The $Xe_{(1)}$−$O_{(1,1A)}$ bond orders are comparable among the three species, ranging from 0.321 to 0.342. The $Xe_{(2,2A)}$−$O_{(1,1A)}$ bond orders are similar for free $[XeOXeOXe]^{2+}$ (0.486) and for the ion pair (0.461). In contrast, the $Xe_{(2,2A)}$−$O_{(1,1A)}$ bond orders of FXeOXeOXeF (0.395) are smaller, indicating that the $Xe_{(2,2A)}$−$O_{(1,1A)}$ bonds are less covalent than the $Xe_{(1)}$−$O_{(1,1A)}$ bonds. The $Xe_{(2,2A)}$---$F_{(1,1A)}$ bridge bond orders of the ion pair (0.141) are approximately half of the $Xe_{(2,2A)}$−$F_{(1,1A)}$ bond orders of FXeOXeOXeF (0.259), indicating significantly weaker covalent interactions for the $Xe_{(2,2A)}$---$F_{(1,1A)}$ bridge bonds of the ion pair than for the terminal $Xe_{(2,2A)}$−$F_{(1,1A)}$ bonds of FXeOXeOXeF. The $Xe_{(1)}$ valences of the ion pair (0.656) and FXeOXeOXeF (0.692) are only slightly greater than that of the free cation (0.636), whereas the $Xe_{(2,2A)}$ valences increase significantly from $[XeOXeOXe]^{2+}$ (0.484) to the ion-pair (0.600), and are highest in FXeOXeOXeF (0.660). The $O_{(1,1A)}$ valences of the ion pair (0.786) are comparable to those of the free cation (0.808) and slightly greater than the $O_{(1,1A)}$ valences of FXeOXeOXeF (0.741). The $F_{(1,1A)}$ atom valences are in accordance with the semi-ionic characters of the $Xe_{(2,2A)}$---$F_{(1,1A)}$ bonds in the ion pair (0.443) and FXeOXeOXeF

(0.260). The higher valences of the bridging $F_{(1,1A)}$ atoms of the ion pair are in accordance with their higher coordination numbers.

6.2.4.3. QTAIM Analyses

The natures of the Xe−O and Xe−F bonds in the free $[XeOXeOXe]^{2+}$ cation, the $[XeOXeOXe][\mu\text{-}F(ReO_2F_3)_2]_2$ ion pair, and the hypothetical FXeOXeOXeF molecule have been investigated by complimentary use of the quantum theory of atoms in molecules QTAIM[316] and the topological[317] analysis of the Becke and Edgecombe electron localization function (ELF).[318]

The contour maps of the charge densities showing the bond paths and intersections of atomic surfaces (Figure 6.3), charge density contour maps of the Laplacian distributions ($\nabla^2\rho$) (Figure 6.3), and valence shells of charge concentration (VSCC) relief maps ($-\nabla^2\rho$) (Figure D4) are provided for $[XeOXeOXe]^{2+}$, $[XeOXeOXe][\mu\text{-}F(ReO_2F_3)_2]_2$, and FXeOXeOXeF.

For two atoms to be bonded to one another, they must be linked by a bond path, indicating that some electronic charge is accumulated between the two nuclei. The presence of a bond path implies the existence of a bond critical point along it, where the charge density, ρ, is at its minimum value, but is a maximum with respect to lines perpendicular to its bond path.[316] The charge distributions (Figure 6.3) of the aforementioned species exhibit such bond paths between the Xe and O nuclei and between the Xe and F nuclei. Several AIM properties (Tables 6.5 and D10) evaluated at

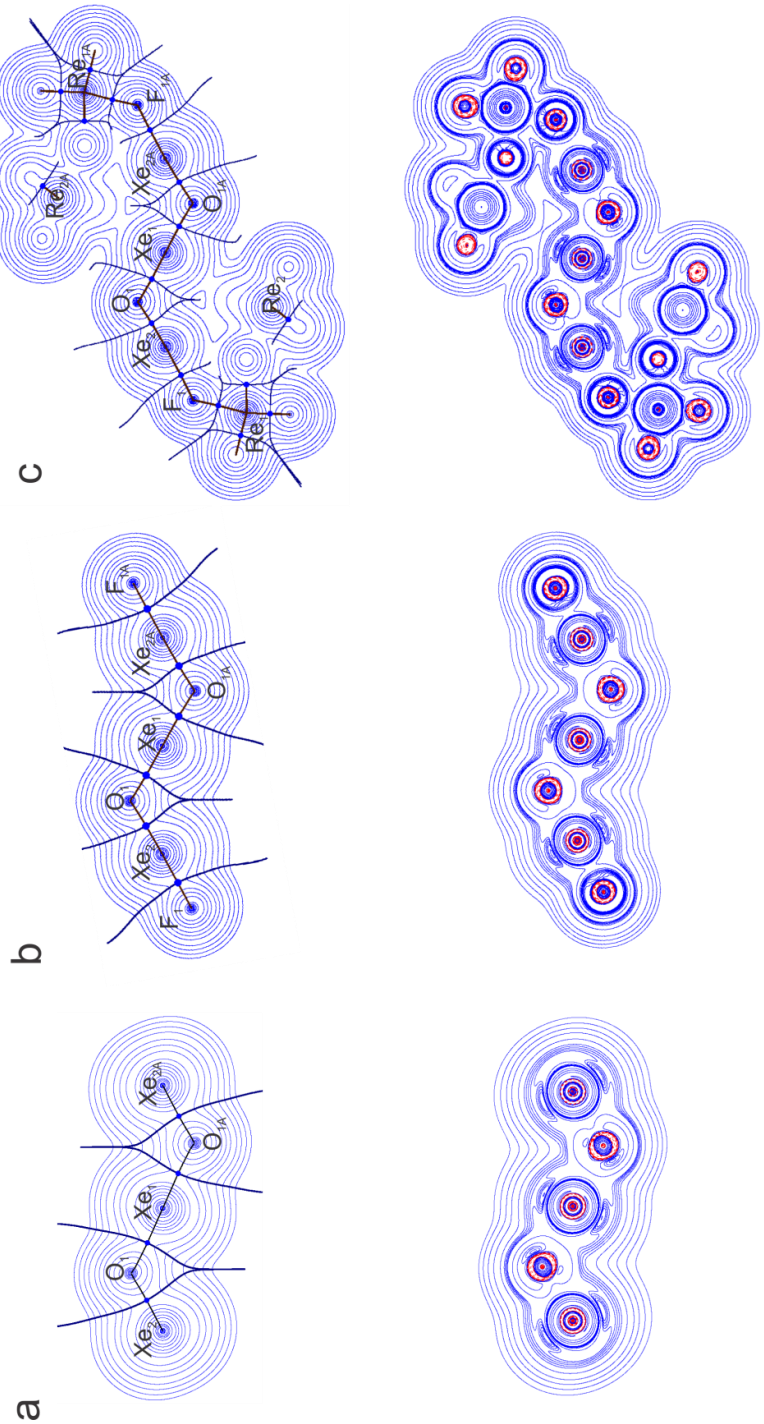

Figure 6.3. Contour maps of the charge density showing the bond paths and the intersection of the interatomic surfaces (top) and charge density contour maps of the Laplacian distribution (bottom) in (a) $[XeOXeOXe]^{2+}$, (b) FXeOXeOXeF, and (c) $[XeOXeOXe][\mu\text{-}F(ReO_2F_3)_2]_2$. The nuclear positions in the contour maps of the charge density are identical to those in the contour maps of the Laplacian distribution. The contour values start at ±0.001 a.u. and increase in the order ±2 x 10^n, ±4 x 10^n, and ±8 x 10^n with n starting at −3 and increasing in steps of 1 to give a maximum contour value of 8 x 10^6 with several additional contour values on the contour maps of the Laplacian distribution (±0.05, ±0.06, ±0.07, ±0.5, ±0.55, ±0.6, ±0.65, ±0.7, ±0.75 a.u.). Bond critical points are denoted by blue dots. Solid blue contours denote positive and dashed red lines denote negative values of $\nabla^2\rho$.

Table 6.5. QTAIM Density of all Electrons (ρ_b), Laplacian of Electron Density ($\nabla^2\rho_b$), Energy Density (H_b), QTAIM Delocalization Indexes (δ), QTAIM Atomic Populations ($\bar{N}$), and ELF Basin Populations ($\bar{N}$) in $[XeOXeOXe]^{2+}$, FXeOXeOXeF, and $[XeOXeOXe][\mu\text{-}F(ReO_2F_3)_2]_2$ [a,b,c]

Bond	ρ_b	$\nabla^2\rho_b$	H_b	δ	$\bar{N}$		$\bar{N}$[A]	
				$[XeOXeOXe][\mu\text{-}F(ReO_2F_3)_2]_2$				
Xe_1-O_1	0.091	0.170	−0.023	0.81	$\bar{N}(Xe_1)$	52.96	$\bar{N}[C(Xe_1)]^d$	46.34
Xe_2-O_1	0.123	0.161	−0.048	1.12	$\bar{N}(Xe_2)$	52.92	$\bar{N}[V(Xe_1)]$	7.15
Xe_2---F_1	0.058	0.168	−0.008	0.43	$\bar{N}(O_1)$	8.75	$\bar{N}[C(Xe_2)]^d$	46.34
					$\bar{N}(F_1)$	9.68	$\bar{N}[V(Xe_2)]$	7.02
							$\bar{N}[C(O_1)]$	2.12
							$\bar{N}[V(O_1)]$	6.78
							$\bar{N}[C(F_1)]$	2.18
							$\bar{N}[V(F_1)]$	7.57
				$[XeOXeOXe]^{2+}$				
Xe_1-O_1	0.084	0.162	−0.018	0.78	$\bar{N}(Xe_1)$	52.94	$\bar{N}[C(Xe_1)]^d$	46.42
Xe_2-O_1	0.125	0.142	−0.049	1.26	$\bar{N}(Xe_2)$	52.93	$\bar{N}[V(Xe_1)]$	7.16
					$\bar{N}(O_1)$	8.59	$\bar{N}[C(Xe_2)]^d$	46.42
							$\bar{N}[V(Xe_2)]$	7.05
							$\bar{N}[C(O_1)]$	2.12
							$\bar{N}[V(O_1)]$	6. 62
				FXeOXeOXeF				
Xe_1-O_1	0.096	0.171	−0.027	0.86	$\bar{N}(Xe_1)$	53.09	$\bar{N}[C(Xe_1)]^e$	45.79
Xe_2-O_1	0.108	0.173	−0.036	0.97	$\bar{N}(Xe_2)$	52.97	$\bar{N}[V(Xe_1)]$	7.24
Xe_2-F_1	0.098	0.233	−0.028	0.77	$\bar{N}(O_1)$	8.86	$\bar{N}[C(Xe_2)]^e$	45.79
					$\bar{N}(F_1)$	9.63	$\bar{N}[V(Xe_2)]$	7.10
							$\bar{N}[C(O_1)]$	2.13
							$\bar{N}[V(O_1)]$	6.85
							$\bar{N}[C(F_1)]$	2.16
							$\bar{N}[V(F_1)]$	7.46

[a] B3LYP/aug-cc-pVDZ (-PP). [b] The au for $\nabla^2\rho_b$ is e/a_0^5 (1 au = 24.098 e Å^{-5}). The au for ρ_b is e/a_0^3 (1 au = 6.748 e Å^{-3}). The au for H is e^2/a_0^4 (1 au = E_h/a_0^3 = 6.748 E_h/Å^3). a_0 = Bohr radius = 0.52918 Å. e = charge on an electron. E_h = hartree = e^2/a_0. [c] For atom labeling, see Figures 6.1 and D3. [d] $\bar{N}[C(Xe_1)] = \frac{1}{3}\{178 - (2\,\bar{N}[C(O_1)] + 2\,\bar{N}[V(O_1)])\} - \bar{N}[V(Xe_1)]$; $\bar{N}[C(Xe_2)] = \frac{1}{3}\{178 - (2\,\bar{N}[C(O_1)] + 2\,\bar{N}[V(O_1)])\} - \bar{N}[V(Xe_2)]$. [e] $\bar{N}[C(Xe_1)] = \frac{1}{3}\{196 - (2\bar{N}[C(O)] + 2\bar{N}[V(O)] + 2\bar{N}[C(F)] + 2\bar{N}[V(F)])\} - \bar{N}[V(Xe_1)]$; $\bar{N}[C(Xe_2)] = \frac{1}{3}\{196 - (2\bar{N}[C(O)] + 2\bar{N}[V(O)] + 2\bar{N}[C(F)] + 2\bar{N}[V(F)])\} - \bar{N}[V(Xe_2)]$.

.

the bond critical points (denoted by subscripted b in the ensuing discussion and by blue dots in Figure 6.3) can be used to assess the nature of a bond.[316] For example, all significantly negative values for the Laplacian of the electron density ($\nabla^2\rho_b$) and a density of electrons (ρ_b) greater than 0.2 au are associated with covalent bonding. Significantly negative values for the total energy density of Cremer and Kraka (H_b) are also consistent with strong covalent bonds. The energy, H_b, is defined as the sum of G_b and V_b, where G_b is the Lagrangian kinetic energy and V_b is the potential energy density. In covalent bonds, G_b is dominated by V_b, giving a negative value for H_b. When dealing with semi-ionic bonds such as encountered in the present study, the sign or the small absolute values of the above properties can be ambiguous, and it is necessary to look at the combined properties to characterize the nature of the bond. In the present case, the delocalization indices (δ) were also considered, where the delocalization index provides a quantitative measure of the number of electron pairs delocalized between two atomic spaces.

The Xe−O bond properties of $[XeOXeOXe]^{2+}$, $[XeOXeOXe][\mu\text{-}F(ReO_2F_3)_2]_2$, and FXeOXeOXeF are consistent with resonance structures **(1)** and **(2)** and with the NBO analyses (see above). The small ρ_b values ($Xe_{(1)}$–$O_{(1,1A)}$, 0.084–0.096 au; $Xe_{(2,2A)}$–$O_{(1,1A)}$, 0.108–0.125 au) and positive $\nabla^2\rho_b$ values ($Xe_{(1)}$–$O_{(1,1A)}$, 0.162–0.171 au; $Xe_{(2,2A)}$–$O_{(1,1A)}$, 0.142–0.173 au) are consistent with semi-ionic Xe–O bonds. This description is supported by small delocalization indices, δ_{Xe-O} ($Xe_{(1)}$–$O_{(1,1A)}$, 0.78–0.86; $Xe_{(2,2A)}$–$O_{(1,1A)}$, 0.97–1.26). The delocalization indices of the terminal $Xe_{(2,2A)}$−$O_{(1,1A)}$ bonds are greater than those of the central $Xe_{(1)}$−$O_{(1,1A)}$ bonds and are consistent with the shorter, more covalent, $Xe_{(2,2A)}$−$O_{(1,1A)}$ bonds observed for $[XeOXeOXe]^{2+}$ in the crystal structure of

$[XeOXeOXe][\mu\text{-}F(ReO_2F_3)_2]_2$ and those calculated for $[XeOXeOXe]^{2+}$, the $[XeOXeOXe][\mu\text{-}F(ReO_2F_3)_2]_2$ ion pair, and FXeOXeOXeF. In the case of FXeOXeOXeF, the gap between $\delta_{Xe(1)-O(1,1A)}$ and $\delta_{Xe(2,2A)-O(1,1A)}$ is smaller, in accordance with terminal and central semi-ionic Xe–O bonds that possess similar covalent characters. The very small negative values of the total energy densities, H_b ($Xe_{(1)}$–$O_{(1,1A)}$, −0.018 to −0.027 au; $Xe_{(2,2A)}$–$O_{(1,1A)}$, −0.036 to −0.049 au), are also in agreement with semi-ionic description for the Xe−O bonds, where the more negative H_b values correspond to the shorter, more covalent terminal $Xe_{(2,2A)}$−$O_{(1,1A)}$ bonds of all three species.

The $Xe_{(2,2A)}$---$F_{(1,1A)}$ bond properties of $[XeOXeOXe][\mu\text{-}F(ReO_2F_3)_2]_2$ and FXeOXeOXeF (ρ_b, 0.058 and 0.098 au; $\nabla^2 r_b$, 0.168 and 0.233 au; $\delta_{Xe(2,2A)---F(1,1A)}$, 0.43 and 0.77 au; H_b, –0.008 and –0.028 au, respectively) show that the $Xe_{(2,2A)}$---$F_{(1,1A)}$ bridge bonds of $[XeOXeOXe][\mu\text{-}F(ReO_2F_3)_2]_2$ are considerably more ionic than the terminal $Xe_{(2,2A)}$–$F_{(1,1A)}$ bonds of FXeOXeOXeF. This is consistent with the ionic formulations that have been adopted for the gas-phase and solid state ion pairs.

The Xe and O valence electron lone pair (VELP) charge densities are readily discernable on the contour maps of $\nabla^2\rho$ (Figure 6.3). The charge densities of the three Xe VELPS combine to form tori around each Xe atom (see ELF Analyses). The tori lie in planes that are perpendicular to the molecular planes of $[XeOXeOXe]^{2+}$, FXeOXeOXeF, and the XeOXeOXe-plane of $[XeOXeOXe][\mu\text{-}F(ReO_2F_3)_2]_2$ so that the plane of the charge density contour map depicted in Figure 6.3 passes through each torus to give two VELP charge concentrations on either side of each Xe core.

Although the $F_{(1,1A)}$ VELP charge densities exhibit essentially spherical distributions in FXeOXeOXeF and $[XeOXeOXe][\mu\text{-}F(ReO_2F_3)_2]_2$, the Laplacian contour plot of the electron density around $F_{(1,1A)}$ and $Xe_{(2,2A)}$ in FXeOXeOXeF differs slightly from that of the ion pair. The Laplacian distribution of the charge density in FXeOXeOXeF (Figure 6.3b) exhibits a contour line enclosing $F_{1,1A}$ and $Xe_{2,2A}$, whereas the contours of $F_{1,1A}$ and $Xe_{2,2A}$ are not joined in the plot of the Laplacian distribution in the ion pair (Figure 6.3c). This is in agreement with the more ionic characters of the $Xe_{(2,2A)}$---$F_{(1,1A)}$ bridge bonds relative to those of the terminal $Xe_{(2,2A)}$−$F_{(1,1A)}$ bonds in FXeOXeOXeF.

Maxima in the relief maps ($-\nabla^2\rho$) of $[XeOXeOXe]^{2+}$, FXeOXeOXeF, and $[XeOXeOXe][\mu\text{-}F(ReO_2F_3)_2]_2$ (Figure D4) denote maxima in charge concentrations. When the inner spike at its nucleus is counted, the Xe atom exhibits five alternating regions of charge concentration and depletions corresponding to five quantum shells. The VSCCs are not strongly linked for the Xe−O, Xe−F, and Xe---F bonds. Rather, their charges are predominantly concentrated in their atomic basins with small, shared charge concentrations. The Xe and O VELP densities are considerably more diffuse and less apparent in the VSCC relief maps (Figure D4) than in their $\nabla^2\rho$ contour maps. Nevertheless, cusps are discernable on the Xe atoms that correspond to the combined charge concentrations of the Xe VELPS, whereas the O VELPS are not discernable. Small charge concentration cusps are visible between the Xe and O atoms. In the case of FXeOXeOXeF and $[XeOXeOXe][\mu\text{-}F(ReO_2F_3)_2]_2$, cusps between F and Xe are not clearly distinguishable.

6.2.4.4. Electron Localization Function (ELF) Analyses

ELF analyses were carried out for $[XeOXeOXe]^{2+}$ (C_{2h}), FXeOXeOXeF (C_i), and $[XeOXeOXe][\mu\text{-}F(ReO_2F_3)_2]_2$ (C_i) primarily to visualize the behaviors of the Xe VELPs of these species. In the ensuing discussion, the following abbreviations denote an atomic basin population, $\bar{N}$[A]; the electron localization function, $\eta(\mathbf{r})$; a core basin, C(A); a monosynaptic valence basin, V(A); and a closed isosurface, $\eta(\mathbf{r}) = f$ value, at which a specific isosurface can be visualized. ELF parameters are provided in Tables 6.5 and D10 and ELF isosurface plots at the isosurface contour value $\eta(\mathbf{r}) = 0.60$ are shown for the localization domains of $[XeOXeOXe]^{2+}$, FXeOXeOXeF, and $[XeOXeOXe][\mu\text{-}F(ReO_2F_3)_2]_2$ in Figures 6.4 and D5, respectively.

The ELF population analyses (Tables 6.5 and D10) are in agreement with the QTAIM results (see above). The ELF basin populations of the $Xe_{(1)}$ and $Xe_{(2,2A)}$ cores are comparable for $[XeOXeOXe]^{2+}$, FXeOXeOXeF, and the ion pair. In all cases, the $Xe_{(1)}$ and $Xe_{(2,2A)}$ core populations are close to the ideal core population of the Xe atom, [Kr] $4d^{10}$ = 46 e. The ELF valence population analyses suggest an interpretation of the bonding in terms of a significant delocalization of electron density between the valence shells of Xe and those of its neighboring atoms. Overall, the electron density transfer from the xenon atoms to O in free $[XeOXeOXe]^{2+}$ and to F and O in FXeOXeOXeF and the ion pair leads to O and F valence population increases of 0.5 to 0.9 e, consistent with semi-ionic bonding. A similar interpretation applies to the bonding in XeF_2 [319] and KrF_2.[320]

The localization domain reduction tree diagrams[321] provide the hierarchies of the ELF basins and the corresponding basin separation values (f_{sep}) for $[XeOXeOXe]^{2+}$,

a

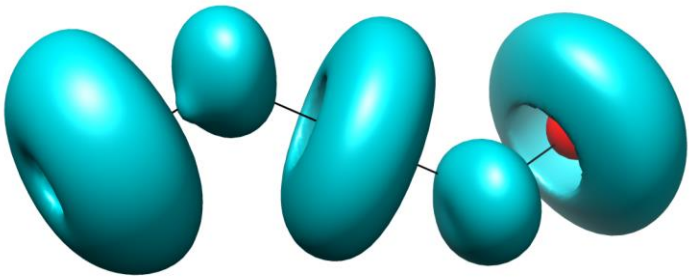

b

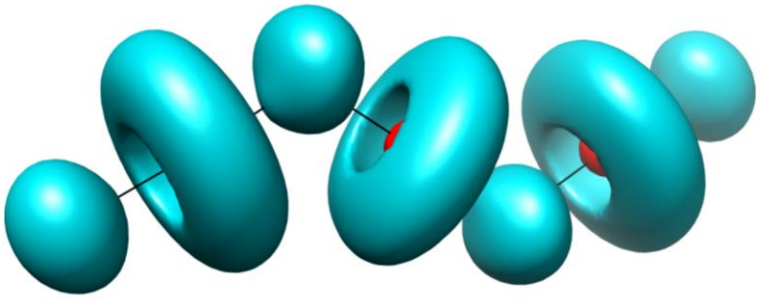

Figure 6.4. ELF isosurface plots at $\eta(\mathbf{r})$ = 0.60 (B3LYP/aug-cc-pVDZ(-PP)) for (a) $[XeOXeOXe]^+$ and (b) [FXeOXeOXeF]. Color code: red = core; blue = monosynaptic basin.

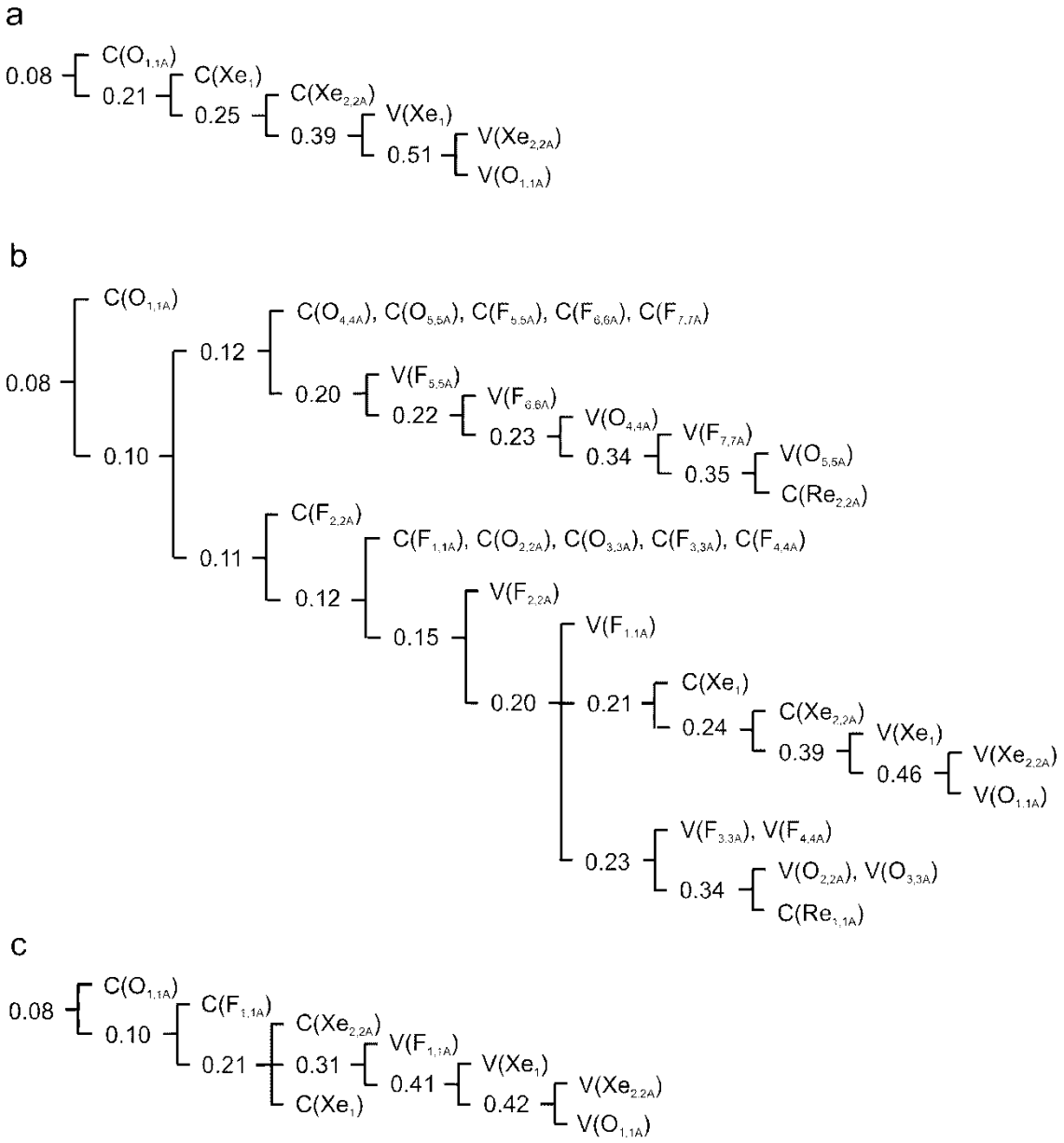

Figure 6.5. Reduction of the localization diagrams for (a) $[XeOXeOXe]^{2+}$, (b) $[XeOXeOXe][\mu\text{-}F(ReO_2F_3)_2]_2$, and (c) FXeOXeOXeF showing the ordering of localization nodes and the boundary isosurface values, $\eta(\mathbf{r})$ (also referred to as f_{sep}-values), at which the reducible domains split.

FXeOXeOXeF, and [XeOXeOXe][μ-F(ReO_2F_3)$_2$]$_2$ (Figure 6.5). The ELF reduction of localization diagram of [XeOXeOXe][μ-F(ReO_2F_3)$_2$]$_2$ shows that the ion pair initially separates (f_{sep} = 0.10) into [XeOXeOXe][($Re_{(1,1A)}O_2F_4$)]$_2$ and two $Re_{(2,2A)}O_2F_3$ *f*-localization domains. The former separates (f_{sep} = 0.15) into V($F_{(2,2A)}$) and the [XeOXeOXe][μ-$F_{(1,1A)}$($Re_{(1,1A)}O_2F_2$)]$_2$ *f*-localization domain. The latter subsequently separates (f_{sep} = 0.20) into V($F_{(1,1A)}$), and the $Re_{(1,1A)}O_2F_2$ and XeOXeOXe *f*-localization domains. The XeOXeOXe domain separates (f_{sep} = 0.39) into V($Xe_{(1)}$) and the $Xe_{(2,2A)}O_{(1,1A)}$ *f*-localization domains, which finally separate (f_{sep} = 0.46) into V($Xe_{(2,2A)}$) and V($O_{(1,1A)}$). For comparison, the XeOXeOXe domain separates at similar values for $[XeOXeOXe]^{2+}$ (f_{sep} = 0.39) and FXeOXeOXeF (f_{sep} = 0.41), whereas V($Xe_{(2,2A)}$) and V($O_{(1,1A)}$) separate at f_{sep} = 0.51 for $[XeOXeOXe]^{2+}$ and at f_{sep} = 0.42 for FXeOXeOXeF. The earlier separations of the V($Xe_{(1)}$) basins from their XeOXeOXe domains relative to those of V($Xe_{(2,2A)}$) is consistent with central $Xe_{(1)}$–$O_{(1,1A)}$ bonds that are more ionic than the terminal $Xe_{(2,2A)}$–$O_{(1,1A)}$ bonds and with resonance structures (**1**) and (**2**), their NBO analyses (Tables D9), and the QTAIM findings (Table 6.5, D10). The ELF isosurface values at which the V($F_{(1,1A)}$) valence basins separate ([XeOXeOXe][μ-F(ReO_2F_3)$_2$]$_2$, f_{sep} = 0.20; FXeOXeOXeF, f_{sep} = 0.31) are consistent with the lower covalent characters of the $Xe_{(2,2A)}$---$F_{(1,1A)}$ bridge bonds in the ion pair relative to those of the $Xe_{(2,2A)}$–$F_{(1,1A)}$ bonds in FXeOXeOXeF, and their respective bond orders obtained from the NBO analyses, i.e., [XeOXeOXe][μ-F(ReO_2F_3)$_2$]$_2$ (0.141) and FXeOXeOXeF (0.259).

The Xe valence basins consist of the toroidal-shaped valence electron densities resulting from the combination of the three non-bonding VELP domains of Xe with

exposed atomic core densities at their centers. Such torus-shaped basins have been calculated for XeF_2,[319,322] $[XeF_3]^-$,[322] $[XeOTeF_5]^+$,[242] and for the NgF_2 (Ng = Kr or Xe) ligands in $[BrOF_2][AsF_6]\cdot 2NgF_2$.[319,320] Variations in VELP behavior have been noted for the NgF_2 adducts of the $[BrOF_2]^+$ cation in $[BrOF_2][AsF_6]\cdot 2NgF_2$ where NgF_2 and $[AsF_6]^-$ are fluorine bridged to Br(V). In this case, the Br(V) valence basin is an electron lone pair that accommodates its shape and volume to the environment available to it in its complex. This contrasts with the Br(V) VELP of the free cation, $[BrOF_2]^+$, which is dramatically expanded in its less constrained environment.

In the present series, the volumes of the toroidal $V(Xe_{(1)})$ and $V(Xe_{(2,2A)})$ valence basins ($\eta(\mathbf{r}) = 0.60$) increase with decreasing NBO charge of the XeOXeOXe moiety, i.e., $[XeOXeOXe]^{2+}$ (1.88 $Å^3$ ($Xe_{(1)}$), 1.93 $Å^3$ ($Xe_{(2,2A)}$); +2.00), $[XeOXeOXe][\mu\text{-}F(ReO_2F_3)_2]_2$ (2.41 $Å^3$ ($Xe_{(1)}$), 2.86 $Å^3$ ($Xe_{(2,2A)}$); +1.67), FXeOXeOXeF (3.01 $Å^3$ ($Xe_{(1)}$), 3.37 $Å^3$ ($Xe_{(2,2A)}$); +1.23). Plots of the xenon valence basin volumes versus charge are near-linear for both the terminal and central xenon valence basin volumes. In all three cases, the volume of $V(Xe_{(2,2A)})$ is larger than that of $V(Xe_{(1)})$. In general, the valence basin of the central $Xe_{(1)}$ atom is symmetrically bonded to oxygen and is more confined than the corresponding $Xe_{(2,2A)}$ valence basins. In FXeOXeOXeF, where the $Xe_{(2,2A)}$–$F_{(1,1A)}$ bonds are stronger and more confining than the $Xe_{(2,2A)}$---$F_{(1,1A)}$ bridge bonds of $[XeOXeOXe][\mu\text{-}F(ReO_2F_3)_2]_2$, the terminal and central Xe valence basins are the most symmetric and their toroidal holes most open, exposing the $Xe_{(2,2A)}$ core charges for interaction with the $F_{(1,1A)}$ ligands of the anions. The similar shapes of the $Xe_{(1)}$ and $Xe_{(2,2A)}$ tori of FXeOXeOXeF are consistent with their similar bonding environments and

abilities to confine their Xe VELP volumes and shapes. The $Xe_{(2,2A)}$ tori of the ion pair are considerably more expanded and their valence holes more contracted, in accordance with the asymmetries that result from their weaker $Xe_{(2,2A)}$---$F_{(1,1A)}$ interactions. The $Xe_{(2,2A)}$ tori of the free $[XeOXeOXe]^{2+}$ cation, where the isosurface is the least confined, are the most asymmetric among the series, standing in marked contrast to those of FXeOXeOXeF and the ion pair. The $Xe_{(2,2A)}$ tori of $[XeOXeOXe]^{2+}$ are significantly contracted at the extremities of the cation, giving somewhat conical-shaped tori and significantly narrowed toroidal holes that correspond to σ-holes (see MEPS discussion).

Similar bonding modalities arise for the $[FNgNCH]^{+}$ cations (Ng = Kr or Xe), as described in 1989 by MacDougall, Bader, and Schrobilgen,[323] where the Lewis acid behaviors of the $[NgF]^{+}$ cations towards HCN were also shown to be due to the presence of holes in the valence shells of charge concentrations for Kr(II) and Xe(II) which expose their Ng cores to the nitrogen VELP of HCN.

6.2.4.5. Molecular Electrostatic Potential Surface (MEPS Analyses)

The MEPSs of the $[XeOXeOXe]^{2+}$ cation, FXeOXeOXeF, and the $[XeOXeOXe][\mu\text{-}F(ReO_2F_3)_2]_2$ ion pair have been calculated at the 0.001 electron $bohr^{-3}$ contour level. The color scale used in Figure 6.6a differs from that used in Figures 6.6b and 6.6c, whereas the energy scales are directly comparable. The $[XeOXeOXe]^{2+}$ cation displays high positive electrostatic potentials on the terminal $Xe_{(2,2A)}$ atoms (895 kJ mol^{-1}) and between the $Xe_{(1)}$ and $Xe_{(2,2A)}$ atoms (901 kJ mol^{-1}) (Figure 6.6a). The most positive

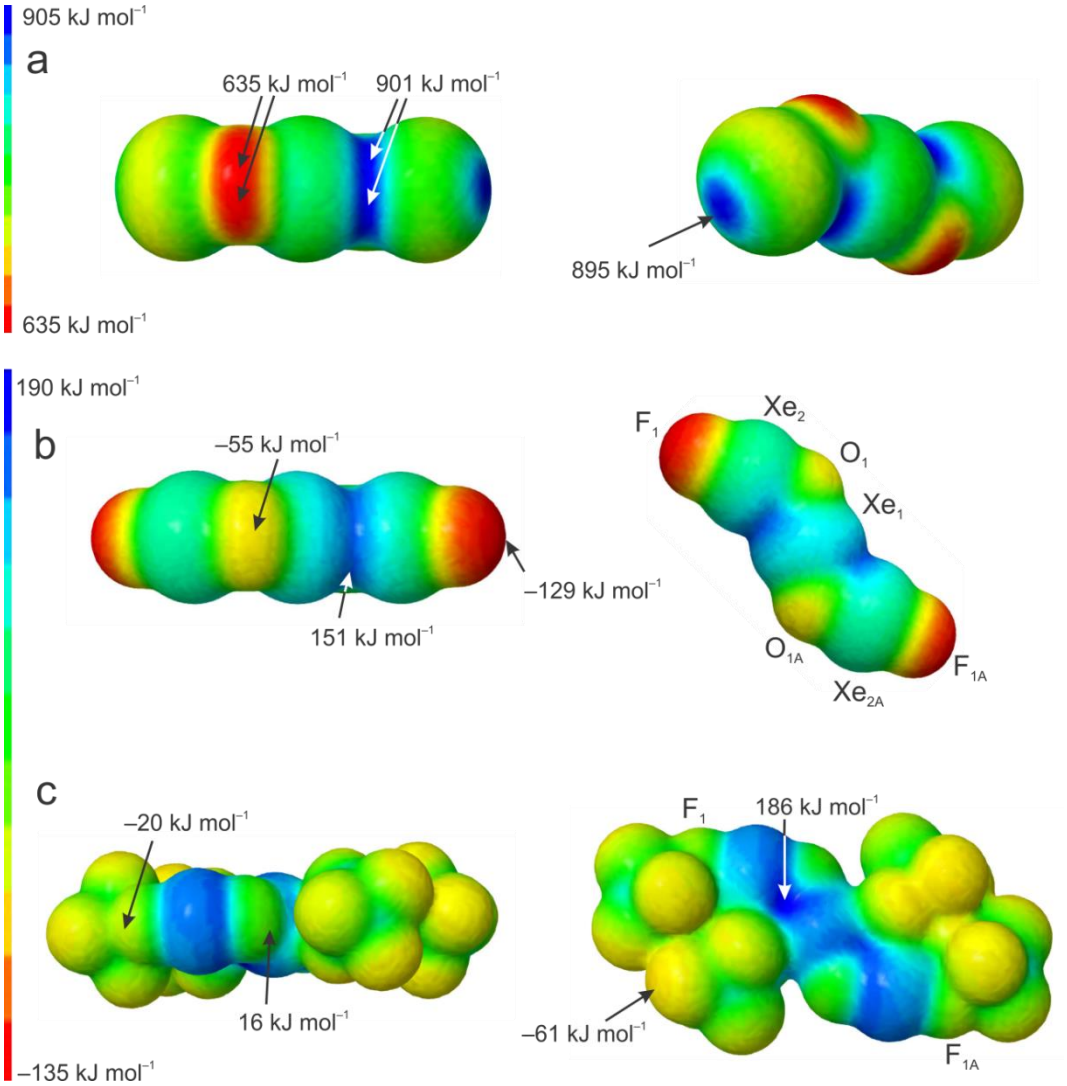

Figure 6.6. Calculated molecular electrostatic potentials at the 0.001 electron bohr^{-3} surfaces of (a) the $[XeOXeOXe]^{2+}$ cation, (b) FXeOXeOXeF, and (c) the $[XeOXeOXe][\mu\text{-}F(ReO_2F_3)_2]_2$ ion pair. The color scales range from red (−905 kJ mol^{-1}) to blue (635 kJ mol^{-1}) for $[XeOXeOXe]^{2+}$ and from red (−135 kJ mol^{-1}) to blue (190 kJ mol^{-1}) for FXeOXeOXeF and $[XeOXeOXe][\mu\text{-}F(ReO_2F_3)_2]_2$. Maximum and minimum electrostatic potentials are indicated by arrows. The optimized geometries and molecular surface electrostatic potentials were calculated at the B3LYP/aug-cc-pVDZ(-PP) level of theory.

electrostatic potentials occur between $Xe_{(1)}$ and $Xe_{(2,2A)}$, and are opposed to the lowest electrostatic potential values which are located on the O atoms (635 kJ mol^{-1}). The highest electrostatic potentials on the $Xe_{(2,2A)}$ atoms are opposite to the $Xe_{(2,2A)}$–O bonds and correspond to highly directional σ-holes.[324-328] In the ELF analysis described above, the σ-holes correspond to the exposed $Xe_{(2,2A)}$ cores situated at the centers of the toroidal $Xe_{(2,2A)}$ valence basins.

The formation of the hypothetical FXeOXeOXeF molecule by donation of a F^- VELP into the σ-hole of each $Xe_{(2,2A)}$ atom results in electrostatic potentials that are lower than those of $[XeOXeOXe]^{2+}$. The highest electrostatic surface potential still occurs between $Xe_{(1)}$ and $Xe_{(2,2A)}$ (151 kJ mol^{-1}), whereas the lowest electrostatic surface potentials now occurs on the terminal fluorine atoms (–129 kJ mol^{-1}). The electrostatic surface potentials of the fluorine-bridged $[XeOXeOXe]^{2+}$ cation of $[XeOXeOXe][\mu\text{-}F(ReO_2F_3)_2]_2$ are somewhat higher than those of FXeOXeOXeF, but are significantly lower than those of the naked $[XeOXeOXe]^{2+}$ cation. This is corroborated by the NBO analyses (see NBO Analyses), which show that the total charge of the XeOXeOXe-moiety in the ion pair is significantly greater than that of the FXeOXeOXeF molecule. The most negative electrostatic potential values on the isosurfaces of the bridging fluorines of the ion pair (–20 kJ mol^{-1}) are significantly more positive than those of the terminal F atoms of FXeOXeOXeF (–129 kJ mol^{-1}) and the $[\mu\text{-}F(ReO_2F_3)_2]^-$ anions (–61 to –32 kJ mol^{-1}). This observation is consistent with the ionic formulation of $[XeOXeOXe][\mu\text{-}F(ReO_2F_3)_2]_2$ in its crystal structure.

6.3. Conclusion

The low-temperature synthesis of a kinetically stable salt of the novel $[XeOXeOXe]^{2+}$ cation has been accomplished by reaction of ReO_3F with XeF_2 in aHF. The synthetic approach is reliant upon ReO_3F as the oxygen source and as the progenitor of the counter ion, $[\mu\text{-}F(ReO_2F_3)_2]^-$. The reaction pathway likely involves HOXeF as an intermediate in a series of oxygen/fluorine metathesis steps that lead to $[XeOXeOXe]^{2+}$ and the $[\mu\text{-}F(ReO_2F_3)_2]^-$ anion. The $[XeOXeOXe][\mu\text{-}F(ReO_2F_3)_2]_2$ salt is the first instance where the $[\mu\text{-}F(ReO_2F_3)_2]^-$ anion has been used to stabilize a strong oxidant cation. The $[XeF_5]^+$ and $[Xe_2F_{11}]^+$ cations are the only other noble-gas cations to have been stabilized by metal oxide fluoride anions, namely, $[XeF_5][\mu\text{-}F(OsO_3F_2)_2]$ and $[M][fac\text{-}OsO_3F_3]$ ($[M]^+ = [XeF_5]^+, [Xe_2F_{11}]^+$).[315]

The $[XeOXeOXe]^{2+}$ cation is unique in several respects. Its discovery provides the first examples of a xenon(II) oxide, a noble-gas oxide cation, and a rare example of a noble-gas dication.[329] It is also the first noble-gas dication for which a crystal structure is available. Not only has $[XeOXeOXe][\mu\text{-}F(ReO_2F_3)_2]_2$ been unambiguously characterized by low-temperature single-crystal X-ray diffraction, its Raman spectrum and vibrational assignments have been confirmed by quantum-chemical calculations and ^{18}O-enrichment studies.

The Xe–O and Xe–F bonding in free $[XeOXeOXe]^{2+}$, the hypothetical neutral oxide fluoride, FXeOXeOXeF, and the ion pair, $[XeOXeOXe][\mu\text{-}F(ReO_2F_3)_2]_2$, were studied with the aid of NBO, QTAIM, ELF, and MEPS analyses. The Xe–O bonds of $[XeOXeOXe]^{2+}$ are semi-ionic, with the terminal Xe–O bonds exhibiting more covalent

character. The terminal Xe atoms of $[XeOXeOXe]^{2+}$ show regions of high positive electrostatic potential, opposite to their Xe–O bonds, which correspond to σ-holes. The cation-anion F-bridge interaction can be accounted for in terms of a σ-hole bond, where F atoms of the anions donate electron density to the electrophilic regions (σ-holes) of the terminal Xe atoms. As shown by the NBO, QTAIM, and ELF analyses, the Xe---F bridge bonds are weakly covalent and consistent with a true ion-pair and σ-hole bonds.

CHAPTER 7

REACTION OF MnO_3F WITH NOBLE-GAS FLUORIDES, KrF_2 AND XeF_6

7.1. Introduction

In contrast to Tc(VII) and Re(VII), for which several oxide fluorides are known,[1−37] only one Mn(VII) oxide fluoride, MnO_3F, has been synthesized and structurally characterized.[6,31,32,35,51−62] Manganese trioxide fluoride is an unstable compound at temperatures above 0 ^oC that decomposes in the pure state to MnF_2, MnO_2, and O_2 and under aHF to MnF_2 and O_2. Challenges associated with handling MnO_3F have previously prevented detailed studies of its reactivity. Moreover, the syntheses of MnO_2F_3 and $MnOF_5$ have not yet been reported.

Attempts to synthesize $MnOF_5$ and MnO_2F_3 by the reactions of MnO_3F with KrF_2 and XeF_6 are described in this Chapter. The synthetic procedures are analogous to those used to synthesize MO_2F_3 (M = Tc, Re)[17,19] and $TcOF_5$[1,2] and have led to the isolation and preliminary characterization of what is assumed to be MnF_5 and to the isolation of the previously known $[Xe_2F_{11}]_2[MnF_6]$[169,170] and $[XeF_5]_2[MnF_6]$[169,171] salts of $[Mn^{IV}F_6]^{2-}$. Reaction of MnO_3F with KrF_2 in the presence of $K[HF_2]$ in aHF also resulted in the isolation of the first example of a $[Mn^{V}F_6]^-$ salt, $K[MnF_6]$.

The $[Xe_2F_{11}]_2[MnF_6]$[169,170] and $[XeF_5]_2[MnF_6]$[169,171] salts have been previously synthesized by reaction of MnF_2 with XeF_6 at 60 ^oC and by subsequent removal of XeF_6 under dynamic vacuum at room temperature and 60 ^oC, respectively, (eqs 7.1-7.3). Both

$$MnF_2 + 5XeF_6 \xrightarrow{60\ ^oC} 4XeF_6{\cdot}MnF_4 + XeF_4 \qquad (7.1)$$

$$4XeF_6{\cdot}MnF_4 \xrightarrow[\text{vac.}]{24\ ^oC} [Xe_2F_{11}]_2[MnF_6] + 2XeF_6 \quad (7.2)$$

$$[Xe_2F_{11}]_2[MnF_6] \xrightarrow[\text{vac.}]{60\ ^oC} [XeF_5]_2[MnF_6] + XeF_6 \quad (7.3)$$

products were characterized by chemical analyses, magnetic measurements and infrared spectroscopy, and by their X-ray powder diffraction patterns which only provided incomplete structural characterizations of these compounds. Žemva and Slivnik[171] have also synthesized $[NH_4][XeF_5][MnF_6]$ by reaction of $[NH_4][MnF_3]$ with neat $nXeF_6$ ($n \geq 15$) (eq 7.1) and isolated the yellow salt, $[NH_4][XeF_5][MnF_6]$, at room temperature. The

$$[NH_4][MnF_3] + nXeF_6 \xrightarrow{0 \text{ to } 60\ ^oC} [NH_4][XeF_5][MnF_6] + XeF_x + Xe + XeF_6$$
$$n \geq 15,\ x = 2, 4 \quad (7.1)$$

product was characterized by chemical analysis, magnetic susceptibility measurements, thermogravimetric studies, and infrared and Raman spectroscopies. The vibrational assignments of the Raman spectrum were made by comparison with the experimental Raman spectrum of $[XeF_5]_2[MnF_6]$.

The only evidence for the existence of a Mn(V) fluoride is the observation of $[MnF_4]^+$ in the mass spectrum of the MnF_3–F_2 system, however, the origin of this cation is presently unclear.[172,173]

This Chapter describes the syntheses and preliminary characterizations of two new manganese(V) fluorides, which are tentatively identified as $K[MnF_6]$ and MnF_5. Additionally, the syntheses of $[Xe_2F_{11}]_2[MnF_6]$ and $[XeF_5]_2[MnF_6]$ from the reaction of MnO_3F with XeF_6 are also described. The $K[MnF_6]$, $[Xe_2F_{11}]_2[MnF_6]$, and $[XeF_5]_2[MnF_6]$ salts were structurally characterized for the first time by single-crystal X-ray diffraction. The latter two salts were also characterized by Raman spectroscopy and quantum-

chemical calculations were used to aid in vibrational assignments of their Raman spectra. A preliminary solution of the single-crystal X-ray structure of MnF_5 is also provided.

7.2. Results and Discussion

7.2.1. Reaction of MnO_3F with KrF_2 in aHF

Manganese trioxide fluoride has been synthesized in admixture with Mn_2O_7 by solvolysis of $K[MnO_4]$ in aHF (eq 7.1) (Figure E1). The resulting reaction mixture was subsequently fluorinated with F_2 gas at −15 °C in order to oxidatively fluorinate H_2O to O_2 and HF (eq 7.2). The MnO_3F/Mn_2O_7/HF mixture was isolated from $K[HF_2]$ by static

$$K[MnO_4] + HF \longrightarrow MnO_3F, Mn_2O_7, [H_3O][HF_2], K[HF_2] \quad (7.1)$$

$$H_2O + F_2 \longrightarrow 2HF + \tfrac{1}{2}O_2 \quad (7.2)$$

distillation at −20 °C into a pre-cooled (−196 °C) reactor. Subsequent addition of KrF_2 to the MnO_3F/Mn_2O_7/HF mixture and warming of the mixture to room temperature resulted in O_2 and Kr evolution. The reaction was quenched by cooling the reactor to −196 °C after the deep green solution became pale pink and a red oil had also formed at the bottom of the reaction vessel. The Raman spectrum recorded on the red oil under the frozen solution corresponded to a mixture of KrF_2 and unidentified manganese fluoride(s) (Figure E2, Appendix E). The reaction was subsequently allowed to proceed at room temperature until gas evolution ceased and the color of the oil and solution became red-violet. The Raman spectrum was recorded on the solid material that had been isolated by removal of aHF at room temperature (Figure E3, Appendix E). The latter differed from the Raman spectrum recorded on the red oil under the pale pink frozen solution (Figure

E2). Other than a band at 1840 cm^{-1}, the highest frequency bands occurred in the 600−700 cm^{-1} range and correspond to Mn−F stretching modes, confirming the formation of manganese fluoride(s). An important feature of the spectrum was a band at 1840 cm^{-1}, which corresponded to the $[O_2]^+$ stretch. Previous studies of the $[O_2]^+$ salts of manganese(IV) fluoro-anions revealed that a possible product of this reaction could be $[O_2][Mn_2F_9]$,[165] for which the ν(O−O) stretch was reported at 1838 cm^{-1}, whereas the ν(O−O) stretch occurs at 1805 cm^{-1} for $[O_2]_2[MnF_6]$.[151]

Crystallization of the resulting product was attempted by dissolving the solid in aHF which resulted in the precipitation of a grey solid under a red-purple solution. The grey solid was separated by decanting the supernatant and the solid into the side arm of the reaction vessel and then decanting only the supernatant back into the main tube of the reactor. The supernatant was maintained at −78 ^oC for three weeks. The solution was subsequently combined with the grey solid, which resulted in the dissolution and a solution color change from red-purple to very pale green. Crystallization of the product by static distillation of aHF into the pre-cooled (−78 ^oC) side arm was attempted which resulted in the formation of ruby-red, needle-shaped crystals and a small amount of a pale pink/grey solid. Low-temperature single-crystal X-ray diffraction data was collected and solved as MnF_5, however, due to twinning issues, the structure solution requires further refinement. All subsequent reactions reproduced a solid which showed an $[O_2]^+$ band in the Raman spectrum (Figure E3). In all subsequent cases, attempts to regrow crystals of MnF_5 failed.

A possible reaction sequence leading to the formation of MnF_5 that would account for $[O_2]^+$ observed at 1840 cm^{-1} (Figure E3, Appendix E) is given in eqs 7.3−7.5. The

$$2MnO_3F + 3\,KrF_2 \xrightarrow{20\,^oC} [O_2][MnF_6] + MnF_2 + 2\,O_2 + 3\,Kr \quad (7.3)$$

$$[O_2][MnF_6] \xrightarrow{20\,^oC} MnF_5 + O_2F \quad (7.4)$$

$$MnF_2 + O_2F \xrightarrow{20\,^oC} MnF_3\ (\text{grey solid}) + O_2 \quad (7.5)$$

reaction of MnO_3F with KrF_2 could have resulted in the formation of MnF_2 and $[O_2][MnF_6]$, which decomposed to MnF_5 and O_2F (eqs 7.3 and 7.4). Dioxygen fluoride subsequently oxidized MnF_2 to MnF_3, which precipitated as a grey solid (eq 7.5).

Alternatively, the reaction of MnO_3F with KrF_2 could have resulted in the formation of $[O_2][Mn_2F_9]$[165] (eq 7.6) which could also account for the peak at 1840 cm^{-1}. The

$$2MnO_3F + 3.5\,KrF_2 \longrightarrow [O_2][Mn_2F_9] + 2\,O_2 + 3.5\,Kr \quad (7.6)$$

$[O_2][Mn_2F_9]$ salt subsequently disproportionated to manganese (V), $[O_2][MnF_6]$, and manganese (III), MnF_3 (eq 7.7). The dioxygen cation $[O_2]^+$, is a powerful one-electron

$$[O_2][Mn_2F_9] \xrightarrow{20\,^oC} [O_2][MnF_6] + MnF_3\ (\text{grey solid}) \quad (7.7)$$

oxidant, which has been previously shown to act as an oxidizing agent converting Pt(IV) to Pt(V),[330] Au(III) to Au(V),[330] Ni(II) to Ni(IV),[330] and Xe to Xe(II).[264] The decomposition of the $[O_2][MnF_6]$ salt at room temperature resulted in the formation of MnF_5, which crystallized as ruby-red crystals (eq 7.8).

$$[O_2][MnF_6] \xrightarrow{20\,^oC} MnF_5 + O_2F \quad (7.8)$$

When MnO_3F reacted with KrF_2 in the presence of $K[HF_2]$, a dark red oil formed at the bottom of a red-orange solution. An attempt to record the Raman spectrum of the oil failed. Upon removal of aHF at −78 °C and room temperature, the red oil transformed

into an orange solid. The Raman spectrum was recorded on the isolated product (Figure E4), which was shown to contain $K[MnF_6]$ by single-crystal X-ray diffraction (see below). Moreover, the most intense ν(MnF) stretching band (693 cm^{-1}) appears at lower frequency than the most intense and characteristic bands of MnF_4 (744 cm^{-1})[124] and to higher frequency of MnF_3 (651 cm^{-1}).[124] The most intense band of the MnF_3 Raman spectrum, however, coincides with one of the bands of the broad Raman spectrum shown in Figure E4 and appears as a shoulder. Therefore, the broad Raman spectrum was assigned to a solid mixture that contained at least two species, $K[MnF_6]$ and MnF_3 (Figure E4, Appendix E).

The solid was divided into two portions which were dissolved in aHF to form red-orange solutions. One solution was used for ^{19}F NMR characterization (see NMR Section), and the other was used for crystal growth (see X-ray Crystallography Section).

Colorless or pale pink cubic crystals of $K[MnF_6]$ that were of a quality suitable for an X-ray structure determination were grown from HF by slow cooling of the red-orange solution from −25 to −30 °C over a period of 3 h. An insoluble grey solid, presumably MnF_3, also precipitated from the solution; however, it was not structurally identified.

The formation of $K[MnF_6]$ may result from the displacement of the $[O_2]^+$ cation by the K^+ cation (7.9). All subsequent attempts to synthesize $K[MnF_6]$ resulted in the

$$[O_2][MnF_6] + K^+ + F^- \longrightarrow K[MnF_6] + O_2F \qquad (7.9)$$

formation of a solid mixture which Raman spectrum (Figure E5) was similar to that shown in (Figure E4), additionally bands of $K_2[MnF_6]$ (601, 516, 309 cm^{-1}) were also observed. Dissolution of this solid mixture in aHF always resulted in the reappearance of

the red oil. Attempts to crystallize the product by maintaining the solution at −78 °C or by slow removal of aHF under dynamic vacuum at −78 °C failed.

7.2.2. Reaction of MnO_3F with XeF_6 in aHF

Manganese trioxide fluoride did not react with XeF_6 in aHF up to room temperature as was confirmed by Raman spectroscopy. The reaction proceeded very slowly at room temperature and was accompanied by slow gas evolution. The Raman spectrum of the solid mixture indicated that only partial reaction of MnO_3F with XeF_6 had occurred at room temperature and was assigned to MnO_3F, $XeF_6{\cdot}1.5HF$, $[Xe_2F_{11}]_2[MnF_6]$, $XeOF_4$ and/or $XeOF_4{\cdot}XeF_6$, which was identified by comparison with the $XeOF_4{\cdot}XeF_2$ adduct[189] (Figure E6, Appendix E). The reaction of MnO_3F with XeF_6 differs significantly from the analogous reactions of its heavy transition metal analogues, MO_3F (M = Tc, Re), which react with XeF_6 in a series of oxygen/fluorine metathesis reactions that result in the formation of MO_2F_3 and $XeOF_4$.[17,19] The complete reaction of MnO_3F with XeF_6 was indicated by a change of the solution color from deep green to dark orange. The resulting product mixture, $[Xe_2F_{11}]_2[MnF_6]$, $XeOF_4$ and/or $XeOF_4{\cdot}XeF_6$, and $XeF_6{\cdot}1.5HF$ (eq 7.2)

$$MnO_3F + 7XeF_6 \xrightarrow{HF} [Xe_2F_{11}]_2[MnF_6],\ XeOF_4 \text{ and/or } XeOF_4{\cdot}XeF_6,\ XeF_6{\cdot}1.5HF \qquad (7.2)$$

was isolated upon removal of HF under dynamic vacuum at −78 °C. The $[Xe_2F_{11}]_2[MnF_6]$ salt exhibits thermochromic behaviour, changing color from orange to yellow when the compound is cooled below −50 °C, in agreement with previous observations.[169] Needle-shaped crystals of $[Xe_2F_{11}]_2[MnF_6]$ that were of a quality suitable for an X-ray crystal

structure determination were grown by cooling the HF solution of the salt from −10 to −15 °C over a 4 h period. The Raman spectrum was recorded on the resulting isolated crystalline compound.

Orange $[XeF_5]_2[MnF_6]$ was synthesized from $[Xe_2F_{11}]_2[MnF_6]$ by removal of XeF_6 under dynamic vacuum at room temperature (eq 7.3). The solid readily dissolved in aHF

$$[Xe_2F_{11}]_2[MnF_6] \xrightarrow{\text{vac.}} [XeF_5]_2[MnF_6] + 2XeF_6 \quad (7.3)$$

forming an orange solution. The $[XeF_5]_2[MnF_6]$ salt also exhibited thermochromic behaviour in the solid state and in solution, as observed for $[Xe_2F_{11}]_2[MnF_6]$. Orange needle-shaped crystals of $[XeF_5]_2[MnF_6]$ were grown at room temperature (3 days) by slow static distillation of HF, under 1.1 atm of N_2 gas, into the pre-cooled (–78 °C) side arm of the FEP reaction vessel. The crystalline sample was characterized by Raman spectroscopy and single-crystal X-ray diffraction.

7.2.3. ^{19}F and ^{55}Mn NMR Spectroscopy

Manganese trioxide fluoride was characterized by room temperature ^{19}F, ^{55}Mn, and ^{55}Mn–^{19}F COSY NMR spectroscopies. The broad ($\Delta\nu_{½}$ = 1553 Hz) saddle-shaped resonance observed in the ^{19}F spectrum of MnO_3F ($\delta(^{19}F)$ = –169.4 ppm) (Figure 7.1a) results from partial quadrupole collapse of the equal-intensity six-line multiplet ($2I + 1$, where $I = {}^5/_2$) that arises from $^1J(^{19}F–^{55}Mn)$ spin-spin coupling. The ^{55}Mn NMR spectrum of MnO_3F (Figure 7.1b) shows a doublet at 6.1 ppm referenced to aqueous $K[MnO_4]$ ($\Delta\nu_{½}$ = 120 Hz) and provides the first example of a $^1J(^{19}F–^{55}Mn)$ coupling constant (285.56

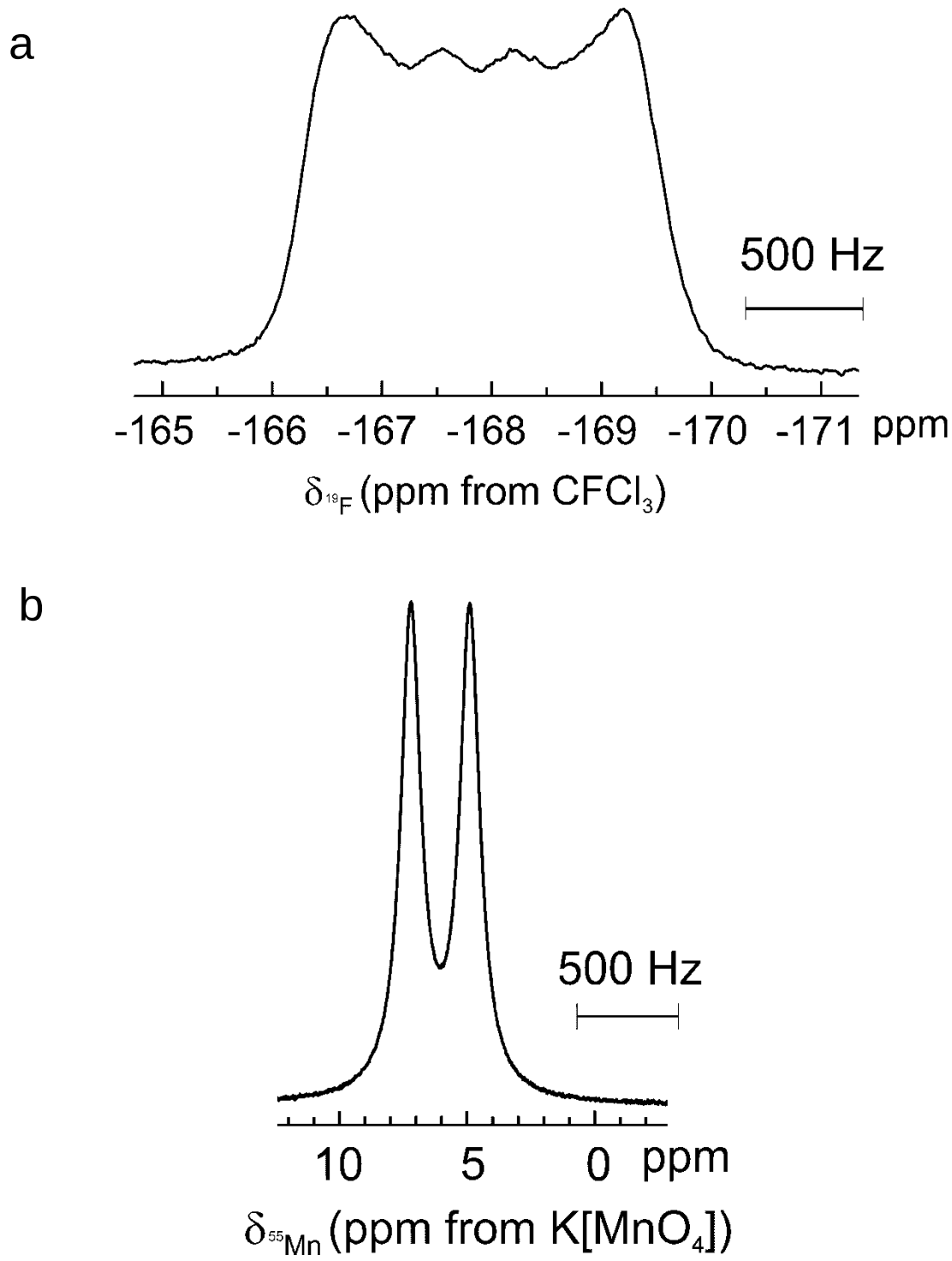

Figure 7.1. (a) The ^{19}F NMR spectrum (470.51 MHz) of MnO_3F; (b) The ^{55}Mn NMR spectrum (123.98 MHz). All spectra were recorded in HF solvent at 25 ^{o}C.

Hz). The ^{55}Mn–^{19}F COSY spectrum (Figure 7.2) shows a strong correlation between the doublet and the partially quadrupole-collapsed sextet. The ^{55}Mn chemical shift occurs at significantly lower frequency than those of $[(CO)_4(C_{18}H_{15}P)Mn]Cl$ ($\delta(^{55}Mn)$ = 150 ppm)[331] and $[(CO)_4(C_{18}H_{15}P)Mn]Br$ ($\delta(^{55}Mn)$ = 149 ppm).[331]

When MnO_3F and $K[HF_2]$ were allowed to react with KrF_2 in HF at room temperature, a red-orange solid resulted that was isolated by removal of HF under dynamic vacuum at room temperature (see Section 2.7.2). The solid was divided into two portions, one portion was used for crystal growth from HF solution and the other was used for a ^{19}F NMR study in HF. The room-temperature ^{19}F NMR spectrum of the red-orange HF solution showed a broad resonance centered at –65.4 ppm ($\Delta\nu_{1/2}$ = 3004 Hz) (Figure 7.3), which corresponds to a partially quadrupole-collapsed quartet having equally intense integrated multiplet lines. The outer lines are moved inwards and the broader inner lines are moved outwards with respect to the center of the multiplet. A similar resonance shape has been previously observed for the ^{19}F NMR spectra of BF_3 (^{11}B, $I = {}^3/_2$)[332] and ClO_3F ($^{35/37}$Cl, $I = {}^3/_2$).[332] The intensities of the lines were determined based on the empirical calculations of the individual line shapes of the corresponding partially quadrupole-collapsed resonances for $0.1 \leq \eta^2 \geq 100$, where $\eta = 2\pi J\tau$ and τ is the correlation time for molecular reorientation. The ^{19}F resonance is significantly shifted to higher frequency than that of MnO_3F, consistent with the lower polarities of the Mn−F bonds in the new manganese fluoride when compared with the Mn−F bond of $Mn^{VII}O_3F$. It is therefore reasonable to assign the ^{19}F NMR spectrum to $[Mn^{V}F_6]^-$. In view of the fact that coupling between ^{55}Mn and ^{19}F nuclei was observed in the ^{19}F spectrum, it should be

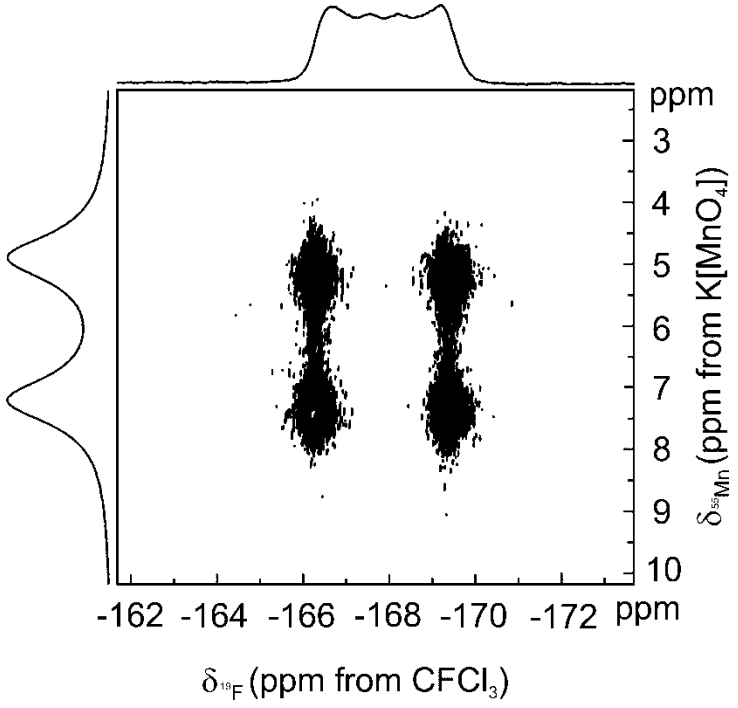

Figure 7.2. The $^{9}F-^{55}Mn$ COSY NMR spectrum (^{19}F, 470.51 MHz; ^{55}Mn, 123.98 MHz) of MnO_3F recorded in HF solvent at 25 ^{o}C.

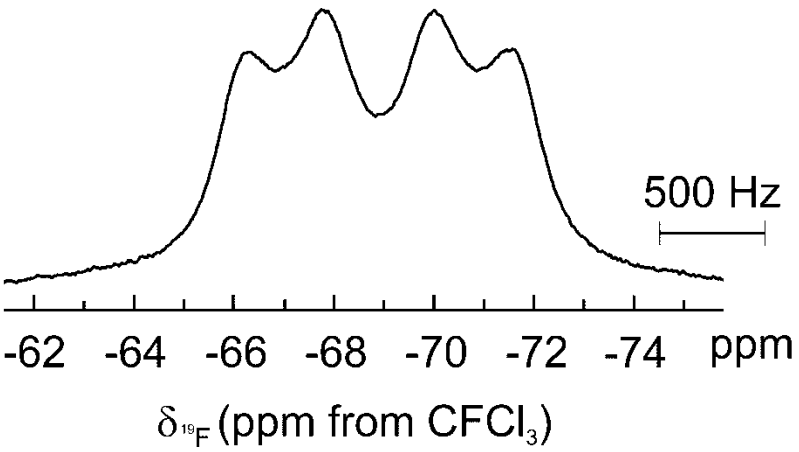

Figure 7.3. (a) The ^{19}F NMR spectrum (470.56 MHz) of the product formed in the reaction of MnO_3F with KrF_2 and $K[HF_2]$ in HF. The spectrum was recorded in HF at 25 ^{o}C and is tentatively assigned to $[MnF_6]^{-}$.

possible to obtain the ^{55}Mn NMR spectrum of $[Mn^{V}F_6]^-$, ideally a 1:6:15:20:15:6:1 septet, which would confirm the above assignment.

7.2.4. X-ray Crystallography

A summary of refinement results and other crystallographic information for MnF_5, $K[MnF_6]$, $[Xe_2F_{11}]_2[MnF_6]$, $[XeF_5]_2[MnF_6]$, and $K_2[MnF_6]\cdot 4HF$ (see Experimental Section 2.7.4) is provided in Table 7.1. Important bond lengths and angles along with calculated values are listed in Tables 7.2, 7.3, 7.4, E1, and E2. The structural parameters of the $[Xe_2F_{11}]^+$ and $[XeF_5]^+$ cations are comparable to those of $[Xe_2F_{11}][OsO_3F_3]$,[315] $[XeF_5][\mu\text{-}F(OsO_3F_2)_2]$,[315] $[XeF_5][OsO_3F_3]$,[315] $[Xe_2F_{11}]_2[NiF_6]$,[333] and $[XeF_5]_2[PdF_6]$,[334] and, therefore, require no further discussion. Although the experimental geometrical parameters of $K_2[MnF_6]$ have been improved for the crystal structure of $K_2[MnF_6]\cdot 4HF$, they are not further discussed (Figure E7 and Table E2).

7.2.4.1. MnF_5

Preliminary findings suggest that MnF_5 has been synthesized and isolated for the first time and structurally characterized by single-crystal X-ray diffraction. A preliminary solution in *C*2/c reveals that the crystal structure of MnF_5 consists of linear infinite chains formed by MnF_6 pseudo-octahedra that are *trans*-linked to each other through fluorine bridges. The chains run parallel to the *a*-axis and are packed along the *c*-axis (Figure E8). The crystal structure of MnF_5 is analogous to those of α-UF_5[335] and BiF_5[336] as they also

Table 7.1. Summary of Crystal Data and Refinement Results for MnF_5 **(1)**, $K[MnF_6]$ **(2)**, $[Xe_2F_{11}]_2[MnF_6]$ **(3)**, $[XeF_5]_2[MnF_6]$ **(4)**, and $K_2[MnF_6]\cdot 4HF$ **(5)**

chem formula	**(1)**	**(2)**	**(3)**	**(4)**	**(5)**
space group	*C*2/c	$R\bar{3}$	*C*2/c	*P*ca2$_1$	*P*2$_1$/n
a (Å)	5.6068(6)	7.2890(9)	21.581(2)	9.21740(10)	6.4909(2)
b (Å)	9.8503(10)	7.2890(9)	5.5438(4)	12.5607(2)	6.9208(2)
c (Å)	7.1707(7)	7.1879(9)	17.4799(12)	9.20800(10)	10.0683(3)
α (deg)	90	90	90	90	90
β (deg)	107.348(4)	90	115.586(4)	90	107.948(2)
γ (deg)	90	120	90	90	90
V (Å)^3	378.01(7)	330.73(9)	1886.3(2)	1066.07(2)	430.28(2)
molecules/unit cell	4	3	4	4	4
mol wt (g mol^{-1})	599.76	624.12	4448.56	2486.16	646.28
calcd density (g cm^{-3})	2.635	3.134	3.916	3.872	2.494
T (^{o}C)	–173	–173	–173	–173	–173
μ (mm^{-1})	3.47	3.97	8.02	7.70	2.62
R_1[a]	0.0463	0.0391	0.0261	0.0184	0.0226
wR_2[b]	0.1228	0.0915	0.0430	0.0342	0.0506

[a] R_1 is defined as $\Sigma \| F_o | - | F_c \| \Sigma | F_o |$ for $I > 2\sigma(I)$. [b] wR_2 is defined as $[\Sigma[w(F_o^2 - F_c^2)^2]/\Sigma w(F_o^2)^2]^{1/2}$ for $I > 2\sigma(I)$.

Table 7.2. Experimental Bond Lengths and Bond Angles for Polymeric MnF_5 and Calculated Bond Lengths and Bond Angles for the Hypothetical $[Mn_3F_{16}]^-$ (C_{2h}) Anion

MnF_5		$[Mn_3F_{16}]^-$		
exptl[a]		calcd[b]		
			B3LYP	PBE1PBE
Bond lengths (Å)				
$Mn–F_1$	1.9646(5)	$Mn–F_1$	1.853	1.838
$Mn–F_2$	1.950(2)	$Mn–F_2$	1.730	1.715
$Mn–F_3$	1.912(2)			
Bond Angles (°)				
$F_1–Mn_1–F_{1A}$	180.00	$F_1–Mn_1–F_{1A}$	180.0	180.0
$F_1–Mn_1–F_2$	90.14(7)	$F_1–Mn_1–F_2$	90.8	90.8
$F_1–Mn_1–F_{2A}$	89.85(7)	$F_1–Mn_1–F_{2A}$	89.2	89.2
$F_1–Mn_1–F_3$	91.19(6)	$F_1–Mn_1–F_{2B}$	90.8	90.8
$F_1–Mn_1–F_{3A}$	88.81(6)	$F_1–Mn_1–F_{2C}$	89.2	89.2
$F_2–Mn_1–F_{1A}$	92.5(3)	$F_2–Mn_1–F_{1A}$	89.2	89.2
$F_2–Mn_1–F_{2A}$	180.00	$F_2–Mn_1–F_{2A}$	180.0	180.0
$F_2–Mn_1–F_3$	91.43(7)	$F_2–Mn_1–F_{2B}$	90.1	90.1
$F_2–Mn_1–F_{3A}$	88.57(7)	$F_2–Mn_1–F_{2C}$	89.9	89.9
$Mn_{1A}–F_{1A}–Mn_1$	155.09(13)	$Mn_1–F_1–Mn_2$	144.7	143.1

[a] For the atom labeling scheme, see Figure 7.4a. [b] The aug-cc-pVTZ basis set was used. For the atom labeling scheme, see Figure 7.4b.

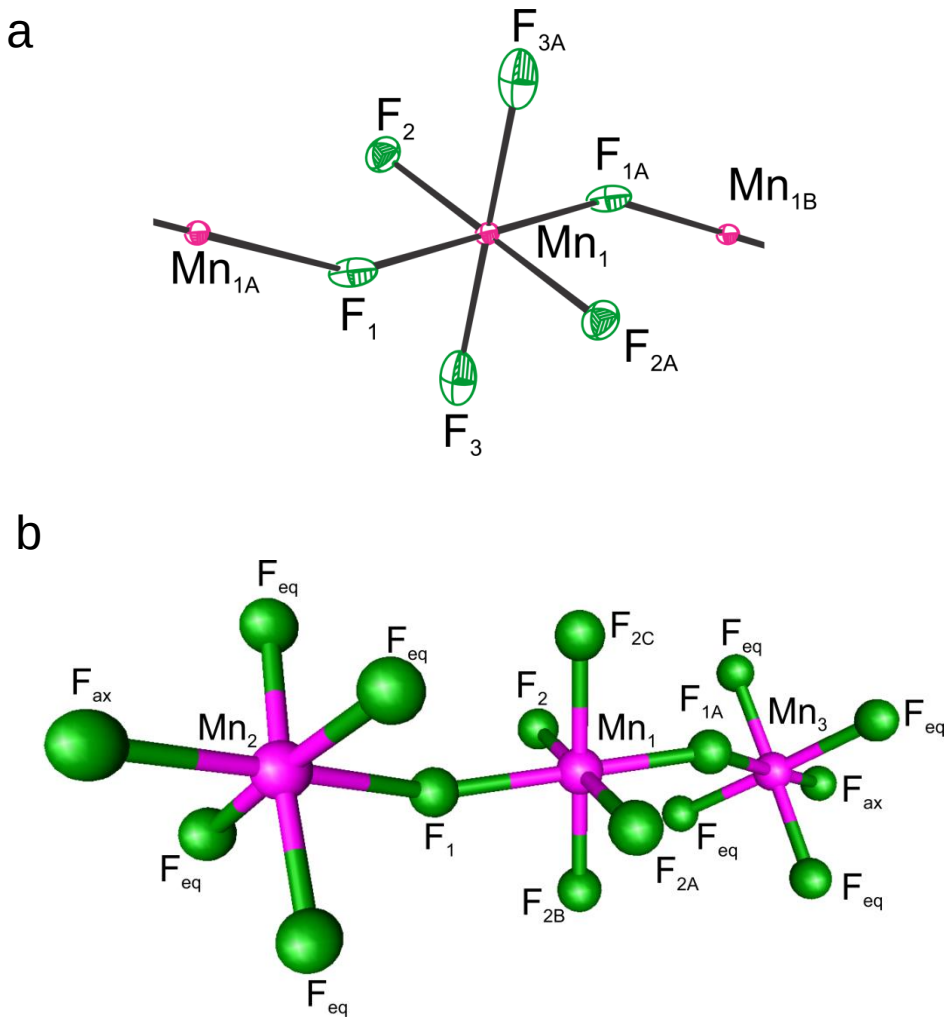

Figure 7.4. (a) The repeat unit in the crystal structure of MnF_5; thermal ellipsoids are shown at the 50% probability level. (b) The calculated structure of the hypothetical $[Mn_3F_{16}]^-$ anion (B3LYP/aug-cc-pVTZ).

have *trans*-bridge structures and differs from the *cis*-bridge structures of CrF_5[337] and VF_5.[338] The elongated thermal ellipsoids suggest the possibility of a unsolved disorder or twinning. Furthermore, the Mn(V)−F bonds are significantly longer than the Mn(IV)−F bonds in $K[MnF_6]$, $K_2[MnF_6]\cdot 4HF$, $[Xe_2F_{11}]_2[MnF_6]$, and $[XeF_5]_2[MnF_6]$ (see below) and the calculated Mn(V)−F bonds in the hypothetical $[Mn_3F_{16}]^-$ anion (Table 7.4). This appears to result from twinning issues associated with the crystal structure of MnF_5. The bond elongation due to twinning is reminiscent of what was observed in the crystal structures $Cs[MnF_4]$.[339,340] Moreover, the absence of ν(Mn−O) stretches in the Raman spectrum (Figure E3) is consistent with the crystal structure being that of a manganese fluoride.

7.2.4.2. $K[MnF_6]$

The $[MnF_6]^-$ anion would correspond to only the second example of a manganese(V) fluoride which has been isolated and structurally characterized by single-crystal X-ray diffraction. Although the crystal structure of $K[MnF_6]$ could be solved using both the *R*3 and $R\bar{3}$ space groups (Figure E9), the latter provided a better overall solution. In this space group, the $[MnF_6]^-$ anion has essentially an octahedral geometry which is imposed by symmetry. This contrasts with the fact that the d^2 electron configuration of manganese in $[MnF_6]^-$ is expected to result in a Jahn-Teller distortion from O_h to D_{4h} symmetry.

Each F atom in $[MnF_6]^-$ interacts with two K^+ cations (K···F, 2.847(2) and

Table 7.3. Experimental Bond Lengths, Contacts, and Bond Angles for $K[MnF_6]$ and Calculated Bond Lengths and Bond Angles for $[MnF_6]^-$

	$K[MnF_6]$ exptl[a]		$[MnF_6]^-$ (D_{4h}) calcd[a,b]	
			B3LYP	PBE1PBE
Bond Lengths (Å)				
$Mn_1–F_1$	1.729(3)	$Mn_1–F_1$	1.789	1.774
		$Mn_1–F_2$	1.759	1.744
$K---F_1$	2.847(2)			
$K---F_{1H}$	2.940(3)			
Bond Angles (°)				
$F_1–Mn_1–F_{1A}$	180.0(1)	$F_1–Mn_1–F_{1A}$	180.0	
$F_1–Mn_1–F_{1B}$	89.3(1)	$F_1–Mn_1–F_2$	90.0	
$F_1–Mn_1–F_{1C}$	90.7(1)			

[a] For the atom labeling scheme see Figure 7.5. [b] The aug-cc-pVTZ basis set was used.

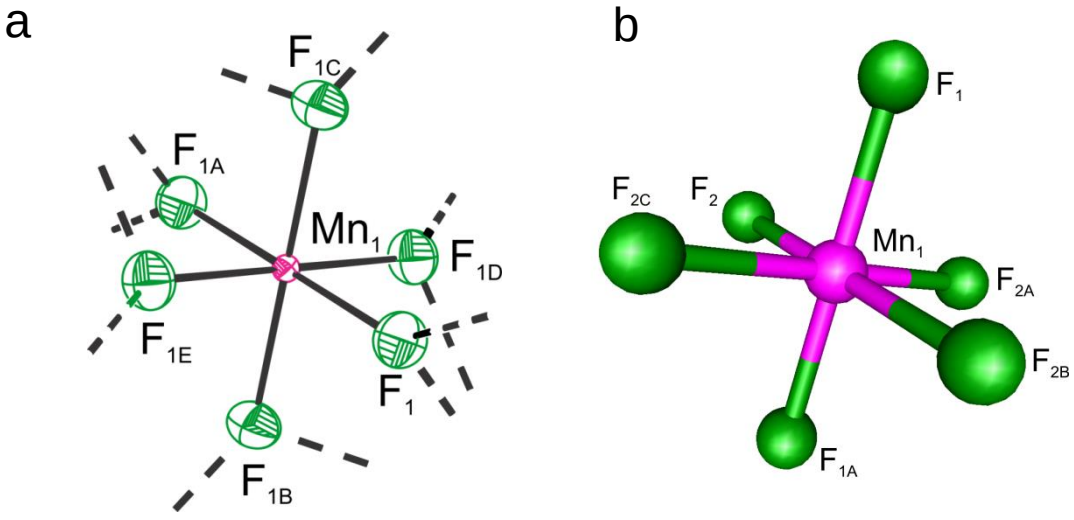

Figure 7.5. (a) The $[MnF_6]^-$ anion in the crystal structure of $K[MnF_6]$ showing the K^+ contacts around the MnF_6-octahedron. Thermal ellipsoids are shown at the 50% probability levels for both compounds. (b) The calculated structure of the $[MnF_6]^-$ anion (B3LYP/aug-cc-pVTZ).

2.940(3) Å) and, in turn, each cation interacts with twelve fluorine atoms (Figure E10). The Mn−F bond lengths (1.729(3) Å) of $[MnF_6]^-$ (Table 7.2) are shorter than those of $[MnF_6]^{2-}$ ($[Xe_2F_{11}]_2[MnF_6]$, 1.806(2)−1.807(2) Å; $[XeF_5]_2[MnF_6]$, 1.798(2)−1.817(2) Å; $K_2[MnF_6]\cdot 4HF$, 1.7895(5)−1.8064(5) Å), consistent with the higher oxidation state of the Mn atoms in $[Mn^{V}F_6]^-$ when compared to $[Mn^{IV}F_6]^{2-}$. The F−Mn−F bond angles (89.3 and 90.7°) are close to 90°.

7.2.4.3. $[Xe_2F_{11}]_2[MnF_6]$ and $[XeF_5]_2[MnF_6]$

The crystal structure of $[Xe_2F_{11}]_2[MnF_6]$ represents a rare example in which two $[Xe_2F_{11}]^+$ cations bridge to a common anion. The $[MnF_6]^{2-}$ anions and $[Xe_2F_{11}]^+$ cations stack along the *b*-axis (Figure E11, Appendix E). Each $[Xe_2F_{11}]^+$ cation interacts with two $[MnF_6]^{2-}$ anions through four short Xe---F bridge bonds (Xe_1---F_1, 2.554(2) Å; Xe_1---F_3, 2.778(2) Å; Xe_2---F_{2B}, 2.776(2) Å; Xe_2---F_{3B} (2.559(2) Å) (Figures 7.6 and E12, Appendix E). This type of interaction contrasts with the one observed in $[Xe_2F_{11}]_2[NiF_6]$,[333] where one XeF_5-group of the $[Xe_2F_{11}]^+$ cation interacts with the same anion and a second XeF_5-group interacts with two anions. The Xe---F contacts are significantly shorter than the sum of the Xe···F van der Waals radii (3.63 Å).[241] Each XeF_5-group of the $[Xe_2F_{11}]^+$ cation also interacts with two $[MnF_6]^{2-}$ anions through long Xe_2---F_{1A} (3.623(2) Å) and Xe_1---F_{2C} (3.623(2) Å) bridging bonds, which are equal to the sum of the Xe···F van der Waals radii. In addition, there are several interionic F···F contacts, where the shortest cation/anion interaction is 2.677(2) Å and anion/anion interaction is 2.806(2) Å.

Table 7.4. Selected Experimental Bond Lengths, Contacts, and Bond Angles for $[Xe_2F_{11}]_2[MnF_6]$ **(1)** and $[XeF_5]_2[MnF_6]$ **(2)** and Selected Calculated Bond Lengths and Bond Angles for $\{[Xe_2F_{11}]_4[MnF_6]\}^{2+}$ **(3)** and $\{[XeF_5]_4[MnF_6]\}^{2+}$ **(4)**

exptl[a]		calcd[b]		exptl[c]		calcd[d]	
(1)		**(3)**		**(2)**		**(4)**	
Bond Lengths (Å)							
Mn_1-F_1	1.807(2)	Mn_1-F_1	1.828	Mn_1-F_1	1.817(2)	Mn_1-F_1	1.804
Mn_1-F_2	1.806(2)	Mn_1-F_2	1.825	Mn_1-F_2	1.800(2)	Mn_1-F_2	1.844
Mn_1-F_3	1.806(2)	Mn_1-F_3	1.819	Mn_1-F_3	1.802(2)	Mn_1-F_3	1.811
		Mn_1-F_4	1.824	Mn_1-F_4	1.798(2)	Mn_1-F_4	1.846
		Mn_1-F_5	1.829	Mn_1-F_5	1.807(2)	Mn_1-F_5	1.810
		Mn_1-F_6	1.819	Mn_1-F_6	1.804(2)	Mn_1-F_6	1.802
$Xe_1\cdots F_1$	2.554(2)	$Xe\cdots F_1$	2.768	$Xe_1\cdots F_1$	2.521(2)	$Xe_1\cdots F_1$	2.637
$Xe_2\cdots F_2$	2.559(2)	$Xe\cdots F_2$	2.711	$Xe_2\cdots F_{2A}$	2.579(2)	$Xe_2\cdots F_2$	2.457
$Xe_1\cdots F_3$	2.778(2)	$Xe\cdots F_3$	2.790	$Xe_1\cdots F_3$	2.558(2)	$Xe_1\cdots F_3$	2.572
$Xe_2\cdots F_3$	2.777(2)	$Xe\cdots F_3$	2.846	$Xe_2\cdots F_{4A}$	2.572(2)	$Xe\cdots F_4$	2.450
		$Xe\cdots F_4$	2.725	$Xe_1\cdots F_{5A}$	2.483(2)	$Xe\cdots F_5$	2.573
		$Xe\cdots F_5$	2.755	$Xe_2\cdots F_6$	2.470(2)	$Xe\cdots F_6$	2.640
		$Xe\cdots F_6$	2.801				
		$Xe\cdots F_6$	2.832				
Bond Angles (deg)							
$F_1-Mn_1-F_{1A}$	90.0(1)	$F_1-Mn_1-F_4$	89.7	$F_1-Mn_1-F_2$	175.7(1)		176.1
$F_1-Mn_1-F_2$	175.3(1)	$F_1-Mn_1-F_2$	173.4	$F_1-Mn_1-F_3$	85.4(1)		86.3
$F_1-Mn_1-F_{2A}$	90.1(1)	$F_1-Mn_1-F_5$	90.7	$F_1-Mn_1-F_4$	90.7(1)		90.3
$F_1-Mn_1-F_3$	87.5(1)	$F_1-Mn_1-F_3$	93.3	$F_1-Mn_1-F_5$	91.7(1)		91.2
$F_1-Mn_1-F_{3A}$	92.3(1)	$F_1-Mn_1-F_6$	86.6	$F_1-Mn_1-F_6$	91.4(1)		88.8
$F_2-Mn_1-F_{1A}$	90.1(1)	$F_2-Mn_1-F_4$	90.6	$F_2-Mn_1-F_3$	91.5(1)		89.9
$F_2-Mn_1-F_{2A}$	90.2(1)	$F_2-Mn_1-F_5$	89.8	$F_2-Mn_1-F_4$	86.4(1)		90.6
$F_2-Mn_1-F_3$	87.8(1)	$F_2-Mn_1-F_3$	86.7	$F_2-Mn_1-F_5$	91.4(1)		92.6
$F_2-Mn_1-F_{3A}$	92.4(1)	$F_2-Mn_1-F_6$	93.2	$F_2-Mn_1-F_6$	91.6(1)		90.6
$F_3-Mn_1-F_{1A}$	92.3(1)	$F_3-Mn_1-F_4$	93.3	$F_3-Mn_1-F_4$	90.7(1)		92.4
$F_3-Mn_1-F_{2A}$	92.4(1)	$F_3-Mn_1-F_5$	93.3	$F_3-Mn_1-F_5$	177.1(1)		176.6
$F_3-Mn_1-F_{3A}$		$F_3-Mn_1-F_6$	179.9	$F_3-Mn_1-F_6$	89.8(1)		91.2
		$F_4-Mn_1-F_5$	173.4	$F_4-Mn_1-F_5$	90.1(1)		89.9
		$F_4-Mn_1-F_6$	86.8	$F_4-Mn_1-F_6$	178.0(1)		176.1
		$F_5-Mn_1-F_6$	86.8	$F_5-Mn_1-F_6$	89.5(1)		86.4

[a] For the atom labeling scheme, see Figure 7.6a. [b] B3LYP/def2-SVP (Mn, F)/aug-cc-pVTZ(-PP) (Xe). For the atom labeling scheme, see Figure 7.6b. [c] For the atom labeling scheme, see Figure 7.7a. [d] B3LYP/def2-SVP (Mn, F)/aug-cc-pVTZ(-PP) (Xe). For the atom labeling scheme, see Figure 7.7b.

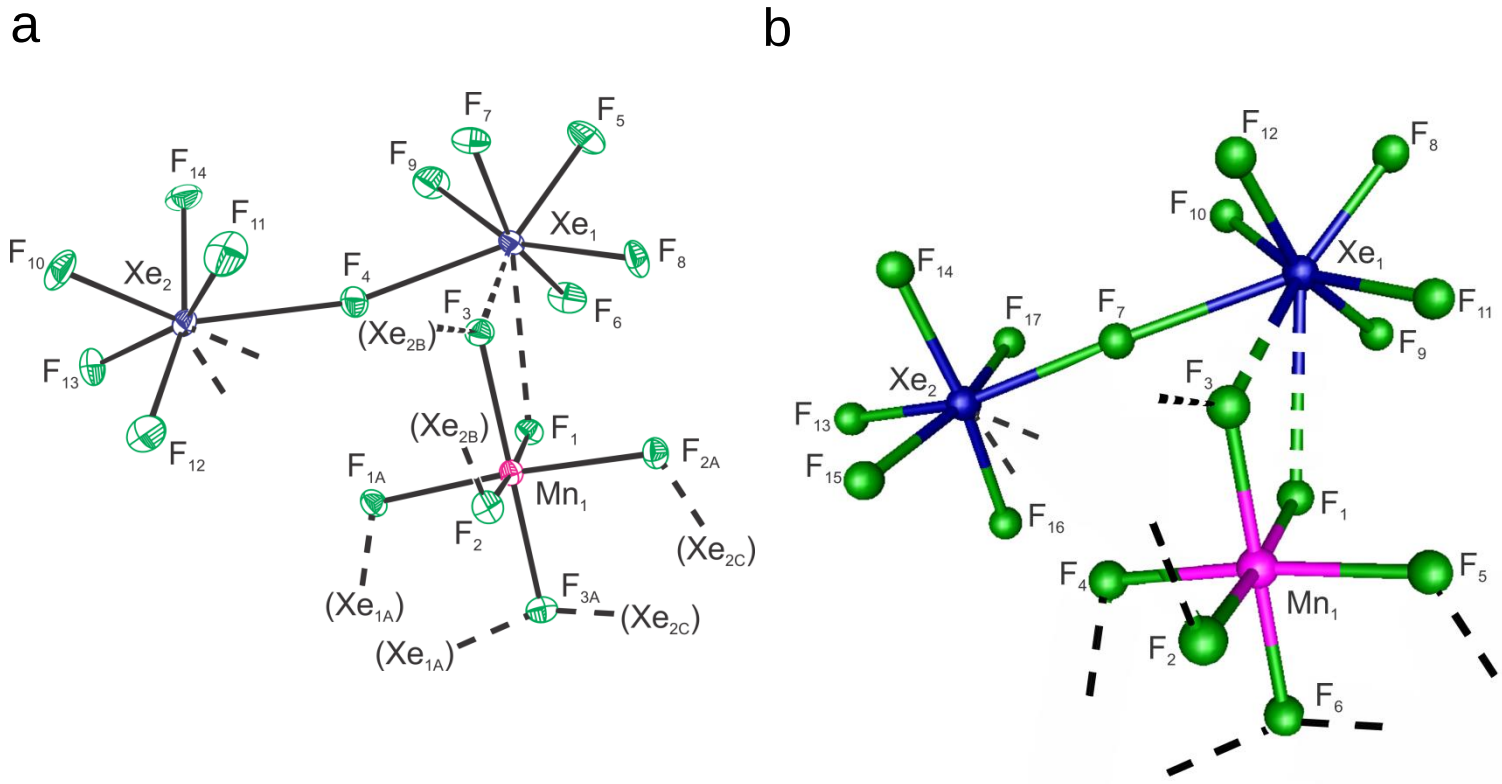

Figure 7.6. (a) A portion of the crystal structure of $[Xe_2F_{11}]_2[MnF_6]$ showing the contacts around the $[MnF_6]^-$ anion. Thermal ellipsoids are shown at the 50% probability level. The symmetry-related $[Xe_2F_{11}]^+$ cation is omitted for clarity. (b) A portion of the calculated structure of $\{[Xe_2F_{11}]_4[MnF_6]\}^{2+}$ showing the contacts around the MnF_6 octahedron. The remaining $[Xe_2F_{11}]^+$ cations are omitted for clarity (B3LYP/def2-SVP (Mn, F)/aug-cc-pVTZ(-PP) (Xe)).

a

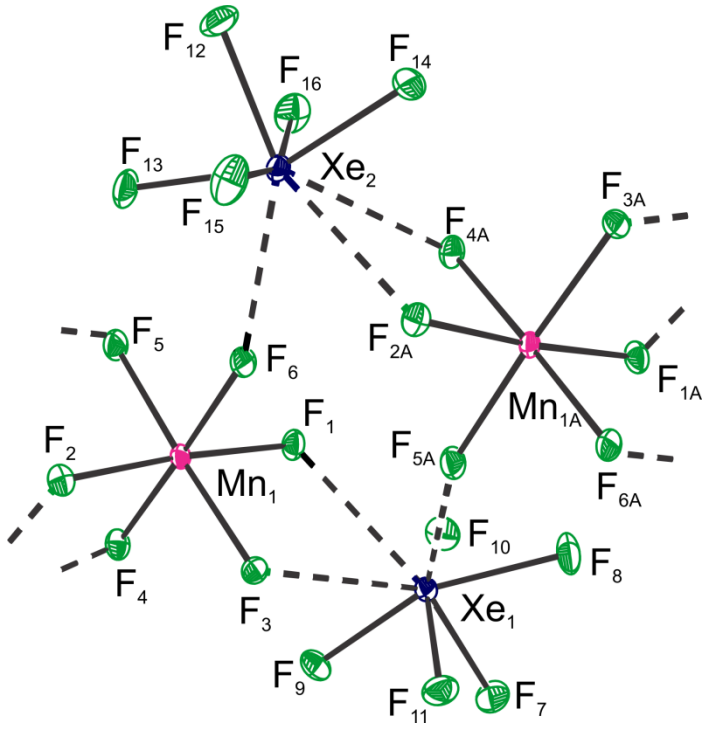

b

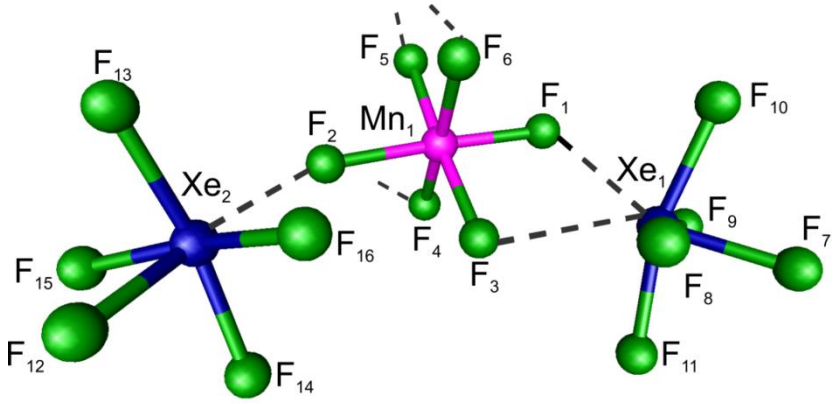

Figure 7.7. (a) View of a dimeric ring in $[XeF_5]_2[MnF_6]$; thermal ellipsoids are drawn at the 50% probability level. (b) A portion of the calculated structure of $\{[XeF_5]_4[MnF_6]\}^{2+}$ showing the contacts around the $[MnF_6]^-$ anion. The remaining $[XeF_5]^+$ cations are omitted for clarity (B3LYP/def2-SVP (Mn, F)/aug-cc-pVTZ(-PP) (Xe)).

The crystal structure of $[XeF_5]_2[MnF_6]$ consists of rings composed of the $[MnF_6]^{2-}$ anions and the $[XeF_5]^+$ cations, which run along the *b*-axis (E13, Appendix E). Each $[XeF_5]^+$ cation interacts with two $[MnF_6]^-$ anions, with one $[MnF_6]^-$ anion interacting by means of two fluorine bridge-bonds (Xe_1---F, 2.521(2) and 2.558(2) Å; Xe_2---F, 2.579(2) and 2.572(2) Å) and the other interacting with another anion by means of one fluorine bridge-bond (Xe_1---F, 2.483(2) Å; Xe_2---F, 2.470(2) Å). This results in rings (Figures 7.7 and E13) which are linked to each other in the Mn_1, Xe_1, Mn_{1A}, Xe_{2A}-plane. All the contacts are significantly shorter than the sum of the Xe···F van der Waals radii (3.63 Å),[241] implying that the $[XeF_5]^+$ cations are extensively associated with the $[MnF_6]^-$ anions. This type of coordination is analogous to that observed in $[XeF_5]_2[PbF_6]$.[334] There are also several interionic F···F contacts ($F_{Mn}\cdots F_{Mn}$, 2.752(3) Å; $F_{Xe}\cdots F_{Mn}$, 2.486(3) Å), which are shorter than the sum of the van der Waals radii (2.94 Å).[241]

The $[MnF_6]^{2-}$ anion of $[Xe_2F_{11}]_2[MnF_6]$ is essentially octahedral (Mn−F, 1.806(2) and 1.807(2) Å; ∠(F−Mn−F), 87.5(1)−92.4(1)°) (Figure 7.6a); whereas in $[XeF_5]_2[MnF_6]$, the $[MnF_6]^{2-}$ anion is a distorted octahedron (Figure 7.7a) with the Mn−F bond lengths varying from 1.798(2) to 1.817(2) Å, and the F−Mn−F bond angles from 85.4(1)° to 91.7(1)°. These Mn−F bond lengths are comparable to those of $K_2[MnF_6]\cdot 4HF$ (Table E2, Appendix E), $K_2[MnF_6]$ (1.792 and 1.785 Å),[160] and $[NH_4]_2[MnF_6]$ (1.801(1) Å).[149]

7.2.5. Raman Spectroscopy

The low-temperature Raman spectra were recorded on $[XeF_5]_2[MnF_6]$ (Figure 7.8), $[Xe_2F_{11}]_2[MnF_6]$ (Figure 7.9), and $K_2[MnF_6]\cdot 4HF$ (Figure E14). The observed and

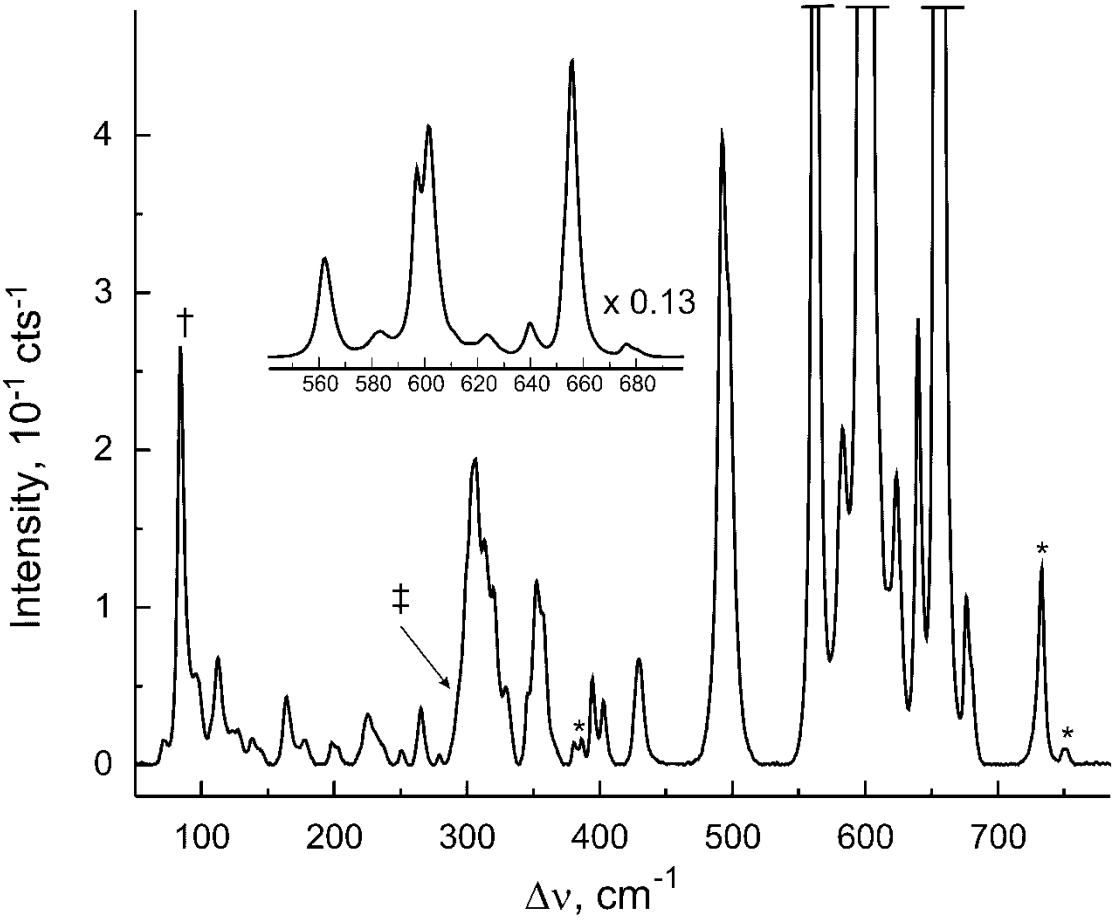

Figure 7.8. Raman spectrum of $[XeF_5]_2[MnF_6]$ recorded at –140 ^{o}C using 1064-nm excitation. Symbols denote an FEP line (*), instrumental artifact (†), and overlap of a $[XeF_5]_2[MnF_6]$ line with an FEP line (‡).

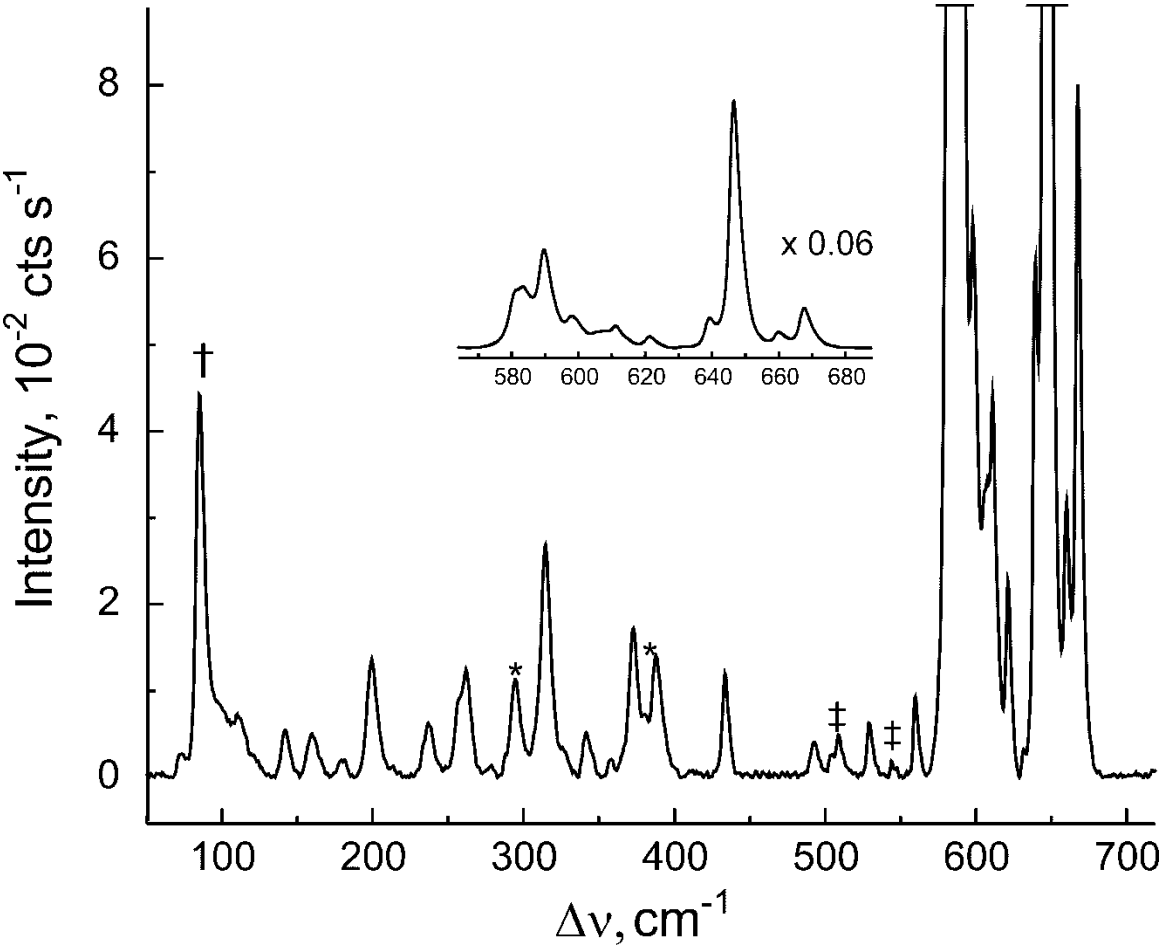

Figure 7.9. Raman spectrum of $[Xe_2F_{11}]_2[MnF_6]$ recorded at –140 °C using 1064-nm excitation. Symbols denote an FEP line (*), a $XeOF_4 \cdot XeF_6$ line (‡), and an instrumental artifact (†).

calculated frequencies and mode descriptions for $[XeF_5]_2[MnF_6]$, $[Xe_2F_{11}]_2[MnF_6]$, and $K_2[MnF_6]\cdot 4HF$ are provided in Tables 7.5, E3, and E4 (Appendix E). Spectral assignments for $[XeF_5]_2[MnF_6]$, $[Xe_2F_{11}]_2[MnF_6]$, and $K_2[MnF_6]\cdot 4HF$ were made by comparison with the calculated frequencies and Raman intensities for the hypothetical gas-phase cations, $\{[XeF_5]_4[MnF_6]\}^{2+}$ (C_1) (Table 7.5 and E3) and $\{[Xe_2F_{11}]_4[MnF_6]\}^{2+}$ (C_1) (Table 7.5 and E4), and for $[MnF_6]^{2-}$ (O_h) (Table E5), which were optimized at the B3LYP/def2-SVP (Mn, F)/aug-cc-pVTZ(-PP) (Xe) levels of theory. The frequencies observed for $[XeF_5]_2[MnF_6]$ and $[Xe_2F_{11}]_2[MnF_6]$ agree with the previously published infrared frequencies.[169] The trace of a room-temperature Raman spectrum was reported for $[XeF_5]_2[MnF_6]$.[171] Although the frequencies were not listed, bands associated with the $[XeF_5]^+$ cation and $[MnF_6]^-$ anion were assigned by comparison with those observed in the Raman spectrum of $[NH_4][XeF_5][MnF_6]$.[171] The frequencies associated with $[XeF_5]^+$ and $[Xe_2F_{11}]^+$ agree with those in $[NH_4][XeF_5][MnF_6]$,[171] $[Xe_2F_{11}]_2[PbF_6]$,[341] $[Xe_2F_{11}]_2[SnF_6]$,[341] $[XeF_5][\mu\text{-}F(OsO_3F_2)_2]$,[315] $[XeF_5][OsO_3F_3]$,[315] and $[Xe_2F_{11}][OsO_3F_3]$.[315] The Raman frequencies of the latter ion pairs were fully assigned with the aid of quantum-chemical calculations in $[XeF_5][\mu\text{-}F(OsO_3F_2)_2]$,[315] $[XeF_5][OsO_3F_3]$,[315] and $[Xe_2F_{11}][OsO_3F_3]$.[315]

7.2.5.1. $[XeF_5]_2[MnF_6]$ (4) and $[Xe_2F_{11}]_2[MnF_6]$ (3)

Although the present assignments well agree with those reported earlier, they provide a more detailed description of the vibrational modes of $[XeF_5]_2[MnF_6]$, which

Table 7.5. Experimental Raman Frequencies and Intensities for $[XeF_5]_2[MnF_6]$ **(4)** and $[Xe_2F_{11}]_2[MnF_6]$ **(3)** and Calculated Vibrational Frequencies, Intensities and Assignments for $\{[XeF_5]_4[MnF_6]\}^{2+}$ (C_1) **(7)** and $\{[Xe_2F_{11}]_4[MnF_6]\}^{2+}$ (C_1) **(6)**

(4) exptl[a,b]	**(7)** calcd[a,c]	**(3)** exptl[a,b]	**(6)** calcd[a,c]	assgnts[d]
640(12) 623(7) 602(78) 597(64)	621(19)[124] 617(35)[49] 595(31)[74] 591(25)[54] 589(1)[46]	619(5) 611(9) 597(13) 589(40)	598(<1)[84] 594(4)[106] 586(1)[57]	
583(9)	573(8)[228]	582(25) 581 sh	579(12)[4] 575(1)[171] 572(16)[23]	$[\nu(MnF_b) - \nu(XeF_b)]$
563(33)	544(47)[153]	560(2)	566(23)[55] 563(22)[56] 561(4)[57]	
497 sh 493(16)	470(20)[99]			
430(3) 402(2) 394(2)	447(27)[297]	433(2)	471(2)[<1] 462(3)[1]	
358 sh 352(5) 346 sh	356(4)[37] 352(5)[80]	373(3)	360(6)[80] 356(20)[15]	
320(5)	315(1)[7]	341(1)	337(4)[60] 335(1)[28] 332(4)[110] 331(<1)[126 329(3)[36] 319(1)[131] 318(3)[153]	$\delta(F_bMnF_b)$
312(6) 306(8) 298 sh 279(<1)	306(2)[96] 300(12)[1] 298(<1)[118] 295(3)[63] 286(6)[9] 281(20)[38] 278(2)[7]	295(1)	302(2)[62] 301(1)[9] 288(7)[<1]	

Table 7.5. (continued…)

236 sh	239(1)[2]	238(<1)	244(3)[<1] 240(1)[4] 234(1)[<1]	δ(F_bMnF_b)
226(1)	215(<1)[5] 213(<1)[2]			
	200(<1)[2]	214(1)	224(<1)[22] 222(<1)[1]	
200(1)	197(<1)[4]			$\rho_t(F_bMnF_b)$
137(1)	135(2)[42]	143(1)	138(<1)[17]	$\rho_r(F_bMnF_b)$

[a] Frequencies are given in cm^{-1}. [b] Values in parentheses denote relative Raman intensities. The Raman spectrum was recorded in an FEP sample tube at –140 °C using 1064-nm excitation. [c] Values in parentheses denote calculated Raman intensities ($Å^4\ u^{-1}$). Values in square brackets denote calculated infrared intensities (km mol^{-1}). The B3LYP/def2-SVP(Mn, F)/aug-cc-pVTZ(-PP) (Xe) method was used. [d] The abbreviations denote stretch (ν), bend (δ), twist (ρ_t), rock (ρ_r), and bridging (b). Complete assignment of the vibrational modes is provided in Tables E5 for **(3)** and E6 for **(4)**.

takes into account vibrational coupling between the ν(MnF) and ν(XeF) stretching modes and δ(FMnF) and δ(FXeF) deformational modes (Tables 7.5 and E3).

The highest frequency bands in both $[XeF_5]_2[MnF_6]$ and $[Xe_2F_{11}]_2[MnF_6]$ are assigned to the ν(XeF) stretching modes (**(4)**, 597, 602, 640−681 cm^{-1}; **(3)**, 560−666 cm^{-1}), which are predicted to appear at 587−612, 659−678 cm^{-1} and 545, 546, 570, 571, 581, 582, 589, 590, 629−668 cm^{-1}, respectively. The band at 597 **(4)** and 581−619 cm^{-1} **(3)** overlap with ν(MnF). The ν(XeF) stretching modes in **(4)** and **(3)** are comparable to those of $[XeF_5]_2[NiF_6]$ (582−657 cm^{-1}),[342] $[XeF_5][\mu\text{-}F(OsO_3F_2)_2]$ (596, 612, 656−680 cm^{-1}),[315] $[XeF_5][OsO_3F_3]$ (599−654 cm^{-1}),[315] $[Xe_2F_{11}]_2[PbF_6]$ (571−664 cm^{-1}),[341] $[Xe_2F_{11}]_2[PdF_6]$ (583−668 cm^{-1}),[341] $[Xe_2F_{11}]_2[SnF_6]$ (599−674 cm^{-1}),[341] and $[Xe_2F_{11}][OsO_3F_3]$ (580, 591, 613−656 cm^{-1}),[315] with the most intense band occurring at 656 cm^{-1} **(4)** and 646 cm^{-1} **(3)**. The highest intensity bands are comparable to those of $[XeF_5]_2[NiF_6]$ (650 cm^{-1}),[342] $[Xe_2F_{11}]_2[PbF_6]$ (650 cm^{-1})[341] $[Xe_2F_{11}]_2[PdF_6]$ (651 cm^{-1}),[341] and $[Xe_2F_{11}]_2[SnF_6]$ (657 cm^{-1}).[341] The F−Xe−F deformation modes appear below 346 cm^{-1} **(4)** and 378 cm^{-1} **(3)**.

The $\nu(MnF_b)$ stretching modes in **(3)** (exptl, 433−619 cm^{-1}; calcd, 462−598 cm^{-1}) and **(4)** (exptl, 394−640 cm^{-1}; calcd, 447−621 cm^{-1}) are strongly coupled with the $\nu(XeF_b)$ stretching modes and are comparable in both salts. The $\delta(F_bMnF_b)$ deformation modes are also strongly coupled with the δ(FXeF) deformational modes and appear below 373 cm^{-1} (calcd, 360 cm^{-1}) in **(4)** and 358 cm^{-1} (calcd, 356 cm^{-1}) in **(3)**.

7.2.6. Computational Results

Quantum-chemical calculations for $\{[Xe_2F_{11}]_4[MnF_6]\}^{2+}$ (C_1), $\{[XeF_5]_4[MnF_6]\}^{2+}$ (C_1), and $[MnF_6]^{2-}$ (O_h), were carried out using the B3LYP/def2-SVP (Mn, F)/aug-cc-pVTZ(-PP) (Xe) level of theory. The optimization of $[MnF_6]^{2-}$ (O_h) resulted in a stationary point with all frequencies real (Table E5), whereas the optimizations of both $\{[Xe_2F_{11}]_4[MnF_6]\}^{2+}$ (C_1) and $\{[XeF_5]_4[MnF_6]\}^{2+}$ (C_1) (Tables E3 and E4) each gave one negative frequency. Attempts to follow the negative frequencies resulted in convergence failures. Quantum-chemical calculations were also carried out for the $[MnF_6]^-$ (D_{4h}), hypothetical $[Mn_3F_{16}]^-$ (C_{2h}), and $[MnF_6]^{2-}$ (O_h) anions using the B3LYP/aug-cc-pVTZ and PBE1PBE/aug-cc-pVTZ levels of theory. The optimizations of $[MnF_6]^-$ (D_{4h}) (Table 7.3) and $[MnF_6]^{2-}$ (O_h) (Table 7.3) resulted in stationary points with all frequencies real, whereas the optimization of $[Mn_3F_{16}]^-$ (C_{2h}) resulted in one (B3LYP) and two (PBE1PBE) negative frequencies, respectively.

$[Mn_3F_{16}]^-$ (C_{2h}) and $[MnF_6]^-$ (D_{4h}). The starting geometry used for the hypothetical $[Mn_3F_{16}]^-$ (C_{2h}) anion was part of the MnF_5 chain (see X-ray Crystallography), which reproduced the geometry of the central MnF_6-moiety.

The calculated terminal Mn−F_t and bridging Mn−F_μ bond lengths in $[Mn_3F_{16}]^-$ (Mn−F_t, 1.730 [1.715] Å; Mn−F_μ, 1.853 [1.838] Å) are significantly shorter than the corresponding experimental Mn−F bonds (Mn−F_t, 1.950(2) and 1.912(2) Å; Mn−F_μ, 1.9646 (5) Å), whereas the calculated F_t−Mn−F_t, F_t−Mn−F_μ, and F_μ−Mn−F_μ bond angles well reproduce the corresponding experimental bond angles (Table 7.2). The Mn−F_μ−Mn bond angle is bent (144.7° [143.1]°] as observed experimentally (155.09(13)°). The

calculated Mn−F_t bond lengths in the $[Mn_3F_{16}]^-$ anion are shorter than those calculated for the $[MnF_6]^-$ anion (1.789 [1.774] and 1.759 [1.744] Å), consistent with the increased polarity of the Mn−F_t bonds in the $[MnF_6]^-$ anion.

Although the $[MnF_6]^-$ anion is predicted to have two long (2x 1.789 Å) and four short (4x 1.759 Å) bonds in its D_{4h} ground state due to Jahn-Teller distortion of the d^2 six-coordinate manganese fluoride, the effect is not very pronounced because the t_{2g} orbitals are not pointing directly at the ligands. The calculated Mn−F bond lengths are slightly longer than the experimental Mn−F bond lengths (6x 1.729(3) Å), whereas the F−Mn−F bond angles well reproduce the experimental values (Table 7.3).

$\{[Xe_2F_{11}]_4[MnF_6]\}^{2+}$ (C_1), $\{[XeF_5]_4[MnF_6]\}^{2+}$ (C_1), and $[MnF_6]^{2-}$ (O_h). The starting geometries used for the hypothetical $\{[Xe_2F_{11}]_4[MnF_6]\}^{2+}$ (C_1) and $\{[XeF_5]_4[MnF_6]\}^{2+}$ cations were the crystallographic geometries of $[Xe_2F_{11}]_2[MnF_6]$ and $[XeF_5]_2[MnF_6]$ (see X-ray Crystallography) which reproduced the coordination environments of the $[MnF_6]^{2-}$ anions in both salts. The starting geometry of the $[MnF_6]^{2-}$ (O_h) anion, which was calculated in order to assess the effect of ion-pairing (Table E2), was the crystallographic geometry of the $[MnF_6]^{2-}$ anion in $K_2[MnF_6]\cdot 4HF$.

The geometry of the isolated $[MnF_6]^{2-}$ anion is a regular octahedron (Mn−F, 6x 1.8266 Å); ∠(F−Mn−F), 90°), where the t_{2g} orbitals of Mn are equally occupied (Table E2). The geometry of the $[MnF_6]^{2-}$ in $\{[Xe_2F_{11}]_4[MnF_6]\}^{2+}$ (C_1) and $\{[XeF_5]_4[MnF_6]\}^{2+}$ (Table 7.4) are slightly distorted from the ideal octahedral geometry of the isolated $[MnF_6]^{2-}$ anion (Table E2) which is caused by ion-pairing. The calculated average Mn−F bond lengths in $\{[Xe_2F_{11}]_4[MnF_6]\}^{2+}$ (1.824 Å) and $\{[XeF_5]_4[MnF_6]\}^{2+}$ (1.820 Å) are

longer than the corresponding average experimental Mn−F bond lengths (1.806(2) and 1.805(2) Å, respectively). The analogous trend was observed for the calculated Xe---Mn contact distances ($\{[Xe_2F_{11}]_4[MnF_6]\}^{2+}$, 2.779 Å; $\{[XeF_5]_4[MnF_6]\}^{2+}$, 2.555 Å), which are slightly longer than the corresponding experimental contact distances (2.667(2) and 2.534(2) Å, respectively). The calculated F−Mn−F bond angles are in a very good agreement with the experimental bond angles (Table 7.4).

7.3 Conclusion

The reaction of MnO_3F with KrF_2 resulted in the syntheses and isolation in the solid state of the first manganese(V) fluorides, MnF_5 and $K[MnF_6]$. Although the refinement of the crystal structure of MnF_5 is not yet finalized due to unresolved twinning issues, it is clear that MnF_5 is polymeric and that the crystal structure of MnF_5 consists of MnF_6-octahedra, which are linked to each other through *trans*-bridging fluorine atoms. The crystal structure of $[MnF_6]^-$ is imposed by the symmetry of the crystallographic space group. This results in an octahedral geometry and does not reflect the expected Jahn-Teller distortion which would result in D_{4h} symmetry for the anion.

The ^{19}F NMR spectrum was acquired for the solution that was used for crystal growth of $K[MnF_6]$. The ^{19}F resonance signal was significantly shifted to higher frequency when compared to that of MnO_3F which was studied by ^{19}F and ^{55}Mn NMR spectroscopy. The $^1J(^{19}F–^{55}Mn)$ coupling was also determined for the first time.

The reaction of MnO_3F with XeF_6 resulted in the isolation of the $[Xe_2F_{11}]_2[MnF_6]$ and $[XeF_5]_2[MnF_6]$ salts and their characterization by low-temperature single-crystal X-

ray diffraction. In both structures, the pseudo-octahedral $[MnF_6]^{2-}$ anions strongly interact with their respective cations, $[Xe_2F_{11}]^+$ and $[XeF_5]^+$. The $[Xe_2F_{11}]_2[MnF_6]$ salt was also characterized by low-temperature Raman spectroscopy, whereas the assignment of the known Raman spectrum of $[XeF_5]_2[MnF_6]$ has been improved in the present work. The vibrational assignments of both Raman spectra were aided by quantum-chemical calculations.

CHAPTER 8

CONCLUSIONS AND DIRECTIONS FOR FUTURE WORK

8.1. Conclusions

The fundamental chemistry of ReO_3F has been significantly extended with the development of its high-yield high-purity synthesis. The availability of ReO_3F in bulk amounts has enabled further investigation of its Lewis acid and fluoride ion donor-acceptor properties. The Lewis acid-base complex, $(HF)_2ReO_3F{\cdot}HF$, the only known example of an HF complex with rhenium, was characterized by Raman spectroscopy and single-crystal X-ray diffraction. The study of the fluoride-ion acceptor properties of ReO_3F has led to the isolation of the novel anions, $[\{ReO_3(\mu\text{-}F)\}_3(\mu_3\text{-}O)]^{2-}$, *fac*-$[ReO_3F_3]^{2-}$, and $[ReO_3F_2]^-$ and their characterization in the solid state by Raman spectroscopy and single-crystal X-ray diffraction. The $[\{ReO_3(\mu\text{-}F)\}_3(\mu_3\text{-}O)]^{2-}$ anion was also studied in CH_3CN solvent by ^{19}F NMR spectroscopy. The $[\{ReO_3(\mu\text{-}F)\}_3(\mu_3\text{-}O)]^{2-}$ cage anion provides the only example of a rhenium oxide fluoride species containing a triply coordinated oxygen atom. The facial arrangement of oxygen ligand atoms in *fac*-$[ReO_3F_3]^{2-}$ anion in the $K^+[H_3O]^+$ salt contrasts with the meridional geometry reported for the *fac*-$[ReO_3F_3]^{2-}$ anion based on the infrared and Raman spectroscopic findings. The $[ReO_3F_2]^-$ anion represents an example of an open-chain structure, where the ReO_3F units are fluorine bridged to each other.

The study of the fluoride ion-donor properties of ReO_3F has led to the isolation of the new compounds, $\mu\text{-}O(ReO_2F)(AsF_5){\cdot}2AsF_5$ and $[ReO_3][Sb_3F_{16}]$, and their

characterization in the solid state by Raman spectroscopy. The μ-$O(ReO_2F)(AsF_5)\cdot 2AsF_5$ molecule provides the first example of AsF_5 molecule coordinated to a transition metal through an oxygen atom. Attempts to synthesize the $[ReO_3][PnF_6]$ (Pn = As, Sb), $[ReO_3][Sb_2F_{11}]$, $[ReO_3][BF_4]$, and [μ-$F(ReO_3)$][SbF_6] in aHF solvent failed due to HF solvolysis of ReO_3F and formation of known ReO_2F_3 and $[H_3O][HF_2]$. Both, μ-$O(ReO_2F)(AsF_5)\cdot 2AsF_5$ and $[ReO_3][Sb_3F_{16}]$, reacted with CH_3CN forming $[ReO_3\cdot 3CH_3CN][PnF_6]$ (Pn = As, Sb), which were characterized by solid-state Raman spectroscopy. The compounds are not soluble in CH_2Cl_2 and SO_2ClF, which prevented their structural characterization by single-crystal X-ray diffraction. An attempt to grow crystals of $[ReO_3][Sb_3F_{16}]$ by sublimation resulted in the formation of the known $[ReO_2F_2][SbF_6]$.

The development of a high-yield, high-purity synthesis of ReO_3F has extended the number of known Re(VII) oxide fluorides. Reaction of ReO_3F with ReO_2F_3 in SO_2ClF yielded the new neutral rhenium(VII) oxide fluoride, $(\mu\text{-}F)_4\{[\mu\text{-}O(ReO_2F)_2](ReO_2F_2)_2\}$, which is also a rare example of an O-bridged rhenium oxide fluoride. It was characterized by single-crystal X-ray diffraction and solid-state Raman spectroscopy. The vibrational assignments of the $(\mu\text{-}F)_4\{[\mu\text{-}O(ReO_2F)_2](ReO_2F_2)_2\}$ Raman spectrum were confirmed by ^{18}O-enrichment studies.

Rhenium trioxide fluoride has been shown to act as the oxygen source and as the progenitor of the counter ion, $[\mu\text{-}F(ReO_2F_3)_2]^-$, in the synthesis of [XeOXeOXe][μ-$F(ReO_2F_3)_2]_2$, where the $[XeOXeOXe]^{2+}$ cation provides the first example of an isolated xenon(II) oxide and a noble-gas oxide cation. The synthesis of [XeOXeOXe][μ-

$F(ReO_2F_3)_2]_2$ was accomplished by the low-temperature reaction of ReO_3F with XeF_2 in aHF. The reaction pathway involving HOXeF as an intermediate in the oxygen/fluorine metathesis steps was proposed. The $[XeOXeOXe][\mu\text{-}F(ReO_2F_3)_2]_2$ salt was unambiguously characterized by low-temperature single-crystal X-ray diffraction and solid-state Raman spectroscopy with aid of quantum-chemical calculations and ^{18}O-enrichment studies. The nature of the Xe–O and Xe–F bonds in free $[XeOXeOXe]^{2+}$, the hypothetical neutral oxide fluoride, FXeOXeOXeF, and the ion pair, $[XeOXeOXe][\mu\text{-}F(ReO_2F_3)_2]_2$, were studied with the aid of NBO, QTAIM, ELF, and MEPS analyses.

The reactions of MnO_3F with noble-gas fluorides, KrF_2 and XeF_6, have been studied with the aim to synthesize the missing Mn(VII) oxide fluorides, $MnOF_5$ and MnO_2F_3. Both reactions, however, resulted in the oxidative elimination of O ligands and the formation of manganese(V), MnF_5 and $K[MnF_6]$, and manganese(IV), $[Xe_2F_{11}]_2[MnF_6]$ and $[XeF_5]_2[MnF_6]$, fluorides, respectively. An HF solution of MnO_3F was characterized by ^{19}F, ^{55}Mn, and $^{19}F–^{55}Mn$ COSY NMR spectroscopies and the first $^1J(^{19}F–^{55}Mn)$ coupling constant was determined. A preliminary characterization of $[MnF_6]^-$ by ^{19}F NMR spectroscopy is also provided. The $K[MnF_6]$, $[Xe_2F_{11}]_2[MnF_6]$, and $[XeF_5]_2[MnF_6]$ were structurally characterized for the first time by single-crystal X-ray diffraction. The crystal structure of MnF_5 is polymeric, however, the geometrical parameters could not be finalized due to unresolved twinning issues. Additionally, $[Xe_2F_{11}]_2[MnF_6]$ has been characterized by Raman spectroscopy and the vibrational assignment of the Raman spectrum of $[XeF_5]_2[MnF_6]$ was improved in the present work.

8.2. Future Work

8.2.1. Development of the Fluoride Ion Donor-Acceptor Properties of TcO_3F

The neutral TcO_3F, TcO_2F_3, $TcOF_5$ and technetium anions and cations derived from TcO_2F_3 and $TcOF_5$ are known and well characterized. The only isolated derivative of TcO_3F that has been well characterized by single-crystal X-ray diffraction is the $[\{TcO_3(\mu\text{-}F)\}_3(\mu_3\text{-}F)]^-$ anion.[23] the latter has been synthesized by reaction of K/$[NH_4][TcO_4]$ with aHF. The $[TcO_3]^+$ cation was shown to exist by ^{99}Tc and ^{17}O NMR spectroscopy. However, a subsequent study of this reaction revealed that TcO_3F undergoes solvolysis in PnF_5/aHF (Pn = As, Sb) media to form $[TcO_2F_2][PnF_6]$ salts.[23]

The knowledge of the fundamental chemistry of ReO_3F can be applied to develop the chemistry of its radioactive analogue, TcO_3F. A detailed knowledge of TcO_3F reactivity is vital to improve methods for the effective removal of $^{99}TcO_3F$ from re-enriched UF_6 prior to refabrication into nuclear fuel elements composed of UO_2.

The fluoride ion-acceptor properties of TcO_3F can be studied by its reactions with fluoride ion donors, CsF or [NO]F, (eq 8.1) which have been used to synthesize the *fac*-

$$n\text{XF} + TcO_3F \longrightarrow X_n[TcO_3F_{n+1}] \quad (\text{X} = \text{Cs, [NO]}) \quad (n = 1,2) \qquad (8.1)$$

$[ReO_3F_3]^{2-}$ and $[ReO_3F_2]^-$ anions. Facial arrangements of oxygen ligands are expected for both anions, as observed for their rhenium analogues, because in the d^0 trioxo transition metal complexes, a *cis* arrangement of oxygen atoms minimizes the competition of the oxo ligands for the empty $d_{t_{2g}}$ orbitals of the metal. Structural characterization of the $[TcO_3F_2]^-$ anion is of particular interest because $[ReO_3F_2]^-$ (see Chapter 4) and OsO_3F_2[247]

are polymeric, fluorine-bridged structures, whereas the polymeric $[MoO_3F_2]^{2-}$ [343] and $[WO_3F_2]^{2-}$ [344] anions exhibit asymmetric oxygen-bridges.

In view of the solvolysis of ReO_3F and TcO_3F in aHF and in the presence of strong Lewis acids, AsF_5 and SbF_5, the use of aHF as a reaction solvent should be avoided in the synthesis of the $[TcO_3]^+$ cation. Therefore, it should be possible to synthesize the $[TcO_3]^+$ cation by analogy with the synthesis of the $[ReO_3]^+$ cation (eq. 8.2). If soluble in SO_2ClF

$$TcO_3F + 3SbF_5 \xrightarrow{SO_2ClF} [TcO_3][Sb_3F_{16}] \quad (8.2)$$

or CH_2Cl_2, the single-crystal structure determination of the $[TcO_3][Sb_3F_{16}]$ salt should be possible. Dissolution of $[TcO_3][Sb_3F_{16}]$ in CH_3CN is expected to yield the pseudo-octahedral compounds, $[O_3Tc(NCCH_3)_3][SbF_6]$ (eq 8.3). The complex $[O_3Tc(NCCH_3)_3]^+$ cation can be

$$[TcO_3][Sb_3F_{16}] + 3CH_3CN \longrightarrow [O_3Tc(NCCH_3)_3][SbF_6] + 2SbF_5{\cdot}CH_3CN \quad (8.4)$$

studied by ^{99}Tc NMR spectroscopy and $^1J(^{99}Tc-^{17}O)$ coupling should be observed.

8.2.2. Further Development of the MnO_3F Chemistry

The fundamental chemistry of MnO_3F is least studied among other group VII d^0 transition metal oxide fluorides. In the present work, attempts to study its fluoride ion acceptor properties by reactions of MnO_3F with AF (K, Cs) in aHF failed because MnO_3F was shown to be a weaker fluoro-acid than HF and, as a result, only $A[HF_2]$ formed. Manganese trioxide fluoride was reported not to react with AsF_5 and SbF_5; however, the reaction conditions were not described.[43] In order to avoid competition of HF solvent in reactions with fluoride ion donors, it may be possible to synthesize MnO_3F by reaction of $K[MnO_4]$ with XeF_2 in CH_2Cl_2 (eq 8.6). Moreover, XeF_2 has recently been shown by ^{19}F

$$K[MnO_4] + XeF_2 \xrightarrow{CH_2Cl_2} MnO_3F + Xe + KF + \tfrac{1}{2}O_2 \quad (8.6)$$

NMR studies to be stable in CH_2Cl_2 at room temperature in PTFE-FEP for ≥ 168 h[345] and CH_2Cl_2 was used as a solvent in oxidation of organic compounds by $K[MnO_4]$.[346] Manganese trioxide fluoride can subsequently react with CsF or $[N(CH_3)_4]F$ at temperatures below 0 °C (eq 8.7). The reaction of MnO_3F with Lewis acids in CH_2Cl_2 should be also attempted (8.8).

$$nXF + MnO_3F \longrightarrow X_n[MnO_3F_{n+1}] \ (X = Cs, [N(CH_3)_4]) \ (n = 1,2) \quad (8.7)$$

$$xPnF_5 + MnO_3F \longrightarrow [MnO_3][Pn_xF_{5x+1}] \ (Pn = As, Sb; x = 1-3) \quad (8.8)$$

The $[MnO_3F_3]^{2-}$ anion is expected to possess C_{3v} symmetry in the solid state as observed for its third row transition metal analogue, *fac*-$[ReO_3F_3]^{2-}$. If synthesized, $[MnO_3F_2]^-$ anion may differ structurally from oligomeric $[ReO_3F_2]^-$. By analogy with the neutral compounds, where ReO_3F is a polymer, TcO_3F is a dimer, and MnO_3F is a monomer, the $[MnO_3F_2]^-$ anion may be a pentacoordinated monomer.

8.2.3. Improved Synthesis of MnF_5 and the Development of Its Fundamental Chemistry

Although the solid isolated from the reaction of MnO_3F with KrF_2 has been tentatively assigned to MnF_5 based on its preliminary single-crystal X-ray structure, the solution of the latter structure suffers from unresolved twinning issues requiring further refinement. Moreover, attempts to regrow crystals of MnF_5 from aHF failed. Therefore, a high-yield and high-purity synthesis of MnF_5 will allow its unambiguous characterization by Raman and ^{19}F NMR spectroscopies, and magnetic measurements. In the course of the

current research work, it has been shown that MnF_5 reacts with $K[HF_2]$ in situ (Chapter 7). The resulting salt, $K[MnF_6]$, has only been characterized by single-crystal X-ray diffraction. Therefore, the availability of MnF_5 in larger amounts should allow full characterization of the $[MnF_6]^-$ anion by magnetic measurements and Raman spectroscopy. Although a resonance observed in the ^{19}F NMR spectrum recorded on an HF solution of the solid containing $K[MnF_6]$ was assigned to the $[MnF_6]^-$ anion, a more in-depth study is required to confirm the latter assignment. In particular, the acquisition of the ^{55}Mn spectrum would confirm the assignment from the septet that is expected to be observed in the ^{55}Mn NMR spectrum.

8.2.4. Synthesis of FXeOXeOXeF and the $[FXeOXeOXe]^+$ Cation

The synthesis of the neutral FXeOXeOXeF molecule may be achieved by the low-temperature reaction of $[XeOXeOXe][\mu\text{-}F(ReO_2F_3)_2]_2$ with a fluoride-ion source, CsF or $[N(CH_3)_4]F$ (eq 8.9) in aHF. The compound, FXeOXeOXeF, will provide the first

$$[XeOXeOXe][\mu\text{-}F(ReO_2F_3)_2]_2 + 2\ CsF/[N(CH_3)_4]F \longrightarrow FXeOXeOXeF + 2Cs/[N(CH_3)_4][\mu\text{-}F(ReO_2F_3)_2] \quad (8.9)$$

example of a neutral Xe(II) oxide fluoride. The characterization of FXeOXeOXeF by single-crystal X-ray diffraction will provide the first determination of a Xe−O bond length in a neutral Xe(II) oxide fluoride. The study of the $[XeOXeOXe]^{2+}$ cation (Chapter 6) and FXeOXeOXeF compound by ^{129}Xe, ^{19}F, and ^{17}O NMR spectroscopy is of particular interest because it will allow the determination of a $^2J(^{129}Xe–^{129}Xe)$ coupling.

Availability of high-purity FXeOXeOXeF in reasonable amounts may enable the synthesis of the $[FXeOXeOXe]^+$ cation by stoichiometric reaction of FXeOXeOXeF with PnF_5 (Pn = As, Sb). The latter cation may be structurally characterized by single-crystal X-ray diffraction, ^{129}Xe and ^{19}F NMR and Raman spectroscopies.

References

1. LeBlond, N.; Schrobilgen, G. J. *J. Chem. Soc., Chem. Commun*. **1996**, 2479−2480.
2. LeBlond, N.; Mercier, H. P. A.; Dixon, D. A.; Schrobilgen, G. J. *Inorg. Chem*. **2000**, *39*, 4494−4509.
3. Aynlsey, E. E.; Peacock, R. D.; Robinson, P. L. *J. Chem. Soc*. **1950**, 1622−1624.
4. Sunder, W. A.; Stevie F. A. *J. Fluorine Chem.*, **1975**, *6*, 449–463.
5. Roesky, H. W. *Efficient Preparations of Fluorine Compounds*, Wiley: New York, **2013**, pp 100–107.
6. Brisdon, A. K.; Holloway, J. H.; Hope, E. G.; Townson, P. J.; Levason, W.; Ogden, J. S. *J. Chem. Soc. Dalton Trans*. **1991**, 3127−3132.
7. Holloway, J. H.; Selig, H.; Claasen, H. H. *J. Chem. Phys*. **1971**, *54*, 4305−4311.
8. Bartlett, N.; Jha, N. K. *J. Chem. Soc. (A)* **1968**, 536−543.
9. Bartlett, N.; Beaton, S.; Reeves, L. W.; Wells, E. J. *Can. J. Chem*. **1964**, *42*, 253−2540.
10. Alekseichuk, I. S.; Ugarov, V. V.; Sokolov, V. B.; Rambidi, N. G. *Zh. Strukt. Khim.*, **1981**, *22*, 795−796.
11. Shalabi, A. S.; Nour, E. M. E. *Gazz. Chim. Ital.* **1991**, *121*, 555−558.
12. Supel J. Ph.D. Dissertation, Free University of Berlin, Berlin, 2007.
13. Schrobilgen, G. J.; Holloway, J. H.; Russell, D. R. *J. Chem. Soc. Dalton Trans*. **1984**, 1411−1415.
14. LeBlond, N. Ph. D. Thesis, McMaster University, Hamilton, ON, Canada, **1998**.
15. Selig, H.; Karpas, Z. *Izrael J. Chem*. **1971**, 9, 53−56.
16. Giese, S.; Seppelt, K. *Angew. Chem., Int. Ed. Engl*. **1994**, *33*, 461−463.
17. Mercier, H. P. A.; Schrobilgen, G. J. *Inorg. Chem*. **1993**, *32*, 145−151.
18. LeBlond, N.; Schrobilgen, G. J. *Inorg. Chem*. **2001**, *40*, 1245−1249.
19. Casteel, W. J., Jr.; Dixon, D. A.; LeBlond, N.; Lock, P. E.; Mercier, H. A. P.; Schrobilgen, G. J. *Inorg. Chem*. **1999**, *38*, 2340−2358.

20. Beattie, I. R.; Crocombe, R. A.; Ogden, S. *J. Chem. Soc. Dalton. Trans.* **1977**, 1481–1489.
21. Supel, J.; Marx, R.; Seppelt, K. *Z. Anorg. Allg. Chem*. **2005**, *631*, 2979–2986.
22. LeBlond, N.; Dixon, D. A.; Schrobilgen, G. J. *Inorg. Chem*. **2000**, *39*, 2473−2487.
23. Supel, J.; Abram, U.; Hagenbach, A.; Seppelt, K. *Inorg. Chem*. **2007**, *46*, 5591−5595.
24. Peterson, S. W.; Willett, R. D.; Huston, J. L. *J. Chem. Phys*. **1973**, *59*, 453−459.
25. Casteel, W. J. Jr.; Dixon, D. A.; LeBlond, N.; Mercier, H. P. A.; Schrobilgen, G. J. *Inorg. Chem.* **1998**, *37*, 340–353.
26. Franklin, K. J.; Lock, C. J. L.; Sayer, B. G.; Schrobilgen, G. J. *J. Am. Chem. Soc*. **1982**, *104*, 5303−5306.
27. Yagodin, G. A.; Oplavskii, E. G.; Rakov, E. G.; Dudin, A. S. *Dokl. Akad. Nauk SSSR*. **1980**, *252*(6), 1400–1402.
28. Peacock, R. D. *J. Chem. Soc*. **1955**, 602−603.
29. Selig, H.; Malm, J. G. *J. Inorg. Nucl. Chem*. **1963**, *25*, 349–351.
30. Binenboym, J.; El-Gad, U.; Selig, H. *Inorg. Chem*. **1974**, *13*, 319–321.
31. Wiechert, K. *Z. Anorg. Allg. Chem*. **1950**, *261*, 310–323.
32. Engelbrecht, A.; Grosse, V. *J. Am. Chem. Soc*. **1954**, *76*, 2042–2045.
33. Ansley, E. E.; Hair, M. L. *J. Chem. Soc.* **1954**, *76*, 3747–3748.
34. Selig, H.; El-Gad, U. *J. Inorg. Nucl. Chem*. **1973**, *35*, 3517–3522.
35. Brisdon, A. K.; Holloway, J. H.; Hope, E. G. *J. Fluorine Chem*. **1998**, *89*, 35–37.
36. Kuhlmann, W.; Sawodny, W. *J. Fluorine Chem*. **1977**, *9*, 337–340.
37. Gerlach, U.; Ringel, C. *Z. Chem*. **1977**, *17*, 307–309.
38. Lis T. *Acta Crystallograph*. **1983**, *C39*, 961−962.
39. Gerken, M.; Dixon, D. A.; Schrobilgen, G. J. *Inorg. Chem.* **2000**, *39*, 4244−4255.
40. (a) Herrmann, W. A.; Voss, E.; Flöel, M. *J. Organomet. Chem.* **1985**, *297*, C5−C7; (b) Herrmann, W. A.; Flöel, M.; Kulpe, J.; Felixberger, J. K.; Herdtweck, E. *J. Organomet. Chem*. **1988**, *355*, 297−313.

41. (a) Wieghardt, K.; Pomp, C.; Nuber, B.; Weiss, J. *Inorg. Chem*. **1986**, *25*, 1659−1661; (b) Herrmann, W. A.; Roesky, P. W.; Kühn, F. E.; Scherer, W.; Kleine, M. *Angew. Chem. Int. Ed. Engl.* **1993**, *32*, 1714−1716; (c) Herrmann, W. A.; Roesky, P. W.; Kühn, F. E.; Elison, M.; Artus, G.; Scherer, W.; Romão, C. C.; Lopes, A.; Basset, J.-M. *Inorg. Chem*. **1995**, *34*, 4701−4707.
42. Küppers, H.-J.; Nuber, B.; Weiss, J.; Cooper, S. R. *J. Chem. Soc., Chem, Commun*. **1990**, 979−980.
43. Supel, J.; Hagenbach, A.; Abram, U.; Seppelt, K. *Z. Anorg. Allg. Chem.* **2008**, *634*, 646−648.
44. Allred, A. L. *J. Inorg. Nucl. Chem*. **1961**, *17*, 215−221.
45. Birchall, T.; Myers, R. D.; de Waard, H.; Schrobilgen, G. J. *Inorg. Chem*. **1982**, *21*, 1068−1073.
46. Huppmann, P.; Labischinski, H.; Lentz, D.; Pritzkow, H.; Seppelt, K. *Z. Anorg. Allg. Chem.* **1982**, *487*, 7−25.
47. Casteel, W. J., Jr.; MacLeod, D. M.; Mercier, H. P. A.; Schrobilgen, G. J. *Inorg. Chem*. **1996**, *35*, 7279−7288.
48. Turowsky, L.; Seppelt, K. *Z. Anorg. Allg. Chem.* **1990,** *590*, 37−47.
49. Huppmann, P. Dissertation, Freie Univ. Berlin(W), **1983.**
50. Ansley, E. E. *J. Chem. Soc.* **1958**, 2425–2426.
51. Varetti, E. L.; Müller, A. *Z. Anorg. Allg*. *Chem*. **1978**, *442*, 230–234.
52. Jasinski, J. P.; Holt, S. L.; Wood, J. H.; Moskowitz, J. W. *J. Chem. Phys*. **1975**, *63*, 1429–1444.
53. Aymonino, P. J.; Schulze, H.; Müller, A. *Z. Naturforsch*. **1969**, *24b*, 1508–1510.
54. Javan, A.; Engelbrecht, A. *Phys. Rev*, **1954**, *96*, 649–658.
55. Hog, J.; Pederson, T. *J. Mol. Spectrosc*. **1976**, *61*, 243–248.
56. Bürger, H.; Weinrath, P.; Dressler, S.; Hansen, T.; Thiel. W. *J. Mol. Spectrosc*. **1997**, *183*, 139–150.
57. Reisfeld, M. J.; Asprey, L. B.; Matwiyoff, N. A.; *Spectrochim. Acta (A)*. **1971**, *27*, 765

58. Varetti, E. L.; Filgueira, R. R; Müller, *Spectrochim. Acta (A)*. **1981**, *37*, 369–373.
59. Diemann, E.; Varetti, E. L.; Müller, A. *Chem. Phys. Let*. **1977**, *51*, 460–463.
60. Varetti, E. L. *J. Raman Spectrosc*. **1991**, *22*, 307–309.
61. Levason, W.; Ogden, J. S.; Saad, A. K.; Young, N. A.; Brisdon, A. K.; Holliman, P. J.; Holloway, J. H.; Hope, E. G. *J. Fluorine Chem*. **1991**, *53*, 43–51.
62. Spandl, J.; Supel, J.; Drews, T.; Seppelt, K. *Z. Anorg. Allg. Chem*. **2006**, *632*, 2222–2225.
63. Malm, J. G.; Selig, H.; Fried, S. *J. Am. Chem. Soc*. **1960**, *82*, 1510.
64. Malm, J. G.; Selig, H. *Inorg. Nucl. Chem*. **1961**, *20*, 189–197.
65. Bartlett, N.; Beaton, S.; Reeves, L. W.; Wells, E. J. *Can. J. Chem*. **1964**, *42*, 2531–2540.
66. Mutterties, E. L.; Packer, K. J.; *J. Am. Chem. Soc*. **1964**, *86*, 293–294.
67. Claassen, H. H.; Selig, H. *J. Chem. Phys*. **1965**, *43*, 103–105
68. Claassen, H. H.; Gasner, E. L.; Selig, H. *J. Chem. Phys*. **1968**, *49*, 1803–1807.
69. Jacob, J.; Bartell, L. S. *J. Chem. Phys*. **1970**, *53*, 2235–2242.
70. Vogt, T.; Fitch, A. N.; Cockcroft, J. K. *Science* **1994**, *263*, 1265–1267.
71. Jacob, E.; Fähnle, M. *Angew. Chem. Int. Ed. Engl*. **1976**, *15*, 159−160.
72. Baran, E. J. *Angew. Chem*. **1976**, *31A*, 1733−1734.
73. Yeh, S. M. Ph.D. Thesis, Lawrence Berkeley National Laboratory, 1984.
74. Yeh, S. M.; Bartlett, N. *Rev. Chim. Miner*. **1986**, *23*, 676−689.
75. Hwang, I.-C.; Seppelt, K. *J. Fluorine Chem*. **2000**, *102*, 69−72.
76. Gaunt, J. *Trans. Faraday Soc*. **1954**, *50*, 209-212.
77. Moffit, W.; Goodman, G. L.; Fred, M.; Weinstock, B. *Mol. Phys*.**1959**, *2*, 109−122.
78. Claassen, H. H.; Malm, J. G.; Selig, H. *J. Chem. Phys*. **1962**, *36*, 2890–2892.
79. Siegel, S.; Northrop, D. A. *Inorg. Chem*. **1966**, *5*, 2187−2188.
80. Claassen, H. H.; Goodman, G. L.; Holloway, J. H.; Selig, H. *J. Chem. Phys*. **1970**, *53*, 341–348.
81. Richardson, A. D.; Hedberg, K.; Lucier, G. M. *Inorg. Chem*. **2000**, *39*, 2787–2793.

82. Drews, T.; Supel, J.; Hagenbach, A.; Seppelt, K. *Inorg. Chem*. **2006**, *45*, 3782–3788.
83. Molski, M.; Seppelt, K. *Dalton Trans*. **2009**, 3379−3383.
84. Craciun, R.; Picone, D.; Long, R. T.; Li, S.; Dixon, D. A.; Peterson, K. A.; Christe, K. O. *Inorg. Chem.* **2010**, *49*, 1056−1070.
85. Nikolaev, N. S.; Ippolitov, E. G. *Dokl. Akad. Nauk* **1961**, *140*, 129–133.
86. Ippolitov, E. G.; Nikolaev, N. S. *Izv. Akad. Nauk, Ser. Khim*. **1962**, 748–755.
87. Beuter, A.; Kuhlman, W.; Sawodny, W. *J. Fluorine Chem*. **1975**, *6*, 367–378.
88. Koz'min, P. A. *Zh. Strukt. Khim*. **1964**, *1*, 70–76.
89. Adam, S.; Ellern, A.; Seppelt, K. *Chem.-Eur. J*. **1996**, *2*, 398−402.
90. Selig, H.; Chernick, C. C.; Malm, J. G.; *J. Inorg. Nucl. Chem*. **1961**, *19*, 377–381.
91. Claassen, H. H.; Selig, H.; Malm, J. G. *J. Chem. Phys*. **1962**, *36*, 2888–2890.
92. Craciun, R.; Long, R. T.; Dixon, D. A.; Christe, K. O. *J. Phys. Chem. A*. **2010**, *114*, 7571−7582.
93. Holloway, J. H.; Selig, H.; *J. Inorg. Nucl. Chem*. **1968**, *30*, 473−478.
94. Hargreaves, G. B.; Peacock, R. D. *J. Chem. Soc*. **1960**, 1099–1103.
95. Falconer, W. E.; Jones, G. R.; Sunder, W. A.; Haigh, I.; Peacock, R. D. *J. Inorg. Nucl. Chem*. **1973**, *35*, 751–753.
96. Paine, R. T.; Asprey, L. B. *Inorg. Chem*. **1975**, *14*, 1111–1113.
97. Hoskins, B. F.; Linden, A.; Mulvaney, P. C.; O'Donnell, T. A. *Inorg. Chim. Acta* **1984**, *88*, 217−222.
98. Peacock, R. D. *J. Chem. Soc*. **1957**, 467−469.
99. Shamir, J.; Malm, J. *J. Inorg. Nucl. Chem. Suppl*. **1976**, 107−111.
100. Sunder, W. A.; Wayda, A. L.; Distefano, D.; Falconer, W. E. *J. Fluorine Chem*. **1979**, *14*, 299–325.
101. Casteel, W. Jr.; Horwitz, T. *Eur. J. Solid State Inorg. Chem*. **1992**, *29*, 649-657.
102. Edwards, A. J.; Hugill, D.; Peacock, R. D. *Nature* **1963**, *200*, 672.
103. Binenboym, J.; Selig, H. *Inorg. Nucl. Chem*. Herbert H. Hyman Mem. Vol. **1976**, 231−232.

104. Gibson, J. K. *J. Fluorine Chem*. **1991**, *55*, 299−311.
105. Hugill, D.; Peacock, R. D. *J. Chem. Soc. A* **1966**, 1339−1341.
106. Peakock, R. D. *J. Chem. Soc*. **1956**, 1291−1293.
107. Weise, L. C. *Z. Anorg. Chem*. **1956**, *283*, 377−389.
108. Schwochau, K. W. *Z. Naturforsch.* **1964**, *19A*, 1237−1238.
109. LaValle, D. E.; Steele, R. M.; Smith, W. T. Jr. *J. Inorg. Nucl. Chem*. **1966**, *28*, 260−263.
110. Schwochau, K.; Krasser, W. *Z. Naturforsch.* **1969**, *24A*, 403−407.
111. Krasser, W.; Schwochau, K. *Z. Naturforsch.* **1970**, *25A*, 206−210.
112. Black, A. M.; Flint, C. D. *J. Mol. Spectrosc*. **1978**, *70*, 481−483.
113. Clark, G. R.; Russell, D. R. Acta Crystallogr. **1978**, *B34*, 894−895.
114. Lomenzo, J.; Patterson, H.; Strobridge, S.; Engstrom, H. *Mol. Phys*. **1980**, *40*, 1401−1420.
115. Bettinelli, M.; Di Sipio, L.; Pasquetto, A.; Ingletto, G.; Montenero, A. *Inorg. Chim. Acta* **1985**, *99*, 37−42.
116. Bettinelli, M.; Di Sipio, L.; Ingletto, G.; Razzetti, C. *Inorg. Chim. Acta* **1987**, *133*, 7−9.
117. Schwochau, K.; Herr, W. *Angew. Chem. Int. Ed. Engl*. **1963**, *2*, 97.
118. Schwochau, K. *Z. Naturforsch.* **1964**, *19A*, 1237−1238.
119. Alberto, R.; Anderegg, G. *Polyhedron* **1985**, *4*, 1067.
120. Balasekaran, S. M.; Molski, M.; Spandl, J.; Hagenbach, A.; Alberto, R.; Abram, U. *Inorg. Chem*. **2013**, *52*, 7094−7099.
121. Housecroft, C. E.; Sharpe, A. G. *Inorganic Chemistry*; Pearson Education Ltd: Essex, 2001; pp 507-508.
122. Baur, W. H.; Khan, A. A. *Acta Crystallogr*. **1971**, *B27*, 2133−2139.
123. Hoppe, R.; Liebe, W.; Dähne, W. *Z. Anorg. Allg. Chem*. **1961**, *307*, 276−289.
124. Mazej, Z. *J. Fluorine Chem*. **2002**, *114*, 75−80.
125. Hepworth, M. A.; Jack, K. H.; *Acta Crystallogr*. **1957**, *10*, 345−351.
126. Schrötter, F.; Müller, B. G. *Z. Anorg. Allg. Chem*. **1993**, *619*, 1426−1430.

127. Hepworth, M. A.; Jack, K. H.; Nyholm, R. S. *Nature*, **1957**, *179*, 211–212.
128. Osin, S. B.; Davlyatshin, D. I.; Shevelkov, V. F.; Mit'kin, V. N. *Russ. J. Phys. Chem*. **1995**, *69*, 794
129. Bukhmarina, V. N.; Predtechenskii, Y. B. *Opt. Spektrosk.* **1996**, *80*, 762−765.
130. Girichev, G. V.; Giricheva, N. I.; Petrova, V. N.; Shlykov, S. A.; Rakov, E. G. *Zh. Strukt. Khim*. **1994**, *35*, 61−67.
131. Solomonik, V. G.; Sliznev, V. V.; Balabanov, N. B. *Z. Phys. Chem*. **1997**, *200*, 77−82.
132. Hargittai, M.; Réffy, B.; Kolonits, M.; Marsden, C. J.; Heully, J.-L. *J. Am. Chem. Soc*. **1997**, *119*, 9042−9048.
133. Lutar, K.; Jeshih, A.; Žemva, B. *Polyhedron* **1988**, *7*, 1217–1219.
134. Rakov, E. G.; Khaustov, S. V.; Ostropikov, V. V. *Russ. J. Inorg. Chem*. **1998**, *43*, 465−469.
135. (a) Hoppe, R.; Dähne, W.; Klemm, W. *Naturwissenschaften* **1961**, *48*, 429–5. (b) Hoppe, R.; Dähne, W.; Klemm, W. *Liebigs. Ann. Chim*. **1962**, *658*, 1–5.
136. Hoppe, R. *Israel. J. Chem*. **1978**, *17*, 48–2048.
137. Roesky, H. W.; Glemser, O.; Hellberg, K. H. *Chem. Ber*. **1965**, *98*, 2046–2048.
138. Cesaro, S. N.; Rau, J. V.; Chilingarov, N. S.; Balducci, G.; Sidorov, L. N. *Inorg. Chem.* **2001**, *40*, 179–181.
139. Müller, B. G.; Serafin, M. *Z. Naturforsch*. **1987**, *42b*, 1102–1106.
140. Ehlert, T. C.; Hsia, M. *J. Fluorine Chem*. **1972**, *2*, 33–51.
141. Rakov, E. G.; Khaustov, S. V.; Pomadchin, S. A. *Z. Neorg. Khim.* **1997**, *42*, 1800–1803.
142. Kadosov, D. B.; Bagaturjants, A. A.; Rakov, E. G.; Kazanskii, V. B. *Dokl. Akad. Nauk* **1986**, *290*, 387–389.
143. Adelhelm, A.; Jacob, E. *J. Fluorine Chem.* **1991**, *54*, 21.
144. Wilson, W. W.; Christe, K. O. *Inorg. Synthesis* **1986**, 24, 48–50.
145. Hoppe; Blinne, K. *Z. Anorg. Allg. Chem*. **1957**, *291*, 269–275.
146. Hoppe; Siebert, G. *Z. Anorg. Allg. Chem*. **1970**, *376*, 261–267.

147. Artukhov, A. A; Klimov, V. D.; Krasulin, S. V.; Nabiev, SH. Sh.; Tolmachjova, N. S. *Koord. Khim.* **1990**, *16*, 1348–1349.
148. Cox, B.; Sharpe, A. G. *J. Chem. Soc.* **1954**, 1798–1803.
149. Kaskel, S.; Strähle, J. *Z. Anorg. Allg. Chem.* **1997**, *623*, 1259–1263.
150. Christe, K. O.; Wilson, W. W.; Wilson, R. D. *Inorg. Chem.* **1980**, *19*, 3254–3256.
151. Bougon, R. A.; Christe, K. O.; Wilson, W. W. *J. Fluorine Chem.* **1985**, *30*, 237–239.
152. Asprey, L. B.; Reisfeild, M. J.; Matwiyoff, N. A. *J. Mol. Spectrosc.* **1970**, *34*, 361–369.
153. Pfeil, A. *Theor. Chim. Acta* **1971**, *20*, 159–369.
154. Flint, C. D. *J. Mol. Spectrosc.* **1971**, *37*, 414–422.
155. Flint, C. D. *Chem. Comm.* **1970**, *8*, 482–483.
156. Reisfeld, M. J.; Matwiyoff, N. A.; Asprey, L. B. *J. Mol. Spectrosc.* **1971**, *39*, 8–20.
157. Hoppe, R.; Hofman, B. *Z. Anorg. Allg. Chem.* **1977**, *436*, 65–74.
158. Hoppe, R.; Wander, K.-H. *J. Fluorine Chem.* **1983**, *23*, 589–592.
159. Bode, H.; Wendt, W. *Z. Anorg. Allg. Chem.* **1952**, *269*, 165–172.
160. Bukovec, P.; Hoppe, R. *J. Fluorine Chem.* **1983**, *23*, 579–587.
161. Bukovec, P.; Hoppe, R. *J. Fluorine Chem.* **1988**, *38*, 107–114.
162. Chaudhuri, M. K.; Das, J. C.; Dasgupta, H. S. *J. Inorg. Nucl. Chem.* **1981**, *43*, 85–87.
163. Sharpe, A. G.; Woolf, A. A. *J. Chem. Soc.* **1951**, 798–801.
164. Allen, G. C.; McMeeking, R. F.; Hoppe, R. *J. Fluorine Chem.* **1973**, *2*, 333–336.
165. Müller, B. G. *J. Fluorine Chem.* **1981**, *17*, 409–421.
166. Mazej, Z.; Lutar, P. B.; Žemva, B. *Zbornik Referatov s Poscetovanja Slovenski Kemijski Dnevi.* **2000**, 187–190.
167. Žemva, B.; Zupan, J.; Slivnik, J. *J. Inorg. Nucl. Chem.* **1971**, *33*, 3955–3957.
168. Jeshih, A.; Žemva, B. *Vestn. Slov. Kem. Drus.* **1987**, *34*, 343–349.
169. Bohinc, M.; Grannec, J.; Slivnik, J.; Žemva, B. *J. Inorg. Nucl. Chem.* **1976**, *38*, 75–76.

170. Aubert, J.; Cady, G. H. *Inorg. Chem*. **1970**, *9*, 2600–2602.
171. Žemva, B.; Slivnik, J. *J. Fluorine Chem*. **1981**, *17*, 375–379.
172. Nikitin, M. I.; Rakov, E. G.; Tsirel'nikov, V. I.; Khaustov, S. V. *Zh. Neorg. Khim*. **1997**, *42*, 1354.
173. Nikitin, M. I.; Rakov, E. G. *Russ. J. Inorg. Chem*. **1998**, *43*, 314–318.
174. Gerken, M.; Moran, M. D.; Mercier, H. P. A.; Pointner, B. E.; Schrobilgen, G. J.; Hoge, B.; Christe, K. O.; Boatz, J. A. *J. Am. Chem. Soc*. **2009**, *131*, 13474−13489.
175. *Oak Ridge Nat. Lab., [Rep] ORNL (US)* **2009**, *ORNL/TM-2007/207*.
176. Winfield, J, M. *J. Fluorine Chem.* **1984**, *25*, 91–98.
177. Casteel, W. J., Jr.; Dixon, D. A.; Mercier, H. P. A.; Schrobilgen, G. J. *Inorg. Chem*. **1996**, *35*, 4310−4322.
178. Gillespie, R. J.; Netzer, A.; Schrobilgen, G. J. *Inorg. Chem*. **1974**, *13*, 1455−1459.
179. Christe, K. O.; Wilson, W. W.; Wilson, R. D.; Bau, R.; Feng, J. *J. Am. Chem. Soc.* **1990**, *112*, 7619−7625.
180. Emara, A. A. A.; Lehmann, J. F.; Schrobilgen, G. J. *J. Fluorine Chem*. **2005**, *126*, 1373−1376.
181. Ruff, O.; Menzel, W.; Neumann, W. *Z. Anorg. Allg. Chem.* **1932,** *208*, 293–303.
182. Mercier, H. P. A.; Sanders, J. C. P.; Schrobilgen, G. J.; Tsai, S. S. *Inorg. Chem*. **1993**, *32*, 386−393.
183. Kinkead, S. A; FitzPatrick, J. R.; Foropoulos, J. J.; Kissane, R. J.; Purson, J. D. *In Fluorine Chemistry Toward the 21st Century*; Thrasher, J. S., Strauss, S. H., Eds.; ACS Symposium Series 555; American Chemical Society: Washington, DC, 1994; Chapter 3, pp 40−55.
184. Bezmel'nitsyn, V. N.; Legasov, V. A.; Chaivanov, B. B. *Dokl. Akad. Nauk SSSR* **1977**, *235*, 365−367.
185. Lehmann, J. F. Ph. D. Thesis, McMaster University, Hamilton, ON, Canada, **2000**.
186. Chernick, C. L.; Malm, J. G. *Inorg. Synth*. **1966**, *8*, 259−260.
187. Ulbricht, K.; Kriegsmann, H. *Z. Chem*. **1966**, *6*, 232−233.
188. Tsao, P.; Cobb, C. C.; Claassen, H. H. *J. Chem. Phys*. **1971**, *54*, 5247−5253.

189. Hughes, M. J.; Brock,, D. S.; Mercier, H. P. A.; Schrobilgen, G. J. *J. Fluorine Chem.* **2011**, *132*, 660−668
190. *APEX2*, release v2011.6-1; Bruker AXS Inc.: Madison, WI, **1995**.
191. Sheldrick, G. M. SADABS (Siemens Area Detector Absorption Corrections), version 2.03; Siemens Analytical X-ray Instruments, Inc.: Madison, WI, **1999**.
192. Sheldrick, G. M. SHELXTL-Plus, release 5.1; Siemens Analytical X-ray Instruments, Inc.: Madison, WI, **1998**.
193. Spek, A. L. *J. Appl. Crystallogr.* **2003**, *36*, 7−13.
194. Brock, D. S.; Bilir, V.; Mercier, H. P. A.; Schrobilgen, G. J. *J. Am. Chem. Soc.* **2007**, *129*, 3598−3611.
195. Frisch, M. J.; Trucks, G. W.; Schlegel, H. B.; Scuseria, G. E.; Robb, M. A.;. Cheeseman, J. R;Zakrzewski, V. G.; Montgomery, J. A.; Stratmann, Jr., R. E.; Burant, J. C.; Dapprich, S.; Millam, J. M.; Daniels, A. D.; Kudin, K. N.; Strain, M. C.; Farkas, O.; Tomasi, J.; Barone, V.;Cossi, M.; Cammi, R.; Mennucci, B.; Pomelli, C.; Adamo, C.; Clifford, S.; Ochterski, J.; Petersson, G. A.; Ayala, P. Y.; Cui, Q.; Morokuma, K.; Salvador, P.; Dannenberg, J. J.;Malick, D. K.; Rabuck, A. D.; Raghavachari, K.; Foresman, J. B.; Cioslowski, J. V.; Ortiz, A.; Baboul, G.; Stefanov, B. B.; Liu, G.; Liashenko, A.; Piskorz, P. K. I.; Gomperts, R.;Martin, R. L.; Fox, D. J.; Keith, T.; Al-Laham, M. A.; Peng, C. Y.; Nanayakkara, A.; Challacombe, M.; Gill, P. M. W.; Johnson, B.; Chen, W.; Wong, M. W.; Andres, J. L; Gonzalez, C.; Head-Gordon, M.; Replogle, E. S.; Pople, J. A. *Gaussian 98*, Revision A.11; Gaussian, Inc.: Pittsburgh, PA, 2004 (**g03_D.01**).
196. Frisch, M. J.; Trucks, G. W.; Schlegel, H. B.; Scuseria, G. E.; Robb, M. A.; Cheeseman, J. R.; Scalmani, G.; Barone, V.; Mennucci, B.; Petersson, G. A.; Nakatsuji, H.; Caricato, M.; Li, X.; Hratchian, H. P.; Izmaylov, A. F.; Bloino, J.; Zheng, G.; Sonnenberg, J. L.; Hada, M.; Ehara, M.; Toyota, K.; Fukuda, R.; Hasegawa, J.; Ishida, M.; Nakajima, T.; Honda, Y.; Kitao, O.; Nakai, H.; Vreven, T.; Montgomery, J. A.; Peralta, Jr., J. E.; Ogliaro, F.; Bearpark, M.; Heyd, J. J.; Brothers, E.; Kudin, K. N.; Staroverov, V. N.; Keith, T.; Kobayashi, R.; Normand,

J.; Raghavachari, K.; Rendell, A.; Burant, J. C.; Iyengar, S. S.; Tomasi, J.; Cossi, M.; Rega, N.; Millam, J. M.; Klene, M.; Knox, J. E.; Cross, J. B.; Bakken, V.; Adamo, C.; Jaramillo, J.; Gomperts, R.; Stratmann, R. E.; Yazyev, O.; Austin, A. J.; Cammi, R.; Pomelli, C.; Ochterski, J. W.; Martin, R. L.; Morokuma, K.; Zakrzewski, V. G.; Voth, G. A.; Salvador, P.; Dannenberg, J. J.; Dapprich, S.; Daniels, A. D.; Farkas, O.; Foresman, J. B.; Ortiz, J. V.; Cioslowski, J.; Fox, D. J. Gaussian, Inc., Wallingford CT, 2010 (**g09_C.01**).

197. Basis sets and pseudopotentials were obtained from the Extensible Computational Chemistry Environment Basis set Database, version 2/25/04, as developed and distributed by the Molecular Science Computing Facility, Environmental and Molecular Science Laboratory, which is part of the Pacific Northwest Laboratory, P.O. Box 999, Richland, WA 99352.
198. Feller, D. *J. Comput. Chem.* **1996**, *17*, 1571–1586.
199. Schuchardt, K. L.; Didier, B. T. Elsethagen, T.; Sun, L.; Gurumoorthi, V.; Chase, J.; Li, J.; Windus, T. L. *J. Chem. Inf. Model* **2007**, *47*, 1045–1052.
200. NBO 6.0. Glendening, E. D.; Badenhoop, J. K.; Reed, A. E.; Carpenter, J. E.; Bohmann, J. A.; Morales, C. M.; Landis, C. R.; Weinhold, F. Theoretical Chemistry Institute, University of Wisconsin, Madison, **2013**.
201. Multiwfn, version 3.3.8; Lu, T.; Chen, F. *J. Comput. Chem.* **2012**, *33*, 580−592.
202. GaussView, version 3.0; Gaussian Inc.: Pittsburgh, PA, **2003**.
203. Jmol, an open-source Java viewer for chemical structures in 3D (http://www.jmol.org/).
204. Pettersen, E. F; Goddard, T. D.; Huang, C. C.; Couch, G. S.; Greenblatt, D. M.; Meng, E. C.; Ferrin, T. E. *J. Comput. Chem.* **2004**, *25*, 1605−1612.
205. te Velde, G.; Bickelhaupt, F. M.; Baerends, E. J.; Fonseca Guerra, C.; van Gisbergen, S. J. A.; Snijders, J. G.; Ziegler, T. *J. Comput. Chem.* **2001**, *22*, 931–967.
206. Fonseca Guerra, C.; Snijders, J. G.; te Velde, G.; Baerends, E. J. *Theor. Chem. Acc.* **1998**, *99*, 391–403.

207. Baerends, E. J.; et al. *ADF 2010*, SCM, Theoretical Chemistry, Vrije Universiteit, Amsterdam, The Netherlands, http://www.scm.com.
208. Krykunov, M.; Ziegler, T.; van Lenthe, E. *Int. J. Quant. Chem.* **2009**, *109*, 1676–1683.
209. Schreckenbach, G.; Ziegler, T. *J. Phys. Chem.* **1995**, *99*, 606–611.
210. Schreckenbach, G.; Ziegler, T. *Int. J. Quant. Chem.* **1997**, *61*, 899–918.
211. Wolff, S. K.; Ziegler, T. *J. Chem. Phys*. **1998**, *109*, 895–905.
212. Wolff, S. K.; Ziegler, T; van Lenthe, E; Baerends, E. J. *J. Chem. Phys.* **1999**, *110*, 7689–7698.
213. Okrasinski, S.; Mitra, G. *J. Inorg. Nucl. Chem*. **1974**, *36*, 1908–1909.
214. Saielli, G.; Bini, R.; Bagno, A. *Theor. Chem. Acc*. **2012**, *131*, 1140−1150 and references therein.
215. Saielli, G.; Bini, R.; Bagno, A. *Theor. Chem. Acc.* **2012**, *131*, 1283.
216. Christe, K. O.; Curtis, E. C.; Mercier, H. P.; Sanders, J. C. P.; Schrobilgen, G. J.; Dixon, D. A. *J. Am. Chem. Soc.* **1991**, *113*, 3351−3361.
217. Hughes, M. J.; Gerken, M.; Mercier, H. P. A.; Schrobilgen, G. J. *Inorg. Chem*. **2010**, *49*, 4768−4780.
218. Krebs, B.; Hasse, K.-D. *Acta Crystallogr*. **1976**, *B32*, 1334−1337.
219. Kruger, G. J.; Reynhardt, E. C. *Acta Crystallogr*. **1978**, *B34*, 259−261.
220. Tramšek, M.; Goreshnik, E.; Žemva, B. *J. Fluorine Chem.* **2009**, *130*, 1093–1098.
221. Gerken, M; Dixon, D. A.; Schrobilgen, G. J. *Inorg. Chem.*, **2002**, *41*, 259–277.
222. Mattes, R.; Mennemann, K. *Z. Anorg. Allg. Chem*. **1977**, *437*, 175–182.
223. Cotton, F. A.; Mague, J. T. *Inorg. Chem.* **1964**, *3*, 1402−1407.
224. Mucker, K.; Smith, G. S.; Johnson, Q. *Acta Crystallogr*. **1968**, *B24*, 874−879.
225. Watson, W. H., Jr.; Waser, J. *Acta Crystallogr*. **1958**, *11*, 689−692.
226. Tragl, S.; Ströbele, J.; Vicent, C.; Llusar, R.; Meyer, H.-J. *Inorg. Chem.* **2009**, *48*, 3825−3831.
227. Krebs, B.; Müller, A.; Beyer, H. H. *Inorg. Chem*. **1969**, *8*, 436–443.

228. Bertolucci, A.; Freni, M.; Romiti, P.; Ciani, G.; Sironi, A.; Albano, V. G. *J. Organomet. Chem*. **1976**, *113*, C61−C64.
229. Roesky, H. W.; Hesse, D.; Bohra, R.; Noltemeyer, M. *Chem. Ber*. **1991**, *124*, 1913−1915.
230. Kabisch, G.; Klose, M. *J. Raman Spectrosc*. **1978**, *7*, 311–315.
231. Kabisch, G. *J. Raman Spectrosc*. **1980**, *9*, 279–285.
232. Berg, R. W. *Spectrochim. Acta*. **1978**, *34A*, 655–659.
233. Korppi-Tommola, J.; Brown, R. J. C.; Shurvell, H. F. *J. Raman Spectrosc*. **1981**, *11*, 363–368.
234. Park, Y. S.; Shurvell, H. F.; Brown, R. J. C. *J. Raman Spectrosc*. **1986**, *17*, 351–354.
235. Ivanova, M. V.; Köchner, T.; Mercier H. P. A.; Schrobilgen G. *Inorg. Chem.* **2013**, *52*, 6806–6819.
236. Grove, D. E.; Johnson, N. P.; Wilkinson, G. *Inorg. Chem*. **1969**, *8*, 1196.
237. Gerlach, U.; Ringel, C. *Z. Anorg. Allg. Chem*. **1974**, *408*, 180–186.
238. Lis, T. *Acta Crystallogr*. **1983**, *C39*, 961−962.
239. Hołyńska, M.; Lis, T. *J. Chem. Crystallogr*, **2010**, 707−711.
240. Masterton, W. L.; Bolocofsky, D.; Lee, P. T. *J. Phys. Chem.* **1971**, *75*, 2809−2815.
241. Bondi, A. *J. Phys. Chem*. **1964**, *68*, 441−451.
242. Mercier, H. P. A.; Moran, M. D.; Sanders, J. C. P.; Schrobilgen, G. J. *Inorg. Chem.* **2005**, *44*, 49−60.
243. Craig, N. C.; Futamura, K. *Spectrochim. Acta*, **1989**, *45*, 507−509.
244. Qureshi, A. M.; Aubke, F. *Can. J. Chem*. **1970**, *48*, 3117−3123.
245. Mazej. Z.; Ponikar-Svet, M.; Liebman, J. F.; Passmore, J.; Jenkins, J. D. B. *J. Fluorine Chem.* **2009**, *130*, 788−791.
246. Beattie, I. R.; Ozin, G. A. *J. Chem. Soc. A,* **1969**, 2615−2619.
247. Hughes, M. J.; Mercier, H. P. A.; Schrobilgen, G. J. *Inorg. Chem*. **2009**, *48*, 4478−4490.

248. Niboer, J.; Mack, J. P.; Mercier, H. P. A.; Gerken, M. *Inorg. Chem*. **2010**, *49*, 6153−6159.

249. (a) Herrmann, W. A.; Kuchler, J. G.; Wagner, W.; Felixberger, J. K.; Herdtweck, E. *Angew. Chem. Int. Ed. Engl*. **1988**, *27*, 394−396; (b) Herrmann, W. A; Kiprof, P.; Rypdal, K.; Tremmel, J.; Blom, R.; Alberto, R.; Behm, J.; Albach, R. W.; Bocj, H.; Soluki, B.; Mink, J.; Lichtenberger, D.; Gruhn, N. E. *J. Am. Chem. Soc*. **1991**, *113*, 6527−6537; (c) Kühn, F. E.; Herrmann, W. A.; Hahn, R.; Elison, M.; Blümel. J.; Herdtweck, E. *Organomet*. **1994**, *13*, 1601−1606; (d) Parker, S. F.; Herman, H. *Spectrochim. Acta, Part A*. **2006**, *56*, 1123−1129.

250. Cunin, F.; Favier, F.; Pascal, J. L. *Spectrochim. Acta, Part A,* **2002**, *58*, 2869−2875.

251. Byler, D. M.; Shriver, D. F. *Inorg. Chem*. **1973**, *12*, 1412−1416.

252. Byler, D. M.; Shriver, D. F. *Inorg. Chem*. **1974**, *13*, 2697−2705.

253. Ahsen, B.; Bley, B.; Proemmel, S.; Wartchow, R.; Willner, H.; Aubke, F. *Z. Anorg. Allg. Chem*. **1998**, *624*, 1225–1234.

254. Benkič, P.; Jenkins, H. D. B.; Ponikvar, M.; Mazej, Z. *Eur. J. Inorg. Chem*. **2006**, 1084−1092.

255. de Méric de Bellefon, C.; Herrmann, W. A.; Kiprof, P.; Whitaker, C. R. *Organomet*. **1992**, *11*, 1072−1081.

256. Burrell, A. K.; Cotton, F. A.; Daniels, L. M.; Petricek, V. *Inorg. Chem*. **1995**, *34*, 4253−4255.

257. Herrmann, W. A.; Taillefer, M.; de Méric de Bellefon, C.; Behm, J. *Inorg. Chem*. **1991**, *30*, 3247−3248.

258. Gerken, M.; Kolb, P.; Wegner, A.; Mercier, H. P. A.; Borrmann, H.; Dixon, D. A.; Schrobilgen, G. J. *Inorg. Chem*. **2000**, *39*, 2813−2824.

259. Mercier, H. P. A.; Sanders, J. C. P.; Schrobilgen, G. J. *J. Am. Chem. Soc.* **1994**, *116*, 2921−2937.

260. Haupt, S.; Seppelt, K. *Z. Anorg. Allg. Chem*. **2002**, *628*, 729–734.

261. Brosius, A.; Haas, A. *Chem. Ber*. **1995**, *128*, 651.

262. Minkwitz, R.; Koch, M.; Nowicki, J. *Z. Anorg. Allg. Chem*. **1990**, *590*, 93–102.

263. Bencze, É. Mink, J.; Németh, C.; Herrmann, W. A.; Lokshin, B. V.; Kühn, F. E. *J. Organomet. Chem.* **2002**, *642*, 246−258.
264. Bartlett, N. *Proc. Chem. Soc*. **1962**, 218.
265. Brock, D. S.; Schrobilgen, G. J.; Žemva, B. In *Comprehensive Inorganic Chemistry II*; Reedijk J.; Poepplemeier, K., Eds.; Elsevier: Oxford, U.K.; 2013, Vol. 1, pp. 755−822.
266. Brock, D. S.; Schrobilgen, G. J. *J. Am. Chem. Soc*. **2011**, *133*, 6265−6269.
267. Smith, D. F. *J. Am. Chem. Soc*. **1963**, *85*, 816−817.
268. Templeton, D. H.; Zalkin, A.; Forrester, J. D.; Williamson, S. M. *J. Am. Chem. Soc*. **1963**, *85*, 817.
269. Gunn, S. R. In *Noble Gas Compounds*; Hyman, H. H., Ed.; University of Chicago Press: Chicago, IL, 1963; pp 149−151.
270. Appelman, E. H.; Malm, J. G. *J. Am. Chem. Soc*. **1964**, *86*, 2141−2148.
271. Claassen, H. H.; Knapp, G. *J. Am. Chem. Soc.* **1964**, *86*, 2341−2342.
272. Spittler, T. M.; Jaselskis, D. *J. Am. Chem. Soc.* **1965**, *87*, 3357−3360.
273. Selig, H.; Claassen, H. H.; Chernick, C. L.; Malm, J. G.; Huston, J. L. *Science* **1964**, *143*, 1322−1323.
274. Huston, J. L.; Studier, M. H.; Sloth, E. N. *Science* **1964**, *143*, 1161−1162.
275. Gunn, S. R. *J. Am. Chem. Soc*. **1965**, *87*, 2290−2291.
276. Gundersen, G.; Hedberg, K.; Huston, J. L. *J. Chem. Phys*. **1970**, *52*, 812−815.
277. Huston, J. L.; Claassen, H. H. *J. Chem. Phys.* **1970**, *52*, 5646−5648.
278. Gerken, M.; Schrobilgen, G. J. *Inorg. Chem*. **2002**, *41*, 198−204.
279. Vent-Schmidt, T.; Goettel, J. T.; Schrobilgen, G. J.; Riedel, S. *Chem. Eur. J*. **2015**, *21*, 11244−11252.
280. Siegel, S.; Gebert, E. In *Noble-Gas Compounds*; Hyman, H. H., Ed.; University of Chicago Press: Chicago, IL, 1963; pp 193−194.
281. Hamilton, W. C.; Ibers, J. A.; Mackenzie, D. R. *Science* **1963**, *141*, 532−534.
282. Zalkin, A.; Forrester, J. D.; Templeton, D. H.; Williamson, S. M.; Koch, C. W. *Science* **1963**, *142*, 501−502.

283. Ibers, J. A.; Hamilton, W. C.; Mackenzie, D. R. *Inorg. Chem*. **1964**, *3*, 1412−1416.
284. Zalkin, A.; Forrester, J. D.; Templeton, D. H.; Williamson, S. M.; Koch, C. W. *J. Am. Chem. Soc*. **1964**, *86*, 3569−3571.
285. Zalkin, A.; Forrester, J. D.; Templeton, D. H. *Inorg. Chem*. **1964**, *3*, 1417−1421.
286. Marcus, Y.; Cohen, D. *Inorg. Chem.* **1966**, *5*, 1740−1743.
287. Appelman, E. H.; Williamson, S. M. *Inorg. Synth*. **1968**, *11*, 210−213.
288. Hauck, J. *Z. Naturforsch*. **1970**, *25b*, 226.
289. Peterson, J. L.; Claassen, H. H.; Appelman, E. H. *Inorg. Chem*. **1970**, *9*, 619−621.
290. Downey, G. D.; Claassen, H. H.; Appelman, E. H. *Inorg. Chem*. **1971**, *10*, 1817−1820.
291. Jørgensen, C. K.; Berthou, H. *Chem. Phys. Lett*. **1975**, *36*, 432−435.
292. Schrobilgen, G. J.; Holloway, J. H.; Granger, P.; Brevard, C. *Inorg. Chem*. **1978**, *17*, 980−987.
293. de Waard, H.; Bukshpan, S.; Schrobilgen, G. J.; Holloway, J. H.; Martin, D. *J. Chem. Phys*. **1979**, *70*, 3247−3253.
294. Foropoulos, J. Jr.; DesMarteau, D. D. *Inorg. Chem*. **1982**, *21*, 2503−2504.
295. Kläning, U. K.; Appelman, E. H. *Inorg. Chem*. **1988**, *27*, 3760−3762.
296. Shustov, L. D.; Tolmacheva, N. S.; Nabiev, Sh. Sh.; Il'in. E. K.; Klimov, V. D.; Ushakov, V. P. *Russ. J. Inorg. Chem*. **1989**, *34*, 946−949.
297. Forgeron, M. A. M.; Wasylishen, R. E.; Gerken, M.; Schrobilgen, G. J. *Inorg. Chem*. **2007**, *46*, 3585−3592.
298. Lehmann J. F.; Mercier, H. P. A.; Schrobilgen, G. J. *Coord. Chem. Rev.* **2002**, *233-234*, 1−39.
299. Dunning, T. H.; Hay, P. J. *J. Chem. Phys*. **1977**, *66*, 3767−3777.
300. Yamanishi, M.; Hirao, K.; Yamashita, K. *J. Chem. Phys*. **1998**, *108*, 1514−1521.
301. Ault, B. S.; Andrews, L. *Chem. Phys. Lett*. **1976**, *43*, 350−352.
302. Gerken, M.; Moran, M. D.; Mercier, H. P. A.; Pointner, B. E.; Schrobilgen, G. J.; Hoge, B.; Christe, K. O.; Boatz, J. A. *J. Am. Chem. Soc*. **2009**, *131*, 13474−13489.
303. Mootz, D.; Ohms, U.; Poll, W. *Z. Anorg. Allg. Chem*. **1981**, *479*, 75−83.

304. Mootz, D.; Poll, W. *Z. Anorg. Allg. Chem*. **1982**, *484*, 158−164.
305. Brown, I. D. *The Chemical Bond in Inorganic Chemistry: The Bond Valence Model*; Oxford University Press: Oxford, 2006.
306. Fir, B. A.; Mercier, H. P. A.; Sanders, C. P. Dixon, D. A. Schrobilgen, G. J. *J. Fluorine Chem*. **2001**, *110*, 89−107.
307. Bartlett, N.; Wechsberg, M.; Jones, G. R.; Burbank, R. D. *Inorg. Chem*. **1972**, *11*, 1124−1127.
308. Malischewski, M.; Seppelt, K. *Acta Crystallogr*. **2015**, *E71*, 363−365.
309. Moran, M. D.; Brock, D. S.; Mercier, H. P. A.; Schrobilgen, G. J. *J. Am. Chem. Soc*. **2010**, *132*, 13823−13839.
310. Turowsky, L.; Seppelt. K. *Z. Anorg. Allg. Chem.* **1992**, *609*, 153−156.
311. Elliot, H. St. A.; Lehmann, J. F.; Mercier, H. P. A. Jenkins, B. H. D.; Schrobilgen, G. J. *Inorg. Chem*. **2010**, *49*, 8504−8523.
312. Zalkin, A.; Ward, D. L.; Biagioni, R. N.; Templeton, D. H.; Bartlett, N. *Inorg. Chem*. **1978**, *12*, 1318−1322.
313. Gillespie, R. J.; Hargittai, I. In *The VSEPR Model of Molecular Geometry*; Allyn and Bacon: Boston, MA, 1991; pp 127−130.
314. Bougon, R.; Buu, B.; Seppelt, K. *Chem. Ber*. **1993**, *126*, 1331–1336.
315. Hughes, M. J.; Mercier, H. P. A.; Schrobilgen, G. J. *Inorg. Chem*. **2010**, *49*, 3501−3515.
316. Bader, R. F. W. *Atoms in Molecules: A Quantum Theory*; Oxford University Press: Oxford, 1990.
317. Silvi, B.; Savin, A. *Nature* **1994**, *371*, 683–686.
318. Becke, A. D.; Edgecombe, K. E. *J. Chem. Phys.* **1990**, *92*, 5397–5403.
319. Brock, D. S.; Casalis de Pury, J. J.; Mercier, H. P. A.; Schrobilgen, G. J., Silvi, B. *Inorg. Chem*. **2010**, *49*, 6673−6689.
320. Brock, D. S.; Casalis de Pury, J. J.; Mercier, H. P. A.; Schrobilgen, G. J., Silvi, B. *J. Am. Chem. Soc*. **2010**, *132*, 3533−3542.
321. Savin, A.; Silvi, B.; Colonna, F. *Can. J. Chem.* **1996**, *74*, 1088–1096.

322. Vasdev, N.; Moran, M. D.; Tuononen, H. M.; Chirakal, R.; Suontamo, R.; Bain, A. D.; Schrobilgen, G. J. *Inorg. Chem*. **2010**, *49*, 8997−9004.
323. MacDougall, P. J.; Schrobilgen, G. J.; Bader, R. F. W. *Inorg. Chem.* **1989**, *28*, 763–769.
324. Clark, T.; Hennemann, M.; Murray, J. S.; Politzer, P. *J. Mol. Chem.* **2007**, *13*, 291−296.
325. Legon, A. C. *Phys. Chem. Chem. Phys.* **2010**, *12*, 7736−7747.
326. Politzer, P.; Murray, J. S.; Clark, T. *Phys. Chem. Chem. Phys.* **2010**, *12*, 7748−7757.
327. Politzer, P.; Murray, J. S.; Clark, T. *Phys. Chem. Chem. Phys.* **2013**, *15*, 11178–11189.
328. Kolář, M.H.; Deepa, P.; Ajani, H.; Pecina, A.; Hobza P. *Top. Curr. Chem.* **2015**, 1–26.
329. Frohn. H.-J.; Bilir, V.; Westphal, U. *Inorg. Chem.* **2012**, *51*, 11251−11258.
330. Lucier, G. M.; Shen, C.; Elder, S. H.; Bartlett, N. *Inorg. Chem*. **1998**, *37*, 3829−3834.
331. Egorochkin, A. N.; Kuznetsova, O. V.; Khamaletdinova, N. M.; Kurskii, Y. A.; Domratcheva-Lvova, L. D.; Domrachev, G. A. *Magn. Reson. Chem*. **2009**, *47*, 782−790.
332. Bacon, J.; Gillespie, R. J.; Quail, J. W. *Can. J. Chem*. **1963**, *41*, 3063−3069.
333. Jesih, A.; Lutar, K.; Leban, I.; Žemva, B. *Inorg. Chem*. **1989**, *28*, 2911−2914.
334. Leary, K.; Templeton, D. H.; Zalkin, A.; Bartlett, N. *Inorg. Chem*. **1973**, *12*, 1726−1730.
335. Eller, P. G.; Larson, A. C.; Peterson, J. R.; Ensor, D. D.; Young, J. P. *Inorg. Chim. Acta* **1979**, *37*, 129−133.
336. Hebecker, C. *Z. Anorg. Allg. Chem*. **1971**, *384*, 111−114.
337. Shorafa, H.; Seppelt, K. *Z. Anorg. Allg. Chem*. **2009**, *635*, 112−114.
338. Edwards, A. J. Jones, G. R. *J. Chem. Soc. (A)* **1969**, 1651−1654.
339. Massa, W.; Steiner, M. *J. Solid State Chem*. **1980**, *32*, 137−143.

340. Molinier, M.; Massa, W. *Z. Naturforsch. B* **1992**, *47*, 783−788.
341. Žemva, B.; Jesih, A. *J. Fluorine Chem.* **1984**, *24*, 281−289.
342. Jesih, A.; Lutar, K.; Leban, I.; Žemva, B. *Eur. J. Solid State Inorg. Chem.* **1991**, *28*, 829−840.
343. Mattes, R.; Müller, G.; Becher, H. J.; *Z. Anorg. Allg. Chem.* **1975**, *416*, 256−262.
344. Torardi, C. C.; Brixner, L. H.; *Mat. Res. Bull.* **1985**, *20*, 137−145.
345. Shaw, M. M.; Smith, R. G.; Ramsden, C. A. *Arch. Org. Chem.* **2001**, 221−228. DOI: http://dx.doi.org/10.3998/ark.5550190.0012.a18.
346. Markgraf, J. H.; Choi, B. Y. *Synth. Commun.* **1999**, *29*, 2405−2411.

APPENDIX A

THE SYNTHESIS AND LEWIS ACID PROPERTIES OF ReO_3F AND THE X-RAY CRYSTAL STRUCTURES OF $(HF)_2ReO_3F{\cdot}HF$ AND $[N(CH_3)_4]_2[\{ReO_3(\mu\text{-}F)\}_3(\mu_3\text{-}O)]{\cdot}CH_3CN$

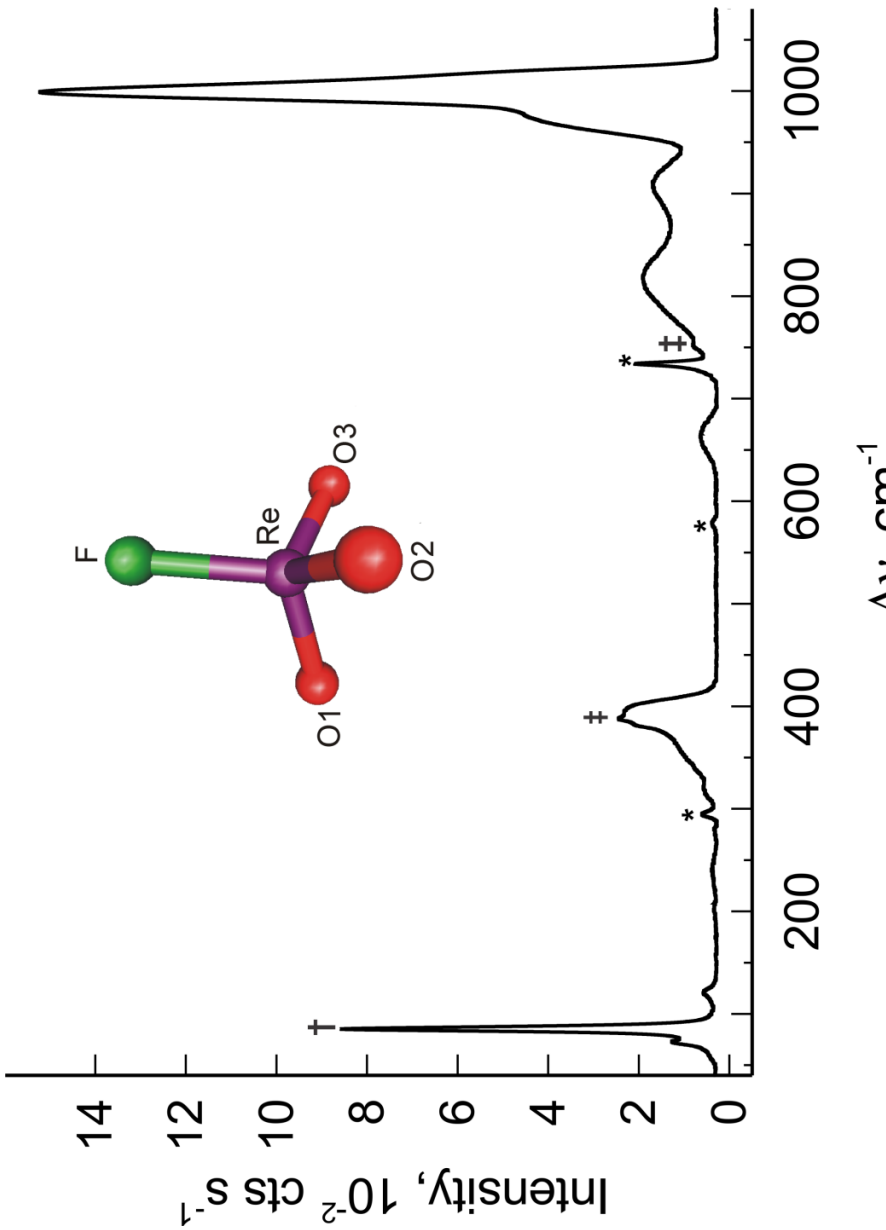

Figure A1. Raman spectrum of ReO_3F recorded at –150 °C using 1064-nm excitation. Symbols denote an FEP sample tube line (*), instrumental artifact (†), and overlap of a ReO_3F line with an FEP sample tube line (‡). The geometry of monomeric ReO_3F (C_{3v}) was calculated at the B3LYP/aug-cc-pVTZ(-PP) level.

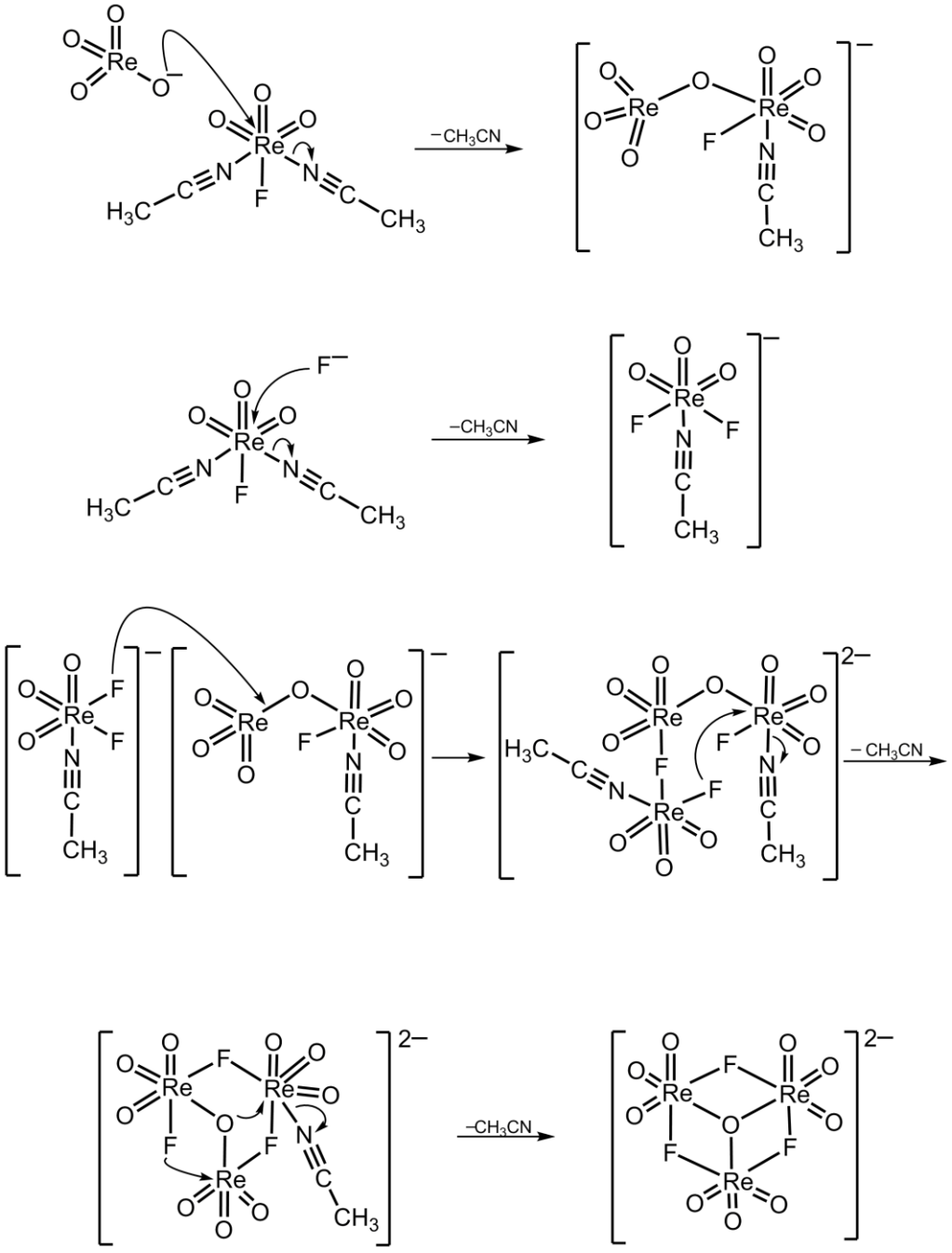

Scheme A1. An alternative proposed reaction pathway leading to the formation of the $[\{ReO_3(\mu\text{-}F)\}_3(\mu_3\text{-}O)]^{2-}$ anion in CH_3CN solvent. The $[ReO_4]^-$ anion is formed in eq 3.6.

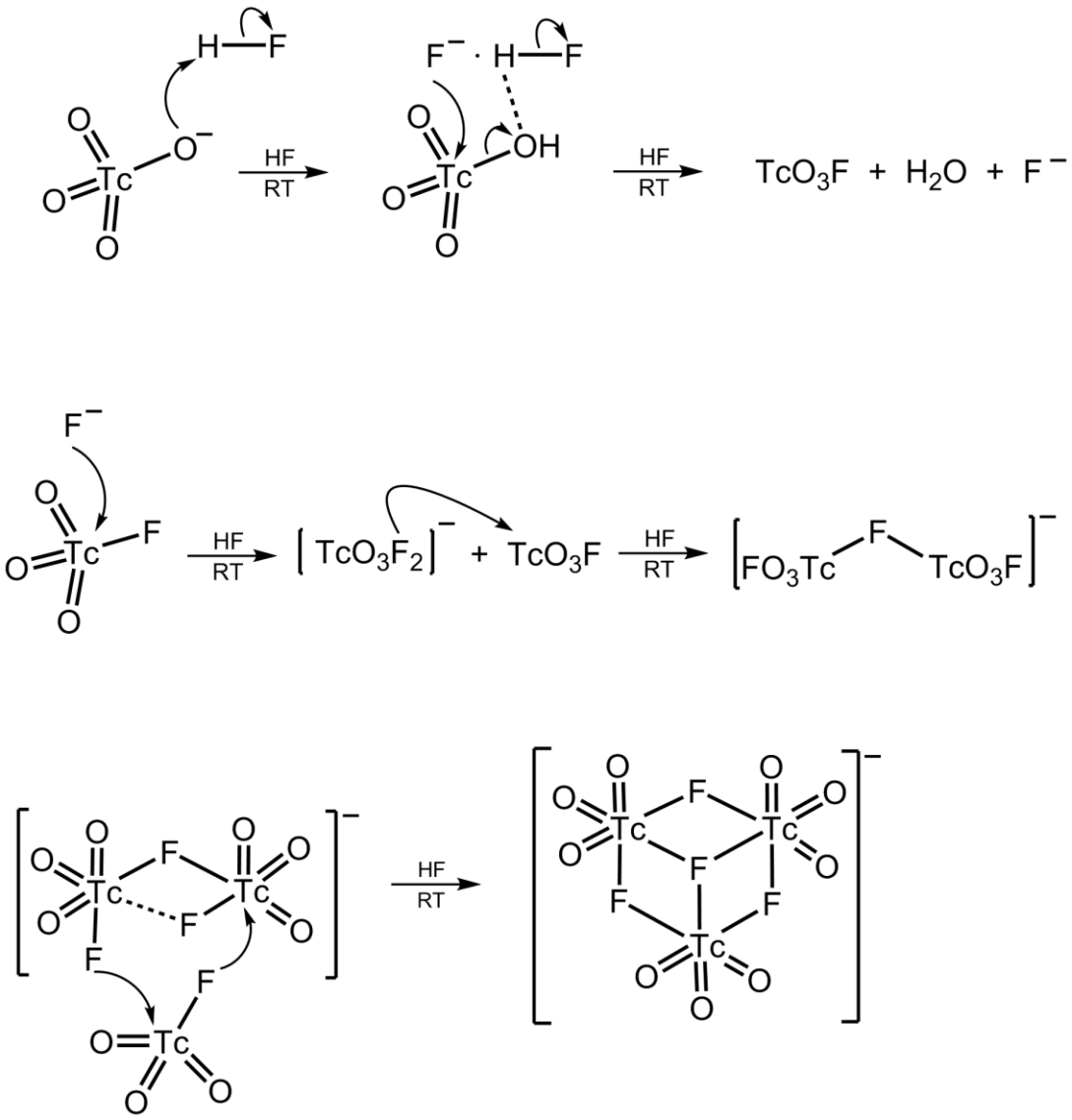

Scheme A2. A plausible reaction pathway leading to the formation of the $[\{TcO_3(\mu\text{-}F)\}_3(\mu_3\text{-}F)]^-$ anion in aHF solvent. The molecular structure of the $[TcO_3F_2]^-$ anion is presently unknown. Two possible geometries are likely: (1) a trigonal bipyramidal D_{3h} geometry, where the three oxygen atoms lie in the equatorial plane and the fluorine atoms are trans to one another and occupy axial positions that are perpendicular to the TcO_3-plane, and (2) a distorted tetrahedral C_s geometry, where two fluorine atoms, one oxygen atom, and the technetium atom are coplanar and the remaining two oxygen atoms are equidistant from the $TcOF_2$-plane.

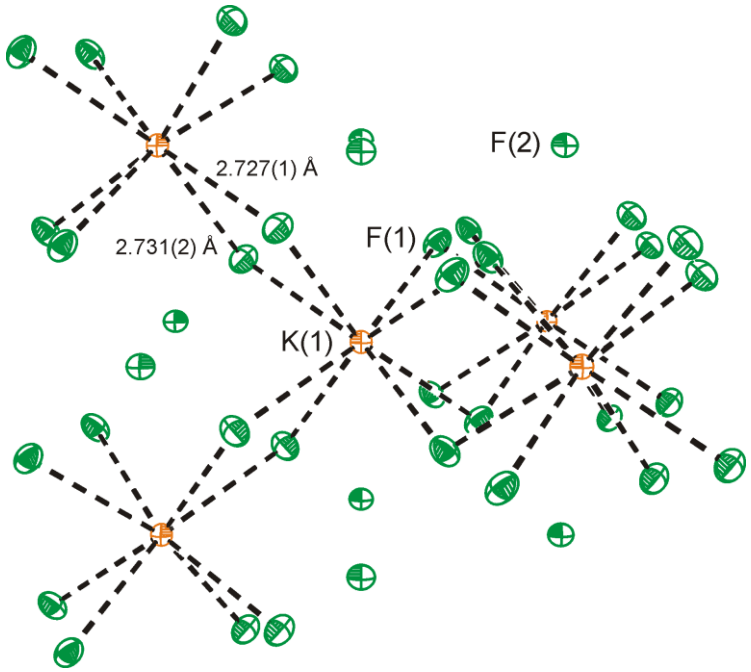

Figure A2. The X-ray crystal structure of KF·4HF. Thermal ellipsoids are shown at the 50% probability level. The "fluorine atoms" that are not coordinated, such as F(2), are HF molecules within the crystal lattice and the "bridging fluorine atoms", such as F(1), are fluoride ions.

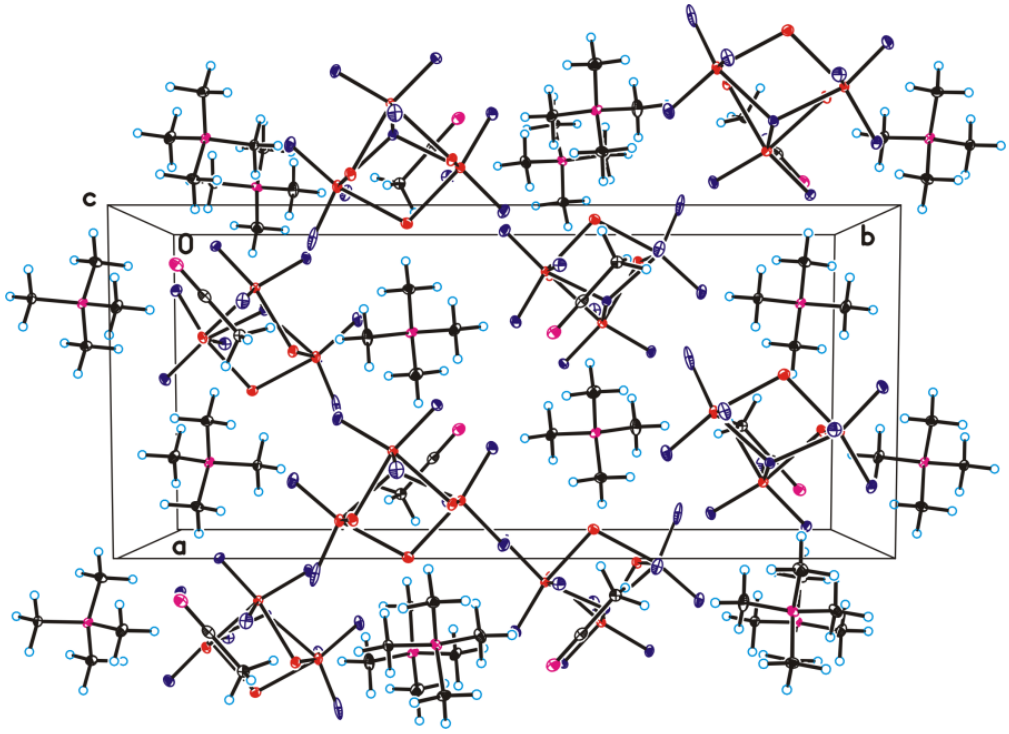

Figure A3. A view of the crystal packing in $[N(CH_3)_4]_2[\{ReO_3(\mu\text{-}F)\}_3(\mu_3\text{-}O)]\cdot CH_3CN$ along the *c*-axis of the unit cell.

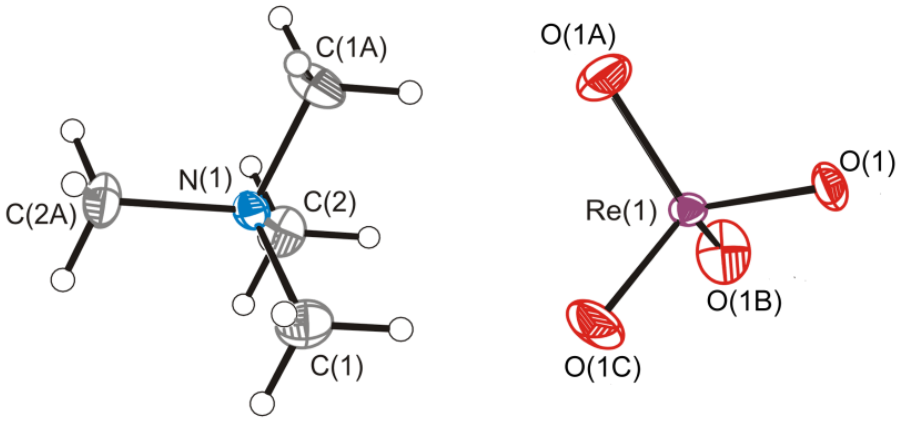

Figure A4. The structural unit in the crystal structure of $[N(CH_3)_4][ReO_4]$. Thermal ellipsoids are shown at the 50% probability level.

Raman Spectrum of $[N(CH_3)_4][ReO_4]$

A low-quality infrared spectrum was previously reported for $[N(CH_3)_4][ReO_4]$[213] that only revealed one intense broad band at ca. 900 cm^{-1} and at least four bands in the 250–350 cm^{-1} region for $[ReO_4]^-$. Reliable Raman data are, however, available for the Na^+,[233] K^+,[233] Rb^+,[233] and $[NH_4]^+$ [233,234] salts of $[ReO_4]^-$. The $[ReO_4]^-$ anion (T_d) is expected to have four Raman-active (A_1, E, $2T_2$), and two infrared-active ($2T_2$) bands. The most intense and highest frequency band of the $[ReO_4]^-$ anion in $[N(CH_3)_4][ReO_4]$ occurs at 964 cm^{-1} and is assigned to ν_s(Re−O) whereas the bands at 899, 909, 928 cm^{-1} are assigned to ν_{as}(Re−O). The bands at 323, 330, 332, and 334 cm^{-1} are assigned to δ(O−Re−O) bending modes. These frequencies are well reproduced by the calculations (Table A1) although the ν_s(Re−O) and ν_{as}(Re−O) stretches are overestimated by about 25 and 15 cm^{-1}, respectively.

Table A1. Experimental Raman Frequencies and Intensities for the $[ReO_4]^-$ Anion in $[N(CH_3)_4][ReO_4]$, $K[ReO_4]$, $[NH_4][ReO_4]$, and $Na[ReO_4]$; and the Calculated Vibrational Frequencies and Intensities for the $[ReO_4]^-$ Anion

exptl[a,b,c,d]					calcd[a,e]	assgnts (T_d)[c]
$[N(CH_3)_4][ReO_4]$[f]	$K[ReO_4]$	$[NH_4][ReO_4]$	$Na[ReO_4]$			$[ReO_4]^-$
964(100)	968(100)	967(100)	957(100)	$\nu_1(A_1)$	989(56)[0]	ν_s(ReO)
928(16) 909(27) 899(14)	927(22) 897(48)	916(14) 894(26)	925(14) 887(39)	$\nu_3(T_2)$	926(13)[276]	ν_{as}(ReO)
334(43) 332 sh	350(35)	356(20)	376 sh 374(17)	$\nu_2(E)$	336(6)[0]	$\delta(O_1ReO_2) + \delta(O_3ReO_4)$
330 sh 323(11)	337(34) 331(11)	343(30) 327 sh	333(18) 320(5)	$\nu_4(T_2)$	333(1)[12]	$\delta(O_1ReO_2) + \delta(O_1ReO_4) - \delta(O_1ReO_3)$

[a] Frequencies are given in cm^{-1}. [b] Values in parentheses denote relative Raman intensities. Raman spectra were recorded in FEP sample tubes at –150 °C using 1064-nm excitation. [c] The abbreviations denote shoulder (sh), stretch (ν), bend (δ), symmetric (s), and asymmetric (as). [d] This work. [e] Values in parentheses denote calculated Raman intensities ($Å^4\ u^{-1}$). Values in square brackets denote calculated infrared intensities (km mol^{-1}). The B3LYP/aug-cc-pVTZ(-PP) level was used. [f] The $[N(CH_3)_4]^+$ cation modes were observed at ν_8(E), 377(1); $\nu_{19}(T_2)$, 463(5), 460(5), 455(5); $\nu_3(A_1)$, 750(3), 757(12); $\nu_{18}(T_2)$, 952(18), 949(8), 943(1); ν_7(E), 1174(1), 1182(2); $\nu_{17}(T_2)$, 1285(1), 1288(2); $\nu_{16}(T_2)$, 1407(5), 14013(3); $\nu_2(A_1)$, ν_6(E), 1461(9), 1467(8); $\nu(CH_3)$ and combination bands, 2801(4), 2810(4), 2904(3), 2915(5), 2953(21), 2962(6), 2992sh, 3026(11), 3034(30) cm^{-1}.

Table A2. Correlation Diagram for the Vibrational Modes of $(HF)_2ReO_3F$ in $(HF)_2ReO_3F \cdot HF$ [a]

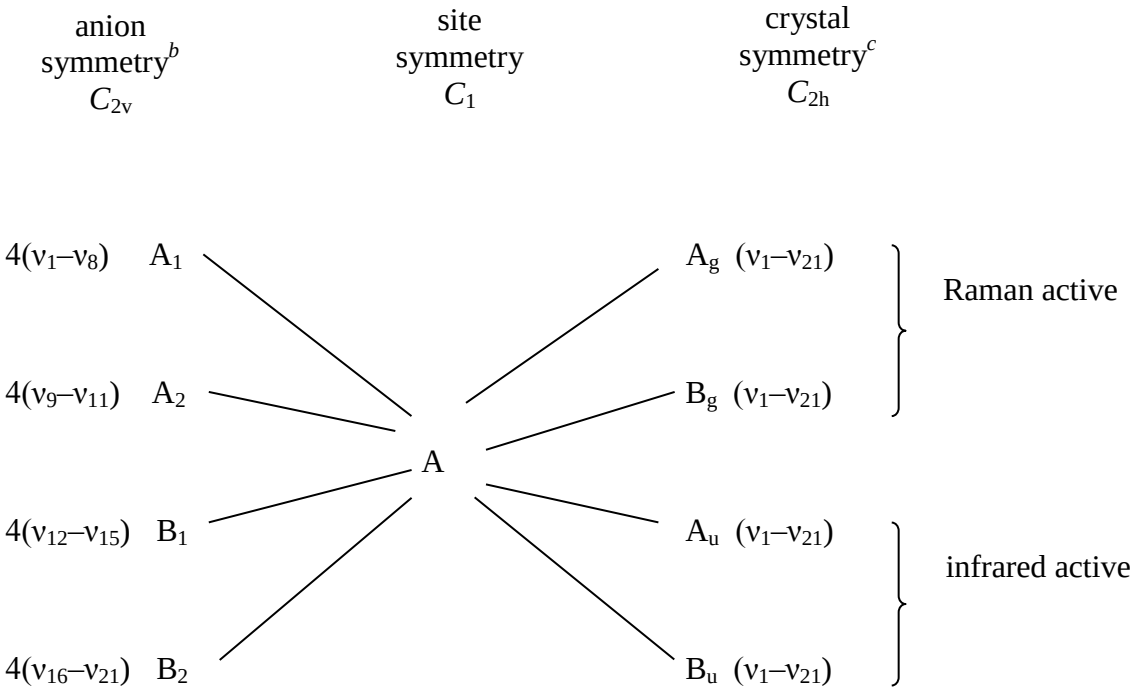

[a] The irreducible representation is $\Gamma = 8A_1 + 4B_1 + 3A_2 + 6B_2$ for $(HF)_2ReO_3F$. [b] The anion (C_{2v}) symmetry is the local symmetry observed in the crystallographic unit cell. [c] The crystallographic space group is $P2_1/c$ with $Z = 4$.

Table A3. Correlation Diagram for the Vibrational Modes of the $[\{ReO_3(\mu\text{-}F)\}_3(\mu_3\text{-}O)]^{2-}$ Anion[a] in $[N(CH_3)_4]_2[\{ReO_3(\mu\text{-}F)\}_3(\mu_3\text{-}O)]\cdot CH_3CN$

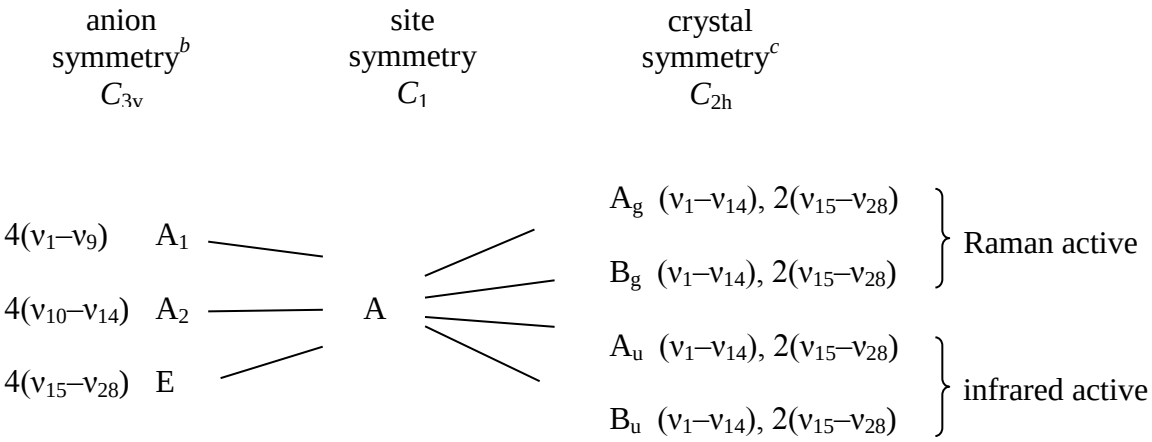

[a] The irreducible representation is $\Gamma = 9A_1 + 5A_2 + 14E$ for the $[\{ReO_3(\mu\text{-}F)\}_3(\mu_3\text{-}O)]^{2-}$ anion. [c] The anion symmetry (C_{3v}) is the symmetry observed in the crystallographic unit cell and for the optimized geometry in the gas phase. [b] The crystallographic space group is $P2_1/c$ with $Z = 4$.

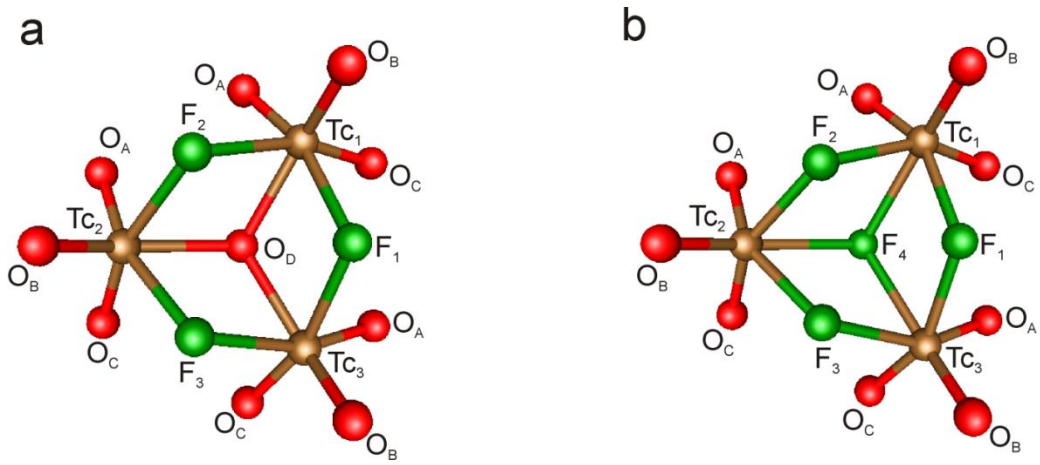

Figure A5. The calculated structures of the (a) $[\{TcO_3(\mu\text{-}F)\}_3(\mu_3\text{-}O)]^{2-}$ and (b) $[\{TcO_3(\mu\text{-}F)\}_3(\mu_3\text{-}F)]^{-}$ anions. The B3LYP/aug-cc-pVTZ(-PP) level was used.

Table A4. Calculated Vibrational Frequencies and Infrared and Raman Intensities for the $[\{TcO_3(\mu\text{-}F)\}_3(\mu_3\text{-}O)]^{2-}$ and $[\{TcO_3(\mu\text{-}F)\}_3(\mu_3\text{-}F)]^{-}$ Anions

$[\{TcO_3(\mu\text{-}F)\}_3(\mu_3\text{-}O)]^{2-}$		assgnts (C_{3v})[c]	$[\{TcO_3(\mu\text{-}F)\}_3(\mu_3\text{-}F)]^{-}$	
calcd[a,d]			calcd[a,d]	
988(173)[94]	$\nu_1(A_1)$	$\nu(Tc_1O_AO_BO_C) + \nu(Tc_2O_AO_BO_C) + \nu(Tc_3O_AO_BO_C)$	$\nu_1(A_1)$	1018(166)[15]
972(5)[197]	$\nu_{10}(E)$	$\nu(Tc_1O_AO_BO_C) - \nu(Tc_2O_AO_BO_C) + \nu(Tc_3O_AO_BO_C)$	$\nu_{10}(E)$	1009(2)[91]
957(27)[521]	$\nu_2(A_1)$	$\nu(Tc_1O_B) + \nu(Tc_2O_B) + \nu(Tc_3O_B)$	$\nu_2(A_1)$	997(6)[482]
960(36)[248]	$\nu_{11}(E)$	$\nu(Tc_1O_A) - \nu(Tc_1O_C) - \nu(Tc_2O_A) + \nu(Tc_2O_C)$	$\nu_{11}(E)$	993(28)[256]
935(54)[112]	$\nu_{12}(E)$	$\nu(Tc_1O_B) - \nu(Tc_2O_B) + \nu(Tc_2O_A) + \nu(Tc_2O_C) - \nu(Tc_1O_A) - \nu(Tc_1O_C)$	$\nu_{12}(E)$	981(25)[66]
551(7)[222]	$\nu_{13}(E)$	$[\nu(Tc_1O_D) + \nu(Tc_3O_D) - \nu(Tc_2O_D)] + [\nu(Tc_1F_1) + \nu(Tc_3F_1) - \nu(Tc_1F_2) - \nu(Tc_2F_2)]$		
499(2)[2]	$\nu_3(A_1)$	$[\nu(Tc_1O_D) + \nu(Tc_2O_D) + \nu(Tc_3O_D)] + [\nu(Tc_1F_1) + \nu(Tc_3F_1) + \nu(Tc_2F_3) + \nu(Tc_3F_3) + \nu(Tc_1F_2) + \nu(Tc_2F_2)]$		
		$[\nu(Tc_2F_4) + \nu(Tc_3F_4)] + [\nu(Tc_1F_1) - \nu(Tc_3F_1) + \nu(Tc_1F_2) - \nu(Tc_2F_2)]$	$\nu_{13}(E)$	471(1)[243]
		$[\nu(Tc_1F_4) + \nu(Tc_2F_4) + \nu(Tc_3F_4)] + [\nu(Tc_1F_1) + \nu(Tc_3F_1) + \nu(Tc_2F_3) + \nu(Tc_3F_3) + \nu(Tc_1F_2) + \nu(Tc_2F_2)] + \delta(O_AO_BTc_1O_C) + \delta(O_AO_BTc_2O_C) + \delta(O_AO_BTc_3O_C)$	$\nu_3(A_1)$	438(3)[17]
		$[\nu(Tc_1F_4) + \nu(Tc_2F_4) + \nu(Tc_3F_4)] + [\nu(Tc_1F_1) + \nu(Tc_3F_1) + \nu(Tc_2F_3) + \nu(Tc_3F_3) + \nu(Tc_1F_2) + \nu(Tc_2F_2)] + [\delta(O_ATc_1O_B) + \delta(O_ATc_2O_B) + \delta(O_ATc_3O_B)]$	$\nu_4(A_1)$	406(4)[3]
420(2)[18]	$\nu_4(A_1)$	$\delta(O_AO_BTc_1O_C) + \delta(O_AO_BTc_2O_C) + \delta(O_AO_BTc_3O_C) + [\nu(Tc_1O_D) + \nu(Tc_2O_D) + \nu(Tc_3O_D)]$		
408(2)[86]	$\nu_{14}(E)$	$[\nu(Tc_1O_D) + \nu(Tc_2O_D) - \nu(Tc_3O_D)] + [\nu(Tc_1F_1) - \nu(Tc_3F_1) + \nu(Tc_2F_3) - \nu(Tc_3F_3)] + [\delta(O_AO_BTc_1O_C) + \delta(O_AO_BTc_2O_C) + \delta(O_AO_BTc_2O_C)]$		
		$[\delta(O_ATc_1O_C) - \delta(O_ATc_2O_C)] + \delta(O_BTc_1F_1F_2) - \delta(O_BTc_2F_3F_2)]$	$\nu_{14}(E)$	400(3)[<1]
		$\delta(O_AO_CRe_1O_B) + \delta(O_AO_CRe_2O_B) + \delta(O_AO_CRe_3O_B) + [\nu(Tc_1F_4) + \nu(Tc_2F_4) + \nu(Tc_3F_4)] + [\nu(Tc_1F_1) + \nu(Tc_3F_1) + \nu(Tc_2F_3) + \nu(Tc_3F_3) + \nu(Tc_1F_2) + \nu(Tc_2F_2)]$	$\nu_5(A_1)$	390(3)[16]
388(6)[8]	$\nu_5(A_1)$	$[\delta(O_ATc_1O_B) - \delta(O_CTc_1O_B) + \delta(O_ATc_2O_B) - \delta(O_CTc_2O_B) + \delta(O_ATc_3O_B) - \delta(O_CTc_3O_B)] + [\nu(Tc_1F_1) - \nu(Tc_3F_1) + \nu(Tc_2F_3) - \nu(Tc_3F_3) - \nu(Tc_1F_2) + \nu(Tc_2F_2)]$		
398(1)[5]	$\nu_{15}(E)$	$[\delta(O_AO_BTc_1O_C) + \delta(O_AO_BTc_2O_C) - \delta(O_ATc_3O_C)] + [\nu(Tc_1F_1) - \nu(Tc_3F_1) + \nu(Tc_2F_3) - \nu(Tc_3F_3)$		
		$[\delta(O_AO_BTc_1O_C) + \delta(O_AO_BTc_2O_C) - \delta(O_ATc_3O_C)] + [\nu(Tc_1F_4) + \nu(Tc_2F_4) - \nu(Tc_3F_4)] + [\nu(Tc_1F_1) + \nu(Tc_3F_1) + \nu(Tc_2F_3) + \nu(Tc_3F_3) - \nu(Tc_1F_2) - \nu(Tc_2F_2)]$	$\nu_{15}(E)$	390(4)[1]
379(4)[47]	$\nu_{16}(E)$	$[\delta(O_ATc_1O_B) - \delta(O_CTc_1O_B) + \delta(O_ATc_2O_C) - \delta(O_ATc_3O_B) - \delta(O_CTc_3O_B)] + [\nu(Tc_3F_1) + \nu(Tc_1F_1)] - [\nu(Tc_1F_2) + \nu(Tc_2F_2)] + [\nu(Tc_2F_3) + \nu(Tc_3F_3)]$		

Table A4. (continued ...)

		$[\delta(O_AO_BTc_1O_C) - \delta(O_AO_BTc_2O_C)]$	$\nu_{16}(E)$	378(<0.1)[<0.1]
376(1)[9]	$\nu_{17}(E)$	$\delta(O_CTc_1O_A) - \delta(O_ATc_2O_B) + \delta(O_BTc_2F_3) + \delta(O_BTc_1F_1F_2)$		
		$[\delta(O_ATc_1O_B) - \delta(O_CTc_1O_B) + \delta(O_ATc_2O_B) - \delta(O_CTc_2O_B)] + [\nu(Tc_1F_4) + \nu(Tc_2F_4) - \nu(Tc_3F_4)] + [\nu(Tc_3F_1) + \nu(Tc_1F_1)] - [\nu(Tc_1F_2) + \nu(Tc_2F_2)] - [\nu(Tc_2F_3) + \nu(Tc_3F_3)]$	$\nu_{17}(E)$	369(2)[12]
365(2)[15]	$\nu_6(A_1)$	$[\rho_w(O_ATc_1O_C) + \rho_w(O_ATc_2O_C) + \rho_w(O_ATc_3O_C)] + [\nu(Tc_1F_2) + \nu(Tc_2F_2)] + [\nu(Tc_2F_3) + \nu(Tc_3F_3)] + [\nu(Tc_3F_1) + \nu(Tc_1F_1)]$		
		$\rho_w(O_ATc_1O_C) + \rho_w(O_ATc_2O_C) + \rho_w(O_ATc_3O_C) + [\nu(Tc_1F_2) + \nu(Tc_2F_2)] + [\nu(Tc_2F_3) + \nu(Tc_3F_3)] + [\nu(Tc_3F_1) + \nu(Tc_1F_1)] + [\nu(Tc_1F_4) + \nu(Tc_2F_4) + \nu(Tc_3F_4)]$	$\nu_6(A_1)$	356(<1)[14]
		$[\nu(Tc_1F_2) + \nu(Tc_2F_2)] + [\nu(Tc_2F_3) + \nu(Tc_3F_3)] + [\nu(Tc_3F_1) + \nu(Tc_1F_1)] - [\nu(Tc_1F_4) + \nu(Tc_2F_4) + \nu(Tc_3F_4)] + [\nu(Tc_3F_1) + \nu(Tc_1F_1)] - [\nu(Tc_1F_2) + \nu(Tc_2F_2)] + [\nu(Tc_2F_3) + \nu(Tc_3F_3)]$	$\nu_7(A_1)$	278(1)[9]
252(7)[<1]	$\nu_7(A_1)$	$[\nu(Tc_1F_2) + \nu(Tc_2F_2)] + [\nu(Tc_2F_3) + \nu(Tc_3F_3)] + [\nu(Tc_3F_1) + \nu(Tc_1F_1)]$		
321(3)[14]	$\nu_{18}(E)$	$[\delta(O_ATc_1O_B) - \delta(O_BTc_1O_C) + \delta(O_BTc_2O_C) - \delta(O_BTc_2O_C)] + [\nu(Tc_1F_1) + \nu(Tc_3F_1) + \nu(Tc_2F_3) + \nu(Tc_3F_3)] + [\nu(Tc_1F_4) + \nu(Tc_2F_4) + \nu(Tc_3F_4) - \nu(Tc_1F_2) - \nu(Tc_2F_2)]$		
		$[\rho_w(O_ATc_2O_C) + \rho_w(O_ATc_3O_C)] + [\nu(Tc_1F_1) + \nu(Tc_3F_1) + \nu(Tc_2F_3) + \nu(Tc_3F_3)] + [\nu(Tc_2F_4) + \nu(Tc_3F_4) - \nu(Tc_1F_4)]$	$\nu_{18}(E)$	275(2)[52]
250(1)[6]	$\nu_{19}(E)$	$[\rho_r(O_ATc_1O_C) + \rho_r(O_ATc_3O_C)] + [\nu(Tc_1F_2) + \nu(Tc_2F_2)] + [\nu(Tc_2F_3) + \nu(Tc_3F_3)] - [\nu(Tc_3F_1) + \nu(Tc_1F_1)]$		
		$[\rho_r(O_ATc_1O_B) + \rho_r(O_ATc_2O_B) + \rho_r(O_ATc_3O_C)] + [\nu(Tc_2F_3) + \nu(Tc_3F_3)] - [\nu(Tc_2F_4) + \nu(Tc_3F_4) - \nu(Tc_1F_4)]$	$\nu_{19}(E)$	257(<1)[1]
202(3)[1]	$\nu_8(A_1)$	$[\nu(Tc_1F_2) + \nu(Tc_2F_2)] + [\nu(Tc_2F_3) + \nu(Tc_3F_3)] + [\nu(Tc_3F_1) + \nu(Tc_1F_1)] + [\nu(Tc_1O_D) + \nu(Tc_2O_D) + \nu(Tc_3O_D)]$		
		$\rho_w(O_BTc_1F_4) + \rho_r(O_BTc_2F_4) + \rho_r(O_BTc_3F_4)$	$\nu_8(A_1)$	193(3)[<1]
196(4)[<0.01]	$\nu_{20}(E)$	$\rho_r(O_ATc_1O_B) + \rho_r(O_AO_BTc_2O_C) + \rho_r(O_AO_BTc_3O_C)$		
		$[\rho_r(O_CTc_1O_B) + \rho_r(O_ATc_2O_C) + \rho_r(O_AO_BTc_3O_C)] + [\nu(Tc_1F_2) + \nu(Tc_2F_2) - \nu(Tc_2F_3) + \nu(Tc_3F_3)]$	$\nu_{20}(E)$	188(2)[<0.1]

Table A4. (continued ...)

166(1)[1]	$\nu_9(A_1)$	$[\nu(Tc_1F_2) + \nu(Tc_2F_2)] + [\nu(Tc_2F_3) + \nu(Tc_3F_3)] + [\nu(Tc_3F_1) + \nu(Tc_1F_1)] + [\nu(Tc_1O_D) + \nu(Tc_2O_D) + \nu(Tc_3O_D)] + \rho_r(O_AO_BTc_1O_C) + \rho_r(O_AO_BTc_2O_C) + \rho_r(O_AO_BTc_3O_C)$		
		$\rho_r(O_AO_BTc_1O_C) + \rho_r(O_AO_BTc_2O_C) + \rho_r(O_AO_BTc_3O_C)$	$\nu_9(A_1)$	132(1)[<1]
130(<0.1)[<0.1]	$\nu_{21}(E)$	$\rho_r(O_AO_BTc_1O_C) - \rho_r(O_AO_BTc_2O_C)$	$\nu_{21}(E)$	108(<1)[<0.1]
92(<1)[<1]	$\nu_{22}(E)$	deformation modes	$\nu_{22}(E)$	97(1)[<0.1]
83(1)[1]	$\nu_{23}(E)$		$\nu_{23}(E)$	57(<1)[<1]

[a] Frequencies are in cm^{-1}. [b] Values in parentheses denote calculated Raman intensities ($Å^4\ u^{-1}$). Values in square brackets denote calculated infrared intensities (km mol^{-1}). The B3LYP/aug-cc-pVTZ(-PP) level was used. [c] The abbreviations denote stretch (ν), bend (δ), rock (ρ_r), and wag (ρ_w). For the atom labeling scheme, see Figure A5.

Table A5. Experimental Geometrical Parameters for the $[\{TcO_3(\mu\text{-}F)\}_3(\mu_3\text{-}F)]^-$ Anion in $K[\{TcO_3(\mu\text{-}F)\}_3(\mu_3\text{-}F)]\cdot 1.5TcO_3F$ and Calculated Geometrical Parameters for the $[\{TcO_3(\mu\text{-}F)\}_3(\mu_3\text{-}O)]^{2-}$ and $[\{TcO_3(\mu\text{-}F)\}_3(\mu_3\text{-}F)]^-$ Anions

calcd[a,b]				exptl[c]	
$[\{TcO_3(\mu\text{-}F)\}_3(\mu_3\text{-}O)]^{2-}$		$[\{TcO_3(\mu\text{-}F)\}_3(\mu_3\text{-}F)]^-$			
Bond Lengths (Å)					
$Tc_1–O_A$	1.693	$Tc_1–O_A$	1.680	$Tc_1–O_{11}$	1.685(4)
$Tc_1–O_B$	1.700	$Tc_1–O_B$	1.681	$Tc_1–O_{12}$	1.677(4)
$Tc_1–O_C$	1.693	$Tc_1–O_C$	1.680	$Tc_1–O_{13}$	1.682(4)
$Tc_2–O_A$	1.693	$Tc_2–O_A$	1.680	$Tc_2–O_{21}$	1.680(4)
$Tc_2–O_B$	1.700	$Tc_2–O_B$	1.681	$Tc_2–O_{22}$	1.683(4)
$Tc_2–O_C$	1.693	$Tc_2–O_C$	1.680	$Tc_2–O_{23}$	1.687(4)
$Tc_3–O_A$	1.693	$Tc_3–O_A$	1.680	$Tc_3–O_{33}$	1.667(4)
$Tc_3–O_B$	1.700	$Tc_3–O_B$	1.681	$Tc_3–O_{32}$	1.685(4)
$Tc_3–O_C$	1.693	$Tc_3–O_C$	1.680	$Tc_3–O_{31}$	1.691(4)
$Tc_1–O_D$	2.096	$Tc_1–F_4$	2.302	$Tc_1–F_{10}$	2.266(3)
$Tc_2–O_D$	2.096	$Tc_2–F_4$	2.302	$Tc_2–F_{10}$	2.246(3)
$Tc_3–O_D$	2.096	$Tc_3–F_4$	2.302	$Tc_3–F_{10}$	2.223(3)
$Tc_1–F_1$	2.165	$Tc_1–F_1$	2.128	$Tc_1–F_1$	2.132(3)
$Tc_1–F_2$	2.165	$Tc_1–F_2$	2.128	$Tc_1–F_2$	2.102(3)
$Tc_2–F_2$	2.165	$Tc_2–F_2$	2.128	$Tc_2–F_2$	2.098(3)
$Tc_2–F_3$	2.165	$Tc_2–F_3$	2.128	$Tc_2–F_3$	2.113(3)
$Tc_3–F_3$	2.165	$Tc_3–F_3$	2.128	$Tc_3–F_3$	2.110(3)
$Tc_3–F_1$	2.165	$Tc_3–F_1$	2.128	$Tc_3–F_1$	2.112(3)
Bond Angles (deg)					
$O_A–Tc_1–O_B$	104.9	$O_A–Tc_1–O_B$	105.8	$O_{12}–Tc_1–O_{13}$	105.5(2)
$O_B–Tc_1–O_C$	104.9	$O_B–Tc_1–O_C$	105.8	$O_{12}–Tc_1–O_{11}$	105.4(2)
$O_C–Tc_1–O_A$	102.8	$O_C–Tc_1–O_A$	103.6	$O_{13}–Tc_1–O_{11}$	104.1(2)
$O_A–Tc_1–O_D$	95.1	$O_A–Tc_1–F_4$	89.1	$O_{11}–Tc_1–F_{10}$	88.1(2)
$O_B–Tc_1–O_D$	147.5	$O_B–Tc_1–F_4$	155.3	$O_{12}–Tc_1–F_{10}$	157.3(2)
$O_C–Tc_1–O_D$	95.1	$O_C–Tc_1–F_4$	89.1	$O_{13}–Tc_1–F_{10}$	88.2(2)
$O_A–Tc_2–O_B$	104.9	$O_A–Tc_2–O_B$	105.8	$O_{21}–Tc_2–O_{22}$	105.5(2)
$O_B–Tc_2–O_C$	104.9	$O_B–Tc_2–O_C$	105.8	$O_{22}–Tc_2–O_{23}$	105.9(2)
$O_C–Tc_2–O_A$	102.8	$O_C–Tc_2–O_A$	103.6	$O_{23}–Tc_2–O_{21}$	103.6(2)
$O_A–Tc_2–O_D$	95.1	$O_A–Tc_2–F_4$	89.1	$O_{23}–Tc_2–F_{10}$	86.9(2)
$O_B–Tc_2–O_D$	147.5	$O_B–Tc_2–F_4$	155.3	$O_{21}–Tc_2–F_{10}$	157.3(2)
$O_C–Tc_2–O_D$	95.1	$O_C–Tc_2–F_4$	89.1	$O_{22}–Tc_2–F_{10}$	89.0(2)
$O_A–Tc_3–O_B$	104.9	$O_A–Tc_3–O_B$	105.8	$O_{33}–Tc_3–O_{31}$	104.9(2)
$O_B–Tc_3–O_C$	104.9	$O_B–Tc_3–O_C$	105.8	$O_{32}–Tc_3–O_{33}$	105.3(2)
$O_C–Tc_3–O_A$	102.8	$O_C–Tc_3–O_A$	103.6	$O_{31}–Tc_3–O_{32}$	103.5(2)
$O_A–Tc_3–O_D$	89.1	$O_A–Tc_3–F_4$	89.1	$O_{31}–Tc_3–F_{10}$	88.0(2)
$O_B–Tc_3–O_D$	147.5	$O_B–Tc_3–F_4$	155.3	$O_{33}–Tc_3–F_{10}$	157.3(2)
$O_C–Tc_3–O_D$	95.1	$O_C–Tc_3–F_4$	89.1	$O_{32}–Tc_3–F_{10}$	89.2(2)
$O_A–Tc_1–F_2$	87.7	$O_A–Tc_1–F_2$	87.3	$O_{12}–Tc_1–F_2$	93.0(2)
$O_B–Tc_1–F_2$	85.2	$O_B–Tc_1–F_2$	92.7	$O_{11}–Tc_1–F_2$	87.9(2)

Table A5. (continued…)

O_C–Tc_1–F_2	162.7	O_C–Tc_1–F_2	154.6	O_{13}–Tc_1–F_2	154.0(2)
O_D–Tc_1–F_2	70.0	F_4–Tc_1–F_2	67.9	F_{10}–Tc_1–F_2	68.9(1)
O_A–Tc_1–F_1	162.7	O_A–Tc_1–F_1	154.6	O_{11}–Tc_1–F_1	154.6(2)
O_B–Tc_1–F_1	85.2	O_B–Tc_1–F_1	92.7	O_{12}–Tc_1–F_1	94.1(2)
O_C–Tc_1–F_1	87.7	O_C–Tc_1–F_1	87.3	O_{13}–Tc_1–F_1	85.8(2)
O_D–Tc_1–F_1	70.0	F_4–Tc_1–F_1	67.9	F_{10}–Tc_1–F_1	68.5(1)
O_A–Tc_2–F_2	87.5	O_A–Tc_2–F_2	87.3	O_{21}–Tc_2–F_2	93.5(2)
O_B–Tc_2–F_2	85.2	O_B–Tc_2–F_2	92.7	O_{22}–Tc_2–F_2	87.6(2)
O_C–Tc_2–F_2	162.7	O_C–Tc_2–F_2	154.6	O_{23}–Tc_2–F_2	153.7(2)
O_D–Tc_2–F_2	70.0	F_4–Tc_2–F_2	67.9	F_{10}–Tc_2–F_2	69.3(1)
O_A–Tc_2–F_3	162.7	O_A–Tc_2–F_3	154.6	O_{22}–Tc_2–F_3	155.1(2)
O_B–Tc_2–F_3	85.2	O_B–Tc_2–F_3	92.7	O_{21}–Tc_2–F_3	92.3(2)
O_C–Tc_2–F_3	87.7	O_C–Tc_2–F_3	87.3	O_{23}–Tc_2–F_3	87.6(2)
O_D–Tc_2–F_3	70.0	F_4–Tc_2–F_3	67.9	F_{10}–Tc_2–F_3	69.2(1)
O_A–Tc_3–F_3	162.7	O_A–Tc_3–F_3	154.6	O_{32}–Tc_3–F_3	156.5(2)
O_B–Tc_3–F_3	85.2	O_B–Tc_3–F_3	92.7	O_{31}–Tc_3–F_3	92.1(2)
O_C–Tc_3–F_3	87.7	O_C–Tc_3–F_3	87.3	O_{33}–Tc_3–F_3	86.7(2)
O_D–Tc_3–F_3	70.0	F_4–Tc_3–F_3	67.9	F_{10}–Tc_3–F_3	69.7(1)
O_A–Tc_3–F_1	87.7	O_A–Tc_3–F_1	87.3	O_{32}–Tc_3–F_1	87.5(2)
O_B–Tc_3–F_1	85.2	O_B–Tc_3–F_1	92.7	O_{33}–Tc_3–F_1	93.2(2)
O_C–Tc_3–F_1	162.7	O_C–Tc_3–F_1	154.6	O_{31}–Tc_3–F_1	155.2(2)
O_D–Tc_3–F_1	68.0	F_4–Tc_3–F_1	67.9	F_{10}–Tc_3–F_1	69.7(1)
F_1–Tc_1–F_2	79.1	F_1–Tc_1–F_2	74.5	F_1–Tc_1–F_2	74.6(1)
F_2–Tc_2–F_3	79.1	F_2–Tc_2–F_3	74.5	F_2–Tc_2–F_3	73.9(1)
F_3–Tc_3–F_1	79.1	F_3–Tc_3–F_1	74.5	F_3–Tc_3–F_1	75.6(1)
Tc_1–O_D–Tc_2	110.0	Tc_1–F_4–Tc_2	103.5	Tc_1–F_{10}–Tc_2	103.0(1)
Tc_2–O_D–Tc_3	110.0	Tc_2–F_4–Tc_3	103.5	Tc_2–F_{10}–Tc_3	104.2(1)
Tc_3–O_D–Tc_1	110.0	Tc_3–F_4–Tc_1	103.5	Tc_3–F_{10}–Tc_1	105.0(1)
Tc_1–F_2–Tc_2	104.9	Tc_1–F_2–Tc_2	117.3	Tc_1–F_2–Tc_2	114.4(1)
Tc_2–F_3–Tc_3	104.9	Tc_2–F_3–Tc_3	117.3	Tc_2–F_3–Tc_3	113.2(1)
Tc_3–F_1–Tc_1	104.9	Tc_3–F_1–Tc_1	117.3	Tc_3–F_1–Tc_1	114.1(1)

[a] For the atom labeling scheme, see Figure A5. [b] The B3LYP/aug-cc-pVTZ (-PP) level was used. [c] For the atom labeling scheme see Ref 23.

APPENDIX B

SYNTHESES AND STRUCTURAL CHARACTERIZATION OF THE $[ReO_3F_2]^-$ AND *fac*–$[ReO_3F_3]^{2-}$ ANIONS AND $(\mu\text{-}F)_4\{[\mu\text{-}O(ReO_2F)_2](ReO_2F_2)_2$

Table B1. Experimental Geometrical Parameters for $(\mu\text{-}F)_4\{[\mu\text{-}O(ReO_2F)_2](ReO_2F_2)_2\}$ in $(\mu\text{-}F)_4\{[\mu\text{-}O(ReO_2F)_2](ReO_2F_2)_2\}\cdot SO_2ClF$ and Calculated Geometrical Parameters for $(\mu\text{-}F)_4\{[\mu\text{-}O(ReO_2F)_2](ReO_2F_2)_2\}$

	exptl[a]			calcd[b]	
				B3LYP	PBE1PBE
Bond Lengths (Å)					
$Re_5–O_{10}$	1.666(12)	$Re_7–O_{14}$	1.700(11)	1.671	1.659
$Re_5–O_{11}$	1.690(11)	$Re_7–O_{15}$	1.671(11)	1.671	1.659
$Re_6–O_{12}$	1.677(11)	$Re_8–O_{16}$	1.646(11)	1.674	1.662
$Re_6–O_{13}$	1.694(11)	$Re_8–O_{17}$	1.673(10)	1.674	1.662
$Re_6–O_{18}$	1.853(10)	$Re_8–O_{18}$	1.883(10)	1.876	1.862
$Re_5–F_{11}$	1.826(8)	$Re_7–F_{14}$	1.857(9)	1.840	1.826
$Re_5–F_{12}$	1.816(9)	$Re_7–F_{15}$	1.842(9)	1.850	1.836
$Re_6–F_{13}$	1.848(9)	$Re_8–F_{16}$	1.823(8)	1.844	1.831
$Re_5–F_{17}$	2.081(8)	$Re_7–F_{18}$	2.083(9)	2.115	2.097
$Re_5–F_{20}$	2.091(9)	$Re_7–F_{19}$	2.089(8)	2.115	2.097
$Re_6–F_{17}$	2.139(8)	$Re_8–F_{19}$	2.099(8)	2.131	2.112
$Re_6–F_{18}$	2.078(8)	$Re_8–F_{20}$	2.092(9)	2.131	2.112
$S_1–O_{20}$	1.40(2)				
$S_1–O_{19}$	1.47(3)				
$S_1–F_{21}$	1.53(3)				
$S_1–Cl_1$	1.94(3)				
$F_{(11)}\text{---}O_{(5)}$	2.683(13)				
$O_{(13)}\text{---}O_{(16A)}$	2.71(2)				
$O_{(20)}\text{---}O_{(6)}$	2.80(3)				
$F_{(21)}\text{---}O_{(7B)}$	2.96(3)				
$F_{(21)}\text{---}F_{(6B)}$	2.98(3)				
$Cl_{(1)}\text{---}O_{(6C)}$	2.80(1)				
$Cl_{(1)}\text{---}F_{(16C)}$	3.05(2)				
Bond Angles (deg)					
$O_{10}–Re_5–O_{11}$	102.6(6)	$O_{14}–Re_7–O_{15}$	103.2(5)	103.1	103.0
$O_{12}–Re_6–O_{13}$	102.4(6)	$O_{16}–Re_8–O_{17}$	103.5(5)	102.7	102.8
$O_{12}–Re_6–O_{18}$	97.9(5)	$O_{16}–Re_8–O_{18}$	97.8(5)	98.2	98.2
$O_{13}–Re_6–O_{18}$	98.0(5)	$O_{17}–Re_8–O_{18}$	97.5(5)	98.2	98.2
$O_{10}–Re_5–F_{11}$	98.5(5)	$O_{14}–Re_7–F_{14}$	96.8(5)	98.4	98.6
$O_{10}–Re_5–F_{12}$	97.7(5)	$O_{14}–Re_7–F_{15}$	98.4(5)	97.9	98.0
$O_{10}–Re_5–F_{17}$	165.7(5)	$O_{14}–Re_7–F_{19}$	168.0(4)	166.5	166.5
$O_{10}–Re_5–F_{20}$	89.6(5)	$O_{14}–Re_7–F_{18}$	91.1(4)	90.4	90.4
$O_{11}–Re_5–F_{11}$	96.0(5)	$O_{15}–Re_7–F_{14}$	97.5(5)	98.4	98.6
$O_{11}–Re_5–F_{12}$	99.7(5)	$O_{15}–Re_7–F_{15}$	97.7(6)	97.9	98.0
$O_{11}–Re_5–F_{17}$	91.7(4)	$O_{15}–Re_7–F_{19}$	88.7(5)	90.4	90.4
$O_{11}–Re_5–F_{20}$	167.6(4)	$O_{15}–Re_7–F_{18}$	165.7(5)	166.5	166.5
$O_{12}–Re_6–F_{13}$	96.9(5)	$O_{16}–Re_8–F_{16}$	98.0(5)	98.0	98.0
$O_{12}–Re_6–F_{17}$	89.3(5)	$O_{16}–Re_8–F_{19}$	89.7(4)	90.1	90.2
$O_{12}–Re_6–F_{18}$	166.3(5)	$O_{16}–Re_8–F_{20}$	167.7(4)	167.1	166.9
$O_{13}–Re_6–F_{13}$	97.1(5)	$O_{17}–Re_8–F_{16}$	97.3(5)	98.0	98.0
$O_{13}–Re_6–F_{17}$	168.0(5)	$O_{17}–Re_8–F_{19}$	166.7(4)	167.1	166.9

Table B1. (continued…)

O_{13}−Re_6−F_{18}	90.9(5)	O_{17}−Re_8−F_{20}	88.7(4)	90.1	90.2
O_{18}−Re_6−F_{13}	156.0(4)	O_{18}−Re_8−F_{16}	155.1(4)	154.0	153.9
O_{18}−Re_6−F_{17}	82.7(4)	O_{18}−Re_8−F_{19}	81.0(4)	81.3	81.2
O_{18}−Re_6−F_{18}	77.2(3)	O_{18}−Re_8−F_{20}	81.9(4)	81.3	81.2
F_{11}−Re_5−F_{12}	154.3(4)	F_{14}−Re_7−F_{15}	155.4(4)	153.6	153.2
F_{11}−Re_5−F_{17}	80.7(4)	F_{14}−Re_7−F_{18}	79.9(4)	79.9	79.7
F_{11}−Re_5−F_{20}	79.5(4)	F_{14}−Re_7−F_{19}	79.5(4)	79.9	79.7
F_{12}−Re_5−F_{17}	78.7(4)	F_{15}−Re_7−F_{18}	80.6(4)	79.4	79.2
F_{12}−Re_5−F_{20}	80.9(5)	F_{15}−Re_7−F_{19}	81.6(5)	79.4	79.2
F_{17}−Re_5−F_{20}	76.3(3)	F_{18}−Re_7−F_{19}	77.0(3)	76.1	76.1
F_{13}−Re_6−F_{17}	78.6(4)	F_{16}−Re_8−F_{19}	80.0(4)	78.5	78.4
F_{13}−Re_6−F_{18}	78.1(4)	F_{16}−Re_8−F_{20}	78.6(4)	78.5	78.4
F_{17}−Re_6−F_{18}	77.2(3)	F_{19}−Re_8−F_{20}	78.1(4)	77.1	76.7
Re_5−F_{17}−Re_6	145.2(5)	Re_6−F_{18}−Re_7	153.9(5)	150.9	149.8
Re_8−F_{20}−Re_5	142.6(4)	Re_7−F_{19}−Re_8	156.6(4)	150.9	149.8
Re_6−O_{18}−Re_8	160.6(6)			163.6	163.7
O_1−Re_1−O_2	103.1(6)	O_5−Re_3−O_6	102.4(6)	103.1	103.0
O_3−Re_2−O_4	103.5(6)	O_7−Re_4−O_8	102.4(8)	102.7	102.8
O_3−Re_2−O_9	98.4(5)	O_7−Re_4−O_9	98.5(5)	98.2	98.2
O_4−Re_2−O_9	98.3(5)	O_8−Re_4−O_9	98.3(5)	98.2	98.2
O_1−Re_1−F_1	97.8(5)	O_5−Re_3−F_4	96.9(5)	98.4	98.6
O_1−Re_1−F_2	97.1(5)	O_5−Re_3−F_5	98.3(5)	97.9	98.0
O_1−Re_1−F_7	166.2(5)	O_5−Re_3−F_9	168.0(5)	166.5	166.5
O_1−Re_1−F_{10}	88.4(5)	O_5−Re_3−F_8	91.2(5)	90.4	90.4
O_2−Re_1−F_1	98.2(6)	O_6−Re_3−F_4	98.8(5)	98.4	98.6
O_2−Re_1−F_2	97.8(6)	O_6−Re_3−F_5	98.1(6)	97.9	98.0
O_2−Re_1−F_7	90.7(5)	O_6−Re_3−F_9	89.6(5)	90.4	90.4
O_2−Re_1−F_{10}	168.5(5)	O_6−Re_3−F_8	166.4(5)	166.5	166.5
O_3−Re_2−F_3	97.3(6)	O_7−Re_4−F_6	97.7(6)	98.0	98.0
O_3−Re_2−F_7	90.3(6)	O_7−Re_4−F_9	89.9(7)	90.1	90.2
O_3−Re_2−F_8	166.4(6)	O_7−Re_4−F_{10}	167.0(7)	167.1	166.9
O_4−Re_2−F_3	96.7(5)	O_8−Re_4−F_6	98.1(5)	98.0	98.0
O_4−Re_2−F_7	166.0(5)	O_8−Re_4−F_9	167.6(6)	167.1	166.9
O_4−Re_2−F_8	89.8(5)	O_8−Re_4−F_{10}	90.6(6)	90.1	90.2
O_9−Re_2−F_3	155.1(4)	O_9−Re_4−F_6	153.9(4)	154.0	153.9
O_9−Re_2−F_7	81.8(4)	O_9−Re_4−F_9	81.6(4)	81.3	81.2
O_9−Re_2−F_8	82.2(4)	O_9−Re_4−F_{10}	80.3(4)	81.3	81.2
F_1−Re_1−F_2	155.0(5)	F_4−Re_3−F_5	154.2(4)	153.6	153.2
F_1−Re_1−F_7	81.9(4)	F_4−Re_3−F_8	80.2(4)	79.9	79.7
F_1−Re_1−F_{10}	79.2(5)	F_4−Re_3−F_9	80.0(5)	79.9	79.7
F_2−Re_1−F_7	78.9(4)	F_5−Re_3−F_8	78.8(4)	79.4	79.2
F_2−Re_1−F_{10}	81.3(5)	F_5−Re_3−F_9	80.8(5)	79.4	79.2
F_7−Re_1−F_{10}	77.9(3)	F_8−Re_3−F_9	76.8(4)	76.1	76.1
F_3−Re_2−F_7	78.9(4)	F_6−Re_4−F_9	78.2(4)	78.5	78.4
F_3−Re_2−F_8	78.1(4)	F_6−Re_4−F_{10}	79.4(4)	78.5	78.4
F_7−Re_2−F_8	76.3(4)	F_9−Re_4−F_{10}	77.1(4)	77.1	76.7
Re_1−F_7−Re_2	150.8(5)	Re_2−F_8−Re_3	147.4(5)	150.9	149.8
Re_4−F_{10}−Re_1	154.2(5)	Re_3−F_9−Re_4	150.3(5)	150.9	149.8
Re_2−O_9−Re_4	162.7(6)			163.6	163.7
O_{20}−S−O_{19}	116(2)				

Table B1. (continued…)

O_{20}−S_1−F_{21}	117(2)
O_{20}−S_1−Cl_1	108(1)
O_{19}−S_1−F_{21}	109(2)
O_{19}−S_1−Cl_1	96(1)
F_{21}−S_1−Cl_1	108(1)

[a] For the atom labeling scheme, see Figure B1. [b] For the atom labeling scheme, see Figure 4.3b. The aug-cc-pVTZ(-PP) basis set was used.

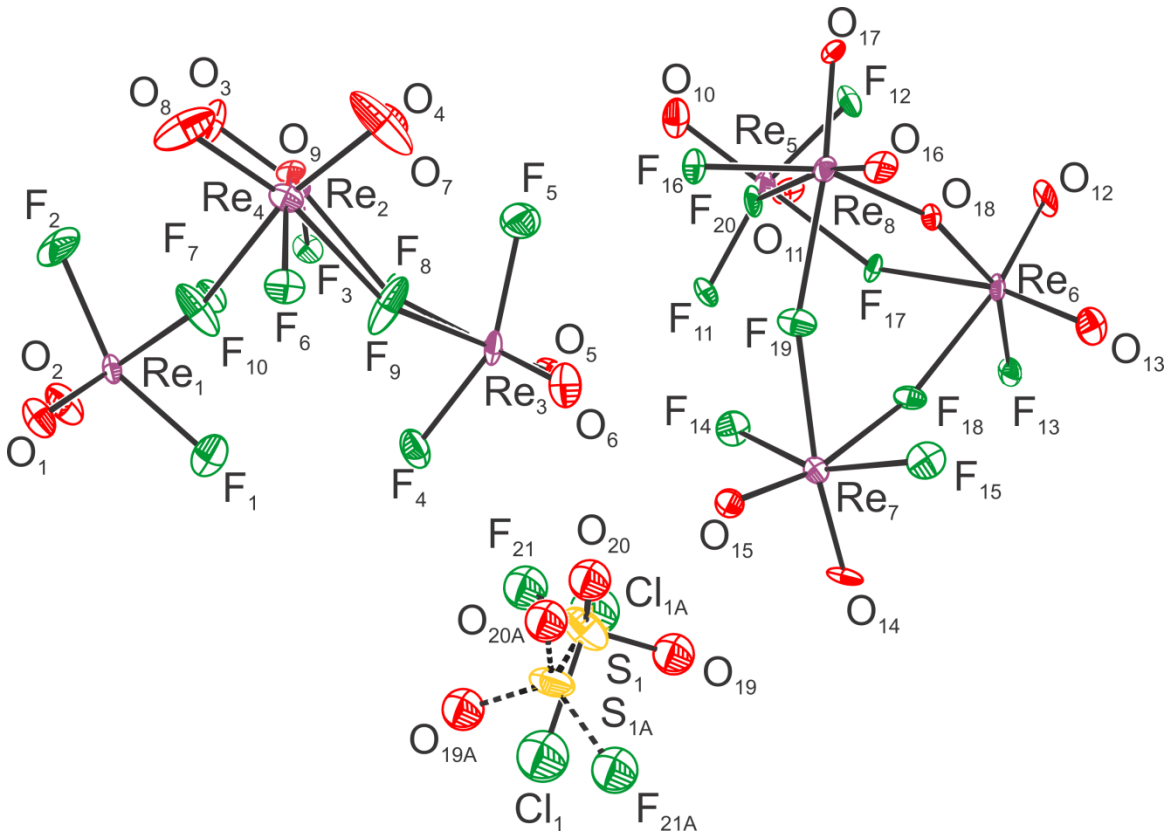

Figure B1. Crystal structure of (μ-F)$_4${[μ-O(ReO$_2$F)$_2$](ReO$_2$F$_2$)$_2$}·SO$_2$ClF; thermal ellipsoids are shown at the 50% probability level. The two orientations of the positionally disordered (50/50) SO$_2$ClF molecule are shown.

The $Cs[ReO_2F_4]$ and $Cs[\mu\text{-}F(ReO_2F_3)_2]$ Salts

The $[\mu\text{-}F(ReO_2F_3)_2]^-$ and $[ReO_2F_4]^-$ anions have been previously synthesized as their $Li^+/Na^+/Cs^+/[N(CH_3)_4]^+$ and $[N(CH_3)_4]^+/K^+$ salts, respectively,[19] and characterized by Raman and ^{19}F NMR spectroscopy. The salts of $Li[ReO_2F_4]$ and $K[\mu\text{-}F(ReO_2F_3)_2]$ were additionally characterized by single-crystal X-ray diffraction, however, no crystal structures were obtained for the Cs^+ salts. Overall all bond lengths and angles are comparable among the corresponding cations in the K^+ and Cs^+ salts, except the $Re{-}F_\mu{-}Re$ bond angle (Cs^+, 180.0°; K^+, 139.5(6)° [19]).

Crystals of $Cs[ReO_2F_4]$ and $Cs[\mu\text{-}F(ReO_2F_3)_2]$ were grown from a pale yellow solution prepared by reacting ReO_3F (0.0602 g, 0.2376 mmol) with CsF (0.0698 g, 0.4597 mmol) in aHF in a ¼-in. o.d. FEP reaction vessel equipped with a side arm (T-shaped reactor) and fitted with a Kel-F valve. The main arm of the reaction vessel containing the solution was placed inside the glass dewar of the crystal growing apparatus precooled to −33 °C and the temperature of the dewar and contents was slowly lowered to −40 °C to induce slow crystal growth. Colorless plates formed over a period of 5−6 h. Upon completion of crystal growth, the supernatant was decanted into the side arm, which had been precooled to −196 °C. The crystalline products were dried under dynamic vacuum at −45 °C before the side arm containing the frozen supernatant was heat-sealed off under dynamic vacuum. The portion of the reactor containing the dry crystalline products were backfilled with dry N_2 and stored at −78 °C until the crystals could be mounted. A crystal of $Cs[ReO_2F_4]$ having the dimensions 0.11 x 0.27 x 0.33 mm^3 and a crystal of $Cs[\mu\text{-}F(ReO_2F_3)_2]$ having the dimensions 0.12 x 0.31 x 0.31 mm^3 were selected for a low-temperature X-ray structure determination.

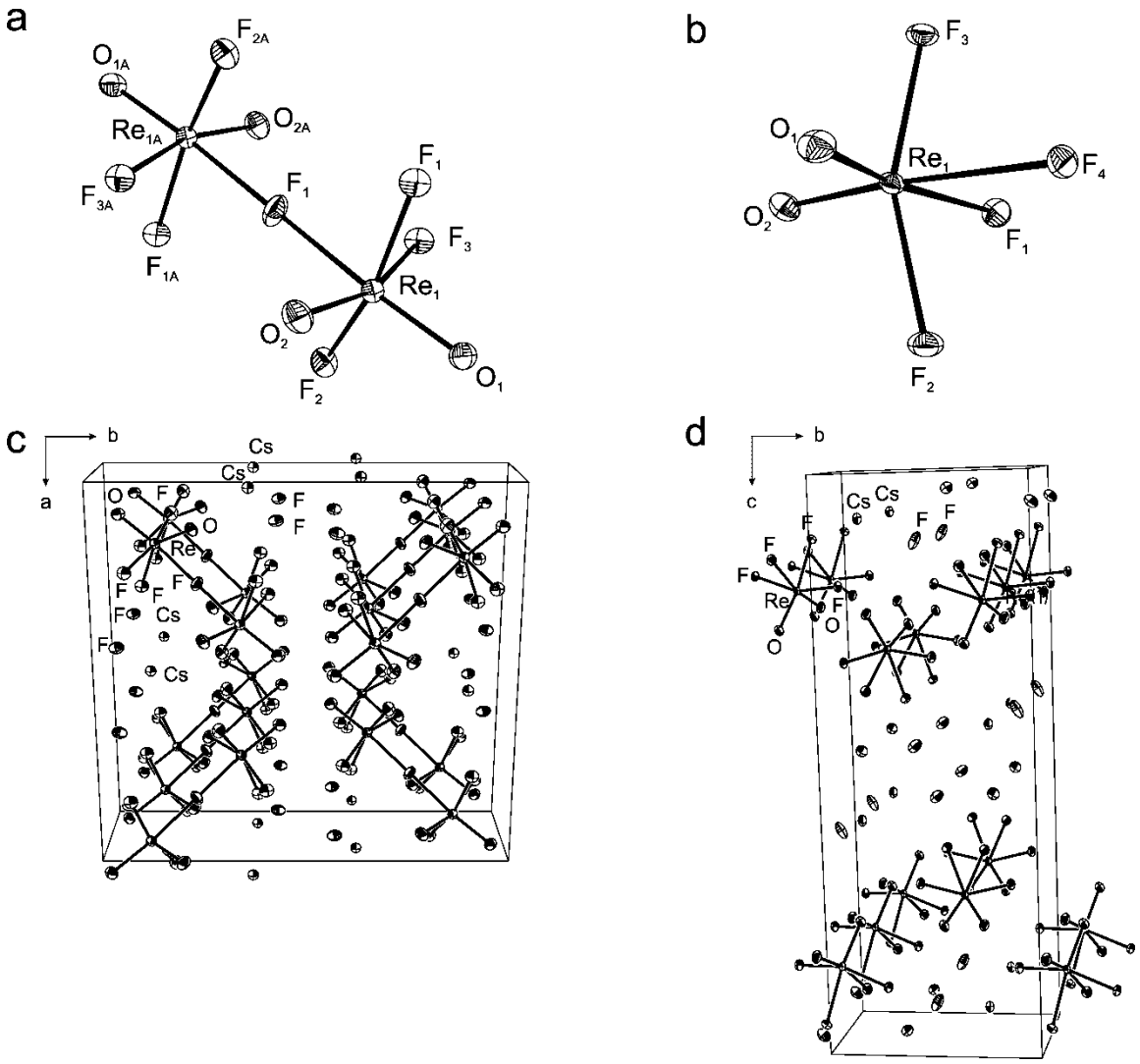

Figure B2. The (a) $[\mu\text{-}F(ReO_2F_3)_2]^-$ and (b) $[ReO_2F_4]^-$ anions in the crystal structures of $Cs[\mu\text{-}F(ReO_2F_3)_2]\cdot 2HF$ and $Cs[ReO_2F_4]\cdot 3HF$, respectively. Packing diagrams for (c) $Cs[\mu\text{-}F(ReO_2F_3)_2]\cdot 2HF$ and (d) $Cs[ReO_2F_4]\cdot 3HF$ are shown along the *c*- and *a*-axes, respectively. Thermal ellipsoids are shown at the 50 % probability level.

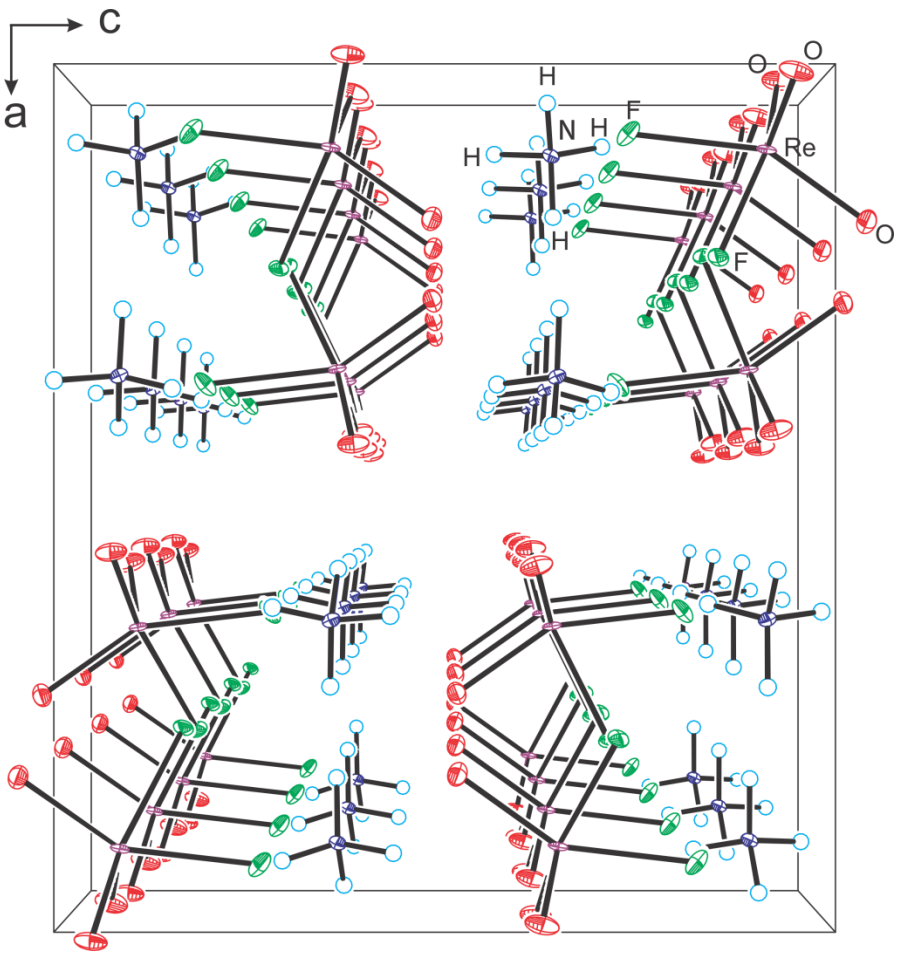

Figure B3. The packing diagram for $[NH_4][ReO_3F_2]$ is shown along the *b*-axis. Thermal ellipsoids are shown at the 50 % probability level.

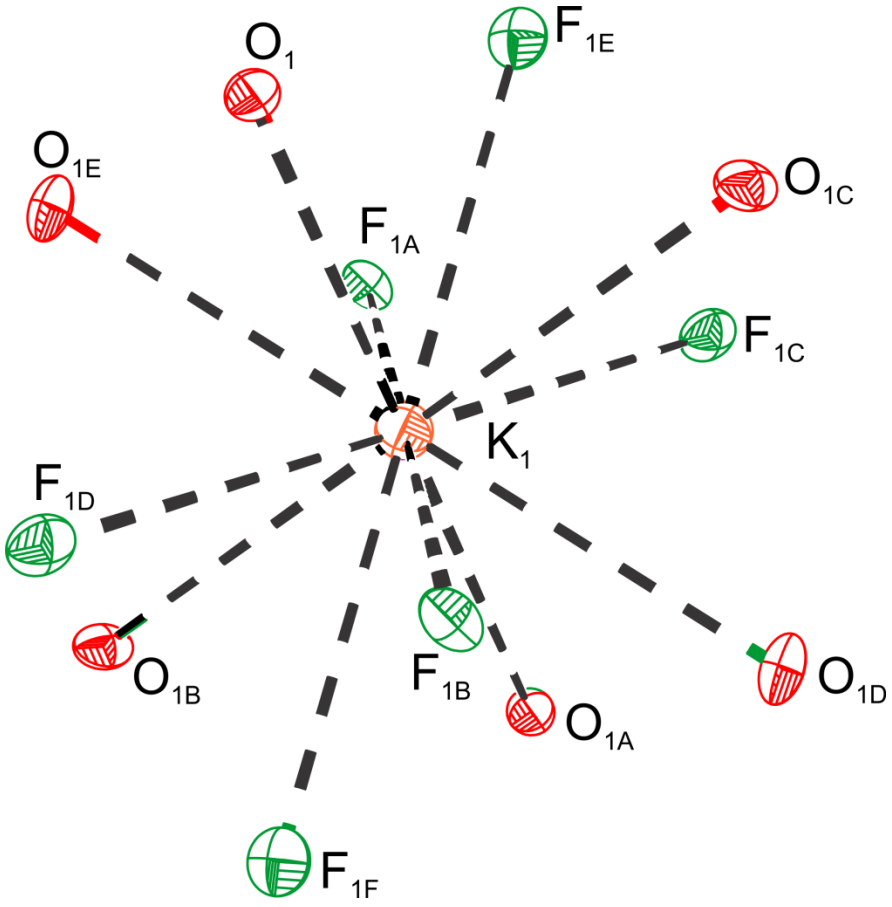

Figure B4. The coordination environment around the K^+ cation in the crystal structure of $K[H_3O][ReO_3F_3]$. Thermal ellipsoids are shown at the 50 % probability level.

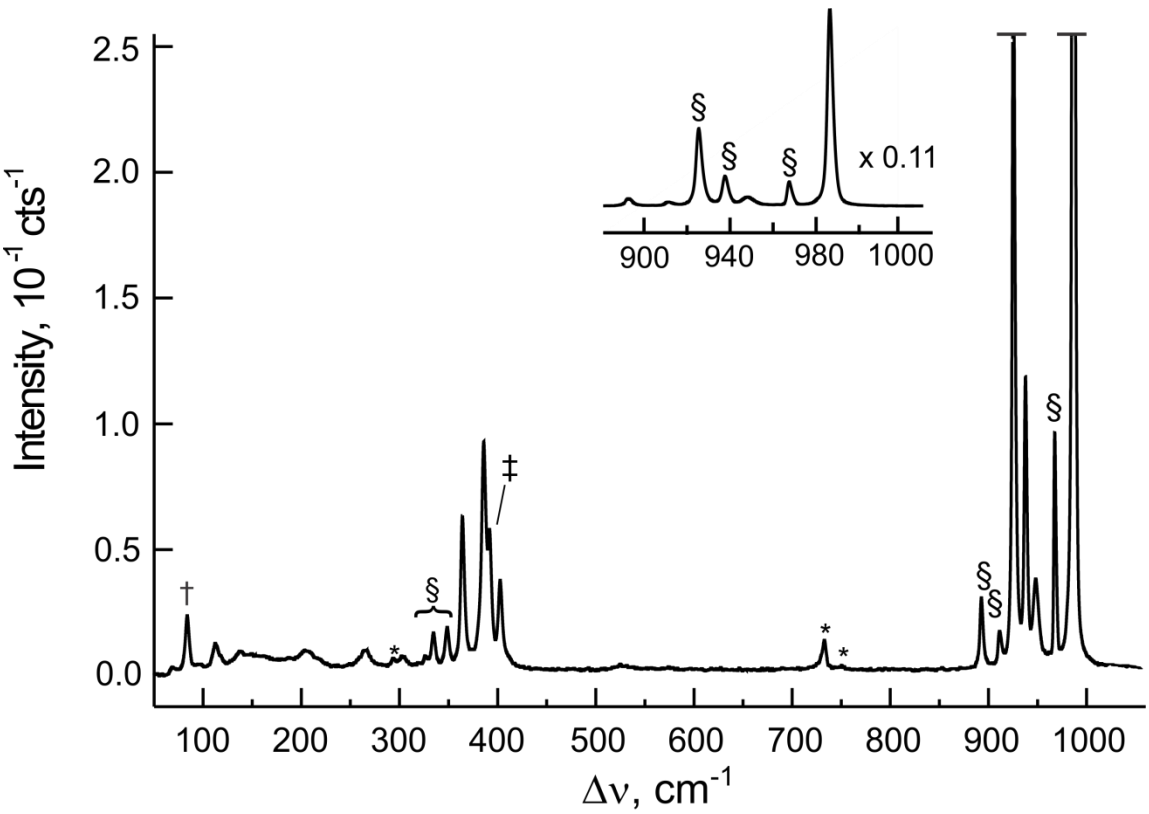

Figure B5. Raman spectrum of crystalline $[NH_4][ReO_3F_2]$ recorded at –150 ^{o}C using 1064-nm excitation. Symbols denote an FEP sample tube line (*), instrumental artifact (†), overlap of a $[NH_4][ReO_3F_2]$ line with an FEP sample tube line (‡), and a $[NH_4][ReO_4]$ line (§). The $[NH_4]^+$ cation modes were observed at 214 sh, 265(1), 1439(<1), 3137(1), and 3191(1) cm^{-1}.

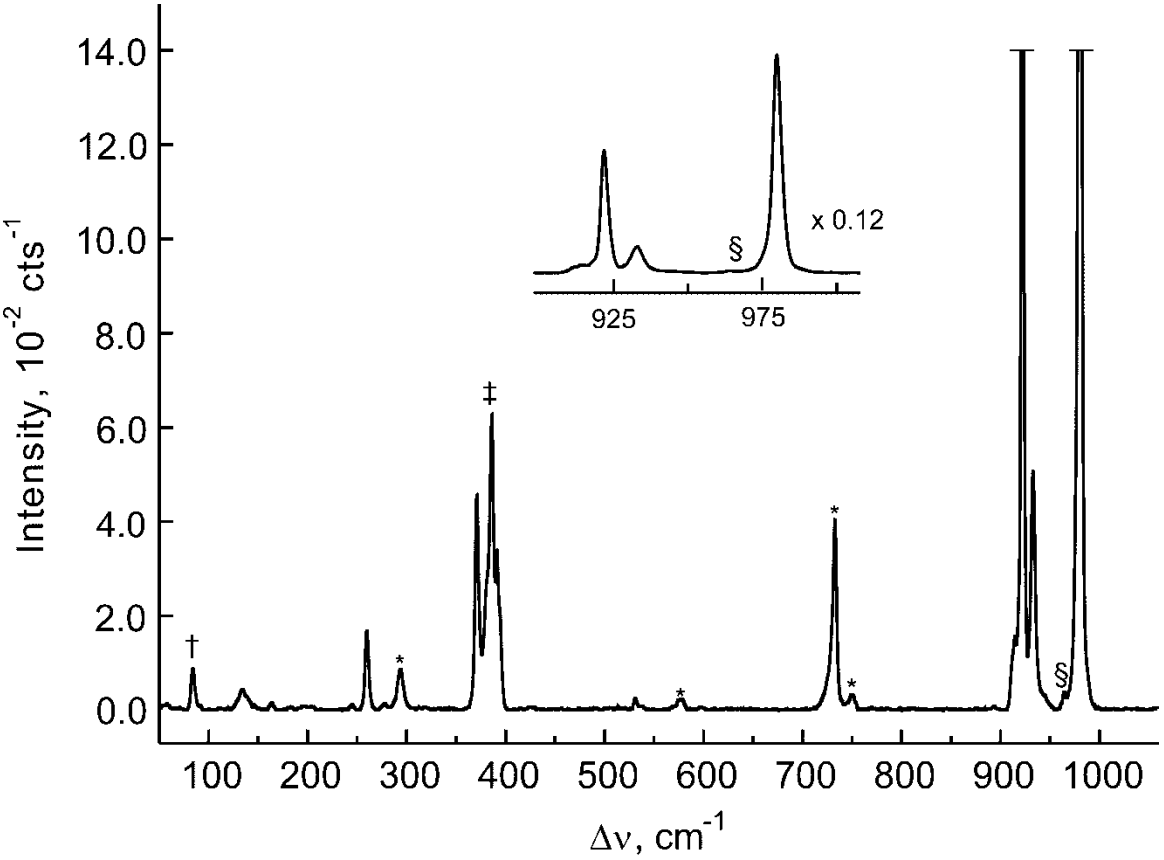

Figure B6. Raman spectrum of crystalline $Cs[ReO_3F_2]$ recorded at –150 ^{o}C using 1064-nm excitation. Symbols denote an FEP sample tube line (*), instrumental artifact (†), overlap of a $Cs[ReO_3F_2]$ line with an FEP sample tube line (‡), and a $Cs[ReO_4]$ line (§).

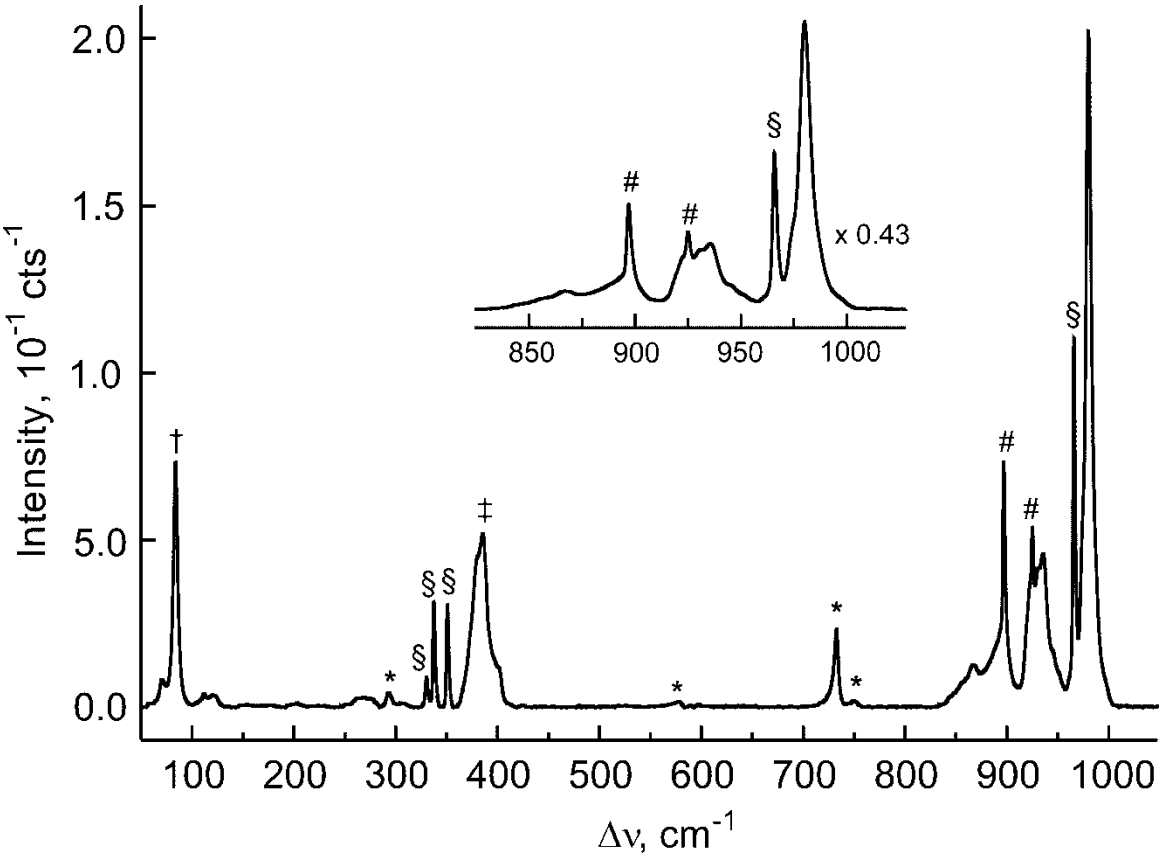

Figure B7. Raman spectrum of a solid mixture of crystalline $K[ReO_3F_2]$, crystalline $K[H_3O][ReO_3F_3]$, and $K[ReO_4]$ recorded at –150 ^{o}C using 1064-nm excitation. Symbols denote an FEP sample tube line (*), instrumental artifact (†), overlap of a $K[ReO_3F_2]$ line with a $K[ReO_4]$ line (#), overlap of a $K[ReO_3F_2]$ line with an FEP sample tube line (‡), and a $K[ReO_4]$ line (§).

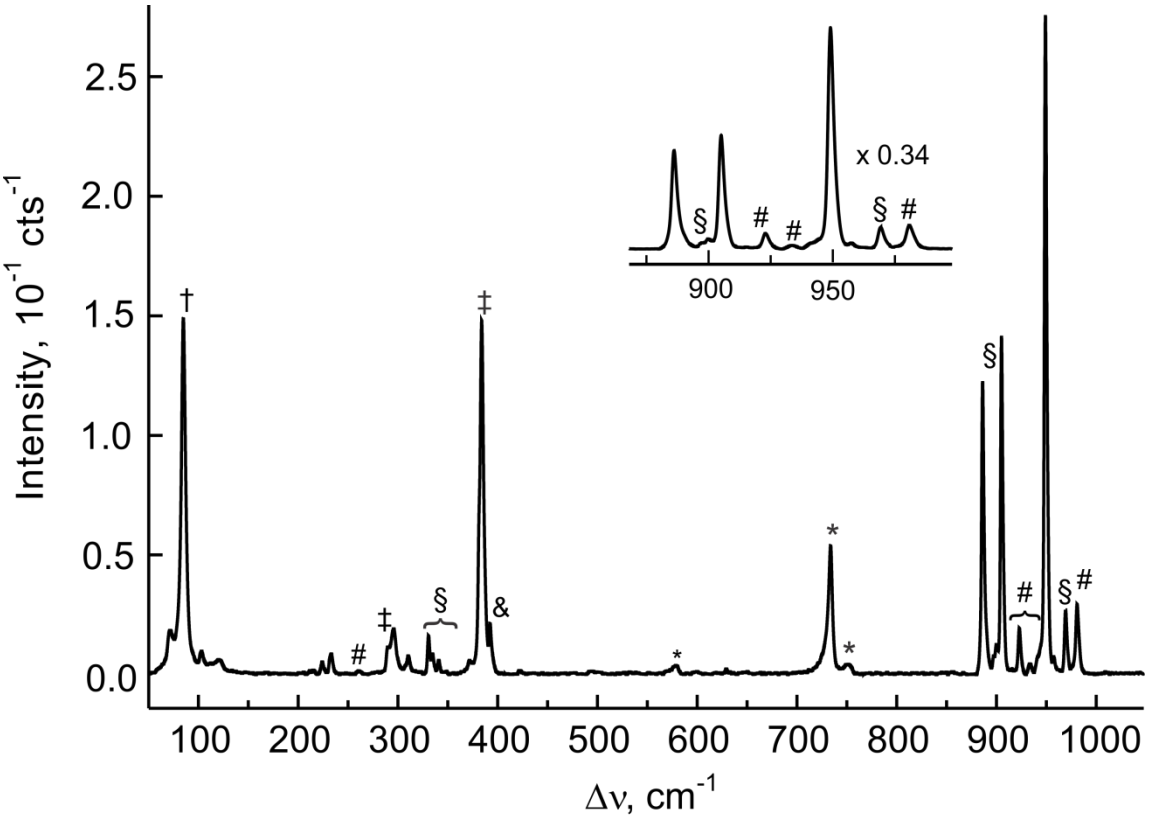

Figure B8. Raman spectrum of a solid mixture of crystalline $Cs_2[ReO_3F_3]$ recorded at –150 ^{o}C using 1064-nm excitation. Symbols denote an FEP sample tube line (*), instrumental artifact (†), overlap of a $Cs_2[ReO_3F_3]$ line with an FEP sample tube line (‡), a $Cs[ReO_4]$ line (§), a $Cs[ReO_3F_2]$ line (#), and overlap of a $Cs[ReO_3F_2]$ line with a $Cs_2[ReO_3F_3]$ line (&).

Table B2. Experimental Raman Frequencies and Intensities for $(\mu\text{-}F)_4\{[\mu\text{-}^{18}O(Re^{16/18}O_2F)_2](Re^{16/18}O_2F_2)_2\}$ in $(\mu\text{-}F)_4\{[\mu\text{-}^{16/18}O(Re^{16/18}O_2F)_2](Re^{16/18}O_2F_2)_2\}\cdot SO_2ClF$ and Calculated Raman and Infrared Frequencies, Intensities, and Assignments for $(\mu\text{-}F)_4\{[\mu\text{-}^{16/18}O(Re^{16/18}O_2F)_2](Re^{16/18}O_2F_2)_2\}$

B3LYP/aug-cc-pVT(-PP)

exptl[a,b]			calcd[a,c]			assgnts (C_s)[d]
^{16}O	^{18}O	Δν	^{16}O	^{18}O	Δν	
			1077.9(159)[9]	1020.2(143)[8]	−57.7	$[\nu(Re_1O_1) + \nu(Re_1O_2)] + [\nu(Re_3O_5) + \nu(Re_3O_6)]$
1024.0(100)	969.1(100)	−54.9	1075.1(14)[115]	1017.4(13)[101]	−57.7	$[\nu(Re_1O_1) + \nu(Re_1O_2)] - [\nu(Re_3O_5) + \nu(Re_3O_6)]$
			1072.1(11)[<1]	1014.1(10)[<1]	−58.0	$[\nu(Re_2O_3) + \nu(Re_2O_4)] - [\nu(Re_4O_7) + \nu(Re_4O_8)] + [\nu(Re_2O_9) - \nu(Re_4O_9)]_{small}$
1012.6(97)	958.8(94)	−53.8	1066.0(58)[145]	1008.7(50)[132]	−57.3	$[\nu(Re_2O_3) + \nu(Re_2O_4)] + [\nu(Re_4O_7) + \nu(Re_4O_8)]$
996.3(24)	945.8(30)	−50.5	1042.2(7)[328]	988.6(6)[301]	−53.6	$[\nu(Re_1O_1) - \nu(Re_1O_2)] + [\nu(Re_3O_6) - \nu(Re_3O_5)]$
			1041.5(44)[0]	988.1(39)[0]	−53.4	$[\nu(Re_1O_1) - \nu(Re_1O_2)] + [\nu(Re_3O_5) - \nu(Re_3O_6)]$
991.3(46)	940.5(44)	−50.8	1032.0(23)[330]	978.9(20)[307]	−53.1	$[\nu(Re_2O_3) - \nu(Re_2O_4)] + [\nu(Re_4O_8) - \nu(Re_4O_7)]$
988.7 sh	937.0 sh	−51.7	1028.5(4)[0]	975.3(3)[0]	−53.2	$[\nu(Re_2O_3) - \nu(Re_2O_4)] + [\nu(Re_4O_7) - \nu(Re_4O_8)]$
863.7(4)	819(4)[e]	−44.7	887.2(5)[813]	841.1(4)[709]	−46.1	$[\nu(Re_2O_9) - \nu(Re_4O_9)]$
700.8(2)	700.8(2)	0.0	704.0(7)[198]	704.0(7)[198]	−0.0	$[\nu(Re_1F_1) - \nu(Re_1F_2)] + [\nu(Re_3F_4) - \nu(Re_3F_5)]$
691.3(2)	691.7(3)	0.0	695.3(8)[133]	695.2(8)[134]	−0.1	$[\nu(Re_2F_3) + \nu(Re_4F_6)] - [\nu(Re_1F_1) + \nu(Re_1F_2)] + [\nu(Re_3F_4) + \nu(Re_3F_5)]$
			690.0(1)[166]	690.0(1)[165]	0.0	$[\nu(Re_1F_1) - \nu(Re_3F_4)]$
675.9 sh	675.9 sh	0.0	676.1(<1)[4]	676.0(<1)[4]	−0.1	$[\nu(Re_1F_2) - \nu(Re_3F_5)]$
668.5(9)	668.4(13)	−0.1	675.3(13)[54]	675.2(13)[54]	−0.1	$[\nu(Re_1F_2) + \nu(Re_3F_5)] + [\nu(Re_2F_3) + \nu(Re_4F_6)]$
			672.7(1)[303]	671.9(1)[327]	−0.8	$[\nu(Re_2F_3) - \nu(Re_4F_6)]$
			505.1(1)[191]	504.2(1)[197]	−0.9	$[\nu(Re_1F_{10}) + \nu(Re_1F_7)] - [\nu(Re_2F_7) + \nu(Re_2F_8)] + [\nu(Re_3F_8) + \nu(Re_3F_9)] - [\nu(Re_4F_9) + \nu(Re_4F_{10})]$
			467.2(<1)[341]	466.2(<1)[355]	−1.0	$[\nu(Re_1F_{10}) + \nu(Re_1F_7)] + [\nu(Re_2F_8) - \nu(Re_2F_7)] - [\nu(Re_3F_8) + \nu(Re_3F_9)] + [\nu(Re_4F_9) - \nu(Re_4F_{10})]$
			439.3(<1)[28]	437.2(<1)[25]	−2.1	$[\nu(Re_1F_{10}) - \nu(Re_1F_7)] + [\nu(Re_2F_7) + \nu(Re_2F_8)] + [\nu(Re_3F_9) - \nu(Re_3F_8)] - [\nu(Re_4F_9) + \nu(Re_4F_{10})]$
414.2(5)	397.5(5)	−16.7	421.1(2)[22]	402.2(2)[12]	−18.9	$[\nu(Re_2O_9) + \nu(Re_4O_9)] + [\delta(O_3Re_2O_4) + \delta(O_7Re_4O_8)]$
			415.3(1)[0]	412.9(1)[0]	−2.4	$[\nu(Re_1F_{10}) - \nu(Re_1F_7)] + [\nu(Re_2F_7) - \nu(Re_2F_8)] + [\nu(Re_3F_8) - \nu(Re_3F_9)] + [\nu(Re_4F_9) - \nu(Re_4F_{10})]$
405.4(9)	385.2(9)	−20.2	413.6(2)[<1]	393.4(2)[1]	−20.2	$\delta(O_1Re_1O_2) + \delta(O_3Re_2O_4) + \delta(O_5Re_3O_6) + \delta(O_7Re_4O_8)$
400.2(10)	380.1(10)	−20.1	411.0(1)[17]	391.5(1)[14]	−19.5	$\delta(O_1Re_1O_2) - \delta(O_5Re_3O_6)$
395.7(6)	376.6(7)	−19.1	407.6(1)[2]	386.7(1)[2]	−20.9	$\delta(O_3Re_2O_4) - \delta(O_7Re_4O_8)$
			407.1(6)[2]	386.4(5)[3]	−20.7	$[\delta(O_1Re_1O_2) + \delta(O_5Re_3O_6)] - [\delta(O_3Re_2O_4) + \delta(O_7Re_4O_8)] + [\nu(Re_2O_9) + \nu(Re_4O_9)]$
			402.3(<1)[7]	384.2(<1)[<1]	−18.1	$[\delta(O_3Re_2O_9) - \delta(O_4Re_2O_9)] + [\delta(O_8Re_4O_9) - \delta(O_7Re_2O_9)]$
347.9(4)	345.1(3)	−2.8	348.2(2)[7]	344.3(2)[16]	−3.9	$[\delta(F_2Re_1F_7F_{10}) + \delta(F_4Re_3F_8F_9)] - [\delta(F_1Re_1O_1O_2) + \delta(F_5Re_3O_5O_6)]_{small}$
			340.0(3)[1]	335.5(2)[<1]	−4.5	$[\rho_t(O_5Re_3O_6) - \rho_t(O_1Re_1O_2)] + [\rho_t(F_8Re_3F_9) - \rho_t(F_7Re_1F_{10})] + [\rho_t(F_4Re_3F_5) - \rho_t(F_1Re_1F_2)]$
329.1(2)	327.4 sh	−1.7	337.9(1)[8]	331.1(1)[4]	−6.8	$[\delta(O_1Re_1O_2F_1) - \delta(F_7Re_1F_{10})] + [\delta(O_5Re_3O_6F_4) - \delta(F_8Re_3F_9)] + \delta(O_3Re_2O_4F_3) + \delta(O_7Re_4O_8F_6)]$
			336.8(2)[5]	326.4(1)[4]	−10.4	$[\delta(O_1Re_1F_1) - \delta(O_2Re_1F_2)] + [\delta(O_5Re_3F_5) - \delta(O_6Re_3F_4)]$
			329.4(<1)[0]	323.5(<1)[0]	−5.9	$[\rho_t(O_1Re_1O_2) - \rho_t(F_7Re_1F_{10})] + [\rho_t(O_5Re_3O_6) - \rho_t(F_8Re_3F_9)] + [\rho_t(F_1Re_1F_2) - \rho_t(F_4Re_3F_5)]$
325.9 sh	317.0 sh	−8.5	321.4(3)[57]	312.7(3)[52]	−8.7	$[\rho_w(O_1Re_1O_2) + \rho_w(F_7Re_1F_{10})] + [\rho_w(O_5Re_3O_6) + \rho_w(F_8Re_3F_9) + [\delta(F_3Re_2O_9) + \delta(F_6Re_4O_9)]_{small}$
			320.3(<1)[90]	308.7(<1)[76]	−11.6	$\delta(F_3Re_2O_3O_4) - \delta(F_6Re_4O_7O_8)$
312.6(11)[e]	307.5(11)	−5.1	312.4(2)[0]	306.6(2)[0]	−5.8	$[\delta(F_3Re_2O_3) + \rho_t(O_3Re_2O_4)] + [\delta(F_6Re_4O_7) + \rho_t(O_1Re_4O_8)] + [\delta(O_2Re_1F_2) - \delta(O_1Re_1F_2)]_{small}$

Table B2. (continued…)

300.0 sh	309.0 sh	−9.0	295.4(<1)[4]	290.2(<1)[47]	−5.2	$[\delta(F_2Re_1F_7F_{10}) - \delta(F_4Re_3F_8F_9)] + [\delta(O_3Re_2O_9) - \delta(O_4Re_2O_9)] + [\delta(O_8Re_4O_9) - \delta(O_7Re_2O_9)]$
294.4(4)	290.1(5)	−4.3	296.3(2)[60]	291.8(2)[66]	−4.5	$[\delta(F_2Re_1O_1) - \delta(F_2Re_1O_2)] + [\delta(F_5Re_3O_6) - \delta(F_5Re_3O_5)] - [\delta(F_3Re_2F_7F_8) + \delta(F_6Re_4F_9F_{10})]$
287.9(5)	283.5(7)	−4.4	292.5(1)[117]	287.4(1)[73]	−5.1	$[\rho_t(O_7Re_4O_8) + \rho_t(O_3Re_2O_4)] + [\delta(F_3Re_2O_9) - \delta(F_6Re_4O_9)] + [\delta(F_7Re_1F_{10}) - \delta(F_9Re_3F_8)]$
272.6(7)	267.1(11)	−5.5	267.9(2)[16]	263.6(2)[14]	−4.3	$[\delta(F_8Re_3F_9) + \delta(F_7Re_1F_{10})] + [\delta(F_6Re_4O_9) + \delta(F_3Re_2O_9)]$
262.6(3)	260.2(6)	−2.4	263.1(3)[0]	256.6(2)[0]	−6.5	$[\rho_w(F_2Re_1F_1) + \rho_t(O_2Re_1O_1) + \rho_t(F_7Re_1F_{10})] + [\rho_w(F_4Re_3F_5) + \rho_t(O_5Re_3O_6) + \rho_t(F_8Re_3F_9)] + [\rho_t(O_7Re_4O_8) + \rho_t(O_3Re_2O_4)]$
256.7 sh	253.6 sh	−3.1	262.4(<1)[59]	260.3(1)[56]	−2.1	$[\delta(F_1Re_1F_7F_{10}) - \delta(F_4Re_3F_8F_9)]$
245.5(1)	239.5(2)	−4.0	248.3(1)[2]	244.3(1)[1]	−4.0	$[\rho_t(O_2Re_1O_1) + \rho_t(F_7Re_1F_{10})] + [\rho_t(O_5Re_3O_6) + \rho_t(F_8Re_3F_9)]$
			247.2(<1)[8]	246.4(1)[9]	−0.8	$[\delta(F_1Re_1F_2) + \delta(F_4Re_3F_5)]$
235.0(1)	232.4(2)	−2.6	236.9(3)[0]	230.2(3)[0]	−6.7	$[\rho_t(O_8Re_4O_7) - \rho_t(F_9Re_4F_{10})] - [\rho_t(O_3Re_2O_4) - \rho_t(F_8Re_2F_7)]$
			232.7(<1)[39]	230.4(<1)[37]	−2.3	$[\delta(F_1Re_1F_2) - \delta(F_4Re_3F_5)]$
229.4(1)	229.0 sh	−0.4	223.3(<1)[2]	222.9(<1)[2]	−0.4	$[\delta(F_8Re_2F_7) - \delta(F_9Re_4F_{10})] + [\rho_w(F_1Re_1F_2) + \rho_w(F_4Re_3F_5)]$
202.8(15)	199.8(20)	−3.0	196.7(4)[<1]	193.7(4)[<1]	−3.0	$[(O_3O_4Re_2F_3)_{trans} + (O_3O_4Re_4F_3)_{trans}]$
182.0(<1)	180.4(<1)	−1.6	187.6(<1)[0]	185.9(<1)[0]	−1.7	$[\rho_w(F_1Re_1F_2) + \rho_w(F_4Re_3F_5)] + [\rho_t(F_8Re_2F_7) + \rho_t(F_9Re_4F_{10})]$
160.0 (1)	157.8(2)	−2.2	153.7(<1)[1]	151.9(<1)[1]	−1.8	$[\delta(F_3Re_2O_9) + \delta(F_6Re_4O_9)] + \rho_t(F_1Re_1F_2) + \rho_t(F_4Re_3F_5)$
			150.2(<1)[0]	148.1(<1)[0]	−2.1	$[\rho_t(O_3Re_2O_4) + \rho_t(F_7F_8Re_2F_3)] + [\rho_t(O_8Re_4O_7) + \rho_t(F_6F_9Re_4F_{10})]$
			148.9(<1)[6]	143.6(<1)[5]	−5.3	$[\rho_t(O_4Re_2O_3) + \rho_t(O_7Re_4O_8)] + [\rho_t(F_1Re_1F_2) + \rho_t(F_4Re_3F_5)]_{small}$
143.5(<1)	139.7(1)	−3.8	141.5(<1)[1]	139.8(<1)[1]	−1.7	$[\rho_t(O_3O_4Re_1F_3) - \rho_t(O_7O_8Re_3F_6)]$
128.6(1)	127.6(2)	−1.0	133.3(<1)[<1]	130.9(<1)[<1]	−2.4	$[\rho_t(O_3O_4Re_1F_3) + \rho_t(O_7O_8Re_3F_6)]$
119.2(1)	119.1 sh	0.0	121.6(<1)[4]	120.7(<1)[4]	−0.9	$\rho_w(O_9Re_2F_3) + \rho_w(O_9Re_4F_6) + [\rho_w(Re_1F_1) + \rho_w(Re_3F_4)]_{small}$
			119.1(<1)[0]	115.2(<1)[0]	−3.9	$[\rho_t(O_3O_4Re_2F_3) + \rho_t(O_7O_8Re_4F_6)] + [\rho_t(O_1O_2Re_1F_2) + \rho_t(O_5O_6Re_3F_5)]_{small}$
			117.1(<1)[<1]	115.7(<1)[<1]	−1.4	$[\rho_t(O_1O_2Re_1F_1) - \rho_t(O_5O_6Re_3F_4)] + \rho_t(O_3O_4Re_2F_3) - \rho_t(O_7O_8Re_4F_6)]$
			108.8(<1)[<1]	104.2(<1)[<1]	−4.6	$[\rho_t(O_1O_2Re_1F_2) + \rho_t(O_5O_6Re_3F_5)]$
99.2(2)	99.2(2)	0.0	97.5(<1)[1]	94.1(0)[<1]	−3.4	lattice modes
			95.7(<1)[0]	92.2(<1)[0]	−3.5	
			87.4(<1)[0]	85.5(<1)[0]	−1.9	
			83.6(<1)[<1]	83.1(<1)[<1]	−0.5	
			64.7(<1)[<1]	63.4(<1)[<1]	−1.3	
			30.3(<1)[<1]	29.7(<1)[<1]	−0.7	
			23.7(<1)[<1]	23.4(<1)[<1]	−0.3	
			22.3(0)[0]	21.8(0)[0]	−0.5	

PBE1PBE/aug-cc-pVTZ(-PP)

expt[a,b]			calcd[a,c]			assgnt (C_{2v})[d]
^{16}O	^{18}O	Δν	^{16}O	^{18}O	Δν	
1024.0(100)	969.1(100)	−54.9	1111.2(156)[7]	1051.6(141)[5]	−59.6	$[\nu(Re_1O_1) + \nu(Re_1O_2)] + [\nu(Re_3O_5) + \nu(Re_3O_6)]$
			1108.1(12)[126]	1048.6(11)[110]	−59.5	$[\nu(Re_1O_1) + \nu(Re_1O_2)] - [\nu(Re_3O_5) + \nu(Re_3O_6)]$
			1105.5(10)[<1]	1045.8(9)[<1]	−59.7	$[\nu(Re_2O_3) + \nu(Re_2O_4)] - [\nu(Re_4O_7) + \nu(Re_4O_8)] + [\nu(Re_2O_9) - \nu(Re_4O_9)]_{small}$
1012.6(97)	958.8(94)	−53.8	1099.1(50)[151]	1040.1(43)[137]	−59.0	$[\nu(Re_2O_3) + \nu(Re_2O_4)] + [\nu(Re_4O_7) + \nu(Re_4O_8)]$
996.3(24)	945.8(30)	−50.5	1071.9(6)[354]	1016.8(5)[325]	−55.1	$[\nu(Re_1O_1) - \nu(Re_1O_2)] + [\nu(Re_3O_6) - \nu(Re_3O_5)]$
			1071.3(42)[0]	1016.3(38)[0]	−55.0	$[\nu(Re_1O_1) - \nu(Re_1O_2)] + [\nu(Re_3O_5) - \nu(Re_3O_6)]$
991.3(46)	940.5(44)	−50.8	1062.1(22)[355]	1007.5(19)[329]	−54.6	$[\nu(Re_2O_3) - \nu(Re_2O_4)] + [\nu(Re_4O_8) - \nu(Re_4O_7)]$

Table B2. (continued…)

988.7 sh	937.0 sh	−51.7	1057.8(3)[0]	1003.2(3)[0]	−54.6	$[\nu(Re_2O_3) - \nu(Re_2O_4)] + [\nu(Re_4O_7) - \nu(Re_4O_8)]$
863.7(4)	819(4)[e]	−44.7	911.0(5)[836]	863.8(4)[728]	−47.2	$[\nu(Re_2O_9) - \nu(Re_4O_9)]$
700.8(2)	700.8(2)	0.0	721.0(7)[227]	720.9(7)[227]	−0.1	$[\nu(Re_1F_1) - \nu(Re_1F_2)] + [\nu(Re_3F_4) - \nu(Re_3F_5)]$
691.3(2)	691.7(3)	0.0	714.1(7)[123]	714.0(7)[123]	−0.1	$[\nu(Re_2F_3) + \nu(Re_4F_6)] - [\nu(Re_1F_1) + \nu(Re_1F_2)] + [\nu(Re_3F_4) + \nu(Re_3F_5)]$
			708.3(1)[166]	708.2(1)[166]	−0.1	$[\nu(Re_1F_1) - \nu(Re_3F_4)]$
675.9 sh	675.9 sh	0.0	694.0(<1)[3]	693.9(<1)[3]	−0.1	$[\nu(Re_1F_2) - \nu(Re_3F_5)]$
668.5(9)	668.4(13)	−0.1	693.3(11)[57]	693.2(11)[57]	−0.1	$[\nu(Re_1F_2) + \nu(Re_3F_5)] + [\nu(Re_2F_3) + \nu(Re_4F_6)]$
			690.3(1)[316]	689.4(1)[341]	−0.9	$[\nu(Re_2F_3) - \nu(Re_4F_6)]$
			519.5(1)[190]	518.7(1)[195]	−0.8	$[\nu(Re_1F_{10}) + \nu(Re_1F_7)] - [\nu(Re_2F_7) + \nu(Re_2F_8)] + [\nu(Re_3F_8) + \nu(Re_3F_9)] - [\nu(Re_4F_9) + \nu(Re_4F_{10})]$
			480.9(<1)[366]	480.0(<1)[377]	−0.9	$[\nu(Re_1F_{10}) + \nu(Re_1F_7)] + [\nu(Re_2F_8) - \nu(Re_2F_7)] - [\nu(Re_3F_8) + \nu(Re_3F_9)] + [\nu(Re_4F_9) - \nu(Re_4F_{10})]$
			454.5(<1)[32]	452.6(<1)[29]	−1.9	$[\nu(Re_1F_{10}) - \nu(Re_1F_7)] + [\nu(Re_2F_7) + \nu(Re_2F_8)] + [\nu(Re_3F_9) - \nu(Re_3F_8)] - [\nu(Re_4F_9) + \nu(Re_4F_{10})]$
			428.5(2)[17]	409.6(1)[8]	−18.9	$[\nu(Re_2O_9) + \nu(Re_4O_9)] + [\delta(O_3Re_2O_4) + \delta(O_7Re_4O_8)]$
414.2(5)	397.5(5)	−16.7	427.8(1)[0]	425.4(1)[0]	−2.4	$[\nu(Re_1F_{10}) - \nu(Re_1F_7)] + [\nu(Re_2F_7) - \nu(Re_2F_8)] + [\nu(Re_3F_8) - \nu(Re_3F_9)] + [\nu(Re_4F_9) - \nu(Re_4F_{10})]$
			421.7(2)[<1]	401.0(2)[2]	−20.7	$\delta(O_1Re_1O_2) + \delta(O_3Re_2O_4) + \delta(O_5Re_3O_6) + \delta(O_7Re_4O_8)$
405.4(9)	385.2(9)	−20.2	419.1(1)[14]	399.3(1)[11]	−19.8	$\delta(O_1Re_1O_2) - \delta(O_5Re_3O_6)$
400.2(10)	380.1(10)	−20.1	415.4(1)[1]	394.0(1)[1]	−21.4	$\delta(O_3Re_2O_4) - \delta(O_7Re_4O_8)$
395.7(6)	376.6(7)	−19.1	414.6(6)[1]	393.6(5)[2]	−21.0	$[\delta(O_1Re_1O_2) + \delta(O_5Re_3O_6)] - [\delta(O_3Re_2O_4) + \delta(O_7Re_4O_8)] + [\nu(Re_2O_9) + \nu(Re_4O_9)]$
			408.8(<1)[5]	390.7(<1)[<1]	−18.1	$[\delta(O_3Re_2O_9) - \delta(O_4Re_2O_9)] + [\delta(O_8Re_4O_9) - \delta(O_7Re_2O_9)]$
347.9(4)	345.1(3)	−2.8	357.0(2)[11]	353.5(1)[19]	−3.5	$[\delta(F_2Re_1F_7F_{10}) + \delta(F_4Re_3F_8F_9)] - [\delta(F_1Re_1O_1O_2) + \delta(F_5Re_3O_5O_6)]_{small}$
			348.8(3)[<1]	344.7(2)[<1]	−4.1	$[\rho_t(O_5Re_3O_6) - \rho_t(O_1Re_1O_2)] + [\rho_t(F_8Re_3F_9) - \rho_t(F_7Re_1F_{10})] + [\rho_t(F_4Re_3F_5) - \rho_t(F_1Re_1F_2)]$
329.1(2)	327.4 sh	−1.7	342.6(1)[6]	336.3(1)[3]	−6.3	$[\delta(O_1Re_1O_2F_1) - \delta(F_7Re_1F_{10})] + [\delta(O_5Re_3O_7F_4) - \delta(F_8Re_3F_9)] + \delta(O_3Re_2O_4F_3) + \delta(O_7Re_4O_8F_6)]$
			341.9(2)[5]	331.7(2)[4]	−10.2	$[\delta(O_1Re_1F_1) - \delta(O_2Re_1F_2)] + [\delta(O_5Re_3F_5) - \delta(O_6Re_3F_4)]$
			337.0(<1)[0]	331.6(<1)[0]	−5.5	$[\rho_t(O_1Re_1O_2) - \rho_t(F_7Re_1F_{10})] + [\rho_t(O_5Re_3O_6) - \rho_t(F_8Re_3F_9)] + [\rho_t(F_1Re_1F_2) - \rho_t(F_4Re_3F_5)]$
325.9 sh	317.0 sh	−8.5	326.5(3)[56]	316.9(3)[51]	−9.6	$[\rho_w(O_1Re_1O_2) + \rho_w(F_7Re_1F_{10})] + [\rho_w(O_5Re_3O_6) + \rho_w(F_8Re_3F_9) + [\delta(F_3Re_2O_9) + \delta(F_6Re_4O_9)]_{small}$
			324.2(<1)[85]	312.7(<1)[68]	−11.5	$\delta(F_3Re_2O_3O_4) - \delta(F_6Re_4O_7O_8)$
312.6(11)[e]	307.5(11)	−5.1	317.3(2)[0]	311.3(1)[0]	−6.0	$[\delta(F_3Re_2O_3) + \rho_t(O_3Re_2O_4)] + [\delta(F_6Re_4O_7) + \rho_t(O_1Re_4O_8)] + [\delta(O_2Re_1F_2) - \delta(O_1Re_1F_2)]_{small}$
300.0 sh	309.0 sh	−9.0	302.4(<1)[14]	296.6(<1)[42]	−5.8	$[\delta(F_2Re_1F_7F_{10}) - \delta(F_4Re_3F_8F_9)] + [\delta(O_3Re_2O_9) - \delta(O_4Re_2O_9)] + [\delta(O_8Re_4O_9) - \delta(O_7Re_2O_9)]$
294.4(4)	290.1(5)	−4.3	297.2(1)[102]	291.8(1)[72]	−5.1	$[\delta(F_2Re_1O_1) - \delta(F_2Re_1O_2)] + [\delta(F_5Re_3O_6) - \delta(F_5Re_3O_5)] - [\delta(F_3Re_2F_7F_8) + \delta(F_6Re_4F_9F_{10})]$
287.9(5)	283.5(7)	−4.4	301.2(2)[66]	296.4(2)[74]	−4.8	$[\rho_t(O_7Re_4O_8) + \rho_t(O_3Re_2O_4)] + [\delta(F_3Re_2O_9) - \delta(F_6Re_4O_9)] + [\delta(F_7Re_1F_{10}) - \delta(F_9Re_3F_8)]$
272.6(7)	267.1(11)	−5.5	273.4(2)[14]	268.9(2)[13]	−5.4	$[\delta(F_8Re_3F_9) + \delta(F_7Re_1F_{10})] + [\delta(F_6Re_4O_9) + \delta(F_3Re_2O_9)]$
262.6(3)	260.2(6)	−2.4	267.5(2)[0]	261.2(2)[0]	−6.3	$\{[\rho_w(F_2Re_1F_1) + \rho_t(O_2Re_1O_1) + \rho_t(F_7Re_1F_{10})] + [\rho_w(F_4Re_3F_5) + \rho_t(O_5Re_3O_6) + \rho_t(F_8Re_3F_9)] + [\rho_t(O_7Re_4O_8) + \rho_t(O_3Re_2O_4)]$
256.7 sh	253.6 sh	−3.1	266.9(1)[65]	264.8(1)[63]	−2.1	$[\delta(F_1Re_1F_7F_{10}) - \delta(F_4Re_3F_8F_9)]$
245.5(1)	239.5(2)	−4.0	254.8(1)[2]	250.5(1)[1]	−4.3	$[\rho_t(O_2Re_1O_1) + \rho_t(F_7Re_1F_{10})] + [\rho_t(O_5Re_3O_6) + \rho_t(F_8Re_3F_9)]$

Table B2. (continued…)

			252.6(<1)[8]	251.8(1)[9]	−0.8	$[\delta(F_1Re_1F_2) + \delta(F_4Re_3F_5)]$
235.0(1)	232.4(2)	−2.6	243.0(3)[0]	235.8(3)[0]	−7.2	$[\rho_t(O_8Re_4O_7) - \rho_t(F_9Re_4F_{10})] - [\rho_t(O_3Re_2O_4) - \rho_t(F_8Re_2F_7)]$
			237.5(<1)[34]	235.0(<1)[32]	−2.5	$[\delta(F_1Re_1F_2) - \delta(F_4Re_3F_5)]$
			228.4(<1)[2]	228.0(<1)[2]	−0.4	$[\delta(F_8Re_2F_7) - \delta(F_9Re_4F_{10})] + [\rho_w(F_1Re_1F_2) + \rho_w(F_4Re_3F_5)]$
202.8(15)	199.8(20)	−3.0	201.5(4)[<1]	198.3(4)[<1]	−3.2	$[(O_3O_4Re_2F_3)_{trans} + (O_3O_4Re_4F_3)_{trans}]$
182.0(<1)	180.4(<1)	−1.6	191.4(<1)[0]	189.5(<1)[0]	−1.9	$[\rho_w(F_1Re_1F_2) + \rho_w(F_4Re_3F_5)] + [\rho_t(F_8Re_2F_7) + \rho_t(F_9Re_4F_{10})]$
160.0 (1)	157.8(2)	−2.2	157.2(<1)[1]	155.5(<1)[1]	−1.6	$[\delta(F_3Re_2O_9) + \delta(F_6Re_4O_9)] + \rho_t(F_1Re_1F_2) + \rho_t(F_4Re_3F_5)$
			153.2(<1)[0]	151.1(<1)[0]	−2.1	$[\rho_t(O_3Re_2O_4) + \rho_t(F_7F_8Re_2F_3)] + [\rho_t(O_8Re_4O_7) + \rho_t(F_6F_9Re_4F_{10})]$
			150.9(<1)[5]	145.7(<1)[4]	−5.2	$[\rho_t(O_4Re_2O_3) + \rho_t(O_7Re_4O_8)] + [\rho_t(F_1Re_1F_2) + \rho_t(F_4Re_3F_5)]_{small}$
143.5(<1)	139.7(1)	−3.8	146.0(<1)[1]	144.4(<1)[1]	−1.6	$[\rho_t(O_3O_4Re_1F_3) - \rho_t(O_7O_8Re_3F_6)]$
128.6(1)	127.6(2)	−1.0	137.1(<1)[<1]	134.4(<1)[<1]	−2.7	$[\rho_t(O_3O_4Re_1F_3) + \rho_t(O_7O_8Re_3F_6)]$
			125.8(<1)[5]	124.7(<1)[5]	−1.1	$\rho_w(O_9Re_2F_3) + \rho_w(O_9Re_4F_6) + [\rho_w(Re_1F_1) + \rho_w(Re_3F_4)]_{small}$
119.2(1)	119.1 sh	0.0	121.1(<1)[0]	117.2(<1)[0]	−3.9	$[\rho_t(O_3O_4Re_2F_3) + \rho_t(O_7O_8Re_4F_6)] + [\rho_t(O_1O_2Re_1F_2) + \rho_t(O_5O_6Re_3F_5)]_{small}$
			120.1(<1)[<1]	118.6(<1)[<1]	−1.5	$[\rho_t(O_1O_2Re_1F_1) - \rho_t(O_5O_6Re_3F_4)] + \rho_t(O_3O_4Re_2F_3) - \rho_t(O_7O_8Re_4F_6)]$
			111.1(0)[<1]	106.4(<1)[<1]	−4.7	$[\rho_t(O_1O_2Re_1F_2) + \rho_t(O_5O_6Re_3F_5)]$
			99.1(<1)[1]	95.6(0)[<1]	−3.5	lattice modes
			98.1(<1)[0]	94.7(<1)[0]	−3.4	
			90.0(<1)[0]	87.9(<1)[0]	−1.9	
			84.7(<1)[<1]	84.1(<1)[<1]	−0.6	
99.2(2)			66.8(<1)[<1]	65.5(<1)[<1]	−1.3	
			30.9(<1)[<1]	30.3(<1)[<1]	−0.6	
			20.7(<1)[<1]	20.4(<1)[<1]	−0.3	
			22.9(0)[0]	22.5(0)[0]	−0.4	

[a] Frequencies are given in cm^{-1}. $\Delta\nu^{16/18} = \nu(^{18}O) - \nu(^{16}O)$. [b] Values in parentheses denote relative Raman intensities. Raman spectra were recorded in FEP sample tubes at –130 °C using 1064-nm excitation. The abbreviation denotes shoulder (sh). The SO_2ClF modes were observed at 424(3), 431(4), 474(<1), 502(1), 626(1), 824(1), 1218(4), and 1444(1) cm^{-1}. [c] Values in parentheses denote calculated Raman intensities ($Å^4\ u^{-1}$). Values in square brackets denote calculated infrared intensities (km mol^{-1}). [d] The atom numbering scheme corresponds to that used in Figure 4.3b. The abbreviations denote stretch (ν), bend (δ), translation (trans), wag (ρ_w), twist (ρ_t), and rock (ρ_r). [e] Overlap with SO_2ClF

Table B3. Calculated Vibrational Frequencies and Infrared and Raman Intensities for *mer*–$[ReO_3F_3]^{2-}$

calcd[a]		assgnt[b,c]
B3LYP	PBE1PBE	
928(60)[109]	958(59)[106]	$\nu(ReO_1) + \nu(ReO_3) + \nu(ReO_2)$
872(55)[187]	900(49)[206]	$\nu(ReO_1) + \nu(ReO_2) - \nu(ReO_3)$
835(6)[555]	860(5)[579]	$\nu(ReO_1) - \nu(ReO_2)$
506(5)[132]	522(4)[132]	$\nu(ReF_1)$
462(4)[126]	475(3)[133]	$\nu(ReF_2)$
402(5)[2]	411(4)[1]	$\delta(O_3ReO_1) + \delta(F_3ReO_2)$
394(<1)[52]	408(<1)[59]	$\nu(ReF_3) + \delta(O_1ReO_2) - \delta(F_1ReO_3)_{small}$
364(4)[<1]	374(4)[<1]	$\delta(O_1ReF_2) + \delta(O_3ReO_2)$
337(4)[30]	348(3)[24]	$\delta(O_2ReO_1) + \delta(O_3ReF_1) - \delta(O_3ReF_2)$
327(<1)[9]	334(<1)[9]	$\delta(F_3F_2ReF_1O_3)_{umb} + \rho_r(O_1ReO_2)_{small}$
302(8)[100]	311(6)[93]	$\nu(ReF_3) + \delta(F_2ReF_1) + \delta(O_2ReO_1) - \delta(O_3ReF_1)$
282(2)[91]	291(2)[96]	$\delta(F_1ReF_3) + \delta(O_2ReO_1O_3)$
202(1)[1]	201(1)[1]	$\rho_t(O_3ReF_2) + \rho_t(F_1ReF_3)$
191(2)[7]	200(2)[9]	$\delta(F_3ReF_1) - \delta(O_3ReF_2) + \rho_w(O_2ReO_1)$
69(3)[2]	73(3)[2]	$\delta(F_2ReF_3) - \delta(O_2ReO_1)$

[a] Values in parentheses denote calculated Raman intensities ($Å^4\ \mu^{-1}$). Values in square brackets denote calculated infrared intensities (km mol^{-1}). The aug-cc-pVTZ(-PP) basis set was used. [b] The abbreviations denote stretch (ν), bend (δ), wag (ρ_w), rock (ρ_r), twist (ρ_t), umbrella (umb). [c] For the atom labeling scheme, see Figure B9b.

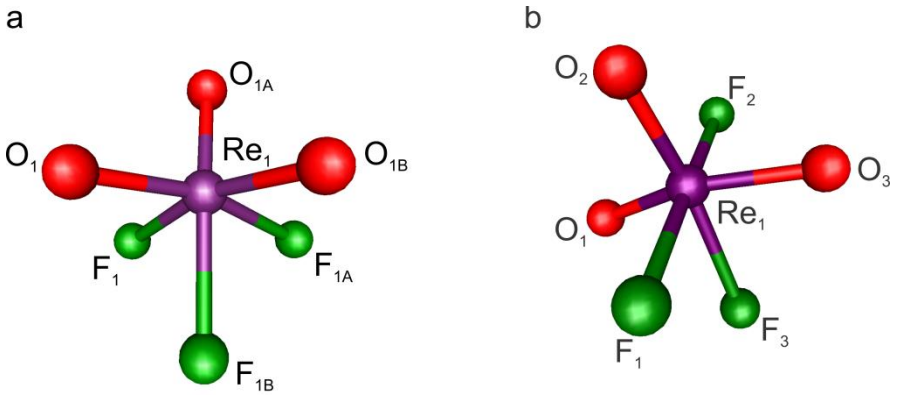

Figure B9. Calculated Structures of the (a) *fac*-$[ReO_3F_3]^{2-}$ (C_{3v}) and (b) *mer*-$[ReO_3F_3]^{2-}$ (C_s) anions (B3LYP/aug-cc-pVTZ(-PP)).

Table B4. Calculated Vibrational Frequencies and Infrared and Raman Intensities for $[ReO_3F_2]^-$ Monomer (C_s)

$[ReO_3F_2]^-$ (C_s)		
calcd[a]		assgnt[b]
B3LYP	PBE1PBE	
1004(54)[54]	1035(52)[56]	$\nu(ReO_2) + \nu(ReO_3) + \nu(ReO_1)$
949(13)[262]	975(12)[277]	$\nu(ReO_2) - \nu(ReO_3)$
938(19)[274]	964(18)[289]	$\nu(ReO_2) + \nu(ReO_3) - \nu(ReO_1)$
577(3)[159]	594(3)[164]	$\nu(ReF_1) + \nu(ReF_2)$
495(2)[70]	511(2)[73]	$\nu(ReF_1) - \nu(ReF_2)$
406(3)[4]	414(3)[3]	$\delta(F_2ReF_1) + \delta(O_3O_2ReO_1)$
392(5)[3]	399(4)[3]	$\delta(O_2ReO_1) - \delta(O_3ReO_1)$
350(<1)[22]	358(<1)[22]	$\delta(F_1ReF_1) + \rho_w(O_2ReO_3)$
342(2)[14]	349(2)[12]	$\delta(O_3ReO_2) + \delta(O_1ReF_1)_{small}$
282(1)[14]	286(1)[14]	$\rho_t(O_3ReO_2) + \rho_w(F_1F_2ReO_1)$
249(2)[26]	254(2)[27]	$\delta(O_1ReF_2) + \rho_w(O_2ReO_3)$
68(1)[<1]	69(1)[<1]	$\rho_t(F_1ReF_2) + \rho_r(O_1ReO_2O_3)$

[a] Values in parentheses denote calculated Raman intensities ($Å^4$ μ^{-1}). Values in square brackets denote calculated infrared intensities (km mol^{-1}). The aug-cc-pVTZ(-PP) basis set was used. [b] The abbreviations denote stretch (ν), bend (δ), wag (ρ_w), rock (ρ_r), twist (ρ_t). For the atom labeling scheme, see Figure B10.

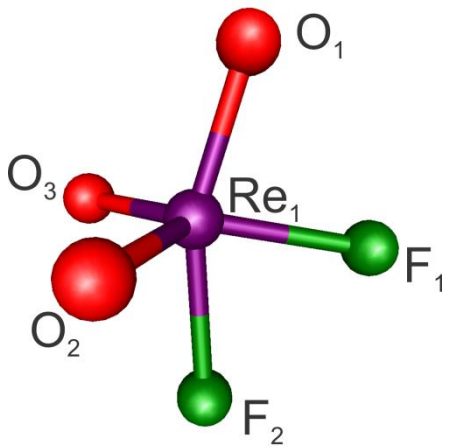

Figure B10. Calculated Structure of $[ReO_3F_2]^-$ Monomer (C_s) (B3LYP/aug-cc-pVTZ(-PP)).

Table B5. Correlation Diagram for the Vibrational Modes of the *fac*-$[ReO_3F_3]^{2-}$ Anion[a] in $K[H_3O][ReO_3F_3]$

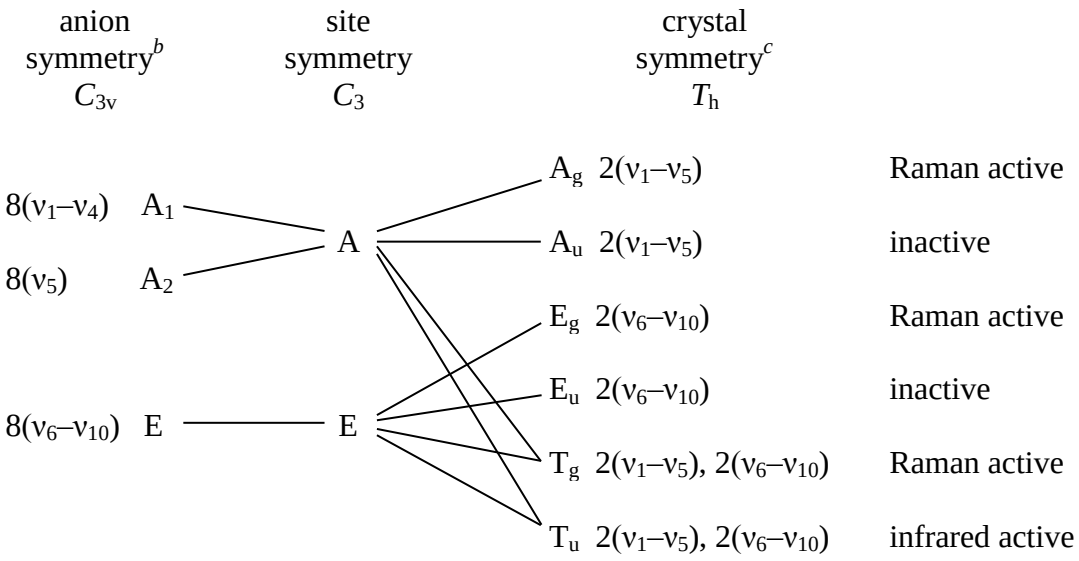

[a] The irreducible representations are $\Gamma = 4A_1 + A_2 + 5E$ for the *fac*-$[ReO_3F_3]^{2-}$ anion. [b] The anion symmetry (C_{3v}) is the symmetry observed in the crystallographic unit cell and for the optimized geometry in the gas phase.[c] The crystallographic space group is $Pa\bar{3}$ with $Z = 8$.

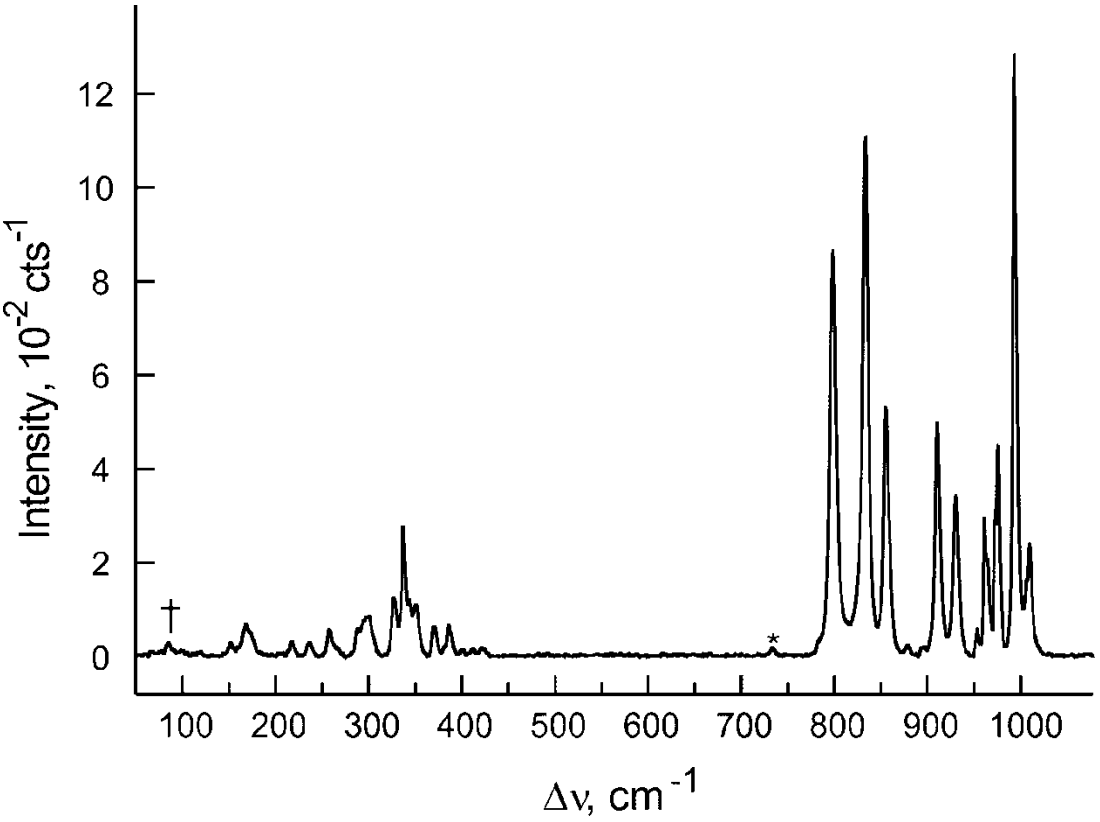

Figure B11. Raman spectrum of solid Re_2O_7 recorded at –150 ^{o}C using 1064-nm excitation. Symbols denote an FEP sample tube line (*) and instrumental artifact (†). (1009(18), 1007 sh, 993(100), 976(35), 973(24), 965 sh, 961(23), 954(4), 930(27), 910(39), 895(1), 879(2), 855(41), 833(86), 798(67), 782 sh, 421(1), 412(1), 401(1), 386(5), 370(5), 351(8), 344(9), 336(21), 329(10), 300(6), 288(6), 266 sh, 258(4), 236(2), 217(2), 173 sh, 168(5), 152(2) cm^{-1}).

Table B6 Calculated [a] Bond Lengths and Bond Angles for $[ReO_3F_2]^-$ Monomer

	$[ReO_3F_2]^-$ (C_s)[b]	
	B3LYP	PBE1PBE
Bond Length (Å)		
Re_1-O_1	1.721	1.709
Re_1-O_2	1.712	1.699
Re_1-O_3	1.712	1.699
Re_1-F_1	1.938	1.922
Re_1-F_2	1.975	1.959
Re_1-F_3		
Bond Angle (deg)		
$O_1-Re_1-O_2$	101.3	101.3
$O_1-Re_1-O_3$	101.3	101.3
$O_2-Re_1-O_3$	109.8	109.7
$O_1-Re_1-F_1$	84.7	84.6
$O_2-Re_1-F_1$	123.8	123.9
$O_3-Re_1-F_1$	123.8	123.9
$O_1-Re_1-F_2$	159.3	159.2
$O_2-Re_1-F_2$	90.5	90.5
$O_3-Re_1-F_2$	90.5	90.5
$O_1-Re_1-F_3$		
$O_2-Re_1-F_3$		
$O_3-Re_1-F_3$		
$F_1-Re_1-F_2$	74.6	74.5
$F_1-Re_1-F_3$		
$F_3-Re_1-F_2$		

[a] The aug-cc-pVTZ(-PP) basis set was used. [b] For the atom labeling scheme, see Figure B10.

Table B7. Calculated [a] Bond Lengths and Bond Angles for *fac*- and *mer*-$[ReO_3F_3]^{2-}$

fac-$[ReO_3F_3]^{2-}$ (C_{3v})[b]			*mer*-$[ReO_3F_3]^{2-}$ (C_s)[c]		
	B3LYP	PBE1PBE		B3LYP	PBE1PBE
Bond Length (Å)					
$Re_1–O_1$	1.735	1.722	$Re_1–O_1$	1.763	1.749
			$Re_1–O_2$	1.763	1.749
			$Re_1–O_3$	1.731	1.718
$Re_1–F_1$	2.035	2.017	$Re_1–F_1$	1.962	1.946
			$Re_1–F_2$	2.002	1.987
			$Re_1–F_3$	2.089	2.068
Bond Angle (deg)					
$O_1–Re_1–O_{1A}$	100.9	101.0	$O_1–Re_1–O_2$	152.6	151.4
			$O_1–Re_1–O_3$	102.0	102.4
			$O_2–Re_1–O_3$	102.0	102.4
$O_1–Re_1–F_1$	89.0	89.0	$O_1–Re_1–F_1$	97.2	97.8
			$O_2–Re_1–F_1$	97.2	97.8
			$O_3–Re_1–F_1$	87.0	86.4
$O_1–Re_1–F_{1A}$	164.2	164.0	$O_1–Re_1–F_2$	82.7	82.2
			$O_2–Re_1–F_2$	82.7	82.2
			$O_3–Re_1–F_2$	93.1	93.3
$O_1–Re_1–F_{1B}$	89.0	89.0	$O_1–Re_1–F_3$	80.0	80.0
			$O_2–Re_1–F_3$	80.0	80.0
			$O_3–Re_1–F_3$	165.6	164.3
$O_1–Re_1–F_{1A}$	78.8	78.8	$F_1–Re_1–F_2$	179.4	179.8
			$F_1–Re_1–F_3$	78.7	77.9
			$F_3–Re_1–F_2$	100.8	102.3

[a] The aug-cc-pVTZ(-PP) basis set was used. [b] For the atom labeling scheme, see Figure B9a. [c] For the atom labeling scheme, see Figure B9b.

Table B8. NBO Natural Charges and Wiberg Valencies and Bond Indices for the Hypothetical $[(\mu\text{-}F)_4(ReO_3F)_4]^{4-}$ Anion (C_{4v})[a]

	B3LYP		PBE1PBE		Bond	Bond Index	
Atom	Charge	Valence	Charge	Valence		B3LYP	PBE1PBE
Re_1	2.20	5.58	2.20	5.59	Re_1-O_1	1.52	1.52
O_1	−0.68	2.08	−0.68	2.08	Re_1-O_2	1.52	1.52
O_2	−0.68	2.08	−0.68	2.08	Re_1-O_3	1.56	1.56
O_3	−0.62	2.15	−0.63	2.15	Re_1-F_1	0.50	0.50
F_1	−0.59	0.75	−0.59	0.75	Re_1-F_2	0.24	0.24
F_2	−0.63	0.72	−0.63	0.71	$Re-F_{2A}$	0.24	0.24
F_{2A}	−0.63	0.72	−0.63	0.71			

[a] The aug-cc-pVTZ(-PP) basis set was used.

Table B9. NBO Natural Charges and Wiberg Valencies and Bond Indices for the $[fac\text{-}ReO_3F_3]^{2-}$ Anion (C_{3v})[a]

	B3LYP		PBE1PBE		Bond	Bond Index	
Atom	Charge	Valence	Charge	Valence		B3LYP	PBE1PBE
Re_1	2.18	5.61	2.18	5.63	Re_1-O_1	1.47	1.48
O_1	−0.72	2.04	−0.72	2.04	Re_1-F_1	0.40	0.40
F_1	−0.68	0.60	−0.68	0.60			

[a] The aug-cc-pVTZ(-PP) basis set was used.

Table B10. NBO Natural Charges and Wiberg Valencies and Bond Indices for $(\mu\text{-}F)_4\{[\mu\text{-}O(ReO_2F)_2](ReO_2F_2)_2\}$ (C_{2v})[a]

	B3LYP		PBE1PBE			B3LYP	PBE1PBE
Atom	Charge	Valence	Charge	Valence	Bond	Bond Index	Bond Index
Re_1	2.23	5.54	2.34	5.56	$Re_1-O_{1,2}$	1.81	1.82
Re_2	2.30	5.56	2.30	5.57	$Re_2-O_{3,4}$	1.79	1.80
F_1	−0.43	1.02	−0.43	1.01	Re_2-O_9	0.74	0.74
F_2	−0.45	0.98	−0.45	0.98	Re_1-F_1	0.71	0.71
F_3	−0.43	1.01	−0.43	1.01	Re_1-F_2	0.69	0.70
$F_{7,8,10}$	−0.61	0.76	−0.61	0.75	Re_2-F_3	0.70	0.70
$O_{1,2}$	−0.40	2.36	−0.40	2.36	$Re_1-F_{7,10}$	0.25	0.25
$O_{3,4}$	−0.40	2.37	−0.40	2.37	$Re_2-F_{7,8}$	0.24	0.24
O_9	−0.78	2.11	−0.79	2.09			

[a]The aug-cc-pVTZ(-PP) basis sets were used.

APPENDIX C

FLUORIDE ION-DONOR PROPERTIES OF ReO_3F

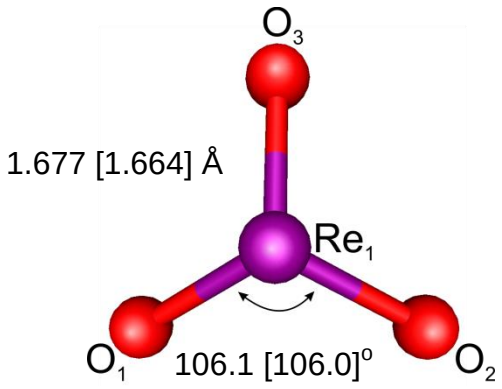

Figure C1. Calculated structure (C_{3v}) of the $[ReO_3]^+$ cation (B3LYP [PBE1PBE]/aug-cc-pVTZ(-PP)).

Table C1. Calculated[a] Vibrational Frequencies, Intensities, and Assignments for the $[ReO_3]^+$ cation (C_{3v})

B3LYP	PBE1PBE		assgnts [b]
1084(39)[<1]	1120(39)[<1]	A_1	$\nu(ReO_1) + \nu(ReO_2) + \nu(ReO_3)$
1016(16)[64]	1048(16)[76]	E	$\nu(ReO_2) - \nu(ReO_3)$
378(4)[<1]	387(4)[<1]	E	$\delta(ReO_1O_2O_3)_{oop}$
340(2)[8]	347(2)[9]	A_1	$\delta(O_1ReO_2)$

[a] Values in parentheses denote calculated Raman intensities ($Å^4\ u^{-1}$). Values in square brackets denote calculated infrared intensities (km mol^{-1}). The aug-cc-pVTZ(-PP) basis set was used. [b] For atom labeling see Figure C1. Abbreviations denote stretch (ν), bend (δ), and out-of-plane (oop).

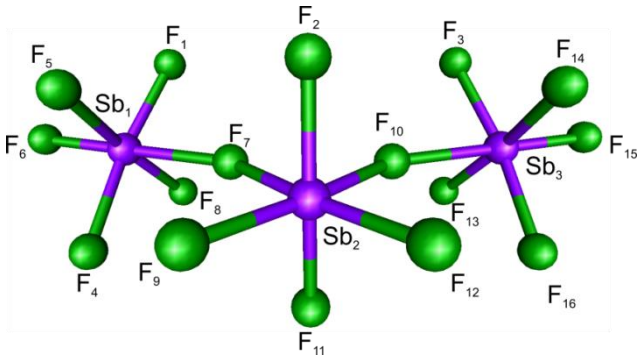

Figure C2. Calculated structure (C_s) of the $[Sb_3F_{16}]^-$ anion (B3LYP/aug-cc-pVTZ(-PP)).

Table C2. Calculated[a] Vibrational Frequencies, Intensities, and Assignments for the $[Sb_3F_{16}]^-$ anion (C_s)

B3LYP	PBE1PBE	B3LYP	PBE1PBE
701(0)[189]	725(<1)[193]	261(<1)[0]	266(<1)[0]
681(<1)[272]	703(<1)[288]	257(1)[10]	261(1)[9]
679(<1)[71]	701(<1)[67]	245(<1)[65]	256(<1)[46]
678(<1)[158]	700(<1)[165]	244(<1)[89]	248(<1)[86]
677(<1)[<1]	700(<1)[0]	226(<1)[300]	230(<1)[308]
664(1)[43]	687(1)[48]	218(2)[<1]	221(2)[0]
663(26)[10]	686(24)[8]	206(<1)[1]	209(<1)[1]
648(9)[48]	668(10)[39]	206(1)[<1]	209(1)[<1]
646(1)[220]	667(<1)[215]	196(1)[4]	202(1)[3]
630(2)[19]	653(3)[24]	180(<1)[0]	184(<1)[0]
626(<1)[30]	648(<1)[44]	172(<1)[2]	176(<1)[2]
623(56)[1]	644(44)[1]	133(<1)[<1]	136(<1)[<1]
585(5)[<1]	602(4)[<1]	133(<1)[0]	135(<1)[0]
585(1)[0]	601(<1)[0]	126(<1)[<1]	129(<1)[<1]
503(5)[93]	521(3)[86]	119(<1)[<1]	122(<1)[<1]
457(1)[194]	474(<1)[193]	113(1)[1]	116(<1)[1]
322(2)[31]	335(2)[33]	100(<1)[1]	103(<1)[6]
288(<1)[6]	295(<1)[8]	97(<1)[0]	100(<1)[0]
287(<1)[79]	294(<1)[77]	63(<1)[<1]	64(<1)[<1]
279(<1)[0]	286(<1)[0]	43(<1)[<1]	46(<1)[<1]
276(1)[29]	282(<1)[26]	26(<1)[<1]	28(<1)[<1]
275(2)[7]	281(2)[4]	19(<1)[<1]	20(<1)[<1]
275(<1)[<1]	280(<1)[<1]	19(<1)[0]	19(<1)[0]
266(<1)[41]	271(<1)[54]	17(0)[0]	17(<1)[0]
262(<1)[20]	268(<1)[29]	13(<1)[<1]	12(<1)[<1]
261(<1)[27]	266(<1)[35]		

[a] Values in parentheses denote calculated Raman intensities ($Å^4\ u^{-1}$). Values in square brackets denote calculated infrared intensities (km mol^{-1}). The aug-cc-pVTZ(-PP) basis set was used. For atom labeling see Figure C2.

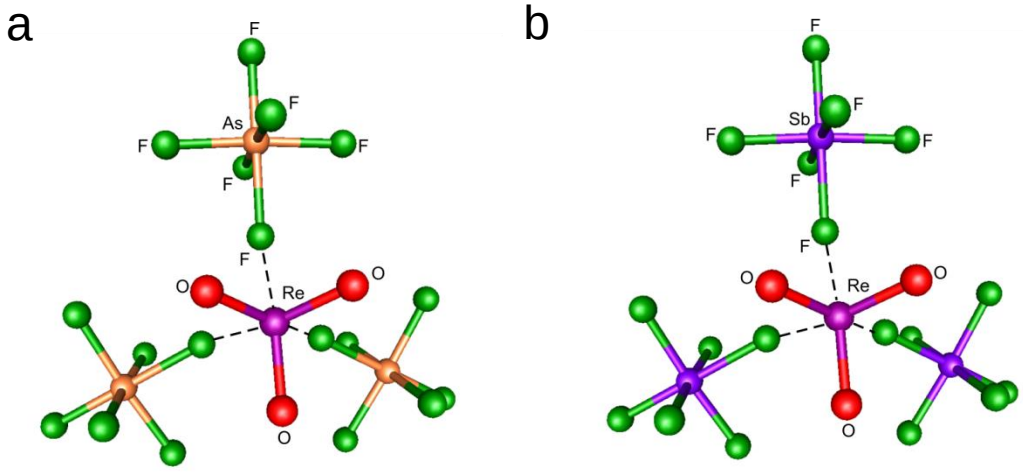

Figure C3. Calculated structures (C_{3v}) of the (a) $\{[ReO_3][AsF_6]_3\}^{2-}$ and (b) $\{[ReO_3][SbF_6]_3\}^{2-}$ ion-pairs (B3LYP/aug-cc-pVTZ(-PP)).

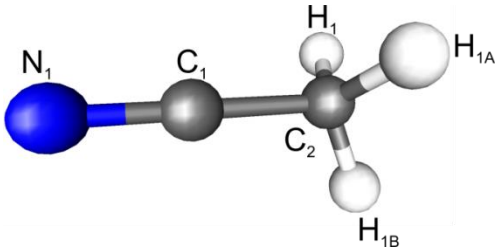

Figure C4. Calculated structure (C_{3v}) of CH_3CN (B3LYP/aug-cc-pVTZ(-PP)).

Table C3. Calculated[a] Bond Lengths and Bond Angles for CH_3CN (C_{3v})

	B3LYP	PBE1PBE
Bond Length (Å)		
N_1-C_1	1.149	1.149
C_1-C_2	1.455	1.449
C_2-H_1	1.089	1.090
Bond Angles (deg)		
$N_1-C_1-C_2$	180.0	180.0
$C_1-C_2-H_1$	110.2	110.1
$H_1-C_2-H_2$	108.7	108.9

[a] The aug-cc-pVTZ basis set was used. For the atom labeling scheme see Figure C4.

Table C4. Experimental Raman Frequencies and Intensities and Calculated Vibrational Frequencies, Intensities, and Assignments for $[ReO_3][Sb_3F_{16}]$

exptl[a,b]	calcd[a,c]		assgnts (C_s)[d]
	B3LYP	PBE1PBE	
1038(100) 1018(14) 1010(40)	1066(55)[19]	1099(52)[21]	$\nu(Re_1O_1) + \nu(Re_1O_2) + \nu(Re_1O_3)$
972(11)	1014(18)[156]	1042(15)[172]	$[\nu(Re_1O_1) - \nu(Re_1O_2)]$
	1011(21)[139]	1040(19)[153]	$[\nu(Re_1O_1) + \nu(Re_1O_2)] - \nu(Re_1O_3)$
704(8)	716(<1)[180]	739(<1)[194]	$[\nu(Sb_1F_8) - \nu(Sb_1F_5)] + [\nu(Sb_3F_{13}) - \nu(Sb_3F_{14})]$
	712(<1)[43]	735(<1)[38]	$[\nu(Sb_1F_8) - \nu(Sb_1F_5)] + [\nu(Sb_3F_{14}) - \nu(Sb_3F_{13})]$
	696(3)[161]	719(2)[159]	$[\nu(Sb_1F_6) + \nu(Sb_3F_{15})] + [\nu(Sb_2F_9) + \nu(Sb_2F_{12}) - \nu(Sb_2F_{11})]$
	696(3)[43]	719(3)[49]	$[\nu(Sb_1F_6) - \nu(Sb_3F_{15})] + [\nu(Sb_2F_{12}) - \nu(Sb_2F_9)]$
	691(11)[43]	713(15)[22]	$[\nu(Sb_1F_6) + \nu(Sb_3F_{15})] - \nu(Sb_2F_{11})$
657(16)	688(3)[29]	709(3)[27]	$[\nu(Sb_1F_6) - \nu(Sb_1F_4)] + [\nu(Sb_2F_9) - \nu(Sb_2F_{12})] + [\nu(Sb_3F_{16}) - \nu(Sb_3F_{15})]$
	686(28)[128]	709(18)[159]	$[\nu(Sb_1F_4) + \nu(Sb_3F_{16})] + [\nu(Sb_2F_9) + \nu(Sb_2F_{12}) + \nu(Sb_3F_{11})]$
	677(4)[41]	699(6)[35]	$[\nu(Sb_1F_6) + \nu(Sb_1F_4)] - [\nu(Sb_2F_9) + \nu(Sb_2F_{12}) + \nu(Sb_2F_{11})] + [\nu(Sb_3F_{16}) + \nu(Sb_3F_{15})]$
	676(2)[146]	698(1)[148]	$[\nu(Sb_1F_6) + \nu(Sb_1F_4)] - [\nu(Sb_3F_{16}) + \nu(Sb_3F_{15})]$
632(37)	640(34)[11]	662(27)[12]	$[\nu(Sb_1F_8) + \nu(Sb_1F_5)] + [\nu(Sb_3F_{13}) + \nu(Sb_3F_{14})]$
	638(<1)[34]	660(<1)[44]	$[\nu(Sb_1F_8) + \nu(Sb_1F_5)] - [\nu(Sb_3F_{13}) + \nu(Sb_3F_{14})]$
590(11)	578(29)[196]	599(22)[202]	$[\nu(Sb_2F_2) - \nu(Re_1F_2)] + [\nu(Sb_2F_7) + \nu(Sb_2F_{10})]$
	534(3)[150]	552(2)[144]	$[\nu(Sb_1F_1) - \nu(Re_1F_1)] + [\nu(Sb_1F_7) - \nu(Sb_2F_7)] + [\nu(Sb_3F_{10}) - \nu(Sb_2F_{10})] + [\nu(Sb_3F_3) - \nu(Sb_1F_3)]$
	487(2)[283]	504(2)[284]	$[\nu(Sb_1F_1) - \nu(Re_1F_1)] + [\nu(Sb_1F_7) - \nu(Sb_2F_7)] + [\nu(Sb_2F_{10}) - \nu(Sb_3F_{10})] + [\nu(Re_1F_3) - \nu(Sb_3F_3)]$
	474(2)[25]	492(2)[21]	$[\nu(Sb_1F_1) - \nu(Re_1F_1)] + [\nu(Sb_3F_3) - \nu(Re_1F_3)] + [\nu(Re_1F_2) - \nu(Sb_2F_2)] + [\nu(Sb_2F_7) - \nu(Sb_1F_2)] + [\nu(Sb_2F_{10}) - \nu(Sb_3F_{10})]$
	435(1)[<1]	452(1)[<1]	$[\nu(Sb_1F_1) - \nu(Re_1F_1)] + [\nu(Sb_2F_7) - \nu(Sb_2F_{10})] + [\nu(Re_1F_3) - \nu(Sb_3F_3)] + [\nu(Sb_3F_{10}) - \nu(Sb_2F_{10})]$
406(8)	388(3)[2]	395(3)[2]	$\delta(O_1Re_1O_2)$
	383(3)[5]	391(3)[4]	$\delta(O_1Re_1O_3) - \delta(O_2Re_1O_3)$
	375(2)[18]	384(2)[18]	$\delta(Re_1O_1O_2O_3)$
380 sh 375(19)	334(2)[49]	348(2)[50]	$[\nu(Sb_1F_7) + \nu(Sb_2F_7)] + [\nu(Sb_3F_{10}) + \nu(Sb_2F_{10})]$

Table C4. (continued ...)

347(5)	317(<1)[20]	327(<1)[21]	$\delta(F_8Sb_1F_1) + \delta(F_7Sb_2F_{10}) + \delta(F_3Sb_3F_{13})$
	312(<1)[3]	324(<1)[3]	$\delta(F_5Sb_1F_1) + [\delta(F_2Sb_2F_7) - \delta(F_2Sb_2F_{10})] + \delta(F_3Sb_3F_{14})$
	304(<1)[2]	312(<1)[2]	$[\nu(Sb_1F_1) + \nu(Re_1F_1)] + [\nu(Sb_2F_2) + \nu(Re_1F_2)] + [\nu(Sb_3F_3) + \nu(Re_1F_3)] + \delta(F_7Sb_2F_{10})$
330(4)	295(<1)[27]	306(<1)[21]	$[\delta(F_{10}Sb_2F_{11}) + [\delta(F_7Sb_2F_{11})] + [\delta(F_3Sb_3F_{13}) - \delta(F_1Sb_1F_8)]$
	278(<1)[<1]	285(<1)[1]	$[\delta(F_7Sb_2F_9) - \delta(F_{10}Sb_2F_{12}) - \delta(F_1Sb_2F_{11})] + [\delta(F_1Sb_1F_5) - \delta(F_3Sb_3F_{14})$
	272(1)[72]	279(1)[78]	$[\delta(F_9Sb_2F_{12}) + \delta(F_7Sb_2F_{10})] + [\delta(F_1Sb_1F_5) + \delta(F_3Sb_3F_{14})]$
286(8)	265(<1)[15]	271(<1)[14]	$[\delta(F_9Sb_2F_{12}) + \delta(F_7Sb_2F_{10})_{small}] + \rho_t(F_2Sb_2F_{11}) + [\rho_w(F_4Sb_1F_5) - \rho_w(F_{13}Sb_3F_{14})]_{small}$
	262(<1)[64]	268(<1)[70]	$[\delta(F_5Sb_1F_8F_6) - \delta(F_{13}F_{14}Sb_3F_{15})]$
	259(1)[6]	264(1)[6]	$[\delta(Sb_1F_5F_1F_6) + \delta(Sb_3F_{14}F_3F_{15})] - [\delta(Sb_2F_9F_2F_{12} + \delta(F_7Sb_3F_{10})]$
	255(1)[40]	259(1)[43]	$[\delta(F_5Sb_1F_6) - \delta(F_4Sb_1F_8)] + [\delta(F_{15}Sb_3F_{14}) - \delta(F_{13}Sb_3F_{16})]$
	254(1)[6]	258(1)[5]	$[\delta(F_5Sb_1F_6) - \delta(F_4Sb_1F_8)] + [\delta(F_{13}Sb_3F_{16}) - \delta(F_{15}Sb_3F_{14})]$
	243(1)[135]	247(1)[133]	$\delta(Sb_1F_1F_4F_5F_8)_{umb} + \delta(Sb_3F_3F_{13}F_{14}F_{16})_{umb} + [\rho_w(F_2Sb_2F_{11}) - \delta(F_9Sb_2F_{12})]$
	236(<1)[36]	244(<1)[31]	$\delta(F_1Sb_1F_4F_6) + \delta(F_3Sb_3F_{13}F_{15}) + \rho_r(F_7Sb_2F_2F_{10})$
	222(<1)[113]	227(<1)[124]	$\delta(Sb_1F_1F_4F_5F_8)_{umb} - \delta(Sb_3F_3F_{13}F_{14}F_{16})_{umb} + [\delta(F_2Sb_2F_9) - \delta(F_2Sb_2F_{12})]$
229(5)	213(2)[1]	217(1)[1]	$[\delta(F_5Sb_1F_8) + \delta(F_6Sb_1F_4)] + \delta(F_9Sb_2F_{12}) + [\delta(F_{13}Sb_1F_{15}) + \delta(F_{14}Sb_1F_{16})]$
	208(1)[1]	212(<1)[4]	$[\delta(F_8Sb_1F_4) + \rho_t(F_6Sb_1F_1)] + [\delta(F_{13}Sb_3F_{16}) + \rho_t(F_3Sb_3F_{15})]$
	204(1)[4]	209(<1)[4]	$[\delta(F_1Sb_1F_6) - \delta(F_6Sb_1F_4) + \delta(F_5Sb_1F_8)] + \delta(F_7Sb_2F_{10}) + [\delta(F_3Sb_3F_{15}) - \delta(F_{15}Sb_3F_{16}) + \delta(F_{14}Sb_3F_{13})]$
	203(1)[39]	207(1)[36]	$[\delta(F_6Sb_1F_4) - \delta(F_{15}Sb_3F_{16})] + [\delta(F_9Sb_2F_{11}) - \delta(F_{11}Sb_2F_{12}) + \rho_t(F_7Sb_2F_{10})_{small}]$
	183(1)[1]	187(1)[1]	$[\delta(F_2Sb_2F_{11}) - \delta(F_7Sb_2F_{10}) - \delta(F_9Sb_2F_{12})] + [\delta(F_6Sb_1F_4) + \delta(F_{15}Sb_3F_{16})]_{small}$
	177(<1)[2]	180(<1)[1]	$[\rho_t(F_5Sb_1F_6) + \rho_t(F_{14}Sb_3F_{15})] + [\rho_r(F_7Sb_2F_{11}F_{10}) + \rho_r(F_9Sb_2F_2F_{12})]$
180(2)	164(1)[1]	168(<1)[1]	$[\delta(F_4Sb_1F_6) - \delta(F_5Sb_1F_8)_{small}] + [\delta(F_{13}Sb_3F_{14})_{small} - \delta(F_{15}Sb_3F_{16})] + [\delta(F_9Sb_2F_{12}) + \delta(F_{11}Sb_2F_2) + \rho_r(Re_1O_1O_2O_3)_{small}$
155(4)	152(<1)[1]	157(<1)[1]	$\rho_r(Re_1O_1O_2) + [\rho_w(F_5Sb_1F_8) - \rho_w(F_1Sb_1F_4)] - [\rho_w(F_{13}Sb_3F_{14}) - \rho_w(F_3Sb_3F_{16})]$
	151(1)[4]	156(1)[4]	$\rho_w(O_1Re_1O_2)$
	139(1)[1]	142(<1)[<1]	$\rho_r(Re_1O_1O_2O_3)$
	138(<1)[<1]	142(<1)[<1]	$\rho_r(O_1Re_1O_2) + [\delta(F_4Sb_1F_1) - \delta(F_5Sb_1F_8)] + [\delta(F_{13}Sb_3F_{14}) - \delta(F_3Sb_3F_{16})] + \rho_r(F_7Sb_2F_{10})$
119(7)	133(1)[2]	136(1)[2]	$\rho_r(F_2Sb_2F_{11}) + \delta(F_7Sb_2F_{10})_{small}$
	124(<1)[<1]	128(<1)[<1]	$[\rho_w(F_2Sb_2F_{11}) + \rho_r(F_9Sb_2F_{12})] + \rho_r(Re_1O_1O_2O_3)_{small}$
	112(<1)[1]	116(<1)[1]	$\rho_w(Re_1O_1O_2) + [\rho_r(F_4Sb_1F_8F_6) + \rho_r(F_{13}Sb_3F_{15}F_{16})] + \rho_r(F_7Sb_2F_1F_{10})_{small}$
	103(<1)[3]	108(<1)[3]	$\rho_r(O_1Re_1O_2) + [\rho_r(F_1F_4F_5Sb_1F_8F_6) + \rho_r(F_3F_{13}F_{14}Sb_3F_{15}F_{16})]$

Table C4. (continued ...)

97(<1)[1]	101(<1)[2]	deformational modes
88(<1)[1]	91(<1)[1]	
87(<1)[1]	89(<1)[1]	
81(<1)[<1]	84(<1)[<1]	
76(<1)[2]	79(<1)[2]	
70(<1)[3]	74(<1)[2]	
61(<1)[<1]	65(<1)[<1]	
55(<1)[1]	60(<1)[1]	
34(<1)[<1]	39(<1)[<1]	
25(<1)[<1]	32(<1)[<1]	
15(<1)[<1]	18(<1)[<1]	

[a] Frequencies are given in cm^{-1}. [b] Values in parentheses denote relative Raman intensities. Raman spectrum was recorded in FEP sample tubes at –140 °C using 1064-nm excitation. The abbreviation denotes shoulder (sh). [c] Values in parentheses denote calculated Raman intensities ($Å^4\ u^{-1}$). Values in square brackets denote calculated infrared intensities (km mol^{-1}). The aug-cc-pVTZ(-PP) basis set was used. [d] The atom numbering corresponds to that used in Figure 5.1a. The abbreviations denote stretch (ν), bend (δ), wag (ρ_w), rock (ρ_r), twist (ρ_t), and umbrella (umb).

Table C5. Experimental Raman Frequencies and Intensities and Calculated Vibrational Frequencies, Intensities, and Assignments for μ-O(ReO_2F)(AsF_5)·2AsF_5

exptl[a,b]	calcd[a,c]		assgnts (C_s)[d]
	B3LYP	PBE1PBE	
1038(5) 1030(100)	1082(51)[37]	1116(48)[40]	$\nu(Re_1O_1) + \nu(Re_1O_2)$
1015(29) 1006(15) 1002(3)	1045(21)[140]	1077(20)[153]	$\nu(Re_1O_1) - \nu(Re_1O_2)$
886(2) 878(3)	938(4)[609]	962(3)[659]	$\nu(Re_1O_3) - \nu(As_2O_3)$
829(2)	783(1)[234]	810(1)[252]	$[\nu(As_1F_8) - \nu(As_1F_5)] + [\nu(As_3F_{13}) - \nu(As_3F_{14})]$
	777(<1)[40]	804(<1)[35]	$[\nu(As_1F_8) - \nu(As_1F_5)] + [\nu(As_3F_{14}) - \nu(As_3F_{13})]$
808(6)	762(6)[125]	783(5)[123]	$\nu(As_1F_6) + \nu(As_3F_{15})$
	761(5)[14]	783(4)[3]	$\nu(As_1F_6) - \nu(As_3F_{15})$
752(16) 743 sh	744(24)[188]	771(25)[173]	$\nu(As_1F_4) + \nu(As_2F_{11}) + \nu(As_3F_{16})$
	737(1)[103]	764(1)[15]	$\nu(As_1F_4) - \nu(As_3F_{16})$
	736(1)[28]	763(1)[21]	$\nu(As_1F_4) - \nu(As_2F_{11}) + \nu(As_3F_{16})$
	732(<1)[207]	762(<1)[301]	$\nu(As_2F_9) - \nu(As_2F_{12})$
712(3) 707(6)	726(6)[88]	754(3)[94]	$\nu(As_2F_9) - \nu(As_2F_{12}) + \nu(As_2F_{11})_{small}$
	703(2)[141]	719(2)[140]	$\nu(Re_1F_2)$
680(14)	674(30)[14]	697(24)[16]	$[\nu(As_1F_8) + \nu(As_1F_5)] + [\nu(As_3F_{13}) + \nu(As_3F_{14})]$
	674(<1)[49]	697(<1)[61]	$[\nu(As_1F_8) + \nu(As_1F_5)] - [\nu(As_3F_{13}) + \nu(As_3F_{14})]$
535(1)	549(1)[93]	556(1)[91]	$[\nu(Re_1F_1) + \nu(Re_1F_3)] - [\nu(As_1F_1) + \nu(As_3F_3)] + [\nu(As_2F_7) + \nu(As_2F_{10})] - [\nu(As_1F_7) + \nu(As_3F_{10})]$
523(1)	523(4)[155]	528(2)[171]	$[\nu(Re_1F_1) + \nu(As_3F_3)] - [\nu(Re_1F_3) + \nu(As_1F_1)]$
510(3)	520(20)[36]	520(12)[32]	$[\nu(Re_1F_1) + \nu(Re_1F_3)] - [\nu(As_1F_1) + \nu(As_3F_3)] - [\nu(As_2F_7) + \nu(As_2F_{10})] + [\nu(As_1F_7) + \nu(As_3F_{10})]$
	472(3)[9]	475(2)[3]	$[\nu(As_2F_7) - \nu(As_2F_{10})] + [\nu(As_3F_{10}) + \nu(As_1F_7)]$
423(2)	420(1)[11]	440(1)[7]	$[\nu(Re_1O_3) + \nu(As_2O_3)] + \rho_w(O_1Re_1O_2)_{small}$
	417(<1)[6]	431(<1)[3]	$\delta(O_1Re_1O_2) - \delta(O_1Re_1O_2) + [\delta(F_1As_1F_5) - \delta(F_3As_3F_{14})]$
407(13)	407(2)[3]	418(3)[6]	$\delta(O_1Re_1O_2)$
	403(1)[111]	425(1)[106]	$\delta(O_1Re_1O_2) + \delta(F_{11}As_2F_7F_{10}) + [\delta(F_1As_1F_5) + \delta(F_3As_3F_{14})]_{small}$
	391(1)[51]	405(<1)[49]	$\delta(F_1As_1F_8) + \delta(F_3As_3F_{13})$

Table C5. (continued ...)

384(4)	383(1)[5]	394(<1)[15]	$[\delta(F_1As_1F_8) - \delta(F_3As_3F_{13})] + [\delta(O_3As_2F_7) - \delta(O_3As_2F_{10})]_{small}$
380(3)	379(2)[62]	391(1)[73]	$[\delta(F_7As_2F_{10}) - \delta(F_9As_2F_{12}F_{11})] - [\delta(F_4As_1F_5) + \delta(F_{14}As_3F_{16})]$
367(8)	374(<1)[70]	384(<1)[37]	$[\delta(F_4As_1F_5) - \delta(F_{14}As_3F_{16})] + [\delta(F_7F_9As_2F_{11}) - \delta(F_{11}As_2F_{12}F_{10})]$
	366(<1)[21]	374(1)[12]	$\delta(F_{12}F_9As_2F_{11}) + [\delta(F_4As_1F_5) - \delta(F_4As_1F_8)] + [\delta(F_{14}As_3F_{16}) - \delta(F_{13}As_3F_{16})]$
	364(1)[3]	373(1)[23]	$[\delta(F_4F_5As_1F_6) - \delta(F_{14}F_{15}As_3F_{16})] + [\delta(F_{10}As_2F_{11}) - \delta(F_{11}As_2F_7)]$
353(1)	358(<1)[7]	364(<1)[16]	$[\delta(F_1F_5As_1F_6) - \delta(F_6F_8As_1F_4)] + [\delta(F_{13}F_{15}As_3F_{16}) - \delta(F_3F_{10}As_3F_{14})]$
	352(<1)[75]	361(<1)[70]	$[\delta(F_8F_4As_1F_6) - \delta(F_5As_1F_1)_{small}] + [\delta(F_{13}F_{15}As_3F_{16}) - \delta(F_3As_3F_{14})_{small}] - [\delta(F_9F_{11}As_2F_{12}) - \delta(F_7As_2F_{10})_{small}]$
	344(<1)[31]	354(<1)[20]	$[\delta(F_9As_2F_{12}) - \delta(F_7As_2F_{10})] - [\delta(F_8F_4As_1F_6) + \delta(F_{13}F_{15}As_3F_{16})]_{small}$
333(2)	338(2)[46]	347(1)[76]	$\delta(O_1Re_1O_2F_2) + [\delta(F_9As_2F_{12}) - \delta(F_7As_2F_{10}]_{small} + [\delta(F_1As_1F_6) + \delta(F_3As_3F_{15})]_{small}$
312(4)	322(1)[36]	338(1)[28]	$[\delta(O_1Re_1O_3) - \delta(O_2Re_1O_3)] + [\delta(F_{14}As_3F_{10}) - \delta(F_7As_1F_5]$
	307(1)[51]	315(<1)[51]	$[\delta(O_1Re_1O_2F_2) + \delta(O_3As_2F_9F_{12})] + [\rho_w(F_1As_1F_5) + \rho_w(F_3As_3F_{14})]$
290(18)	294(1)[120]	305(1)[118]	$[\delta(O_1Re_1F_2) - \delta(O_2Re_1F_2)] + [\delta(F_1As_1F_6) - \delta(F_3As_3F_{15})] + \rho_t(F_9As_2F_{12})]$
	286(1)[31]	294(2)[45]	$[\delta(O_1Re_1F_2) - \delta(O_2Re_1F_2)] + [\delta(F_4As_1F_6) - \delta(F_{16}As_3F_{15})]$
283(8)	283(1)[5]	291(1)[7]	$[\delta(F_8As_1F_6) + \delta(F_4As_1F_1)_{small}] + [\delta(F_{13}As_3F_{15}) - \delta(F_3As_3F_{16})_{small}]$
	280(1)[1]	288(<1)[<1]	$[\delta(F_8As_1F_6) + \delta(F_4As_1F_1)_{small}] + [\delta(F_3As_3F_{16})_{small} - \delta(F_{13}As_3F_{15})]$
267(<1)			
260(<1)	271(2)[<1]	275(1)[1]	$[\delta(F_1As_1F_6) - \delta(F_4As_1F_6) + \delta(F_8As_1F_5)] + [\delta(F_3As_3F_{15}) - \delta(F_{15}As_3F_{16}) + \delta(F_{13}As_3F_{14})] + \delta(F_7As_3F_{10})_{small}$
259(<1)			
246(5)	252(2)[2]	261(2)[2]	$[\delta(O_3Re_1F_2) + \delta(O_3As_2F_{11})] + [\delta(F_7As_2F_{10}) - \delta\ (F_9As_2F_{12})]$
	247(<1)[<1]	255(1)[54][i]	$[\rho_t(F_9As_2F_{12}) + \rho_r(F_7F_{10}As_2F_{11})] + [\delta(F_4As_1F_6) - \delta(F_{16}As_3F_{15})]_{small} + \delta(O_3Re_1F_2)_{small}$
234(3)	239(1)[113]	243(1)[81][j]	$[\rho_t(F_9As_2F_{12}) + \rho_t(F_7As_2F_{10})] + [\delta(F_1As_1F_4) - \delta(F_{16}As_3F_3)]_{small} + \rho_t(O_1Re_1O_2)_{small}$
206(13)	207(3)[2]	224(2)[2]	$\delta(O_3Re_1F_2) + [\delta(F_8As_1F_5) - \delta(F_1As_1F_4)] + [\delta(F_{13}As_3F_{14}) - \delta(F_3As_3F_{16})]$
196(3)	201(<1)[2]	205(<1)[14]	$\rho_r(F_2O_1Re_1O_2) + \rho_r(F_7As_2F_{10}) + [\delta(F_8As_1F_5) - \delta(F_{13}As_3F_{14})]$
188(1)	189(1)[1]	205(2)[2]	$\rho_r(F_1Re_1F_2F_3) + \rho_r(F_9As_2F_{12}) + [\rho_t(F_1As_1F_4) + \rho_t(F_{14}As_3F_{16})]$
180(1)	177(<1)[2]	193(<1)[5]	$[\rho_t(F_1As_1F_5) + \rho_t(F_4As_1F_8)] + [\rho_t(F_3As_3F_{14}) + \rho_t(F_{13}As_3F_{16})] + \rho_r(F_{11}As_2F_7F_{10}F_9F_{12})$
170(1)	165(1)[1]	179(1)[3]	$\rho_r(F_2O_1Re_1O_2) + \rho_w(F_9As_2F_{12}F_{11})$
158(1)	151(<1)[2]	162(<1)[2]	$[\rho_r(O_1Re_1O_2) + \rho_r(F_9As_2F_{12})] + [\rho_r(F_8As_1F_6) + \rho_r(F_{13}As_3F_{15})$
141(3)	149(<1)[<1]	165(<1)[<1]	$\rho_r(O_3Re_1F_2) + [\rho_t(F_1As_1F_8) + \rho_t(F_3As_3F_{13})]$
135(2)	131(<1)[3]	145(<1)[5]	$\rho_r(F_1F_4As_1F_5F_6F_7F_8) + \rho_r(F_3F_{10}As_3F_{13}F_{14}F_{15}F_{16})$
	106(<1)[6]	119(<1)[4]	$[\rho_r(F_5As_1F_6) + \rho_r(F_{14}As_3F_{15})] + \rho_r(F_{11}O_3As_2F_7F_{10}F_9F_{12})$

Table C5. (continued ...)

118(3)	122(<1)[4]	121(<1)[9]	$\rho_r(F_2O_1Re_1O_2) + [\rho_r(F_4As_1F_5) + \rho_r(F_{14}As_3F_{16})]$
	112(<1)[2]	128(<1)[2][k]	$\rho_r(F_2O_1Re_1O_2) + [\rho_r(F_1F_4As_1F_6) + \rho_r(F_3F_{16}As_3F_{15})]$
	106(<1)[6]	119(<1)[4]	$[\rho_r(F_5As_1F_6) + \rho_r(F_{14}As_3F_{15})] + \rho_r(F_{11}O_3As_2F_7F_{10}F_9F_{12})$
	99(<1)[<1]	107(<1)[<1]	deformational modes
	94(<1)[4]	108(<1)[2]	
	81(<1)[22]	97(<1)[22]	
	62(<1)[4]	82(<1)[5]	
	46(<1)[8]	72(<1)[10]	
	39(<1)[9]	51(<1)[<1]	
	36(<1)[2]	58(<1)[1]	
	29(<1)[2]	37(<1)[<1]	
	18(<1)[<1]	24(<1)[<1]	

[a] Frequencies are given in cm^{-1}. [b] Values in parentheses denote relative Raman intensities. Raman spectrum was recorded in FEP sample tubes at –140 °C using 1064-nm excitation. Modes at 967(<1), 922(<1), 786(<1), 775(<1), 645(5) are unassigned. The abbreviation denotes shoulder (sh). [c] Values in parentheses denote calculated Raman intensities ($Å^4\ u^{-1}$). Values in square brackets denote calculated infrared intensities (km mol^{-1}). The aug-cc-pVTZ(-PP) basis set was used. [d] The atom numbering corresponds to that used in Figure 5.1b. The abbreviations denote stretch (ν), bend (δ), wag (ρ_w), rock (ρ_r), and twist (ρ_t).

Table C6. Experimental Raman Frequencies and Intensities for $[O_3Re(NCCH_3)_3][SbF_6]$ **(3)** and CH_3CN and Calculated Vibrational Frequencies, Intensities, and Assignments for $[O_3Re(NCCH_3)_3]^+$ and CH_3CN

exptl[a,b]		calcd[a,c]		assgnts[d]
(3)[e]	CH_3CN[f]	$[O_3Re(NCCH_3)_3]^+$ (C_{3v})		
		B3LYP	PBE1PBE	
3007 sh 2997(20)[g]		3125(164)[7] 3125(11)[2]	3154(158)[12] 3154(11)[2]	$\nu_{as}(CH_3)$
		3123(100)[7] 3123(0)[0]	3151(97)[11] 3151(0)[0]	$\nu_{as}(CH_2)$
2953 sh 2939(78)[g] 2934(100)		3049(699)[3] 3049(32)[14]	3066(695)[5] 3066(33)[19]	$\nu_s(CH_3)$
2331(38) 2303(16)		2405(394)[87] 2400(171)[214]	2433(389)[94] 2428(170)[230]	$\nu(CN)$
1413(2)		1458(2)[35] 1458(10)[2] 1457(7)[23] 1457(0)[0]	1447(2)[38] 1447(9)[3] 1446(7)[25] 1446(0)[0]	$\delta_{as}(CH_3)$
1370(11) 1366(9) 1361(8)		1408(22)[3] 1407(14)[5]	1395(19)[4] 1394(13)[7]	$\delta_{as}(CH_3)$
1037(1)[i]		1059(1)[9] 1058(1)[2] 1055(1)[7] 1054(0)[0]	1047(1)[10] 1047(1)[3] 1043(1)[8] 1042(0)[0]	$\rho_r(CH_3)$
975(27)		1039(68)[26]	1069(66)[30]	$\nu(ReO_1) + \nu(ReO_{1A}) + \nu(ReO_{1B})$
946(43)		993(19)[202]	1019(18)[218]	$\nu(ReO_1) - \nu(ReO_{1A})$
935(20)		950(18)[12]	975(20)[12]	$\nu_s(CC)$
922 sh		946(2)[11]	971(2)[11]	$\nu_{as}(CC)$
424(4)		434(2)[6] 433(2)[1]	439(2)[6] 438(2)[1]	$\delta_s(NCC)_{ip}$ $\delta_s(NCC)_{oop}$
399(2)		424(<1)[4] 421(0)[0]	429(<1)[3] 426(0)[0]	$\delta_{as}(NCC)_{ip}$ $\delta_{as}(NCC)_{oop}$
390(8) 386(3)[g,h] 380 sh[h]		386(2)[33]	393(2)[34]	$\delta_s(ReO_1O_{1A}O_{1B})$
371(14) 365(14)		377(5)[6]	383(5)[6]	$\delta_{as}(ReO_1O_{1A}O_{1B})$
		251(<1)[8]	256(<1)[7]	$\delta(OReN)$
		250(<1)[12]	258(<1)[11]	$\nu_s(Re\text{---}N)$
213(2)		213(1)[9]	220(1)[11]	$\nu_{as}(Re\text{---}N)$
		199(<1)[1]	205(<1)[1]	$\delta_s(ReNC)_{ip}$
		178(0)[0]	181(0)[0]	$\rho_r(ReO_1O_{1A}O_{1B}) - \rho_r(CH_3CN)$
		158(1)[13]	166(1)[13]	$\delta(OReN)$
115(5)[g]		71(<1)[<1]	72(<1)[<1]	$\delta(OReN)$
106(9)		69(0)[0]	70(0)[0]	$\rho_r(ReO_1O_{1A}O_{1B}) + \rho_r(CH_3CN)$

Table C6. (continued ...)

		43(3)[15]	43(3)[15]	CH_3CN deformation modes
		38(4)[4]	38(4)[4]	
		22(<1)[<1]	16(<1)[<1]	
		21(0)[0]	14(0)[0]	
129 sh				lattice modes
115(5)[g]				
106(9)				
99 sh				
(3)	CH_3CN	CH_3CN (C_{3v})		
2997(39)[i]	2999(54)	3115(58)[1]	3148(56)[<1]	$\nu_{as}(CH_3)$
2938(77)[i]	2938(97)	3048(195)[3]	3067(193)[2]	$\nu_s(CH_3)$
2247(71)	2248(100)	2363(81)[11]	2389(80)[13]	ν(CN)
1457(7)	1457(11), 1454(7)	1475(5)[10]	1464(5)[12]	$\delta_{as}(CH_3)$
1424(4)	1425(3), 1420(4)			
1377 sh	1376(15)	1413(6)[2]	1399(6){3]	$\delta_s(CH_3)$
1370(11)	1371(3)			
1367(9)	1368(2)			
1037(1) br[i]	1042(1)	1063(<1)[2]	1053(<1)[2]	$\rho_r(CH_3)$
919(12)	920(20)	928(5)[1]	948(5)[1]	ν(CC)
399(2)	400(3)	382(1)[1]	387(1)[1]	δ(NCC)
394 sh	395(12)			
390(8)	392(9)			
386(9)[i]	386(5)			
	380 sh			
115(12)[i]	116(18)			deformational modes
107(8)[i]	108(13)			
	102(15)			
	96(32)			

[a] Frequencies are given in cm^{-1}. [b] Values in parentheses denote relative Raman intensities. Raman spectrum was recorded on the products under small amount of frozen CH_3CN in FEP sample tubes at –140 °C using 1064-nm excitation. The abbreviation denotes shoulder (sh). [c] Values in parentheses denote calculated Raman intensities ($Å^4$ u^{-1}). Values in square brackets denote calculated infrared intensities (km mol^{-1}). The aug-cc-pVTZ(-PP) basis set was used. [d] The atom numbering corresponds to that used in Figure 5.1c. The abbreviations denote stretch (ν), symmetric (s), asymmetric (as), bend (δ), rock (ρ_r), in-plane (ip), out-of-plane (oop). [e] The $[SbF_6]^-$ anion modes were observed at $\nu_1(A_{1g})$, 645(23), $\nu_2(E_g)$, 574(2); $\nu_5(T_{2g})$, 278(4) cm^{-1}. Overtone and combination bands were observed at 1454 sh, 1445(1) cm^{-1}. The broad peak at 668(1) cm^{-1} was assigned to $SbF_5 \cdot NCCH_3$. [f] Combination band was observed at 2732(2) cm^{-1}. [g] Band overlapping with CH_3CN. [h] Band overlapping with the FEP lines. [i] Band overlapping with the $[O_3Re(NCCH_3)_3][SbF_6]$ line.

Table C7. Calculated[a] Bond Lengths and Bond Angles for $[ReO_3][Sb_3F_{16}]$ and μ-$O(ReO_2F)(AsF_5)\cdot 2AsF_5$

	$[ReO_3][Sb_3F_{16}]$ (C_s)		μ-$O(ReO_2F)(AsF_5)\cdot 2AsF_5$ (C_s)		
	B3LYP	PBE1PBE		B3LYP	PBE1PBE
Bond Length (Å)					
Re_1-O_1	1.686	1.674	Re_1-O_1	1.670	1.657
Re_1-O_2	1.686	1.674	Re_1-F_2	1.835	1.822
$Re_1\cdots F_1$	2.197	2.178	$Re_1\cdots F_1$	2.381	2.297
$Re_1\cdots F_2$	2.401	2.368	Re_1-O_3	1.791	1.797
Sb_1-F_1	2.006	1.988	As_1-F_1	1.805	1.805
Sb_1-F_4	1.872	1.857	As_1-F_4	1.698	1.684
Sb_1-F_5	1.873	1.858	As_1-F_5	1.704	1.693
Sb_1-F_6	1.868	1.853	As_1-F_6	1.687	1.676
Sb_1-F_8	1.870	1.856	As_1-F_8	1.698	1.685
Sb_1-F_7	2.147	2.123	$As_1\cdots F_7$	2.165	2.063
Sb_2-F_2	1.939	1.924	As_2-O_3	1.848	1.799
Sb_2-F_{11}	1.866	1.851	As_2-F_{11}	1.699	1.685
Sb_2-F_9	1.865	1.850	As_2-F_9	1.702	1.686
Sb_2-F_{12}	1.865	1.850	As_2-F_{12}	1.702	1.686
Sb_2-F_7	2.017	2.000	As_2-F_7	1.830	1.841
Bond Angles (deg)					
$O_1-Re_1-O_2$	104.8	104.8	$O_1-Re_1-O_2$	103.5	103.4
$O_1-Re_1-O_3$	105.3	105.3	$O_1-Re_1-F_2$	100.7	99.8
$O_1-Re_1\cdots F_1$	88.8	88.9	$O_1-Re_1\cdots F_1$	88.8	90.0
$O_1-Re_1\cdots F_2$	88.8	88.9	$O_1-Re_1-O_3$	103.1	102.1
$O_1-Re_1\cdots F_3$	153.1	153.2	$O_1-Re_1\cdots F_3$	166.7	165.9
$O_3-Re_1\cdots F_1$	93.0	92.8	$F_2-Re_1\cdots F_1$	71.8	73.1
$O_3-Re_1\cdots F_2$	161.2	161.0	$F_2-Re_1-O_3$	141.0	144.3
$F_1\cdots Re_1\cdots F_2$	71.9	71.8	$F_1\cdots Re_1-O_3$	78.3	79.1
$F_1\cdots Re_1\cdots F_3$	70.4	70.3	$F_1\cdots Re_1\cdots F_3$	78.5	76.3
$Re_1\cdots F_1-Sb_1$	152.5	150.8	$Re_1\cdots F_1-As_1$	142.1	140.1
$Re_1\cdots F_2-Sb_2$	156.2	156.6	$Re_1-O_3-As_2$	164.5	162.1
$F_1-Sb_1-F_4$	168.3	168.3	$F_1-As_1-F_4$	166.7	168.0
$F_1-Sb_1-F_5$	85.5	85.4	$F_1-As_1-F_5$	86.3	86.2
$F_1-Sb_1-F_6$	91.7	91.7	$F_1-As_1-F_6$	93.7	92.7
$F_1-Sb_1-F_7$	81.6	81.6	$F_1-As_1\cdots F_7$	82.6	82.8
$F_1-Sb_1-F_8$	84.7	84.6	$F_1-As_1-F_8$	86.2	86.0
$F_4-Sb_1-F_5$	93.4	93.4	$F_4-As_1-F_5$	91.7	92.2
$F_4-Sb_1-F_6$	100.0	100.1	$F_4-As_1-F_6$	99.6	99.3
$F_4-Sb_1-F_7$	86.7	86.7	$F_4-As_1\cdots F_7$	84.2	85.2
$F_4-Sb_1-F_8$	94.5	93.6	$F_4-As_1-F_8$	92.0	92.6
$F_5-Sb_1-F_6$	96.8	97.0	$F_5-As_1-F_6$	98.0	96.9
$F_5-Sb_1-F_7$	82.7	82.6	$F_5-As_1\cdots F_7$	82.6	83.5
$F_5-Sb_1-F_8$	163.3	163.0	$F_5-As_1-F_8$	162.4	163.9
$F_6-Sb_1-F_7$	173.3	173.2	$F_6-As_1\cdots F_7$	176.1	175.4
$F_6-Sb_1-F_8$	97.0	97.1	$F_6-As_1-F_8$	98.4	97.4
$F_7-Sb_1-F_8$	82.5	82.3	$F_7\cdots As_1-F_8$	80.6	81.6
$Sb_1-F_7-Sb_2$	146.5	145.1	$As_1\cdots F_7-As_2$	144.6	143.3
$F_2-Sb_2-F_7$	83.8	83.7	$O_3-As_2-F_7$	86.5	86.9
$F_2-Sb_2-F_9$	91.6	91.6	$O_3-As_2-F_9$	89.8	91.0
$F_2-Sb_2-F_{10}$	83.8	83.7	$O_3-As_2-F_{10}$	86.5	86.9
$F_2-Sb_2-F_{11}$	166.9	166.8	$O_3-As_2-F_{11}$	172.6	170.9

Table C7. (continued ...)

F_2−Sb_2−F_{12}	91.6	91.6	O_3−As_2−F_{12}	89.8	91.0
F_7−Sb_2−F_9	89.8	89.8	F_7−As_2−F_9	90.1	90.2
F_7−Sb_2−F_{10}	82.2	81.8	F_7−As_2−F_{10}	84.1	83.2
F_7−Sb_2−F_{11}	86.4	86.3	F_7−As_2−F_{11}	88.0	86.4
F_7−Sb_2−F_{12}	171.1	170.8	F_7−As_2−F_{12}	173.4	173.1
F_9−Sb_2−F_{10}	171.1	170.8	F_9−As_2−F_{10}	173.4	173.1
F_9−Sb_2−F_{11}	96.9	97.1	F_9−As_2−F_{11}	95.2	95.0
F_9−Sb_2−F_{12}	98.0	98.2	F_9−As_2−F_{12}	95.4	96.4
F_{10}−Sb_2−F_{11}	86.4	86.3	F_{10}−As_2−F_{11}	88.0	86.4
F_{10}−Sb_2−F_{12}	89.8	89.8	F_{10}−As_2−F_{12}	90.1	90.2
F_{11}−Sb_2−F_{12}	96.9	97.1	F_{11}−As_2−F_{12}	95.2	95.0

[a] The aug-cc-pVTZ(-PP) basis set was used. For the atom labeling scheme see Figure 5.4a and 5.4b. The bond length and bond angles around Pn_3 (Pn = As, Sb) are equal to those around Pn_1 by symmetry.

Table C8. Calculated[a] Bond Lengths and Bond Angles for the $[Sb_3F_{16}]^-$ anion (C_s)

	B3LYP	PBE1PBE		B3LYP	PBE1PBE
Bond Length (Å)					
Sb_1-F_1	1.891	1.876	Sb_2-F_2	1.879	1.864
Sb_1-F_4	1.891	1.877	Sb_2-F_{11}	1.879	1.864
Sb_1-F_5	1.891	1.877	Sb_2-F_9	1.881	1.866
Sb_1-F_6	1.891	1.876	Sb_2-F_{12}	1.881	1.866
Sb_1-F_8	1.891	1.876	Sb_2-F_7	2.019	2.004
Sb_1-F_7	2.146	2.120			
Bond Angles (deg)					
$F_1-Sb_1-F_4$	169.5	169.4	$F_2-Sb_2-F_7$	85.9	85.7
$F_1-Sb_1-F_5$	89.5	89.5	$F_2-Sb_2-F_9$	93.7	93.8
$F_1-Sb_1-F_6$	95.3	95.4	$F_2-Sb_2-F_{10}$	85.9	85.7
$F_1-Sb_1-F_7$	84.4	84.3	$F_2-Sb_2-F_{11}$	169.0	168.7
$F_1-Sb_1-F_8$	89.5	89.5	$F_2-Sb_2-F_{12}$	93.7	93.8
$F_4-Sb_1-F_5$	89.6	89.6	$F_7-Sb_2-F_9$	90.6	90.7
$F_4-Sb_1-F_6$	95.2	95.3	$F_7-Sb_2-F_{10}$	82.8	82.4
$F_4-Sb_1-F_7$	85.1	85.0	$F_7-Sb_2-F_{11}$	85.9	85.7
$F_4-Sb_1-F_8$	89.5	89.5	$F_7-Sb_2-F_{12}$	173.4	173.1
$F_5-Sb_1-F_6$	95.2	95.3	$F_9-Sb_2-F_{10}$	173.4	173.1
$F_5-Sb_1-F_7$	85.1	85.0	$F_9-Sb_2-F_{11}$	93.7	93.8
$F_5-Sb_1-F_8$	169.5	169.4	$F_9-Sb_2-F_{12}$	96.0	96.2
$F_6-Sb_1-F_7$	179.6	179.6	$F_{10}-Sb_2-F_{11}$	85.9	85.7
$F_6-Sb_1-F_8$	95.3	95.4	$F_{10}-Sb_2-F_{12}$	90.6	90.7
$F_7-Sb_1-F_8$	84.4	84.3	$F_{11}-Sb_2-F_{12}$	93.7	93.8
$Sb_1-F_7-Sb_2$	150.5	148.5			

[a] The aug-cc-pVTZ(-PP) basis set was used. For the atom labeling scheme see Figure C2. The bond length and bond angles around Sb_3 are equal to those around Pn_1 by symmetry.

Table C9. Calculated[a] Bond Lengths and Bond Angles for $[O_3Re(NCCH_3)_3]^+$ (C_{3v})

Bond Length (Å)	
$Re{-}O_1$	1.684
$Re{---}N_1$	2.271
$N_1{-}C_1$	1.144
$C_1{-}C_2$	1.441
$C_2{-}H_1$	1.091

Bond Angles (deg)	
$O_1{-}Re{-}O_2$	105.5
$O_1{-}Re{---}N_1$	86.6
$O_1{-}Re{---}N_{1A}$	86.6
$O_1{-}Re{---}N_{1B}$	159.4
$Re{---}N_1{-}C_1$	164.4
$C_1{-}N_1{-}C_2$	179.3
$N_1{-}C_2{-}H$	109.3
$H_1{-}C_2{-}H_2$	109.2

[a] PBE1PBE/aug-cc-aVTZ(-PP). For the atom labeling scheme, see Figure 5.1c.

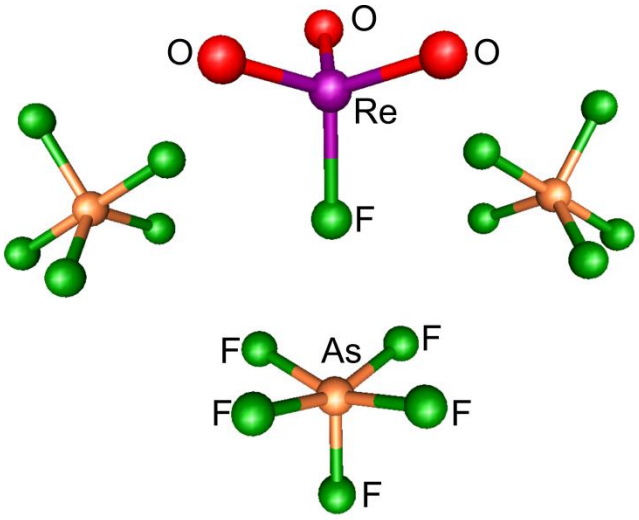

Figure C5. Calculated transitional state of the "$[ReO_3][As_3F_{16}]$" structure (C_s) (B3LYP/aug-cc-pVTZ(-PP)).

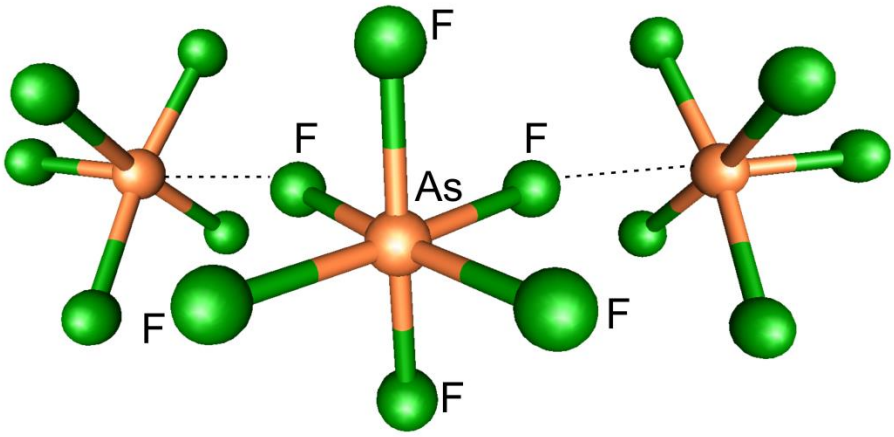

Figure C6. Calculated structure of the "$[As_3F_{16}]^-$" anion (C_{2v}) (B3LYP/aug-cc-pVTZ(-PP)).

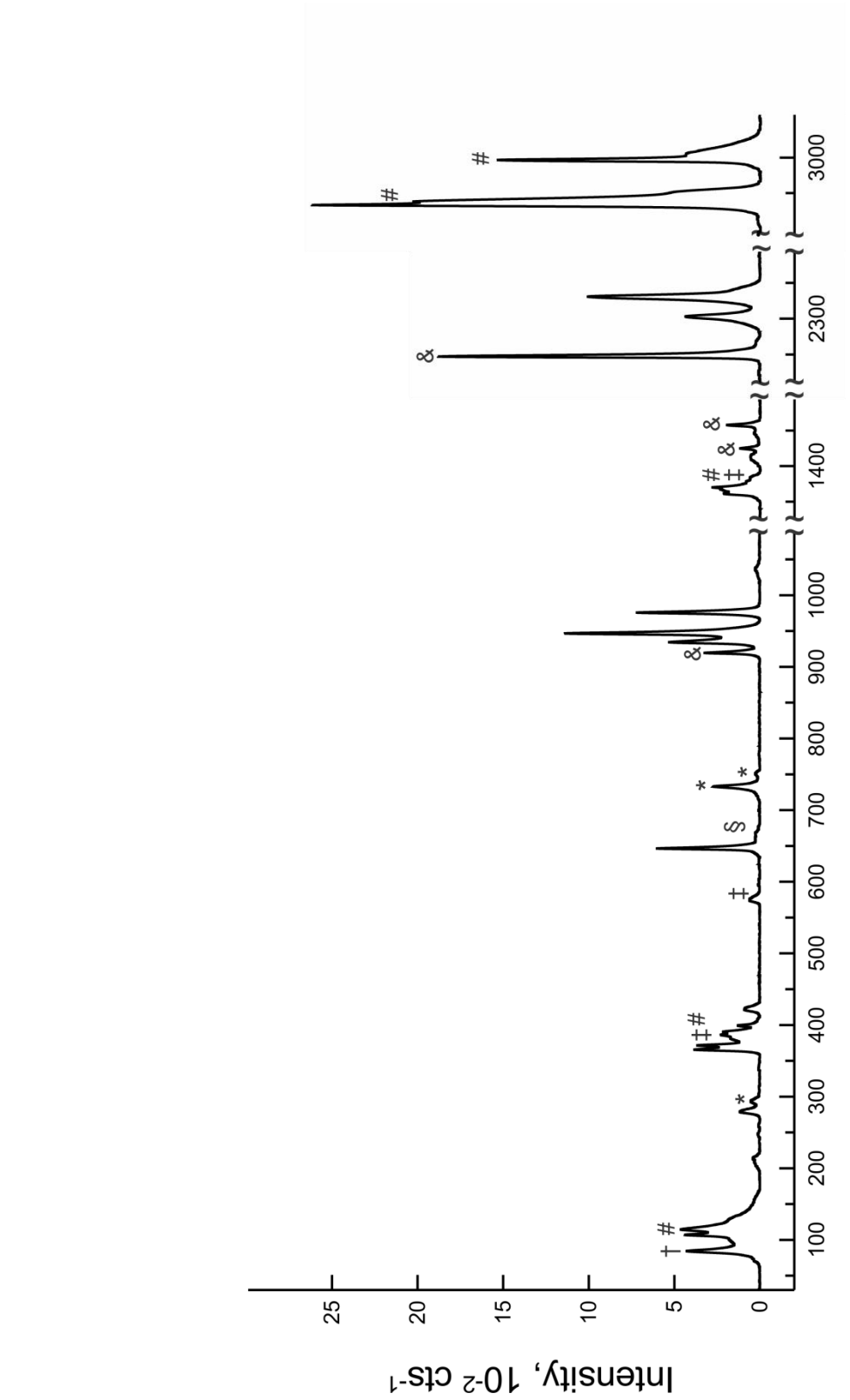

Figure C7. Raman spectrum of $[O_3Re(NCCH_3)_3][SbF_6]$ recorded on a crystalline material under frozen CH_3CN at −140 °C using 1064-nm excitation. Symbols denote an FEP sample tube line (*), free CH_3CN line (&), an instrumental artifact (†), a $SbF_5{\cdot}NCCH_3$ line (§), a $[O_3Re(NCCH_3)_3][SbF_6]$ line overlapping with an FEP sample tube line (‡) or a free CH_3CN line (#).

Table C10. NBO Charges and Wiberg Valencies for $[ReO_3][Sb_3F_{16}]$ and μ-$O(ReO_2F)(AsF_5)\cdot 2AsF_5$

	$[ReO_3][Sb_3F_{16}]$ (C_s)[a]				μ-$O(ReO_2F)(AsF_5)\cdot 2AsF_5$ (C_s)[a]			
Atom	Charge	Valence	Charge	Valence	Charge	Valence	Charge	Valence
	B3LYP		PBE1PBE		B3LYP		PBE1PBE	
Re_1	2.14	5.51	2.14	5.52	2.27	5.50	2.27	5.53
O_1	–0.50	2.27	–0.50	2.27	–0.41	2.36	–0.40	2.37
O_2	–0.50	2.27	–0.50	2.27	–0.41	2.36	–0.40	2.37
O_3	–0.49	2.27	–0.49	2.27	–0.86	1.96	–0.89	1.92
F_1	–0.65	0.67	–0.65	0.67	–0.60	0.73	–0.59	0.74
F_2	–0.65	0.65	–0.65	0.65	–0.43	1.02	–0.42	1.02
F_3	–0.65	0.67	–0.65	0.67	–0.60	0.73	–0.59	0.74
Pn_1	3.07	2.80	3.08	2.81	2.70	3.19	2.70	3.23
Pn_2	3.09	2.80	3.10	2.80	2.68	3.23	2.69	3.24
Pn_3	3.07	2.80	3.08	2.81	2.70	3.19	2.70	3.13
F_4	–0.61	0.68	–0.61	0.68	–0.53	0.79	–0.54	0.79
F_5	–0.60	0.69	–0.61	0.68	–0.54	0.79	–0.54	0.78
F_6	–0.61	0.68	–0.61	0.68	–0.54	0.78	–0.54	0.78
F_7	–0.65	0.64	–0.65	0.65	–0.59	0.74	–0.58	0.76
F_8	–0.60	0.70	–0.60	0.69	–0.52	0.80	–0.53	0.80
F_9	–0.60	0.70	–0.60	0.69	–0.54	0.78	–0.54	0.79
F_{10}	–0.65	0.64	–0.65	0.65	–0.59	0.74	–0.58	0.76
F_{11}	–0.65	0.70	–0.60	0.70	–0.53	0.80	–0.53	0.80
F_{12}	–0.60	0.70	–0.60	0.69	–0.54	0.78	–0.54	0.79
F_{13}	–0.60	0.70	–0.60	0.69	–0.52	0.80	–0.53	0.80
F_{14}	–0.60	0.69	–0.61	0.68	–0.54	0.79	–0.54	0.78
F_{15}	–0.61	0.68	–0.61	0.68	–0.54	0.78	–0.54	0.78
F_{16}	–0.61	0.68	–0.61	0.68	–0.53	0.79	–0.54	0.79

[a] The aug-cc-pVTZ(-PP) basis set was used. For the atom labeling scheme see Figure 5.4a and 5.4b.

Table C11. Wiberg Bond Indices for $[ReO_3][Sb_3F_{16}]$ and μ-$O(ReO_2F)(AsF_5)\cdot 2AsF_5$

	$[ReO_3][Sb_3F_{16}]$ (C_s)[a]		μ-$O(ReO_2F)(AsF_5)\cdot 2AsF_5$ (C_s)[a]	
	B3LYP	PBE1PBE	B3LYP	PBE1PBE
Bond				
Re_1-O_1	1.68	1.68	1.79	1.80
Re_1-O_2	1.68	1.68	1.79	1.80
Re_1-O_3	1.69	1.69	0.97	0.90
Re_1---F_1	0.18	0.18	0.11	0.13
Re_1---F_2/Re_1-F_2	0.09	0.10	0.70	0.71
Re_1---F_3	0.18	0.18	0.11	0.13
Pn_1-F_1	0.32	0.32	0.45	0.43
Sb_2-F_2/As_2-O_3	0.41	0.41	0.46	0.51
Pn_3-F_3	0.32	0.32	0.45	0.43
Pn_1-F_4	0.56	0.57	0.64	0.65
Pn_1-F_5	0.56	0.56	0.63	0.63
Pn_1-F_6	0.57	0.57	0.65	0.65
Pn_1-F_7	0.20	0.21	0.16	0.20
Pn_1-F_8	0.57	0.57	0.65	0.65
Pn_2-F_7	0.31	0.31	0.42	0.39
Pn_2-F_9	0.58	0.58	0.63	0.64
Pn_2-F_{10}	0.31	0.31	0.42	0.39
Pn_2-F_{11}	0.58	0.58	0.64	0.65
Pn_2-F_{12}	0.58	0.58	0.63	0.64
Pn_3-F_{10}	0.20	0.21	0.16	0.20
Pn_3-F_{13}	0.57	0.57	0.65	0.65
Pn_3-F_{14}	0.57	0.56	0.65	0.63
Pn_3-F_{15}	0.57	0.57	0.65	0.65
Pn_3-F_{16}	0.56	0.56	0.64	0.65

[a] The aug-cc-pVTZ(-PP) basis set was used. For the atom labeling scheme see Figure 5.4a and 5.4b.

Table C12. NBO Charges and Wiberg Valencies and Bond Indices for $[O_3Re(NCCH_3)_3]^{+}$[a]

	B3LYP		PBE1PBE			B3LYP	PBE1PBE
Atom	Charge	Valence	Charge	Valence	Bond	Bond Index	Bond Index
Re_1	1.93	5.64	1.92	5.66	Re_1-O_1	1.62	1.62
O	−0.50	2.28	−0.50	2.28	Re_1---N	0.25	0.26
N	−0.44	3.26	−0.44	3.27	$N-C_1$	2.74	2.74
C_1	0.51	3.91	0.52	3.92	C_1-C_2	1.11	1.12
C_2	−0.71	3.82	−0.73	3.81	C_2-H	0.89	0.88
H	0.27	0.92	0.29	0.92			

[a]The aug-cc-pVTZ(-PP) (C_{3v}) basis sets were used. For the atom labeling scheme see Figure 5.4c.

Table C13. NBO Charges and Wiberg Valencies and Bond Indices for $[ReO_3]^{+}$ [a]

	B3LYP		PBE1PBE			B3LYP	PBE1PBE
Atom	Charge	Valence	Charge	Valence	Bond	Bond Index	Bond Index
Re_1	2.12	5.47	2.13	5.47	Re_1−O_1	1.82	1.82
O	−0.37	2.34	−0.38	2.33			

[a]The aug-cc-pVTZ(-PP) (C_{3v}) basis sets were used. For the atom labeling scheme see Figure C3.

Table C14. NBO Charges and Wiberg Valencies and Bond Indices for $[Sb_3F_{16}]^{-}$ [a]

	B3LYP		PBE1PBE			B3LYP	PBE1PBE
Atom	Charge	Valence	Charge	Valence	Bond	Bond Index	Bond Index
Sb_1	3.06	2.81	3.05	2.83	Sb_1−F_1	0.52	0.53
Sb_2	3.08	2.80	3.07	2.81	Sb_1−F_4	0.52	0.53
F_1	−0.63	0.64	−0.63	0.64	Sb_1−F_5	0.52	0.53
F_2	−0.62	0.67	−0.62	0.67	Sb_1−F_6	0.51	0.52
F_4	−0.64	0.64	−0.63	0.64	Sb_1−F_7	0.20	0.20
F_5	−0.64	0.64	−0.63	0.64	Sb_1−F_8	0.52	0.53
F_6	−0.65	0.62	−0.65	0.62	Sb_2−F_2	0.55	0.55
F_7	−0.66	0.63	−0.66	0.63	Sb_2−F_9	0.54	0.54
F_8	−0.63	0.64	−0.63	0.64	Sb_2−F_{10}	0.31	0.31
F_9	−0.63	0.65	−0.63	0.65	Sb_2−F_{11}	0.55	0.55
F_{10}	−0.66	0.63	−0.66	0.63	Sb_2−F_{12}	0.54	0.54
F_{11}	−0.62	0.67	−0.62	0.67	Sb_2−F_7	0.31	0.31
F_{12}	−0.63	0.65	−0.63	0.65			

[a]The aug-cc-pVTZ(-PP) (C_{3v}) basis sets were used. For the atom labeling scheme see Figure C4.

Table C15. NBO Charges and Wiberg Valencies and Bond Indices for CH_3CN[a]

	B3LYP		PBE1PBE			B3LYP	PBE1PBE
Atom	Charge	Valence	Charge	Valence	Bond	Bond Index	Bond Index
N	−0.33	3.02	−0.32	3.02	N−C_1	2.90	2.90
C_1	0.28	4.00	0.28	4.00	C_1−C_2	1.09	1.09
C_2	−0.69	3.85	−0.71	3.84	C_2−H	0.91	0.90
H	0.24	0.94	0.25	0.94			

[a]The aug-cc-pVTZ(-PP) (C_{3v}) basis sets were used. For the atom labeling scheme see Figure C2.

APPENDIX D

$[XeOXeOXe]^{2+}$, THE MISSING OXIDE OF XENON(II); SYNTHESIS, RAMAN SPECTRUM, AND X-RAY CRYSTAL STRUCTURE OF $[XeOXeOXe][\mu\text{-}F(ReO_2F_3)_2]_2$

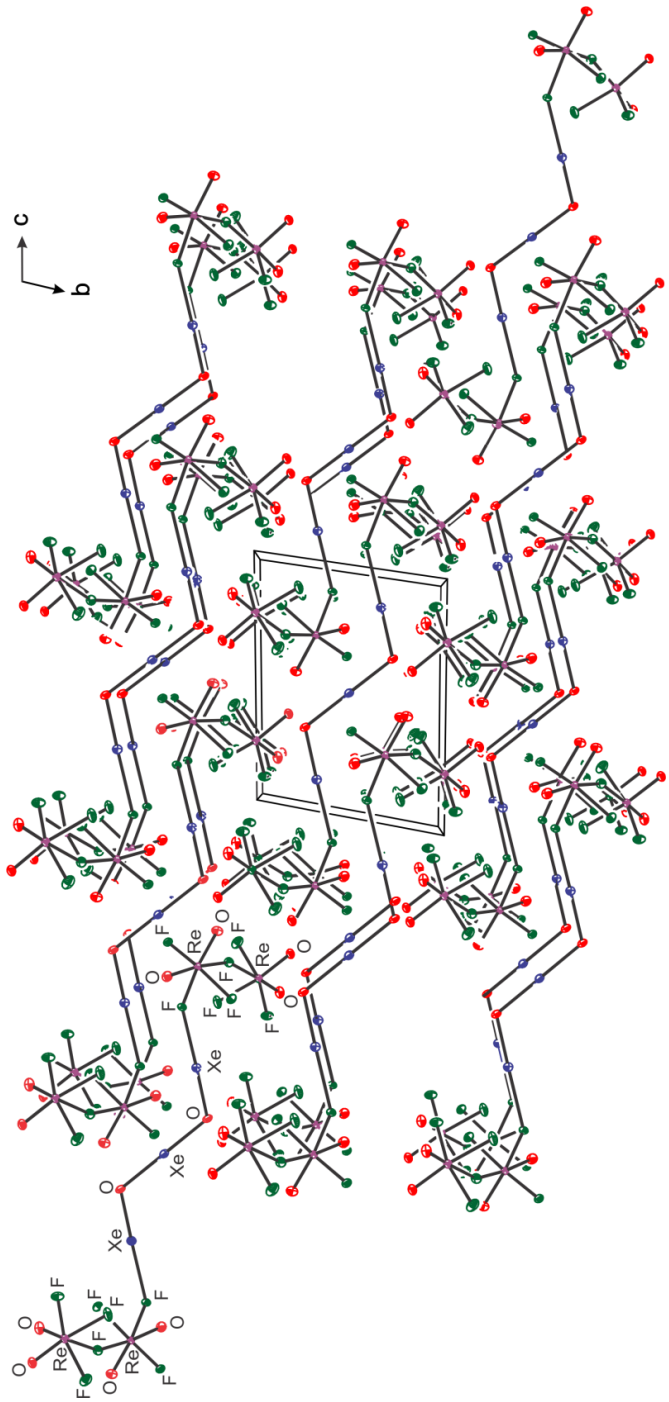

Figure D1. A view of the crystal packing in $[XeOXeOXe][\mu\text{-}F(ReO_2F_3)_2]_2$ along the *a*-axis of the unit cell.

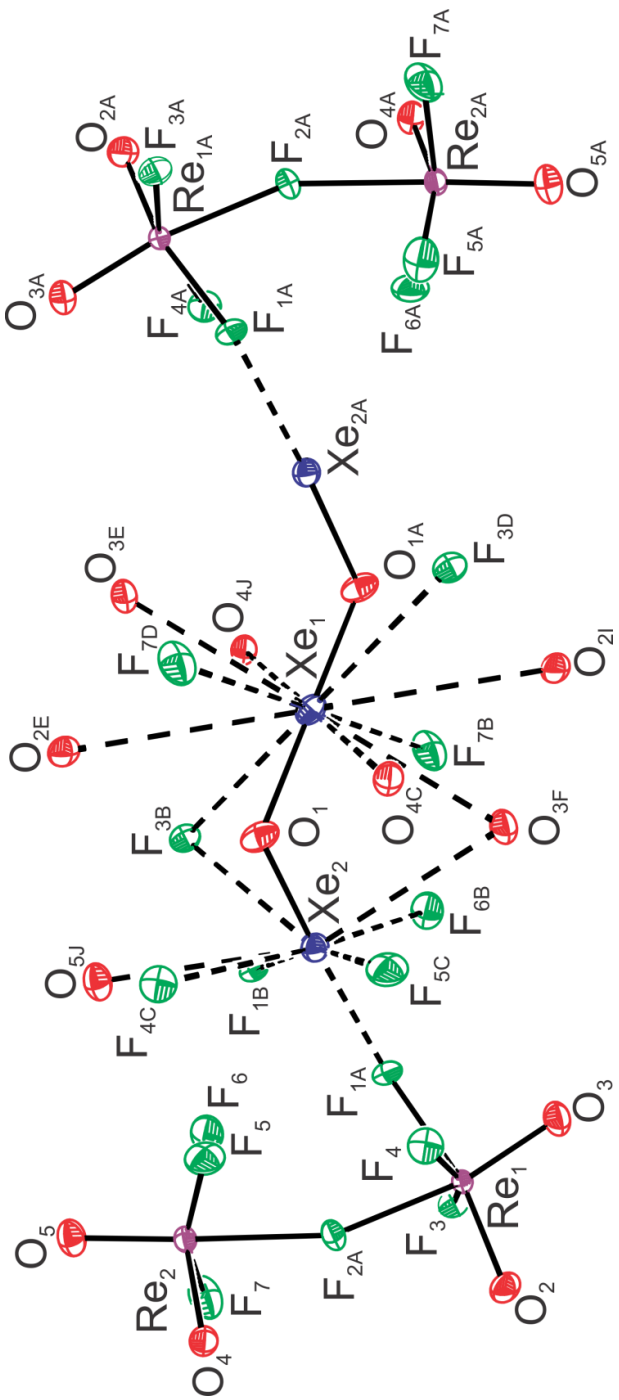

Figure D2. The crystal structure of $[XeOXeOXe][\mu\text{-}F(ReO_2F_3)_2]_2$ showing the immediate coordination environments around $Xe_{(1)}$ and $Xe_{(2)}$ in the structural unit. Thermal ellipsoids are shown at the 50% probability level. Intermolecular distances are given in Table 6.2.

Table D1. Selected Experimental and Calculated Bond Lengths and Contacts[a] for [XeOXeOXe][μ-F(ReO_2F_3)$_2$]$_2$ and Corresponding Bond Valences[b]

exptl			calcd[c]		
Bond Lengths (Å)		Bond Valences (v.u.)	Bond Lengths (Å)		Bond Valences (v.u.)
$Xe_{(1)}$–$O_{(1)}$	2.135(6)	0.78	$Xe_{(1)}$–$O_{(1)}$	2.174	0.70
$Xe_{(1)}$–$O_{(1A)}$	2.135(6)	0.78	$Xe_{(1)}$–$O_{(1A)}$	2.174	0.70
$Xe_{(1)}$---$O_{(1E)}$	3.324(6)	0.03			
$Xe_{(1)}$---$O_{(1F)}$	3.324(6)	0.03			
$Xe_{(1)}$---$O_{(4J)}$	3.330(6)	0.03			
$Xe_{(1)}$---$O_{(4C)}$	3.330(6)	0.03			
$Xe_{(1)}$---$O_{(2E)}$	3.663(6)	0.01			
$Xe_{(1)}$---$O_{2(2I)}$	3.663(6)	0.01			
$Xe_{(1)}$---$F_{(3D)}$	3.429(5)	0.02	$Xe_{(1)}$---$F_{(5)}$	3.295	0.03
$Xe_{(1)}$---$F_{(3B)}$	3.429(5)	0.02	$Xe_{(1)}$---$F_{(6)}$	3.675	0.01
$Xe_{(1)}$---$F_{(7D)}$	3.119(5)	0.05	$Xe_{(1)}$---$F_{(5A)}$	3.295	0.03
$Xe_{(1)}$---$F_{(7B)}$	3.119(5)	0.05	$Xe_{(1)}$---$F_{(6A)}$	3.675	0.01
		1.84[d]			**1.48**[d]
$Xe_{(2)}$–$O_{(1)}$	1.987(6)	1.20	$Xe_{(2)}$–$O_{(1)}$	2.034	1.05
$Xe_{(2)}$–$F_{(1)}$	2.392(4)	0.37	$Xe_{(2)}$–$F_{(1)}$	2.310	0.46
$Xe_{(2)}$---$O_{(3J)}$	3.239(6)	0.03			
$Xe_{(2)}$---$O_{(1F)}$	3.311(6)	0.03			
$Xe_{(2)}$---$F_{(1B)}$	3.248(5)	0.04	$Xe_{(1)}$---$F_{(2)}$	3.158	0.05
$Xe_{(2)}$---$F_{(4C)}$	3.419(5)	0.02	$Xe_{(1)}$---$F_{(4)}$	3.977	0.01

Table D1. (continued….)

$Xe_{(2)}$---$F_{(5C)}$	3.114(5)	0.05	$Xe_{(1)}$---$F_{(5)}$	3.586	0.01
$Xe_{(2)}$---$F_{(6B)}$	3.168(5)	0.04	$Xe_{(1)}$---$F_{(6)}$	3.302	0.03
$Xe_{(2)}$---$F_{(3B)}$	3.266(5)	0.03			
		1.81[d]			**1.61**[d]

[a] See Figures D2 for the atom labeling scheme. [b] Bond valence units (v.u.) are defined in ref 46. R_0 = 2.05 and B_0 = 0.35 (Xe^{II}–O). R_0 = 2.02 and B_0 = 0.37 (Xe^{II}–F) (from *Accumulated Table of Bond Valence Parameters* (http://www.iucr.org/__data/assets/file/0006/81087/bvparm2013.cif) by I. D. Brown). [c] The B3LYP/aug-cc-pVDZ(-PP) method was used. [d] Total bond valence values (v.u.) are given in bold.

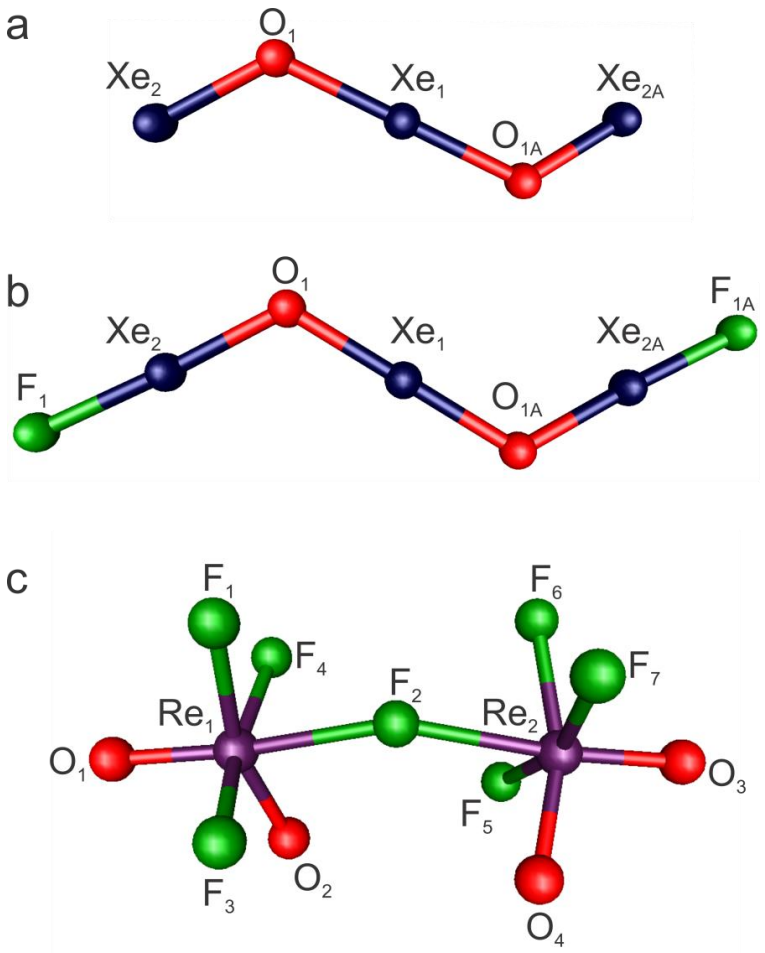

Figure D3. The calculated structures of (a) $[XeOXeOXe]^{2+}$, (b) FXeOXeOXeF, and (c) $[\mu\text{-}F(ReO_2F_3)_2]^-$. See Table 6.2 for the calculated geometric parameters. The B3LYP/aug-cc-pVDZ(-PP) level of theory was used.

Table D2. Experimental and Calculated (B3LYP, C_i) Vibrational Frequencies for $[Xe^{16/18}OXe1^{6/18}OXe][\mu\text{-}F(Re^{16/18}O_2F_3)_2]_2$

exptl[a]			calcd[b]			assgnts[c]
^{16}O	^{18}O	$\Delta\nu^{16/18}$	^{16}O	^{18}O	$\Delta\nu^{16/18}$	
1016.8(90)	962.4(7)	−54.4	1061.7(256)[0]	1004.8(228)[0]	−56.9	$[\nu(Re_1O_3) + \nu(Re_1O_2)] + [\nu(Re_{1A}O_{3A}) + \nu(Re_{1A}O_{2A})] + \{[\nu(Re_2O_4) + \nu(Re_2O_5)] + [\nu(Re_{2A}O_{4A}) + \nu(Re_{2A}O_{5A})]\}_{small}$
			1061.1(0)[212]	1004.2(0)[188]	−56.9	$[\nu(Re_1O_3) + \nu(Re_1O_2)] - [\nu(Re_{1A}O_{3A}) + \nu(Re_{1A}O_{2A})] + \{[\nu(Re_2O_4) + \nu(Re_2O_5)] - [\nu(Re_{2A}O_{4A}) + \nu(Re_{2A}O_{5A})]\}_{small}$
			1055.0(0)[158]	998.5(0)[144]	−56.5	$\{[\nu(Re_1O_3) + \nu(Re_1O_2)] - [\nu(Re_{1A}O_{3A}) + \nu(Re_{1A}O_{2A})]\}_{small} - [\nu(Re_2O_4) + \nu(Re_2O_5)] - [\nu(Re_{2A}O_{4A}) + \nu(Re_{2A}O_{5A})]$
1002.7(47)	948.9(41)	−53.8	1054.9(15)[0]	998.4(13)[0]	−56.5	$\{[\nu(Re_1O_3) + \nu(Re_1O_2)] + [\nu(Re_{1A}O_{3A}) + \nu(Re_{1A}O_{2A})]\}_{small} - [\nu(Re_2O_4) + \nu(Re_2O_5)] + [\nu(Re_{2A}O_{4A}) + \nu(Re_{2A}O_{5A})]$
979.6 sh 975.2(27)	929.8(22) 924.7(21)	−49.8 −50.5	1030.3(74)[0]	977.3(66)[0]	−53.0	$[\nu(Re_1O_3) - \nu(Re_1O_2)] + [\nu(Re_1O_{3A}) - \nu(Re_1O_{2A})]$
			1030.2(0)[258]	977.3(0)[241]	−52.9	$[\nu(Re_1O_3) - \nu(Re_1O_2)] + [\nu(Re_{1A}O_{2A}) - \nu(Re_{1A}O_{3A})]$
			1017.0(0)[337]	964.6(0)[310]	−52.4	$[\nu(Re_2O_4) - \nu(Re_2O_5)] + [\nu(Re_{2A}O_{5A}) - \nu(Re_{2A}O_{4A})]$
964.7 960.2 sh	914.7(17) 910.6 sh	−50.0 −49.6	1016.9(25)[0]	964.5(23)[0]	−52.4	$[\nu(Re_2O_4) - \nu(Re_2O_5)] + [\nu(Re_{2A}O_{4A}) - \nu(Re_{2A}O_{5A})]$
			678.7(0)[540]	678.6(0)[541]	−0.1	$[\nu(Re_1F_4) + \nu(Re_2F_5) - \nu(Re_1F_3)] - [\nu(Re_{1A}F_{4A}) + \nu(Re_{2A}F_{5A}) - \nu(Re_{1A}F_{3A})]$
			678.0(8)[0]	678.0(8)[0]	0.0	$[\nu(Re_1F_4) + \nu(Re_2F_5) - \nu(Re_1F_3)] + [\nu(Re_{1A}F_{4A}) + \nu(Re_{2A}F_{5A}) - \nu(Re_{1A}F_{3A})]$
665.7(12)	666.0(14)	0.3	669.6(3)[0]	669.5(3)[0]	−0.1	$[\nu(Re_1F_4) - \nu(Re_2F_5)] + [\nu(Re_{1A}F_{4A})] - \nu(Re_{2A}F_{5A})]$
			669.4(0)[39]	669.4(0)[39]	0.0	$[\nu(Re_1F_4) - \nu(Re_2F_5)] + [\nu(Re_{1A}F_{5A})] - \nu(Re_{2A}F_{4A})]$
			661.4(18)[0]	661.3(18)[0]	−0.1	$[\nu(Re_1F_4) + \nu(Re_1F_3)] + [\nu(Re_{1A}F_{4A}) + \nu(Re_{1A}F_{3A})]$
			661.2(0)[82]	661.1(0)[83]	−0.1	$[\nu(Re_1F_4) + \nu(Re_1F_3)] - [\nu(Re_{1A}F_{4A}) + \nu(Re_{1A}F_{3A})]$
645.9(8)	646.4(8)	0.5	634.6(7)[0]	634.4(7)[0]	−0.2	$[\nu(Re_2F_7) + \nu(Re_2F_6)] + [\nu(Re_{2A}F_{7A})] + [\nu(Re_{2A}F_{6A})]$
			632.7(0)[288]	632.6(0)[290]	−0.1	$[\nu(Re_2F_7) + \nu(Re_2F_6)] - [\nu(Re_{2A}F_{7A})] + [\nu(Re_{2A}F_{6A})]$
581.6(31)	549.3(30)	−32.3	580.1(110)[0]	550.3(94)[0]	−29.8	$[\nu(Xe_1O_1) + (Xe_1O_{1A})] - [\nu(Xe_2O_1) + (Xe_{2A}O_{1A})]$
			565.0(0)[322]	535.6(0)[304]	−29.4	$[\nu(Xe_1O_1) - (Xe_1O_{1A})] - [\nu(Xe_2O_1) - (Xe_{2A}O_{1A})]$
569.8(5)	573.0(4)	3.2	544.0(2)[0]	543.2(8)[0]	−0.8	$[\nu(Re_2F_7) - \nu(Re_2F_6)] + [\nu(Re_{2A}F_{7A}) - \nu(Re_{2A}F_{6A})]$
			542.9(0)[177]	542.9(0)[142]	0.0	$[\nu(Re_2F_7) - \nu(Re_2F_6)] - [\nu(Re_{2A}F_{7A}) - \nu(Re_{2A}F_{6A})]$

Table D2. (continued….)

			465.5(0)[201]	440.1(0)[165]	−25.4	$[\nu(Xe_1O_1) - (Xe_1O_{1A})] + [\nu(Xe_2O_1) - (Xe_{2A}O_{1A})] - \{[\nu(Xe_2F_1) - \nu(Re_1F_1)] - [\nu(Re_1F_2) - \nu(Re_2F_2)] - [\nu(Xe_{2A}F_{1A}) - \nu(Re_{1A}F_{1A})] - [\nu(Re_{1A}F_{2A}) - \nu(Re_{2A}F_{2A})]\}_{small}$
440.8(7)	438.6(7)	−2.2	461.3(14)[0]	460.8(15)[0]	−0.5	$[\nu(Xe_2F_1) - \nu(Re_1F_1)] + [\nu(Re_1F_2) - \nu(Re_2F_2)] + [\nu(Xe_{2A}F_{1A}) - \nu(Re_{1A}F_{1A})] + [\nu(Re_{1A}F_{2A}) - \nu(Re_{2A}F_{2A})]$
			452.6(0)[488]	458.6(0)[547]	6.0	$\{[\nu(Xe_1O_1) - (Xe_1O_{1A})] + [\nu(Xe_2O_1) - (Xe_{2A}O_{1A})]\}_{small} - [\nu(Re_1F_2) - \nu(Re_2F_2)] + [\nu(Re_{1A}F_{2A}) - \nu(Re_{2A}F_{2A})]$
			408.5(1)[0]	382.9(6)[0]	−25.6	$[\delta(O_2Re_1O_3) - \delta(O_3Re_1F_1)] + [\delta(O_{2A}Re_{1A}O_{3A}) - \delta(O_{3A}Re_{1A}F_{1A})]$
			405.6(0)[17]	385.8(0)[29]	−19.8	$[\delta(O_2Re_1O_3) - \delta(O_{2A}Re_{1A}O_{3A})]$
406.2(10)	384.7(12)	−21.5	398.9(10)[0]	378.4(8)[0]	−20.5	$[\delta(O_4Re_2O_5) + \delta(O_{4A}Re_{2A}O_{5A})] - [\delta(O_2Re_1O_3)] + \delta(O_{2A}Re_{1A}O_{3A})]_{small}$
			398.5(0)[19]	378.4(0)[8]	−20.1	$[\delta(O_4Re_2O_5) - \delta(O_{4A}Re_{2A}O_{5A})] - [\delta(O_2Re_1O_3)] - \delta(O_{2A}Re_{1A}O_{3A})]_{small}$
394.9(12)	376.1(13)	−18.8	395.5(10)[0]	398.6(6)[0]	3.1	$\{[\nu(Xe_1O_1) + (Xe_1O_{1A})] + [\nu(Xe_2O_1) + (Xe_{2A}O_{1A})]\}_{small} + [\nu(Xe_2F_1) - \nu(Re_1F_1)] + [\nu(Re_1F_2) - \nu(Re_2F_2)] - [\nu(Xe_{2A}F_{1A}) - \nu(Re_{1A}F_{1A})] - [\nu(Re_{1A}F_{2A}) - \nu(Re_{2A}F_{2A})]$
379.6, sh 358.7(100) 348.5, sh	358.3, sh 340.9(100) 331.2, sh	−20.0 −17.8 −17.3	376.2(139)[0]	357.3(125)[0]	−18.9	$[\nu(Xe_1O_1) + (Xe_1O_{1A})] + [\nu(Xe_2O_1) + (Xe_{2A}O_{1A})]$
			367.4(0)[756]	362.5(0)[735]	−4.9	$[\nu(Xe_2F_1) - \nu(Re_1F_1)] - [\nu(Xe_{2A}F_{1A}) - \nu(Re_{1A}F_{1A})]$
337.9(10)			346.1(7)[0]	340.9(7)[0]	−5.2	$[\delta(O_4Re_2F_5) + \delta(F_7Re_2F_6)] + [\delta(O_{4A}Re_{2A}F_{5A}) + \delta(F_{7A}Re_{2A}F_{6A})]$
			345.8(0)[6]	340.4(0)[10]	−5.4	$[\delta(O_4Re_2F_5) + \delta(F_7Re_2F_6)] - [\delta(O_{4A}Re_{2A}F_{5A}) + \delta(F_{7A}Re_{2A}F_{6A})]$
329.6, sh			333.7(5)[0]	327.8(3)[0]	−5.9	$[\delta(O_3Re_1F_4) + \delta(F_2Re_1F_3)] + [\delta(O_{3A}Re_{1A}F_{4A}) + \delta(F_{2A}Re_{1A}F_{3A})]$
			333.6(0)[23]	327.7(0)[52]	−5.9	$[\delta(O_3Re_1F_4) + \delta(F_2Re_1F_3)] - [\delta(O_{3A}Re_{1A}F_{4A}) + \delta(F_{2A}Re_{1A}F_{3A})]$
			326.6(0)[68]	322.0(0)[67]	−4.6	$[\delta(O_2Re_1F_3) - \delta(F_2Re_1F_1)] - [\delta(O_{2A}Re_{1A}F_{3A}) - \delta(F_{2A}Re_{1A}F_{1A})]$
			326.5(2)[0]	321.4(2)[0]	−5.1	$[\delta(O_2Re_1F_4) - \delta(F_2Re_1F_1)] + [\delta(O_{2A}Re_{1A}F_{4A}) - \delta(F_{2A}Re_{1A}F_{1A})]$
			320.8(0)[35]	313.8(0)[20]	−7.0	$[\delta(O_2Re_1F_4) + \delta(F_2Re_1F_1) + \delta(O_5Re_1F_5)] - [\delta(O_{2A}Re_{1A}F_{4A}) + \delta(F_{2A}Re_{1A}F_{1A}) + \delta(O_{5A}Re_{1A}F_{5A})]$
321.9 sh	315.2(10)	−6.7	320.6(4)[0]	313.8(4)[0]	−6.8	$[\delta(O_2Re_1F_4) + \delta(F_2Re_1F_1) + \delta(O_5Re_1F_5)] + [\delta(O_{2A}Re_{1A}F_{4A}) + \delta(F_{2A}Re_{1A}F_{1A}) + \delta(O_{5A}Re_{1A}F_{5A})]$
313.9(12)	303.4(12)	−10.5	315.0(6)[0]	304.5(6)[0]	−10.5	$[\delta(O_5Re_2F_5) - \delta(O_5Re_2F_6)] + [\delta(O_{5A}Re_{2A}F_{5A}) - \delta(O_{5A}Re_{2A}F_{6A})]$
			314.3(0)[56]	304.2(0)[27]	−10.1	$[\delta(O_5Re_2F_5) + \delta(O_{5A}Re_{2A}F_{6A})] - [\delta(O_{5A}Re_{2A}F_{5A}) - \delta(O_{5A}Re_{2A}F_{6A})]$
288.2(7)	284.2(8)	−4.0	300.7(4)[0]	296.6(3)[0]	−4.1	$[\rho_r(F_1Re_1F_2) + \rho_r(O_4Re_2O_5) + \rho_w(F_5Re_2F_7)] + [\rho_r(F_{1A}Re_{1A}F_{2A}) + \rho_r(O_{4A}Re_{2A}O_{5A}) + \rho_w(F_{5A}Re_{2A}F_{7A})]$
			300.7(0)[78]	296.3(0)[87]	−4.4	$[\rho_r(F_1Re_1F_2) + \rho_r(O_4Re_2O_5) + \rho_w(F_5Re_2F_7)] - [\rho_r(F_{1A}Re_{1A}F_{2A}) + \rho_r(O_{4A}Re_{2A}O_{5A}) + \rho_w(F_{5A}Re_{2A}F_{7A})]$

Table D2. (continued….)

266.7(5)	264.9(5)	−1.8	286.7(2)[0]	282.5(2)[0]	−4.2	$[\rho_w(F_1Re_1F_2) + \delta(O_3Re_1F_3)] + [\rho_w(F_{1A}Re_{1A}F_{2A}) + \delta(O_{3A}Re_{1A}F_{3A})]$
			286.0(0)[106]	281.9(0)[106]	−4.0	$[\rho_w(F_1Re_1F_2) + \delta(O_3Re_1F_3)] - [\rho_w(F_{1A}Re_{1A}F_{2A}) + \delta(O_{3A}Re_{1A}F_{3A})]$
			260.1(0)[50]	258.2(0)[48]	−1.9	$[\delta(O_4Re_2F_5) - \delta(F_7Re_2F_6) + \rho_w(F_3Re_1F_4)] - [\delta(O_{4A}Re_{2A}F_{5A}) - \delta(F_{7A}Re_{2A}F_{6A}) + \rho_w(F_{3A}Re_{1A}F_{4A})]$
			260.1(1)[0]	258.3(1)[0]	−1.8	$[\delta(O_4Re_2F_5) - \delta(F_7Re_2F_6) + \rho_w(F_3Re_1F_4)] + [\delta(O_{4A}Re_{2A}F_{5A}) - \delta(F_{7A}Re_{2A}F_{6A}) + \rho_w(F_{3A}Re_{1A}F_{4A})]$
248.6(2)	248.6(2)	0.0	255.9(6)[0]	254.0(7)[0]	−1.9	$[\rho_r(F_1Re_1F_2) - \delta(F_5Re_2F_7)] + [\rho_r(F_{1A}Re_{1A}F_{2A}) - \delta(F_{5A}Re_{2A}F_{7A})] + [\delta(O_4Re_2F_6) + \delta(O_{4A}Re_{2A}F_{6A})]_{small} + [\rho_w(F_3Re_1F_4) + \rho_w(F_{3A}Re_{1A}F_{4A})]_{small}$
			255.1(0)[50]	253.7(0)[47]	−1.4	$[\delta(O_4Re_2F_7) - \delta(F_5Re_2F_6) + \rho_r(F_1Re_1F_2)] - [\delta(O_{4A}Re_{2A}F_{7A}) - \delta(F_{5A}Re_{2A}F_{6A}) + \rho_r(F_{1A}Re_{1A}F_{2A}) + [\rho_w(F_3Re_1F_4) + \rho_w(F_{3A}Re_{1A}F_{4A})]_{small}$
			241.2(0)[14]	238.0(0)[21]	−3.2	$[\rho_t(F_1Re_1F_3) + \rho_w(O_4Re_2F_6)] - [\rho_t(F_{1A}Re_{1A}F_{3A}) + \rho_w(O_{4A}Re_{2A}F_{6A})]$
238.2(2)	234.5(3)	−2.5	240.9(4)[0]	237.8(4)[0]	−3.1	$[\rho_t(F_1Re_1F_3) + \rho_w(O_4Re_2F_6)] + [\rho_t(F_{1A}Re_{1A}F_{3A}) + \rho_w(O_{4A}Re_{2A}F_{6A})]$
230.4(3)	229.0(4)	−1.4	227.0(1)[0]	225.9(1)[0]	−1.1	$[\rho_w(F_3Re_1F_4) + \rho_r(F_1Re_1F_2)] + [\rho_w(F_{3A}Re_{1A}F_{4A}) + \rho_r(F_{1A}Re_{1A}F_{2A})]$
			226.0(0)[108]	224.7(0)[103]	−1.3	$[\delta(F_3Re_1F_4) + \rho_t(F_1Re_1F_2)] - [\delta(F_{3A}Re_{1A}F_{4A}) + \rho_t(F_{1A}Re_{1A}F_{2A})]$
216.9(2)	213.3(2)	−3.6	224.2(1)[0]	222.6(1)[0]	−1.6	$[\delta(F_3Re_1F_4) + \rho_r(F_1Re_1F_2) + \delta(Re_2O_4F_5F_6F_7)_{umb}] + [\delta(F_{3A}Re_{1A}F_{4A}) + \rho_r(F_{1A}Re_{1A}F_{2A}) + \delta(Re_{2A}O_{4A}F_{5A}F_{6A}F_{7A})_{umb}]$
			224.1(0)[83]	222.4(0)[75]	−1.7	$[\rho_w(F_3Re_1F_4) + \rho_r(F_1Re_1F_2) + \delta_{umb}(Re_2O_4F_5F_6F_7)] - [\rho_w(F_{3A}Re_{1A}F_{4A}) + \rho_r(F_{1A}Re_{1A}F_{2A}) + \delta_{umb}(Re_{2A}O_{4A}F_{5A}F_{6A}F_{7A})]$
			208.4(0)[15]	203.4(0)[12]	−5.0	$[\rho_t(O_3Re_1O_2) + \rho_t(F_1Re_1F_2)] + [\rho_t(O_3Re_1O_2) + \rho_t(F_1Re_1F_2)]$
198.3(2)	195.5(2)	−2.8	205.2(1)[0]	201.0(1)[0]	−4.2	$[\rho_t(O_3Re_1O_2) + \rho_t(F_1Re_1F_2)] - [\rho_t(O_3Re_1O_2) + \rho_t(F_1Re_1F_2)]$
			178.4(0)[1]	177.8(0)[1]	−0.6	$[\rho_w(F_5Re_2F_7) - \rho_w(O_4Re_2F_6)] - [\rho_w(F_{5A}Re_{2A}F_{7A}) - \rho_w(O_{4A}Re_{2A}F_{6A})]$
179.9(1)	175.8(2)	−4.1	178.9(1)[0]	178.0(1)[0]	−0.9	$[\rho_w(F_5Re_2F_7) - \rho_w(O_4Re_2F_6)] + [\rho_w(F_{5A}Re_{2A}F_{7A}) - \rho_w(O_{4A}Re_{2A}F_{6A})]$
			182.0(0)[5]	180.7(0)[8]	−1.3	$[\delta(Xe_2O_1Xe_1) - \delta(Xe_{2A}O_{1A}Xe_1)]_{i.p.} + \rho_t(F_7Re_2F_6) - [\rho_t(F_{7A}Re_{2A}F_{6A})]$
			179.9(0)[5]	172.9(0)[2]	−7.0	$[\delta(Xe_2O_1Xe_1) - \delta(Xe_{2A}O_{1A}Xe_1)]_{o.o.p.}$
142.5 sh	138.8 sh	−3.4	134.3(1)[0]	130.4(1)[0]	−3.9	$[\rho_r(O_3Re_1O_2) + \rho_r(O_4Re_1O_5)] + [\rho_r(O_{3A}Re_{1A}O_{2A}) + \rho_r(O_{4A}Re_{1A}O_{5A})]$
			129.3(0)[8]	124.9(0)[4]	−4.4	$[\rho_r(O_3Re_1O_2) + \rho_r(O_4Re_1O_5)] - [\rho_r(O_{3A}Re_{1A}O_{2A}) + \rho_r(O_{4A}Re_{1A}O_{5A})]$
131.4(19)	127.2(19)	−3.9	129.0(1)[0]	126.4(<1)[0]	−2.6	$[\rho_r(O_3Re_1F_3) + \rho_r(O_{3A}Re_{1A}F_{3A})] + \{[\delta(Xe_2O_1Xe_1) + \delta(Xe_{2A}O_{1A}Xe_1)]_{o.o.p.}\}$
			127.2(<1)[0]	122.8(<1)[0]	−4.4	$[\delta(Xe_2O_1Xe_1) + \delta(Xe_{2A}O_{1A}Xe_1)]_{o.o.p.} + [\rho_r(O_4Re_1O_5) + \rho_r(O_{4A}Re_{1A}O_{5A})]$
			121.0(0)[53]	118.9(0)[51]	−2.1	$[\rho_r(O_3Re_1O_2) + \rho_w(F_3Re_1F_4)] + [\rho_r(O_{3A}Re_{1A}O_{2A}) + \rho_w(F_{3A}Re_{1A}F_{4A})]$
			114.7(0)[2]	112.6(0)[4]	−2.1	}
106.9(30)	104.6(39)	−2.3	109.8(<1)[0]	107.2(<1)[0]	−2.6	} Rocking of $Re_2O_4F_7$ groups
92.8(25)	90.3(23)	−2.5	94.4(19)[0]	94.1(19)[0]	−0.3	$[\delta(Xe_2O_1Xe_1) + \delta(Xe_{2A}O_{1A}Xe_1)]_{i.p.}$
			91.6(0)[9]	91.2(0)[8]	−0.4	$[\rho_r(Xe_2O_1Xe_1) - \rho_r(Xe_{2A}O_{1A}Xe_1)] + [\rho_r(Re_2O_4O_5F_5F_6F_7) - \rho_r(Re_{2A}O_{4A}O_{5A}F_{5A}F_{6A}F_{7A})]_{small}$

Table D2. (continued….)

84.2(1)[0]	83.8(1)[0]	−0.4	deformation modes
74.0(0)[5]	73.5(0)[6]	−0.5	
59.9(2)[0]	58.5(2)[0]	−1.4	
57.8(0)[2]	56.9(0)[1]	−0.9	
40.2(0)[<1]	39.6(0)[<1]	−0.6	
40.4(<1)[0]	40.0(<1)[0]	−0.4	
30.0(3)[0]	30.0(3)[0]	0.0	
34.3(0)[1]	23.8(0)[1]	−10.5	
23.5(0)[<1]	23.1(0)[<1]	−0.4	
23.7(<1)[0]	23.4(<1)[0]	−0.3	
18.9(1)[0]	18.7(1)[0]	−0.2	
12.9(1)[0]	12.5(<1)[0]	−0.4	
10.7(0)[<1]	10.6(0)[<1]	−0.1	
5.8(<1)[0]	5.7(<1)[0]	−0.1	
5.4(0)[<1]	5.3(0)[<1]	−0.1	
2.7(0)[1]	2.6(0)[<1]	−0.1	
-5.1(0)[<1]	-5.1(0)[<1]	0.0	

[a] Frequencies are given in cm^{-1}. $\Delta\nu^{16/18} = \nu(^{18}O) - \nu(^{16}O)$. Band corresponding to $\nu_1(\Sigma_g^+)$ XeF_2 were observed at 496.5 cm^{-1} in both spectra. Two weak bands were observed in the ^{16}O (487.9 cm^{-1}) and ^{18}O (484.0 cm^{-1}) spectra but were not assigned. Values in parentheses denote relative Raman intensities. Raman spectra were recorded in FEP sample tubes at –140 °C using 1064-nm excitation. [b] Values in parentheses denote calculated Raman intensities ($Å^4$ amu^{-1}). Values in square brackets denote calculated infrared intensities (km mol^{-1}). The B3LYP/aug-cc-pVDZ(-PP) method was used. [c] Bond elongations and angle openings are denoted by plus (+) signs and bond contractions and angle compressions are denoted by minus (–) signs. The abbreviations denote shoulder (sh), stretch (ν), bend (δ), twist (ρ_t), wag (ρ_w), rock (ρ_r), in-plane (i.p.), and out-of-plane (o.o.p.). The atoms labeling scheme is given in Figure 6.1.

Table D3. Experimental and Calculated (PBE1PBE, C_i) Vibrational Frequencies for $[Xe^{16/18}OXe1^{6/18}OXe][\mu\text{-}F(Re^{16/18}O_2F_3)_2]_2$

exptl[a]			calcd[b]			assgnts[c]
^{16}O	^{18}O	$\Delta\nu^{16/18}$	^{16}O	^{18}O	$\Delta\nu^{16/18}$	
1016.8(90)	962.4(7)	−54.4	1094.9(217)[0]	1036.2(194)[0]	−58.7	$[\nu(Re_1O_3) + \nu(Re_1O_2)] + [\nu(Re_2O_4) + \nu(Re_2O_5)] + \{[\nu(Re_{1A}O_{3A}) + \nu(Re_{1A}O_{2A})] + [\nu(Re_{2A}O_{4A}) + \nu(Re_{2A}O_{5A})]\}_{small}$
			1094.3(0)[226]	1035.7(0)[201]	−58.6	$[\nu(Re_1O_3) + \nu(Re_1O_2)] + [\nu(Re_2O_4) + \nu(Re_2O_5)] - \{[\nu(Re_{1A}O_{3A}) + \nu(Re_{1A}O_{2A})] + [\nu(Re_{2A}O_{4A}) + \nu(Re_{2A}O_{5A})]\}_{small}$
			1086.8(0)[157]	1028.5(0)[143]	−58.3	$\{[\nu(Re_1O_3) + \nu(Re_1O_2)] - [\nu(Re_2O_4) + \nu(Re_2O_5)]\}_{small} + [\nu(Re_{2A}O_{4A}) + \nu(Re_{2A}O_{5A})] - [\nu(Re_{1A}O_{3A}) + \nu(Re_{1A}O_{2A})]$
1002.7(47)	948.9(41)	−53.8	1086.6(19)[0]	1028.4(16)[0]	−58.2	$\{[\nu(Re_1O_3) + \nu(Re_1O_2)] - [\nu(Re_2O_4) + \nu(Re_2O_5)]\}_{small} + [\nu(Re_{1A}O_{3A}) + \nu(Re_{1A}O_{2A})] - [\nu(Re_{2A}O_{4A}) + \nu(Re_{2A}O_{5A})]$
979.6 sh 975.2(27)	929.8(22) 924.7(21)	−49.8 −50.5	1060.6(66)[0]	1006.2(58)[0]	−54.4	$[\nu(Re_1O_3) - \nu(Re_1O_2)] + [\nu(Re_1O_5) - \nu(Re_1O_4)]$
			1060.6(0)[265]	1006.2(0)[247]	−54.4	$[\nu(Re_1O_3) - \nu(Re_1O_2)] + [\nu(Re_{1A}O_{2A}) - \nu(Re_{1A}O_{3A})]$
			1045.3(0)[374]	991.5(0)[343]	−53.8	$[\nu(Re_2O_4) - \nu(Re_2O_5)] + [\nu(Re_{2A}O_{5A}) - \nu(Re_{2A}O_{4A})]$
964.7 960.2 sh	914.7(17) 910.6 sh	−50.0 −49.6	1045.2(21)[0]	991.4(19)[0]	−53.8	$[\nu(Re_2O_4) - \nu(Re_2O_5)] + [\nu(Re_{2A}O_{4A}) - \nu(Re_{2A}O_{5A})]$
			695.9(0)[532]	695.9(0)[533]	0.0	$[\nu(Re_1F_4) + \nu(Re_2F_5) - \nu(Re_1F_3)] - [\nu(Re_{1A}F_{4A}) + \nu(Re_{2A}F_{5A}) - \nu(Re_{1A}F_{3A})]$
			695.3(12)[0]	695.3(12)[0]	0.0	$[\nu(Re_1F_4) + \nu(Re_2F_5) - \nu(Re_1F_3)] + [\nu(Re_{1A}F_{4A}) + \nu(Re_{2A}F_{5A}) - \nu(Re_{1A}F_{3A})]$
665.7(12)	666.0(14)	0.3	688.0(2)[0]	688.0(2)[0]	0.0	$[\nu(Re_1F_4) - \nu(Re_2F_5)] + [\nu(Re_{1A}F_{4A})] - \nu(Re_{2A}F_{5A})]$
			687.9(0)[37]	687.8(0)[37]	−0.1	$[\nu(Re_1F_4) - \nu(Re_2F_5)] + [\nu(Re_{1A}F_{5A})] - \nu(Re_{2A}F_{4A})]$
			676.9(14)[0]	676.8(14)[0]	−0.1	$[\nu(Re_1F_4) + \nu(Re_1F_3)] + [\nu(Re_{1A}F_{4A}) + \nu(Re_{1A}F_{3A})]$
			676.6(0)[118]	676.6(0)[120]	0.0	$[\nu(Re_1F_4) + \nu(Re_1F_3)] - [\nu(Re_{1A}F_{4A}) + \nu(Re_{1A}F_{3A})]$
645.9(8)	646.4(8)	0.5	647.6(8)[0]	647.3(6)[0]	−0.3	$[\nu(Re_2F_7) + \nu(Re_2F_6)] + [\nu(Re_{2A}F_{7A})] + [\nu(Re_{2A}F_{6A})]$
			645.2(0)[288]	645.0(0)[310]	−0.2	$[\nu(Re_2F_7) + \nu(Re_2F_6)] - [\nu(Re_{2A}F_{7A})] + [\nu(Re_{2A}F_{6A})]$
581.6(31)	549.3(30)	−32.3	621.8(97)[0]	589.3(91)[0]	−32.5	$[\nu(Xe_1O_1) + (Xe_1O_{1A})] - [\nu(Xe_2O_1) + (Xe_{2A}O_{1A})]$
			601.8(0)[400]	571.0(0)[322]	−30.8	$[\nu(Xe_1O_1) - (Xe_1O_{1A})] - [\nu(Xe_2O_1) - (Xe_{2A}O_{1A})]$
569.8(5)	573.0(4)	3.2	560.0(2)[0]	559.6(2)[0]	−0.4	$[\nu(Re_2F_7) + \nu(Re_2F_5) - \nu(Re_2F_6)] + [\nu(Re_{2A}F_{7A}) + \nu(Re_{2A}F_{5A}) - \nu(Re_{2A}F_{6A})]$
			559.2(0)[160]	558.8(0)[174]	−0.4	$[\nu(Re_2F_7) + \nu(Re_2F_5) - \nu(Re_2F_6)] - [\nu(Re_{2A}F_{7A}) + \nu(Re_{2A}F_{5A}) - \nu(Re_{2A}F_{6A})]$

Table D3. (continued….)

			488.5(0)[113]	476.0(0)[437]	−12.5	$[\nu(Xe_1O_1) - (Xe_1O_{1A})] + [\nu(Xe_2O_1) - (Xe_{2A}O_{1A})] - \{[\nu(Xe_2F_1) - \nu(Re_1F_1)] - [\nu(Re_1F_2) - \nu(Re_2F_2)] - [\nu(Xe_{2A}F_{1A}) - \nu(Re_{1A}F_{1A})] - [\nu(Re_{1A}F_{2A}) - \nu(Re_{2A}F_{2A})]\}_{small}$
440.8(7)	438.6(7)	−2.2	476.8(8)[0]	476.3(8)[0]	−0.5	$[\nu(Xe_2F_1) - \nu(Re_1F_1)] + [\nu(Re_1F_2) - \nu(Re_2F_2)] + [\nu(Xe_{2A}F_{1A}) - \nu(Re_{1A}F_{1A})] + [\nu(Re_{1A}F_{2A}) - \nu(Re_{2A}F_{2A})]$
			469.5(0)[594]	461.6(0)[283]	−7.9	$\{[\nu(Xe_1O_1) - (Xe_1O_{1A})] + [\nu(Xe_2O_1) - (Xe_{2A}O_{1A})]\}_{small} - [\nu(Re_1F_2) - \nu(Re_2F_2)] + [\nu(Re_{1A}F_{2A}) - \nu(Re_{2A}F_{2A})]$
			419.3(11)[0][d]	411.7(4)[0]	−7.6	$[\delta(O_2Re_1O_3) - \delta(O_3Re_1F_1)] + [\delta(O_{2A}Re_{1A}O_{3A}) - \delta(O_{3A}Re_{1A}F_{1A})]$
			413.0(0)[22]	393.0(0)[41]	−20.0	$[\delta(O_2Re_1O_3) - \delta(O_{2A}Re_{1A}O_{3A})]$
406.2(10)	384.7(12)	−21.5	405.5(11)[0]	384.9(8)[0]	−20.6	$[\delta(O_4Re_2O_5) + \delta(O_{4A}Re_{2A}O_{5A})] - [\delta(O_2Re_1O_3)] + \delta(O_{2A}Re_{1A}O_{3A})]_{small}$
			405.4(0)[9]	385.0(0)[1]	−20.4	$[\delta(O_4Re_2O_5) - \delta(O_{4A}Re_{2A}O_{5A})] - [\delta(O_2Re_1O_3)] - \delta(O_{2A}Re_{1A}O_{3A})]_{small}$
394.9(12)	376.1(13)	−18.8	409.5(32)[0]	391.1(8)[0][e]	−18.4	$\{[\nu(Xe_1O_1) + (Xe_1O_{1A})] + [\nu(Xe_2O_1) + (Xe_{2A}O_{1A})]\} + [\delta(O_2Re_1O_3) + \delta(O_{2A}Re_{1A}O_{3A})]$ $\{[\nu(Xe_2F_1) - \nu(Re_1F_1)] + [\nu(Re_1F_2) - \nu(Re_2F_2)] - [\nu(Xe_{2A}F_{1A}) - \nu(Re_{1A}F_{1A})] - [\nu(Re_{1A}F_{2A}) - \nu(Re_{2A}F_{2A})]\}_{small}$
379.6, sh 358.7(100) 348.5, sh	358.3, sh 340.9(100) 331.2, sh	−20.0 −17.8 −17.3	397.5(93)[0][f]	380.2(113)[0]	−17.3	$[\nu(Xe_1O_1) + (Xe_1O_{1A})] + [\nu(Xe_2O_1) + (Xe_{2A}O_{1A})]$
			378.2(0)[779]	373.5(0)[753]	−4.7	$[\nu(Xe_2F_1) - \nu(Re_1F_1)] - [\nu(Xe_{2A}F_{1A}) - \nu(Re_{1A}F_{1A})] + \{[\nu(Xe_1O_1) - (Xe_1O_{1A})] + [\nu(Xe_2O_1) - (Xe_{2A}O_{1A})]\}_{small}$
337.9(10)			351.9(7)[0]	347.0(6)[0]	−4.9	$[\delta(O_4Re_2F_5) + \delta(F_7Re_2F_6)] + [\delta(O_{4A}Re_{2A}F_{5A}) + \delta(F_{7A}Re_{2A}F_{6A})]$
			351.4(0)[10]	346.3(0)[19]	−5.1	$[\delta(O_4Re_2F_5) + \delta(F_7Re_2F_6)] - [\delta(O_{4A}Re_{2A}F_{5A}) + \delta(F_{7A}Re_{2A}F_{6A})]$
329.6, sh			340.8(4)[0]	337.3(2)[0]	−3.5	$[\delta(O_3Re_1F_4) + \delta(F_2Re_1F_3)] + [\delta(O_{3A}Re_{1A}F_{4A}) + \delta(F_{2A}Re_{1A}F_{3A})]$
			340.5(0)[62]	337.4(0)[85]	−3.1	$[\delta(O_3Re_1F_4) + \delta(F_2Re_1F_3)] - [\delta(O_{3A}Re_{1A}F_{4A}) + \delta(F_{2A}Re_{1A}F_{3A})]$
			336.9(0)[28][g]	331.4(0)[12]	−5.5	$[\delta(O_2Re_1F_3) - \delta(F_2Re_1F_1)] - [\delta(O_{2A}Re_{1A}F_{3A}) - \delta(F_{2A}Re_{1A}F_{1A})]$
			336.4(2)[0][h]	330.9(2)[0]	−5.5	$[\delta(O_2Re_1F_4) - \delta(F_2Re_1F_1)] + [\delta(O_{2A}Re_{1A}F_{4A}) - \delta(F_{2A}Re_{1A}F_{1A})]$
			323.9(0)[27]	316.3(0)[32]	−7.6	$[\delta(O_2Re_1F_4) + \delta(F_2Re_1F_1) + \delta(O_5Re_1F_5)] - [\delta(O_{2A}Re_{1A}F_{4A}) + \delta(F_{2A}Re_{1A}F_{1A}) + \delta(O_{5A}Re_{1A}F_{5A})]$
321.9 sh	315.2(10)	−6.7	323.9(4)[0]	316.6(4)[0]	−7.3	$[\delta(O_2Re_1F_4) + \delta(F_2Re_1F_1) + \delta(O_5Re_1F_5)] + [\delta(O_{2A}Re_{1A}F_{4A}) + \delta(F_{2A}Re_{1A}F_{1A}) + \delta(O_{5A}Re_{1A}F_{5A})]$
313.9(12)	303.4(12)	−10.5	317.8(6)[0]	307.3(6)[0]	−10.5	$[\delta(O_5Re_2F_5) - \delta(O_5Re_2F_6)] + [\delta(O_{5A}Re_{2A}F_{5A}) - \delta(O_{5A}Re_{2A}F_{6A})]$
			317.1(0)[51]	307.0(0)[27]	−10.1	$[\delta(O_5Re_2F_5) + \delta(O_{5A}Re_{2A}F_{6A})] - [\delta(O_{5A}Re_{2A}F_{5A}) - \delta(O_{5A}Re_{2A}F_{6A})]$
288.2(7)	284.2(8)	−4.0	310.7(4)[0][i]	305.3(4)[0]	−5.4	$[\rho_r(F_1Re_1F_2) + \rho_r(O_4Re_2O_5) + \rho_w(F_5Re_2F_7)] + [\rho_r(F_{1A}Re_{1A}F_{2A}) + \rho_r(O_{4A}Re_{2A}O_{5A}) + \rho_w(F_{5A}Re_{2A}F_{7A})]$
			310.6(0)[84]	305.1(0)[84]	−5.5	$[\rho_r(F_1Re_1F_2) + \rho_r(O_4Re_2O_5) + \rho_w(F_5Re_2F_7)] - [\rho_r(F_{1A}Re_{1A}F_{2A}) + \rho_r(O_{4A}Re_{2A}O_{5A}) + \rho_w(F_{5A}Re_{2A}F_{7A})]$

$[\rho_r(F_1Re_1F_2) + \rho_r(O_4Re_2O_5) + \rho_w($
$+ \rho_w(F_{5A}Re_{2A}F_{7A})]$

Table D3. (continued….)

266.7(5)	264.9(5)	−1.8	290.7(2)[0]	285.5(2)[0]	−5.2	$[\rho_w(F_1Re_1F_2) + \delta(O_3Re_1F_3)] + [\rho_w(F_{1A}Re_{1A}F_{2A}) + \delta(O_{3A}Re_{1A}F_{3A})]$
			288.9(0)[112]	284.6(0)[110]	−4.3	$[\rho_w(F_1Re_1F_2) + \delta(O_3Re_1F_3)] - [\rho_w(F_{1A}Re_{1A}F_{2A}) + \delta(O_{3A}Re_{1A}F_{3A})]$
			267.4(0)[48]	264.5(0)[46]	−2.9	$[\delta(O_4Re_2F_5) - \delta(F_7Re_2F_6) + \rho_w(F_3Re_1F_4)] - [\delta(O_{4A}Re_{2A}F_{5A}) - \delta(F_{7A}Re_{2A}F_{6A}) + \rho_w(F_{3A}Re_{1A}F_{4A})]$
			266.7(2)[0]	263.8(2)[0]	−2.9	$[\delta(O_4Re_2F_5) - \delta(F_7Re_2F_6) + \rho_w(F_3Re_1F_4)] + [\delta(O_{4A}Re_{2A}F_{5A}) - \delta(F_{7A}Re_{2A}F_{6A}) + \rho_w(F_{3A}Re_{1A}F_{4A})]$
248.6(2)	248.6(2)	0.0	262.8(3)[0]	261.5(3)[0]	−1.3	$[\delta(F_5Re_2F_6) + \delta(F_{5A}Re_{2A}F_{6A})] + \{[\rho_r(F_{1A}Re_{1A}F_{2A}) + \rho_r(F_1Re_1F_2)]\}_{small}$
			261.4(0)[47]	260.3(0)[45]	−1.1	$[\delta(F_5Re_2F_6) + \delta(F_{5A}Re_{2A}F_{6A})] - \{[\rho_r(F_{1A}Re_{1A}F_{2A}) + \rho_r(F_1Re_1F_2)]\}_{small}$
			243.5(0)[25]	240.7(0)[34]	−2.8	$[\rho_t(F_1Re_1F_3) + \rho_w(O_4Re_2F_6)] - [\rho_t(F_{1A}Re_{1A}F_{3A}) + \rho_w(O_{4A}Re_{2A}F_{6A})]$
238.2(2)	234.5(3)	−2.5	243.1(3)[0]	240.5(3)[0]	−2.6	$[\rho_t(F_1Re_1F_3) + \rho_w(O_4Re_2F_6)] + [\rho_t(F_{1A}Re_{1A}F_{3A}) + \rho_w(O_{4A}Re_{2A}F_{6A})]$
230.4(3)	229.0(4)	−1.4	230.7(1)[0]	229.4(1)[0]	−1.3	$[\rho_w(F_3Re_1F_4) + \rho_r(F_1Re_1F_2)] + [\rho_w(F_{3A}Re_{1A}F_{4A}) + \rho_r(F_{1A}Re_{1A}F_{2A})]$
			226.0(0)[108]	224.7(0)[103]	−1.3	$[\delta(F_3Re_1F_4) + \rho_t(F_1Re_1F_2)] - [\delta(F_{3A}Re_{1A}F_{4A}) + \rho_t(F_{1A}Re_{1A}F_{2A})]$
216.9(2)	213.3(2)	−3.6	224.2(1)[0]	222.6(1)[0]	−1.6	$[\delta(F_3Re_1F_4) + \rho_r(F_1Re_1F_2) + \delta(Re_2O_4F_5F_6F_7)_{umb}] + [\delta(F_{3A}Re_{1A}F_{4A}) + \rho_r(F_{1A}Re_{1A}F_{2A}) + \delta(Re_{2A}O_{4A}F_{5A}F_{6A}F_{7A})_{umb}]$
			224.1(0)[83]	222.4(0)[75]	−1.7	$[\rho_w(F_3Re_1F_4) + \rho_r(F_1Re_1F_2) + \delta_{umb}(Re_2O_4F_5F_6F_7)] - [\rho_w(F_{3A}Re_{1A}F_{4A}) + \rho_r(F_{1A}Re_{1A}F_{2A}) + \delta_{umb}(Re_{2A}O_{4A}F_{5A}F_{6A}F_{7A})]$
			208.4(0)[15]	203.4(0)[12]	−5.0	$[\rho_t(O_3Re_1O_2) + \rho_t(F_1Re_1F_2)] + [\rho_t(O_3Re_1O_2) + \rho_t(F_1Re_1F_2)]$
198.3(2)	195.5(2)	−2.8	205.2(1)[0]	201.0(1)[0]	−4.2	$[\rho_t(O_3Re_1O_2) + \rho_t(F_1Re_1F_2)] - [\rho_t(O_3Re_1O_2) + \rho_t(F_1Re_1F_2)]$
			178.4(0)[1]	177.8(0)[1]	−0.6	$[\rho_w(F_5Re_2F_7) - \rho_w(O_4Re_2F_6)] - [\rho_w(F_{5A}Re_{2A}F_{7A}) - \rho_w(O_{4A}Re_{2A}F_{6A})]$
179.9(1)	175.8(2)	−4.1	178.9(1)[0]	178.0(1)[0]	−0.9	$[\rho_w(F_5Re_2F_7) - \rho_w(O_4Re_2F_6)] + [\rho_w(F_{5A}Re_{2A}F_{7A}) - \rho_w(O_{4A}Re_{2A}F_{6A})]$
			182.0(0)[5]	180.7(0)[8]	−1.3	$[\delta(Xe_2O_1Xe_1) - \delta(Xe_{2A}O_{1A}Xe_1)]_{i.p.} + \rho_t(F_7Re_2F_6) - [\rho_t(F_{7A}Re_{2A}F_{6A})]$
			179.9(0)[5]	172.9(0)[2]	−7.0	$[\delta(Xe_2O_1Xe_1) - \delta(Xe_{2A}O_{1A}Xe_1)]_{o.o.p.}$
142.5 sh	138.8 sh	−3.4	134.3(1)[0]	130.4(1)[0]	−3.9	$[\rho_r(O_3Re_1O_2) + \rho_r(O_4Re_1O_5)] + [\rho_r(O_{3A}Re_{1A}O_{2A}) + \rho_r(O_{4A}Re_{1A}O_{5A})]$
			129.3(0)[8]	124.9(0)[4]	−4.4	$[\rho_r(O_3Re_1O_2) + \rho_r(O_4Re_1O_5)] - [\rho_r(O_{3A}Re_{1A}O_{2A}) + \rho_r(O_{4A}Re_{1A}O_{5A})]$
131.4(19)	127.2(19)	−3.9	129.0(1)[0]	126.4(<1)[0]	−2.6	$[\rho_r(O_3Re_1F_3) + \rho_r(O_{3A}Re_{1A}F_{3A})] + \{[\delta(Xe_2O_1Xe_1) + \delta(Xe_{2A}O_{1A}Xe_1)]_{o.o.p.}\}$
			127.2(<1)[0]	122.8(<1)[0]	−4.4	$[\delta(Xe_2O_1Xe_1) + \delta(Xe_{2A}O_{1A}Xe_1)]_{o.o.p.} + [\rho_r(O_4Re_1O_5) + \rho_r(O_{4A}Re_{1A}O_{5A})]$
			121.0(0)[53]	118.9(0)[51]	−2.1	$[\rho_r(O_3Re_1O_2) + \rho_w(F_3Re_1F_4)] + [\rho_r(O_{3A}Re_{1A}O_{2A}) + \rho_w(F_{3A}Re_{1A}F_{4A})]$
			114.7(0)[2]	112.6(0)[4]	−2.1	} Rocking of $Re_2O_4F_7$ groups
106.9(30)	104.6(39)	−2.3	109.8(<1)[0]	107.2(<1)[0]	−2.6	
92.8(25)	90.3(23)	−2.5	94.4(19)[0]	94.1(19)[0]	−0.3	$[\delta(Xe_2O_1Xe_1) + \delta(Xe_{2A}O_{1A}Xe_1)]_{i.p.}$
			91.6(0)[9]	91.2(0)[8]	−0.4	$[\rho_r(Xe_2O_1Xe_1) - \rho_r(Xe_{2A}O_{1A}Xe_1)] + [\rho_r(Re_2O_4O_5F_5F_6F_7) - \rho_r(Re_{2A}O_{4A}O_{5A}F_{5A}F_{6A}F_{7A})]_{small}$

Table D3. (continued….)

84.9(0)[1]	84.5(0)[1]	−0.4	deformation modes
84.2(1)[0]	83.8(1)[0]	−0.4	
74.0(0)[5]	73.5(0)[6]	−0.5	
59.9(2)[0]	58.5(2)[0]	−1.4	
57.8(0)[2]	56.9(0)[1]	−0.9	
40.2(0)[<1]	39.6(0)[<1]	−0.6	
40.4(<1)[0]	39.9(<1)[0]	−0.5	
30.0(3)[0]	29.6(3)[0]	0.4	
34.3(0)[1]	33.8(0)[1]	−0.5	
23.5(0)[<1]	23.1(0)[<1]	−0.4	
23.7(<1)[0]	23.4(<1)[0]	−0.3	
18.9(1)[0]	18.7(1)[0]	−0.2	
12.8(1)[0]	12.5(<1)[0]	−0.3	
10.7(0)[<1]	10.6(0)[<1]	−0.1	
5.8(<1)[0]	5.7(<1)[0]	−0.1	
5.4(0)[<1]	5.3(0)[<1]	−0.1	
2.7(0)[1]	2.6(0)[<1]	−0.1	
−5.1(0)[<1]	−5.1(0)[<1]	0.1	

Frequencies are given in cm^{-1}. $\Delta\nu^{16/18} = \nu(^{18}O) - \nu(^{16}O)$. Band corresponding to $\nu_1(\Sigma_g^+)$ XeF_2 were observed at 496.5 cm^{-1} in both spectra. Two weak ban ere observed in the ^{16}O (487.9 cm^{-1}) and ^{18}O (484.0 cm^{-1}) spectra but were not assigned. Values in parentheses denote relative Raman intensities. Ram ɔectra were recorded in FEP sample tubes at –130 °C using 1064-nm excitation. [b] Values in parentheses denote calculated Raman intensities ($Å^4$ u alues in square brackets denote calculated infrared intensities (km mol^{-1}). The B3LYP/aug-cc-pVDZ(-PP) method was used. [c] Bond elongations and ang ɔenings are denoted by plus (+) signs and bond contractions and angle compressions are denoted by minus (–) signs. The abbreviations denote shoulc h), stretch (ν), bend (δ), twist (ρ_t), wag (ρ_w), rock (ρ_r), in-plane (i.p.), and out-of-plane (o.o.p.). The atoms labeling scheme is given in Figure 6.1 dditional minor contribution: $[\nu(Xe_1O_1) + (Xe_1O_{1A})] + [\nu(Xe_2O_1) + (Xe_{2A}O_{1A})]$. [e] Only contribution: $[\delta(O_2Re_1O_3) + \delta(O_{2A}Re_{1A}O_{3A})]$. [f] Additional mir ɔntribution: $[\nu(Xe_2F_1) - \nu(Re_1F_1)] + [\nu(Xe_{2A}F_{1A}) - \nu(Re_{1A}F_{1A})]$. [g] Additional minor contribution: $\delta(O_3Re_1F_3) + \delta(O_{3A}Re_{1A}F_{3A})$. [h] Additional mir ɔntribution: $\delta(O_3Re_1F_3) - \delta(O_{3A}Re_{1A}F_{3A})$. [i] Additional minor contribution: $\delta(O_3Re_1F_2) - \delta(O_{3A}Re_{1A}F_{2A})$.

Table D4. Calculated (B3LYP, C_{2h}) Raman and Infrared Frequencies,[a] Intensities, and Assignments for $[XeOXeOXe]^{2+}$ [b]

^{16}O	^{18}O	$\Delta\nu^{16/18}$	assgnt[c]	
565.3(20)[0]	535.6(17)[0]	−29.7	$\nu_1(A_g)$	$[\nu(Xe_1O_1) + (Xe_1O_{1A})] - [\nu(Xe_2O_1) + (Xe_{2A}O_{1A})]$
548.0(0)[18]	519.5(0)[16]	−28.5	$\nu_4(B_u)$	$[\nu(Xe_1O_1) - (Xe_1O_{1A})] - [\nu(Xe_2O_1) - (Xe_{2A}O_{1A})]$
407.1(0)[90]	387.4(0)[83]	−19.7	$\nu_5(B_u)$	$[\nu(Xe_1O_1) - (Xe_1O_{1A})] + [\nu(Xe_2O_1) - (Xe_{2A}O_{1A})]$
326.1(30)[0]	308.0(27)[0]	−18.1	$\nu_2(A_g)$	$[\nu(Xe_1O_1) + (Xe_1O_{1A})] + [\nu(Xe_2O_1) + (Xe_{2A}O_{1A})]$
160.3(0)[4]	159.9(0)[4]	−0.4	$\nu_6(B_u)$	$[\delta(Xe_2O_1Xe_1) - \delta(Xe_{2A}O_{1A}Xe_1)]_{i.p.}$
115.0(0)[6]	110.4(0)[6]	−4.6	$\nu_8(A_u)$	$[\delta(Xe_2O_1Xe_1) - \delta(Xe_{2A}O_{1A}Xe_1)]_{o.o.p.}$
71.3(35)[0]	70.9(35)[0]	−0.4	$\nu_3(A_g)$	$[\delta(Xe_2O_1Xe_1) + \delta(Xe_{2A}O_{1A}Xe_1)]_{i.p.}$
34.5(0)[<1]	34.3(0)[<1]	−0.2	$\nu_7(B_u)$	$[\rho_r(Xe_2O_1Xe_1) - \rho_r(Xe_{2A}O_{1A}Xe_1)]$
11.3(0)[3]	11.2(0)[3]	−0.1	$\nu_9(A_u)$	$[\rho_t(Xe_2O_1Xe_1) - \rho_t(Xe_{2A}O_{1A}Xe_1)]$

[a] Frequencies are given in cm^{-1}. [b] The aug-cc-pVDZ(-PP) basis set was used. Values in parentheses denote calculated Raman intensities ($Å^4$ amu^{-1}). Values in square brackets denote infrared intensities (km mol^{-1}). $\Delta\nu^{16/18} = \nu(^{18}O) - \nu(^{16}O)$. [c] Bond elongations and angle openings are denoted by plus (+) signs and bond contractions and angle compressions are denoted by minus (–) signs. Abbreviations denote stretch (stretch (ν), bend (δ), rock (ρ_r), wag (ρ_w), twist (ρ_t), in-plane (i.p.), and out-of-plane (o.o.p.). The atoms labeling scheme is given in Figure D3a.

Table D5. Calculated (PBE1PBE, C_{2h}) Raman and Infrared Frequencies,[a] Intensities, and Assignments for $[XeOXeOXe]^{2+}$ [b]

^{16}O	^{18}O	$\Delta\nu^{16/18}$	assgnt[c]	
611.3(16)[0]	579.1(13)[0]	−32.2	$\nu_1(A_g)$	$[\nu(Xe_1O_1) + (Xe_1O_{1A})] - [\nu(Xe_2O_1) + (Xe_{2A}O_{1A})]$
591.3(0)[51]	560.5(0)[46]	−30.8	$\nu_4(B_u)$	$[\nu(Xe_1O_1) - (Xe_1O_{1A})] - [\nu(Xe_2O_1) - (Xe_{2A}O_{1A})]$
434.4(0)[115]	413.5(0)[106]	−20.9	$\nu_5(B_u)$	$[\nu(Xe_1O_1) - (Xe_1O_{1A})] + [\nu(Xe_2O_1) - (Xe_{2A}O_{1A})]$
353.6(36)[0]	334.1(33)[0]	−19.5	$\nu_2(A_g)$	$[\nu(Xe_1O_1) + (Xe_1O_{1A})] + [\nu(Xe_2O_1) + (Xe_{2A}O_{1A})]$
170.0(0)[5]	169.5(0)[5]	−0.5	$\nu_6(B_u)$	$[\delta(Xe_2O_1Xe_1) - \delta(Xe_{2A}O_{1A}Xe_1)]_{i.p.}$
128.2(0)[6]	122.9(0)[6]	−5.3	$\nu_8(A_u)$	$[\delta(Xe_2O_1Xe_1) - \delta(Xe_{2A}O_{1A}Xe_1)]_{o.o.p.}$
74.9(29)[0]	74.6(29)[0]	−0.3	$\nu_3(A_g)$	$[\delta(Xe_2O_1Xe_1) + \delta(Xe_{2A}O_{1A}Xe_1)]_{i.p.}$
37.4(0)[<1]	37.3(0)[<1]	−0.1	$\nu_7(B_u)$	$[\rho_r(Xe_2O_1Xe_1) - \rho_r(Xe_{2A}O_{1A}Xe_1)]$
8.4(0)[3]	8.3(0)[3]	−0.1	$\nu_9(A_u)$	$[\rho_t(Xe_2O_1Xe_1) - \rho_t(Xe_{2A}O_{1A}Xe_1)]$

[a] Frequencies are given in cm^{-1}. [b] The aug-cc-pVDZ(-PP) basis set was used. Values in parentheses denote Raman intensities (Å amu^{-1}). Values in square brackets denote infrared intensities (km mol^{-1}). $\Delta\nu^{16/18} = \nu(^{18}O) - \nu(^{16}O)$. [c] Bond elongations and angle openings are denoted by plus (+) signs and bond contractions and angle compressions are denoted by minus (–) signs. Abbreviations denote stretch (stretch (ν), bend (δ), rock (ρ_r), wag (ρ_w), twist (ρ_t), in-plane (i.p.), and out-of-plane (o.o.p.). The atoms labeling scheme is given in Figure D.3a.

Table D6. Calculated[a] Raman and Infrared Frequencies, Intensities, and Assignments for the [μ-F($Re^{16/18}O_2F_4$)]$^-$ Anion (C_1)

calcd[a]						assgnt[b]
B3LYP			PBE1PBE			
^{16}O	^{18}O	$\Delta\nu^{16/18}$ [c]	^{16}O	^{18}O	$\Delta\nu^{16/18}$	
1034.2(114)[78]	978.9(103)[69]	−55.3	1066.2(108)[88[	1009.1(97)[78]	−57.1	$[\nu(Re_1O_1) + \nu(Re_1O_2)] + [\nu(Re_2O_3) + \nu(Re_2O_4)]$
1027.7(1)[116]	972.5(1)[105]	−55.2	1059.3(1)[111]	1002.5(1)[100]	−56.8	$[\nu(Re_1O_1) + \nu(Re_1O_2)] - [\nu(Re_2O_3) + \nu(Re_2O_4)]$
998.5(24)[96]	947.4(21)[91]	−51.1	1028.1(21)[86]	975.4(18)[82]	−52.7	$[\nu(Re_1O_1) - \nu(Re_1O_2)] + [\nu(Re_2O_3) - \nu(Re_2O_4)]$
991.0(8)[337]	940.0(7)[309]	−51.0	1019.7(9)[378]	967.3(8)[347]	−52.4	$[\nu(Re_1O_1) - \nu(Re_1O_2)] + [\nu(Re_2O_4) - \nu(Re_2O_3)]$
650.7(<1)[254]	650.6(<1)[255]	−0.1	668.1(<1)[231]	668.0(<1)[232]	−0.1	$[\nu(Re_1F_1) + \nu(Re_1F_4)] - [\nu(Re_2F_6) + \nu(Re_2F_7)]$
647.0(19)[153]	647.0(19)[153]	0.0	664.3(17)[152]	664.2(17)[152]	−0.1	$[\nu(Re_1F_1) + \nu(Re_1F_3) + \nu(Re_1F_4)] + [\nu(Re_2F_6) + \nu(Re_2F_7) + \nu(Re_2F_5)]$
644.2(1)[151]	644.1(1)[152]	−0.1	659.7(1)[180]	659.6(1)[180]	−0.1	$[\nu(Re_1F_3) + \nu(Re_1F_3)] - [\nu(Re_2F_7) + \nu(Re_2F_5)]$
635.7(1)[20]	635.6(1)[21]	−0.1	651.3(1)[29]	651.1(1)[29]	−0.2	$[\nu(Re_1F_4) - \nu(Re_1F_3)] + [\nu(Re_2F_7) - \nu(Re_2F_5)]$
572.0(3)[98]	571.9(3)[97]	−0.1	586.4(3)[102]	586.2(3)[101]	−0.2	$[\nu(Re_1F_3) + \nu(Re_1F_4) - \nu(Re_1F_1)] + [\nu(Re_2F_5) + \nu(Re_2F_7) - \nu(Re_2F_6)]$
569.0(3)[18]	568.9(3)[18]	−0.1	583.3(3)[21]	583.1(3)[21]	−0.2	$[\nu(Re_1F_3) + \nu(Re_1F_4) - \nu(Re_1F_1)] - [\nu(Re_2F_5) + \nu(Re_2F_7) - \nu(Re_2F_6)]$
439.0(<1)[197]	437.6(<1)[208]	−1.4	452.4(<1)[207]	451.4(<1)[215]	−1.0	$[\nu(Re_1F_2) - \nu(Re_2F_2)] + [\delta(Re_1O_1F_1F_3F_4)_{umb} - \delta(Re_1O_4F_5F_6F_7)_{umb}]_{small}$
406.1(4)[3]	386.6(4)[2]	−19.5	413.6(5)[2]	394.1(4)[1]	−19.5	$[\nu(Re_1F_2) + \nu(Re_2F_2)] + [\delta(O_1Re_1O_2) + \delta(O_3Re_2O_4)]$
397.6(6)[16]	377.8(5)[9]	−19.8	404.4(5)[11]	384.0(4)[6]	−20.4	$[\delta(O_1Re_1O_2) - \delta(O_3Re_2O_4)]$
339.5(2)[8]	333.5(1)[11]	−6.0	348.1(1)[11]	344.8(1)[12]	−3.3	$[\delta(O_2Re_1F_4) + \delta(F_3Re_1F_1)] - [\delta(O_4Re_2F_5) + \delta(F_7Re_2F_6)]$
339.4(2)[3]	332.3(2)[3]	−7.1	344.0(2)[7]	337.1(2)[<1]	−6.9	$[\delta(O_2Re_1F_4) + \delta(F_3Re_2F_1)] + [\delta(O_4Re_2F_5) + \delta(F_7Re_2F_6)]$
336.4(1)[8]	332.0(2)[1]	−4.4	344.0(2)[<1]	337.0(2)[2]	−7.0	$[\nu(Re_1F_2) + \nu(Re_2F_2)] + \rho_w(O_1Re_1F_3) + \rho_w(O_3Re_2F_5)$
323.9(1)[14]	315.0(1)[9]	−8.9	327.6(1)[12]	318.9(1)[7]	−8.7	$[\delta(O_1Re_1F_3) - \delta(O_1Re_1F_4)] + [\delta(O_3Re_2F_7) + \delta(O_3Re_2F_5)]$
317.2(5)[12]	306.7(5)[10]	−10.5	320.1(5)[11]	309.3(5)[9]	−10.8	$[\delta(O_1Re_1F_3) - \delta(O_1Re_1F_4)] - [\delta(O_3Re_2F_7) + \delta(O_3Re_2F_5)]$
292.8(<1)[38]	289.1(<1)[43]	−3.7	296.1(<1)[40]	291.9(<1)[44]	−4.2	$[\delta(F_1Re_1F_4) - \delta(O_2Re_1F_3)] + [\delta(F_5Re_2O_4) + \delta(F_7Re_2F_6)] + [\rho_w(O_1Re_1F_2) + \rho_w(O_3Re_2F_2)]$
292.0(1)[2]	288.4(1)[2]	−3.6	295.6(1)[2]	291.7(1)[2]	−3.9	$[\delta(Re_1O_1F_1F_3F_4)_{umb}] + [\delta(Re_2O_4F_5F_6F_7)_{umb}] + \delta(Re_2F_2Re_1)$

Table D6. (continue…)

267.8(<1)[52]	265.0(<1)[47]	−2.8	271.4(<1)[54]	268.5(<1)[50]	−2.9	$[\delta(F_1Re_1F_3) - \delta(O_2Re_1F_4)] + [\delta(O_4Re_2F_7) - \delta(F_6Re_2F_5)] + \delta(Re_2F_2Re_1)$
243.0(1)[1]	241.4(1)[1]	−1.6	246.8(1)[1]	245.5(<1)[1]	−1.3	$[\delta(F_1Re_1F_4) - \delta(O_2Re_1F_3)] + [\delta(F_6Re_2F_7) - \delta(O_4Re_2F_5)] + \delta(Re_2F_2Re_1)$
227.6(1)[154]	226.3(1)[152]	−1.3	231.6(1)[137]	230.3(1)[136]	−1.3	$[\nu(Re_1F_2) - \nu(Re_2F_2)] + [\delta(Re_1O_1F_1F_3F_4)_{umb}] - [\delta(Re_2O_4F_5F_6F_7)_{umb}]$
225.9(1)[5]	222.4(1)[5]	−3.5	229.3(1)[5]	225.4(1)[5]	−3.9	$[\nu(Re_1F_2) + \nu(Re_2F_2)] + [\delta(F_1Re_1F_3) - \delta(O_2Re_1F_4)] + [\delta(F_6Re_2F_5) - \delta(O_4Re_2F_7)]$
187.5(<1)[5]	185.0(<1)[4]	−2.5	189.7(<1)[5]	187.3(<1)[4]	−2.4	$[\nu(Re_1F_2) + \nu(Re_2F_2)] + [\delta(O_1Re_1F_4) + \rho_w(O_2Re_1F_1)] + \rho_w(O_4Re_2F_6) - \delta(O_3Re_2F_7)]$
179.6(<1)[1]	177.9(<1)[1]	−1.7	181.7(<1)[1]	180.1(<1)[1]	−1.6	$[\rho_w(F_3Re_1F_4) + \rho_w(O_2Re_1F_1)] + [\rho_w(F_5Re_2F_7) + \rho_w(O_4Re_2F_6)]$
175.7(<1)[8]	173.1(<1)[10]	−2.6	177.1(<1)[8]	174.3(<1)[10]	−2.8	$[\rho_w(F_3Re_1F_4) + \rho_w(O_2Re_1F_1)] - [\rho_w(F_5Re_2F_7) + \rho_w(O_4Re_2F_6)]$
128.5(<1)[1]	124.8(<1)[<1]	−3.7	129.7(<1)[1]	126.0(<1)[1]	−3.7	$[\rho_w(F_3Re_1F_1) + \rho_r(O_2Re_1O_1)] + [\rho_w(F_5Re_2F_6) + \rho_r(O_3Re_2O_4)] + [\nu(Re_1F_2) + \nu(Re_2F_2)]_{small}$
108.6(<1)[<1]	107.2(<1)[<1]	−1.4	113.5(<1)[<1]	112.0(<1)[<1]	−1.5	$[\rho_w(F_1Re_1F_4) + \rho_r(O_2Re_1O_1)] + [\rho_w(F_5Re_2F_7) + \rho_r(O_3Re_2O_4)]$
99.6(<1)[<1]	98.0(<1)[<1]	−1.6	101.2(<1)[<1]	99.4(<1)[<1]	−1.8	$[\rho_w(O_2Re_1F_1) + \rho_r(F_3Re_1O_1)] + [\rho_w(O_4Re_2F_6) + \rho_r(O_3Re_2F_5)]$
33.4(<1)[<1]	32.4(<1)[<1]	−1.0	37.4(<1)[<1]	36.4(<1)[<1]	−1.0	
20.4(<1)[<1]	20.1(<1)[<1]	−0.3	23.1(<1)[<1]	22.8(<1)[<1]	−0.3	deformation modes
19.1(<1)[<1]	18.9(<1)[<1]	−0.2	20.1(<1)[<1]	19.7(<1)[<1]	−0.4	

[a] The aug-cc-pVDZ basis set was used. [b] The abbreviations denote shoulder (sh), stretch (ν), bend (δ), wag (ρ_w), and rock (ρ_r), umbrella (umb). The atoms labeling scheme is given in Figure D3c. [c] $\Delta\nu^{16/18} = \nu(^{18}O) - \nu(^{16}O)$.

Table D7. Calculated (B3LYP, C_i) Raman and Infrared Frequencies, Intensities, and Assignments for FXeOXeOXeF

calcd[a]				assgnts[b]
^{16}O	^{18}O	$\Delta\nu^{16/18}$		
554.1(51)[0]	528.3(63)[0]	−25.8	$\nu_1(A_g)$	$[\nu(Xe_1O_1) + (Xe_1O_{1A})] - [\nu(Xe_2O_1) + (Xe_{2A}O_{1A})]$
534.7(0)[789]	506.9(0)[635]	−27.8	$\nu_7(A_u)$	$[\nu(Xe_1O_1) - (Xe_1O_{1A})] - [\nu(Xe_2O_1) - (Xe_{2A}O_{1A})]$
493.0(0)[288]	484.4(0)[493]	−8.6	$\nu_8(A_u)$	$[\nu(Xe_1O_1) - (Xe_1O_{1A})] + [\nu(Xe_2O_1) - (Xe_{2A}O_{1A})] - [(Xe_2F_1) - (Xe_{2A}F_{1A})]$
477.5(164)[0]	473.3(157)[0]	−4.2	$\nu_2(A_g)$	$[(Xe_2F_1) + (Xe_{2A}F_{1A})]$
436.3(0)[582]	422.3(0)[435]	−14.0	$\nu_9(A_u)$	$[\nu(Xe_1O_1) - (Xe_1O_{1A})] + [\nu(Xe_2O_1) - (Xe_{2A}O_{1A})] + [(Xe_2F_1) - (Xe_{2A}F_{1A})]$
383.0(193)[0]	362.9(169)[0]	−20.1	$\nu_3(A_g)$	$[\nu(Xe_1O_1) + (Xe_1O_{1A})] + [\nu(Xe_2O_1) + (Xe_{2A}O_{1A})]$
210.6(0)[34]	202.4(0)[33]	−8.2	$\nu_{10}(A_u)$	$[\delta(Xe_2O_1Xe_1) - \delta(Xe_{2A}O_{1A}Xe_1)]_{o.o.p.} + [\delta(F_1Xe_2O_1) - \delta(F_{1A}Xe_{2A}O_{1A})]_{o.o.p.}$
183.2(3)[0]	179.2(3)[0]	−4.0	$\nu_4(A_g)$	$[\delta(Xe_2O_1Xe_1) + \delta(Xe_{2A}O_{1A}Xe_1)]_{o.o.p.} + [\delta(F_1Xe_2O_1) + \delta(F_{1A}Xe_{2A}O_{1A})]_{o.o.p.}$
181.9(0)[7]	181.7(0)[7]	−0.2	$\nu_{11}(A_u)$	$[\delta(Xe_2O_1Xe_1) - \delta(Xe_{2A}O_{1A}Xe_1)]_{i.p.} + [\delta(F_1Xe_2O_1) - \delta(F_{1A}Xe_{2A}O_{1A})]_{i.p.}$
141.8(11)[0]	141.6(11)[0]	−0.2	$\nu_5(A_g)$	$[\delta(F_1Xe_2O_1) + \delta(F_{1A}Xe_{2A}O_{1A})]_{i.p.}$
121.1(0)[1]	120.1(0)[2]	−1.0	$\nu_{12}(A_u)$	$[\rho_t(Xe_2O_1Xe_1) - \rho_t(Xe_{2A}O_{1A}Xe_1)] - [\rho_t(F_1Xe_2O_1) - \rho_t(F_{1A}Xe_{2A}O_{1A})]$
120.4(0)[4]	120.3(0)[4]	−0.1	$\nu_{13}(A_u)$	$[\delta(Xe_2O_1Xe_1) - \delta(Xe_{2A}O_{1A}Xe_1)]_{i.p.} - [\delta(F_1Xe_2O_1) - \delta(F_{1A}Xe_{2A}O_{1A})]_{i.p.}$
52.4(27)[0]	52.1(27)[0]	−0.3	$\nu_6(A_g)$	$[\delta(Xe_2O_1Xe_1) + \delta(Xe_{2A}O_{1A}Xe_1)]_{i.p.}$
29.3(0)[2]	29.1(0)[2]	−0.2	$\nu_{14}(A_u)$	$[\rho_r(Xe_2O_1Xe_1) - \rho_r(Xe_{2A}O_{1A}Xe_1)]$
−5.6(0)[1]	−5.5(0)[1]	−0.1	$\nu_{15}(A_u)$	$[\rho_t(Xe_2O_1Xe_1) - \rho_t(Xe_{2A}O_{1A}Xe_1)] - [\rho_t(F_1Xe_2O_1) - \rho_t(F_{1A}Xe_{2A}O_{1A})]$

[a] Frequencies are given in cm^{-1}. Values in parentheses denote Raman intensities ($Å^4$ amu^{-1}). Values in square brackets denote infrared intensities (km mol^{-1}). $\Delta\nu^{16/18} = \nu(^{18}O) - \nu(^{16}O)$. The aug-cc-pVDZ (-PP) basis set was used. [b] Bond elongations and angle openings are denoted by plus (+) signs and bond contractions and angle compressions are denoted by minus (–) signs. Abbreviations denote stretch (stretch (ν), bend (δ), rock (ρ_r), wag (ρ_w), twist (ρ_t), in-plane (i.p.), and out-of-plane (o.o.p.). The atoms labeling scheme is given in Figure D3b.

Table D8. Calculated (PBE1PBE, C_i) Raman and Infrared Frequencies, Intensities, and Assignments for FXeOXeOXeF

calcd[a]				assgnts[b]
^{16}O	^{18}O	$\Delta\nu^{16/18}$		
592.0(38)[0]	562.8(41)[0]	−29.2	$\nu_1(A_g)$	$[\nu(Xe_1O_1) + (Xe_1O_{1A})] - [\nu(Xe_2O_1) + (Xe_{2A}O_{1A})]$
566.7(0)[805]	537.9(0)[580]	−28.8	$\nu_7(A_u)$	$[\nu(Xe_1O_1) - (Xe_1O_{1A})] - [\nu(Xe_2O_1) - (Xe_{2A}O_{1A})]$
521.1(0)[330]	511.4(0)[606]	−9.7	$\nu_8(A_u)$	$[\nu(Xe_1O_1) - (Xe_1O_{1A})] + [\nu(Xe_2O_1) - (Xe_{2A}O_{1A})] - [(Xe_2F_1) - (Xe_{2A}F_{1A})]$
507.2(141)[0]	504.2(143)[0]	−3.0	$\nu_2(A_g)$	$[(Xe_2F_1) + (Xe_{2A}F_{1A})]$
460.8(0)[671]	446.1(0)[512]	−14.7	$\nu_9(A_u)$	$[\nu(Xe_1O_1) - (Xe_1O_{1A})] + [\nu(Xe_2O_1) - (Xe_{2A}O_{1A})] + [(Xe_2F_1) - (Xe_{2A}F_{1A})]$
409.7(195)[0]	388.2(171)[0]	−21.5	$\nu_3(A_g)$	$[\nu(Xe_1O_1) + (Xe_1O_{1A})] + [\nu(Xe_2O_1) + (Xe_{2A}O_{1A})]$
226.6(0)[34]	217.6(0)[33]	−9.0	$\nu_{10}(A_u)$	$[\delta(Xe_2O_1Xe_1) - \delta(Xe_{2A}O_{1A}Xe_1)]_{o.o.p.} + [\delta(F_1Xe_2O_1) - \delta(F_{1A}Xe_{2A}O_{1A})]_{o.o.p.}$
194.6(2)[0]	190.3(2)[0]	−4.3	$\nu_4(A_g)$	$[\delta(Xe_2O_1Xe_1) + \delta(Xe_{2A}O_{1A}Xe_1)]_{o.o.p.} + [\delta(F_1Xe_2O_1) + \delta(F_{1A}Xe_{2A}O_{1A})]_{o.o.p.}$
191.9(0)[6]	191.7(0)[6]	−0.2	$\nu_{11}(A_u)$	$[\delta(Xe_2O_1Xe_1) - \delta(Xe_{2A}O_{1A}Xe_1)]_{i.p.} + [\delta(F_1Xe_2O_1) - \delta(F_{1A}Xe_{2A}O_{1A})]_{i.p.}$
150.4(9)[0]	150.3(9)[0]	−0.1	$\nu_5(A_g)$	$[\delta(F_1Xe_2O_1) + \delta(F_{1A}Xe_{2A}O_{1A})]_{i.p.}$
129.2(0)[2]	128.3(0)[1]	−0.9	$\nu_{12}(A_u)$	$[\rho_t(Xe_2O_1Xe_1) - \rho_t(Xe_{2A}O_{1A}Xe_1)] - [\rho_t(F_1Xe_2O_1) - \rho_t(F_{1A}Xe_{2A}O_{1A})]$
127.0(0)[4]	126.9(0)[4]	−0.1	$\nu_{13}(A_u)$	$[\delta(Xe_2O_1Xe_1) - \delta(Xe_{2A}O_{1A}Xe_1)]_{i.p.} - [\delta(F_1Xe_2O_1) - \delta(F_{1A}Xe_{2A}O_{1A})]_{i.p.}$
53.9(21)[0]	53.6(21)[0]	−0.3	$\nu_6(A_g)$	$[\delta(Xe_2O_1Xe_1) + \delta(Xe_{2A}O_{1A}Xe_1)]_{i.p.}$
29.3(0)[2]	29.2(0)[2]	−0.1	$\nu_{14}(A_u)$	$[\rho_r(Xe_2O_1Xe_1) - \rho_r(Xe_{2A}O_{1A}Xe_1)]$
−2.9(0)[1]	−2.9(0)[1]	0.0	$\nu_{15}(A_u)$	$[\rho_t(Xe_2O_1Xe_1) - \rho_t(Xe_{2A}O_{1A}Xe_1)] - [\rho_t(F_1Xe_2O_1) - \rho_t(F_{1A}Xe_{2A}O_{1A})]$

[a] Frequencies are given in cm^{-1}. Values in parentheses denote Raman intensities (Å amu^{-1}). Values in square brackets denote infrared intensities (km mol^{-1}). $\Delta\nu^{16/18} = \nu(^{18}O) - \nu(^{16}O)$. The aug-cc-pVDZ (-PP) basis set was used. [b] Bond elongations and angle openings are denoted by plus (+) signs and bond contractions and angle compressions are denoted by minus (–) signs. Abbreviations denote stretch (stretch (ν), bend (δ), rock (ρ_r), wag (ρ_w), twist (ρ_t), in-plane (i.p.), and out-of-plane (o.o.p.). The atoms labeling scheme is given in Figure D.3b.

Table D9. Natural Population Analysis Charges, Natural Atomic Orbital Bond Orders, and Valences for [XeOXeOXe][μ-F(ReO_2F_3)$_2$]$_2$ (C_i), $[XeOXeOXe]^{2+}$ (C_{2h}), and FXeOXeOXeF (C_i)[a]

Atom	Charges	Valencies	Charges	Valencies	Bond	Bond order	
	B3LYP		PBE1PBE			B3LYP	PBE1PBE
[XeOXeOXe][μ-F(ReO_2F_3)$_2$]$_2$							
$Xe_{(1)}$	1.061	0.656	1.093	0.682	$Xe_{(1)}$–$O_{(1)}$	0.330	0.342
$Xe_{(2)}$	1.095	0.600	1.116	0.622	$Xe_{(2)}$–$O_{(1)}$	0.461	0.474
$O_{(1)}$	–0.792	0.786	–0.827	0.810	$Xe_{(2)}$–$F_{(1)}$	0.141	0.147
$F_{(1)}$	–0.621	0.443	–0.624	0.453	$Re_{(1)}$–$F_{(1)}$	0.309	0.313
$Re_{(1)}$	2.322	3.912	2.319	3.982	$Re_{(1)}$–$F_{(2)}$	0.326	0.331
$Re_{(2)}$	2.329	3.599	2.326	3.988	$Re_{(1)}$–$F_{(3)}$	0.570	0.577
$O_{(2)}$	–0.417	1.085	–0.416	1.107	$Re_{(1)}$–$F_{(4)}$	0.573	0.584
$O_{(3)}$	–0.424	1.080	–0.424	1.102	$Re_{(1)}$–$O_{(2)}$	1.070	1.089
$O_{(4)}$	–0.452	1.006	–0.454	1.093	$Re_{(1)}$–$O_{(3)}$	1.067	1.088
$O_{(5)}$	–0.442	1.021	–0.442	1.102	$Re_{(2)}$–$F_{(2)}$	0.180	0.219
$F_{(2)}$	–0.643	0.486	–0.639	0.534	$Re_{(2)}$–$F_{(5)}$	0.523	0.586
$F_{(3)}$	–0.466	0.569	–0.469	0.580	$Re_{(2)}$–$F_{(6)}$	0.419	0.481
$F_{(4)}$	–0.459	0.571	–0.454	0.584	$Re_{(2)}$–$F_{(7)}$	0.482	0.542
$F_{(5)}$	–0.458	0.519	–0.456	0.584	$Re_{(2)}$–$O_{(4)}$	0.990	1.073
$F_{(6)}$	–0.590	0.412	–0.586	0.478	$Re_{(2)}$–$O_{(5)}$	1.005	1.083
$F_{(7)}$	–0.513	0.480	–0.517	0.541			
$[XeOXeOXe]^{2+}$							
$Xe_{(1)}$	1.084	0.635	1.118	0.663	$Xe_{(1)}$–$O_{(1)}$	0.321	0.335
$Xe_{(2)}$	1.095	0.484	1.115	0.500	$Xe_{(2)}$–$O_{(1)}$	0.486	0.502
$O_{(1)}$	–0.637	0.808	–0.674	0.834			
FXeOXeOXeF							
$Xe_{(1)}$	0.966	0.692	1.002	0.700	$Xe_{(1)}$–$O_{(1)}$	0.342	0.345
$Xe_{(2)}$	1.044	0.660	1.069	0.669	$Xe_{(2)}$–$O_{(1)}$	0.395	0.399
$O_{(1)}$	–0.911	0.741	–0.947	0.747	$Xe_{(2)}$–$F_{(1)}$	0.259	0.263
$F_{(1)}$	–0.616	0.260	–0.623	0.263			

[a] The aug-cc-pVDZ (-PP) basis set was used.

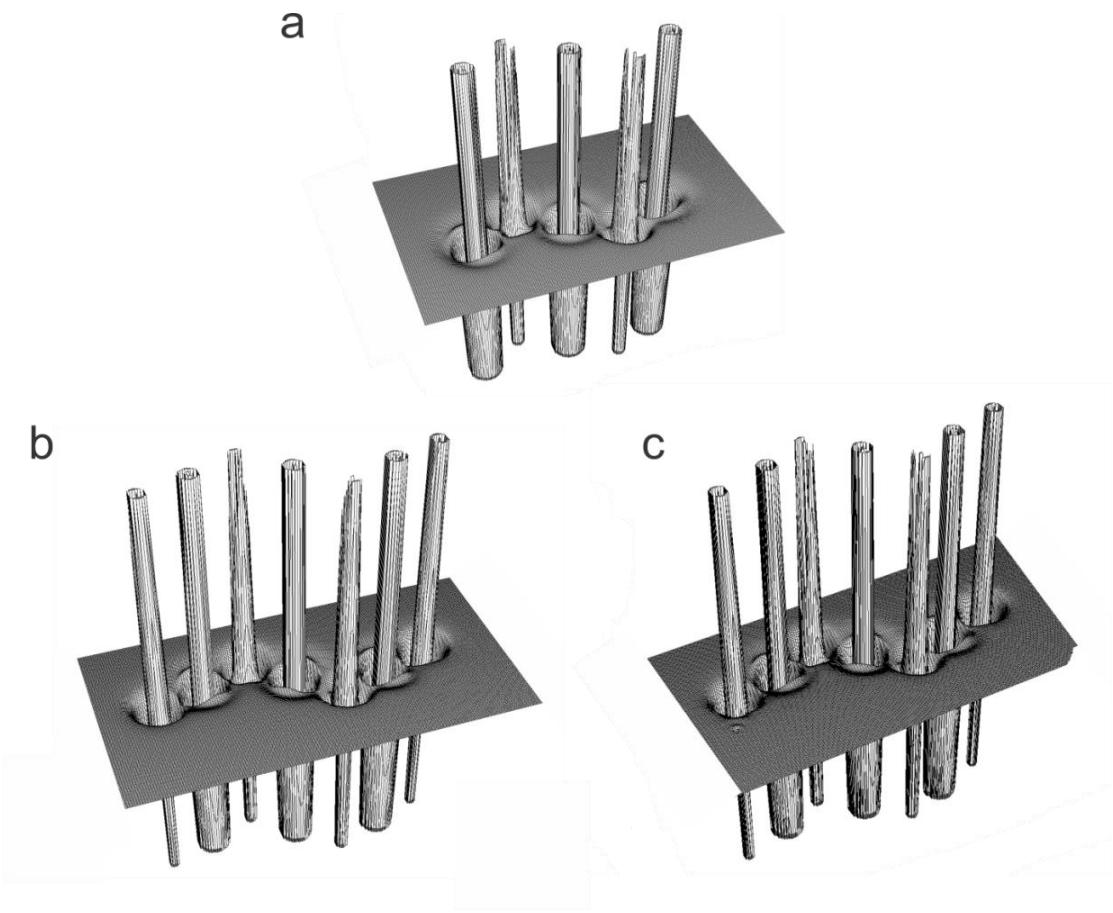

Figure D4. Relief map representations of the electron densities in the plane of (a) $[XeOXeOXe]^{2+}$, (b) FXeOXeOXeF, and (c) the F---XeOXeOXe---F moiety of the ion pair, $[XeOXeOXe][\mu\text{-}F(ReO_2F_3)]_2$.

Table D10. QTAIM Density of all Electrons (ρ_b), Laplacian of Electron Density ($\nabla^2\rho_b$), Energy Density (H_b), QTAIM Delocalization Indexes (δ), QTAIM Atomic Populations ($\bar{N}$), and ELF Basin Populations ($\bar{N}$) in $[XeOXeOXe]^{2+}$, FXeOXeOXeF, and $[XeOXeOXe][\mu\text{-}F(ReO_2F_3)_2]_2$ [a,b,c]

Bond	ρ_b	$\nabla^2\rho_b$	H_b	δ	$\bar{N}$		$\bar{N}$[A]	
$[XeOXeOXe][\mu\text{-}F(ReO_2F_3)_2]_2$								
$Xe_1–O_1$	0.098	0.177	−0.029	0.82	$\bar{N}(Xe_1)$	52.92	$\bar{N}[C(Xe_1)]$[d]	46.26
$Xe_2–O_1$	0.130	0.172	−0.056	1.13	$\bar{N}(Xe_2)$	52.88	$\bar{N}[V(Xe_1)]$	7.05
Xe_2---F_1	0.062	0.179	−0.010	0.44	$\bar{N}(O_1)$	8.80	$\bar{N}[C(Xe_2)]$[d]	46.33
					$\bar{N}(F_1)$	9.68	$\bar{N}[V(Xe_2)]$	6.98
							$\bar{N}[C(O_1)]$	2.16
							$\bar{N}[V(O_1)]$	6.87
							$\bar{N}[C(F_1)]$	2.15
							$\bar{N}[V(F_1)]$	7.58
$[XeOXeOXe]^{2+}$								
$Xe_1–O_1$	0.091	0.168	−0.024	0.80	$\bar{N}(Xe_1)$	52.90	$\bar{N}[C(Xe_1)]$[d]	46.24
$Xe_2–O_1$	0.133	0.148	−0.057	1.27	$\bar{N}(Xe_2)$	52.91	$\bar{N}[V(Xe_1)]$	7.04
					$\bar{N}(O_1)$	8.64	$\bar{N}[C(Xe_2)]$[d]	46.28
							$\bar{N}[V(Xe_2)]$	7.00
							$\bar{N}[C(O_1)]$	2.13
							$\bar{N}[V(O_1)]$	6.70
FXeOXeOXeF								
$Xe_1–O_1$	0.104	0.178	−0.034	0.88	$\bar{N}(Xe_1)$	53.04	$\bar{N}[C(Xe_1)]$[e]	45.73
$Xe_2–O_1$	0.115	0.182	−0.043	0.98	$\bar{N}(Xe_2)$	52.93	$\bar{N}[V(Xe_1)]$	7.12
$Xe_2–F_1$	0.104	0.248	−0.033	0.79	$\bar{N}(O_1)$	8.90	$\bar{N}[C(Xe_2)]$[e]	45.83
					$\bar{N}(F_1)$	9.64	$\bar{N}[V(Xe_2)]$	7.02
							$\bar{N}[C(O_1)]$	2.14
							$\bar{N}[V(O_1)]$	6.93
							$\bar{N}[C(F_1)]$	2.17
							$\bar{N}[V(F_1)]$	7.49

[a] PBE1PBE/aug-cc-pVDZ (-PP). [b] The au for $\nabla^2\rho_b$ is e/a_0^5 (1 au = 24.098 e Å^{-5}). The au for ρ_b is e/a_0^3 (1 au = 6.748 e Å^{-3}). The au for H is e^2/a_0^4 (1 au = E_h/a_0^3 = 6.748 E_h/Å^3). a_0 = Bohr radius = 0.52918 Å. e = charge on an electron. E_h = hartree = e^2/a_0. [c] For atom labeling, see Figures 3.1 and D.3. [d] $\bar{N}[C(Xe_1)] = ⅓\{178 – (2\ \bar{N}[C(O_1)] + 2\ \bar{N}[V(O_1)])\} – \bar{N}[V(Xe_1)]$; $\bar{N}[C(Xe_2)] = ⅓\{178 – (2\ \bar{N}[C(O_1)] + 2\ \bar{N}[V(O_1)])\} – \bar{N}[V(Xe_2)]$.[e] $\bar{N}[C(Xe_1)] = ⅓\{196 – (2\bar{N}[C(O)] + 2\bar{N}[V(O)] + 2\bar{N}[C(F)] + 2\bar{N}[V(F)])\} – \bar{N}[V(Xe_1)]$; $\bar{N}[C(Xe_2)] = ⅓\{196 – (2\bar{N}[C(O)] + 2\bar{N}[V(O)] + 2\bar{N}[C(F)] + 2\bar{N}[V(F)])\} – \bar{N}[V(Xe_2)]$.

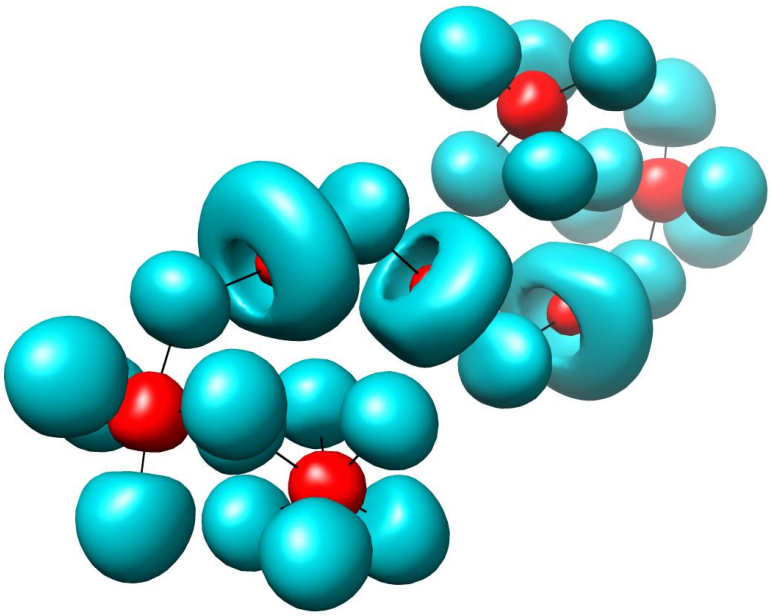

Figure D5. ELF isosurface plots (B3LYP/aug-cc-pVDZ(-PP), $\eta(\mathbf{r})$ = 0.60 for [XeOXeOXe] [μ-F(ReO_2F_3)$_2$]$_2$. Color code: red = core; blue = monosynaptic basin.

APPENDIX E

REACTION OF MnO_3F WITH NOBLE-GAS FLUORIDES, KrF_2 AND XeF_6

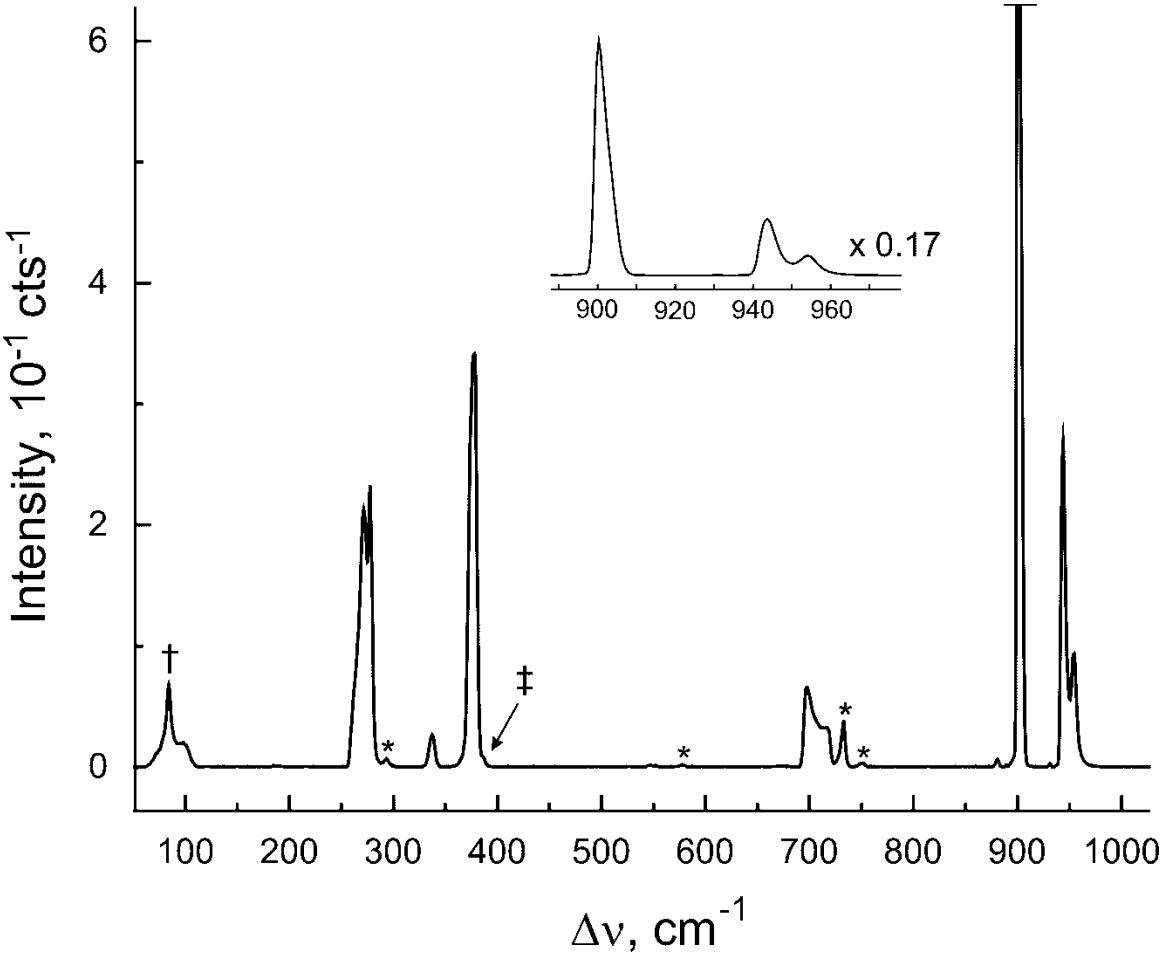

Figure E1. Raman spectrum of MnO_3F recorded at –150 ^{o}C using 1064-nm excitation. Symbols denote an FEP sample tube line (*), a MnO_3F line overlapping with an FEP line (‡), and an instrumental artifact (†). The bands at 881 (<1) and 931(<1) cm^{-1} are unassigned.

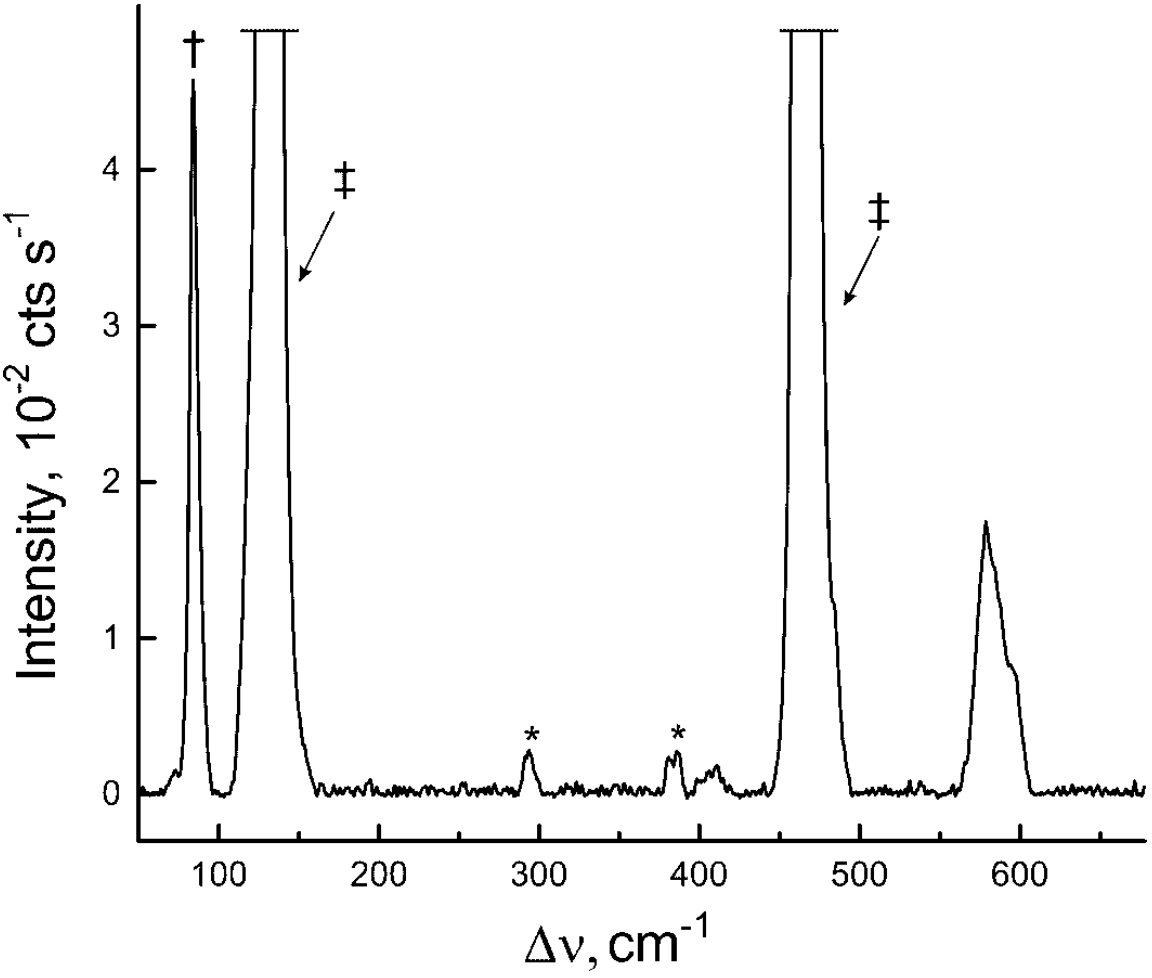

Figure E2. Raman spectrum of a red oil under frozen solution that resulted from the reaction of MnO_3F with KrF_2 in aHF. The spectrum was recorded at –150 ^{o}C using 1064-nm excitation. Symbols denote an FEP sample tube line (*), KrF_2 (‡), and an instrumental artifact (†).

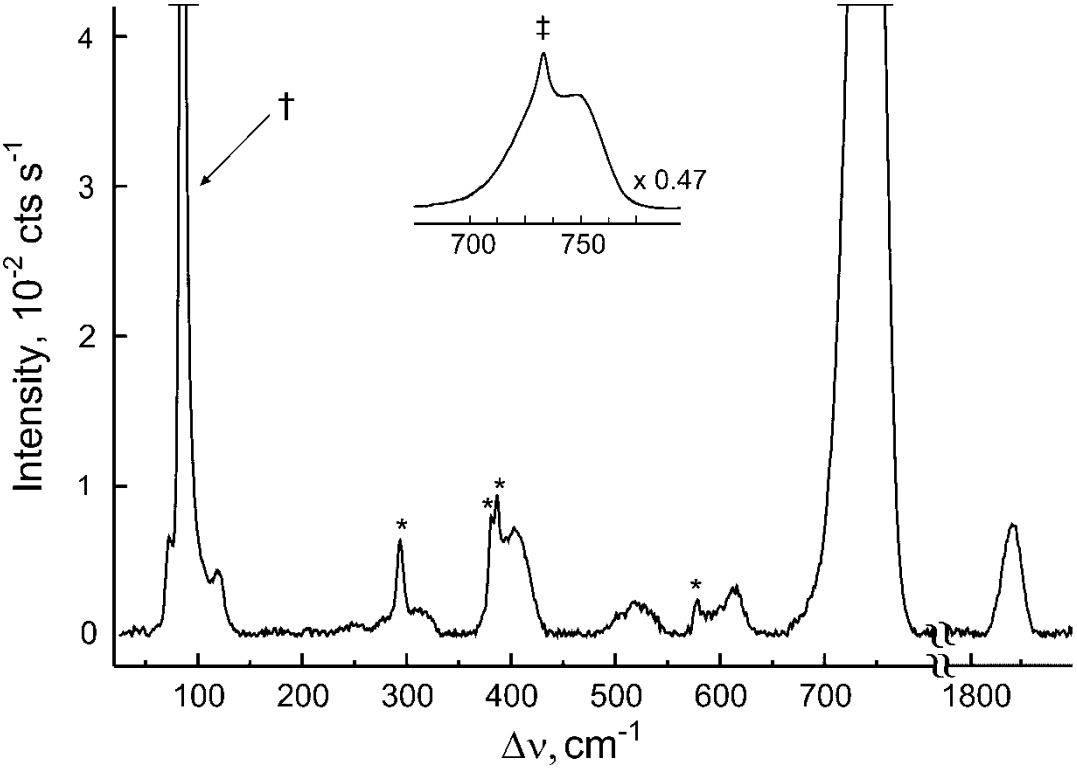

Figure E3. Raman spectrum of the isolated product resulting from the reaction of MnO_3F with KrF_2 in aHF. The spectrum was recorded at –150 ^oC using 1064-nm excitation. Symbols denote an FEP sample tube line (*), an instrumental artifact (†), overlap of a product line with an FEP sample tube line (‡). Broad bands observed at 119(7), 252(2), 401(12), 520(4), 614(5), 732(85), 747(100) cm^{-1} were tentatively assigned to $[O_2][MnF_6]$ or $[O_2][Mn_2F_9]$.

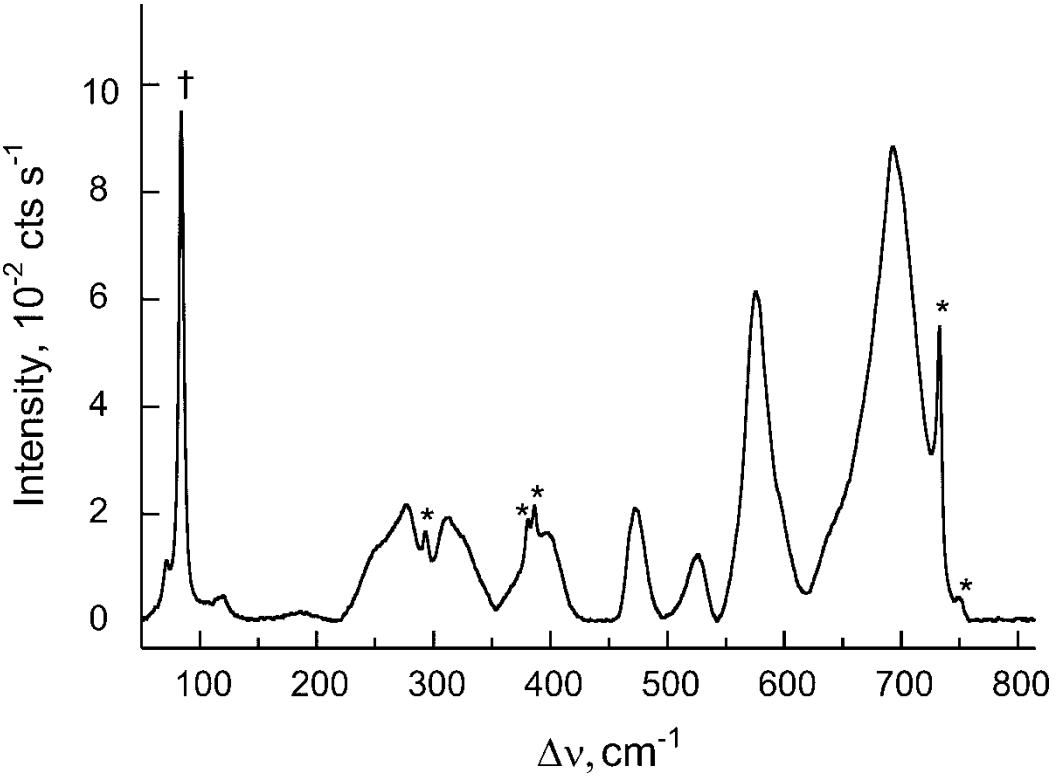

Figure E4. Raman spectrum of the product resulting from the reaction of MnO_3F with KrF_2 and $K[HF_2]$ in aHF. The spectrum was recorded at –150 ^oC using 1064-nm excitation. Symbols denote an FEP sample tube line (*) and an instrumental artifact (†). Broad bands observed at 119(5), 186(2), 247 sh, 276(25), 311(22), 325 sh, 398(17), 473(24), 525(14), 575(70), 595 sh, 645sh, 693(100) cm^{-1} were tentatively assigned to a solid mixture containing at least $K[MnF_6]$ and MnF_3.

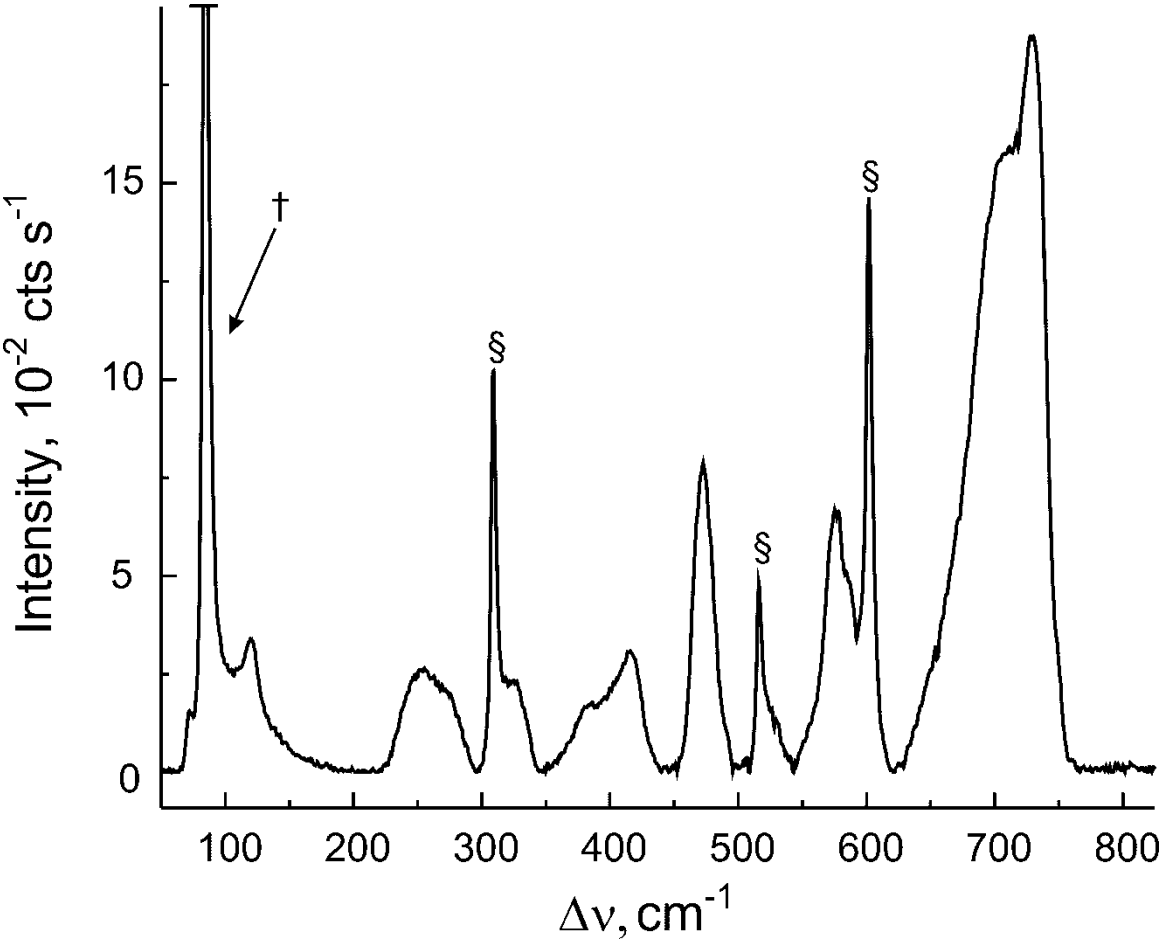

Figure E5. Raman spectrum of the product resulting from the reaction of MnO_3F with KrF_2 and $K[HF_2]$ in aHF. The spectrum was recorded in 4-mm i.d. glass at –140 ^{o}C using 1064-nm excitation. Symbols denote a $K_2[MnF_6]$ line (§) and an instrumental artifact (†).

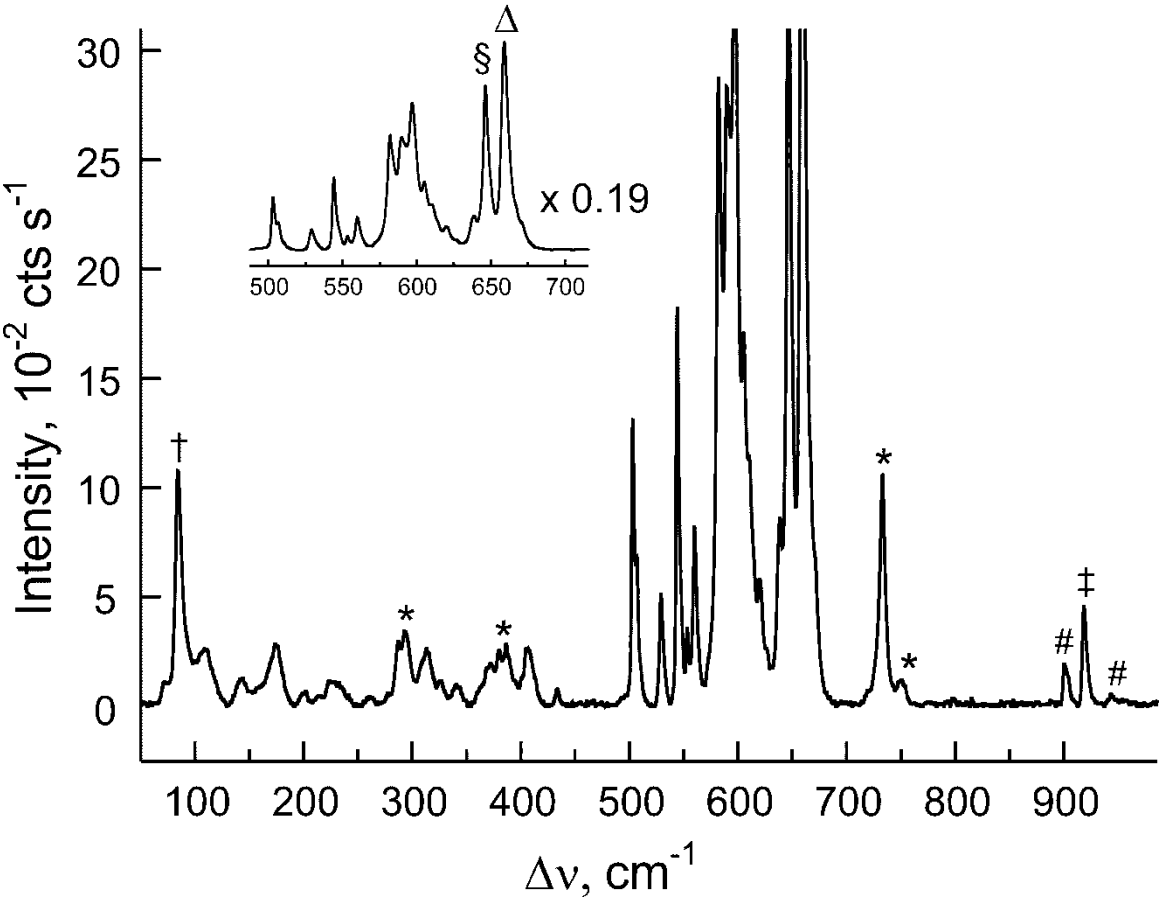

Figure E6. Raman spectrum of a solid mixture comprised of MnO_3F, $XeF_6 \cdot 1.5HF$, $[Xe_2F_{11}]_2[MnF_6]$, and $XeOF_4$ and/or $XeOF_4 \cdot XeF_6$ (see Section 7.2.2) recorded at –150 ^oC using 1064-nm excitation. Symbols denote an FEP sample tube line (*), an instrumental artifact (†), and the most intense lines for MnO_3F (#), $XeOF_4$ and/or $XeOF_4 \cdot XeF_6$ (‡), $[Xe_2F_{11}]_2[MnF_6]$ (§), and $XeF_6 \cdot 1.5HF$ (Δ).

Table E1. Selected Experimental and Calculated Bond Lengths and Bond Angles for the $[Xe_2F_{11}]^+$ and $[XeF_5]^+$ cations in $[Xe_2F_{11}]_2[MnF_6]$ and $[XeF_5]_2[MnF_6]$

$[Xe_2F_{11}]^+$				$[XeF_5]^+$		
exptl[a]		calcd			exptl[c]	calcd[d]
Bond Lengths (Å)						
Xe_1-F_4	2.247(2)	Xe_1-F_7	2.418	Xe_1-F_7	1.825(2)	1.851
Xe_1-F_5	1.834(2)	Xe_1-F_8	1.864	Xe_1-F_8	1.851(2)	1.892
Xe_1-F_6	1.855(2)	Xe_1-F_9	1.902	Xe_1-F_9	1.852(2)	1.894
Xe_1-F_7	1.848(2)	Xe_1-F_{10}	1.890	Xe_1-F_{10}	1.853(2)	1.895
Xe_1-F_8	1.869(2)	Xe_1-F_{11}	1.914	Xe_1-F_{11}	1.853(2)	1.890
Xe_1-F_9	1.861(2)	Xe_1-F_{12}	1.894	Xe_2-F_{12}	1.821(2)	1.848
Xe_2-F_{10}	1.830(2)	Xe_2-F_{13}	1.866	Xe_2-F_{13}	1.851(2)	1.892
Xe_2-F_{11}	1.850(2)	Xe_2-F_{14}	1.897	Xe_2-F_{14}	1.853(2)	1.892
Xe_2-F_{12}	1.864(2)	Xe_2-F_{15}	1.930	Xe_2-F_{15}	1.846(2)	1.894
Xe_2-F_{13}	1.866(2)	Xe_2-F_{16}	1.944	Xe_2-F_{16}	1.861(2)	1.890
Xe_2-F_{14}	1.864(2)	Xe_2-F_{17}	1.895			
Xe_2-F_4	2.260(2)	Xe_2-F_7	2.197			
Bond Angles (°)						
$F_4-Xe_1-F_5$	145.4(1)	$F_7-Xe_1-F_8$	146.0	$F_7-Xe_1-F_8$	78.0(1)	82.3
$F_4-Xe_1-F_6$	111.1(1)	$F_7-Xe_1-F_9$	113.9	$F_7-Xe_1-F_9$	77.9(1)	82.3
$F_4-Xe_1-F_7$	72.0(1)	$F_7-Xe_1-F_{10}$	71.8	$F_7-Xe_1-F_{10}$	79.8(1)	82.2
$F_4-Xe_1-F_8$	133.5(1)	$F_7-Xe_1-F_{11}$	128.9	$F_7-Xe_1-F_{11}$	79.1(1)	82.4
$F_4-Xe_1-F_9$	83.7(1)	$F_7-Xe_1-F_{12}$	80.4	$F_8-Xe_1-F_9$	155.5(1)	164.6
$F_4-Xe_2-F_{10}$	144.8(1)	$F_7-Xe_2-F_{13}$	161.2	$F_8-Xe_1-F_{10}$	84.6(1)	88.3
$F_4-Xe_2-F_{11}$	71.7(1)	$F_7-Xe_2-F_{14}$	87.5	$F_8-Xe_1-F_{11}$	88.6(1)	89.5
$F_4-Xe_2-F_{12}$	111.3(1)	$F_7-Xe_2-F_{15}$	115.1	$F_9-Xe_1-F_{10}$	87.6(1)	89.9
$F_4-Xe_2-F_{13}$	133.7(1)	$F_7-Xe_2-F_{16}$	103.1	$F_9-Xe_1-F_{11}$	90.4(1)	88.2
$F_4-Xe_2-F_{14}$	83.2(1)	$F_7-Xe_2-F_{17}$	81.0	$F_{10}-Xe_1-F_{11}$	158.7(1)	164.6
$F_5-Xe_1-F_6$	80.4(1)	$F_8-Xe_1-F_9$	81.6	$Xe_1---F_1-Mn_1$	108.9(1)	105.8
$F_5-Xe_1-F_7$	77.0(1)	$F_8-Xe_1-F_{10}$	79.7	$Xe_1---F_3-Mn_1$	107.9(1)	108.2
$F_5-Xe_1-F_8$	76.8(1)	$F_8-Xe_1-F_{11}$	79.1	$Xe_2---F_{2A}-Mn_{1A}$	108.0(1)	89.9
$F_5-Xe_1-F_9$	79.9(1)	$F_8-Xe_1-F_{12}$	80.1	$Xe_2---F_{4A}-Mn_{1A}$	108.3(1)	143.4
$F_6-Xe_1-F_7$	84.8(1)	$F_9-Xe_1-F_{10}$	86.2	$F_{12}-Xe_2-F_{13}$	78.0(1)	83.6
$F_6-Xe_1-F_8$	89.3(1)	$F_9-Xe_1-F_{11}$	88.3	$F_{12}-Xe_2-F_{14}$	77.6(1)	83.5
$F_6-Xe_1-F_9$	160.0(1)	$F_9-Xe_1-F_{12}$	162.6	$F_{12}-Xe_2-F_{15}$	80.6(1)	83.0
$F_7-Xe_1-F_8$	153.7(1)	$F_{10}-Xe_1-F_{11}$	158.6	$F_{12}-Xe_2-F_{16}$	79.8(1)	82.7
$F_7-Xe_1-F_9$	87.3(1)	$F_{10}-Xe_1-F_{12}$	89.4	$F_{13}-Xe_2-F_{14}$	155.6(1)	167.1
$F_8-Xe_1-F_9$	89.6(1)	$F_{11}-Xe_1-F_{12}$	89.7	$F_{13}-Xe_2-F_{15}$	85.7(1)	90.0
$Xe_1---F_1-Mn_1$	112.8(1)	$Xe_1---F_1-Mn_1$	110.0	$F_{13}-Xe_2-F_{16}$	86.3(1)	88.5
$Xe_1---F_3-Mn_1$	103.8(1)	$Xe_1---F_3-Mn_1$	109.4	$F_{14}-Xe_2-F_{15}$	89.6(1)	89.7
$Xe_1-F_4-Xe_2$	166.3(1)	$Xe_1-F_7-Xe_2$	173.7	$F_{14}-Xe_2-F_{16}$	90.9(1)	88.6
$F_{10}-Xe_2-F_{11}$	77.0(1)	$F_{13}-Xe_2-F_{14}$	84.4	$F_{15}-Xe_2-F_{16}$	159.9(1)	165.7
$F_{10}-Xe_2-F_{12}$	80.6(1)	$F_{13}-Xe_2-F_{15}$	81.7			
$F_{10}-Xe_2-F_{13}$	77.1(1)	$F_{13}-Xe_2-F_{16}$	83.3			
$F_{10}-Xe_2-F_{14}$	78.0(1)	$F_{13}-Xe_2-F_{17}$	81.8			
$F_{11}-Xe_2-F_{12}$	84.8(1)	$F_{14}-Xe_2-F_{15}$	88.5			
$F_{11}-Xe_2-F_{13}$	153.9(1)	$F_{14}-Xe_2-F_{16}$	167.1			

Table E1. (continued…)

F_{11}−Xe_2−F_{14}	86.8(1)	F_{14}−Xe_2−F_{17}	87.5
F_{12}−Xe_2−F_{13}	89.3(1)	F_{15}−Xe_2−F_{16}	93.5
F_{12}−Xe_2−F_{14}	159.8(1)	F_{15}−Xe_2−F_{17}	163.3
F_{13}−Xe_2−F_{14}	90.3(1)	F_{16}−Xe_2−F_{17}	86.9

[a] For the atom labeling scheme see Figure 7.Xa. [b]For the atom labeling scheme see Figure 7.Xa (B3LYP/def2-SVP(F, Mn)/aug-cc-pVTZ(-PP) (Xe)). [c] For the atom labeling scheme see Figure 7.Xb. [d] For the atom labeling scheme see Figure 7.Xb (B3LYP/def2-SVP(F, Mn)/aug-cc-pVTZ(-PP) (Xe)).

Table E2. Experimental Bond Lengths, Contacts, and Bond Angles for $K_2[MnF_6]$ in the Crystal structure of $K_2[MnF_6]\cdot 4HF$ and Calculated Bond Lengths and Bond Angles for $[MnF_6]^{2-}$

$K_2[MnF_6]$ exptl[a]		$[MnF_6]^{2-}$ (O_h) calcd[b]			
			B3LYP[c]	B3LYP[d]	PBE1PBE[c]
Bond Lengths (Å)					
Mn_1-F_1	1.8064(5)				
Mn_1-F_2	1.7895(5)	Mn_1-F_1	1.8403	1.8266	1.8253
Mn_1-F_3	1.8060(5)				
$K_{1D}---F_1$	2.6938(6)				
K_1---F_2	2.8173(6)				
$K_{1E}---F_2$	2.7156(5)				
$K_{1A}---F_3$	2.7618(6)				
Bond Angles (°)					
$F_1-Mn_1-F_{1A}$	180.00(3)		90.0		
$F_1-Mn_1-F_2$	90.47(3)		180.0		
$F_1-Mn_1-F_{2A}$	89.53(3)		90.0		
$F_1-Mn_1-F_3$	89.94(3)		90.0		
$F_1-Mn_1-F_{3A}$	90.06(3)		90.0		
$F_2-Mn_1-F_{2A}$	180.00(3)		180.0		
$F_2-Mn_1-F_3$	90.22(2)		90.0		
$F_2-Mn_1-F_{3A}$	89.78(2)		90.0		
$F_3-Mn_1-F_{3A}$	180.00(3)		180.0		

[a] For the atom labeling scheme see Figures E6a and E6b. [b] For the atom labeling scheme see Figure E6c. [c] The aug-cc-pVTZ basis set was used. [d] The def2-SVP basis set was used.

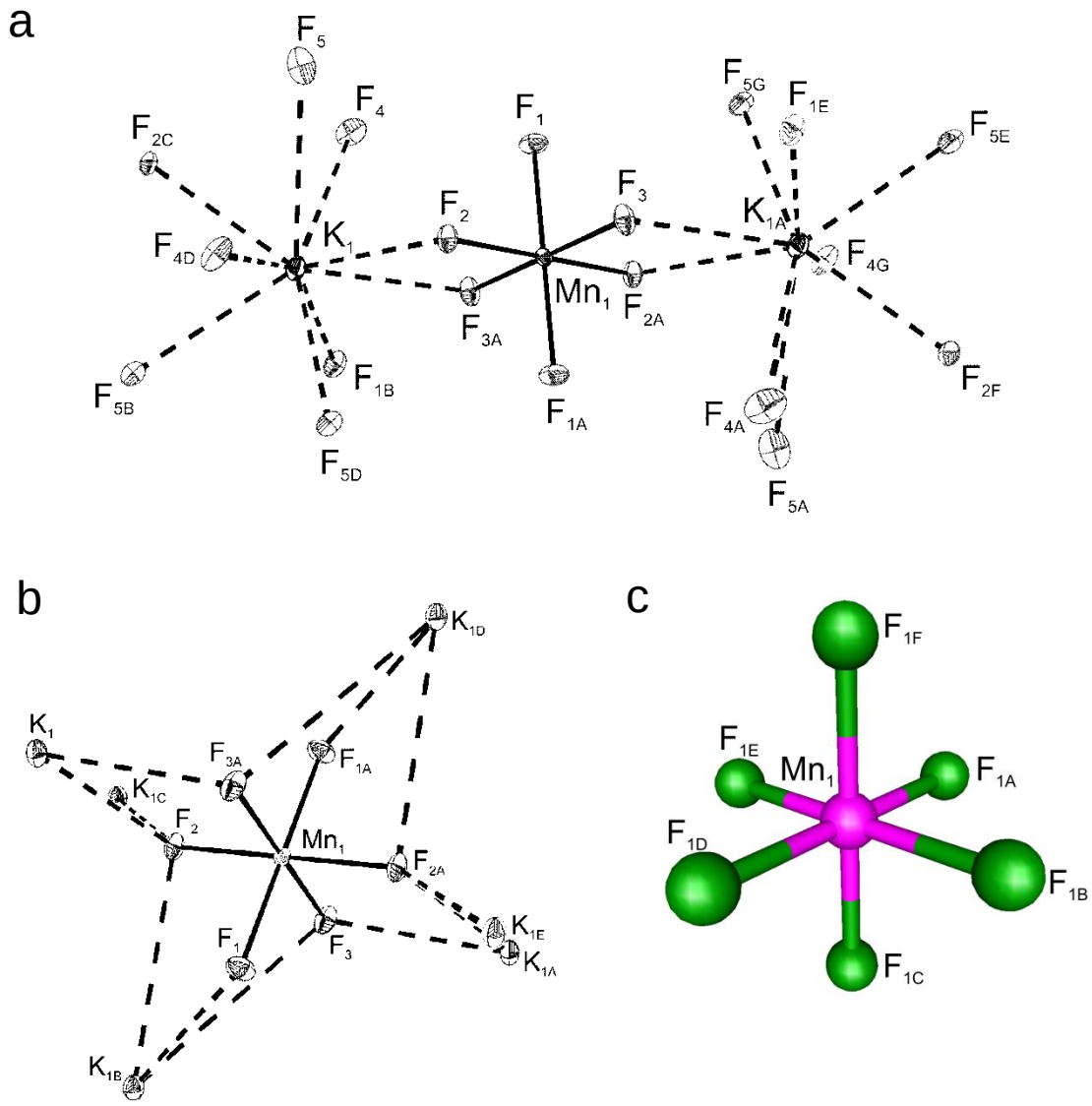

Figure E7. Crystal structure of $K_2[MnF_6]\cdot 4HF$ showing the coordination environment around (a) the K^+ cation and (b) the $[MnF_6]^{2-}$ anion. Thermal ellipsoids are drawn at the 50% probability level. (c) The calculated structure of the $[MnF_6]^{2-}$ anion (B3LYP/aug-cc-pVTZ).

.

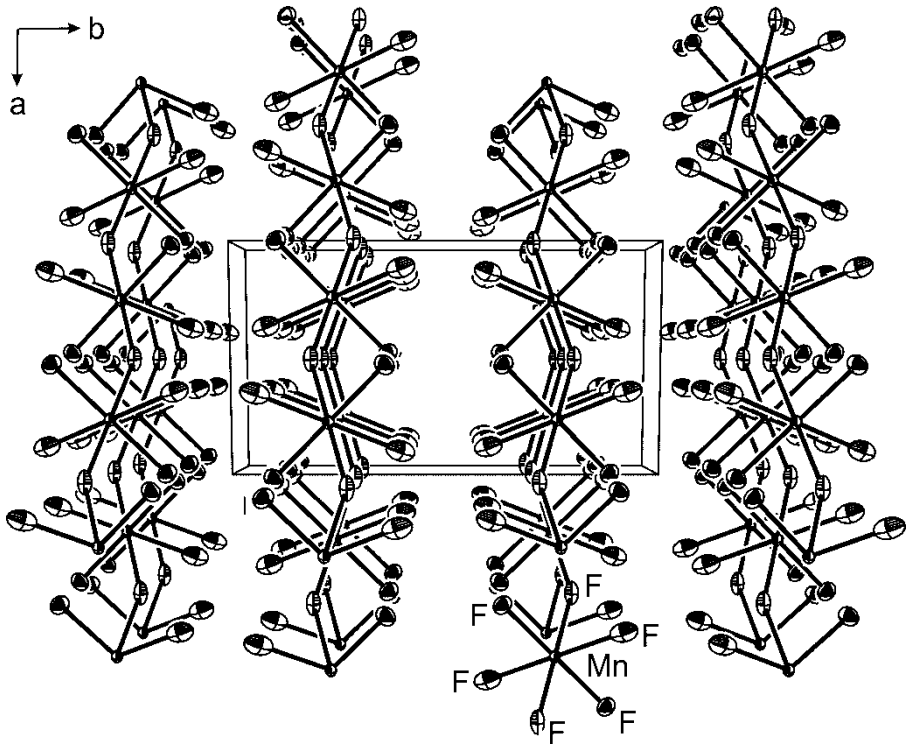

Figure E8. Packing of MnF_5 along the *c*-axis. Thermal ellipsoids are drawn at the 50% probability level.

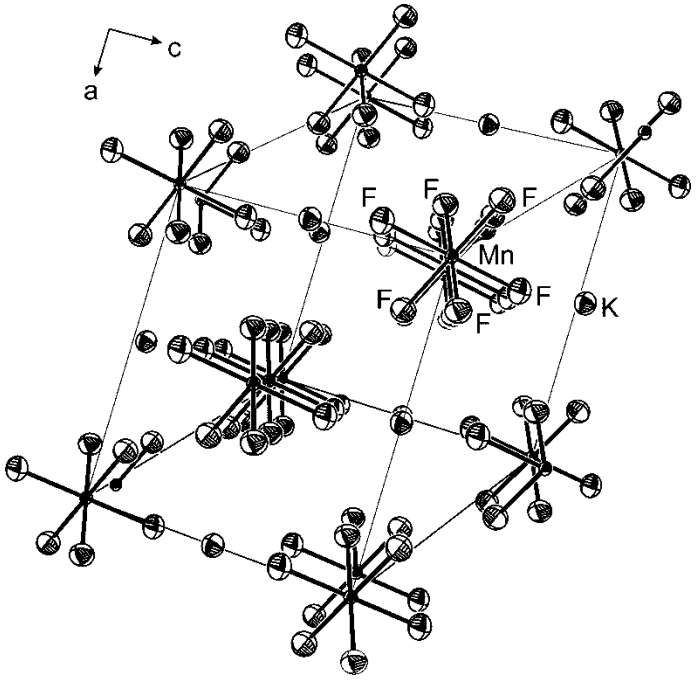

Figure E9. Packing of $K[MnF_6]$ along the *b*-axis. Thermal ellipsoids are drawn at the 50% probability level.

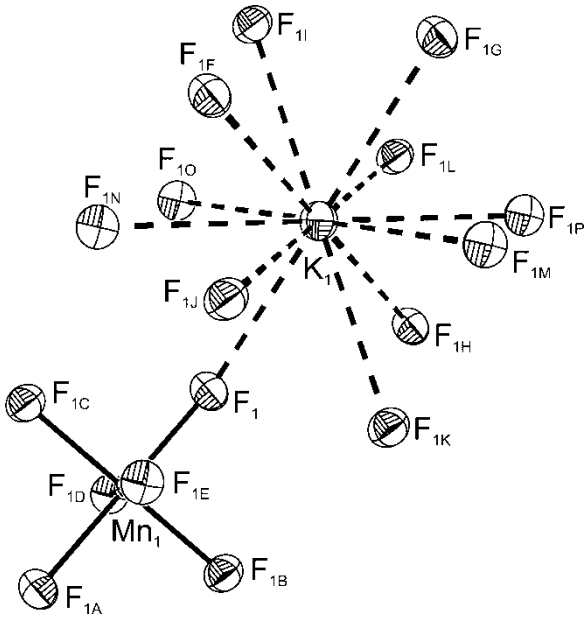

Figure E10. View showing contacts around the K^+ cation in the crystal structure of $K[MnF_6]$. Thermal ellipsoids are drawn at the 50% probability level.

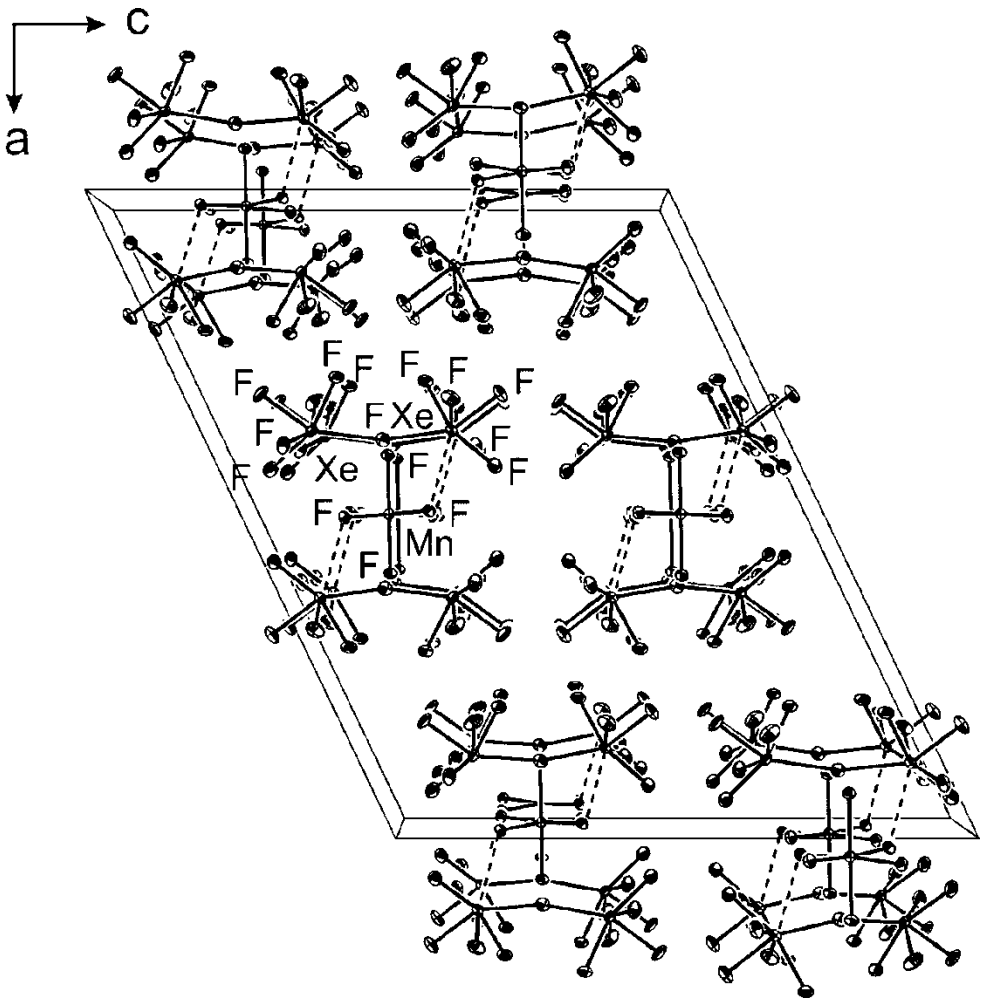

Figure E11. Packing of $[Xe_2F_{11}]_2[MnF_6]$ along the *b*-axis. Thermal ellipsoids are drawn at the 50% probability level.

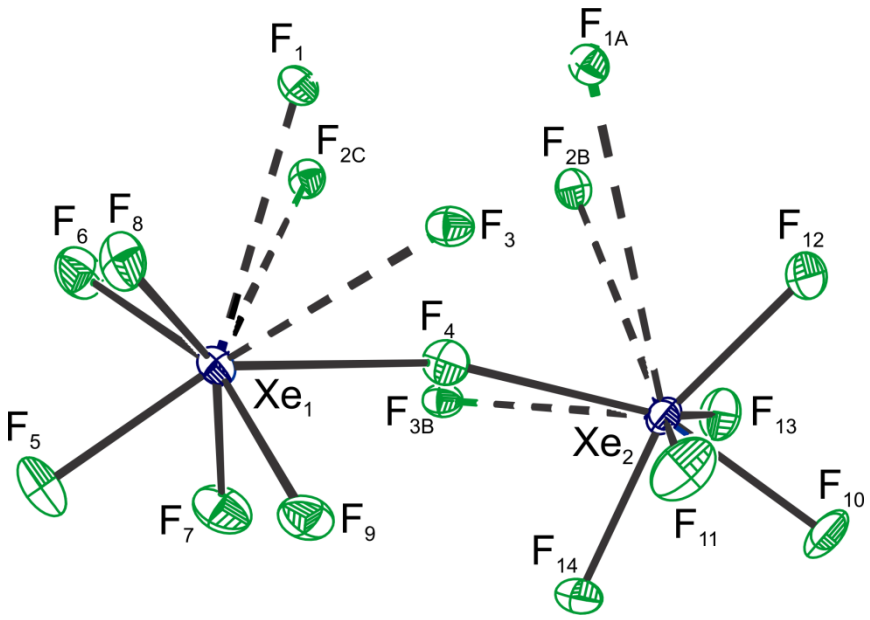

Figure E12. The coordination around the $[Xe_2F_{11}]^+$ cation in the crystal structure of $[Xe_2F_{11}]_2[MnF_6]$. Thermal ellipsoids are drawn at the 50% probability level.

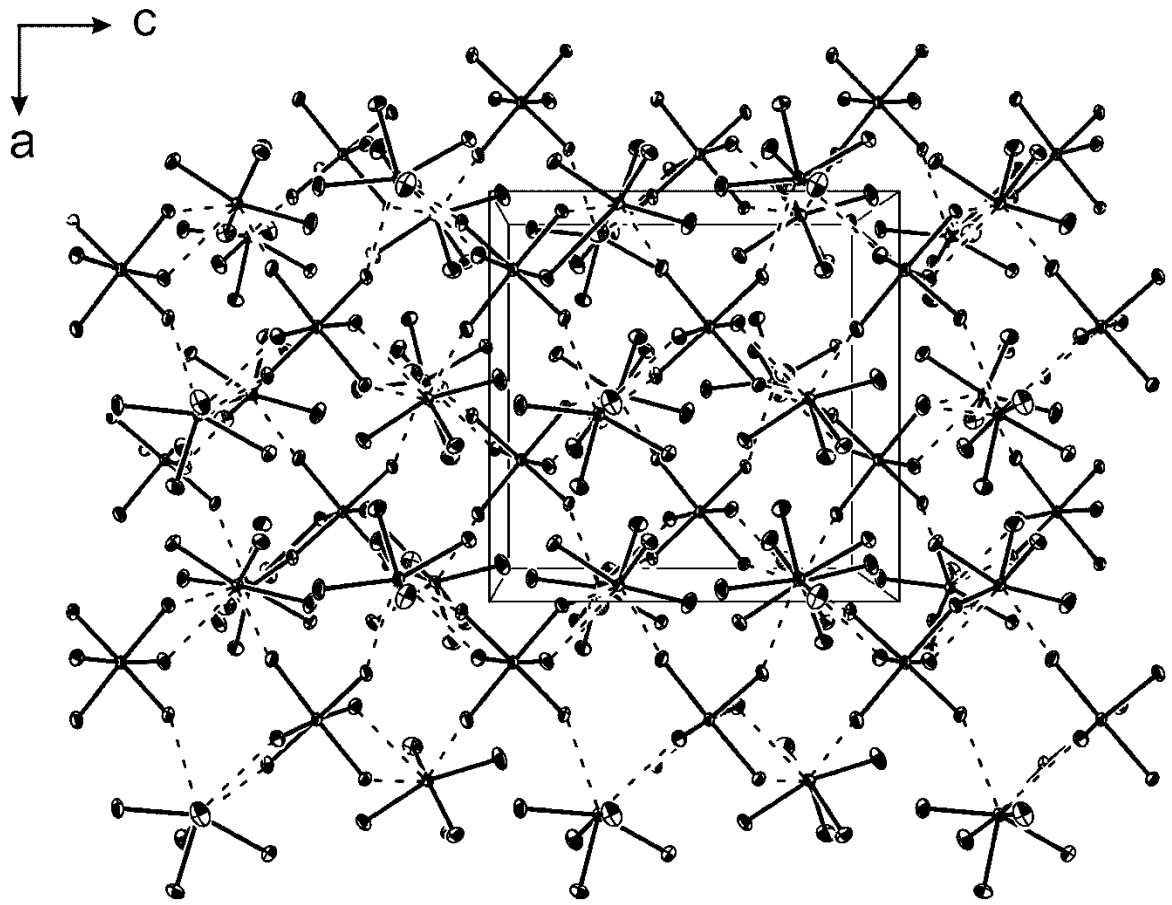

Figure E13. Packing of $[XeF_5]_2[MnF_6]$ along the *b*-axis. Thermal ellipsoids are drawn at the 50% probability level.

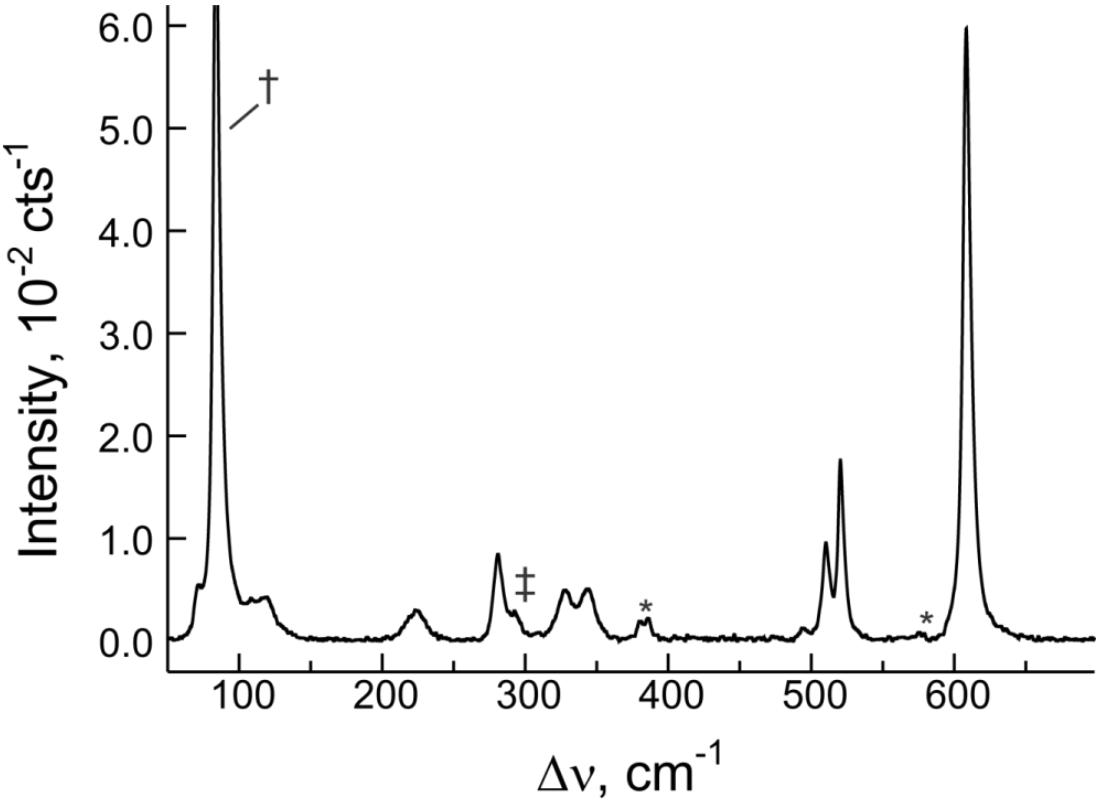

Figure E14. Raman spectrum of $K_2[MnF_6]\cdot 4HF$ recorded at –140 ^{o}C using 1064-nm excitation. Symbols denote FEP sample tube lines (*), an instrumental artifact (†), and overlap of a $K_2[MnF_6]\cdot 4HF$ line with an FEP line (‡).

Table E3. Experimental Raman Frequencies and Intensities for $[XeF_5]_2[MnF_6]$ and Calculated Vibrational Frequencies, Intensities, and Assignments for $\{[XeF_5]_4[MnF_6]\}^{2+}$

$[XeF_5]_2[MnF_6]$	$\{[XeF_5]_4[MnF_6]\}^{2+}$ (C_1)	
exptl[a,b]	calcd[a,c]	assgnts[d]
681 sh 676(4)	678(5)[289] 676(4)[430] 675(5)[487] 672(16)[4] 672(11)[36]	$\nu(XeF_{eq})$
656(100) 640(12)	666(93)[5] 666(7)[87] 665(7)[87] 664(7)[50] 664(8)[15]	$\nu(XeF_{ax}) + \nu(XeF_{eq})$
	660(52)[112] 659(41)[113]	$\nu(XeF_{ax})$
623(7)	621(19)[124]	$[\nu(MnF_b) - \nu(XeF_b)]_{oop} + [\nu(XeF_{ax}) + \nu(XeF_{eq})]$
	617(35)[49]	$[\nu(XeF_{eq}) - \nu(XeF_{ax})] + [\nu(MnF_b) - \nu(XeF_b)]_{small}$
602(78)	612(3)[20] 606(55)[5]	$\nu(XeF_{eq})$
597(64)	595(31)[74] 591(25)[54] 589(1)[46]	$[\nu(MnF_b) - \nu(XeF_b)]_{ip} + \nu(XeF_{eq})$
	590(9)[1] 588(16)[3] 587(2)[8]	$\nu(XeF_{eq})$
583(9)	573(8)[228]	$[\nu(MnF_b) - \nu(XeF_b)]_{oop}$
563(33)	544(47)[153]	$[\nu(MnF_b) - \nu(XeF_b)]_{ip}$
497 sh 493(16)	470(20)[99]	$[\nu(MnF_b) - \nu(XeF_b)]_{oop}$
430(3) 402(2) 394(2)	447(27)[297]	
358 sh 352(5)	356(4)[37] 352(5)[80]	$\delta(F_bMnF_b)$
346 sh 330(2)	346(1)[4] 345(1)[5] 343(1)[3] 342(1)[1] 338(1)[6] 336(1)[5] 335(1)[4] 330(1)[4]	$\delta(F_{ax}XeF_{eq})$

Table E3. (continued…)

320(5) 312(6)	315(1)[7]	$\delta(F_bMnF_b)$
306(8)	306(2)[96] 300(12)[1] 298(<1)[118] 295(3)[63]	$\delta(F_bMnF_b) - \delta(F_{eq}XeF_{eq})_{umb}$
298 sh 279(<1)	286(6)[9] 281(20)[38] 278(2)[7]	$\delta(F_bMnF_b)$
265(2)	260(2)[<1] 259(2)[<1] 259(2)[<1] 258(2)[<1]	$\delta(F_{eq}XeF_{eq})$
236 sh	239(1)[2]	$\delta(F_bMnF_b)$
226(1)	215(<1)[5] 213(<1)[2]	$\delta(F_bMnF_b) - \rho_t(F_{eq}XeF_{eq})$
200(1)	200(<1)[2] 197(<1)[4]	$\rho_t(F_bMnF_b) - \rho_t(F_{eq}XeF_{eq})$
178(1)	191(<1)[1] 189(<1)[1]	$\rho_t(F_{eq}XeF_{eq})$
	188(<1)[3] 188(<1)[1] 186(<1)[7] 185(<1)[<1]	$\delta(F_{eq}XeF_{ax})$
164(2)	180(<1)[1] 180(<1)[2] 179(<1)[2] 177(<1)[2]	$\delta(F_{eq}XeF_{eq}) + \delta(F_{eq}XeF_{ax})$
137(1)	135(2)[42]	$\rho_r(F_bMnF_b)$
126(1) 111(3) 96(2)	114(1)[31] 108(1)[30] 104(1)[15] 98(1)[6] 76(<1)[<1] 70(1)[<1] 64(<1)[<1] 63(1)[1] 55(<1)[1] 44(<1)[<1] 35(<1)[<1] 29(<1)[<1] 25(<1)[1] 18(<1)[<1] 17(<1)[<1] 16(<1)[<1] 13(<1)[<1] 13(<1)[<1] 12(<1)[<1] 10(<1)[<1] 9(<1)[<1]	deformation modes

Table E3. (continued…)

8(<1)[<1] −12(<1)[<1]	deformational modes

[a] Frequencies are given in cm^{-1}. [b] Values in parentheses denote relative Raman intensities. Raman spectrum was recorded in FEP sample tubes at –140 °C using 1064-nm excitation. The abbreviation denotes shoulder (sh). [c] Values in parentheses denote calculated Raman intensities ($Å^4$ u^{-1}). Values in square brackets denote calculated infrared intensities (km mol^{-1}). The B3LYP/def2-SVP (Mn, F)/aug-cc-pVTZ(-PP) (Xe) method was used. [d] The abbreviations denote stretch (ν), bend (δ), rock (ρ_r), twist (ρ_t), umbrella (umb), equatorial (eq), axial (ax), in-phase (ip), out-of-phase (oop), and bridging (b).

Table E4. Experimental Raman Frequencies and Intensities for $[Xe_2F_{11}]_2[MnF_6]$ and Calculated Vibrational Frequencies, Intensities, and Assignments for $\{[Xe_2F_{11}]_4[MnF_6]\}^{2+}$

$[Xe_2F_{11}]_2[MnF_6]$	$\{[Xe_2F_{11}]_4[MnF_6]\}^{2+}$ (C_1)	
exptl[a,b]	calcd[a,c]	assgnts[d]
	668(<1)[344]	
	664(2)[551]	
666(16)	662(19)[55]	
	659(1)[401]	
	659(46)[1]	
	654(27)[59]	
	653(44)[284]	
	653(292)[3]	
646(100)	651(1)[1]	
	647(9)[270]	
	647(17)[670]	
	645(2)[21]	
	645(12)[12]	ν(XeF)
	641(20)[98]	
	641(6)[339]	
	640(21)[92]	
639(12)	639(48)[185]	
	637(1)[2]	
	637(1)[311]	
	635(23)[1]	
	632(<1)[24]	
	630(2)[12]	
631(1)	630(4)[1]	
	629(<1)[10]	
	598(<1)[84]	
619(5)	594(4)[106]	$[\nu(MnF_b) - \nu(XeF_b)] + \nu(XeF)$
611(9)		
	590(4)[3]	
597(13)	589(86)[<1]	ν(XeF)
589(40)		
	586(1)[57]	$[\nu(MnF_b) - \nu(XeF_b)] + \nu(XeF)$
	582(8)[1]	
	581(1)[25]	ν(XeF)
	581(34)[<1]	
582(25)	579(12)[4]	
581 sh	575(1)[171]	$[\nu(MnF_b) - \nu(XeF_b)] + \nu(XeF)$
	572(16)[23]	
	571(35)[5]	
	570(11)[2]	ν(XeF)
	566(23)[55]	
560(2)	563(22)[56]	$[\nu(MnF_b) - \nu(XeF_b)]$
	561(4)[57]	$[\nu(MnF_b) - \nu(XeF_b)] + \nu(XeF)$

Table E4. (continued…)

560(2)	546(16)[4]	ν(XeF)
	546(4)[50]	
	546(28)[2]	
	545(4)[28]	
433(2)	471(2)[<1]	[ν(MnF_b) − ν(XeF_b)]
	462(3)[1]	
387(3)	378(1)[170]	[ν(XeF_b) − ν(XeF_b)]
	377(1)[81]	
	376(1)[48]	
	375(3)[24]	
373(3)	370(2)[391]	δ(F_bMnF_b) + [ν(XeF_b) − ν(XeF_b)] + δ(FXeF)
	360(6)[80]	δ(F_bMnF_b) + [ν(XeF_b) − ν(XeF_b)]
	356(20)[15]	
358(1)	352(8)[2]	δ(FXeF)
	352(2)[9]	
	350(<1)[4]	
	350(1)[3]	
	348(41)[1]	δ(FXeF) + [ν(XeF_b) − ν(XeF_b)] + [ν(XeF_b) + ν(XeF_b)]
341(1)	342(5)[5]	δ(FXeF)
	341 (2)[4]	
	337(4)[60]	δ(F_bMnF_b) + δ(FXeF)
	335(1)[28]	
	332(4)[110]	δ(F_bMnF_b) + δ(FXeF)
	331(<1)[126]	[ν(XeF_b) − ν(XeF_b)] + δ(F_bMnF_b)
	329(3)[36]	δ(F_bMnF_b)
314(5)	319(1)[131]	δ(F_bMnF_b) + δ(FXeF)
	318(3)[153]	
	316(1)[91]	δ(FXeF)
	315(1)[16]	
	312(1)[28]	
	311(1)[13]	
	308(1)[2]	
	307(1)[2]	
295(1)	302(2)[62]	δ(F_bMnF_b)
	301(1)[9]	
	288(7)[<1]	
261(3)	271(1)[3]	δ(FXeF)
	269(2)[9]	
	266(2)[3]	δ(FXeF) + ρ_r(FXeF)
	264(<1)[7]	ρ_r(FXeF)
	264(1)[4]	
	263(5)[9]	δ(FXeF) + ρ_r(FXeF)
	259(4)[14]	
	257(1)[27]	
255 sh	253(2)[12]	δ(FXeF) + δ(FXeF)
	251(<1)[2]	ρ_r(FXeF)
	246(1)[14]	δ(FXeF) + ρ_r(FXeF)

Table E4. (continued…)

238(<1)	244(1)[1]	[ν(XeF$_b$) + ν(XeF$_b$)]
	244(3)[<1]	δ(F$_b$MnF$_b$) + δ(FXeF)
	241(1)[1]	δ(FXeF)
	240(1)[4]	δ(F$_b$MnF$_b$) + δ(FXeF)$_{small}$
	239(<1)[16]	δ(FXeF)
	234(1)[<1]	δ(F$_b$MnF$_b$)
214(1)	224(<1)[22]	δ(F$_b$MnF$_b$) + δ(FXeF)$_{small}$
	222(<1)[1]	
199(3)	205(1)[5]	(FXeF) deformation modes
	204(<1)[13]	
	203(<1)[30]	
	203(<1)[1]	
	202(<1)[4]	
	201(<1)[5]	
	195(<1)[<1]	
	193(2)[2]	
	191(<1)[10]	
	190(<1)[<1]	
	189(<1)[1]	
	187(<1)[1]	
	186(<1)[4]	
	185(<1)[<1]	
176(<1)	180(<1)[3]	
	179(<1)[3]	
	176(1)[5]	
	174(3)[<1]	
	173(1)[7]	
	170(1)[1]	
158(1)	154(<1)[<1]	
	152(<1)[3]	
	149(<1)[5]	
	147(<1)[1]	
143(1)	140(2)[19]	δ(F$_b$MnF$_b$)
	138(<1)[17]	ρ$_r$(F$_b$MnF$_b$)
109(1)	120(<1)[3]	deformation modes
	117(<1)[11]	
	113(3)[1]	
	113(<1)[25]	
	111(1)[9]	
	109(1)[9]	
	105(1)[<1]	
	101(<1)[2]	
	96(<1)[3]	
	95(1)[1]	
	92(<1)[3]	
	90(2)[<1]	
	88(<1)[3]	
	82(1)[<1]	
	80(<1)[<1]	

Table E4. (continued…)

79(<1)[2]	
78(<1)[<1]	
74(<1)[4]	
72(<1)[37]	
60(<1)[<1]	
58(1)[<1]	
57(<1)[1]	
53(<1)[<1]	
52(<1)[2]	
51(<1)[<1]	
50(<1)[<1]	
48(<1)[<1]	
47(<1)[<1]	
46(<1)[<1]	
41(<1)[3]	
41(<1)[<1]	
40(<1)[1]	
37(<1)[1]	deformation modes
36(<1)[1]	
35(<1)[1]	
32(<1)[1]	
32(<1)[1]	
27(<1)[1]	
26(<1)[<1]	
25(<1)[<1]	
23(<1)[<1]	
23(<1)[1]	
19(<1)[<1]	
18(<1)[<1]	
17(<1)[2]	
15(<1)[<1]	
13(<1)[1]	
8(<1)[3]	
7(<1)[<1]	
−3(<1)[<1]	

[a] Frequencies are given in cm^{-1}. [b] Values in parentheses denote relative Raman intensities. Raman spectrum was recorded in FEP sample tubes at –140 °C using 1064-nm excitation. The abbreviation denotes shoulder (sh). [c] Values in parentheses denote calculated Raman intensities ($Å^4$ u^{-1}). Values in square brackets denote calculated infrared intensities (km mol^{-1}). The def2-SVP (Mn, F)/aug-cc-pVTZ(-PP) (Xe) basis sets were used. [d] The abbreviations denote stretch (ν), bend (δ), rock (ρ_r), and bridging (b).

Table E5. Experimental Raman Frequencies and Intensities and Calculated Vibrational Frequencies, Intensities, and Assignments for the $[MnF_6]^{2-}$ anion (O_h)

exptl[a,b]		calcd[a,c]			assgnts[f]
		B3LYP[d]	PBE1PBE[d]	B3LYP[e]	
	T_{1u}	573(0)[360]	590(0)[367]	599(0)[280]	ν_{as}(MnF)
608(100)	A_{1g}	546(34)[0]	561(34)[0]	548(26)[0]	ν_s(MnF)
520(30)					$[\nu(Mn_1F_1) + \nu(Mn_1F_2)] -$
510(16)	E_g	442(11)[0]	458(10)[0]	454(7)[0]	$[\nu(Mn_1F_6) + \nu(Mn_1F_5)]$
494(2)					
	T_{1u}	305(0)[<1]	312(0)[<1]	319(0)[1]	$\delta_{umb}(F_3F_4Mn_1F_5F_6)$
343(9)	T_{2g}	270(3)[0]	276(3)[0]	286(3)[0]	$\delta(F_1Mn_1F_6) + \delta(F_2Mn_1F_5)$
328(9)					
	T_{2u}	193(0)[0]	199(0)[0]	202(0)[0]	$\rho_t(F_1Mn_1F_5) + \rho_t(F_2Mn_1F_6)$
281(14)					
223(5)					
118(6)					lattice modes

[a] Frequencies are given in cm^{-1}. [b] Values in parentheses denote relative Raman intensities. The Raman spectrum was recorded in an FEP sample tube at –140 °C using 1064-nm excitation. [c] Values in parentheses denote calculated Raman intensities ($Å^4\ u^{-1}$). Values in square brackets denote calculated infrared intensities (km mol^{-1}). [d] The aug-cc-pVTZ basis set was used. [e] The def2-SVP basis set was used. [f] The abbreviations denote stretch (ν), bend (δ), twist (ρ_t), symmetric (s), asymmetric (as), umbrella (umb). For atom labeling scheme see Figure E7.